# Upgrade of the HADES RICH photon detector and first performance analyses

**Dissertation**

zur Erlangung des akademischen Grades eines

*Doktors der Naturwissenschaften (Dr. rer. nat.)*

der Fakultät Mathematik und Naturwissenschaften

Fachgruppe Physik

der Bergischen Universität Wuppertal

vorgelegt von

**Jörg Förtsch**

foertsch@uni-wuppertal.de

Wuppertal, 28. Juli 2021

Verteidigt

Wuppertal, 30. September 2021

# Abstract

The 1.58A GeV Ag+Ag beamtime of the High Acceptance Dielectron Spectrometer HADES at GSI in March 2019 marked the first use of the improved HADES RICH covered in this thesis. This new RICH detector utilizes Hamamatsu H12700 MultiAnode Photo electron Multipliers (MAPMT) and the DiRICH readout chain developed at GSI, substantially improving the detector performance in terms of electron detection efficiency and identification. Different aspects related to this upgrade are covered throughout this thesis, beginning with preparatory studies on the MAPMTs and readout electronics. Followed by studies accompanying the construction phase of the RICH detector and finally the optimization of reconstruction procedures improving the performance of the detector on basis of the final beamtime data. The preparatory studies include a characterization of the 1100 MAPMTs obtained for the HADES- and CBM experiments together, monitoring their quality with regards to production time and giving attention to any longterm change in individual MAPMTs characteristics. Using these detailed sensor characteristics, this thesis describes a special procedure that groups the MAPMTs according to their amplification for final installation in the HADES RICH. Another important work described is the controlling of all 856 DiRICH-Front End Boards (FEB) in the HADES RICH detector. As the DiRICH-FEB can only digitize time stamps of incoming hits, and is not capable of measuring signal amplitude directly, a complete tool chain is developed to derive statistical amplitude distributions from threshold dependent rate scans. This data is used to control thresholds in the full detector setup for all 27392 readout channels individually. On basis of the finally obtained beamtime data, procedures are derived to optimize the reconstruction in the new RICH detector. These procedures include an analytical coordinate transformation from particle tracks to RICH ring coordinates, corrections for misalignment of the detector, and a mathematical transformation aiming to unify the measured ring radii over the full detection plane. Finally the time- and time over threshold-spectra (ToT) measured with the DiRICH are discussed. The ToT information is analyzed as a tool to distinguish single photons from simultaneous multi-photon hits in the same readout pixel and background sources. On basis of the timing information the effect of different cuts is examined, deriving also the best timing precision possible with this MAPMT and readout electronics.

# Kurzfassung

Bei der 1.58A GeV Ag+Ag Strahlzeit des High Acceptance Dielectron Spectrometer HADES an der GSI im März 2019 kam das erste mal der verbesserte HADES RICH zum Einsatz, der in dieser Arbeit behandelt wird. Dieser neue RICH-Detektor nutzt Hamamatsu H12700 Mehrkanal-Photoelektronenvervielfacher (MAPMTs) und die an der GSI entwickelte DiRICH-Auslesekette, welche die Detektorleistung erheblich verbessert. Verschiedene Aspekte im Zusammenhang mit diesem Upgrade werden in dieser Arbeit behandelt, beginnend mit vorbereitenden Studien zu den MAPMTs und der Ausleseelektronik, über Studien, die die Bauphase des RICH-Detektors begleiten, bis hin zur Optimierung der Rekonstruktionsverfahren, welche die Leistung des Detektors auf der Basis der Strahlzeitdaten verbessern. Die vorbereitenden Studien beinhalten eine Charakterisierung der 1100 MAPMTs, die für die HADES- und CBM-Experimente zusammen erworben wurden, mit Fokus auf der Überwachung ihrer Qualität in Bezug auf die Produktionszeit und die Untersuchung jeglicher langfristiger Veränderung der Eigenschaften einzelner MAPMTs. Anhand dieser detaillierten Charakterisierung wird in dieser Arbeit ein spezielles Verfahren beschrieben, das die MAPMTs entsprechend ihrer Verstärkung für den endgültigen Einbau im HADES RICH gruppiert. Eine weiterer wichtiger Punkt der in der Thesis behandelt wird, ist die Steuerung aller 856 DiRICH-Front End Boards (FEB) im HADES RICH Detektor. Da das DiRICH-FEB nur Zeitinformationen von eingehenden Treffern misst und nicht in der Lage ist die Signalamplitude direkt zu messen, wird eine Software entwickelt, um statistische Amplitudenverteilungen aus schwellenabhängigen Ratenmessungen abzuleiten. Diese Daten werden verwendet, um die Schwellenwerte im gesamten Detektor-Setup für alle 27392 Auslesekanäle einzeln zu steuern. Auf Basis der schließlich gewonnenen Strahlzeitdaten werden Verfahren zur Optimierung der Rekonstruktion im neuen RICH-Detektor abgeleitet. Diese Verfahren beinhalten eine analytische Koordinatentransformation von Teilchenspuren zu RICH-Ringkoordinaten, Korrekturen für Fehlausrichtungen des Detektors und eine mathematische Transformation mit dem Ziel, gemessene Ringradien über die gesamte Detektionsebene anzugleichen. Schließlich werden die mit dem DiRICH gemessenen Zeit- und Zeit-über-Schwelle-Spektren (ToT) diskutiert. Hierbei wird analysiert inwiefern sich die ToT-Information als Werkzeug eignet, um einzelne Photonen von gleichzeitigen Multi-Photonen-Treffern im gleichen Auslesepixel und Hintergrundquellen zu unterscheiden. Auf Basis der Zeitinformation wird der Effekt verschiedener Zeitschnitte untersucht, wobei auch behandelt wird, welche bestmögliche Zeitpräzision mit diesem MAPMT und dieser Ausleseelektronik möglich wäre.

# Contents

# Introduction

All matter that surrounds us changes under different external conditions such as temperature, pressure and others to form so called phases. One classic example from everyday life is water. Water has distinct phases such as solid (ice), liquid or gaseous. Normally, matter (i.e. here water) undergoes discontinuous changes in its physical properties (e.g. density, heat-capacity and many more) when transitioning between its phases. Albeit these phenomena already being interesting, it is even more interesting to see what happens at exactly the border between two phases. Water for example exhibits a so called triple point. A point where its ice-, gas- and liquid phase meet and coexist.
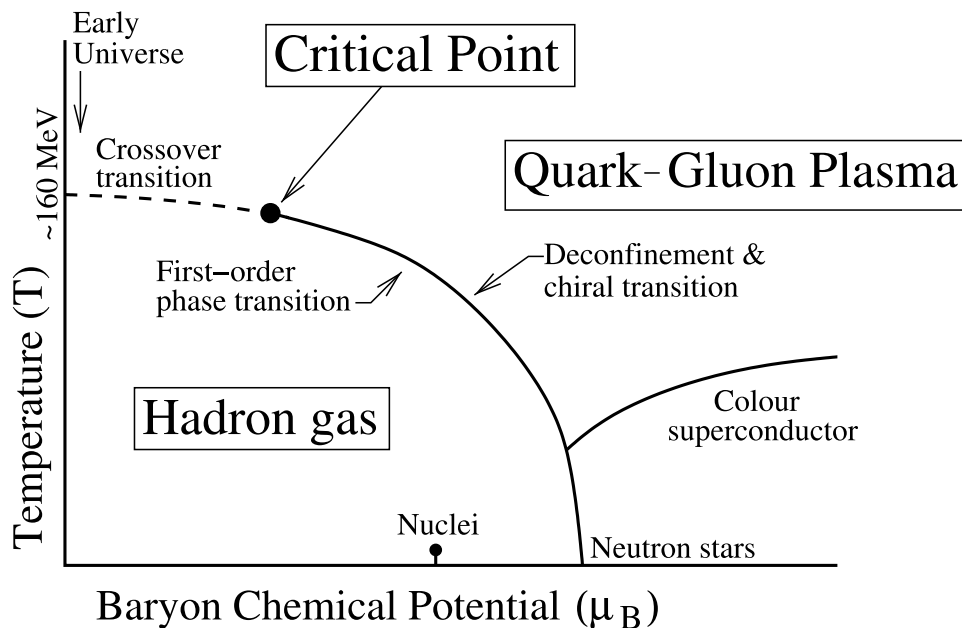


**Figure 1.1** ♦ *Sketch of the phase diagram of nuclear matter. Shown are the cross over region at temperatures of approximately* 160 MeV *and low baryon chemical potential, leading from the hadron gas phase into the quark-gluon plasma phase by means of a smooth transition. Nuclei are depicted as a dot at lowest temperatures. The line connecting the nuclei to an approximate temperature of* 0 MeV *is the so called liquid-gas transition. At moderate temperatures and large baryon chemical potentials a first order phase transition ending in a second order critical point is suspected and depicted. Additionally indicated are the rough position of neutron stars in this phase diagram and the evolution of the early universe. This figure is taken from* [MK14].

In light of this example one might ask what happens to nuclear matter under such extreme conditions. This question is not only relevant for fundamental research, but such dense matter is actually found in e.g. neutron stars. These densely packed but cold stars inhabit a regime in the

phase diagram of nuclei still neither fully understood nor experimentally accessible. Actually when looking at a phase diagram for matter, which shows temperature vs. baryon chemical potential – quasi relatable to the pressure/density axis in a water phase diagram – most of its regions are not yet understood fully. Figure 1.1 depicts a sketch of such a phase diagram, where not only the rough region of neutron stars is depicted but also many other regions of interest. Starting at the most readily understood landmark in this diagram, the nuclei can be seen at lowest temperatures represented by a dot connected to a line starting at a temperature of zero. This line actually indicates one measured landmark in this phase diagram referring to the liquid-gas transition in nuclear matter [Poc+95]. To the very left of this figure, i.e. at very low chemical potentials one finds a continuous phase transition called "Crossover". This phase transition is between the hadronic gas phase and the so called Quark Gluon Plasma (QGP). The QGP is hereby the phase region, where quarks and gluons are deconfined from hadrons and chiral symmetry is restored [Ada+05, p. 92]. This crossover region, at temperatures of approximately $160\,\text{MeV}$ is theoretically still well described using quantum chromodynamical (QCD) models [Bor+10]. These models fail however when moving away from $\mu_\text{B} = 0$. Here it is postulated that there should be a first order phase transition ending in a second order critical point [FK04]. The point is however not yet measured by experiments nor is there theoretical consensus on the exact position.

Those regions, where there is high baryon chemical potential at moderate temperature, can be probed in heavy-ion collisions. As in those collisions many particles are formed they post unique challenges for all detectors involved. Thus utmost performance of these detectors is needed in order to successfully understand the different states of matter.

## 1.1 Motivation for this thesis

The High Acceptance DiElectron Spectrometer Experiment (HADES) which is in operation since 2002 at the GSI[1] in Darmstadt has set itself the task to study the properties of matter at moderate temperatures but high chemical potential through heavy-ion collisions (HIC).

In late 2014 the HADES collaboration started a continuous effort to upgrade the detector. Apart from the addition of the already planed ECAL detector, these upgrade plans foresaw an upgrade of the HADES RICH detector with the goal to increase efficiency in the electron reconstruction. The correct identification of electron pairs ($e^+ + e^-$) is hereby key in understanding the properties of the matter formed in HICs. Electron pairs are of special interest, as they only interact via electromagnetic forces and thus can travel through the fireball undisturbed. This allows the electron pairs to hold information on the temperature and spectral structure of the QCD medium during early phases of the collision. However, reconstructing those electron pairs can be quite challenging, as during HICs also many other fragments are produced. Actually, most of the other collision fragments are produced much more abundant than the electrons. It is therefore very important to have an efficient RICH in place, being able to distinguish well between electrons and other particles. Achieving this is one of the main goals of this thesis, laying out different steps in the build up of the photon detection plane and its read out electronics.

Having the proposed upgrades in place, the HADES detector was granted an Ag+Ag beamtime at $1.58A$ GeV joining the ranks of the first FAIR phase 0 experiments. During a four week long beamtime using an Ag beam on an Ag target during March of 2019, $15.3 \times 10^9$ events were recorded, running at average accepted trigger rates of $10\,\mathrm{kHz}$. Following first chapters on the construction of the new RICH detector an in-depth discussion of its performance based on the data of this first production run is made. In those chapters different improvements in the detector behavior are studied, including an in-depth understanding of the detector response.

---

[1]Gesellschaft für Schwerionenforschung

## 1.2 Outline

This thesis starts continuing this introductory chapter with laying out the HADES spectrometer by means of its components in section 1.3. Hereby the overall working principles as well as parameters needed throughout this thesis are discussed. The HADES RICH is described in detail in section 1.5, after introducing the reader again to the exact workings of the Cherenkov effect in section 1.4. The chapter is concluded by briefly discussing different electron sources relevant for later chapters.

The rest of the thesis is split in two large parts. The first part focuses on measurements of the photon sensor and readout chain in a laboratory environment, whereas the second part focuses on estimating and increasing the performance of the upgraded HADES RICH by means of software calibration on basis of the beamtime data.

First a dedicated analysis of the photon detection hardware is made in chapter 2. In this chapter 1100 Hamamatsu MAPMTs bought by GSI/FAIR are characterized, focusing on possible degradations with time in section 2.3, and development of key characteristics over their time of production in section 2.4. The chapter is closed discussing the final distribution of MAPMTs on the HADES RICH in section 2.5.

This chapter is followed by studies of the readout electronics used in the upgraded HADES RICH in chapter 3. This chapter partially mixes lab measurements with measurements using the partially equipped HADES RICH readout to show key characteristics of DiRICHes overall and in the HADES setup. Starting first with measurements in a lab environment in section 3.2, special methods are developed in section 3.3 to determine the best configuration and settings when employing them in the final RICH upgrade. The results of these methods are discussed using the partially equipped read out chain of the HADES RICH. In addition, the final DiRICH setup in the HADES RICH is also briefly evaluated in subsection 3.2.3, detailing not only its quality but also finding options to improve the setup further in future.

The second part of this thesis, using beamtime data to assess and increase the performance of the upgraded HADES RICH, starts with detailing the workings of the HADES RICH in the analysis chain in chapter 4. Thereafter preparatory studies are discussed in chapter 5, where the impact of the magnetic stray field in the RICH and the used radiator gas are analyzed. The next chapter 6 focuses on the timing and time over threshold behavior of the RICH, detailing the retrieval of cuts and discussing the different artifacts in the time and time over threshold distributions of single channels. On basis of this discussion, an attempt is made extracting the best possible timing precision in chapter 7. Also the time over threshold is further studied to estimate its usefulness as charge or amplitude information equivalent (chapter 8). The last chapter 9 focuses on the alignment of the RICH within HADES and explains an attempt to use the derived procedure to improve the RICH ring finding even further.

## 1.3  The HADES spectrometer

The HADES detector, like most detectors in particle physics, is constructed of several particle identifying detectors (Particle ID detectors, i.e. PID) in conjunction with one momentum resolving tracking system. For the HADES detector the momentum resolving tracking system is built from four layers of mini drift chambers (MDC) intersected by a large toroidal magnetic field. For particle identification a RICH detector as well as a time of flight detector system and an ECAL are employed, as is depicted in figure 1.2. The HADES detector covers an acceptance[2] of
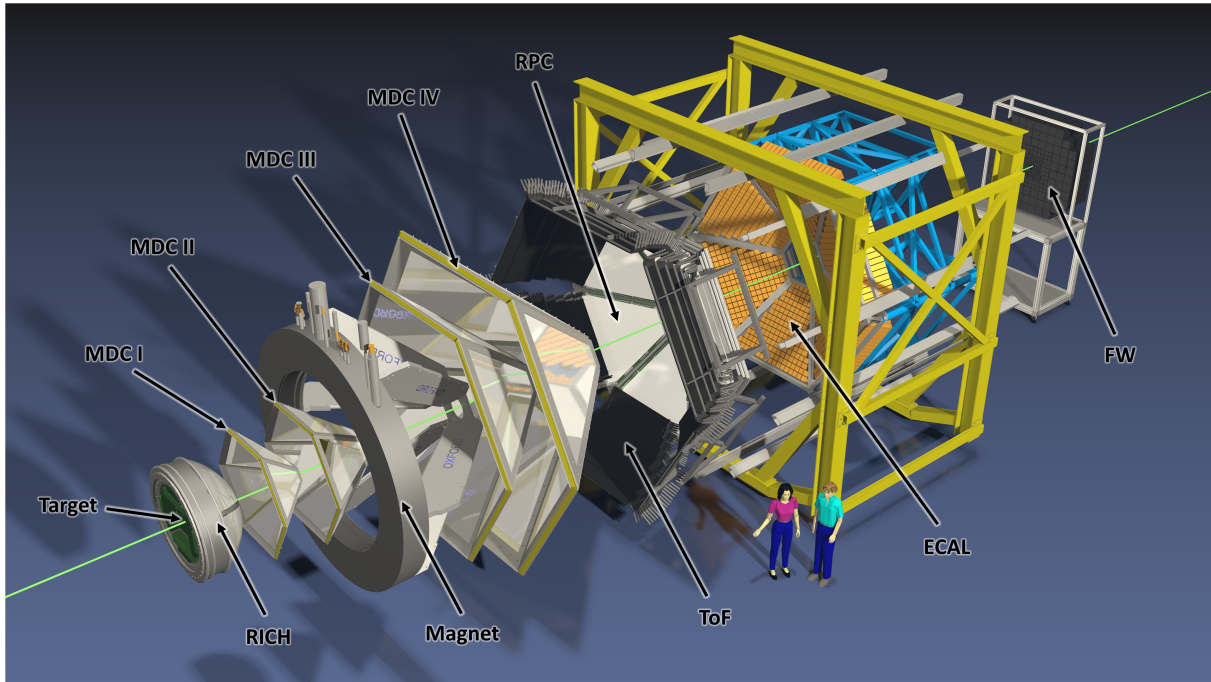


**Figure 1.2** ♦ *CGI render of the artificially spread apart HADES detector. Render made by S. Spies* [Spi21]. *Indicated are the different sub-detectors and the target. The target sits (together with the $T_0$ detector) inside the RICH. MDC stations I and II come before the toroidal field of the magnet, whereas MDC III and IV come thereafter. Time of flight measuring RPC and TOF as well as ECAL are normally directly attached to the MDC positions, whereas the Forward wall (FW) is found only at* 6 m *further downstream.*

85% azimuthally in $\phi$ [The+09]. This is achieved by building most of the HADES detector and especially the MDC tracking out of six identical sectors spaced every $\phi = 30° + n \cdot 60°$ $(n \in \mathbb{N})$. These sectors have a trapezoidal shape such that they can be arranged like a hexagon. For most detectors trapezoidal tiles range from polar angles $\theta = 18°$ to $85°$ [3]. Depicted in figure 1.3 is a transverse cross-section of the HADES detector. In this depiction the four MDC stations are visible with the magnet coil between MDC II and MDC III. Further visible are the time of flight measuring Resistive Plate Chamber (RPC) at polar angles $\theta \lesssim 45°$ and scintillator based TOF (from now on only referred to as TOF) at polar angles $\theta \gtrsim 45°$ sub-detectors which in combination are referred to as META-detectors (Multiplicity Electron Trigger Array). Following downstream one finds the newly added electromagnetic calorimeter (ECAL) as well as the

---

[2]With acceptance meant is the spacial acceptance, i.e. covered area by the detector.
[3]The forward wall obviously measures at much lower polar angles $\sim 0°$–$7°$.

forward hodoscope wall (FW) which represents the end of the HADES detector. The ECAL detector being still under construction makes use of 978 lead glass PMT modules arranged in the HADES common six sector layout. For the Ag+Ag beamtime however only four sectors were built, out of which only sub parts were used. The FW sub-detector employs 287 scintillator PMT compounds of varying size to reconstruct the event plane. Both sub-detectors are not relevant for this thesis and will thus not further be described. For further information on the ECAL concept please see [Svo+14], and for the FW [And+14]. An in depth description of all other detector parts following the beam downstream follows now, excluding the RICH detector, which is detailed in section 1.5.
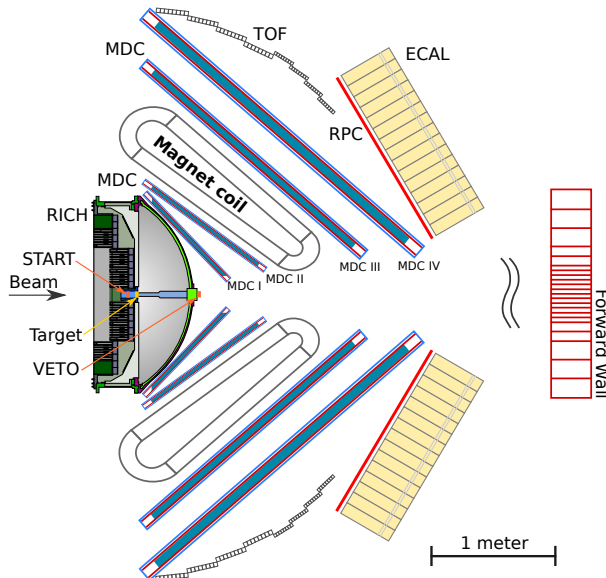


**Figure 1.3** ♦ *Sketch of the HADES detector, showing a cross-section of the HADES detector and explicitly the RICH detector from the top. With the detector being nearly symmetric over all azimuthal angles ϕ, rotating this sketch along x would approximately result in the full HADES detector. The Forward Wall is typically separated by 6 m from the target area. Sketch made by A.A. Weber [Web20b] as a variation of [HAD17]. For illustrative purposes the cross section through the RICH and magnet is chosen such that a horizontal slice is shown, whereas all other sub-detectors show a vertical slice. Thus visible are the top and bottom sectors of each sub-detector except the RICH.*

### 1.3.1 START VETO detectors and the target area

The HADES $T_0$ or START detector is situated in the beam line slightly before the target ($\sim 50\,\mathrm{mm}$ with respect to the target center). It is made of a single crystal CVD (Chemical Vapor Deposit) material, which offers high rate capabilities, radiation hardness and timing precision at low noise levels [The+09]. The $4.7 \times 4.7\,\mathrm{mm^2}$ sensor is only $70\,\mu\mathrm{m}$ thick to reduce interaction probability with beam nucleons [Ros20]. A similarly designed HADES-START detector used during a Au+Au beamtime was found to have an approximate timing precision of around $50\,\mathrm{ps}$ (depending on irradiation levels) [Pie+14]. The START detector in HADES is used primarily in conjunction with the RPC and TOF detectors. Hereby the RPC and TOF, covering different

**(a)** *HADES START detector*     **(b)** *HADES VETO detector*
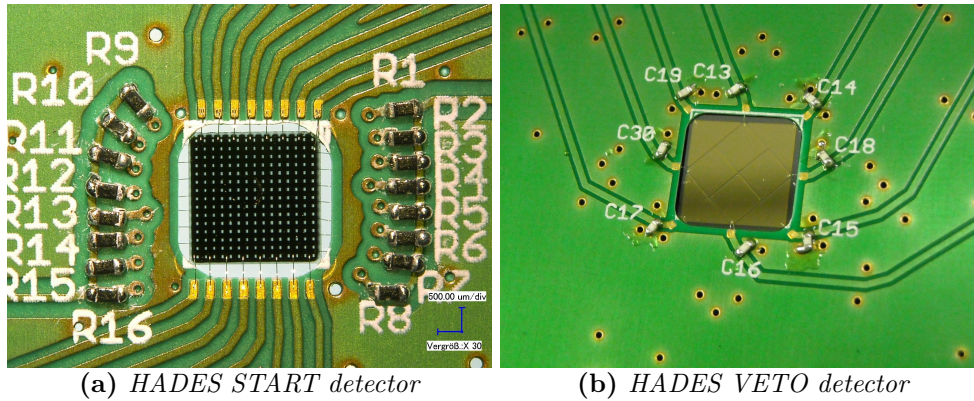
**Figure 1.4** ♦ *Pictures of the $T_0$/START **(a)** and VETO **(b)** detectors. Visible are the 16 distinct stripes on the START and the diamond shaped pixel layout of the VETO detectors. Pictures are taken from* [Pie19b]

polar angles, work as so-called STOP detectors. Together with the START detector they measure the time of flight of any particle traversing through the detector. The START detector, being situated slightly upstream of the target, thereby measures the collision inducing beam particles (here Ag), whereas the RPC and TOF detectors measure the event corresponding collision/decay products. Through the time of flight the velocity $\beta = v/c$ of the individual particle can be extracted. In most cases knowing the particles velocity and momentum allows to determine the particle's ID. In addition to that, the START detector can be used to monitor the beam structure, which was a feature heavily used to ensure best possible beam conditions during the beamtime in 2019. For that, the START detector features 16 individually read out strips on the front and 16 strips rotated by 90° on the backside, all of which are $300\,\mu$m wide (cf. Fig. 1.4a). This is also useful in the regard, that after beam induced wear of certain strips, the detector can be moved slightly such that the beam is focused more on other strips. This helps in keeping a high timing precision and efficiency throughout long measurement campaigns.

Based on a similarly designed pcCVD (poly-crystal CVD), the VETO detector is placed further downstream at a distance of $\sim 550\,$mm with respect to the target center. The detector features a box shaped pixel layout on $8 \times 8\,$mm$^2$ and a $107\mu$m thickness [Pie19b] and is depicted in figure 1.4b. The VETO detector, being aligned with the START detector and target, is used to reject event overlaps, where one event was not properly detected by the START detector.
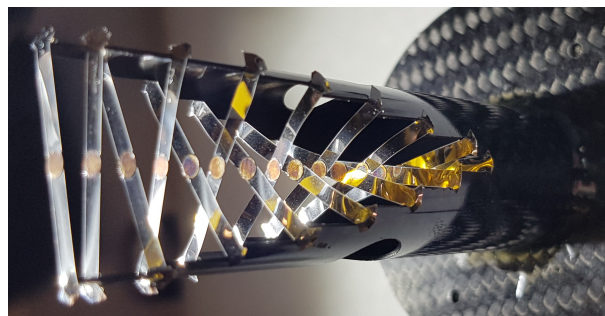


**Figure 1.5** ♦ *Picture showing the 15 fold segmented Ag target used during the 2019 beamtime. The circular target pads are held by Kapton foils and spaced $3\,$mm. Picture taken from* [Pie19a].

Between those two detectors lies the $^{107}$Ag target with an integrated thickness of 0.6 mm. In order to keep the conversion probability of collision fragments inside the target low, the target is 15-fold segmented. Spacing the target segments 3 mm apart, as is depicted in figure 1.5, lowers the conversion probability to 1% only, integrating over the full target (cf. [HAD17]). The full length of the target thus amounts to 45 mm. The circular target slices with diameter $d = 2.2$ mm are glued on Kapton foils attached to the outer carbon based beam pipe such, that they cover the full azimuthal angle equally with material.

### 1.3.2 Mini Drift Chambers and the magnet

The Mini Drift Chambers (being intrinsically Multiwire Drift Chambers, also abbreviated MDC) together with the magnet build the magnet spectrometer with which the momentum over charge ratio of a charged particle can be resolved. The MDC is hereby built out of six sectors, each with four tracking chambers along the beam axis, with the toroidal magnetic field mostly constrained between MDC planes II and III. The toroidal magnetic field is induced by an ironless superconducting magnet. The six magnetic field inducing coils are thereby situated at every $\phi = n \cdot 60°$ ($n \in \mathbb{N}$) and held by a supporting ring located upstream of the target, i.e. outside of the acceptance. This can be seen in figure 1.6a, where a three dimensional cross section of the MDC-magnet configuration is depicted. Applying highest currents of 3500 A the generated field reaches a maximum of approximately 3.6 T at the coils' positions which drops off to levels of about 0.9 T at places between MDC II and III. This is depicted in figure 1.6b, where also the MDC and RICH positions are approximately indicated. Visibly, the field strength at positions of the RICH mirror already drop to the lower milli-Tesla (mT) levels such that the impact of the magnetic field on the RICH can be assumed low. This field produces a transverse kick through which momentum resolutions of $\sigma_p/p \approx 2\%$ for electrons are possible with the given tracking resolution [The+09]. During most of the Ag+Ag beamtime, the magnet was only ramped to 3.2 T [4].

The $4 \times 6$ MDC tracking chambers are each comprised of thirteen internal layers. Out of those, six layers are used to read out the chamber and seven layers are cathode layers. The six read out layers consist of alternating field and sense wires. While the cathode layers always have the same wire angle, the wires of the readout layers are differently rotated each layer. With this setup, a single cell resolution between 60–100 $\mu$m in polar direction and 120–200 $\mu$m in azimuthal direction was found in data from 2001 [Mar06, p. 132]. This is of course momentum dependent, such that lowest momenta result in the worst resolution. According to a simulation analysis described in [Mar06, 109f], the corresponding angular uncertainties would result in angular equivalents of well below 1° for momenta larger than 100 $^{\mathrm{MeV}}/c$. This was found equally in $\theta$ and $\phi$, where only for larger momenta, the angular resolution in $\theta$ tends towards higher precisions compared to $\phi$. Since this analysis, the MDC drift chambers did not change massively. One prominent difference lies only in the gas used for the Ag+Ag beamtime. Here for all chambers

---

[4]During later stages of the beamtime, an additional run using 1.23A GeV and a magnetic current of 2.5 kA was carried out, while even later the magnet was driven with only 200 A for a brief period.

**(a)** *3D cross section of the magnet between the MDC chambers*



**(b)** *Magnetic field strength at the MDC positions*
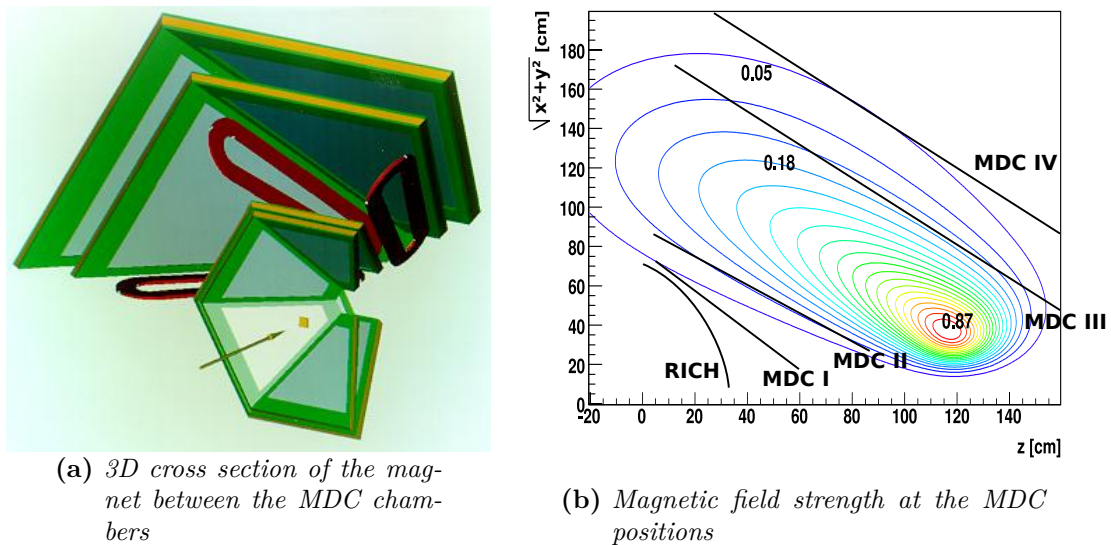
**Figure 1.6** ♦ *Three dimensional cross section of the HADES magnet (red) and MDC (green) setup* **(a)**. *The magnet introduces a toroidal field of which the field strengths are shown for an azimuthal angle of* 90° **(b)**. *Additionally indicated in the field map are the approximate positions of the different MDC stations and the mirror of the RICH. The field strength is noted as numbers for several positions along the gradient map. This field simulation was made using the largest magnet current (*3500 A*). Pictures are taken from* [The+09] *and altered slightly.*

an inorganic gas mixture of $Ar/CO_2$ with ratio 70/30 is used, for aging reasons[5]. Additionally mentioned should be that an additional $\delta$ electron shield out of polypropylene ($C_3H_3$) is deployed between RICH and first MDC station in order to reduce high occupancies induced by these uninteresting particles. Hereby the shield reaches 400 mm radially into the gap between RICH and MDC I and thus covers roughly 50° in $\theta$.

To reconstruct the individual track, a multi step process is used. First the event cluster is searched in the target area. This is done using the information of all fired wires – wires where a signal above threshold was detected – in MDCs I and II. After that, the found target segment is used for an improved cluster – accumulation of fired wires – finding within MDCs I and II. The therethrough extracted track candidates are continued linearly to the "kick-plane", defined by the magnet. Using this point on the kick plane, the same track search is done in MDCs III and IV. This procedure is depicted in figure 1.7a next to an actual overlay of different fired wires as found in one projection plane 1.7b. To include also particles that do not point to the primary vertex, a follow up search for tracks is done using clusters not used before. After finding these tracks, a spline fit is applied using the straight line vectors as start parameters. The resulting tracks in turn are inserted into a fourth order Runge Kutta scheme to solve the particle's trajectory in the magnetic field. The differences between the calculated trajectory and the measured hits in the MDC are minimized by means of a least-square procedure. Therethrough recursively an extremely well fitting particle track is found which provides information about momentum and the initial trajectory vector. The resulting goodness of fit $\chi_{RK}$ is used as a quality parameter for

---

[5]Before this beamtime, MDC III and MDC IV used $Ar/i\text{-}C_4H_{10}$ which led to severe aging of the chambers.

the individual particle candidate track [The+09]. In a final step, the particle track is matched to the closest hit in the TOF/RPC-META detectors giving the META Match Quality $META_{QA}$ [Mar17]. After that, also a matching with rings from the RICH detector is made but discussed in more detail in section 4.1.



**(a)** *Visualization of the linear fitting procedure*

**(b)** *Superposition of fired wires in one projection plane*
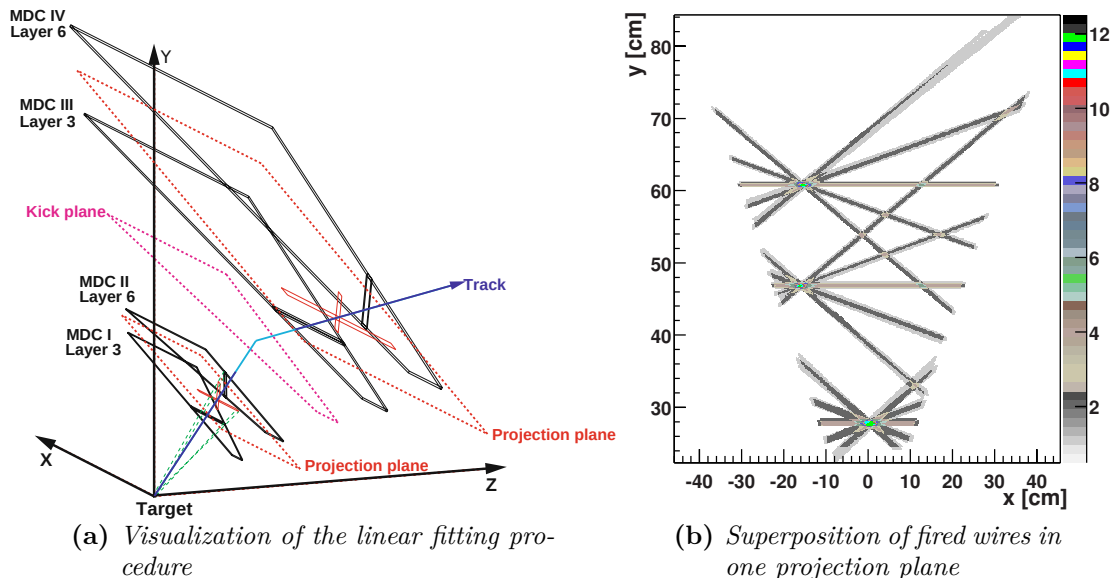
**Figure 1.7 ♦ (a)** *shows a visualization of the linear fitting procedure using the inner and outer projection planes between their corresponding MDC planes (of which here always only a single layer is depicted). The vertex finding is depicted through green dashed lines, the blue line represents a single track. This track features a distinct kink at the kick plane induced by the magnet.* **(b)** *shows the superposition of fired wires in one projection plane of a single segment Both pictures taken from* [The+09].

In addition to resolving the momentum, the MDCs are also capable of measuring the energy loss $dE/dx$ within themselves. This measure does depend on the gas mixture, but is mostly relevant in helping to distinguish particles with larger masses [Har17]. Therefore this procedure is not discussed here.

## 1.3.3 TOF and RPC

Situated directly behind the MDC tracking stations is a setup to measure the time of flight of particles. This setup is often referred to as META detector and is a combination of two sub detectors. A scintillator based TOF wall covers larger polar angles while an RPC setup covers smaller polar angles. The TOF wall is placed at angles between $44°$ and $88°$ and follows the six sector layout of the whole HADES detector. Each TOF sector consists of eight modules each containing eight scintillator strips. One such module is depicted in figure 1.8. The inner rods thereby have a square cross section of $20 \times 20\,mm^2$ and the outer ones $30 \times 30\,mm^2$. This is done to reduce the amount of double hits – particles hitting the same rod during one event – on the inner part of the detector. The length of each rod varies within $1\,m$ to $2\,m$ also depending
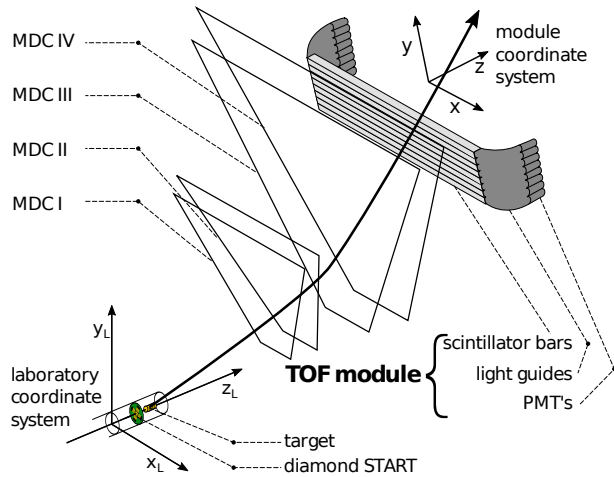
**Figure 1.8** ♦ *Sketch of a single scintillator based TOF detector module in the HADES setup. Further indicated is one full MDC sector as well as the START detector and the target. Sketch taken from [Kor+21]*

on the polar angle. At both ends of each rod, a light guide connects the rectangular rod shape to PMTs with circular front window. The timing precision of this detector in conjunction with the HADES-START was found to be 150 ps after additional calibration [Kor+21].



**(a)** *Single RPC sector*

**(b)** *Sketched cross section showing 3+½ RPC cells*
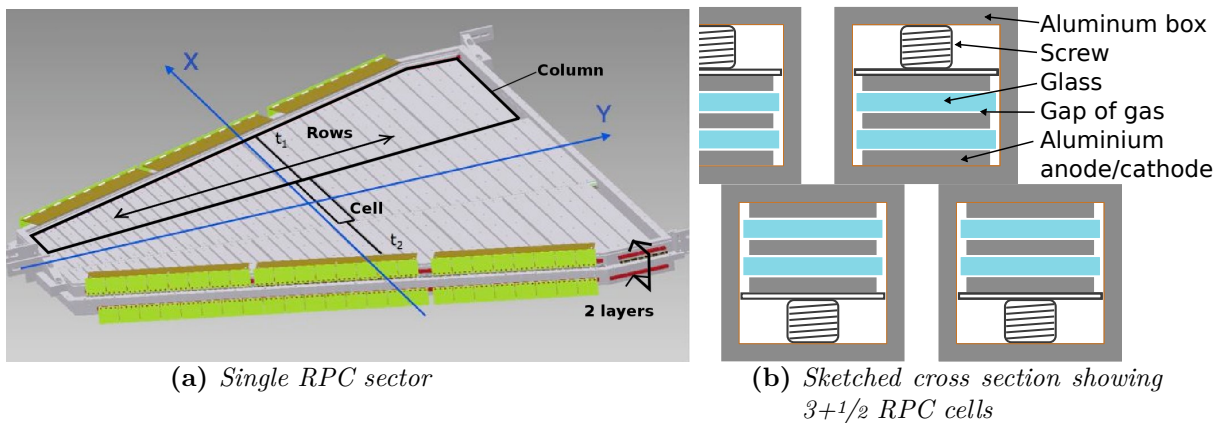
**Figure 1.9** ♦ *CAD drawing of a single RPC sector with markers to several key parts of the detector* **(a)**. *Sub figure* **(b)** *shows a sketch of a cross section through 3+½ RPC cells. The cross section follows the y-axis indicated in the CAD drawing. Pictures taken from [Kor13] and altered slightly for visibility reasons.*

Added in 2010, the RPC provides TOF information in the HADES detector towards lower polar angles ($\theta = 12.8°$ lower geometric acceptance). Also this detector uses the six sector symmetry present in HADES. Hereby 1117 4-gap RPCs with varying dimensions cover an area of $8\,\mathrm{m}^2$. 4-gap hereby refers to the four gaps between the glass resistors and the aluminum anode/cathodes [Kor13]. This design is depicted in figure 1.9b being a cross section of figure 1.9a where one full RPC sector is depicted. The whole "cell" is enclosed in an aluminum shield to reduce cross talk between channels. Therethrough the setup is capable of providing timing information even in the high rate environment of the HADES. The whole RPC detector features a global timing precision of $\sigma = 73\,\mathrm{ps}$ [Bla+09].

### 1.3.4 Trigger setup and data acquisition (DAQ)

The HADES detector runs in a triggered readout setup. Herefore, among other things, sub-detector data is used in order to form a trigger decision. The main trigger used throughout this thesis is the so called "physics trigger 3" (PT3). This trigger requires a simultaneous hit in the START detector and a total of 20 hits in the RPC and TOF detectors. Other triggers include the PT2, START hit and multiplicity 5 in RPC and TOF, and the RICH Laser trigger. The latter is used mainly for RICH stability control and is further discussed in 1.5. After an event is triggered, the central trigger system (CTS) takes care of distributing the trigger information and a reference time to all sub systems. Thereafter the front ends of the individual sub-detector buffer their data internally, responding with an acknowledge and waiting for a read-out request from the CTS. This read-out request, sent out after all sub-systems responded with an acknowledge, also includes the information to which server the data should be sent to. The whole procedure is laid out in figure 1.10, where also the third communication channel of the CTS is shown, which is reserved for monitoring and slow control purposes. The data is then received by up to 16 event building processes, that process and save the raw event data to hard discs and a tape archive.
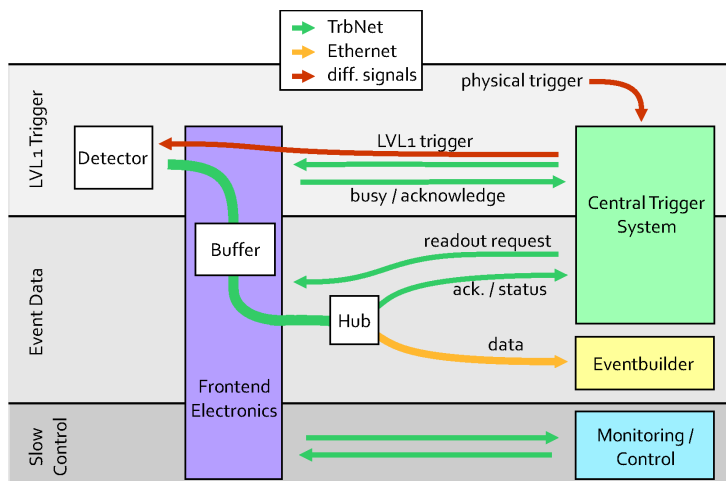


**Figure 1.10** ♦ *Sketch indicating the operating principle of the Central Trigger System (CTS) in conjunction with the event builders (EB) and the monitoring. Picture taken from* [Mic+11]

## 1.4 Cherenkov radiation and RICH detectors

Cherenkov radiation (more properly Wawilow-Čerenkov radiation) is the radiation emitted when a charged particle traverses an isolating medium at velocities larger than the speed of light in that medium. The angle of emission is described through the formula

$$\cos(\theta_c) = \frac{1}{n\beta} \ ,$$

where $\beta = v/c_0$ is the velocity of that particle with respect to the speed of light in vacuum and $n$ is the refractive index of the medium. This can be derived easily through the depiction shown
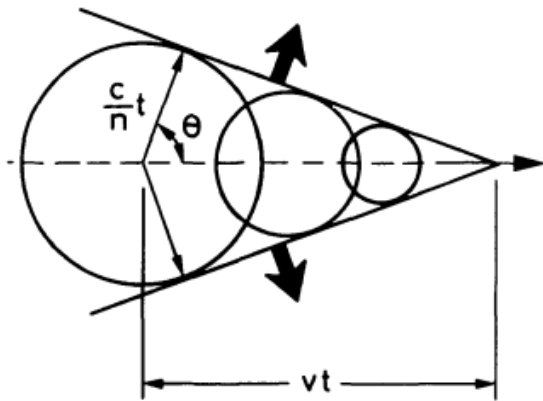


**Figure 1.11** ♦ *Sketch visualizing the Cherenkov effect. Indicated are the Cherenkov angle θ, the velocity of the particle v and the velocity of the electromagnetic wave inside the medium c/n. This depiction is taken from* [Leo94].

in figure 1.11. Here the particle traverses the medium with

$$v_{\mathrm{p}} = \beta_{\mathrm{p}} c_0 \ ,$$

whereas the electromagnetic wave induced through the polarization of the particle traverses the material in all spatial directions equally fast with

$$c_n = \frac{c_0}{n} \ ,$$

as $n = c_n/c_0$. Thus at any given point $t$ in time the newly generated electromagnetic waves meet those generated slightly before at an angle of

$$\cos(\theta_c) = \frac{c_n t}{v_{\mathrm{p}} t} = \frac{1}{n\beta_{\mathrm{p}}} \ .$$

Unfortunately, the refractive index $n(\lambda)$ depends on the wavelength $\lambda$ of the emitted light. Thus one finds not one but a range of $\theta_c(\lambda)$ (dispersion). Assuming a constant $n$ one sees that measuring the emission angle of Cherenkov radiation is a direct measure of the particles velocity. The correlation between opening angle and velocity is depicted in figure 1.12 for different refractive indexes. Here one actually sees that the derivation started with the premise that $v > c_n$ would need to exceed the speed of light in the medium, it is clear that any particle not exceeding this threshold velocity does not induce any Cherenkov effect, and thus produces no light. Therethrough a particle with too low velocity can be immediately rejected, through
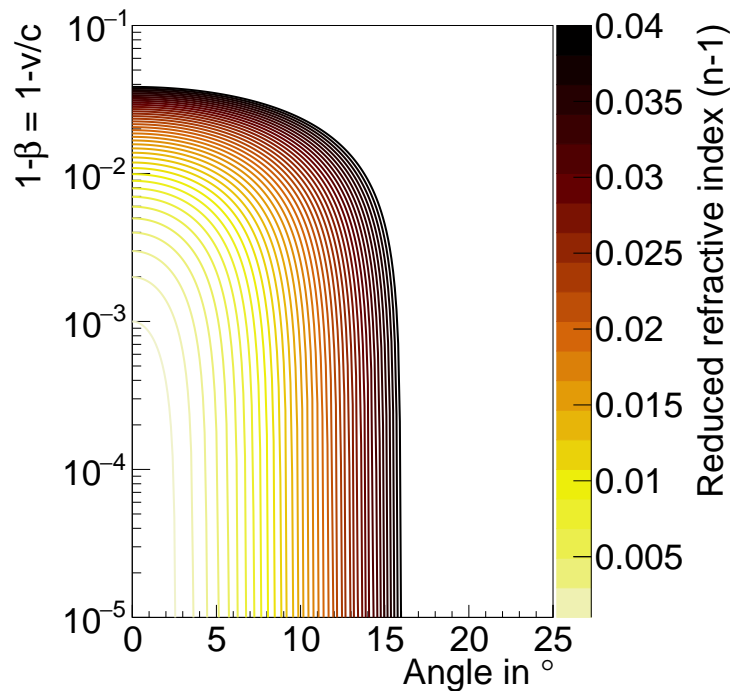
**Figure 1.12** ♦ *Cherenkov angle for different velocities β and refractive indexes. Exactly depicted are hereby the reduced refractive index $n-1$ and the difference from speed of light $1-\beta$.*

the principle of a so called threshold Cherenkov detector, which distinguishes binary between particles exceeding $c_n$ and particles not. Distinguishing different particles below the Cherenkov threshold is however more difficult. With the Cherenkov photons being emitted over the full path the particle traverses through the medium, one has only limited choices on how to reconstruct the emission angle. One way of reconstructing the emission angle is through using a Ring imaging Cherenkov (RICH) detector.

**Ring imaging Cherenkov (RICH)**

The Ring imaging Cherenkov detector (RICH) assumes an approximate knowledge on the direction and the opening angle of the Cherenkov radiation in advance. Then one can build a spherical mirror at the end of the traversed medium, which is bent and oriented such, that all photons produced are focused on a single ring image on a photon detector at a fixed position. More importantly, it is not actually important in which direction the particle traverses through
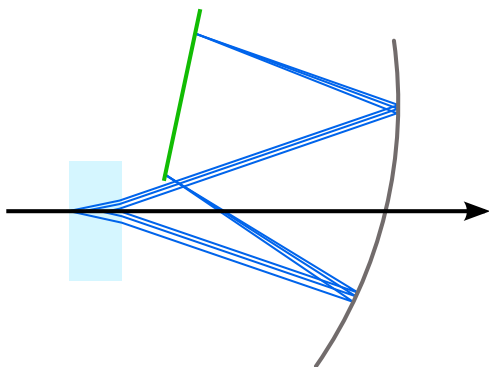


**Figure 1.13** ♦ *Sketch of a mirror imaging RICH setup. A particle (black) produces Cherenkov light (dark blue) inside a thicker medium (light blue) that is detected at the green line after reflection at a mirror (black). Herethrough a sharp ring image is produced. Figure made by and to be distributed according to* [Foe13].

the medium if all particles only start from the same point and the mirror is built large enough. This is sketched in figure 1.13, where after the reflection via mirror, the disperse Cherenkov

light bundles are focused on the photon detection plane. If the detection plane is built flat – like shown in the figure – this comes at a slight cost in terms of ring sharpness which can be recuperated building also the detection plane slightly spherical. This setup gives the additional benefit, that any photon detecting sensors can be moved out of the particles flight path. This is of special interest, as the Cherenkov radiation itself only contributes extremely little to the overall energy loss of a particle traversing a medium (as is discussed later). Very often these RICH detectors are build using a large gas (or liquid) radiator filling the full volume up to the mirror itself.

**The Frank Tamm formula**

As was already touched on before, a critical item using the Cherenkov effect for measurements is the number of photons produced. For that, Frank and Tamm derived the following formula, giving the energy of produced Cherenkov photons per unit length and unit angular frequency in Gaussian units

$$E = \frac{e^2 l}{c^2} \int_{\beta n > 1} \omega \left( 1 - \frac{1}{\beta^2 n^2(\omega)} \right) d\omega \,, \tag{1.1}$$

where $\omega$ is the angular frequency of the emitted photon, $e$ is the elementary charge and $l$ is the length of traversal [FT91]. Approximating the dependency of $n^2(\omega)$ and giving upper threshold for $\omega = \omega_0 = 6 \times 10^{15}$ 1/s they derived that the energy lost by a particle emitting Cherenkov radiation would only lie in the order of "several kilovolts per centimeter, [and is thus] a quantity negligible"[FT91]. Using the relation that $E = \hbar\omega$ is the energy of a single photon and accordingly

$$E_{\text{total}} = N\hbar\omega \,, \tag{1.2}$$

together with

$$\omega = 2\pi \frac{c}{\lambda} \Rightarrow |d\omega| = 2\pi \frac{c}{\lambda^2} \,, \tag{1.3}$$

one finds

$$\begin{aligned} N &= \frac{l e^2}{c^2 \hbar \omega} \int_{\beta n > 1} \omega \left( 1 - \frac{1}{\beta^2 n^2(\omega)} \right) d\omega \\ \Leftrightarrow N &= \frac{\alpha l}{c \omega} \int_{\beta n > 1} \omega \left( 1 - \frac{1}{\beta^2 n^2(\omega)} \right) d\omega \\ \Leftrightarrow N &= 2\pi \alpha l \left( \frac{1}{\lambda_2} - \frac{1}{\lambda_1} \right) d\omega \left( 1 - \frac{1}{\beta^2 n^2} \right) \,, \end{aligned} \tag{1.4}$$

to be the number of photons emitted over the distance $l$ between wavelengths $\lambda_1$ and $\lambda_2$ and $n$ being the average refractive index between those two. Hereby

$$\alpha = \frac{e^2}{\hbar c} \text{ (CGS/Gaussian units)} \ = \frac{e^2}{4\pi\epsilon_0 \hbar c} \text{ (SI units)} \ \approx \frac{1}{137}$$

is the so called fine-structure constant. Nowadays one normally finds the differential expression using SI units for all particles with charge $q = Z \cdot e$:

$$\frac{d^2E}{dxd\omega} = \mu(\omega)\frac{e^2 z^2}{4\pi}\omega\left(1 - \frac{1}{\beta^2 n^2(\omega)}\right) = \mu(\omega)\frac{e^2 z^2}{4\pi}\omega\sin^2(\theta_c(\omega)) \tag{1.5}$$

$$\frac{d^2E}{dxd\omega} = \frac{\hbar\alpha z^2}{c}\omega\left(1 - \frac{1}{\beta^2 n^2(\omega)}\right) \text{, assuming } \mu(\omega) = \mu_0 = \frac{2\alpha h}{e^2 c} = const.$$

$$\Leftrightarrow \frac{d^2N}{dxd\omega} = \frac{\alpha z^2}{c}\left(1 - \frac{1}{\beta^2 n^2(\omega)}\right) \tag{1.6}$$

$$\Leftrightarrow \frac{d^2N}{dxdE} = \frac{\alpha z^2}{\hbar c}\left(1 - \frac{1}{\beta^2 n^2(E)}\right) \text{, using } dE = \hbar d\omega \tag{1.7}$$

$$\Leftrightarrow \frac{d^2N}{dxd\lambda} = \frac{2\pi\alpha z^2}{\lambda^2}\left(1 - \frac{1}{\beta^2 n^2(\lambda)}\right) \text{, using } |d\omega| = 2\pi\frac{c}{\lambda^2}d\lambda \tag{1.8}$$

Equations (1.7) and (1.8) are especially interesting, as they show two key features of the Cherenkov radiation. Firstly, the number of photons emitted is – assuming a constant $n$ – constant over the energy $E$. Secondly, the number of photons increases inverse quadratically towards lower wavelengths. It goes without say that the number of photons does not reach infinity. Following the description of [FT91] (which roughly follows a Sellmeier curve), the maximum is reached when the mediums molecules' average frequency is reached. At that point an infinitely large $n$ is found basically invalidating the whole premise of the derivation. This is the main reason, why many Cherenkov detectors try to be sensitive down into the UV region. An example of the progression of the number of photons with regards to the wavelength is shown in figure 1.14, where a comparison is made between a constant $n$ and a wavelength dependent one. $n(\lambda)$ is hereby approximated via a Sellmeier polynomial using parameters derived for isobutane ($i$-$C_4H_{10}$) in [Arn+88] [6].
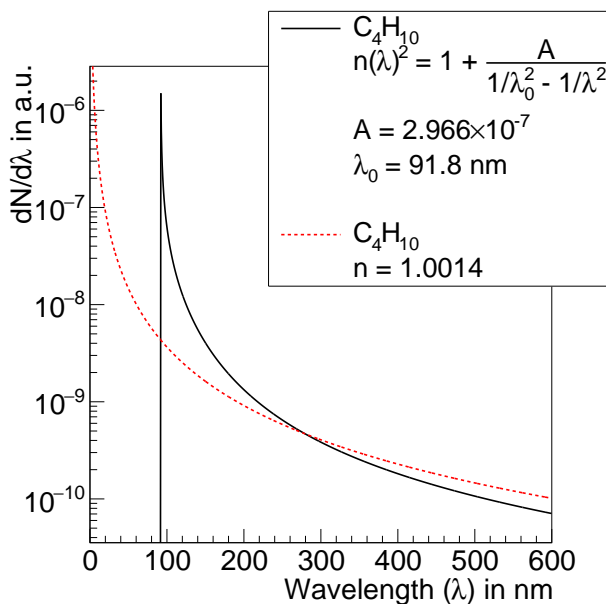


**Figure 1.14** ♦ *Wavelength dependent number of photons* $\mathrm{d}N/\mathrm{d}\lambda$ *with and without wavelength dependent n. The wavelength dependent n is approximated via a Sellmeier form as noted in the legend with parameters extracted from* [Arn+88] *for isobutane. The constant n is taken from its average between* 200 nm *and* 600 nm.

---

[6] Actually derived in this source is the fraction $\frac{n^2-1}{n^2+2}$ in dependence of temperature and pressure (NTP for HADES). This formula is however easily transferable into the here given Sellmeier form.

Instead of what was discussed up to now, most of the time one is not really interested in the particles velocity per se but rather the particle identity. If one knows however the momentum of the particle, the mass and thus identity of the particle are directly retrievable. As a measure of the "quality" of the separation between particles one often finds the Lorentz factor $\gamma_{\text{thr.}}$ as quantity describing the Cherenkov detector

$$\gamma_{\text{thr.}} = \frac{1}{\sqrt{1 - \beta_{\text{thr.}}^2}} = \frac{1}{\sqrt{1 - 1/n^2}} \ .$$

This is handy in a the sense, that one can now easily see at which momentum $p$ the particle with mass $m$ will produce Cherenkov light through

$$\gamma = \sqrt{1 + \left(\frac{p}{mc}\right)^2} \ .$$

One herewith knows that the e.g. the HADES RICH detector with $\gamma_{\text{thr.}} = 18.9 \Rightarrow \sqrt{\gamma_{\text{thr.}}^2 - 1} \approx 18.9$ will only start to see radiation from a neutral pion $\pi^0$ with mass $135 \,\text{MeV}/c^2$ at momenta $p = 135 \cdot 18.9 \approx 2500 \,\text{MeV}/c$.

## 1.5 The HADES RICH

The HADES RICH is conceptualized as a gaseous RICH detector built around the target area. Its goal is to identify electrons with momenta between $100\,^{\text{MeV}}/c$ and $1.5\,^{\text{GeV}}/c$. Main constrains are the limited space between target area and the first tracking station and a harsh limit on the material budged. It therefore uses isobutane as radiator, measuring Cherenkov photons reflected from an aluminum coated mirror with 428 - 64 channel MAPMTs.

**Gas radiator**

Using $i$-$C_4H_{10}$ (isobutane) as radiator gas ($n \approx 1.0014$), the HADES RICH is hadron blind for all momenta measured with the HADES detector as was elaborated before. This is depicted in
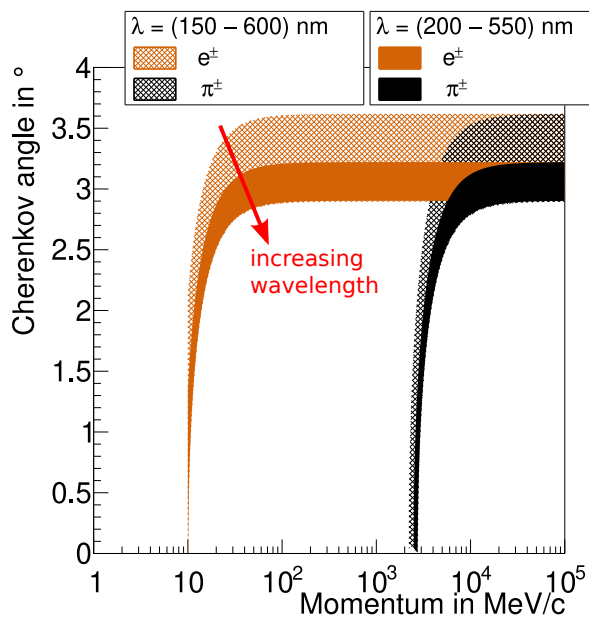


**Figure 1.15** ♦ *Cherenkov angle range for electrons ($e^\pm$) and pions ($\pi^\pm$) at different momenta, assuming the Cherenkov photons to be emitted at wavelengths between either* 150–600 nm *or* 200–550 nm *inside a isobutane ($i$-$C_4H_{10}$) radiator. The wavelength dependent refractive index ($n(\lambda)$) is approximated using a Sellmeier Polynomial for isobutane with parameters from* [Arn+88]. *Note that* $\sim 0.5°$ *difference in the Cherenkov angle corresponds to a width of* $\sim 3$ mm *on the HADES RICH photon detector. Find the same figure for* $C_4F_{10}$ *(the old RICH gas) in figure* A.1 *in the appendix pg.* 171.

figure 1.15, where one sees the onset of the Cherenkov spectra for electrons/positrons as well as pions. Also visible therein is the spread in Cherenkov angle observed for both particles using the Sellmeier Polynomial

$$n^2(\lambda) = 1 + \frac{A}{1/\lambda_0^2 - 1/\lambda^2}$$

$$A = 2.966 \times 10^{-07} \text{nm}^{-2}$$

$$\lambda_0 = 91.8\,\text{nm}$$

extracted from [Arn+88]. The onsets of the different particles' Cherenkov radiation is hereby very similar to that of $C_4F_{10}$, which was the radiator gas used for the former RICH setup (cf. Fig. A.1 pg. 171 appendix). The width in the momentum dependent Cherenkov angle distribution seems large, contributes however only to approximately 3 mm (full wavelength range) measured at the photon detector position. Furthermore, most photons contributing to this large spread are nearly unmeasurable by the photon detector, as is discussed later. Using a reduced wavelength range one thus finds a strong reduction in the angular spread.

Furthermore the gas is nearly transparent for the full wavelength range of interest. The approximate onset of the absorption for this organic gas ($C_NH_{2N+2}$) following the empirical equation of [FU20] is

$$\lambda_{\text{max. abs.}} \approx 181\,\text{nm} - \frac{226\,\text{nm}}{3(N+1)} \approx 166\,\text{nm} .$$

**Geometry**

The detector has a circular base, with a radius of approximately 700 mm, in the middle of which the beampipe sits together with the target setup. A cross section is shown in figure 1.16a. The



**(a)** *Side view*        **(b)** *Front/Photon view*
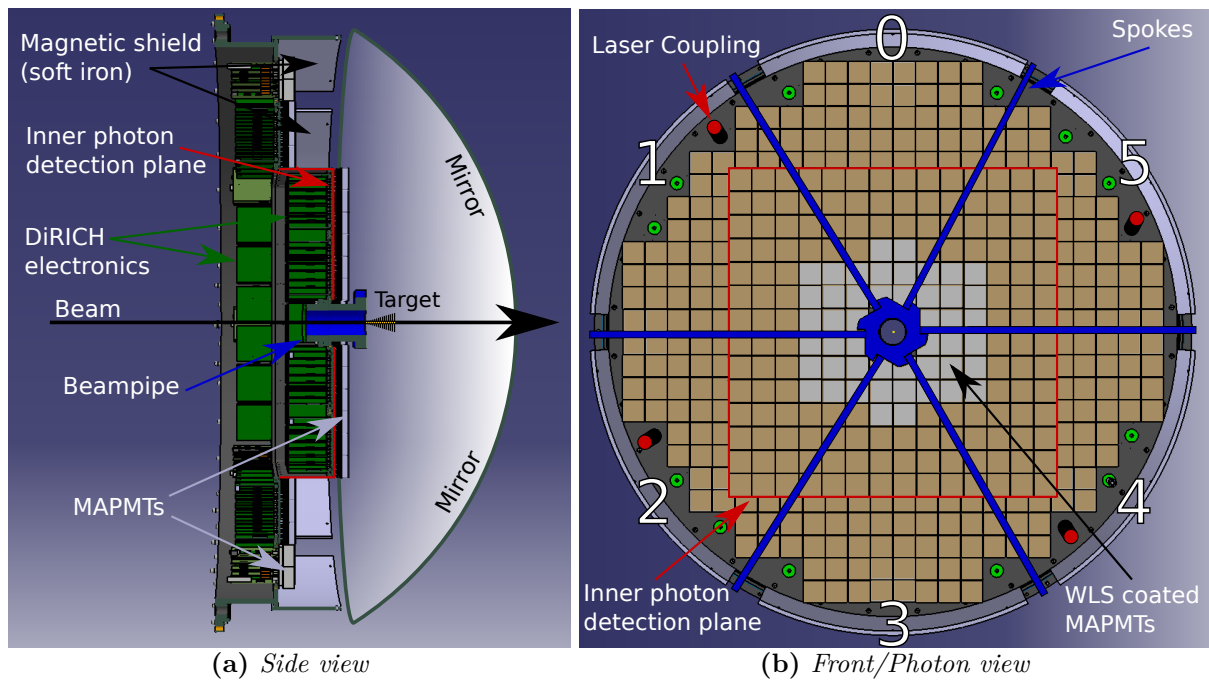
**Figure 1.16** ♦ *Sketch of the HADES RICH from the side* **(a)** *and front (photon/beam upstream view)* **(b)***, based on a CAD drawing. In* **(a)** *in addition to the CAD model, the mirror and target are indicated. Hereby the target is artificially enlarged. As an additional indication, the inner photon detection plane is highlighted with a red line. In* **(a)***, blue lines indicate the spokes supporting the mirror structure, while the red dots indicate the Laser feed through positions for the light pulser system. MAPMTs with gray front indicate MAPMTs with WLS coated front window (cf.* Sec. 2.1*). Numbers (0–5) are added to indicate the different sectors in the RICH.*

MAPMTs are mounted on top of this base plate and form the photon detection plane which is split into an inner and an outer detection plane with different indentations with regards to the beam axis $z$. Hereby the inner photon detection plane is indented by 128 mm with regards to the outer one. This staggered plane setup was chosen in order to closely match the spherical shaped focal plane of the mirror and also to keep ring radii similar over the full reconstruction plane. Both parts of the photon detection plane are equipped with a total of 428 Hamamatsu H12700 MAPMTs to measure the Cherenkov photons. These photons are reflected off of the spherical mirror placed approximately 350 mm downstream of the target. All of these distances are depicted in the mock up sketch shown in figure 1.17. Therein the zero-position in HADES (i.e. in the software framework HYDRA) is depicted together with the RICH and its two staggered

photon detection planes, the START detector and the fifteenfold separated target.
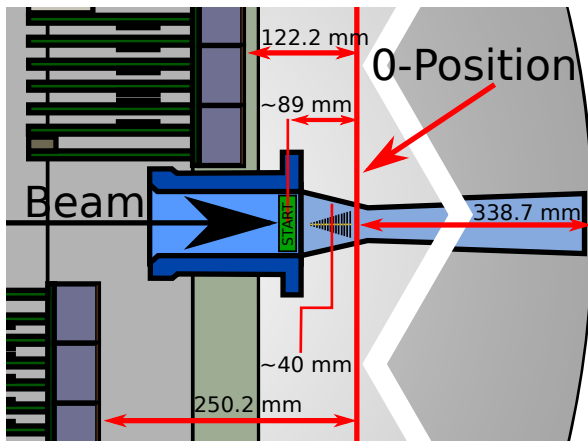


**Figure 1.17** ♦ *Sketch of the HADES target area indicating the spatial separation between target, MAPMTs, HADES-START detector and mirror with respect to the zero position in the HYDRA-Framework. Many objects in the figure are not up to scale. Positions of the START detector and target center are extracted approximately from data, all other distances are taken from the geometry file used for simulation.*

**Mirror setup**

This spherical mirror has a radius of curvature of 872 mm such that the radiator length for particles emitted at a polar angle of 80° reaches 650 mm. A photography of this mirror is shown in figure 1.18. The whole mirror is placed into an aluminum structure supported by six spokes,
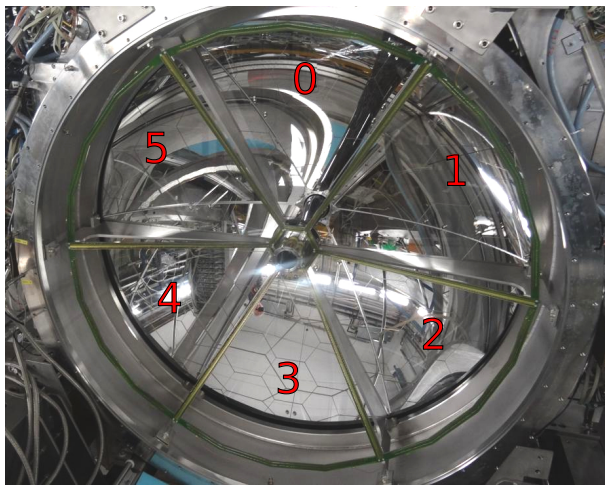


**Figure 1.18** ♦ *Picture of the mirror in the HADES RICH detector. Also visible are the spokes attached to the beam flange supporting the mirror structure. Numbers (0–5) are added to indicate the different sectors in the RICH. Original picture by Jürgen Friese* [Fri18].

indicated in figure 1.16b. Those spokes are congruent with the coils of the superconducting magnet between the different sectors of the MDC. This is important in order to introduce inefficiencies only at those places where either way tracking is infeasible. The spokes are connected on the inside to a newel in whose center the beam pipe lies. The mirror itself is coated with an Al substrate protected by a $MgF_2$ layer. The mirror coating is evaporated on a glassy carbon substrate in nearly all sectors. Only sectors two and five – bottom right and top left looking downstream – are made out of glass instead of carbon. All layers combined are about 2 mm thick reflecting more than 80% of all photons emitted above 150 nm [The+09]. This low material budget mirror setup is in line with the overall design goal of reducing the material budget as can be seen in figure 1.19. There depicted is a simulation of $1 \times 10^8$ photons, emitted in the target's silver segments with angles of $\theta = 10°–90°$ (polar) and $\phi = 0°–360°$ (azimuthal) and momenta ranging from $50 \, \mathrm{MeV}/c$ to $250 \, \mathrm{MeV}/c$. With this simulation setup, one finds the beampipe
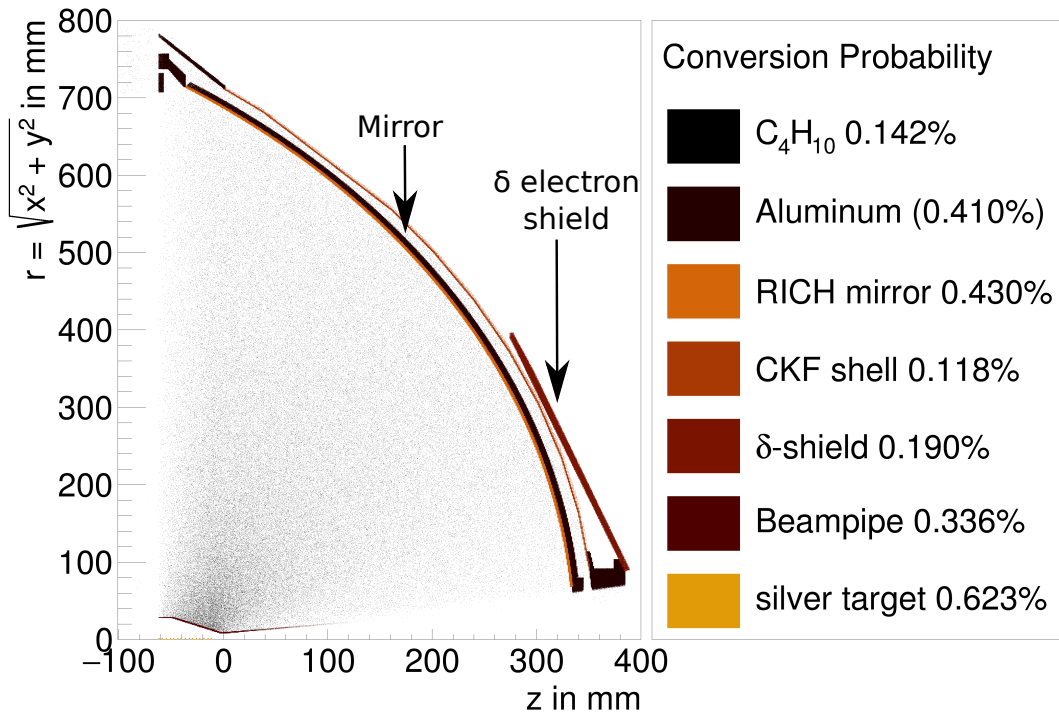
**Figure 1.19** ♦ *Spatially resolved points of conversion and conversion probability broken down per material in the RICH. This plot and data are extracted from a simulation of $1 \times 10^8$ photons emitted over momenta from $50\,\mathrm{MeV}/c$ to $250\,\mathrm{MeV}/c$ and an angular range of $\theta = 10°$–$90°$ (polar) $\phi = 0°$–$360°$ (azimuthal). The calculation for conversion probability divides the number of $\gamma s$ converted in the respective material by all $\gamma s$ simulated. The conversion probability value for the aluminum in the mirror is put in brackets as it does not reflect the conversion probability shown in the spatially resolved plots, but artificially excludes the flange area at $(z, r) = (360, 100)$.*

and target setup to produce approximately $1\%$ [7] conversion in the detector, while the RICH totals a conversion probability of $\sim 1.1\%$ [8] with the $\delta$-electron shield adding another $0.2\%$.

**Readout electronics**

The readout set-up uses the DiRICH readout scheme developed by the TRB group around M. Traxler at GSI. The DiRICH scheme, fully laid out later in section 3.1, reads out 6 MAPMTs× 64 channels = 384 channels, using twelve front end modules (FEB), a data concentrator board and a power board, all connected via a common backplane. This backplane distributes low and high voltage power, as well as trigger, clock and data to its sub-modules. Hereby all power lines are plugged into the power board, which forwards them to the individual sub-module (LV) and the MAPMT (HV) itself. The data concentrator board handles the communication. The DiRICH FEBs each take care of reading out 32 channels. Measured are hereby leading and trailing edges of an MAPMT signal above threshold down to the 10 ps level in timing precision. With leading and trailing edge information the ToT can be determined and therethrough the signals amplitude estimated. The HADES RICH uses 66 3×2-MAPMT modules and an addi-

---

[7] Contributions of other components at the beampipe like the Kapton foils holding the target and the residual air are negligible ($< 0.01\%$).

[8] Adding the flange and the aluminum structure at the top of the RICH to the material budget, the RICH overall reaches a conversion probability total of $1.6\%$

tional eight special $2 \times 2$-MAPMT modules. The orientations and placement of all modules is depicted in figure 1.20a with a photography of its real life pendant shown in figure 1.20b. The



**(a)** *Backplane layout in the HADES RICH*

**(b)** *Picture of the RICH electronics. Backside of the RICH*
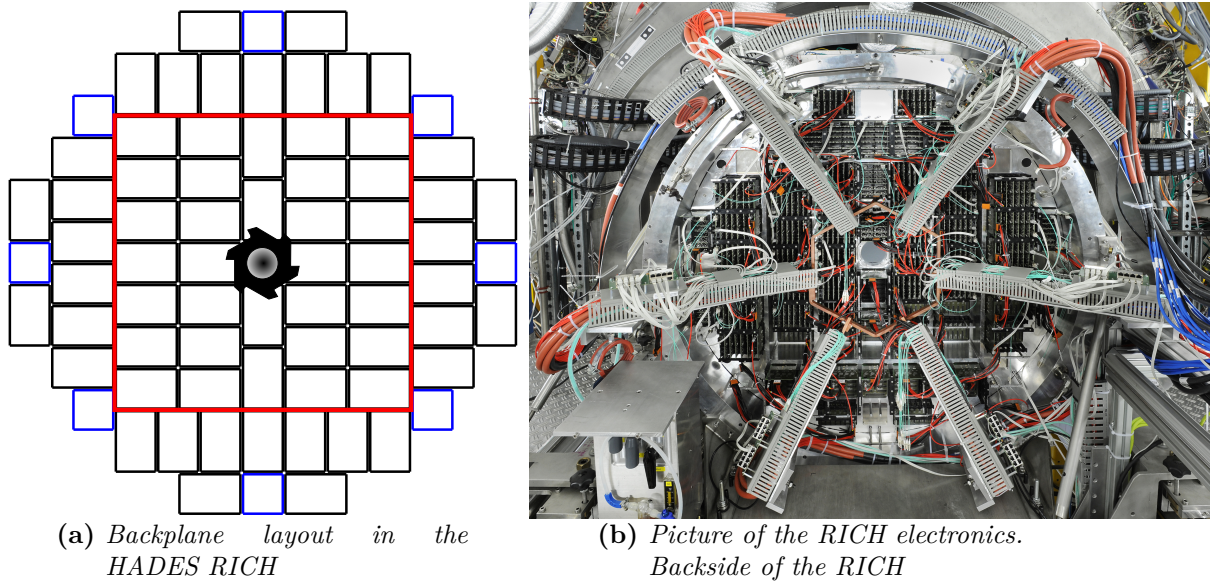
**Figure 1.20** ♦ *Sketch* **(a)** *and picture* **(b)** *of the read out electronics backplane arrangement in the HADES RICH. The sketch indicates each backplane as black rectangle. Blue rectangles indicate 2×2 (MAPMT) backplanes. The large red square indicates the transition from inner to outer photon detection plane. The picture shows the exact same setup installed without the 2×2 backplanes. Six large arms distribute all cabling to the detector. All ground lines are joined together at a common copper ring in the middle of those arms. The picture is taken by Gabi Otto (GSI).*

orientation of each module backplane is chosen such that the combiner module is furthest away from the beam pipe. Additionally the backplanes on the inner part of the HADES RICH are orientated horizontally to ensure optimal air flow through the DiRICH-FEBs. To ensure best working conditions for the MAPMTs, the whole set-up is air cooled to approximately $30\,°C$.

**Photon detection setup**

The photon detection setup consists out of 428 MAPMTs with 64 pixels each. The sensor chosen, H12700 from Hamamatsu, has its quantum efficiency range from $200\,nm$ (10%) to $550\,nm$ (10%) peaking at $350\,nm$ (35%). This is discussed in more detail in section 2.1. Hereby 192 MAPMTs are situated on the inner and 236 MAPMTs on the outer photon detection plane. From the 192 MAPMTs situated on the inner plane, the front windows of 48 MAPMTs are coated with a wavelength shifting coating (WLS). This coating shifts the drop off in efficiency to wavelengths much lower than $200\,nm$ such that at $200\,nm$ an efficiency of nearly 30% is still reached. This is achieved through absorbing photons of lower wavelength in the coating, re-emitting them at larger ones. These WLS coated MAPMTs are shown as gray rectangles in figure 1.16b. Overall, the $428 \times 64$ pixels amount to 27392 total pixels. With an approximate average size of $6.0625 \times 6.0625\,mm^2$ per pixel, the total effective area amounts to approximately $1\,m^2$. Spatial coverage however amounts to a $1.3\,m^2$ circular footprint, or $1.2\,m^2$ taking into account the unfilled edges of the detector. To shield the MAPMTs from magnetic stray fields of the large
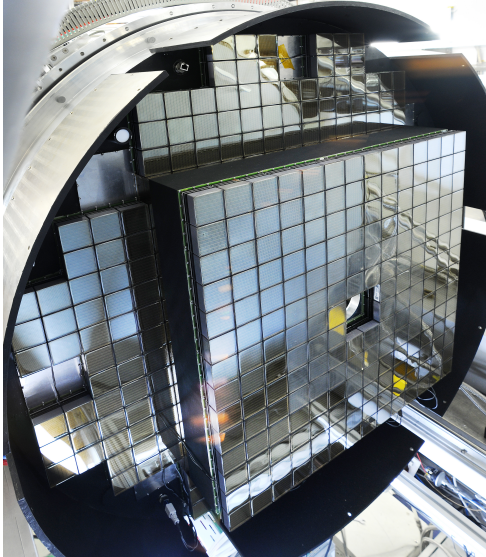
**Figure 1.21** ♦ *Picture of the HADES RICH photon detection plane. The full detector is filled with 428 64 channel Hamamatsu H12700 MAPMTs (here depicted are only 396, as some are still uninstalled). Slightly visible are the WLS coated front windows of the inner most MAPMTs. The inner part of the photon detector is separated clearly by its indentation towards the mirror. On the top left one sees a feed through for a single laser fiber out of four total. On the outer rim of the detector the soft iron magnetic shield is visible. The picture is taken by Gabi Otto (GSI).*

magnetic field in the HADES detector, additional soft iron panels are attached to the rim of the detector. These shields, as well as all other detector surfaces are coated with black spectrometer color[9] on the inside of the RICH.

To cross check the whole setup periodically, a laser system is put in place. This system illuminates the whole setup with 10 Hz while sending a corresponding trigger[10] signal to the data chain. In order to do that, the light of a single laser is split four times and led through four separated fibers and reflected by the mirror onto the detector. A depiction of the lasers' simulated illumination of the whole RICH plane is shown in figure 1.22. Here one finds the full RICH detector illuminated by these four laser couplings. It also becomes clear, that especially the pixels on the rim of the detector are much more illuminated. The lasers' intensity is set such, that most pixels in the detector measure roughly one hit every tenth trigger, i.e. laser pulse.
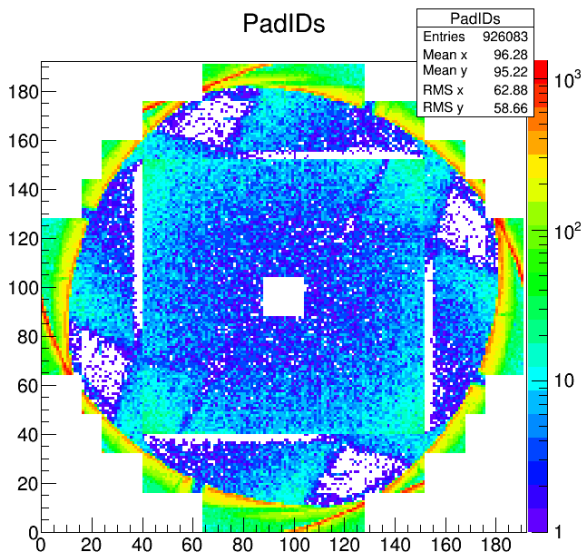


**Figure 1.22** ♦ *Simulated illumination using the four laser couplings attached to the HADES RICH detector. This simulation setup resembles mostly the final laser setup in the real detector. Simulation carried out by Jürgen Friese* [Fri21]. *The same plot using real data is added to the appendix* Fig. A.2 *(pg. 171).*

---

[9] "NEXTEL VELVET COATING 811/21- 9218 black" of company Mankiewicz, suppressing reflection of 98% of all incoming light [Man21].

[10] In analysis one finds data related to the laser trigger by requesting the so called PT6 trigger in the raw data.

## 1.6 Sources of electrons relevant in following analyses

Sources of electrons measured in the RICH detector in HADES are manyfold, and can be separated into two sub-groups; electron-positron pairs from conversion or electron-positron pairs from the collision itself.

Electron-positron pairs (from now on only called electrons/electron-pairs) from conversion originate from high energetic photons, i.e. $\gamma$s that undergo conversion in any material, more precisely near any nucleus. Hereby the $\gamma$s can come directly from the collision or itself be a decay product (e.g. from $\pi^0$). As the photon is massless, the opening angle between the two electrons is extremely narrow, following an exponential like decay. A nonzero (and thus allowed) decay actually happens only due to the recoil of the coulomb field of the corresponding nucleus. This is depicted in figure 1.23, where a simulated opening angle distribution is shown. The detec-
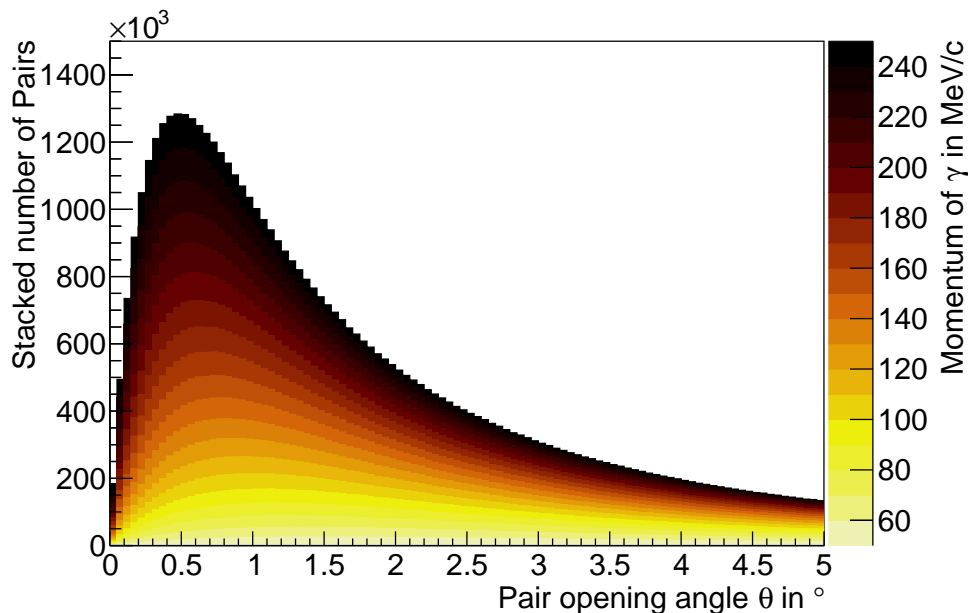


**Figure 1.23** ♦ *Simulated opening angle distribution for electron positron pairs originating from conversion of a photon. $1 \times 10^8$ photons where herefore generated under varying angles and with momenta between $50 \,\mathrm{MeV}/c$ and $250 \,\mathrm{MeV}/c$. The histograms for the different momenta are hereby stacked, meaning that the outer shape of the histogram resembles the histogram over all different momenta.*

tion of these close pairs in the RICH is critical but very hard, as the RICH is very close to the main "conversion"-material of the target. The corresponding rings therefore might overlap substantially and need to be carefully identified.

Electrons that come directly from the collision stem from many sources. This is depicted in figure 1.24, where different electron sources are combined to one mass-cocktail using simulations made for the Ag+Ag beamtime proposal. Distinct features in this spectrum are from the $\pi^0$-Dalitz ($\pi^0 \rightarrow \gamma + \mathrm{e}^+ + \mathrm{e}^-$) decay, which is the main contributor to electron pairs with low invariant masses. More broad and less pronounced spectra arise from $\eta$- and $\omega$-Dalitz decays, whereas the $\omega$ as well as $\phi$ meson $\mathrm{e}^+ + \mathrm{e}^-$-decays introduce peaks at their respective mass. As
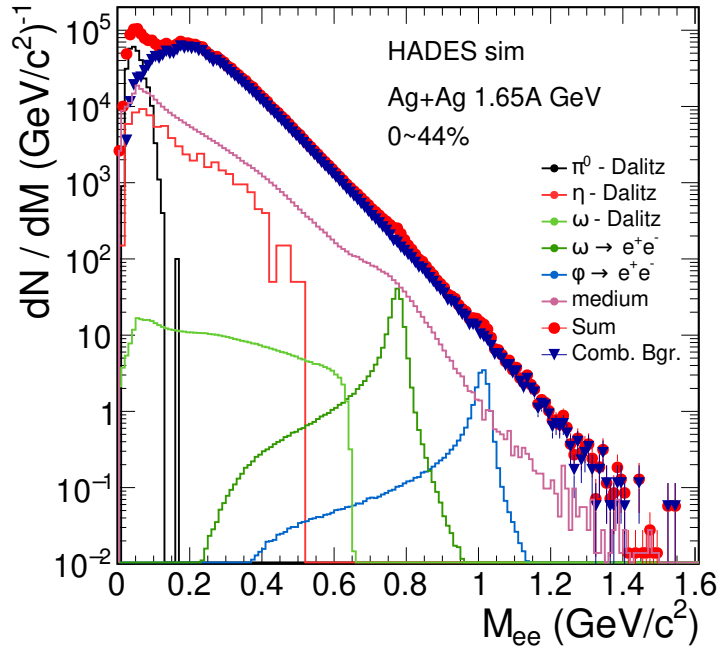
**Figure 1.24** ♦ *Simulated dielectron invariant mass distribution for* Ag+Ag *collisions at* 1.65A GeV *at* 0% *to* ∼ 44% *centrality. Different contributions to the spectrum are indicated with different colors. This figure is taken from* [HAD17].

the mass of the particle is correlated to the opening angle between the two electrons these large masses produce electrons well separated from one another. Thus overlaps between two electrons stemming from these sources can basically be excluded.

# Part I

# Testing the HADES RICH hardware by means of laboratory measurements

# 2

# The upgraded photon detector of the HADES RICH

This chapter will discuss the photo sensitive part of the upgraded HADES RICH detector. The photon sensitive area is equipped with MultiAnode PhotoMultiplier Tubes (MAPMT) of type Hamamatsu H12700. The chapter is coarsely split into two topics, starting with measurements of the MAPMTs in a dedicated test bench and closing with the derivation and description of the final MAPMT layout in the detector. This chapter starts with an introduction to these MAPMTs bought by GSI/FAIR for the future CBM[1] experiment of which a subset is used in the upgraded HADES RICH detector. Thereafter the testing procedure is described, followed up by a study on the long term behavior of selected MAPMTs. The overview over the 1100 MAPMTs is concluded evaluating the behavior of all measured MAPMTs with relation to their production date is studied. On basis of these studies, the chapter is completed discussing the selection criteria for MAPMTs used in the HADES RICH and their final layout in the detector.

## 2.1 The H12700 MultiAnode PhotoMultiplier Tube

The Hamamatsu H12700 is a $52 \times 52 \, \text{mm}^2$ MAPMT[2] with $8 \times 8$ square pixels of size[3] $6 \times 6 \, \text{mm}^2$ [HAM19]. This results in an effective area of theoretically 87%. A picture of one of the MAPMTs used in the upgraded HADES RICH detector is depicted in figure 2.1. The photo cathode of the MAPMT features a large quantum efficiency in the order of 33% peak at approximately 350 nm which is slightly more efficient than the average HAMAMASTU MAPMT with Bialkali (BA) cathode. The photo electron coming from the photo cathode is amplified using ten dynode stages, therewith producing a distinct single photoelectron peak in every channel. Albeit the dynodes being separated for each channel in a so called metal channel MAPMT layout, the voltage dividing stages are common. The last stages of the dynode system are thereby actually driven by an active voltage divider. This setup allows for small transit time spreads and an overall well separable single photoelectron peak. All here analyzed MAPMTs feature a so called blue enhanced photo cathode[4] in conjunction with a UV transparent window (synthetic silica),

---

[1] Compressed Baryonic Matter experiment. The CBM experiment is a future experiment studying the properties of HICs and will be situated at FAIR/GSI. For further information on the CBM experiment cf. [Abl+17] the CBM RICH is found detailed in e.g. [Ada+17]

[2] Note that newer versions of this model feature a glass window of $51.7 \times 51.7 \, \text{mm}^2$ at unchanged effective area. Some of the 1100 MAPMTs discussed feature this new front window.

[3] Please note that the pixels on the MAPMTs rim are actually of size $6.25 \times 6.25 \, \text{mm}^2$.

[4] This was the common naming scheme during the time of buying this MAPMT. Today, all H12700 MAPMTs feature the blue enhanced photo cathode. If one would want an MAPMT more sensitive at larger wavelengths one should choose the structurally identical H14220.
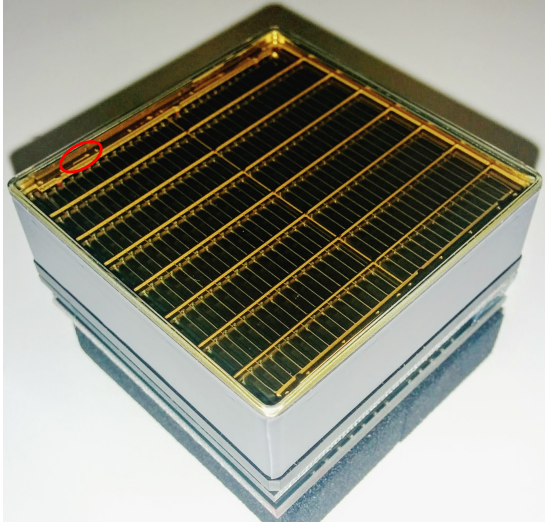
**Figure 2.1** ⬥ *Picture of a Hamamatsu H12700 MAPMT used for the upgraded HADES RICH. Red encircled in the top left is the Hamamatsu "start mark".*

resulting in the quantum efficiency curves depicted in figure 2.2. In the figure depicted are measured quantum efficiency curves for two H12700 MAPMTs and a H8500 MAPMT (normal BA cathode) all with UV transparent window. One of the two H12700 features the blue enhanced photo cathode, while the other does not. Additionally shown are measurements of the two H12700 MAPMTs, where the front window was coated with a WaveLength Shifting film (WLS). This coating, based on $p$-Terphenyl [Ada+15], absorbs photons below 300 nm [Kop14, p. 112] and reemits them at larger wavelengths. As the H12700 is more sensitive at larger wavelengths, but the number of Cherenkov photons increases quadratically towards lower wavelengths, such a coating does improve the overall efficiency for Cherenkov light.

Other important characteristics of any MAPMT are its dark-rate, referring to the number of pulses measured during no illumination, cross-talk, which is the probability that one hit in one pixel induces another hit in another pixel of the same MAPMT, and afterpulsing, meaning the measure of a delayed hit after the first one. The dark-rate (sometimes also called "dark noise") is mostly an artifact of thermal radiation. Hereby an electron is emitted from one of the MAPMTs components like e.g. the front window, cathode or one of the early dynode stages. This electron then undergoes amplification in the amplification stage of the MAPMT and thus becomes detectable. Obviously the dark-rate depends on the temperature the MAPMT is operated in. However, the buying specifications of the here discussed H12700 MAPMTs forbid dark-rates of more than 6.4 kHz at a threshold of larger than 20% of the single photoelectron peak, while no individual pixel is allowed to reach more than 1 kHz dark-rate. Afterpulsing is mostly divided into two separate effects depending on their time constant. Early afterpulses mostly stem from photo electrons elastically scattering off of the first dynode, while late afterpulses mostly come from ionization of residual gases [Tos+07]. Cross talk can also be divided into two categories. One of them is the simple charge sharing, where the electron cloud induced by amplification of a single photo electron in one pixel leaks over into another one, thus inducing a smaller signal therein. The other type of cross talk is the so called capacitive cross talk. Here the sudden drop in potential on the last dynode due to the massive charge produced in a single channel's last dynode, induces a negative pulse in a neighboring pixel. This pulse is followed by an overshoot thereafter, such that the overall integral of this signal is zero. For this particular MAPMT, the
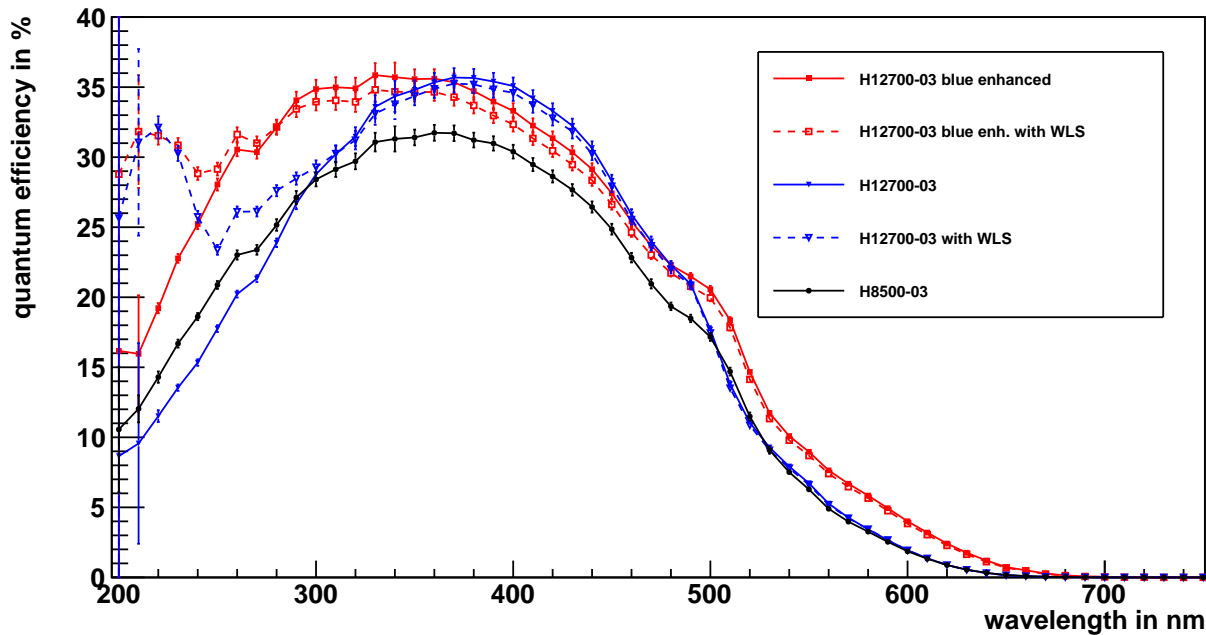
**Figure 2.2** ♦ *Measured quantum efficiencies for two HAMAMASTU H12700 and an H8500 MAPMT. One of the H12700 MAPMTs is called blue enhanced referring to its enhanced quantum efficiency in the blue region. This is the currently sold standard version of the H12700 MAPMT. Both H12700 MAPMTs are measured in their normal configuration and with a wavelength shifting coating applied to their front window. The H8500 is an MAPMT with normal BA cathode.*

delay between actual photon signal and the positive overshoot was found to be in the order of 3 ns [PT18].

## 2.2 Testing procedure and the test bench

All MAPMTs bought for the CBM detector, which are in parts also being deployed in the upgraded HADES RICH, needed to undergo several tests to ensure a proper quality. For this purpose a dedicated test bench was built and is throughly described in [För16]. Still, in this section a brief overview is given introducing the reader to the test bench and briefly detailing each measurand and its uncertainty. Additionally the dark-rate measurand is discussed more in-depth as here changes have been made in the determination procedure comparing it to [För16]. The basic working principle relies on a spatially focused single photon detection using a free triggered data acquisition for each individual channel of four simultaneous measured MAPMTs. The single photons are emitted by an LED and guided, using an optical fiber, onto a small spot on the MAPMT. An LED correlated trigger signal is fed into the data stream in order to later discriminate between measured signals from LED photons and other signals. The optical fiber is then moved over the MAPMT illuminating different spots on all of the MAPMT's pixels. Thus the measured quantities include the spatially resolved single photon efficiency relative to a "reference" PMT and the dark-rate, gain and afterpulse-probability for each individual channel.

Hereby, the "reference" MAPMT[5] stays always inserted in the test bench to keep the derived efficiency comparable despite a slightly fluctuating light intensity in the setup. All of those quantities are derivable as function of supply voltage applied to the MAPMT. Here however mainly the gain varies with different supply voltage settings. The exact measurement principles and derived systematic uncertainties of the test bench can be found in [För16], where a detailed description of the test bench and its results is based on a study of the first 400 MAPMTs from the same order of H12700 MAPMTs. The, for this thesis relevant, measurement variables and their estimated uncertainty are however briefly shown here.

| | |
|---|---|
| **Efficiency index** | The average efficiency of the MAPMT relative to the reference MAPMT. The uncertainty was found to be $\Delta\mathrm{EFF} = 0.003$ |
| **Dark-rate** | The average dark-rate measured over two hours after five hours of storing the switched on MAPMT in darkness. The uncertainty is reevaluated hereafter. |
| **Effective area** | The area of the MAPMT above a relative efficiency of 60% compared to the MAPMTs maximum efficiency. The uncertainty was found to be $\Delta\mathrm{EFFAR} = 0.241\,\mathrm{pp}$ |
| **Skewness** | A quantity indicating the spatial asymmetry in the efficiency, dividing the efficiency of the right half of the MAPMT by the one on the left (w.r.t. the Hamamatsu "start mark"). The uncertainty was found to be $\Delta\mathrm{SKEW} = 0.013$ |
| **Gain** | The average amplification of the single photo electron through the dynode chain. This is extracted from the average single photoelectron equivalent charge measured through fit of a Gaussian profile to each pixels charge distribution. The uncertainty for this measure is quite large with $\Delta\mathrm{Gain} = 0.25 \times 10^5$ |
| **Afterpulse probability** | Measured average probability to measure a hit after the main signal in a time window of up to $4\,\mu\mathrm{s}$ correcting for the dark-rate in each channel. The uncertainty was found to be $\Delta\mathrm{APP} = 0.048\,\mathrm{pp}$ |

In the cited thesis it was found, that the temperature variations, influencing the dark-rate measurement were to large to disregard ([För16, p. 52]). This dependency is now taken into account following the empirically derived formula 2.1 from [ST17] for this Hamamatsu H12700 MAPMT, so that each measured dark-rate is extrapolated to the same temperature via

$$r_{\mathrm{dark}}(T) = r_{\mathrm{dark}}(T_0) \cdot e^{0.12 \cdot (T - T_0)}. \tag{2.1}$$

The validity of the empirically derived formula can be cross checked using the correlation between the dark-rate of the repeatedly measured main reference MAPMT and the temperature during

---

[5]The reference MAPMT is one of the four measured MAPMTs.

the measurement. Using the formula, the correlation between temperature and dark-rate

$$\text{corr}(T, r_{\text{dark}}) = 0.87$$

gets reduced to

$$\text{corr}(T, r_{\text{dark,corrected}}) = -0.18$$

(see Fig. A.3 on pg. 172 in the appendix). With temperature sensors being a late addition to the test bench all following results from the 10-06-2016 onwards focus on the corrected dark-rate, extrapolated to 25 °C. With this correction a reevaluation of the systematic uncertainty on this measurand needs to be carried out. The uncertainty is normally determined by means of the fluctuations of the reference MAPMT, which is always inserted into the test bench. This is feasible, assuming that the measurand for this MAPMT behaves rather constant, or reaches a constant behavior after several repeated measurements. The distribution of the measured corrected dark-rates for the reference MAPMT is shown in figure 2.3. There one finds the standard deviation on all measured corrected dark-rates of the main reference MAPMT after the 10-06-2016 to be

$$\sigma_{\text{dark}} = 0.3087 \, \text{kHz} \,.$$

This number therefore will be referenced as systematic uncertainty on the dark-rate for all measured MAPMTs after that date. In order to estimate the uncertainty on the uncorrected
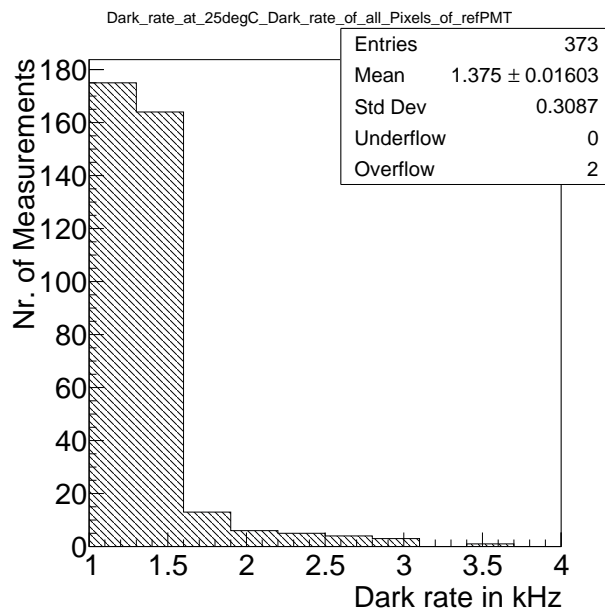


**Figure 2.3** ♦ *Distribution of temperature corrected dark-rate for all measurements of the main reference MAPMT after the 10-06-2016. The dark-rate is hereby the sum over the dark-rates of all pixels of the reference MAPMT. The standard deviation of this distribution is $\sigma_{\text{dark}} = 0.3087 \, \text{kHz}$ and therefore the systematic uncertainty on this measurand.*

dark-rates measured before the 10-06-2016 the procedure is repeated, building the histogram on the uncorrected dark-rates before the key date. The standard deviation of the uncorrected dark-rate distribution for the main reference MAPMT (cf. Fig. A.4 pg. 172 in the appendix) reaches

$$\sigma_{\text{dark}} = 0.4899 \, \text{kHz} \,,$$

which is subsequently used as systematic uncertainty on the measured dark-rates before the 10-06-2016. It needs to be stated however, that this increased systematic uncertainty also takes

MAPMT effects into account, which are discussed in the following section but are unfortunately not distinguishable from the uncertainty of the test bench.

## 2.3 Long term behavior of MAPMT characteristics

To study the long term behavior of this photon sensor, several MAPMTs need to be measured repeatedly over several years. Using the afore described test bench, this comes as some sort of bonus, as the reference MAPMT is always inserted into the setup and thus measured nearly daily over the course of three years. In order to base this study not only on one MAPMT and also to repeatedly cross-check the "main"[6] reference, secondary reference MAPMTs were introduced. These three secondary reference MAPMTs were stored in a lightproof and nitrogen flushed environment to keep their exposure to humid air minimal and only taken out for measurements in the test bench. Measurements with those three MAPMTs were repeated frequently but not following a dedicated schedule. Although the main reference MAPMT was handled in a way, such that the exposed integrated light charge was kept low, the secondary references should show less aging due to exposure to light.

### 2.3.1 Explanation of the analysis

The main measurands this study focuses on are dark-rate, afterpulse-probability, gain, and efficiency. All these measurands are discussed comparing them to the MAPMT individual median after one year of repeated measurements. That means, that first an MAPMT individual median is built using all measurements carried out one year after the MAPMT's first measurement. Now, the derived median is subtracted from the respective measurand in all measurements of that MAPMT, giving the measurand's "deviation from median". This method is chosen as it allows to assess the long term behavior of all four reference MAPMTs at the same time focusing on the change over time rather than the absolute development. For better interpretability, the measurements over one month are combined via averaging. As not all reference MAPMTs have equally many measurements over these periods, the positions and density of these measurement points vary. Same holds true for the measurement uncertainties which vary with the number of measurements of the respective MAPMT in the given month. The uncertainty in $y$-direction is hereby calculated through $\sigma/\sqrt{n}$ using the systematic uncertainty $\sigma$ and number of measurements $n$ of the respective MAPMT in the given month. In $x$-direction, the uncertainty depicted is simply the range in time over which the measurements are spaced. In addition to that, all the $x$-axes, i.e. time-axes, in the following figures are aligned such, that the $0^{\text{th}}$-month indicates the first measurement of each individual MAPMT. This is however not important for the reference and secondary reference MAPMTs as they were all measured for the first time being inserted together into the test bench. In the following, each measurand is discussed individually using the here described visualization. To see all these plots on one side for better correlability please

---

[6]Hereby main reference refers to the reference MAPMT always inserted into the test bench.

see figure A.5 on pgs. 174f in the appendix.

### 2.3.2 Time stability of dark-rate

Measurements of the dark-rate, being the signal rate of the MAPMT uncorrelated[7] to light input, for the reference and secondary reference MAPMTs over the course of three years are depicted in figure 2.4. Here one finds a qualitatively visible drop in the dark-rate reaching negligible levels already after five months of measurement. In the following a quantification of this drop is attempted. Before quantifying this drop, first all other artifacts in the spectrum need to be assessed.

The reference MAPMT shows a spike in dark-rate for its very last measurements. This artifact is not fully understood but seems to be a result of improper storage[8] as no other reference nor other measured MAPMTs during this time period show such a dramatic increase in dark-rate. Additionally the reference MAPMT's dark-rate over all of the last measurements shows erratic spikes and steps of more than $1\,\mathrm{kHz}$ plotting it with regards to the time in measurement. Until a follow-up measurement series is carried out these data points will therefore be excluded from the following discussion. Most predominantly the reference MAPMT, but also one of the secondary reference MAPMTs indicate a drop in their dark-rate over the first few months of operation. A fit to the complete data of all reference MAPMTs indicates, that an exponential
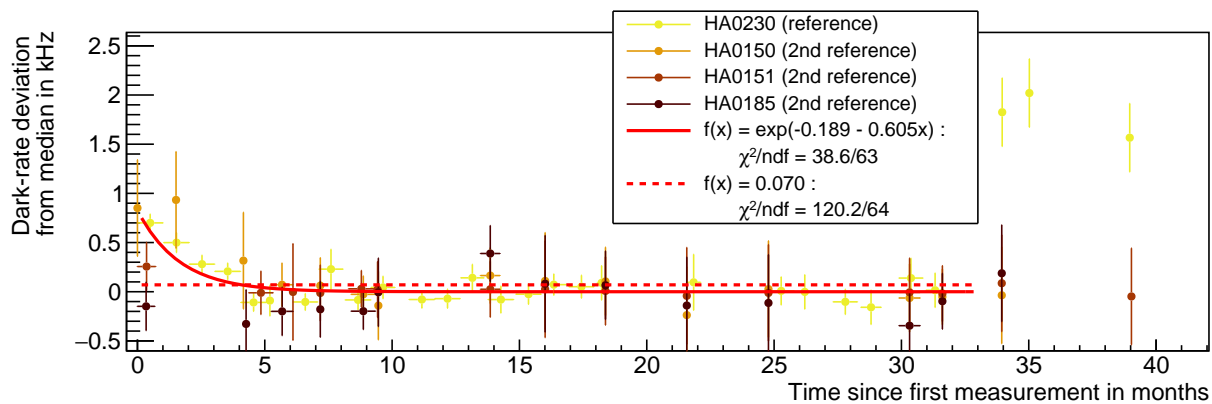


**Figure 2.4 ♦** *Stability of the dark-rate w.r.t. the measurement date for all reference MAPMTs. Details on the depiction chosen here are laid out in subsection* 2.3.1. *An exponential function and a polynomial of $0^{th}$ degree are fitted to the data excluding the time range after the $33^{rd}$ month. The function parameters and the individual $\chi^2$/ndf are denoted in the legend. A corresponding figure not using the uncertainties derived in this thesis, but those derived in* [För16] *(for all data before the 10-06-2016) is found in* Fig. A.5b *in the appendix pg.* 173.

progression describes the data of the reference MAPMTs slightly better than a flat polynomial of $0^{th}$ degree. Fitting an exponential decrease one gains an $\chi^2$/ndf $= 0.6$ whereas the flat hypothesis fits only with an $\chi^2$/ndf $= 1.9$. One can see further, that the exponential decrease fits best to the main reference MAPMT. On the other hand, the hypothesis of a constant dark-rate seems to

---

[7]Uncorrelated hereby means, that the signal is measured in a fixed time window before the trigger-pulse correlated to the LED light source.

[8]Improper storage, like excessive exposure to light might result in a severe increase in dark-rate.

fit the best to the data of the HA0151 and HA0185. Therefore a clear statement favoring the one or other hypothesis is hard to make. Either way, the fitted exponential decrease reaches a negligible difference from the median already after six months since the first measurement. As mainly the main reference MAPMT shows this trend being measured the most of all references, the conclusion that this drop is measurement-time, not time dependent lies close. Assuming this, one can imply that all MAPMTs should reach their final dark-rate latest after approximately 1100 h [9] of partial illumination under operating voltage. As the illumination is only spot wise, it must be assumed, that the main reason for this drop in dark-rate is actually the operation of the MAPMT in a mostly dark environment[10]. Looking at the three outliers in the measurements of the main reference MAPMT and the overall variation of the dark-rates of all MAPMTs individually, it becomes however obvious, that the overall variation is larger than the lowering of the dark-rate with time.

### 2.3.3 Time stability of afterpulse-probability

Figure 2.5 displays the afterpulse-probability, i.e. probability to detect a pulse significantly after the photon was emitted onto the MAPMT, with regards to measurement time. By eye one can immediately see that the afterpulse-probability exhibits an increase over time which is discussed in the following. Evaluating the full distribution again first, the main reference MAPMT (HA0230) again shows three outliers at the very end. This might be a result of the afore mentioned improper storage but might also be an effect of the sudden drops and spikes in the dark-rate distribution during one measurement[11]. Although the outliers are less pronounced in this analysis, these data-points are still disregarded. Excluding those measurements, a fit with an exponential increase is fitted to all reference MAPMTs (red line) and only to the main reference (yellow dashed line). The fit to all MAPMTs is only partially descriptive of their behavior resulting in an $x^2/\mathrm{ndf} = 4.1$. Better description is achieved by solely fitting the main reference MAPMT resulting in $x^2/\mathrm{ndf} = 2.7$ and thus hinting towards a different pace with which the different MAPMTs' afterpulse-probability increases. Nonetheless, the observation of an increase in afterpulse-probability over time is consistent for all reference MAPMTs measured, where the overall maximum seems only to be reached after at least one and a half year.

### 2.3.4 Time stability of gain

The MAPMTs gain is measured as the average over all pixels' single photoelectron gain by fitting the single photoelectron peak in each pixels' pulse charge spectrum. The time dependent varia-

---

[9]160 measurements after six months with seven hours measurement time each.

[10]Obviously the environment the MAPMT is operated in is completely light tight, such that the word "mostly" is chosen with regards to the time the MAPMT is illuminated with single photons on an extremely small spot.

[11]Referring to [För16] the dark-rate is known to be correlated with the afterpulse-probability. This effect is corrected for by subtracting the "dark-rate probability" from the afterpulse-probability. The dark-rate however is measured only at the end of the measurement, whereas the afterpulse-probability is measured during the whole measurement. Therefore erratic dark-rate behavior might significantly influence the quality of the afterpulse-probability measurement.
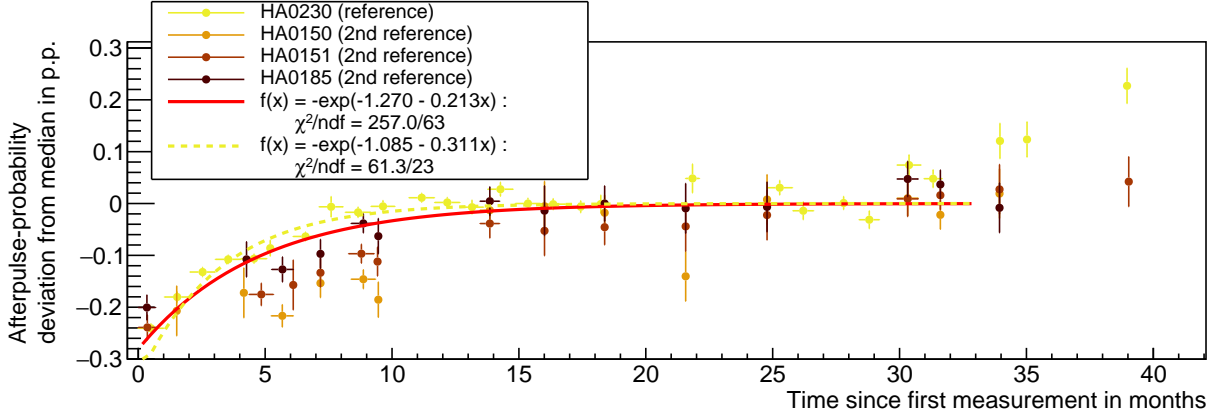
**Figure 2.5** ♦ *Stability of the afterpulse-probability w.r.t. the measurement date for all reference MAPMTs. Details on the depiction chosen here are laid out in subsection* 2.3.1. *The deviation from median is given in units of percentage-points (*pp.*). The function following the red line is fitted to all the measurement-points, excluding the time range after the 33$^{rd}$ month. The yellow dashed line is fitted solely to the main reference MAPMT (HA0230).*

tion of the gain of the reference MAPMTs is depicted in figure 2.6. The systematic uncertainty with which the gain is measured according to [För16, p. 49] is large. Therefore, looking on all secondary reference MAPMTs one can not identify any time dependence of the gain exceeding these uncertainties. The depicted uncertainties for the main reference MAPMT are obviously smaller, as they are the uncertainties on the average ($\sigma/n$) using more data points $n$. For the main reference MAPMT an increase in gain during the first months becomes visible. This is be a behavior also seen by other experiments, where the gain is found to vary within the first months of constant illumination [Cal+15, p. 14]. There, the authors observed an increase in gain for some MAPMTs and a decrease for other, similar ones when illuminating the respective MAPMT over long periods of time. As this variation in gain seems to be dependent mainly
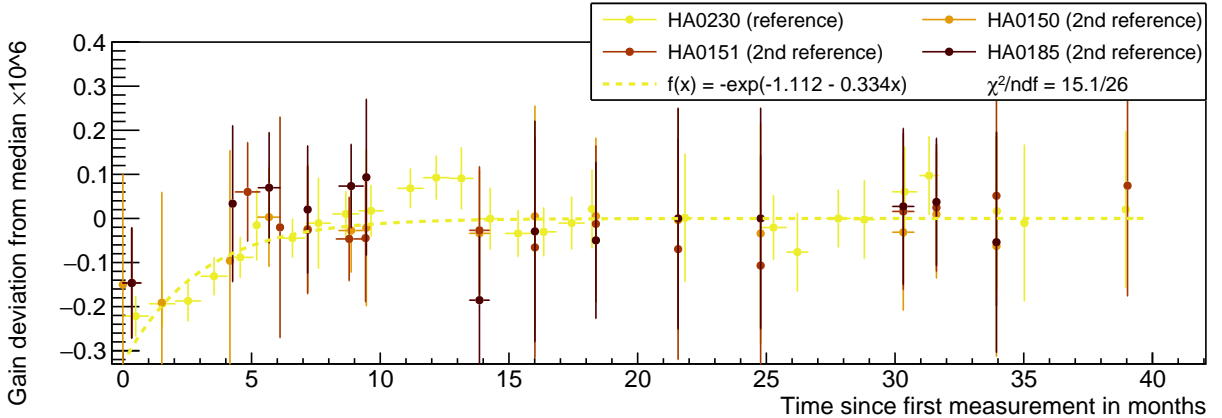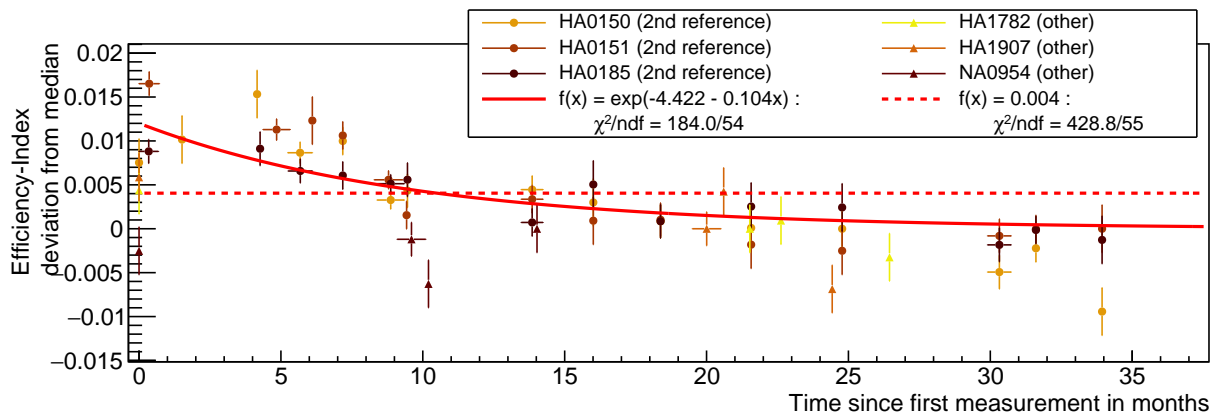


**Figure 2.6** ♦ *Stability of the MAPMT's gain w.r.t. the measurement date for all reference MAPMTs. Details on the depiction chosen here are laid out in subsection* 2.3.1. *The data points of the main reference MAPMT (HA0230) are fitted with an exponential curve.*

on the integrated (photo electron) charge the MAPMT gets exposed to, it is unsurprising that the secondary MAPMTs show no variation in their measured gain, while the main reference MAPMT exhibits a clear increase. To put this into context, the referenced paper describes a 5%

difference in the measured gain in some channels earliest after 500 hours. As the measurement time in this test bench is seven hours only and the MAPMTs are only illuminated at a small spot on the MAPMT, such periods of illumination lie out of reach for any reference MAPMT other than the main reference.

### 2.3.5 Time stability of photon detection efficiency

The photon detection efficiency measured in the test bench is always relative to the main reference MAPMT. This resulting efficiency estimator is called Efficiency-Index. The purpose of this relative efficiency scaling is to counteract variations in the light source intensity. This means that for the analysis on the long term behavior only the secondary reference MAPMTs can be studied. To counteract the lower number of measurement points, three additional MAPMTs are included into the analysis. Those MAPMTs were measured at least four times over the course of at least one year. These additional MAPMTs were also stored in a light tight environment with low humidity, but come from later production charges[12]. Assessing the development of the Efficiency-Index over time, shown in figure 2.7, one sees a slow decrease in efficiency over time for the three secondary reference MAPMTs. This decrease is very hard to explain, as it can only be caused by a (relative speaking) constant efficiency of the main reference MAPMT and a drop in efficiency of the secondary reference MAPMTs, or an increase in the efficiency of the main reference MAPMT and a (relative speaking) constant efficiency of the secondary reference MAPMTs. Both of these hypotheses seem implausible, as they both involve a more drastic deterioration of the secondary reference MAPMTs which were stored under better conditions compared to the main reference which was measured over the course of 481 measurements. In
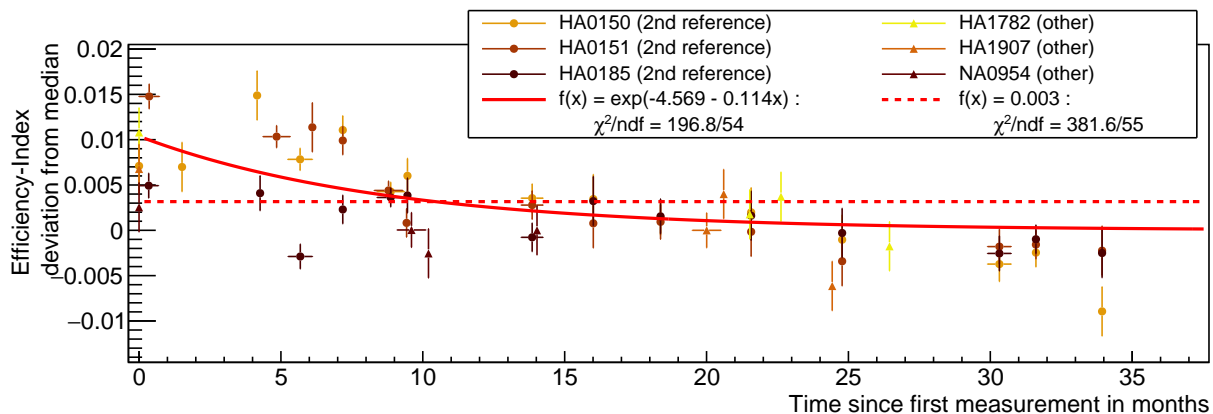


**Figure 2.7 ♦** *Stability of the MAPMT's efficiency w.r.t. the measurement date for all secondary reference- plus some additional MAPMTs. The additional MAPMTs (depicted as triangles) were measured at least four times over the range of at least one year. Details on the depiction chosen here are laid out in subsection 2.3.1. All measurement points are fitted with a exponential decay and a polynomial of $0^{th}$ degree, to assess overall trend of the data points.*

this context it is important to point out, that the whole test bench is operated with a fixed detection threshold, which has advantages and disadvantages. One disadvantage is certainly, that

---

[12]delivered in charges 19 (Jan-2017), 20 (Feb-2017), and 30 (Sep-2017).

MAPMTs with much too low gain have their photon detection efficiency underestimated. This is normally counteracted by remeasuring exactly those MAPMTs with larger supply voltage, thus eliminating the problem of having too low gain for this efficiency estimation. Another disadvantage comes from the calibration with the reference MAPMT. Obviously, if the gain of the reference MAPMT varies drastically over time, sometimes leaving a fraction of normally recognizable hits below the detection threshold, the efficiency of the other MAPMTs measured would be artificially increased. To counteract this, one might imagine using an artificial threshold depending on each MAPMTs' gain, which is set to a certain fraction of the single photoelectron peak of the respective MAPMT. This would eliminate any bias induced by differing or varying gains. One certain disadvantage of this procedure is, that the gain, i.e. the position of the single photoelectron peak, is the measurand with the largest uncertainty of the test bench. Still, in order to exclude the possibility that the variation in gain of the main reference MAPMT induced this drop in efficiency seen here, the same plot is derived using a threshold set to 30% of the respective MAPMT's – thus also the main reference MAPMT's – single photoelectron peak position. This is found depicted in figure 2.8. Both data sets, meaning the one with and without



**Figure 2.8 ♦** *Stability of the MAPMT's efficiency w.r.t. the measurement date for all secondary reference- plus some additional MAPMTs when using a gain dependent detection threshold. The plot is explained in more detail in figure 2.7.*

gain dependent threshold are fitted with a polynomial of $0^{th}$ degree and with an exponential decay, to differentiate if the measurement data shows a decreasing tendency or not. Hereby the before discussed points are found confirmed. Moving from the normal efficiency determination to the one with the gain dependent threshold one finds, that the measured points scatter more drastically which can be attributed to the larger uncertainties in the gain determination. In fact, some of the measurements even need to be discarded to still apply meaningful fits. However, the resulting $\chi^2/\mathrm{ndf}$ value when fitting an exponential decrease, increases when moving from the standard procedure to the gain dependent one, whereas the opposite is visible, when examining the fit with the polynomial, where a decrease in $\chi^2/\mathrm{ndf}$ is visible. Thus one can conclude, that indeed some of the exponential decrease might be contributed to the increase in gain of the reference MAPMT. This is also indicated by all additional (other) MAPMTs – which were measured much later in time – not showing this decreasing trend in the efficiency. It is however also clear that an "efficiency calibration" of the main reference by means of its gain is no proper way of correcting for this, as the uncertainty on the gain is too large. As the effect is too large

to neglect but also not corrigable, the systematic uncertainty on the Efficiency-Index needs to be increased to

$$\sigma_{\text{Efficiency-Index}} = 0.0055$$

comparing it to the uncertainty derived in [För16]. This value is derived taking the weighted average over all MAPMT-individual standard deviations of the Efficiency-Index, and will be used as systematic uncertainty on this measurand from now on. This larger uncertainty is also in line with the much larger variances of the uncalibrated "efficiency" of the main reference MAPMT observed during the first months of measurement (cf. Fig. A.5g pg. 174 in the appendix). These uncalibrated – i.e. not divided by the main reference MAPMT's efficiency – efficiencies are obviously heavily influenced by the luminosity of the test bench's LED at the time of measurement, but still show larger variances during the early months of measurement.

### 2.3.6 Summary

Summarizing all the presented results, one finds an indication of an exponential decrease in the dark-rate of the MAPMT. This decrease seems to reach its final dark-rate level at least after half a year. Further, the afterpulse-probability increases slowly for all measured reference MAPMTs. The steepness of the increase seems to depend on the specific MAPMT but levels off only after one and a half year. Due to the large systematic uncertainties on the measured gain, a significant time dependence can only be made out for the main reference MAPMT where an increase is visible. The measured efficiency shows a distinct drop which can be fitted with an exponential function. The increase in gain of the main reference MAPMT might hereby play a slight role as it could well induce a measured but artificial increase in the efficiency of the main reference MAPMT. As there is no clear explanation for this drop in efficiency over time, the uncertainty on the measurand is increased accordingly. A single page overview over all plots discussed in this section can be found in figure A.5 on pgs. 174f in the appendix.

## 2.4 Development of H12700 MAPMT characteristics over production time

As a discussion on the key parameters of the H12700 was already presented in [För16, pp. 64–71], this section focuses on the development of those features over time of the production. For that, a comparison between different charges is chosen as those charges mostly resemble different production periods. This is achieved by always combining all MAPMTs delivered in one month, as during one month mostly one charge or several smaller charges were successively delivered. Hereby, the parameters of dark-rate, efficiency (Efficiency-Index), effective area, skewness, gain, and afterpulse-probability are analyzed in terms of the different production period, followed up by a look on the overall distribution of the parameters for all measured MAPMTs. In the following discussion, the delivered MAPMTs, which were replaced due to being unrectifiable rejects are disregarded. Here, a total of 19 MAPMTs were found and reclaimed due to not fulfilling the buying specifications[13]. Out of those 19 MAPMTs, one MAPMT was completely broken, ten were found to have too high dark-rates ($> 6.4\,\mathrm{kHz}$) while eight MAPMTs showed efficiency artifacts or too low of an efficiency overall.

### 2.4.1 Explanation of the visualization method

The following discussions focus always on a single measurand individually. The measurand's distribution per delivery-month, i.e. for the different charges of delivery is then discussed based on so called box-plots. These box-plots consist of a box, a median line, so called whiskers and outlier-markers. The central line in the box indicates the median (50%-quantile) with the box visualizing the interquartile range (IQR), marking the position of the first and the third quartile of the measured data. The whiskers, include every data point outside the IQR but extend to a maximum of $\pm 1.5 \times$ IQR, only leaving the so called outliers undescribed, which are indicated by cross-shaped markers. An additional circular marker with error bars depicted for each month visualizes the mean in the individual month, with the error bars depicting the systematic uncertainty on the average ($\sigma/\sqrt{n}$). Additionally, to gain an overview over all MAPMTs delivered, each measurand's distribution over all MAPMTs is depicted in an additional histogram. Hereby the bin widths are always chosen such that they resemble the systematic uncertainty on the respective measurand.

### 2.4.2 Dark-rate versus production time

Figure 2.9 shows the development of the dark-rate over the full production period. It becomes visible, that the dark-rate shows a significant decrease towards later production stages. Furthermore, also the inter-charge spread of the dark-rate gets significantly reduced, reaching levels of the test bench's precision. Although parts of the broadened distribution in the early months

---

[13]In actuality, 27 MAPMTs were found to be worse than all other MAPMTs. However, only 19 out of those were accepted to be defective products by Hamamatsu.

of delivery can be contributed to the larger variations induced by the missing temperature correction in the test bench data at the beginning, some months feature a distinctly larger spread which can therefore not solely be explained by the test bench's worse measurement precision. The overall drop in dark-rate can in parts be contributed to feedback given to the manufacturer during the production. Mainly due to the improvement towards the later production charges, the overall average dark-rate lies at

$$(1.014 \pm 0.030(\text{stat.}) \pm 0.490(\text{syst., max.}))\,\text{kHz}\,.$$
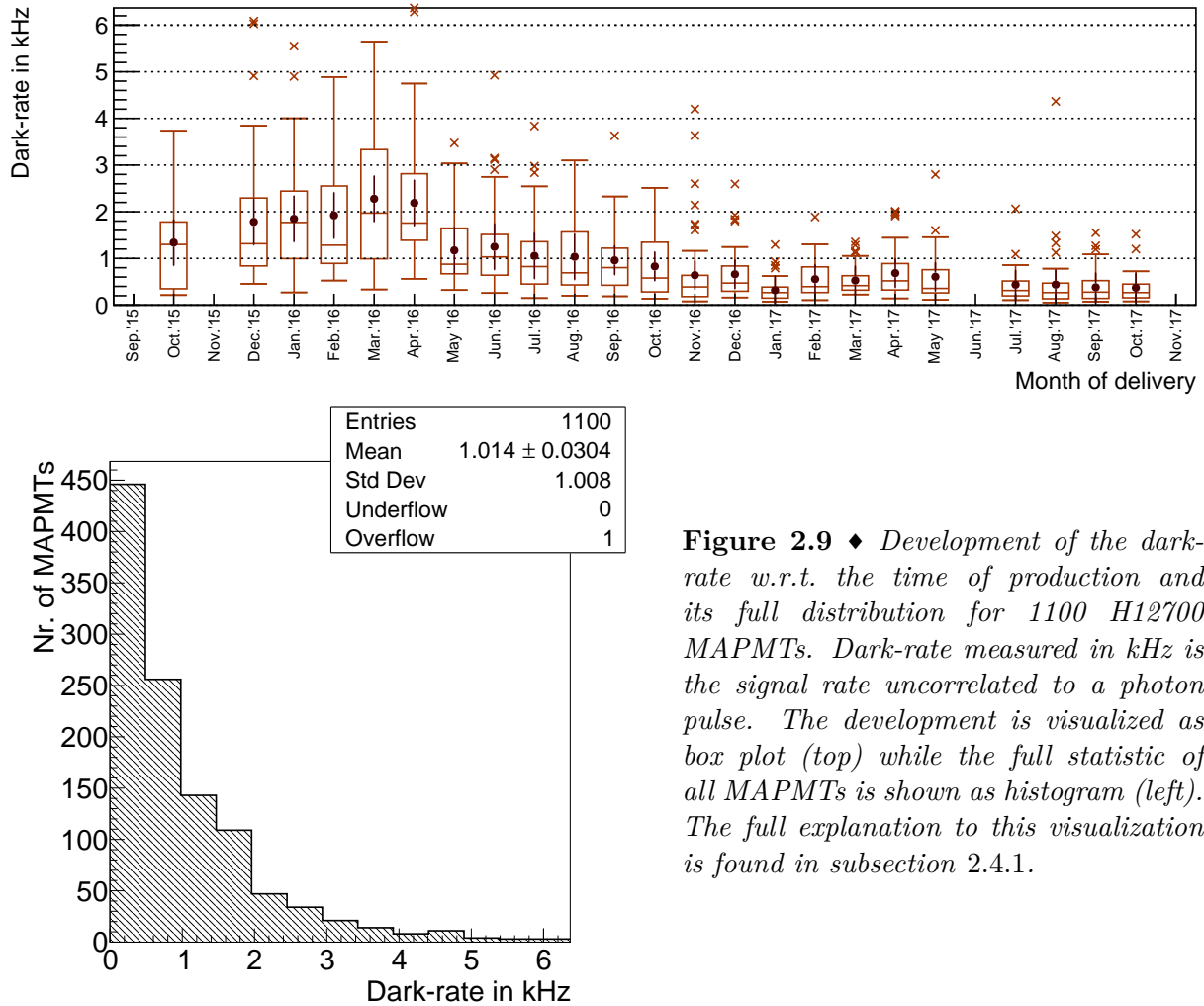


**Figure 2.9** ♦ *Development of the dark-rate w.r.t. the time of production and its full distribution for 1100 H12700 MAPMTs. Dark-rate measured in kHz is the signal rate uncorrelated to a photon pulse. The development is visualized as box plot (top) while the full statistic of all MAPMTs is shown as histogram (left). The full explanation to this visualization is found in subsection 2.4.1.*

### 2.4.3 Efficiency-Index versus production time

The Efficiency-Index, being a measure that compares the measured MAPMT's average efficiency to that of the main reference, is depicted in figure 2.10. The overall distribution is situated at

$$0.9711 \pm 0.0021(\text{stat.}) \pm 0.0055(\text{syst.})$$

indicating that the main reference MAPMT has a slightly higher efficiency than the average MAPMT. The overall distribution is only slightly skewed towards lower Efficiency-Indexes ($\gamma_m = -0.218$) and therefore nearly resembles a Gaussian distribution around its mean. During the summer of 2016 one finds the only time period where MAPMTs were consistently produced with above average efficiency. The lowest median efficiency one finds during May 2017 right before a month-long production stop. This production stop was initiated by the vendor due problems in the production chain and therefore might explain the slight deterioration in the efficiency right before. Apart of these specific months no clear time dependence is visible.
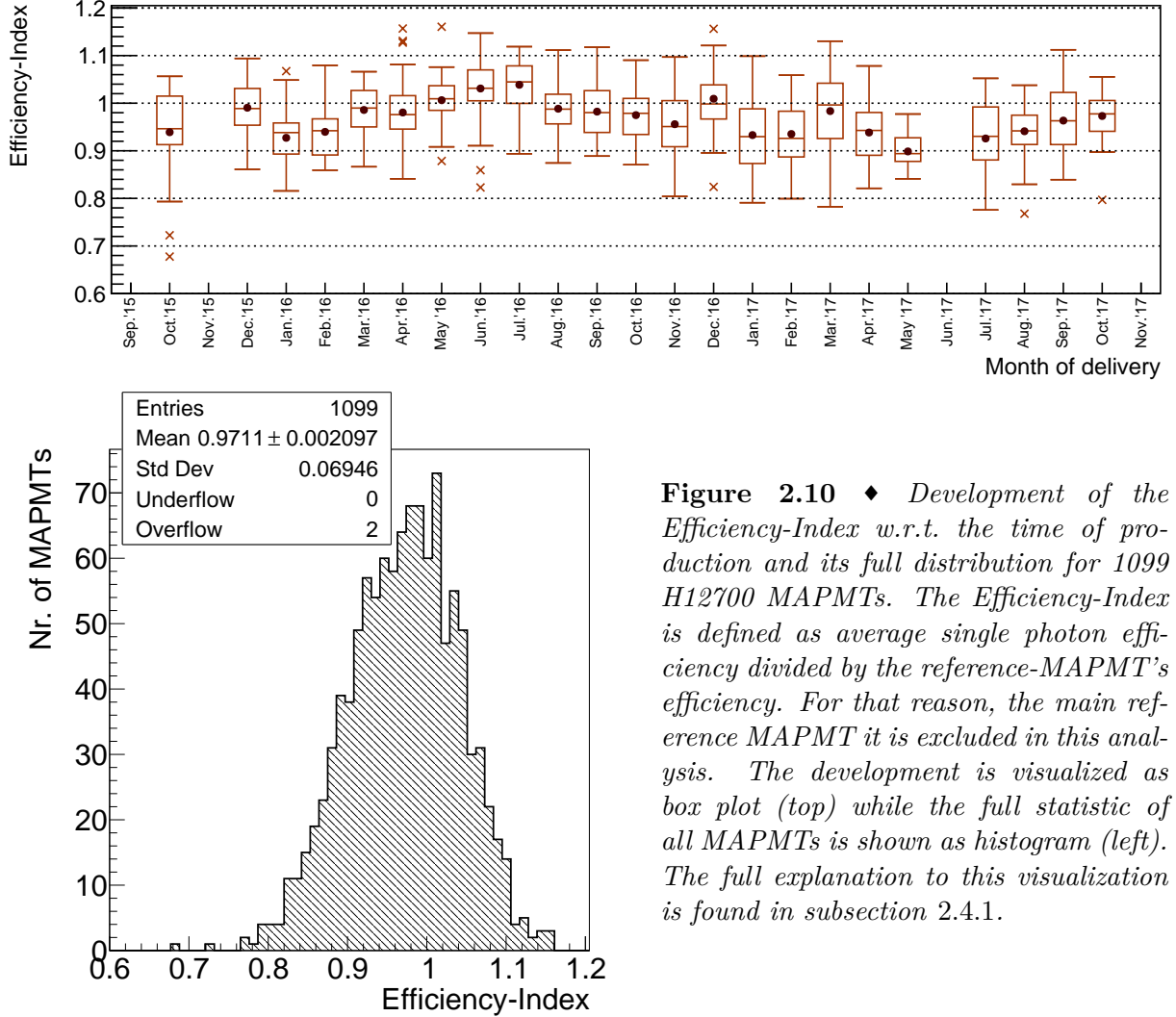


**Figure 2.10** ♦ *Development of the Efficiency-Index w.r.t. the time of production and its full distribution for 1099 H12700 MAPMTs. The Efficiency-Index is defined as average single photon efficiency divided by the reference-MAPMT's efficiency. For that reason, the main reference MAPMT it is excluded in this analysis. The development is visualized as box plot (top) while the full statistic of all MAPMTs is shown as histogram (left). The full explanation to this visualization is found in subsection 2.4.1.*

### 2.4.4 Effective area versus production time

The effective area depicted in figure 2.11 has a structurally conditioned maximum at 87%, defined by the outer dimensions of the MAPMT ($52 \times 52 \, \text{mm}^2$) divided by the coverage of the photo cathode ($48.5 \times 48.5 \, \text{mm}^2$). This theoretical limit is only reached (within errors) by a very limited amount of MAPMTs. This might however also stem from the way of determining the effective area in the test bench, where only those spatial measurement points are assumed

efficient, which do exhibit a relative efficiency – compared to the MAPMTs maximum efficiency – of larger than 60%. On a more positive note, also only a very limited amount of MAPMTs reach
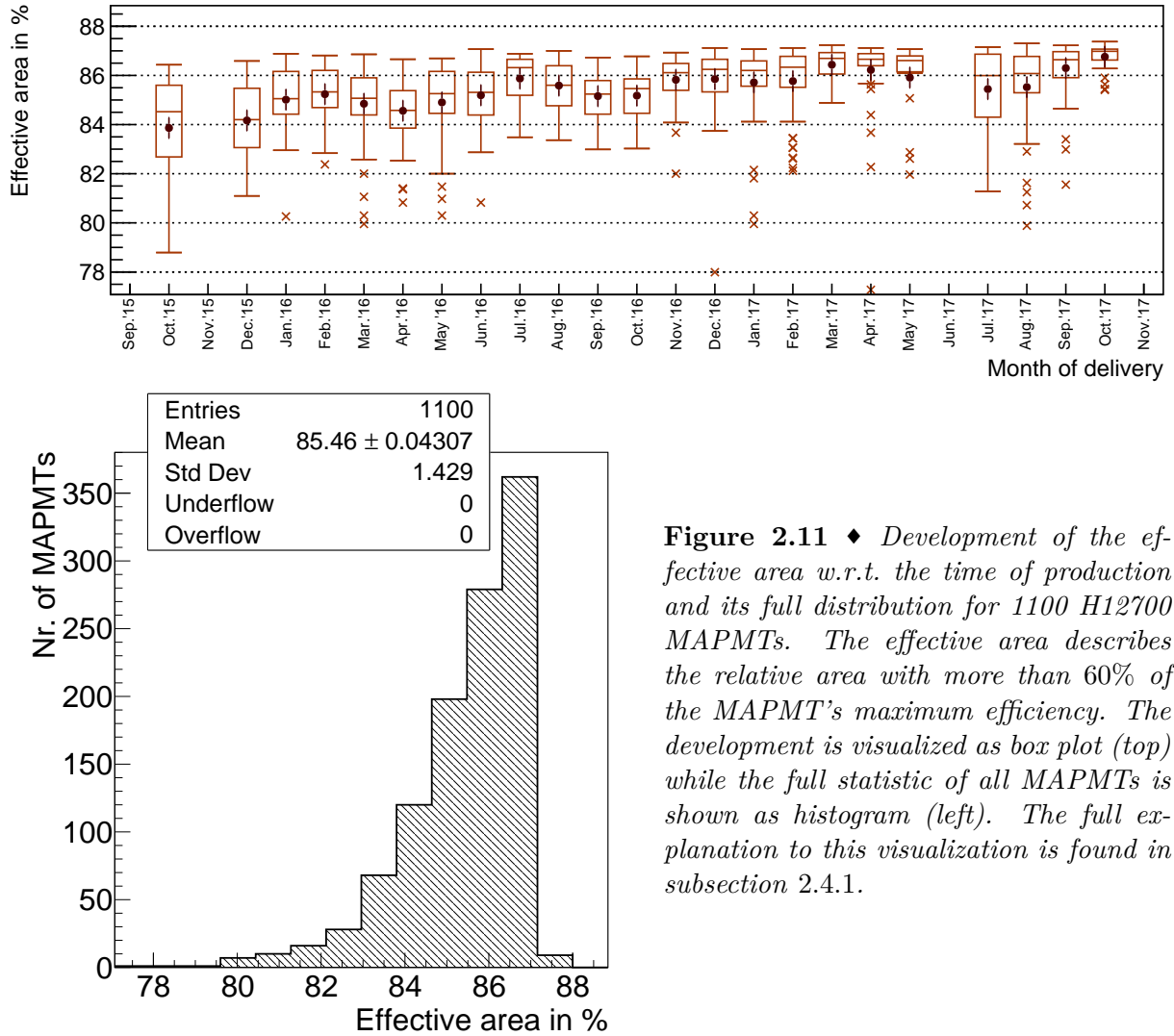


**Figure 2.11** ♦ *Development of the effective area w.r.t. the time of production and its full distribution for 1100 H12700 MAPMTs. The effective area describes the relative area with more than 60% of the MAPMT's maximum efficiency. The development is visualized as box plot (top) while the full statistic of all MAPMTs is shown as histogram (left). The full explanation to this visualization is found in subsection 2.4.1.*

effective area levels of below 80%. An interesting time period to give special attention is the April 2017. From this time on the vendor did deliver H12700 MAPMTs with slightly different form factor. Those MAPMTs (indicated with "NA" in front of their serial number) are slightly more compact featuring outer dimensions of only $51.7 \times 51.7\,\text{mm}^2$. In order to focus mainly on the absolute effective area both MAPMT's effective area is still derived the same way, dividing by $(52 \times 52\,\text{mm}^2)$. This results in the measure being independent of the outer shape only giving comparable results for the sensitive area. From April 2017 onwards however, no drop in the effective area becomes visible, showing that albeit having a slightly smaller entrance-window the MAPMTs sensitive area did not deteriorate. Overall an upwards-trend is visible with the average effective area of the MAPMTs increasing and the spread within one delivery-charge decreasing towards later delivery months. The average effective area of all MAPMTs is, with

$$(85.46 \pm 0.04(\text{stat.}) \pm 0.42(\text{syst.}))\%$$

very close to its theoretical limit of 87%, thus leaving on average only ca. $1/64^{\text{th}}$ of the MAPMT inefficient.

### 2.4.5 Homogeneity/skewness versus production time

Another interesting measure in terms of effective area is the MAPMT's homogeneity. As this MAPMT features distinct inhomogeneities mainly along $x$-direction[14] a good measure comparing the different MAPTMs is the efficiency ratio between the left and the right half of the MAPMT[15]. The thereby defined skewness-parameter (for more details see [För16, p. 46]) is illustrated in figure 2.12 in terms of its development for different production charges and its overall distribution. As the skewness-parameter is derived by division, a skewness of 1.0 is desirable.
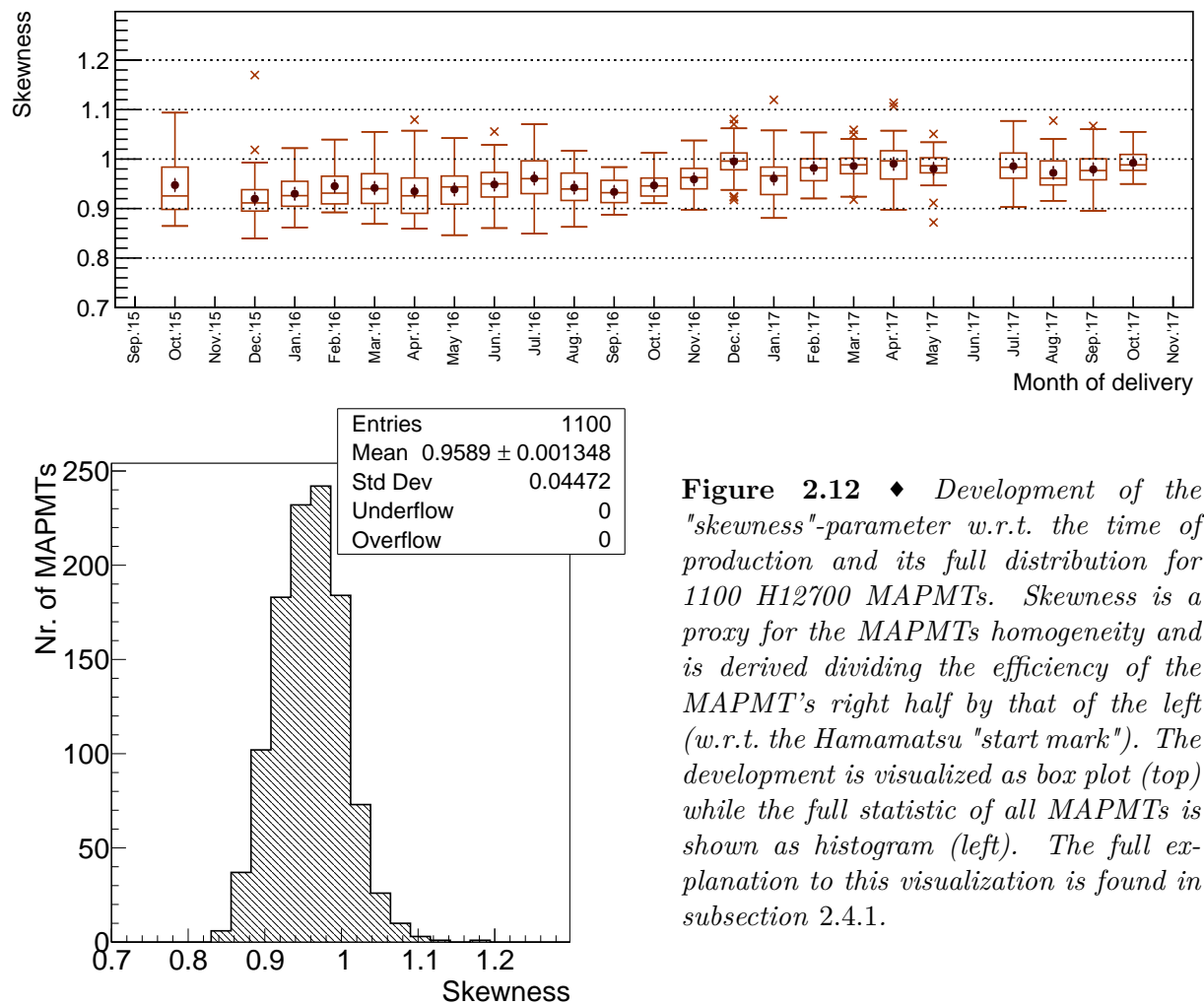


**Figure 2.12** ♦ *Development of the "skewness"-parameter w.r.t. the time of production and its full distribution for 1100 H12700 MAPMTs. Skewness is a proxy for the MAPMTs homogeneity and is derived dividing the efficiency of the MAPMT's right half by that of the left (w.r.t. the Hamamatsu "start mark"). The development is visualized as box plot (top) while the full statistic of all MAPMTs is shown as histogram (left). The full explanation to this visualization is found in subsection 2.4.1.*

Comparing the first few charges to the last, one can see an improvement in the skewness of the MAPMT, as the median of the skewness for the later delivered charges reaches closer to values of 1.0. Albeit the later charges being therefore more homogeneous, averaging all de-

---

[14]Meaning the horizontal w.r.t. the Hamamatsu "start mark" indicated on all H12700 MAPMTs.

[15]Dividing the efficiency of the side of pixels five through eight by the efficiency of the side with pixels one through four.

livered MAPMTs, an overall skewness lower than 1.0 is measured. The overall occurrence of an inhomogeneity in $x$-direction might be contributed to the technique with which the photo cathode is evaporated onto the MAPMT window. An interesting remark can be made for the extreme outlier delivered in December 2015. For this MAPMT it is quite apparent, that the photo cathode must have been evaporated from the other side of the MAPMT, as the overall shape of the efficiency is exactly inverse to all the other MAPMTs.

### 2.4.6 Gain versus production time

The gain, representing the single photoelectron amplification is shown in figure 2.13. This gain, measured for all MAPMTs applying $-1000\,\text{V}$, shows no clear dependence on the time of delivery, i.e. time of production. The overall spread in the gain distribution is large, showing a standard deviation of $\sigma = 0.74 \times 10^6$. The average gain over all MAPMTs is found to be

$$(2.641 \pm 0.0223(\text{stat.}) \pm 0.250(\text{syst.})) \times 10^6\,.$$

These measured MAPMT gains are in very good agreement with those measured by Hamamatsu for the same MAPMT as can be seen in the correlation coefficient

$$\text{corr}(\text{gain}_{\text{test bench}}, \text{gain}_{\text{Hamamatsu}}) = 0.984\,,$$

with the full scatter plot found in figure A.6 pg. 175 in the appendix. This is interesing in so far, as the MAPMT specific gain measured by Hamamatsu is measured by illuminating the full photo cathode with a well defined tungsten lamp measuring the thereby induced current [HAM19]. In the test bench on the contrary, the gain is derived as single photoelectron gain per channel, measuring only the average charge of a single photoelectron response via fit to the extracted charge spectrum of the individual MAPMT pixel. The average over all those single pixel-gains is then given as the gain of the MAPMT. As the average MAPMT gain can be corrected by varying the supply voltage, in this context even more interesting is the pixel to pixel variation in gain over one single MAPMT. As each MAPMT pixel's gain is measured in the test bench, the standard deviation in the pixel-gain for each individual MAPMT can be extracted. The average standard deviation in the pixel-gain per MAPMT is found[16] to be

$$\sigma = (0.333 \pm 0.003(\text{stat.}) \pm 0.177(\text{syst.})) \times 10^6\,,$$

as can be seen in figure A.7 in the appendix pg. A.7. Also this intrinsic variation per MAPMT shows no clear time dependence, but an even larger spread of $\sigma \approx 0.1 \times 10^6$. In simplified terms one can say, that an average MAPMT has a gain of $2.6 \times 10^6$ with most (95.45%) of its pixels lying within the range of $(2.0\text{–}3.3) \times 10^6$. This range is quite large, which immediately explains, why simply "aligning" the average gain of all MAPMTs, by applying different supply voltages to them, does not lead to a constant detection threshold (later to be applied in the detector) for

---

[16]While the measurand itself comes from pixel to pixel variations in one MAPMT, its uncertainty is approximated using the uncertainty of the average $\sigma_{\text{av.}}$ through $\sigma_{\text{std.-dev.}} = \sigma_{\text{av.}}/\sqrt{2}$
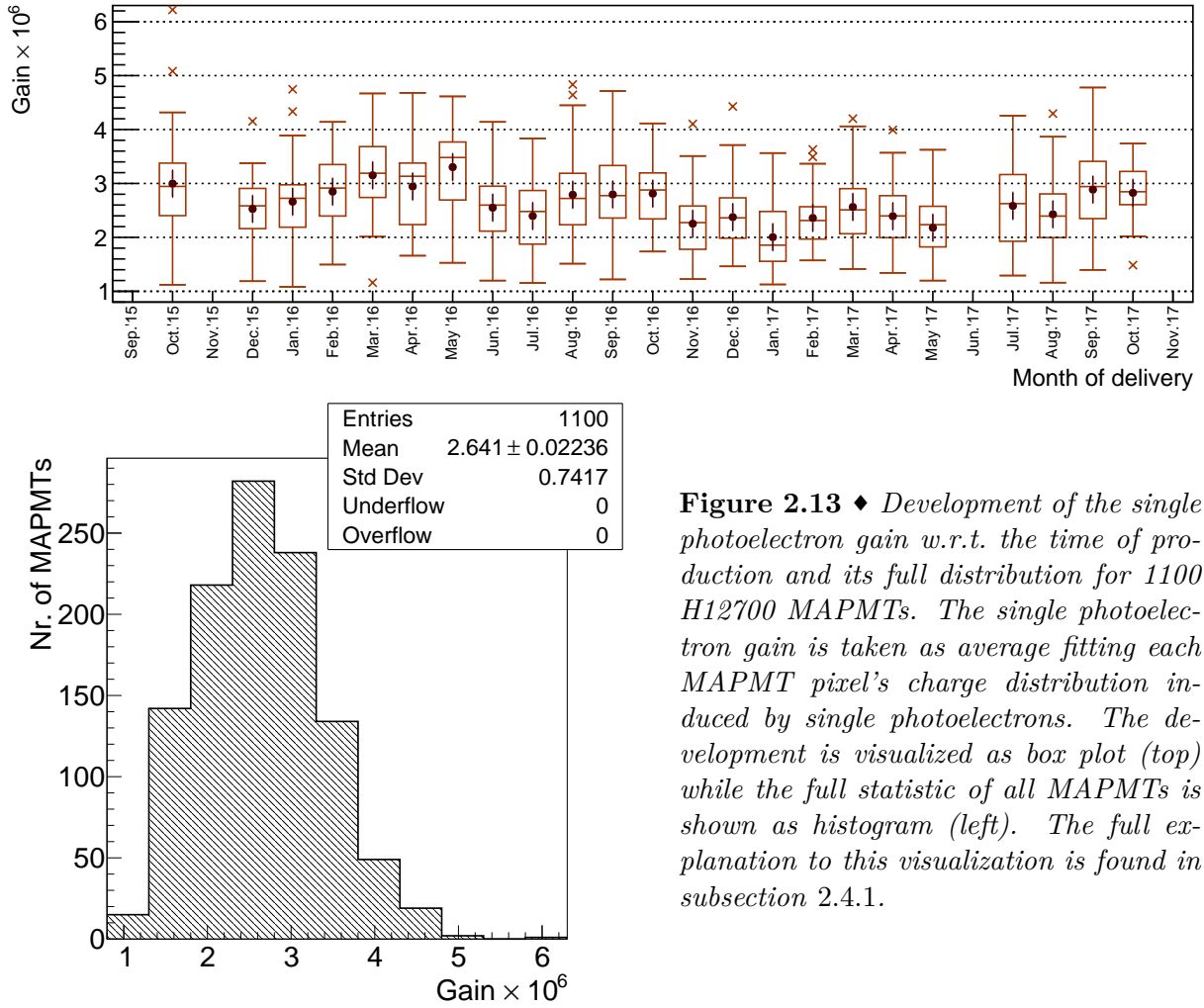
**Figure 2.13** ♦ *Development of the single photoelectron gain w.r.t. the time of production and its full distribution for 1100 H12700 MAPMTs. The single photoelectron gain is taken as average fitting each MAPMT pixel's charge distribution induced by single photoelectrons. The development is visualized as box plot (top) while the full statistic of all MAPMTs is shown as histogram (left). The full explanation to this visualization is found in subsection 2.4.1.*

all individual pixels (discussed in the section hereafter).

### 2.4.7 Afterpulse-probability versus production time

The afterpulse-probability as presented in figure 2.14 is the only key characteristic which did significantly increase from earlier to later charges. The largest afterpulse-probability in median and distribution width is visible for March 2017. This peak is accompanied by a slight increase in its neighboring months. The last months also show a steady increase up to ca. 1.5% in October 2017, there however with a less broadened distribution. The smallest spread in the afterpulse-probability distribution is visible for the first months, where also the median is situated at around 0.5%.
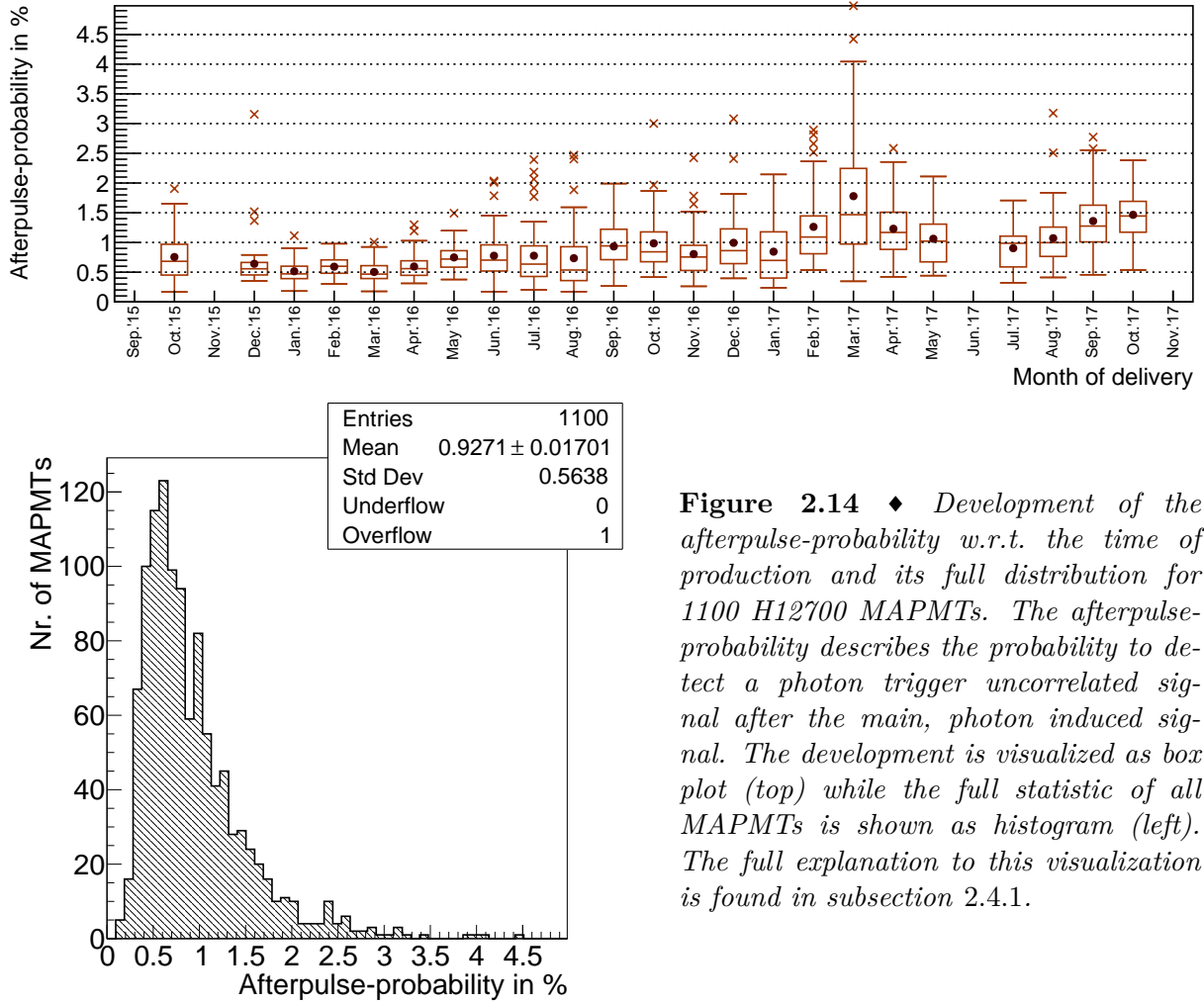
**Figure 2.14** ♦ *Development of the afterpulse-probability w.r.t. the time of production and its full distribution for 1100 H12700 MAPMTs. The afterpulse-probability describes the probability to detect a photon trigger uncorrelated signal after the main, photon induced signal. The development is visualized as box plot (top) while the full statistic of all MAPMTs is shown as histogram (left). The full explanation to this visualization is found in subsection 2.4.1.*

### 2.4.8 Summary

Summarizing all the results, one finds that the dark-rate did decrease for later production charges, whilst the afterpulse-probability increased. Furthermore, over time the homogeneity defining skewness parameter developed towards 1.0 indicating a more homogeneous MAPMT for later production charges. Also the effective area shows a slight upwards-trend towards later production charges, which is interesting in the sense that especially later MAPMTs also have a slightly better form-factor. The variation with time of all other measurands is consistent with zero, showing no clear indication of a decrease or increase of gain and efficiency with time.

# 2.5 MAPMT grouping for the HADES RICH

One key aspect of every detector is its homogeneity. Homogeneity in the case of the HADES RICH means not only homogeneous in efficiency but also homogeneous in the MAPMT gain. Using the DiRICH read out chain, the homogeneity in gain is certainly more important, as one DiRICH module i.e. one fully equipped DiRICH backplane has one common power module and thus supplies six MAPMTs with the same supply voltage. The supply voltage plays a key role because a variation in supply voltage translates to a variation in the pulse amplitude of a photon signal. In the worst case, a too low supply voltage means that the resulting gain of the MAPMT is too low and thus the average single photoelectron signal drops below the detection threshold. Increasing the supply voltage, the total charge delivered over time by the MAPMT's anode pads increases exponentially. This lowers its lifetime exponentially[17] and a compromise between measurability and longevity needs to be found. In the HADES RICH one therefore needs to group MAPMTs with similar gain for a set supply voltage onto one backplane. After deriving suitable groups of six MAPMTs one then needs to derive the correct supply voltage setting to operate all MAPMTs at a suitable gain-level. The derived procedure for grouping MAPMTs is laid out in this chapter also showing results on the final grouping, as well as discussing the final supply voltage settings. The procedure, from now on called "*alignment*", starts with selecting a suitable subgroup of the 1100 MAPMTs, as the HADES RICH only uses 428 out of those. With the HADES RICH being a triggered detector it has less strict requirements on the dark-rate, allowing to chose the MAPMTs with higher dark-rate, leaving MAPMTs with lower dark-rate for other detectors and measurements. To have enough spares and allow for better gain-grouping later, a subgroup of 500 MAPMTs is chosen, by taking the 500 MAPMTs with the highest dark-rate.

## 2.5.1 Definition of a suitable gain-related quantity for the MAPMT grouping procedure

The subgroup of the 500 chosen MAPMTs is now subdivided into gain-classes. Hereby the gain classes must not necessarily be derived using the average MAPMT gain. In fact, as gain variations per pixel are quite large, it might be even better to orient oneself at the lowest pixel-gain of the respective MAPMT such that even this pixel's single photoelectron response always ends up above the detection threshold. Obviously taking only the lowest pixel-gain would not work proper, as the uncertainty on the single pixel-gain measured with the test bench is quite large. In addition, the uncertainty of the test bench is the largest for lowest gains[18]. Therefore, an alternative method using the average gain of the lowest "10+3" pixels is more feasible. The average over "10+3" means, that one takes the 13 pixels with the lowest gain from which the lowest three pixel-gains are disregarded taking the average over the leftover ten pixels. This helps

---

[17]Lifetime for MAPMTs is measured in $^C/_{cm^2}$ and refers to the anode charge seen by the MAPMT after which the MAPMTs performance degrades.

[18]The reason for that lies in the set up of the ADC, whose lower end in the resolvable charge spectrum is too high in order to fully measure lowest gains, thus shifting the measured gain, for pixels with low gain, to slightly larger values.
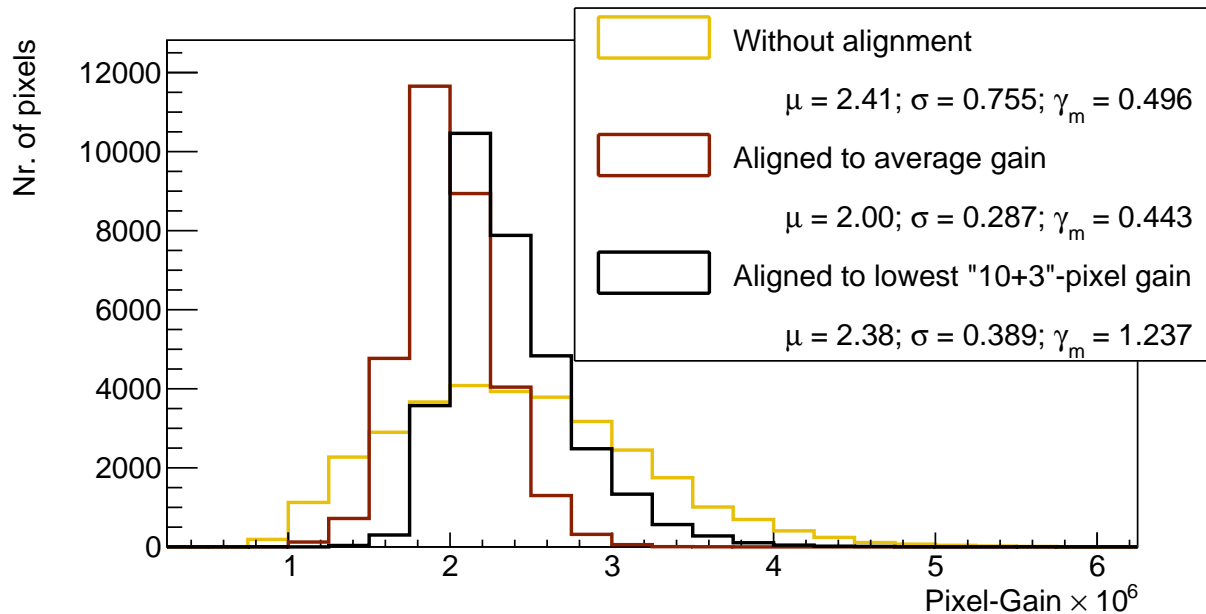
**Figure 2.15** ♦ *Illustrative view on a simulated gain alignment comparing different methods deriving the MAPMT gain used for alignment. The pixel-gain of the 500 noisiest MAPMTs is shown, applying no alignment or different linear shifts to the pixel-individual gain according to an MAPMT individual "representative" gain. This representative gain is either the MAPMT average, or the average over the 13 pixels with the lowest gain but excluding the absolute lowest three pixels ("10+3"). The mean μ, the standard deviation σ and the skewness $\gamma_m$(third standardized moment) are shown for each distribution.*

rejecting outliers but still having a large enough sample to properly determine the response of the pixels with lowest gain. To illustrate the impact of both approaches, "gain-aligning" according to average gain or lowest "10+3" pixel-gain, a toy simulation is made. Hereby, almost like later in the real setup, the average gain or lowest "10+3" pixel-gain is used as baseline. This MAPMT individual "representative" gain is then shifted linearly to a set gain, which is the same for all MAPMTs, thereby shifting also all other pixel-gains linearly[19] by the same amount. This means, that e.g. the average gain of an MAPMT would correspond to the set gain after the this "alignment". This is done by multiplying the fraction of set gain ($2 \times 10^6$) divided by the "representative" gain onto the gain of each individual pixel. The originally measured pixel-gains and resulting pixel-gains for the two different methods are depicted in figure 2.15. One can clearly make out that the distribution using the average MAPMT gain for alignment is the narrowest and peaks at exactly $2 \times 10^6$ as expected. Compared to that, the alignment using the lowest "10+3"-pixel-gain shows a mean slightly right of the set-gain and a slightly larger width. These deteriorations in mean and width are however overshadowed by the steep increase at $2 \times 10^6$. This steep increase can also be seen in the integral over those three distributions in figure 2.16 and in the much larger skewness $\gamma_m$. Thus, as result from this toy simulation one finds support for using the "10+3"-pixel-gain, as through this procedure most pixels with the lowest gain are forced above the set gain, while not loosing much in terms of overall spread in the gain of all pixels.

---

[19]Linear scaling of the gain is hereby only used as an approximation for this toy simulation
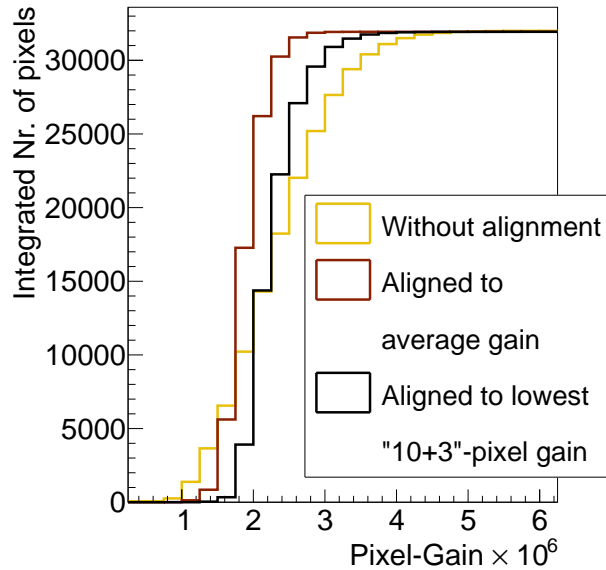
**Figure 2.16** ♦ *Illustrative view on a simulated gain alignment comparing different methods deriving the MAPMT gain used for alignment. The plot represents the integral over all pixels left of the respective bin. This means that all pixel-gains below a certain pixel-gain are shown in the according bin. The non-integrated data is shown and explained in figure 2.15*

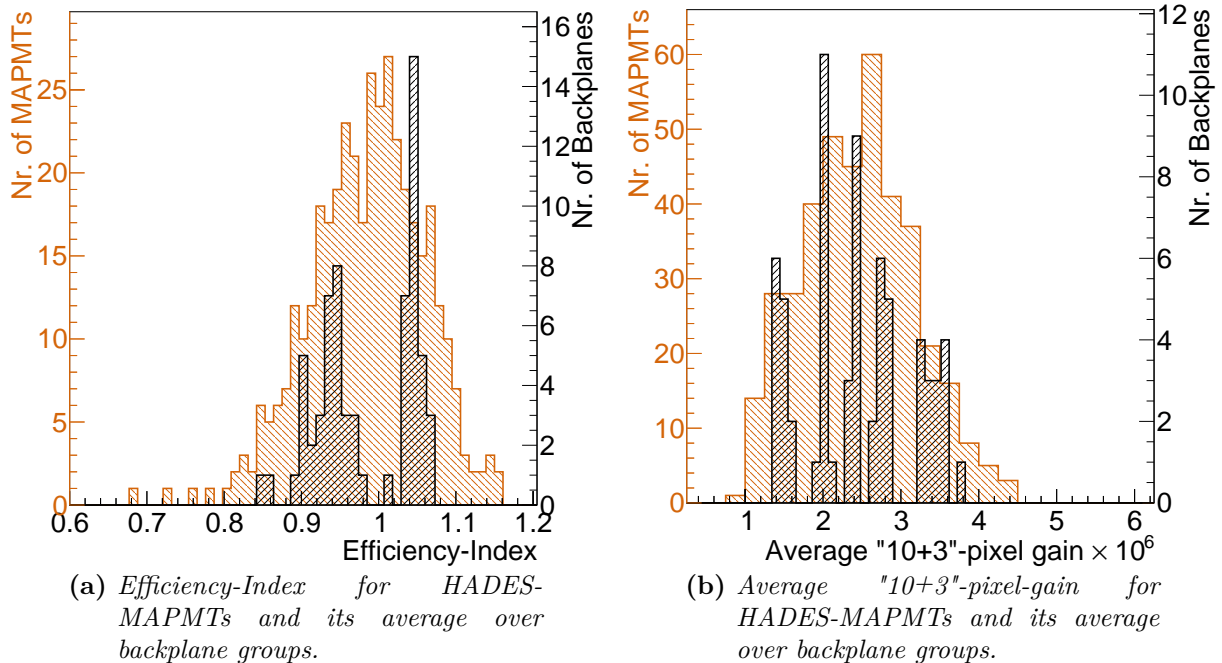### 2.5.2 Grouping the MAPMTs according to their gain and efficiency

After determining a representative gain for each MAPMT it comes to grouping all MAPMTs. For the HADES setup five different gain-classes are chosen based on the presented representative gain estimate for each MAPMT. Those gain-classes shown in table 2.1 are derived by choosing a

**Table 2.1** ♦ *Different gain classes chosen for the HADES RICH. The gain-classes are derived by grouping equal amounts of MAPMTs from the 500 MAPMT subsample into five different classes according to their "10+3"-pixel-gain.*

| Gain-class | Upper bound | Lower bound |
|:---:|:---:|:---:|
| 0 | $5.52 \times 10^6$ | $3.00 \times 10^6$ |
| 1 | $3.00 \times 10^6$ | $2.60 \times 10^6$ |
| 2 | $2.60 \times 10^6$ | $2.24 \times 10^6$ |
| 3 | $2.23 \times 10^6$ | $1.82 \times 10^6$ |
| 4 | $1.81 \times 10^6$ | $0.98 \times 10^6$ |

suitable number of categories first and then populating those with the same number of MAPMTs. Thereby the bounds of each gain-class result from the "10+3"-pixel-gain of the fringe MAPMTs of that class. This subdivision into five gain-classes allows to distribute the MAPMTs within these classes such that all MAPMTs in the same class can be driven with nearly the same supply voltage. As there are still many MAPMTs within one class one furthermore retains the option to focus on a homogeneous efficiency distribution. To further simplify the process, all MAPMTs are again subdivided into two different efficiency-classes from which the more efficient MAPMTs are used in the inner part of the HADES RICH detector whereas the less efficient are placed on the outside. From the sub selected 500 MAPMTs now grouped into gain-classes and within those also in efficiency classes, one now tries to find suitable groups of MAPMTs such that the average efficiency for each backplane is the same. This is achieved by always finding three pairs of high and low efficient MAPMTs from the same category and placing them on one backplane. This iterative process assures that always the highest and lowest efficient MAPMT in one gain and efficiency-class, are found on one backplane. The Efficiency-Index of

all MAPMTs used and the average Efficiency-Index per backplane can be found in figure 2.17a, where it becomes apparent that the procedure produced two rather narrow distributions in efficiency with efficiency varying by $\sim 10\%$ between the two groups. Albeit the last step being the grouping with regards to efficiency, also the average gain per backplane is properly centered in each gain-class as shown in figure 2.17b.



**(a)** *Efficiency-Index for HADES-MAPMTs and its average over backplane groups.*

**(b)** *Average "10+3"-pixel-gain for HADES-MAPMTs and its average over backplane groups.*

**Figure 2.17** ♦ *Distributions of Efficiency-Index and average "10+3"-pixel-gain plotted as average over all backplanes and for all MAPMTs in the HADES RICH. The orange histogram together with the (orange) left y-axis displays the distributions for the MAPMTs whilst the right y-axis (black) together with the black histogram visualize the distribution of the backplane-averages. Backplane-average hereby means, that the individual variable is averaged over all MAPMTs grouped on one backplane.*

### 2.5.3 Determination of backplane individual supply voltages

Having all MAPMTs grouped, one further needs to obtain the supply voltage for each of those backplane-groups aiming for a similar overall gain on each backplane. Before deriving the correct supply voltage setting for each backplane one first needs to understand another measurand acquired by the test bench not fully laid out up to now. The test bench is connected to a remotely controllable supply voltage crate which allows for supply voltage dependent measurements. One such measurement was carried out for each individual MAPMT, where the average gain was studied for a fixed set of supply voltages. This measured dependence of the gain $\mu$ on the supply voltage $V$ can be fitted via

$$\mu = a^n \cdot \left(\frac{V}{n+1}\right)^{kn},$$

with $n = 10$ the number of dynode stages and the free parameters $k$ and $a$, as derived in [Tos+07, p. 47]. The required supply voltage for a certain gain can then be calculated using the

parameters extracted from the measurement and fitted using the inverse formula

$$V = \mu^{1/kn} \cdot \frac{n+1}{a^{1/k}} \,.$$

As only the average gain was measured for different supply voltages and thus the extracted parameters are referring to the behavior of the average gain, a similar dependence of the lowest pixel-gain is adopted. For the HADES RICH, the target-gain was set to $\mu = 2 \times 10^6$, leading
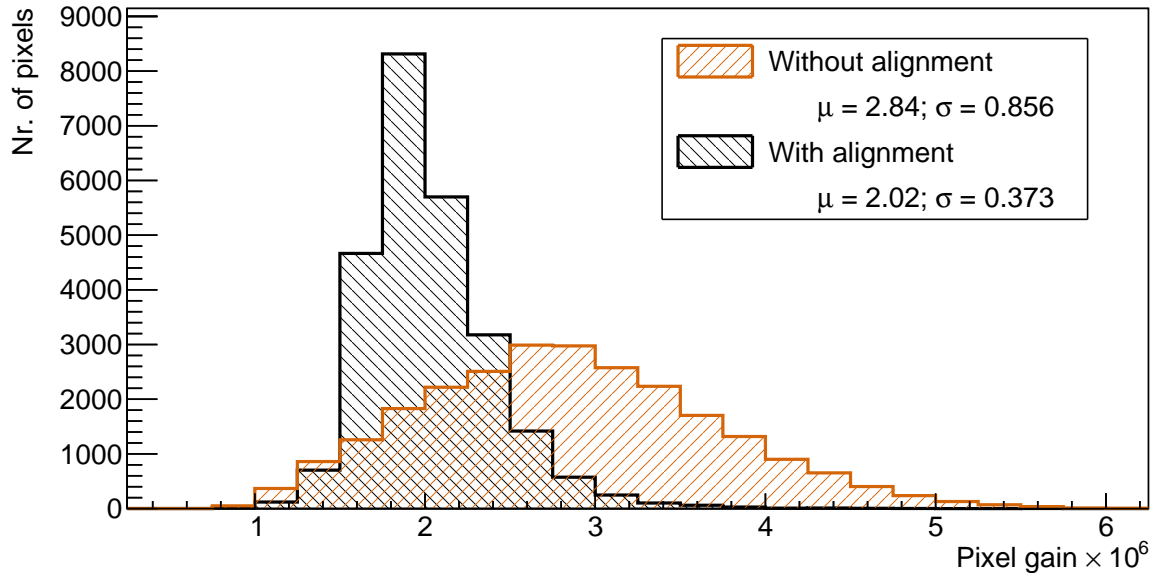


**Figure 2.18 ♦** *Pixel-gain for all MAPMT pixels in the HADES RICH, with and without applied alignment. "Without alignment" refers to the pixel-gain at nominal 1 kV supply voltage. "With alignment" by contrast shows the pixel-gain after applying the derived supply voltage setting for the individual backplane group of MAPMTs. As the exact response of each pixel for different supply voltage settings is not known, the average response is adopted linearly for the individual pixel. The $\mu$- and $\sigma$-values refer to the mean and standard deviation respectively.*

to a good separation between noise and single photoelectron peak[20]. In figure 2.18 the resulting gain per pixel of all MAPMTs is illustrated using the obtained supply voltage settings versus using 1000 V for all backplanes. The narrowing in the overall pixel-gain distribution becomes immediately apparent, featuring a width little more than half of the original standard deviation. Also the average of the distribution moves to the targeted gain of $\mu = 2 \times 10^6$. Comparing this figure to figure 2.15, where the theoretical improvement was laid out, a key observation can be made. In the real setup one can see that the average pixel-gain after applying the correct alignment is much more centered at the target-gain comparing it to the simulation. This behavior stems from the problem, that the obtained supply-voltages could only be derived by means of the MAPMTs' average gain behavior, i.e. the test bench setup only measured the dependency of the average gain on the supply voltage. One could therefore say that the resulting distribution resembles the shape of the "Aligned to lowest 10+3-pixel-gain"-distribution seen in the toy simulation, but with its mean at the target-gain. Albeit being not completely desired, this behavior is not detrimental at all, as the overall steepness of the left side of the distribution

---

[20]The resulting supply voltage settings are depicted in Fig. A.8 appendix pg. 176 where one can still see a slight resemblance of the different gain-classes, derived before.

is still very pronounced. Because of that, only the readout threshold needs to be set slightly lower than one would estimate solely on basis of the target-gain. Still one can clearly conclude, that the applied alignment succeeded in producing a valid set of supply voltage settings.

### 2.5.4 Final MAPMT layout in the upgraded HADES RICH

The final layout of the grouped MAPMTs in the HADES RICH detector is depicted in figure 2.19. There, a visible distinction between inner and outer photon detection plane, and thus grouping of larger and lower efficiency classes, is made through the red rectangle depicted in the figure. Furthermore, red MAPMTs indicate those coated with WLS films. The orientation is shown for each MAPMTs through depiction of the arrow symbolizing Hamamatsu's "start mark". Additionally the serial numbers of all MATPMs are noted.
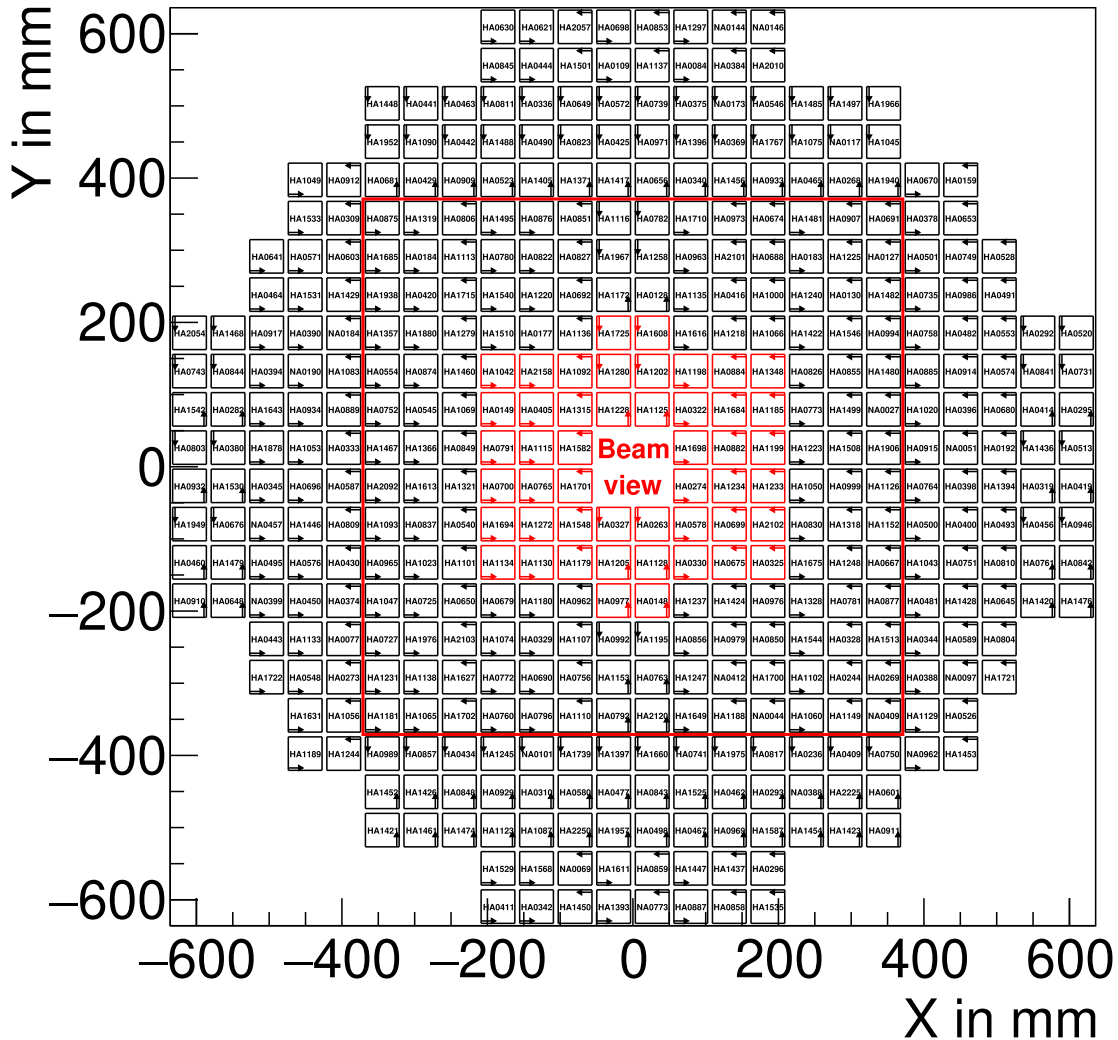
**Figure 2.19** ♦ *Spatial depiction of the arrangement of MAPMTs in the HADES RICH. An arrow at each MAPMT indicates its rotation. The arrow's placement and direction follows that of the "start mark" defined by Hamamatsu in their data sheet [HAM19]. Indicated as red shapes are WLS coated MAPMTs. The large red rectangle marks the transition region from inner to outer photon detection plane. The setup is depicted in a beam downstream view, i.e. from behind the RICH.*

# 3

# Software framework for DIRICH control and first measurements

The DiRICH-FEB being part of the DiRICH read out system, that is used in the HADES RICH, uses a discriminating approach to detect signals. That means, that only signals exceeding a given threshold are measured and the signal's leading edge (LE) time as well as time over threshold (ToT) information stored. Therefore it is extremely important that for each DiRICH channel and thus MAPMT pixel, a suitable signal threshold is found. This chapter will discuss the procedure necessary to derive such a threshold which is incorporated in an according software framework. It starts with a brief introduction to the DiRICH system and especially the DiRICH-FEB (Front End Board). Herein, most notably the discrimination and thus signal detection procedure are discussed. Thereafter the procedure for baseline, i.e. the position of an undiscriminating threshold, determination is discussed. This procedure is based only on low level counters (scalers) in the DiRICH-FEB, counting signals above threshold. By determining this baseline it is always immediately possible to asses the noise band width of the electronics. Thus follows a brief discussion on the impact of different structural modifications to the DiRICH-system with respect to the noise band width. This discussion is based on lab measurements that were carried out before employing the DiRICH system into the HADES RICH. After that, also the final DiRICH set up in the upgraded HADES RICH detector is discussed. Focus lies hereby on the noise in the full detector, the baseline stability and the noise behavior of different channels in the DiRICH-FEB. After discussing the baseline derivation procedure and related analyses, the next step is to derive the actual signal threshold. To derive this threshold, information on the average signal measured by each channel individually is needed. To access this average signal response of the DiRICH, the "differentiated rate spectrum" is introduced. This spectrum again is based on only the low level scaler data and such is the ideal tool to derive the final, channel individual signal threshold. This differentiated rate spectrum is discussed on basis of lab measurements as well as on data gathered in the nearly fully with DiRICH-FEBs equipped HADES RICH.

## 3.1 Introduction to the DiRICH readout chain setup

The DiRICH system consists of twelve front end boards (FEB), a data concentrator (sometimes also called combiner) board, and a power board connected via one common backplane. One such system or backplane group reads out 384 channels, such that every front end board reads out 32 channels. This amount of channels is exactly enough to read out six full MAPMTs. This
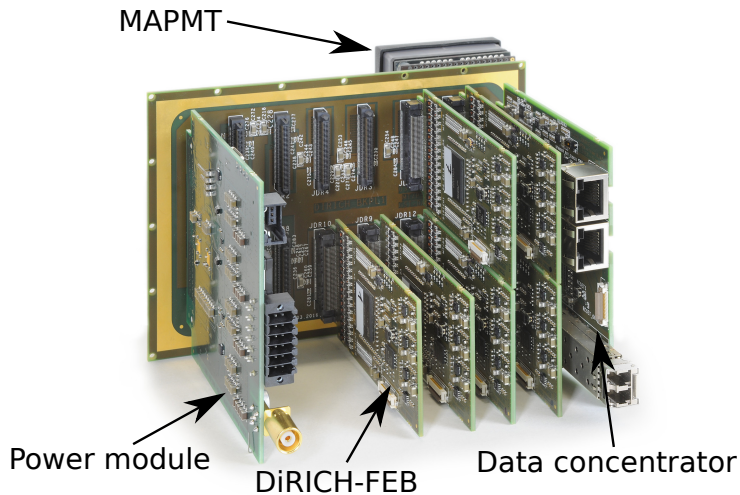
**Figure 3.1** ♦ *Picture of one DiRICH system. Shown are the backplane, the data concentrator module, the power module and six DiRICH-FEBs. On the front side (facing away from the viewer), a single MAPMT is plugged into the backplane. All different components are marked with arrows. This picture was taken by G. Otto (GSI).*

setup is depicted in figure 3.1 showing the backplane with six DiRICH-FEBs, a power and data concentrator module as well as with one MAPMT connected. The backplane is responsible to deliver power to all DiRICH modules and connected MAPMTs, thus delivering high and low voltage. Additionally, all communication between the DiRICH-FEBs as well as the MAPMT signals are routed over this backplane. Thus, running over the backplane are high voltage, low voltage, analog and digital signals. It is for that reason built out of many layers such that spacing between the different traces is large enough. The incoming power connections for MAPMTs and DiRICH modules are connected to the power board. The power board can be equipped with DC/DC converters, such that only one larger voltage needs to be connected to the power module. This one voltage is then transformed to several lower voltages needed by the individual components. For the HADES RICH detector however it was decided that all different voltage lines are directly connected to the power module for reasons discussed in section 3.2. Additionally the power module is used to monitor voltage and current draw by the system. The data concentrator is used to merge the event data measured by all DiRICH-FEBs. It is directly connected to the central data acquisition and also receives the trigger signal from the central trigger system (cf. subsection 1.3.4).

One DiRICH-FEB is used to read out 32 MAPMT channels by means of leading (LE) and trailing edge (TE), and thus time over threshold (ToT). The MAPMT connection to the DiRICH is galvanically decoupled, such that the DiRICH-FEBs ground can be on a different potential to that of its surrounding (especially the MAPMTs). This decoupled input is followed by an amplification stage (pre-amplifier). At this stage, an input capacitance is inserted which works like a low pass on the input stage and thus reduces environmental noise. In several measurements throughout this chapter, this input capacitance was altered to see its impact on e.g. noise suppression. The input signals are then led to an FPGA-based discriminator. This discriminator is based on the LVDS (Low Voltage Differential Signal) input lines of the FPGA. This works as the LVDS input lines come in pairs and give an FPGA internal signal whenever the one line overshoots the (comparative) voltage on its partner line. Thus, if one applies a threshold voltage[1] to one line of the LVDS input, this FPGA input will work as a discriminator. For this

---

[1]The threshold voltages on the DiRICH-FEB are produced by two MachXO3 FPGAs, sitting left and right of

purpose the DiRICH uses one Lattice ECP5 FPGA which has 32 of its LVDS inputs connected to the analog input stages described before. Placed directly after each input on the FPGA is a counting logic which is commonly referred to as "scaler". This scaler simply counts the number of signals crossing the set threshold and thus can give quick access to the current rate in the corresponding channel. The digital input signal is then led from the scaler to the time to digital converter (TDC). One TDC measures the leading and trailing edge of one channel, using the discriminator output described before. In order for that to work, the trailing edge of the channel is delayed through a stretcher. With this setup and after calibration of the stretcher and the TDCs (especially their fine time), timing precisions of up to 7 ps can be reached [Uğu+13]. Throughout this chapter however, focus will not lie on these "high level" TDC-measurands. Instead, only the scaler rate will be used, as it delivers quick low level information on the individual channels without need of any dedicated calibration.

**The setup in the HADES RICH**
The HADES RICH uses 66 3×2-DiRICH modules and an additional eight special 2×2-DiRICH modules. This setup is depicted in figure 3.2. In that figure it is pointed out that some of the 856 DiRICH-FEBs use a different input capacitance. While most DiRICH-FEBs in the HADES RICH run with 1 pF input capacitance, those marked in red use 10 pF. This is mainly a production related artifact but can also be studied in order to better understand the DiRICH system (cf. Subsec. 3.2.3). The orientation of the backplanes is chosen such, that all DiRICH modules on the inner part (which is moved slightly beam downstream compared to the outer) are vertically aligned. This eases the air flow of the cooling applied to the setup, which is particularly important for the inner part.

---

the center FPGA.

# DiRICH map
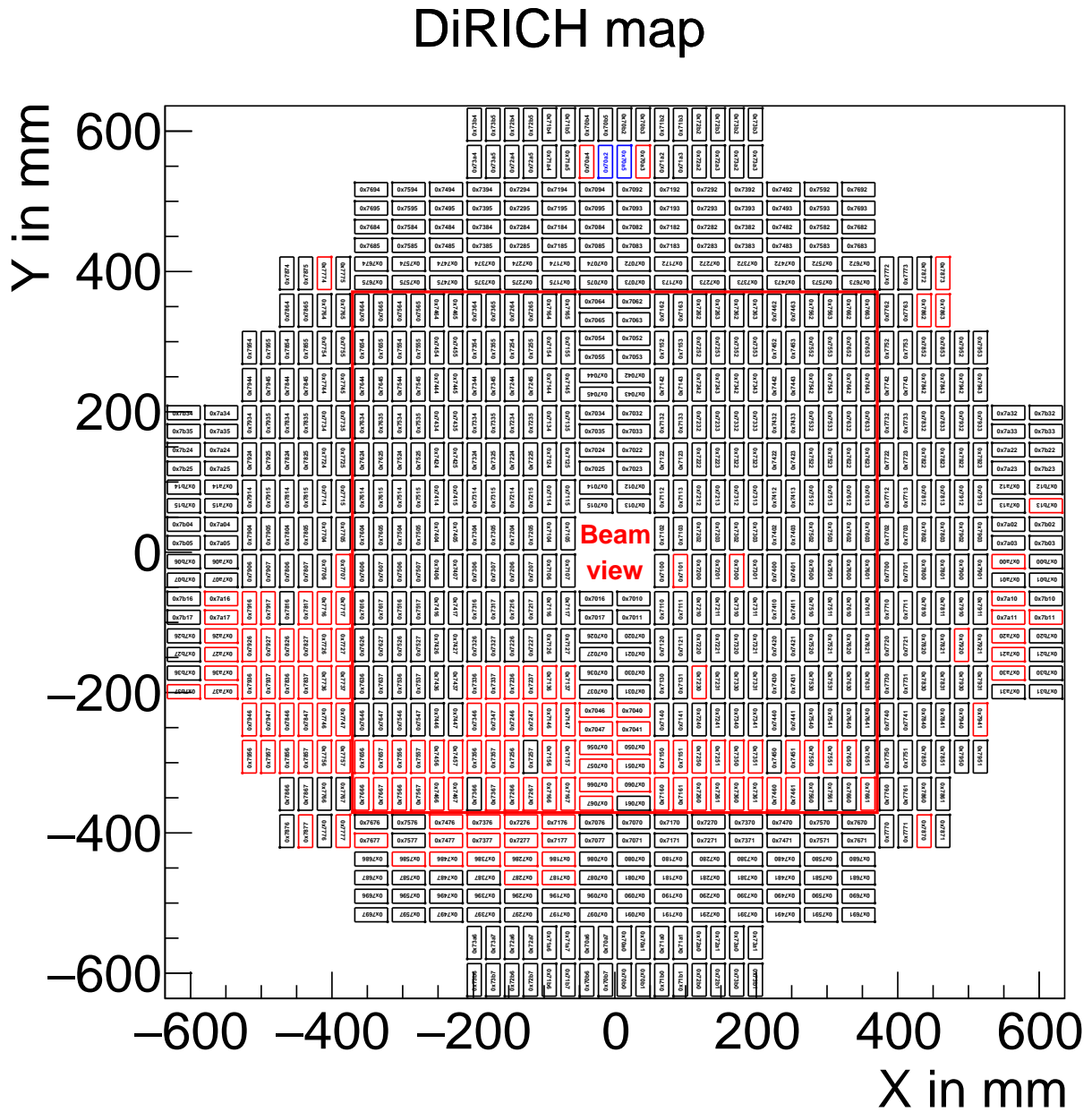


**Figure 3.2 ♦** *Geometrical arrangement of the DiRICH-FEBs in the HADES RICH. A small circle at each DiRICH indicates its first channel and thus orientation. All DiRICH-FEBs are labeled according to the established naming scheme in HADES, thus not depicting which actual DiRICH (referring to serial number) was inserted at the marked place. Indicated through a red shape are DiRICH-FEBs with $10\,\mathrm{pF}$ capacitance at their input stage. In blue indicated are two DiRICH-FEBs at the very top of the HADES RICH detector which were accidentally exchanged among each other. Here depicted is therefore their location following the established mapping scheme. They are later switched in software, i.e. in the HYDRA analysis framework. Indicated as large red rectangle is the transition region from inner to outer photon detection plane. This figure shows the setup in beam view (from behind the RICH). The according backplane map is depicted in* Fig. A.9 *pg. 177 appendix.*

## 3.2 Procedure for baseline determination

As the DiRICH has a floating[2] baseline in combination with a DC-coupled signal discrimination, its determination is key for a precise setting of a signal threshold later. The baseline of one channel refers to that threshold, at which the floating "ground potential" lies. That means, that if the threshold voltage is set exactly to the baseline level, every slight variation in the voltage applied to the channel input produces a signal. For that reason, the baseline can be determined by measuring the rate of pulses exceeding the threshold as a function of threshold voltage. The closer the threshold voltage gets to the individual baseline, the larger the measured signal rate. Thus, the threshold with maximum signal rate directly indicates the baseline position, as there the highest "noise" and thus rate are present. However, this measurement must be altered in a real life measurement as here the maximum rate is capped by the used hardware. This leads to a picture as shown in figure 3.3. Here one can clearly see an exponential increase at the noise edges but a capped rate in the center-region, where the baseline is situated. In this real
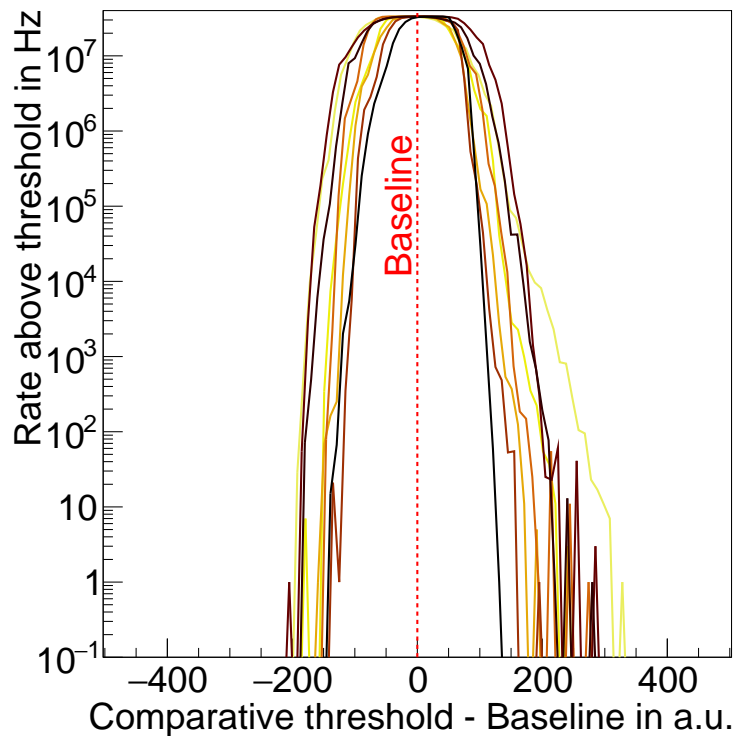


**Figure 3.3** ♦ *Measured rate at varying thresholds for eight of 32 channels of one DiRICH. The thresholds are all centered by subtracting the baseline of each channel from the respective thresholds. The channels of the DiRICH are left open ended leaving only the noise of the baseline visible.*

case the baseline can be derived by searching for the noise edges, where a steep increase is observed. Having both noise edges one can derive the baseline to be centered between those two. Furthermore, with those two edges one can derive a representative noise band width if the method of the noise edge derivation is not altered between measurements. A robust[3] and fast method to search for the noise edges is to search for the first threshold above a certain rate-threshold. The search for this point is carried out by iterating through different thresholds with a fixed step width, each time measuring the rate for that threshold. The rate-threshold

---

[2]Floating hereby refers to a channel individual baseline voltage which might depend on other factors e.g. temperature and supply-voltage.

[3]Robust in this sense means that the procedure should yield reproducible results over many derivations of different channels in different environments.

which needs to be exceeded in order to determine if this threshold is a noise edge, must be chosen relatively high, so that only the noise band reaches larger values. For the DiRICH setup in the HADES RICH a rate-threshold of $50\,\mathrm{kHz}$ was chosen, as it is definitely larger than any rate possibly induced by a single MAPMT pixel[4]. The uncertainty on the derived baseline hereby solely depends on the precision with which the noise band edges are found and thus on the step width. For example, assuming a step width of 100 units the uncertainty of one single noise band edge would equal $2.5\,\mathrm{V} \cdot {}^{100}\!/_{65536} = 3.81\,\mathrm{mV}$. For actual signals, which are pre-amplified at the input of the DiRICH-FEB by an approximate factor of $\mu_{\mathrm{DiRICH}} \approx 25$ (cf. [Kor+20, p. 34]) this means, that this uncertainty of $3.81\,\mathrm{mV}$ actually corresponds to $\sim 150\,\mu\mathrm{V}$ at the input. One simple solution to further reduce the uncertainty given by the step width is to linearly extrapolate between the first measurement point above the rate threshold and last measurement point below. As the improvement using such a simple extrapolation hereby heavily depends on the steepness between the two points, a simple measurement was conducted, measuring the difference in the derived baseline for several measurements of one full DiRICH system, i.e. twelve DiRICH-FEBs, over the course of more than one hour. This measurement can be seen in figure 3.4, where one immediately sees the impact of choosing a step width of $3.81\,\mathrm{mV}$, in the terms of visible peaks at $\pm 1.9\,\mathrm{mV}$. These peaks result from one noise edge being measured one full step width offset compared to the first measurement. Still, using a linear interpolation, also values between those peaks are derived, lowering the standard deviation in the baseline differences to $1.3\,\mathrm{mV}$. Therefore the impact of the linear interpolation can be approximated to $\frac{3.81/\sqrt{2}}{1.3} \approx 2$, where $\sqrt{2}$ is the result of the baseline being an average over two values. It is noteworthy, that no measurement shows a heavily increased standard deviation, indicating that both method and system are stable. To further improve the baseline derivation
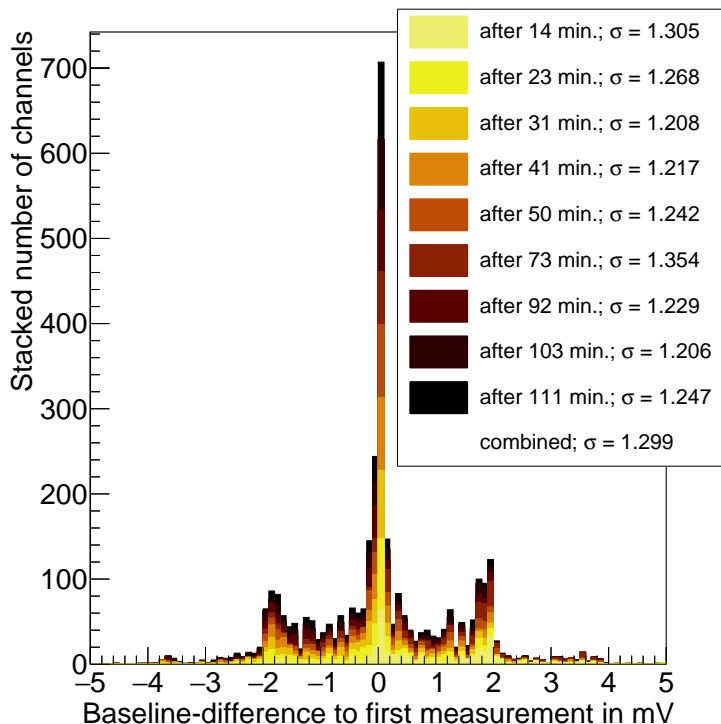


**Figure 3.4** ♦ *Variation of the derived baseline w.r.t. the time of twelve DiRICH-FEBs. Depicted is the difference of each derived baseline compared to the first baseline derived. Each color in this stacked plot represents a different measurement in time. The time difference of each measurement to the first measurement as well as the standard deviation σ can be found in the legend. The baseline is measured with a step width of $3.81\,\mathrm{mV}$ (after pre-amplification). The same visualization for the noise band width can be found in figure A.10 in the appendix.*

in the HADES RICH detector, the search there is performed in two steps. Initially a search

---

[4]Still, during the baseline measurement the MAPMTs are normally left switched off.

with a step width of 75 units is carried out. This search is followed up by a search reducing the step size to 10 units, i.e. 0.4 mV and also limiting the search range to the already estimated baseline position. From there, the linear extrapolation is made with the resulting baseline, being the average of two edges, therefore featuring an uncertainty of approximately $0.4/2\sqrt{2} = 0.14$ mV (after pre-amplification).

### 3.2.1 Impact of input capacitance on the noise band width

The channel individual noise band width of the DiRICH-FEB is influenced by several aspects. Firstly however, the environmental noise impacts the noise band width severely. One way to reduce the environmental noise is to include different input capacitances which work like a low pass filter on the input stage. To test the impact of different input capacitors on the noise band width, a measurement was taken, measuring the noise band width of twelve DiRICH-FEBs with input capacitances ranging from 1 pF to 47 pF. To measure the noise band width, the procedure derived before is used. The measured noise band widths are listed in table 3.1 and clearly show a reduction in noise band width with increasing input capacitance. The reduction herein is

**Table 3.1** ♦ *Impact of different input capacitors at the DiRICH input stage. Measured over three different measurements including seven* 1 pF-*DiRICH-FEBs, one* 10 pF-*DiRICH, two* 22 pF-*DiRICH-FEBs and two* 47 pF-*DiRICH-FEBs.*

| Input capacitance | Noise band width in mV $\pm 1.3$(syst.)[a] |
|:---:|:---:|
| 1 pF | 18.3 |
| 10 pF | 18.1 |
| 22 pF | 13.8 |
| 47 pF | 11.3 |

[a]For this measurement a step width of 100 units was used for the noise band width retrieval.

the largest moving from 10 pF to 22 pF. Also interesting is the minimal change when moving from 1 pF to 10 pF DiRICH-FEBs, this would lead to the assumption, that the effective input capacitance of the 1 pF DiRICH-FEB is actually slightly larger. This assessment is however slightly disfavored, as later studies based on the fully with DiRICH equipped HADES RICH show a more significant difference in these two input capacitances (cf. subsection 3.2.3). This reduction in noise band width is however counteracted by an also lowered pulse height for any measurement signal, i.e. MAPMT-signal which is discussed in section 3.3.

### 3.2.2 Impact of the DC/DC converter on the noise band width

As any DC/DC converter, also that of the DiRICH power-board radiates high frequency noise due to its switching nature. Thus, for the DiRICH read out system one key influence on the environmental noise is that power-board intrinsic DC/DC converter. This DC/DC converter consists of four separate DC/DC-converters all supplied with 35 V. Two of those converters deliver 1.1 V and 1.2 V (PI3311-01) to the rest of the power board, one is responsible for 2.5 V

(PI3312-00) and the last for 3.3 V (PI3301-00). All of those DC/DC converters are buck converters, reducing the input voltage whilst increasing the current through chopping of the input voltage with subsequent smoothing. According to [Vic20b; Vic20a] the switching frequency of these DC/DC converters is in the order of approximately 500 kHz depending on the current drawn by the backplane equipment[5]. This is important, as the described way of estimating the noise band width assumes a minimal noise rate of at least 50 kHz which is clearly exceeded, comparing a single channel measurement in figure A.11 (appendix pg. 178). As an alternative mode of powering the DiRICH system, the different voltages can also be directly supplied to the power module with the DC/DC converter switched off. To determine the influence of said converter, a lab-measurement is made, with and without using the DC/DC converter, i.e. external powering. Additionally, measurements were made attempting to reduce the radiated noise through noise reducing cases (shields), built around the DC/DC converter. These shields are always based on a box shaped copper shield soldered onto the PCB and completely covering the DC/DC stage of the power board. An example picture of this copper shield is found in figure A.12a (appendix pg. 179), where one can see the 0.5 mm copper shielding as a box put over the top of the DC/DC-converters. Additionally tested was an EMV-Shield glued on top of the copper shield (cf. A.12b). The 1 mm EMV-shielding (EFR(10) from Kemet Electronics see [KEM18]) is a self adhesive noise suppression sheet based on a polymer with dispersed magnetic powder throughout the material. Its noise-reducing properties develop their full potential for electromagnetic noise frequencies above 2 GHz. Still there is also an attenuation for noise radiated below 2 GHz, as [KEM18] shows an attenuation of better than $-20$ dB for transmissive noise below 100 MHz. The measurements with the EMV-foil are comprised of three measurements where the EMV-foil was glued on top of the copper caging, below the copper caging, and on both sides. Further, also $\mu$-metal[6] was used as an alternative to the addition of the EMV-foil, to mainly reduce magnetic components of the irradiated noise. This $\mu$-metal also was glued on top of the copper box. Thus overall five individual measurements were made using the different shielding approaches, comparing it two the two standard measurements with and without using the DC/DC converters. For each of those measurements the noise band width is derived and shown in figure 3.5. Clearly visible is that the noise band width gets reduced introducing shielding material. Starting from the measurement without shielding one can see that the full noise band width is mostly impacted by the DiRICH-FEB's position with regard to the power board. The closer the individual DiRICH-FEBs are to the power board the larger the noise band width, hinting towards a large contribution from radiative noise emitted by the DC/DC converters. This irradiated noise seems to have dropped off by roughly a factor of four comparing the DiRICH-FEBs with 1 pF closest and furthest away from the power module. To no surprise one can identify that within one specific distance from the power board, the DiRICH-FEB with the larger input capacitance shows the smaller noise band width. With installation of the copper shielding immediately all noise band widths from all DiRICH-FEBs get reduced significantly. An additional layer of $\mu$-metal on top of the DC/DC converters shows no further reduction whereas the EMV-foil attached to the outside of the copper shielding reduces

---

[5]Due to the hight edge steepness of the switching, probably much higher frequencies, than the switching frequency are radiated by the DC/DC converter.

[6]$\mu$-metal is a metallic alloy comprised of mainly nickel and iron.
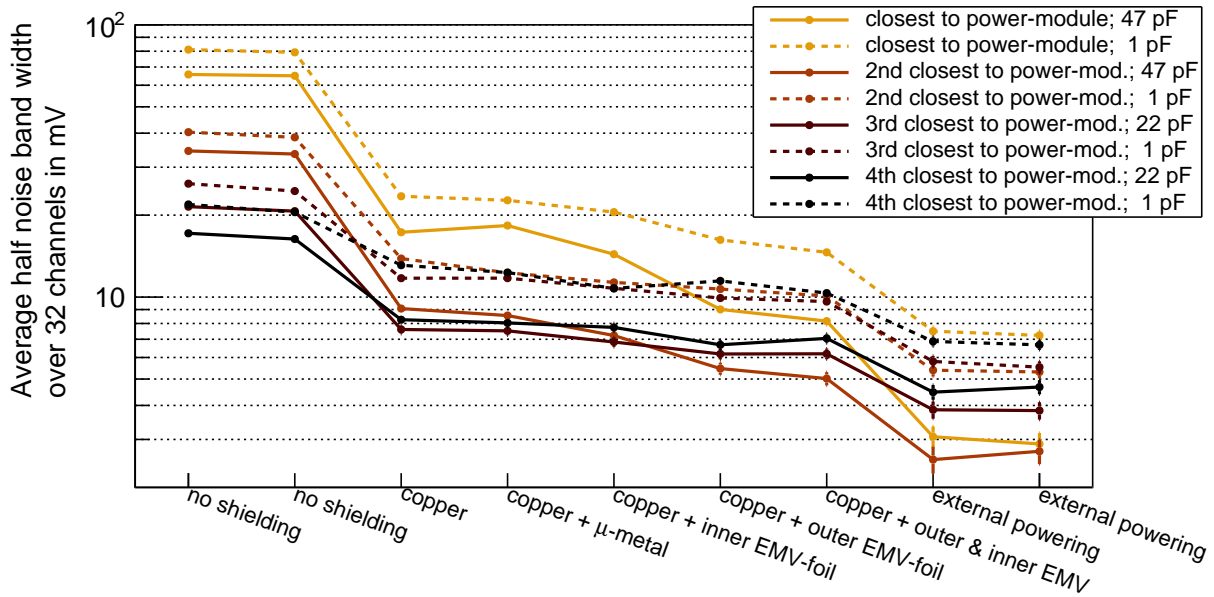
**Figure 3.5 ♦** *Average half noise band width over 32 channels of one DiRICH-FEB with the use of various shielding materials on the power board's DC/DC converters. All measurements except those marked as "external powering" were made with switched on DC/DC converter stage on the power module. The different DiRICH-FEBs have different distances to the power module as indicated in the figure's legend. The solid lines refer to DiRICH-FEBs with larger input capacitances at their input stage. The error bars indicated refer to the systematic error on the measurement.*

the noise band width for those modules closest to the power board even further. In contrast to that, attaching of the EMV-foil to the inside of the copper cage does not show a significant effect on the noise suppression, neither in addition, nor as the only shielding measure. Additionally one can identify that all DiRICH-FEBs further away from the DC/DC converters already reach there maximum in suppression including solely the copper shielding. Only the second closest and closest modules benefit from adding other shielding material. One can therefore argue that the copper shielding eliminates nearly all radiative noise from the DC/DC-converters for DiRICH-FEBs at a distance of at least $4\,\mathrm{cm}$ [7]. This conclusion is supported by the fact, that for those modules no further massive reduction in noise band width can be observed including other layers of shielding material. Clearly visible is, that even with several layers of noise reducing material around the DC/DC-converter one can not achieve a noise band width as small as in the AC-driven mode. This might point to the problem, that not all noise induced by the DC/DC converters is radiatively induced into the DiRICH-FEB input stage but that rather still a small portion of noise is induced by direct coupling over the backplane. Without copper shielding a distance between DC/DC converter and DiRICH-FEB of less than $7\,\mathrm{cm}$ is definitely not sufficient to fully eliminate all radiated noise. To put the noise band widths seen here into context, one can approximate the average single photoelectron signal produced by an MAPMT to be at $\sim 150\,\mathrm{mV}$ after pre-amplification[8], i.e. at the discriminator. This signal level is reached by

---

[7] $4\,\mathrm{cm}$ is the distance between the power module and the second DiRICH-FEB.

[8] The average single photoelectron signal is calculated via $\mu_{\mathrm{MAPMT}} \cdot \mu_{\mathrm{DiRICH}} \cdot R \cdot e / \Delta t = 2\times 10^6 \cdot 25 \cdot 50 \cdot e / 3\times 10^{-9} \approx 150\,\mathrm{mV}$, with MAPMT gain $\mu_{\mathrm{MAPMT}}$, DiRICH-FEB pre-amplification gain $\mu_{\mathrm{DiRICH}}$ (see [Kor+20, p. 34]), $e$ the elementary charge, $R$ the resistivity over which the signal is measured and $\Delta t$ the pulse width.

the noise in the noisiest channel in the unshielded case as can be seen in figure A.13 (appendix pg. 179), immediately rejecting the possibility of using the DiRICH setup with an unshielded DC/DC converter stage. Attaching only a copper shield leaves the measured noise band width to be on average $1/5^{th}$ the size of the average single photoelectron signal. This however does not mean that a detection threshold could be set to such a value as this threshold would still feature a noise contribution in the order of $50\,\text{kHz}$ and, albeit dropping sharply, might still reach out to levels of twice the noise band width. Additionally, even if the average MAPMT signal lies above the noise produced by the DC/DC-converter, the additional noise on the signal might lead to significant deterioration of the ToT, as is described in [GKR15]. Additionally for good ToT measurements one needs a detection threshold far away from the full peak hight, as only then a good separation between different pulse-types can possibly be made. Following the outcome of this measurement that no simple shielding is capable of fully suppressing the DC/DC converter's induced noise, it was decided to drive all DiRICH-FEBs in the HADES RICH detector with external DC supply. Albeit making the process for the HADES RICH more secure one still might consider driving future experiments with the DC/DC converter, if the DC/DC converter is placed further away from all DiRICH-FEBs and/or properly shielded.

### 3.2.3 Noise band width and baseline stability in the HADES RICH

After the discussed lab measurements the DiRICH system was installed in the HADES RICH. Using the external DC powering scheme, i.e. not using the power boards' DC/DC converters, 66 $3\times2$-DiRICH modules and eight $2\times2$-DiRICH modules are distributed according to figure 3.2. The $2\times2$-DiRICH modules are based on special backplanes reading out four MAPMTs using eight DiRICH-FEBs, a concentrator board, and a power board.

For the fully with DiRICH equipped HADES RICH it is interesting to assess the overall noise band width to see if it stays at labratory levels, or if the large system surrounded by other noise sources might negatively impact the performance of the readout chain. Additionally one can use the full setup to also see the impact of the input capacitance as an average over many DiRICH-FEBs. With that many DiRICH-FEBs installed in the HADES RICH, one can even make statements about the channel dependent noise band width w.r.t. the DiRICH-FEBs or the DiRICH-FEB position on the backplane. Measurements in that regard might answer questions if and how the DiRICH system might still be optimized in future. Lastly, it is also necessary to understand the stability of the baseline in the HADES RICH. This baseline stability directly influences how often the channel individual baselines needs to be derived in order to have an overall stable and efficient system.

**Noise band width in the HADES RICH**
Starting with measuring the full noise band width of all channels in the HADES RICH detector using the same procedure as before, the resulting distribution is shown in figure 3.6. This graphic shows clearly, that in all channels an average MAPMT can be read out to half its single photoelectron signal size without any significant noise interference. The average full noise band

width in the HADES RICH detector can be derived to 11.04 mV after pre-amplification. This value is remarkably small reaching levels comparable to that of the lab measurements. To no
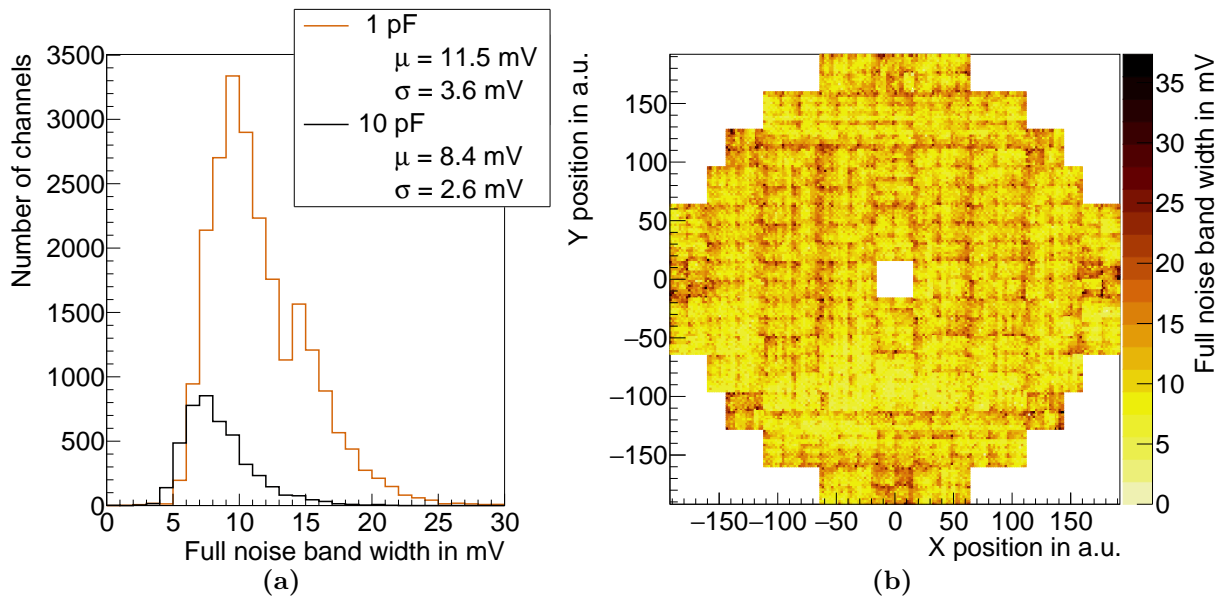


**Figure 3.6** ♦ *Full noise band width distribution over all DiRICH-FEB channels in the HADES RICH detector visualized as histogram **(a)** and spatially resolved distribution **(b)**. The viewpoint in this two dimensional figure is in beam direction. The full noise band width in mV is measured after pre-amplification. The histogram is split for* 1 pF *and* 10 pF *input capacitance with each distributions mean μ and standard deviation σ denoted in the legend.*

surprise the DiRICH-FEBs with larger input capacitance feature a distinctly smaller noise band. It is however remarkable, that this reduction is larger compared to the reduction seen in lab measurements. Additionally one can see in the spatial distribution (fig. 3.6b) that the smaller $2 \times 2$-backplanes show slightly larger noise band widths as can be seen e.g. in the bottom center. Apart from that, the full noise band width is homogeneously spread over the full detector.

**Noise band width variation between backplane and DiRICH channels**

The HADES RICH setup featuring a large quantity of DiRICH-FEBs can be used to study the variation of the noise band width for different DiRICH-FEB channels. This is interesting as one might still decide on slight modifications of the setup for future experiments. Also interesting in that regard is the dependence of the noise band width on the position of the DiRICH-FEB on the backplane. Starting with the full noise band width for the different DiRICH-FEB channels, the distribution showing the average noise band width per channel is depicted in figure 3.7a. Channels one through 16 which are situated on the back side of the DiRICH-FEB, show increasing noise band widths towards the outsides, where channels one and 16 show much larger noise band widths compared to their direct neighbors. On the front side, no such continuous behavior is visible with channel 32 being the noisiest only for an input capacitance of 1 pF. Additionally the average noise band width over all channels on the backside is slightly larger compared to those on the front side. The overall shape of the noise band widths on the back side correlate well with the distances (and thus PCB trace lengths) between connector
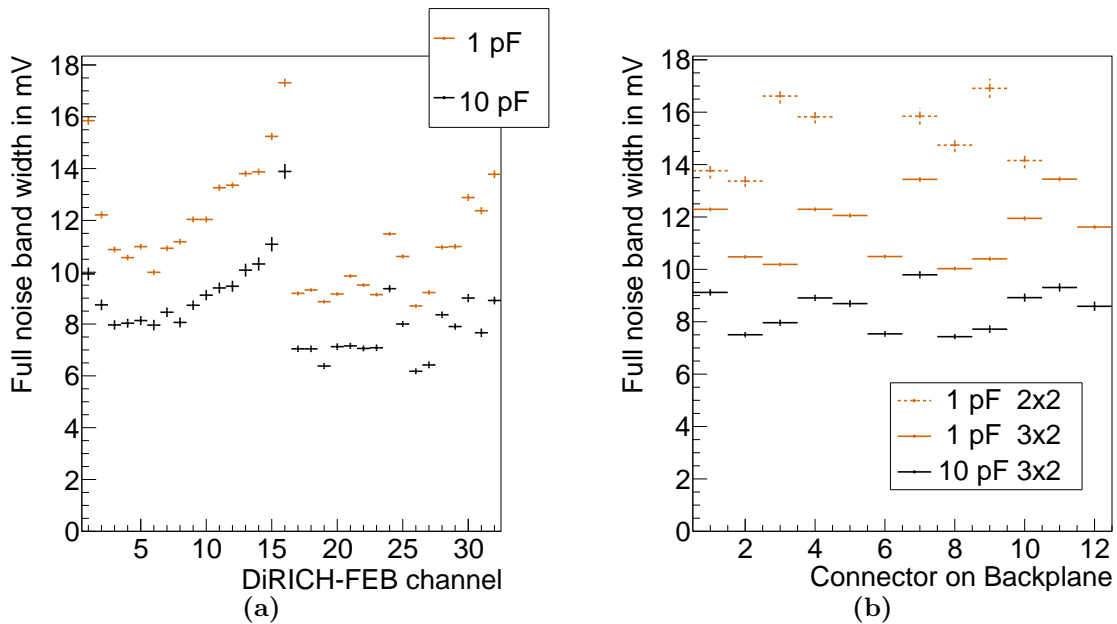
**Figure 3.7 ♦** *Average full noise band width for each DiRICH-FEB channel* **(a)** *and each DiRICH-connector on the backplane* **(b)** *in the full HADES RICH detector. The connectors on the backplane refer to JDR1 through JDR12. The depicted uncertainties in y-direction refer to the statistical uncertainty on the mean. The measured noise band widths are measured after pre-amplification. Each distribution differentiates between DiRICH-FEBs with* 1 pF *and* 10 pF *input capacitance. For the depiction w.r.t. the backplane connector additionally the* 2 × 2*-backplanes and the* 3 × 2*-backplanes are differentiated. For the* 2 × 2*-backplanes using only eight DiRICH-FEBs, connectors JDR5/6 and JDR11/12 do not exist.*

and amplification stage, which are different for each channel, increasing from the center to the sides, with channel 16 having its amplification stage furthest away (cf. [TK17, pp. 11, 22]). The exact behavior, especially for the front side is hard to explain as it certainly relies not only on the exact routing of each channel trace. Taking the average noise band width for each DiRICH position on the backplane, one observes the largest widths for connector JDR7 and JDR11 not exceeding 14 mV after pre-amplification. Both of those connectors are situated on the bottom half of the backplane with the JDR7 being closest to the power board and the JDR11 closest to the concentrator board. With the lowest noise band widths being at 10 mV the overall variation between the different connectors is small. More interesting in that regard are the overall larger noise band widths for the 2 × 2-backplanes as was already observed in the two dimensional distribution hereinbefore. Full noise band widths of up 17 mV after pre-amplification indicate that the 2 × 2-backplane might give the largest room for improvements.

**Baseline stability over time in the HADES RICH**

The last item to check in the fully with DiRICH equipped HADES RICH is its baseline stability over time. This study is important as an unstable baseline would require a repeated baseline determination such that drifting baselines would not lead to inefficient or incorrect measurements. To assess this stability, three measurements over the course of eleven hours were taken, measuring the baseline of all channels in the HADES RICH. The extracted differences between
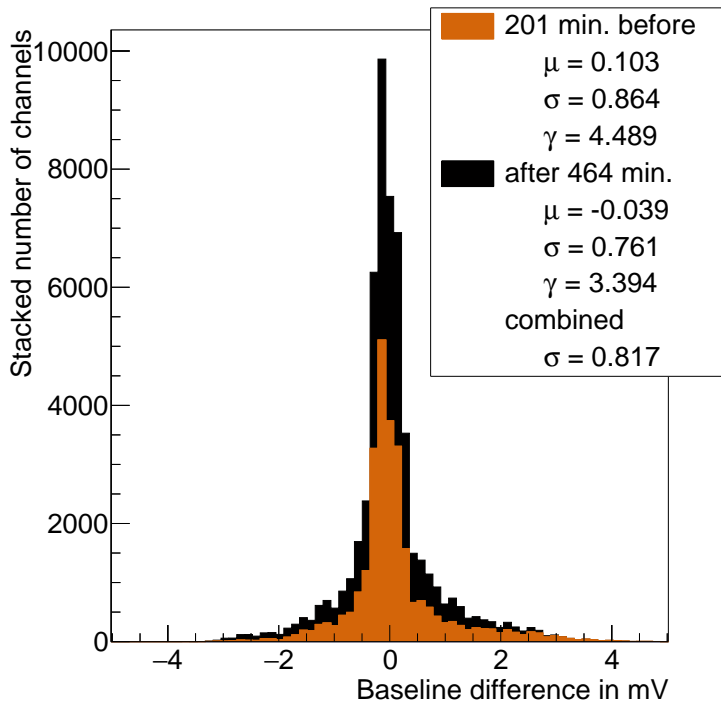
**Figure 3.8** ♦ *Stacked histogram showing the baseline differences in mV after preamplification between three different measurements. All measurements are taken using the fully with DiRICH equipped HADES RICH. The bin width is chosen to be the measurement uncertainty discussed before. The comparison is made between the first and second measurement (201 minutes apart), and between second and third (464 minutes apart). The resulting distributions standard deviation as well as the excess kurtosis are noted in the legend.*

those baselines are depicted in figure 3.8. The total spread of these distributions exceeds the previously derived measurement uncertainty on the baseline by at least a factor five. This behavior is not explicable by temperature variances, which might naturally shift the baselines, as the magnitude of the baseline shift is homogeneously spread over the full detector (see figure A.15 in the appendix), whereas the temperatures are known to fluctuate most in the top region of the inner part of the RICH. Paying closer attention to the shape of the histogram, one can see that indeed the distribution is quite narrow with long tails to both sides, as can be seen in the excess kurtosis[9] being 4.5 and 3.4 respectively indicating leptokurtic distributions. Hereby the center region of $\pm 3 \times 0.14$ still includes 67% of all baseline differences albeit being much lower than the single standard deviation of the whole distribution. This suggests that only very few channels feature larger deviations with the majority of the detector being nearly stable within measurement errors. Furthermore the development over time suggests, that indeed the setup seems to settle over time, as for the later measurement the standard deviation reduces as well as the mean moves closer to zero. The overall variation of the baseline in the (cooled) HADES RICH is therefore so small that a seldom remeasuring of the baseline is fully justified.

## 3.3 Amplitude spectra from rate scans at varying thresholds

After successfully determining the baseline of the individual DiRICH channel, the next step is to find a suitable signal threshold. This detection threshold depends mainly on the actual signal to be measured by the DiRICH, i.e. here the MAPMT signal. A proper threshold for an MAPMT signal provides good discrimination between noise and single photoelectron signal. Normally such a detection threshold is obtained by comparing the charge distributions of noise

---

[9]The excess kurtosis thereby is the kurtosis (fourth statistical moment) minus three.

and single photoelectron signal, which are not retrievable using the DiRICH readout. Therefore an alternative approach will be described in the following, using simple rate measurements at stepwise increasing thresholds.

### 3.3.1 "Integrated" pulse amplitude spectrum

Measuring the signal rate at a given threshold, one naturally measures all pulses above threshold. Thus, measuring this rate for increasing thresholds one retrieves what one might refer to as an "integrated pulse height spectrum". With other words, statistically speaking each pulse with a given height would increase the rate for every threshold lower than its height. Such an



**(a)** *Measured "integral" pulse amplitude spectrum*

**(b)** *Differentiated "statistical" pulse amplitude spectrum*
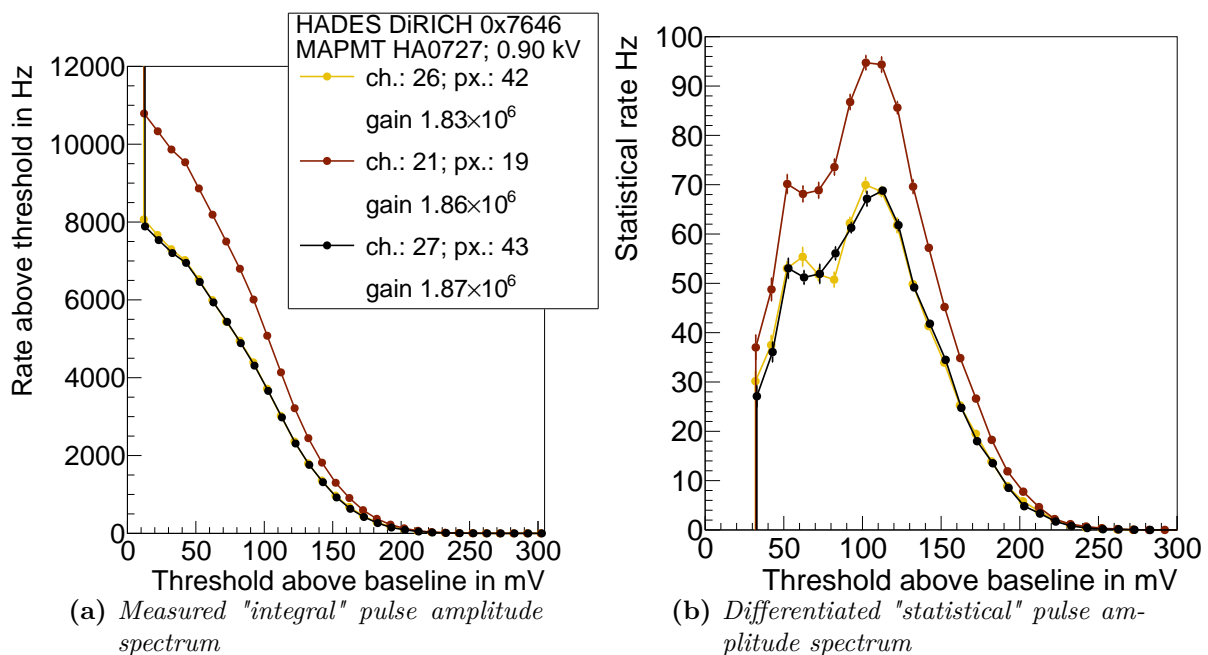
**Figure 3.9** ♦ *Measured rate of pulses above threshold for varying thresholds for three different pixels* **(a)** *and their corresponding differentiated "statistical" pulse amplitude spectra* **(b)**. *The measured pixels are all from the same MAPMT and feature similar gain. On the x-axes the threshold above baseline in mV refers to the threshold of the used DiRICH-FEB relative to its channel-individual baseline after pre-amplification. The measured points in* **(a)** *are the median over ten measurements each measuring the rate of pulses exceeding the threshold, over* 3 *seconds. The statistical rate is derived via the five-point stencil (equation* (B.1)*) with the uncertainties being calculated according to Gaussian error propagation. The Legend shows the used DiRICH-FEB and MAPMT with its supply voltage, as well as the different channels and their gain.*

"integrated pulse height spectrum" is shown in figure 3.9a, where one sees the rate of pulses above threshold for varying thresholds, relative to the baseline. Depicted are three individual MAPMT pixels with comparable gain measured using the same DiRICH-FEB and illuminated with single photons[10] using a laser pulsed with 100 kHz. Each measurement taken at a set threshold consists of ten individual measurements over 3 seconds. To derive the single displayed point per threshold, the median over those ten measurements is taken allowing the rejection of

---

[10]Single photons hereby refers to an average intensity of one measured pulse every ten laser pulses.
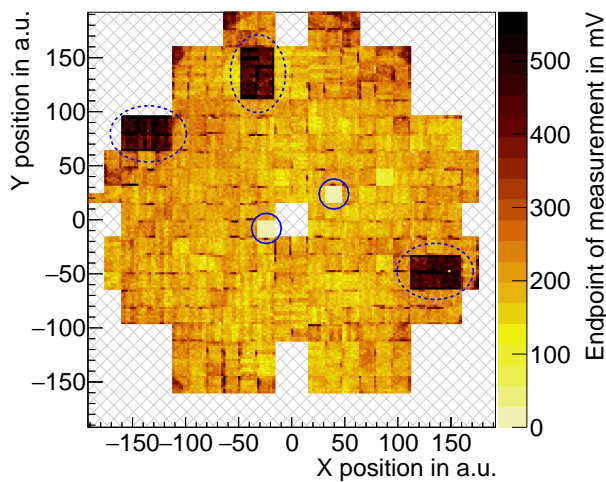
**Figure 3.10** ⬥ *Spatially resolved "endpoints" of rate measurements for each channel in the HADES RICH detector. Endpoint refers to the threshold (mV after pre-ampl.) after which measurements at five consecutive thresholds yield a rate of less than 10 Hz. The gray grid in the background allows to distinguish pixels with early endpoints from unfilled ones. Thereby all empty spaces are either not part of the detector or unequipped for that measurement. The viewpoint in this figure is in beam direction. Two malfunctioning MAPMTs are blue encircled, while three backplanes with too high supply voltage are encircled with a dashed line.*

distinct spikes in the measured rate. The right edge of the noise from the baseline is clearly visible, with the MAPMT's single photoelectron signal being the bump to the right. Directly striking is that one of the three pixels was either exposed to larger amounts of light or to a larger noise contribution. This is visible in the different onsets of the single photoelectron bumps, which equal the integral over the single photoelectron peak. As all the channels have the same gain their measured spectra do end at the same position. This beneficial side effect of measuring the rate above threshold can be used to quickly check large detector systems. Using a partially equipped HADES RICH detector as an example, figure 3.10 shows the endpoints of the rate measurements for each equipped channel. Endpoint of the measurement refers to the threshold at which the measured rate stays below 10 Hz consistently, i.e. for five consecutive increasing threshold settings. With this view one can clearly identify malfunctioning parts in the detector. Those parts include defect MAPMTs where the endpoint is found at a very low threshold (cf. blue encircled MAPMTs). Also incorrectly set supply voltages, where the endpoint of the measurement is at too high thresholds, can be found (cf. blue encircled backplanes).

### 3.3.2 Differentiating the measured integral rate spectrum

Extracting signal information directly from the "integrated pulse height spectrum" is difficult. Easier to interpret is the derivative of this spectrum. This derivative can be understood as difference in the rate between one threshold setting and the next. This difference must then be the rate of pulses with a pulse amplitude in-between those two thresholds. After a special differentiation and smoothing procedure further detailed in the appendix B.1 a statistical pulse height spectrum is retrieved. Such a spectrum is depicted next to its integrated source in figure 3.9b. With this representation of the measured rate spectrum the similar gain of the three depicted pixels becomes observable with the single photoelectron peak being at the same threshold, i.e. pulse height.

This spectrum can be used to understand the behavior of the average single photoelectron
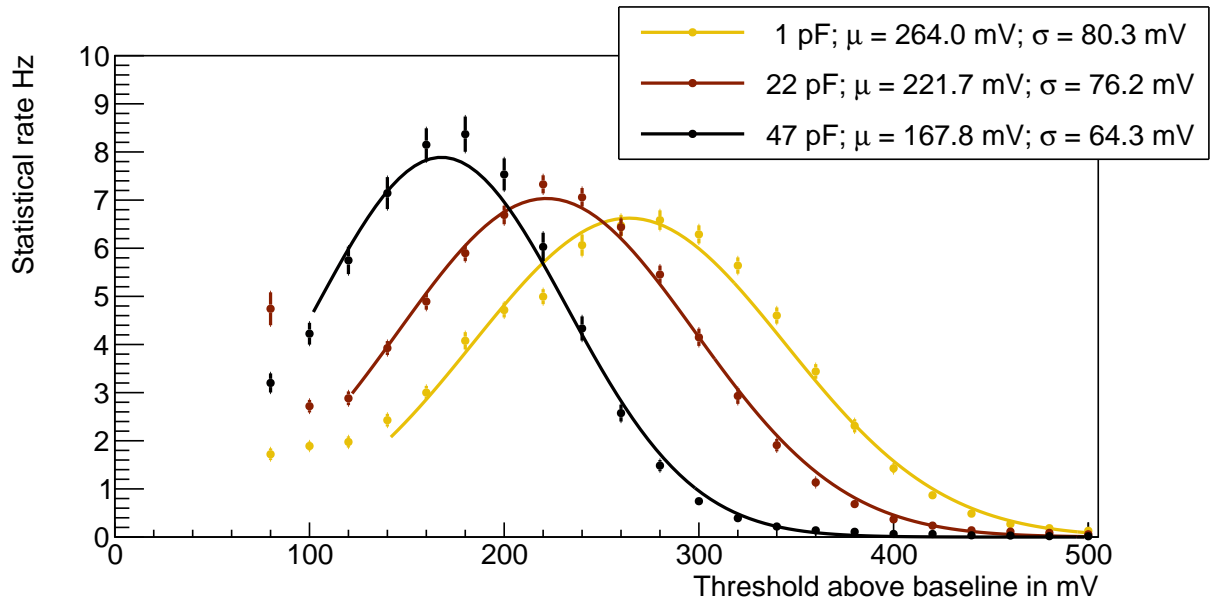
**Figure 3.11** ♦ *Differentiated statistical rate spectrum derived for three DiRICH-FEBs with different input capacitances. All spectra are measured using the same MAPMT half of an MAPMT with a gain of $4.6 \times 10^6$ at $1\,kV$ supply voltage. The derived spectra are fitted with a Gaussian distribution with the mean $\mu$ and standard deviation $\sigma$ denoted in the legend.*

signal amplitude for different capacitances at the DiRICH-FEB input stage. This is done in figure 3.11, where the average single photoelectron signal over one MAPMT half is shown using DiRICH-FEBs with different input capacitance, measured in a lab environment. Shown are the derived statistical rates retrieved as described before. The derived points are then fitted with Gaussian distributions to extract mean and width of the measured single photoelectron signal amplitude spectrum. One can clearly identify the anti-proportional dependence of the average signal amplitude on the input capacitance of the DiRICH-FEB. At the same time also the width of the amplitude spectrum increases with decreasing input capacitance. Dividing each distributions mean by its width to retrieve the relative width one finds a constant reduction moving from lowest to largest capacitance ($3.2 \rightarrow 2.9 \rightarrow 2.6$). This indicates that the measured MAPMT signals indeed get slightly smoothened by larger input capacitances and thus spread less in their width. A large input capacitance of $47\,pF$ however also means, that a detection threshold of $100\,mV$ would result in loosing 30% of all single photoelectron signals while it still includes the 95%-quantile using an input capacitance of $1\,pF$. Therefore the DiRICH-FEBs for the HADES RICH were built with lower input capacitances using a mixture of $1\,pF$ and $10\,pF$ on different DiRICH-FEBs due to availability problems.

### 3.3.3 Estimating the single photoelectron response without differentiation

With prior knowledge of the shape of the MAPMT's single photoelectron response, one can skip the step of differentiation and immediately fit the integral of the assumed single photoelectron signal amplitude distribution to the integrated spectrum. This can be especially helpful to

determine a signal threshold for which one would either way need a final fit to the data[11]. With the single photoelectron signal amplitude distribution assumed to be Gaussian-shaped one therefore must fit an error-function to the (integral) spectrum additionally approximating the tail left of the single photoelectron peak. The resulting fit function to describe the MAPMT response for different thresholds thus is

$$f(x) = \frac{a_{\text{Noise}}}{2} \cdot erfc\left(\frac{x-0}{\sqrt{2}\sigma_{\text{Noise}}}\right) + \frac{a}{2} \cdot erfc\left(\frac{x-\mu}{\sqrt{2}\sigma}\right) \text{, with} \qquad (3.1)$$

$$erfc(x) = 1 - erf(x) = \frac{2}{\sqrt{\pi}} \int_x^\infty e^{\tau^2} d\tau \,, \qquad (3.2)$$

where $x$ corresponds to the threshold and $a$, $a_{\text{Noise}}$, $\mu$, $\sigma$ and $\sigma_{\text{Noise}}$ are fit-parameters. Additionally the edge of the DiRICH-FEB's noise band needs to be approximated. For this purpose the additional error-function is fitted to the left side of the whole distribution, i.e. at center $\mu = 0$. Using this combined fit one then is able to derive the position of the minimum between single photoelectron signal and noise band, commonly referred to as valley via numerical calculations which is shown exemplary for several channels in figure A.14 in the appendix pg. 180. To demonstrate the proper functionality of the described procedure figure 3.12a shows the derived single photoelectron peak amplitude position extracted from the error function plotted against the gain of one MAPMT pixel derived with the test bench described in section 2.4.6. This scatter plot uses the data from a partially with DiRICH-FEBs equipped HADES RICH detector and only includes channels showing an overall proper response. This means that MAPMTs with incorrect HV setting are intentionally left out of this analysis.

A clear distinction is made between fits that approximate the MAPMT's response well and those who do not. To distinguish good from bad fits a high limit on the $\chi^2/\text{ndf}$ is chosen, as the fitted functions must only approximate the measured spectra. Examining the spatial distribution of the $\chi^2/\text{ndf}$ shown in figure 3.12c one can immediately make out that the fit does not approximate those channels well, which are situated on the outer rim of the detector, where the laser intensities are significantly larger compared to the detector's inner part (cf. Fig. 1.22). In the scatter plot comparing the derived single photoelectron peak amplitude position extracted from the fit to the gain of one MAPMT pixel a correlation is visible. This correlation seems to be weak but is to be seen in context of the measurement uncertainties on the MAPMT pixel's gain in the test bench, which is $2.5 \times 10^5$ and therefore quite large. Assuming a linear correlation between MAPMT pixel gain and single photoelectron peak position, one can fit a linear function to the data of the scatter plot. Filling the residuals of the data to the fit into the histogram in figure 3.12b one can see that the spread of this histogram is equal to the uncertainty of the derived pixel gain from the test bench. With this one can conclude that the described procedure produces reliable results. One therefore could use the derived single photoelectron peak position in conjunction with the properly fitted noise tail to set channel individual thresholds. Hereby one should not use the derived thresholds of channels where the difference between measured single pixel gain and extrapolated gain exceeds two times the test bench's measurement uncertainty. Those channels

---

[11]As the individual measurement points for different thresholds still fluctuate significantly, a simple zero-crossing of the second derivative without a preceding smoothing or fitting procedure is infeasible.

(a)



(b)



(c)
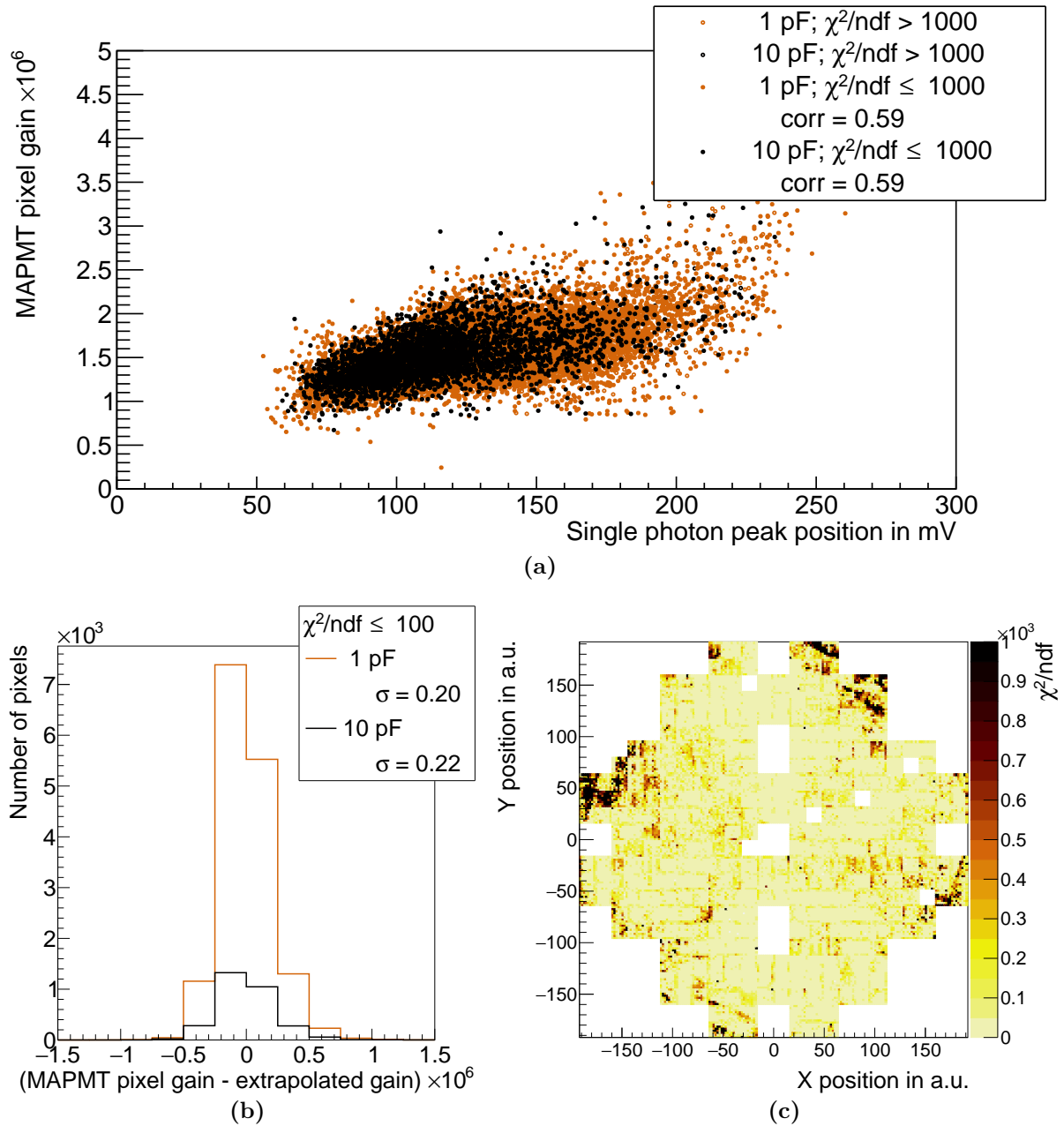
**Figure 3.12** ♦ *Scatter plot comparing the MAPMT pixel-gain derived with a test bench and the single photoelectron peak position derived from a fit of an error function to the measured integral rate spectrum in the HADES RICH* **(a)**. *The Pearson's correlation coefficient using all fits with $\chi^2/\mathrm{ndf} \leq 1000$ is denoted in the legend distinguishing between DiRICH-FEB's with $1\,\mathrm{pF}$ and $10\,\mathrm{pF}$ input capacitance. Residuals with respect to a linear fit to the scatter data are visualized as histogram in* **(b)** *with the standard deviation $\sigma$ noted in the legend for the two different input capacitances separately. Hereby only single photoelectron peak positions from fits with $\chi^2/\mathrm{ndf} \leq 1000$ are taken into account for the fit and the residuals. The spatially resolved $\chi^2/\mathrm{ndf}$ of the fits is shown in* **(c)**, *where the maximum is artificially cut at 1000. The viewpoint in this figure is in beam direction.*

together with the channels featuring a bad fit according to the $\chi^2/\mathrm{ndf}$ make up 1171 channels or approximately 5% of the analyzed part of the HADES RICH detector. For those channels a fixed threshold should be favored.

### 3.3.4 Concluding remarks

The simple integrated rate spectrum and its derivative are great tools to study the detector response directly after its set up without the need of having the full DiRICH readout chain working. Falsely set supply voltages or broken MAPMTs and DiRICH-FEBs can thus easily and quickly be identified. Additionally, the fitted spectra can be used to identify ideal positions for the later signal threshold. The derived spectra and thus thresholds however, depend to a certain degree on the input parameters to the fit. Therefore for the final setup of the HADES RICH detector a more robust approach was chosen, setting the channel thresholds to a fixed offset of 70 mV, after pre-amplification, above baseline. This threshold is far above the DiRICH-FEBs noise band width and still well below the single photoelectron response of all the MAPMTs. This can be deduced extracting the average single photoelectron peak position for an MAPMT pixel with a gain of $2 \times 10^6$ which is according to figure 3.12a above 200 mV after pre-amplification. Using a fixed threshold comes with the additional advantage not to introduce yet another channel dependent parameter[12] which might complicate later low level calibrations such as a ToT calibration. Furthermore the only additional benefit in precisely modeling and fitting the MAPMTs response for different thresholds would lie in a better discrimination with regards to the MAPMT-intrinsic low amplitude noise, which can either way be filtered out to a certain degree using the ToT information.

---

[12]referring to the already existing different pixel gains, supply voltage settings and input capacitances.

# Part II

# Tuning the RICH detector's performance on basis of beam data

The detector performance in many different regards can be optimized through different cuts and calibrations. This part of the thesis starts with an overview on the overall analysis chain employed in HYDRA to then focus on the RICH therein. Further discussed are the event and particle selection, which will be relevant for all following chapters. The analysis results in this part first focuses on preparatory studies (chapter 5), where the effect of the magnetic field in the HADES detector on the RICH is analyzed. Adding onto that, also the choice of radiator gas and the effect of scintillation light from a $CaF_2$ window are investigated, determining any needed changes with regards to the final detector before the first beamtime. From thereon, the following chapters use the data retrieved during the beamtime in spring 2019 to determine cuts and methods to enhance the RICH's performance. First cuts on time and time over threshold are derived, also discussing the different contributions to the time and time over threshold spectra (chapter 6). Following up on that in chapter 7, the best possible global average timing precision in the detector is discussed. This study is not only interesting for the HADES RICH but also helps to estimate which calibrative corrections are necessary in future experiments, using the same readout scheme, to reach certain levels of timing precision. Chapter 8 discusses the usability of the time over threshold information as an estimator for number of photons contributing to the individual signal is covered, aiming for improved separation between single and superimposed double Cherenkov rings. This part of the thesis is completed by focusing on the detector geometry (chapter 9). Deriving a geometry transformation between RICH $x/y$-coordinates and the HADES $\theta/\phi$-coordinates analytically, and additionally investigating the usefulness of a transformation stretching the $x/y$ space in order to reach equal ring radii over the full detection plane.

# 4

# Introduction to the HYDRA analysis chain

Within the HYDRA analysis framework there are two ways of analyzing the recorded data. Most users will only come in touch with the high level analysis of the data which is based on so called DSTs (Data Summary Tape). These DSTs store fully analyzed events and high level data like a reconstructed track and matched RICH ring. DSTs are commonly produced and labeled with a generation tag[1]. Each new generation tag normally results from an improvement in the overall reconstruction quality, mostly due to an improvement in calibration. To retrieve the DST file the full analysis chain starting from the raw .hld-files needs to be run through. This hld-file analysis starts with the data "unpacking". Here, the response of each sub-detectors is unpacked. This, for most detectors, produces first low level hits. Thereon a calibration procedure is applied to form high level hits in the individual detector. Only thereafter the actual matching of e.g. tracks and rings takes place.

**The START calibration**

The important formation and reconstruction of tracks was already discussed in the introductory section 1.3.2 and, in the end, produced a track with a fit quality $\chi_{RK}$ and a matching to the META detectors as well as the RICH. For the RICH of special importance is the START-Hit[2], being the calibrated response of the START detector and thus giving the precise collision time. Building of this hit is done in two steps. First, as all detectors need at least some reference time, the analysis searches for the first START hit within a time window $-25.2\,\text{ns} < t < 25.2\,\text{ns}$. In the second step, after TOF and RPC hits have been reconstructed, the algorithm searches for the exact START hit which sets the average speed of the three fastest particles in the TOF and RPC closest to the speed of light. This new found START-Hit then gives the reference time for all the detector components that need precise timing information.

**Event selection**

Based on the high level information of all detectors, several event selection criteria are established. Those event selection criteria used for most analyses in this thesis will be laid out here. The same cuts are also used in the DST production.

---

[1]Throughout this thesis most results are based on Gen4 data.
[2]More precisely the "HStart2Hit"

| | |
|---|---|
| **kGoodTRIGGER** | Standard trigger, called physics trigger 3 (PT3), requires 20 hits in RPC and TOF coinciding with a hit in the START detector. |
| **kGoodSTART** | Correct START hit according to the afore described procedure. |
| **kGoodVertexClust** (**kGoodVertexCand**) | Vertex cluster (as laid out in the track reconstruction section) has to be found at target area $z > -70\,\text{mm}$, fit of 1(2) particles has to have converged. |
| **kNoSTART** | No further hit with time $t$ on the START detector with calibrated and extracted time $t_{\text{START}}$ with $-15\,\text{ns} < t - t_{\text{START}} < -0.5\,\text{ns}$ and $0.5\,\text{ns} < t - t_{\text{START}} < 15\,\text{ns}$. |
| **kNoVETO** | No VETO detector hit with time $t$ with respect to the START time $t_{\text{START}}$ in the range $-15\,\text{ns} < t - t_{\text{START}} < 15\,\text{ns}$. |
| **kGoodSTARTVETO** | No additional START hit with time $t_{\text{START,add.}}$ from 15 ns to 350 ns that has no correlated VETO hit (meaning found within $t_{\text{START,add.}} \pm 2\,\text{ns}$). |
| **kGoodSTARTMETA** | No additional START hit with $t_{\text{START,add.}}$ from 80 ns to 350 ns that has four correlated hits in the META detectors (meaning found within $t_{\text{START,add.}} + 7\,\text{ns}$ to $t_{\text{START,add.}} + 14\,\text{ns}$). |

Especially the last four cuts are the main cuts to reject event pile up and are thus important to get a clean detector response. As the correct RICH alignment – meaning RICH ring track matching – also depends on the proper reconstruction of the target vertex, also the third cut is very important for a proper functionality of the RICH detector.

**Particle candidate selection**

After selecting proper events next one needs to select good particle candidates. Hereby a particle candidate describes a fitted track that is matched to a META hit and thus has momentum and velocity ($\beta$) information. Momentum hereby actually refers to the momentum over charge information $p/z$ [3], where $z$ refers to the charge number with respect to the elementary charge $e$.

| | |
|---|---|
| **kIsUsed** | This is the standard cut used for particle candidates. In its standard setting it requests that no candidates share hits in any MDC station and the META detector. If any of the detector sub parts are shared, only the one track is used that features overall better fitting. |
| **kIsAcceptedHitInnerMDC** **kIsAcceptedHitOuterMDC** | Requires the inner/outer MDC plane fits to have converged. |
| **kIsAcceptedHitMETA** | Requires a corresponding hit in the META detectors. |
| **kIsAcceptedRK** | Requires the Runge Kutta fit to have converged. |
| **getChi2() < 1000** | Requires additionally that the Runge Kutta fit has to have a good $\chi^2_{\text{RK}} < 1000$ value. |

---

[3]In HYDRA the absolute number of this value is stored as "momentum", where the sign is stored as "charge"

**0 < getMetaMatchQuality() < 3**     Requires a good matching between fitted track and corresponding META cells.

**isGoodMetaCell(4)**     Checks if the fitted particle candidate matches well to a META cell in $y$ after correcting for the measured momentum of the particle. Here the requested maximum distance after correction is $4\,\text{mm}$ (plus the cell's width)

These cuts lay the foundation for a properly reconstructed particle candidate featuring good momentum and velocity ($\beta$) information. When using the RICH detector one should additionally require certain parameters reflecting ring track matching and ring properties, which will be discussed in the next section. When trying to retrieve a pure electron sample, it is helpful to apply additionally sharp cuts on $\beta$ and momentum as well as particle mass $m$ such that the dominating pion contribution in the detector gets reduced. Throughout this thesis, in order to assess the performance of the detector, a very clean electron sample is needed. Therefore cuts on the velocity $0.95 < \beta < 1.05$, the momentum $|p/z| < 250\,\text{MeV}/c$, and mass $m < 50\,\text{MeV}/c^2$ are applied. The effective region of such a cut is visualized in figure A.35 in the appendix pg. 200.

## 4.1 The upgraded RICH detector in HYDRA

The procedure of how the MAPMT responses measured by the DiRICH system are processed to final rings will be laid out here in detail. A brief overview can be described as follows. First, the RICH data is unpacked to form raw-hits ("HRich700Raw"). These raw RICH hits are thereafter calibrated in terms of their leading edge time using the START hit time resulting in so called "RICH-Cals" ("Calibrated hits", "HRichCal"). These "Cals" are used in a ring finding and fitting algorithm to form rings, which in HYDRA are called RICH-Hits ("HRichHit"). However, from now on for the rest of this thesis the more common terms of **"hit"**, describing an MAPMT pixel signal, and **"ring"**, describing a fitted ring, are used.

**Unpacking and creation of raw hits**
Starting with the unpacking procedure, the first step is to calibrate each leading and trailing edge time according to the trigger time of the event. This trigger time is measured by each single DiRICH on input channel number zero as reference time. Per channel a maximum of eleven individual leading or trailing edges can be buffered per event (i.e. readout trigger). Leading and trailing edges within one channel are then combined to form a raw hit with leading edge (LE) and time over threshold (ToT) information. This process of combining the leading and trailing edge is added in form of pseudocode to the appendix algorithm 1 pg. 238. During this combination process a cut on the LE time and ToT is applied. At this point it needs to be mentioned that all leading and trailing edges, i.e. TDC responses are pre-calibrated (i.e. offset adjusted) outside of the HADES unpacker. Therefore a TDC calibration run was made approximately daily using the internal pulser of the DiRICH. This internal pulser produces pulses of fixed width, with

which the DiRICH-FEB's channel individual TDC chain and the corresponding stretcher can be calibrated (cf. [Ama17]). During the production of the raw RICH hits, also the move from a DiRICH-FEB-channel mapping to a PMT-pixel mapping is made. The information, which DiRICH-FEB channel belongs to which PMT pixel is fixed and stored in an according map together with its spatial coordinates. Hereby the naming scheme for the PMTs in HYDRA is shown in figure 4.1. The pixel numbering on the MAPMT always goes from left to right and bottom to top, thus causing pixel one to be on the bottom left and pixel 64 being on the top right of the individual PMT not necessarily reflecting the real pixel numbers of the according MAPMT [4]. It is worth pointing out, that contrary to the normal view beam downstream, the HADES RICH in HYDRA has spatial coordinates such that the view is beam upstream.
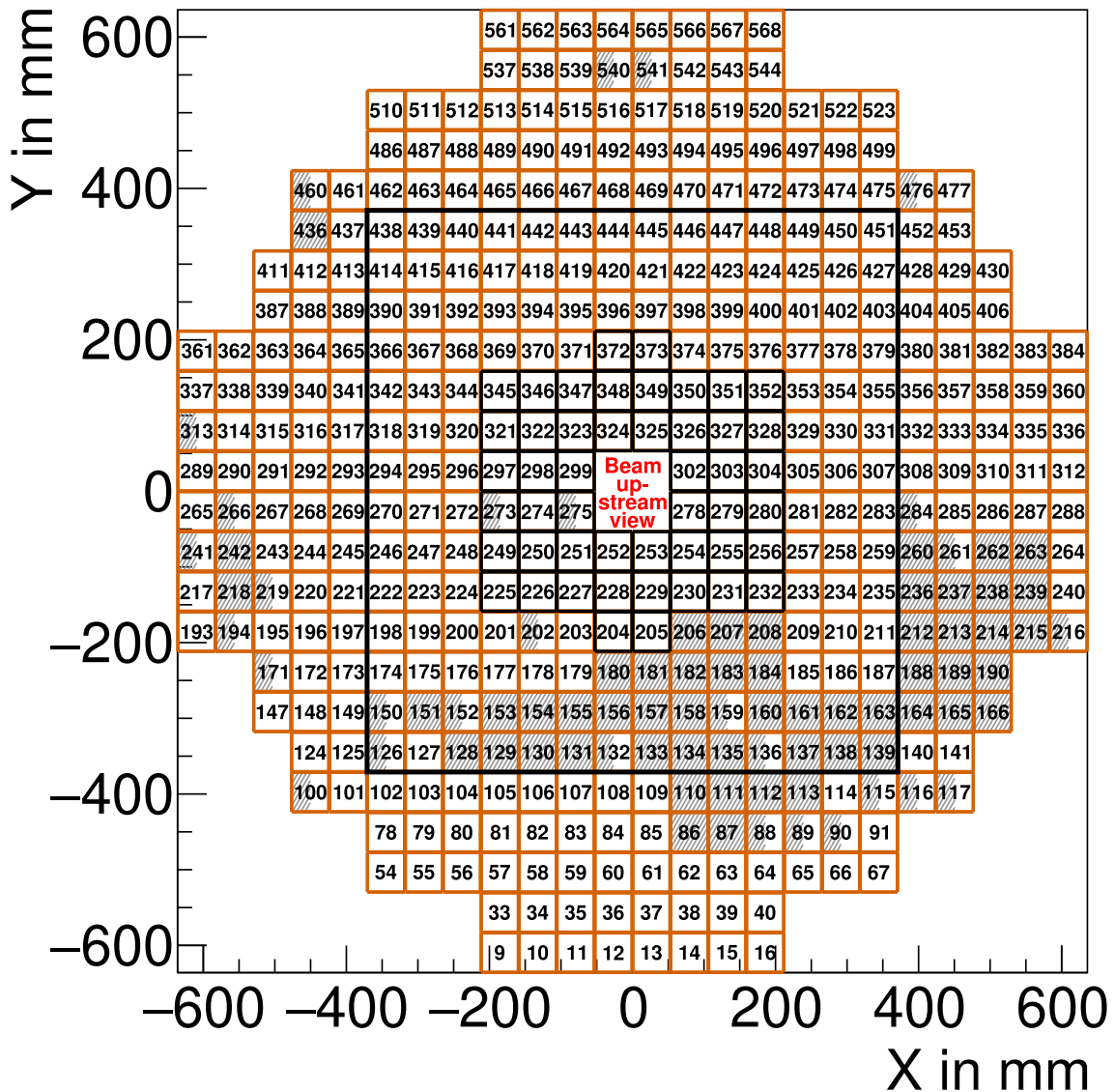


**Figure 4.1** ♦ *Arrangement of PMTs in HYDRA (beam upstream view). Indicated as black boxes are the WLS coated PMTs. The large black box indicates the transition region from inner to outer photon detection plane. Fully hatched boxes indicate PMTs that are read out by two DiRICH-FEBs with 10 pF input capacitance whereas half-hatched boxes indicate those read out by one DiRICH-FEB with 10 pF and one with 1 pF input capacitance.*

---

[4]To see the real orientation of the individual MAPMTs the reader is referred to figure 2.19

**Additional calibration and creation of hits**

The resulting raw RICH hits which at this moment might still be many hits per channel and event are thereafter calibrated using the START detector response. Therefore the event time extracted from the START detector, which is normally found at values around $0\,\mathrm{ns}$, is simply subtracted from the individual raw RICH hit. Thereafter the leading edge time and the ToT of the first raw RICH hit per channel is stored in the RICH hit object. This RICH hit object exists only once per channel and event. Following raw RICH hits are then only used to increase the ToT of the object and the corresponding multiplicity counter. Thus, channel individual RICH hit objects feature the leading edge time of the first raw RICH hit in this channel and the sum over all ToTs of all raw RICH hits in this channel. The impact of this calibration and the overall derivation of corresponding cuts on ToT and LE are further discussed in chapter 6.

**Ring finding and fitting**

In the final step these RICH hits are now used to find and fit rings. The ring finding is based on a localized Hough transformation in $x$, $y$ and ring radius $r$, the details of which are not laid out here but can be found in e.g. [Leb+10]. For this transformation the leading edge time information as well as the ToT of the individual pixel hits are omitted. Based on peaks found in the Hough transform's distribution, rings are fitted to the corresponding area. The extracted rings ("HRichHit" in HYDRA) now have a center position $(x/y)$, a radius, a number of hits contributing to the ring and a fit quality parameter $\chi^2$. This fit quality saved here is easily transformed to the so called ring $dR$ which is used more often throughout this thesis. This ring $dR$ describes the average radial distance of all individual hits to their ring center and is defined through

$$dR = \sqrt{\frac{\sum_n (r_\mathrm{ring} - r_\mathrm{hit})^2}{n}} \; , \tag{4.1}$$

where $n$ is the number of hits counted to the individual ring, $r_\mathrm{ring}$ is the ring's radius and $r_\mathrm{hit}$ the radial distance of the individual hit to the ring center. Using the ring $\chi^2$ saved in HYDRA the equal expression becomes

$$dR = \sqrt{\frac{\chi^2}{n}} \; , \; \text{because } \chi^2 = \sum_n (r_\mathrm{ring} - r_\mathrm{hit})^2 \; . \tag{4.2}$$

The $x/y$ position of the individual ring still needs to be transformed to the HYDRA common $\theta/\phi$ (polar and azimuthal angle) coordinate system. This is done via linear extrapolation between transformation values stored in look up tables, depending on the reconstructed target vertex for this event[5]. A rough $x/y \mapsto \theta/\phi$ is shown in figure 4.2, where also the sector scheme is indicated. This procedure is also discussed in more detail in chapter 9.

---

[5]Actually in a first step only one look up table is used, as the target vertex is not known precisely at the point where RICH rings are first derived. Only after several other reconstruction steps in the whole HYDRA analysis, the $\theta/\phi$ positions are recalculated accordingly.
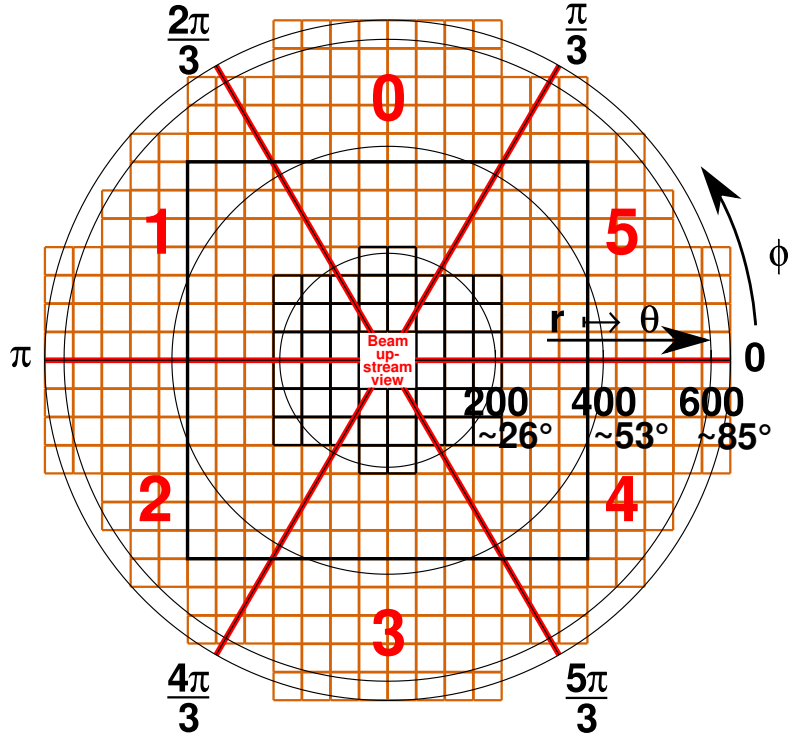
**Figure 4.2 ♦** *Depiction of the RICH configuration in the HYDRA common spherical coordinate system. Red lines repeating every azimuthal angle $\phi = n \cdot 60°$ ($n \in \mathbb{N}$) indicate the spokes in the RICH that split the detector into six sectors. This six sector scheme is found in nearly every HADES sub-detector following the RICH downstream. In the MDC these sectors are separated by gaps between the different MDC planes, such that the RICH spokes do not induce additional inefficiencies. Big red letters indicate the name of the individual $60°$ wide sector. Labels on the radial axis show the radial coordinate in mm and its approximate polar angle $\theta$ equivalent in $°$.*

**Ring matching**

In a last step, the identified rings need to be matched to particle candidates. This is done through the absolute angular difference, sometimes called *dQA*, which is defined as

$$dQA = \sqrt{\Delta\theta_{\text{ring}}^2 + \Delta\phi_{\text{ring}}^2} \, , \tag{4.3}$$

$$\text{where } \Delta\theta_{\text{ring}} = \theta_{\text{ring}} - \theta_{\text{track}}$$

$$\text{and } \Delta\phi_{\text{ring}} = \sin(\theta_{\text{track}})(\phi_{\text{ring}} - \phi_{\text{track}}) \, ,$$

with $\phi_{\text{track}}/\theta_{\text{track}}$ being the particle candidate track's spherical coordinates in the HYDRA framework and $\phi_{\text{ring}}/\theta_{\text{ring}}$ being the spherical coordinates of the ring center. $\Delta\phi$ is multiplied with $\sin(\theta)$ to compensate for the increasing phase space at larger $\theta$ angles.

Later in this thesis not only ring track matching is discussed, but rather bare hits in the vicinity of track candidates are analyzed. A hit is assumed in the vicinity of a track if its distance to the track is lower than a given maximum radial distance plus an additional angular equivalent mirroring the *dQA* parameter discussed before. This procedure is described in full detail in the appendix section B.3 (pg. 239), where the radial distance is detailed in equation (B.3) and the angular equivalent is laid out in equation (B.5).

<div align="right">

# 5

## Preparatory Studies

</div>

Before the RICH detector was taken into full operation, several studies were carried out to answer and fix final open questions and with that ensure good operation of the detector. One of those questions concerned the impact of the magnetic field onto the MAPMTs, with another being related to the scintillation light in the detector. Both those questions are discussed in this section. As this analysis happened way before any calibration of the detector, the extracted spectra are all uncalibrated low level spectra. Thus, the full reconstruction procedure detailed in the section before, was only followed till after the hit building and without any leading edge time and ToT cuts.

## 5.1 Impact of magnetic stray field on efficiency

With the RICH detector being quite close to the toroidal magnetic field in the center of the HADES detector one key check to make, approaching the beamtime in 2019, was the impact of the stray field onto the efficiency of the HADES RICH detector. Already beforehand, measures were taken to reduce the magnetic stray field by attaching a magnetic shield to the outer rim of the RICH detector. This shield is made out of soft iron and encloses the whole RICH detector apart from a few gaps at the points where the spokes are connected to the RICH shell. However, MAPMTs are known to lose efficiency in strong magnetic fields, which is why a measurement series was taken for different magnetic fields using the laser monitoring system in the RICH. For this measurement the magnet was ramped up from 0–3 kA in steps of 1 kA each time measuring the average multiplicity of hits per laser-trigger each pixel in the HADES RICH. Figures 5.1a–c show spatially resolved relative measured rates normalizing each measurement for different magnet currents to the measurement without magnetic field. Immediately eye catching is an increase in relative measured rate near the spoke regions in the RICH. Here the intensities are lowest, due to shadowing of the spokes, such that the relative measured rates show the largest uncertainties. Furthermore, this effect is constant throughout all different magnet currents as can be seen in figure A.17 in the appendix pg. 183 where all measurements are shown relative to the measurement with 1 kA magnet current. Therefore this artifact seems not to be an effect of the increasing magnetic field. Focusing on the histogram in figure 5.1d, where the relative measured rates with respect to the measurement with no magnetic field are displayed for all measurements, one observes an increasing contribution of pixels with relative measured rates below unity for increasing magnetic fields. Those pixels, which are seen as increasingly yellow

spots in the spatially resolved distributions in figures 5.1a–c, are mostly corner rows of single MAPMTs seeing the largest fringe fields. The corner pixels see the largest effects as they are known to be influenced the most from external magnetic fields (cf. Fig. A.18 appendix pg. 184). The largest magnetic field is exerted on the MAPMTs that are placed on the corners of the staggered inner part of the RICH, being much closer to the magnetic coils compared to their direct neighbors on the outer part of the RICH. The edge of the MAPMT suffering the most from the enclosed fringe field is thereby not MAPMT orientation dependent, but is always the edge seeing the largest fields. The strengths of the fringe fields for the different magnet currents can be found in figure A.16 in the appendix. These field strengths are measured by four separated



**(a)** Magnet 1 kA/Magnet Off

**(b)** Magnet 2 kA/Magnet Off

**(c)** Magnet 3 kA/Magnet Off

**(d)** *One dim. comparison histogram*
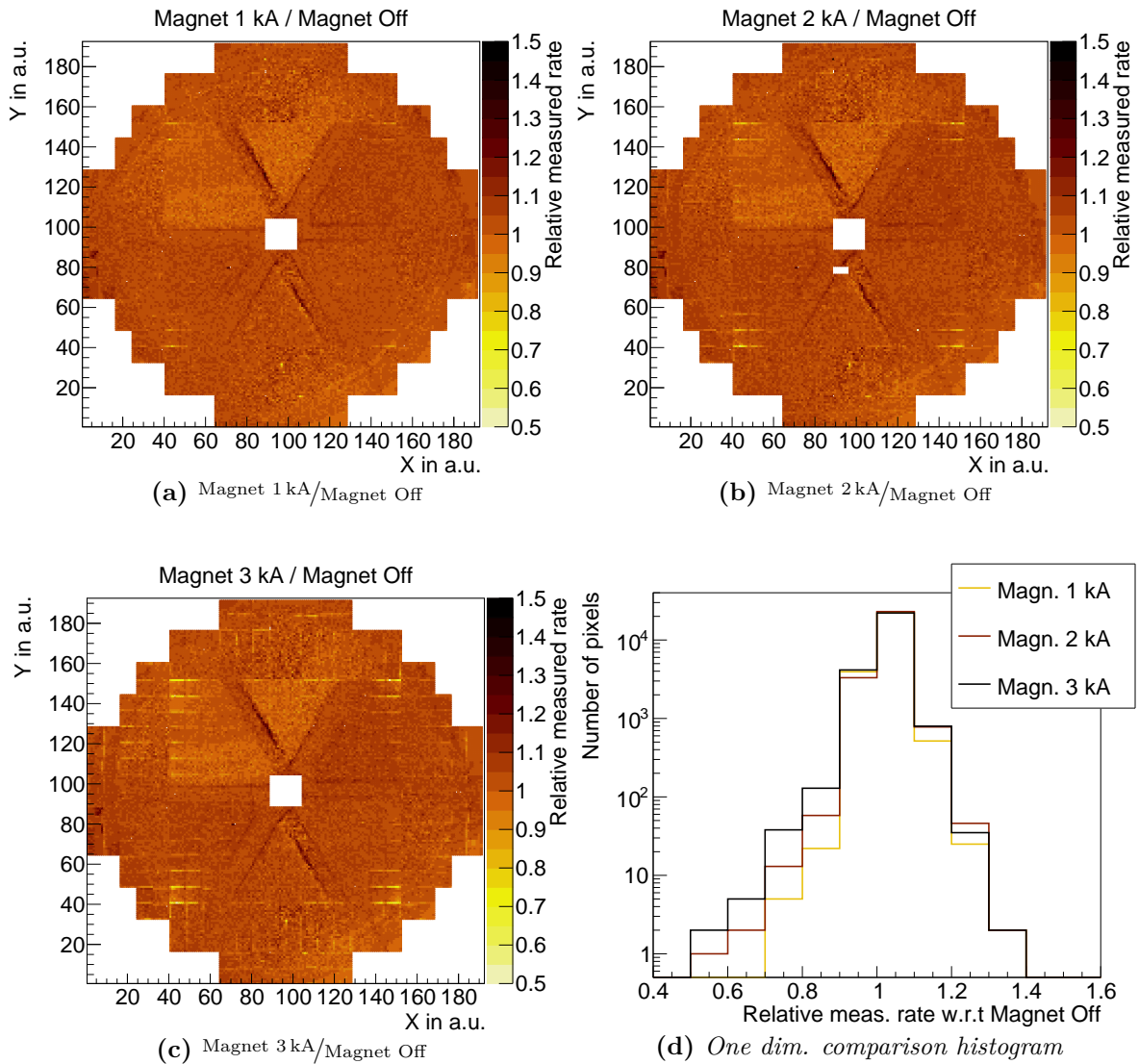
**Figure 5.1 ♦** *Relative measured rate in the HADES RICH for different magnetic fields. Subfigures* **(a)**–**(c)** *display the spatially resolved relative measured rate for different magnetic fields. Thereby for all different magnetic currents the average multiplicity per trigger and pixel in the HADES RICH are normalized to that of the measurement with switched off magnet. Subfigures* **(d)** *displays these relative measured rates as histogram.*

magnetic field sensors on each spoke in the RICH. The measurements show a maximum field of $\sim 2\,\mathrm{mT}$ but also large fluctuations between the sensors on different spokes. Those fluctuations

are not as clearly identifiable looking onto the relative measured rate plots, indicating that the field that acts on the outermost MAPMTs is not exactly that measured by the sensors, which are not situated at exactly the same positions (see A.16d appendix pg. 182). Furthermore, according to measurements carried out by Hamamatsu, the observed efficiency drop of more than 20% would indicate field strengths larger than at least $3\,\text{mT}$ [1].

**Summary**

From the discussed measurements one can only draw the qualitative conclusion that for the analyzed fields only less than 500 of roughly 28000 pixels have an efficiency reduction of more than 20%. Thus, the magnetic fringe fields in the HADES detector do not result in a drastically lowered efficiency of the HADES RICH.

## 5.2 Scintillation light from radiator gas and CaF$_2$ window

Another important preparatory study was carried out checking if the scintillation light emitted by the calcium fluoride CaF$_2$ window, which was needed for the old RICH detector, would produce too much light in the detector and therefore too high rates on the MAPMTs and read out electronics. Therefore test measurements were made, using an Ag beam on Ag target filling the RICH radiator volume with different gases. The Ag beam consisted of approximately $500 \times 10^3$ particles in an average spill hitting the Ag target. During these test measurement the CaF$_2$ window was always inserted. Gases used were C$_4$F$_{10}$, CO$_2$ and N$_2$. Figure 5.2 shows the timing of all registered hits for the N$_2$ filled radiator. Immediately eye catching in this distribution, showing the average number of hits per event, is the long tail after the prompt peak. This tail cannot be produced by the N$_2$ radiator gas, as it's scintillation light features a time constant of $2.5\,\text{ns}$ according to [Leh+15]. The tail is also persistent over all measurements featuring different gases and can thus only be explained by the CaF$_2$ window (see Fig. A.19 and A.20 appendix pg. 185). Additional support for this claim is found by the time constant of CaF$_2$ being $960 \pm 60\,\text{ns}$ (compare [Mik+06]) which compares well to the time constant extracted from exponential fits to the tails in the time distribution of all measurements. This simple exponential decay $(a \cdot e^{-t/\tau})$ is fit to the time range $100\,\text{ns}$ after the prompt peak until the end of data taking in each triggered event, such that scintillation light of the gases – having a small time constant – is negligible. Choosing the fit range this cautiously allows to circumvent an alignment of the timing between different channels, as the decay constant and thus the fit is not impacted by timing offsets. Using the derived parameters of the fit one can extrapolate the impact of the scintillation light from the CaF$_2$ window by taking the integral over different ranges. To study the long term effects of the scintillation light, it is beneficial to compare the amount of light induced by the window to the average dark rate of the MAPMT. For this one needs the average event rate in HADES of $17\,\text{kHz}$, which results in an approximately $58823\,\text{ns}$

---

[1]Here one needs to compare their studies applying magnetic fields along x-axis (moving e.g. over pixels 1,9,17,...,57) from Fig. A.18 (appendix pg. 184), where they find a maximum of $\sim 10\%$ output efficiency loss for $-2\,\text{mT}$ and $\sim 25\%$ for $-4\,\text{mT}$ respectively.
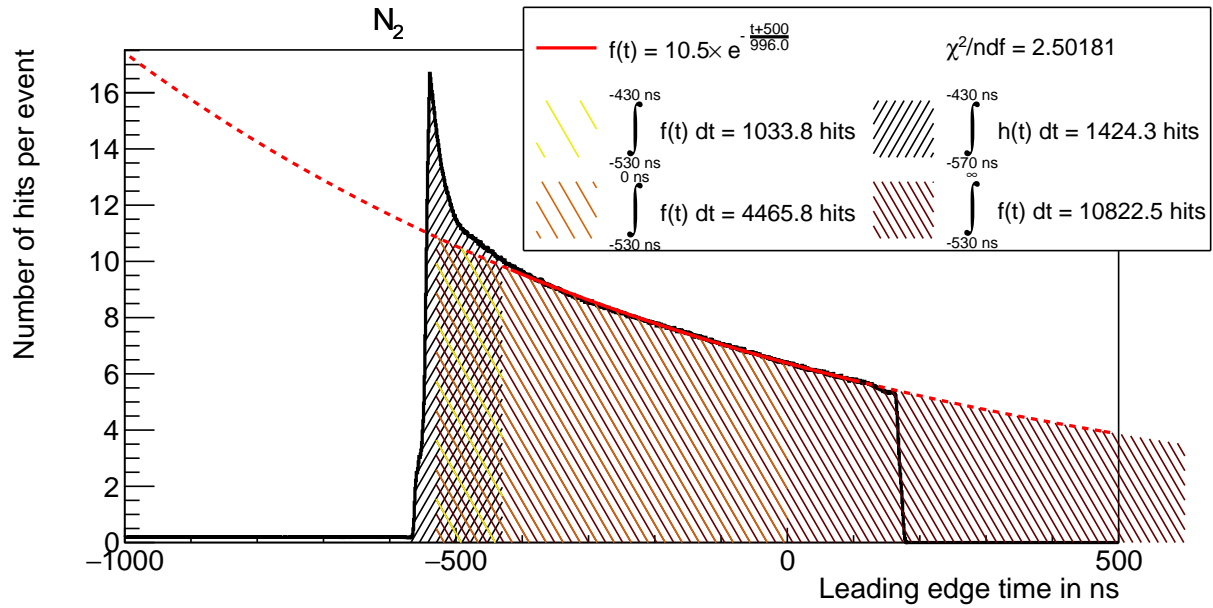
**Figure 5.2** ♦ *Distribution of average hits per event over time measured in the RICH with $N_2$ filled radiator volume, using an Ag beam on Ag target with $500 \times 10^3$ particles per spill. An exponential decay is fitted to the tail of the data (solid red line) being mostly comprised of hits from scintillation photons of the $CaF_2$ window, with the dashed line indicating the shape of the function outside of the fitted range. The dashed areas below the distribution and fitted function indicate the integration ranges denoted in the legend, with the brown dashed area exceeding the drawing pad to indicate the integrals upper edge going to infinity.*

wide time window between two events. Taking the integral from the prompt peak to $58823$ ns [2] and multiplying it with the average event rate then results in the average rate in the detector induced by the window's scintillation light which is to be divided by the number of channels in the detector giving rate per MAPMT pixel

$$17000 \, \frac{\text{events}}{\text{s}} \cdot 10822.5 \, \frac{\text{hits}}{\text{event}} \cdot \frac{1}{27392 \, \text{channel}} = 6.7 \, \frac{\text{kHz}}{\text{channel}} \ .$$

This is much larger than the average dark rate of the MAPMT's pixels in the HADES detector ($\sim 30$ Hz) and therefore would significantly shorten the lifetime of the MAPMTs. This situation is made worse by the fact that most of the scintillation light is produced in the center region of the detector, such that in the most occupied regions in the detector, on average a third of the MAPMT is occupied with scintillation light per event (see figure A.21 in the appendix). Additionally to the problem that the lifetime of the MAPMT gets reduced by the excessive scintillation light one needs to check for immediate effects of the scintillation light during the event. One certain limitation hereby is that the DiRICH readout system is only capable to store up to eleven (leading-/trailing-)edges, meaning maximum five complete hits before it becomes necessary to extract the edges from the DiRICH. This extraction always takes place when a trigger signal arrives at the DiRICH-FEB. That means, that the smallest possible read out window always extends to leading edge time of $0$ ns relative to the trigger. This would mean,

---

[2]Which is equal to the integral from the prompt peak to infinity in the here given precision. This is additionally important, as otherwise the overall amount of light produced by the window would saturate over time, complicating the extraction of an absolute rate.

that an additional $\sim 4500$ hits would be produced per event which, if equally distributed, would correspond to only an additional $\sim 0.16$ hits per channel. Even taking into account the inhomogeneous distribution, this amount of light would only in the rarest cases result in the loss of hits due to buffer overflow[3]. Therefore this limitation of the DiRICH in conjunction with the excess scintillation light does not hinder data taking. As a last check one needs to assess the influence of the scintillation light during the prompt peak. Here one finds that using a 100 ns wide time window starting at the prompt peak ($-530$ ns) results in event averaged hit rates of 1034 hits/event. This number is to compare with the overall number of hits during the prompt peak. Choosing a time window for the integral from $-570$ ns to $-430$ ns allows to definitely capture all hits in the prompt peak but still include the full integrated range from before. One finds that the time distribution features 1424 hits per event on average in the given range. Therefore an average of approximately $1034/1424 \approx 70\%$, of all hits per event can be attributed to the scintillation light from the CaF$_2$ window which supports the first impression gained by only assessing the presented figure 5.2. This even holds true for C$_4$F$_{10}$ as radiator gas ($\sim 60\%$), where additional contributions from Cherenkov light are seen (cf. Fig. A.19 pg. 185).

**Summary**

These results strongly suggest that a removal of the CaF$_2$ window is strongly favored but that data taking would work even with the window still in place. It was therefore finally decided to remove the window which additionally required to also replace the C$_4$F$_{10}$ radiator gas (used in the former RICH detector setup) with the even less scintillating $i$-C$_4$H$_{10}$ (isobutane) (cf. [SFK15]), since the existing gas system was not designed for handling such a large radiator gas volume[4].

---

[3]This assumes all of the produced photons are only hitting MAPMTs in the center of the detector ($192 \cdot$ 64 channels) the probability of having three hits in one channel amounts to a maximum of $\sim 1\%$

[4]Removing the CaF$_2$ window roughly doubles the radiator volume.

# Derivation and impact of time and ToT cuts

This section focuses on the possibility of using leading edge (LE) time and time over threshold (ToT) cuts to improve the detector performance. Such cuts are necessary as otherwise the readout window allows leading edge (LE) times, representing the respective hit arrival time, between $-1000\,\mathrm{ns}$ and $+180\,\mathrm{ns}$ w.r.t. the trigger time. Over the course of such a large time window many additional (noise) hits result in additional reconstructed rings not correlated to electrons, which might falsely be matched to other particles. Having no ToT cut in place results in not only an increased dark noise contribution, but also in an increased contribution of capacitive cross talk and charge sharing. Two noise contributions further laid out during this chapter, which have in lower pulse amplitudes and thus lower ToT. Rejecting hits with too low ToT thus results in cleaner rings as well as less noise in the detector. The discussion in this section starts with establishing the basic cuts on LE time and ToT used as standard in the HADES HYDRA framework. The derivation procedure and impact on the detector performance are discussed. Thereafter several features of the LE time and ToT spectra are discussed. On the basis of this discussion also more narrow LE time cuts are derived, assessing their impact on the detector performance.

## 6.1 Basic LE time and ToT cuts

First cuts on arrival time and ToT are derived solely on RICH basis, not taking into account any other detector. The LE time distribution for individual RICH channels is still contaminated by noise hits resulting from the MAPMT as well as other background hits caused e.g. by scintillation. The main (prompt) peak in these spectra is fitted via a Gaussian distribution extracting its mean. Based on the derived means $\mu_{\mathrm{LE}}(\mathrm{MAPMT}, \mathrm{ch})$ of each individual channel, a rather large acceptance window is derived with fixed width of $60\,\mathrm{ns}$ through

$$\mu_{\mathrm{LE}}(\mathrm{MAPMT}, \mathrm{ch}) - 25\,\mathrm{ns} < t_{\mathrm{LE}} < \mu_{\mathrm{LE}}(\mathrm{MAPMT}, \mathrm{ch}) + 35\,\mathrm{ns} \ .$$

This large time window is chosen mainly for two reasons. Firstly, the uncleaned LE spectrum still features many background contributions showing enhanced number of hits over a broad range of $\sim 15\,\mathrm{ns}$ (see e.g. in Fig. 6.7a). Obviously not all hits in this range are of interest for later ring reconstruction, but before taking into account other detectors to cut on hits from rings of interest, no better cuts can be derived easily. Secondly, for these early studies no time calibration/alignment in terms of the HADES-START detector are made, resulting in arbitrary

shifts in the LE timing of $\sim 10\,\text{ns}$ depending on the measurement day and time (cf. Fig. A.22 appendix pg. 187). These shifts are caused by changes in the trigger of the HADES detector, which can be accounted for by using the timing information extracted from the HADES-START detector. Still, the derived cut on the LE-time is conservative (cf. Fig. A.23 appendix pg. 188).
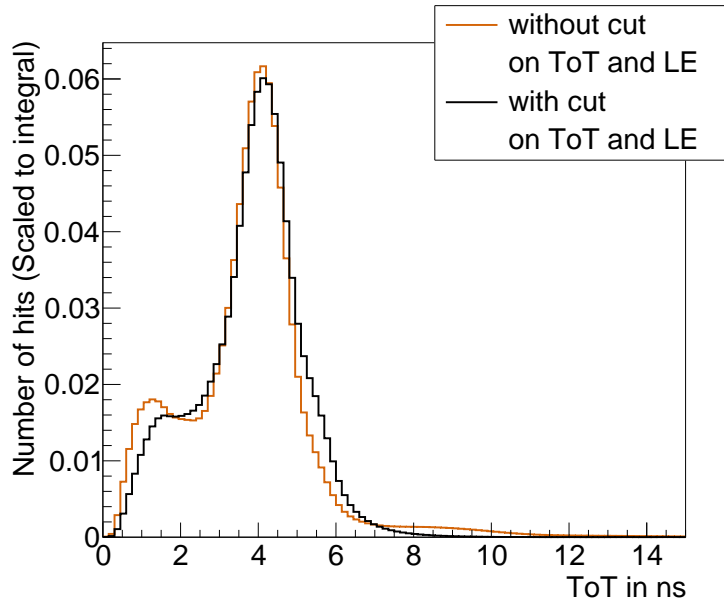


**Figure 6.1** ♦ *Measured Time over Thresholds (ToT) for all channels integrated over days 65, 74, and 80 of the beam-time, with and without applying the standard cut on LE time and ToT. Both distributions are scaled to their integral for visibility reasons. Very large ToTs are an artifact of the way hits are stored in the HYDRA Framework, where the ToT of several hits in one channel during the same event is summed up.*

A similar procedure is used to determine the ToT cuts of each channel, where also the mean ToT position $\mu_{\text{ToT}}$ as well as the width $\sigma_{\text{ToT}}$ of the distribution are approximated through fit of a Gaussian profile. Also here the $0.2\,\text{ns}$-binned spectrum features several artifacts further discussed in chapter 8 which allow only for a conservative cut of

$$\max(\mu_{\text{ToT}} - 4\sigma_{\text{ToT}}, 0) < \text{ToT} < 15\,\text{ns} ,$$

at this first level of ToT extraction. Excluded from both cuts are channels, which over the course of $3.5 \times 10^6$ events did see less than 100 hits. Those channels, most of which are from broken DiRICH-FEBs, are disabled for any further analysis. The $-4\sigma$ region was chosen as lower boundary, as the artifacts discussed in chapter 8 result in sometimes artificially narrow peaks in the ToT distribution of each channel, which need to be accounted for. As a result of that however, the resulting ToT distribution combining all channels still shows a significant contribution of entries with low ToT, resulting (among other things) from capacitive cross talk. This is shown in figure 6.1, showing the integrated ToT spectra of all channels with and without cuts on ToT and LE. At low ToT values, comparing the two distributions, the number of hits gets reduced significantly. Nonetheless, the distribution still shows a visible bump at lower ToTs. Assuming that most MAPMT pixels do have similar gain[1] such low ToTs inside a time window correlated to beam particle times, can mostly be contributed to capacitive cross talk or charge sharing. Charge sharing hereby describes the effect, that the electron cascade induced by a single photoelectron in one of the dynode chains might spill over into one of its neighbors, inducing

---

[1]All MAPMTs were grouped in gain classes and their supply voltage chosen such that the gain is nearly the same for all MAPMTs.

a measurable pulse therein. Capacitive cross talk describes the effect that a massive charge produced in the last dynode of a pixel might induce a sudden drop in potential leading to a measurable pulse of different polarity in one of its neighboring pixels. This pulse being of inverse polarity is followed by a measurable overshoot such that the integrated charge is equal to zero. As those contributions are still visible, they seem not fully eliminated using the conservative cuts derived here. Applying the cuts an additional contribution appears at ToTs larger than the visible single photoelectron peak. Indicating double photon hits this feature of the spectrum is found more pronounced as the cut on the LE time results in a suppression of thermal noise of the MAPMTs situated mostly at the single photoelectron region.



(a) *All particle candidates*

(b) *Particle cand. with ring in RICH*

(c) *Particle cand. with ring in RICH after cut on LE time and ToT*

(d) *Ratio with/without cut on LE time and ToT*
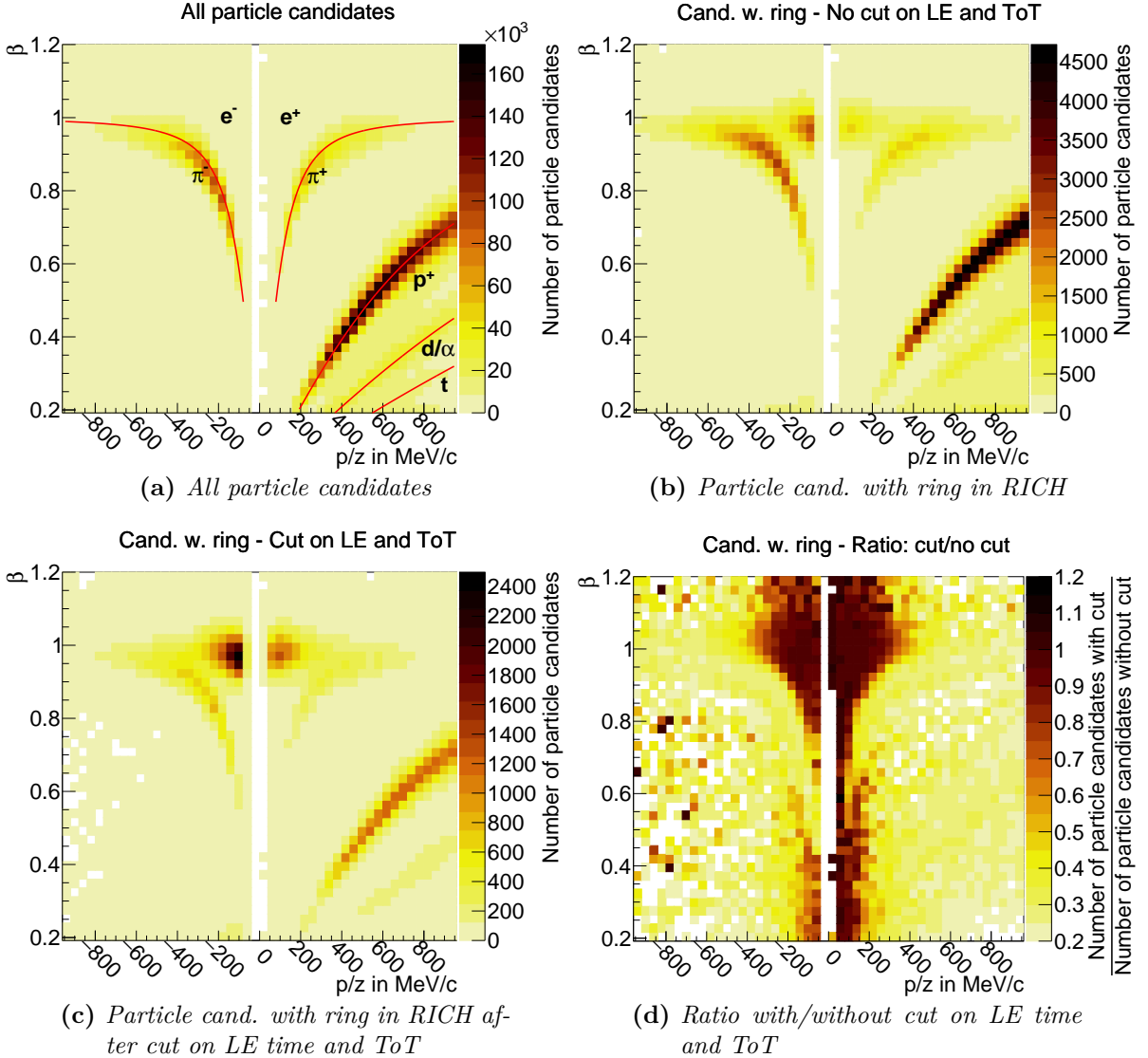
**Figure 6.2 ♦** *β-momentum spectrum of all candidates* **(a)***, candidates featuring a ring in the RICH* **(b)***, candidates featuring a ring in the RICH after application of the LE time and ToT cut* **(c)***, and the ratio of* **(c)**/**(b)** *depicted in sub-figure* **(d)***. Shown data is comprised of partial data retrieved from days 65,74,80. Additionally indicated with red lines in sub-figure* **(a)** *are the visible mass bands in the spectrum. The Enhancement visible in sub-figure* **(d)** *at low β and low momenta stems from an improper β-reconstruction present in this early reconstruction.*

To further study the effects of those conservative cuts, a β-momentum distribution is derived

with and without the use of the derived cut-parameters. For this distribution the velocity $\beta = v/c$ [2] and momentum $p/z$ of only those particles were filled, where a corresponding ring with maximal absolute angular difference ($dQA$, equation (4.3)) of $4°$ was found. Figure 6.2a depicts the spectrum as retrieved, when not requesting a RICH ring in the proximity of the filled particle candidate. Therein one can clearly identify the different particle mass bands characteristic for such a $\beta$-momentum distribution. Hereby of most interest are the pion-bands ($\pi^{\pm}$) which, for large momenta reach into the electron region which is found at $\beta = 1$. This electron region is not visible in this spectrum, as electrons are more seldom compared to the other depicted particles. To see the electron regions one needs to request a RICH ring in the proximity of the particle candidate filled into the spectrum, resulting in figure 6.2b. In this spectrum the contributions of particles other than the electron are already getting suppressed drastically, such that the electron regions $e^{\pm}$ become visible. Even better suppression is now achieved applying the LE time and ToT cuts, resulting in figure 6.2c. Now the electron regions become the most dominant part of the distribution, with the other parts of the spectrum found even more suppressed. To quantify the improvement by applying cuts, figure 6.2d shows the fraction $^{\text{With cut}}/_{\text{Without cut}}$. The electron region itself is nearly untouched by the applied cuts while the contribution of other particles to the spectrum is suppressed to below 30% of the original contents.

## 6.2 Discussion of features in the LE time vs. ToT spectra

To apply stricter time cuts one first needs to understand in more detail the different features of the leading edge time distribution. They are indicated in a single channel LE vs. ToT distribution shown in figure 6.4a. The red contour indicates the regime of hits[3] in the proximity of a definitive electron candidate identified through the use of the MDC, RPC and TOF detectors by requesting the reconstructed candidate to have $0.95 < \beta < 1.05$, $|p/z| < 250\,\text{MeV}/c$, and $m < 50\,\text{MeV}/c^2$ (visualized in Fig. A.35 in the appendix pg. 200). This region of the beta-momentum spectrum is chosen, for its large fraction of electrons with only very low pion contamination. Photon hits in the proximity of the candidate are those which are at most $30\,\text{mm}$ plus an absolute angular equivalent (cf. equation (B.5)) of $2°$ away from the candidate. By comparing the LE-ToT distribution of all hits to those, where an electron candidate was found in the proximity, one can identify several distinct regions. To better understand some of these regions an additional LE-ToT distribution is depicted in figure 6.3 where all cross talk contributions are suppressed. This is achieved through requiring that no direct neighbor measured a signal in the same event as well as a maximum of eight hits on the MAPMT (here PMT 370).[4] In the following, these regions are iterated through using a bulleted list. For readability reasons the more important figure 6.4 is placed next to the bulleted list.

---

[2]Attention needs to be paid with respect to $\beta$, as this value, being a measure overlayed by measurement uncertainties also might induce $\beta$-values larger than one. These values are obviously unphysical and merely an artifact of the incorrectly reconstructed timing of some particles.

[3]The derived contour shows the the outer bound of all LE-ToT bins with more than 5% of the distributions maximum entry.

[4]Similar distributions requiring only the maximum of eight hits on the MAPMT or requiring only a single hit are depicted in figures

**(a)** *Hits in the proximity of an e± cand.*

**(b)** *Hits with no simultaneous hits in neighboring channels*

**(c)** *Ratio*
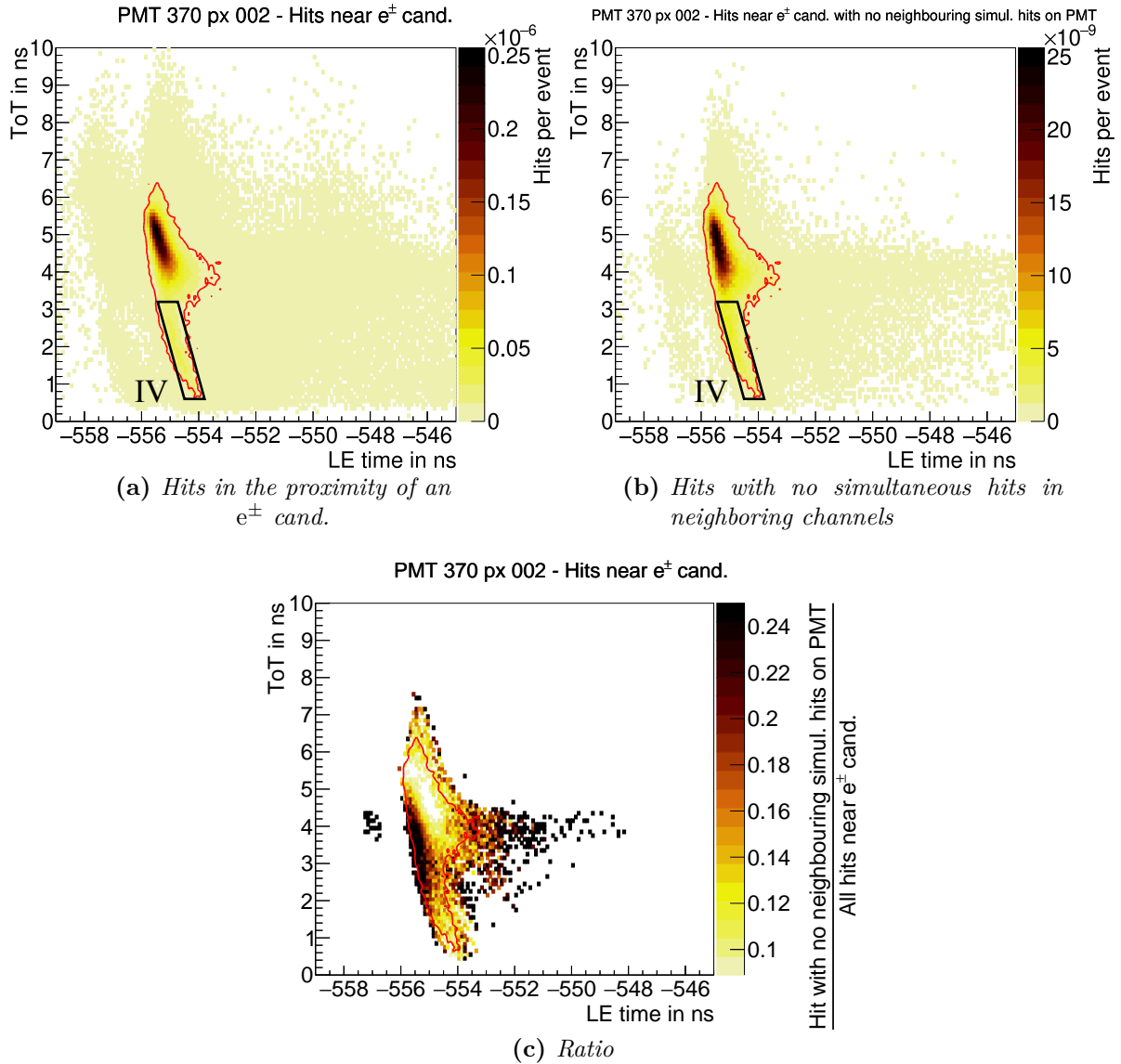
**Figure 6.3 ♦** *Single channel (PMT 370 pixel 2) LE-ToT distribution for hits in the proximity of an electron track for different occupancies on the MAPMT. Sub-figure* **(a)** *shows all those hits whereas* **(b)** *shows only the subsample of hits, where no other hit in its neighboring channels was measured during the same event. This requirement is applied in addition to the requirement that a maximum of eight hits were counted on the same MAPMT during the same event. The ratio of the two distributions is shown in* **(c)**. *The red line in all sub-figures indicates the "5% of maximum" contour of sub-figure* **(b)**, *i.e. the outer bound of LE-ToT bins with more than 5% of the maximum entry. The ratio plot features only bins, where in both used distributions more than 5 hits were counted. This distributions z-scale is additionally cut at the upper and lower 10% quantile, to better visualize its inherent features. Box* **IV** *will be used in the discussion following this figure, with figure* 6.4c *giving a more extensive overview. A figure applying only the cut on the maximum number of hits on the MAPMT (8) is added to the appendix* Fig. A.24 *pg. 189.*

**II** The hits in this region are visible in both sub-figures and thus correlated to electrons reconstructed in the full HADES detector. They hence form the region of interest for the RICH.

**I** Those hits are correlated to the beam hitting the target as they feature a distribution relatively sharp in time. They are spatially uncorrelated to the electrons seen by the rest of the HADES detector, as those arrive approximately 2 ns later (region **II**). Hereby 2.5 ns corresponds roughly to the time which light needs to travel from the target position to the mirror and back to the detection planes ($\sim 2 \cdot 375$ mm). This means, that indeed those hits must be produced at nearly the exact same time the beam hits the target. A possible explanation for this region comes from electrons with very low momenta flying nearly perpendicular to the beam axis and thus passing directly above the MAPMT window. Those electrons produce Cherenkov light, which is directly emitted on the MAPMT and therefore would arrive approximately 2 ns earlier compared to Cherenkov light being reflected off of the mirror. The produced Cherenkov light would thereby be produced in a very narrow cone onto mostly one MAPMT, which is supported by according simulations in [Haa19]. This also explains why a substantial amount of those hits feature very large ToTs and are thus of larger photon count. With the majority of one MAPMT responding to such electrons flying close-by the MAPMTs window, such structures are in the following referred to as **"blob-like" structures**.

**V** This region at low ToTs stems from capacitive cross talk induced by the hits of region **I** and are thus also spatially uncorrelated to electrons seen by the rest of the HADES detector. Those capacitive cross talk hits are positive in polarity and thus produce a measurable negative undershoot only at later times ($\sim 3$ ns according to [PT18]). The amplitude of these cross talk hits scales with the overall occupancy of the MAPMT and is thus more pronounced resulting from the high photon counts of region **I**.

**IV** This region persists even when no signal is measured in one of the pixels neighbors (cf. Fig. 6.3). Thus, this region can not solely consist of hits from charge sharing between neighboring channels. Instead a significant contribution needs to stem from photoelectrons inside the MAPMT producing signals with smaller than average ToT. The resulting hits have a lower pulse height/ToT and arrive slightly later in time due to the so called "walk"-effect. A similar low ToT structure is also visible below region **I** following the same explanation.

**III** The visible band starting already at region **I** and continuing in this region is comprised of scintillation light. The measured hits are mostly comprised of single photons resulting in an average ToT slightly lower than that of region **II**. Contributions of this scintillation light are measured directly and after reflection from the mirror.

**VI** This region is comprised of capacitive cross talk from the main signals of interest in region **II**. The hits in this region are again delayed by up to $\sim 3$ ns. Larger ToTs in this region however seem to reach into region **II**. One possible explanation for this behavior follows the

idea that the negative undershoot induced by a photon signal in its neighboring channels might lower the signal amplitude in that neighboring channel, if this channel too measures a photon signal. Hence this region is not visible in Fig. 6.3. This region is also no artifact of the representation as ratio as can be seen in e.g. Fig. A.30b appendix pg. 195.



(a) *All hits*

(b) *Hits in the proximity of an* $e^{\pm}$ *cand.*

(c) *Ratio*
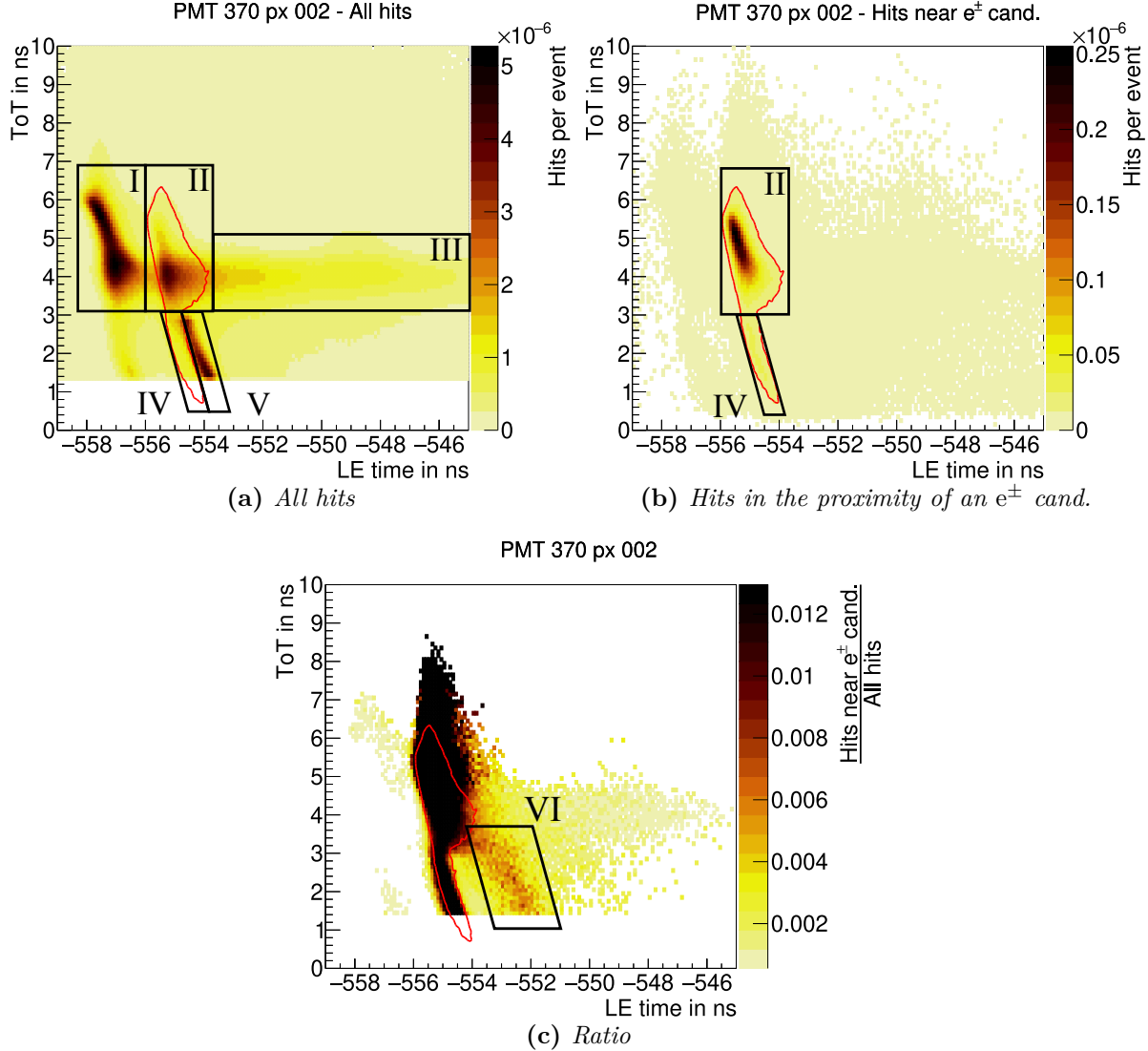
**Figure 6.4** ♦ *Single channel (PMT 370 pixel 2) LE-ToT distribution for all hits* **(a)**, *hits in the proximity of an definitive electron track* **(b)**, *and the fraction of both depicted in* **(c)**. *Indicated with a red line in all sub-figures is the "5% of maximum" contour from sub-figure* **(b)**, *i.e. the outer bound of LE-ToT bins with more than 5% of the maximum entry. For technical reasons the spectrum including all hits is cut off at ToTs smaller than the afore derived cut value on the ToT for this channel. Hits are deemed close to a candidate if they are at most* 30 mm *plus an absolute angular equivalent of* 2° *separated. The ratio plot features only bins, where in both used distributions more than* 5 *hits were counted. Furthermore, this distributions z-scale is artificially cut at the upper and lower* 10% *quantile, to better visualize its inherent features.*

To demonstrate that the distributions shown here capture most features present in all channels, additional LE-ToT distributions of randomly chosen channels are attached to the appendix pgs. 191ff. starting with Fig. A.26. Those figures also include spectra of WLS MAPMTs (e.g.

figure A.31), where a broader time distribution, which is further discussed in chapter 7, is visible.

## 6.3 Derivation and analysis of sharp LE time cuts

Using the spectra including only hits correlated to electron candidates, one can derive sharper LE time cuts to analyze their benefits. In this section two different cuts are derived and discussed, both sharper than the cut derived in the beginning of this chapter. Hereby one cut is chosen narrower and one slightly wider in order to assess if a narrower cut might decrease the efficiency of the detector. The main goal of these cuts is to reduce the amount of capacitive cross talk, the amount of "blob-like" hit structures and the amount of scintillation light. Especially the capacitive cross talk is normally best reduced using a ToT cut which however, following the discussion before, would also reduce the amount of low ToT hits induced by photoelectrons. As the capacitive cross talk, as well as all other background contributions have a distinctly different LE time compared to the signals of interest, a cut on the LE time should already result in a good background suppression. Thus, a sharp ToT in addition to the sharp LE time cut would only spoil the data but not improve the background suppression, which is why in this chapter focuses on a sharp LE time cut only. For this setup, a LE time cut is best determined using the histogram showing the fraction of hits in the proximity of an electron candidate divided by all hits, thus representing a signal-to-noise ratio per LE-ToT-bin as was shown already in figure 6.4c. In order to derive a LE time cut, this two dimensional histogram is projected onto the
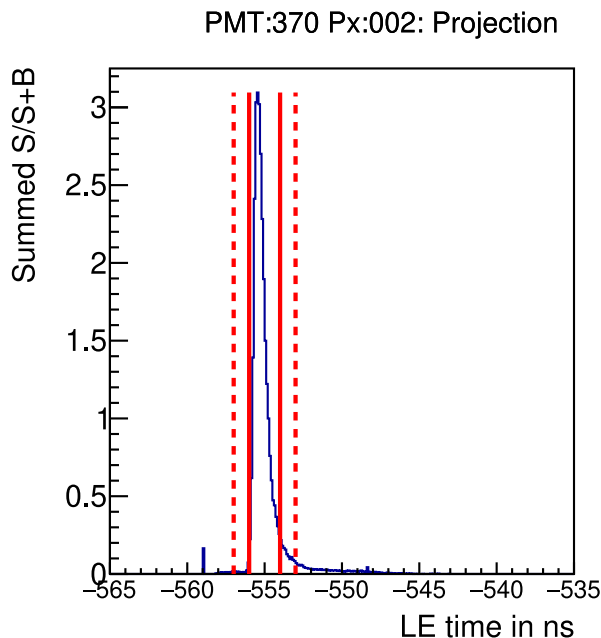


**Figure 6.5** ♦ *One dimensional projection of two dimensional ratio plot dividing hits correlated to an electron by all measured hits for pmt 370 pixel 2. With other words, this plot is the one dimensional projection of figure 6.4c only taking into account LE-ToT bins with ToT larger than 3 ns. The solid red line visualizes the narrow LE cut whereas the dashed line shows the wide LE cut. To see the cut values displayed with respect to the two dimensional distribution the reader is referred to Fig. A.33 on pg. 198 in the appendix.*

time axis. To reduce the influence of low ToT cross talk contributions on this one dimensional ratio spectrum, ToTs lower than 3 ns are discarded. Exemplary this is depicted for the same pmt pixel (pmt 370 pixel 2) in figure 6.5, where also the, in the following derived, cuts are visualized. For the cut derivation only the left most peak in the one dimensional distribution is approximated by searching for the first value above 10% of the maximum in the distribution and

the first value falling below again. This variable cut width is preferred over a fixed one, as some MAPMTs consistently show larger regions of interest (e.g. WLS-PMTs as discussed further in chapter 7). This cut is only derived for channels that do feature a maximum larger than 0.1 a.u. (Summed $S/S+B$)[5]. Channels below the required maximum are not cut on, staying with their original cut on the LE time[6]. For all other channels, the two cut values for the LE time are determined as lower and upper edge independent of the respective ToT of the hit. As the walk is still not corrected for, the extracted cuts on the LE timing are unavoidably wide, still leading to the inclusion of the blob induced capacitive cross talk in some of the channels. To extract a second, more relaxed cut on the LE timing, the extracted cut is widened by a factor of two, still being centered at the same position as before. Even with this relaxed cut a substantial amount of "blob-like" structures, as well as cross talk is suppressed. Both cuts however fail partially to suppress the capacitive cross talk induced by the "blob-like" structures, as its arrival time is too close to that of late signal hits. Excluding those hits is therefore only possible with an additional cut on the ToT or a ToT dependent LE time cut, not further discussed here. Width and mean distributions derived through the described procedure are depicted in figure 6.6. Again visualizing the necessity of having a variable cut width, especially for WLS PMTs.



**(a)** *Cut Mean*    **(b)** *Cut Width*
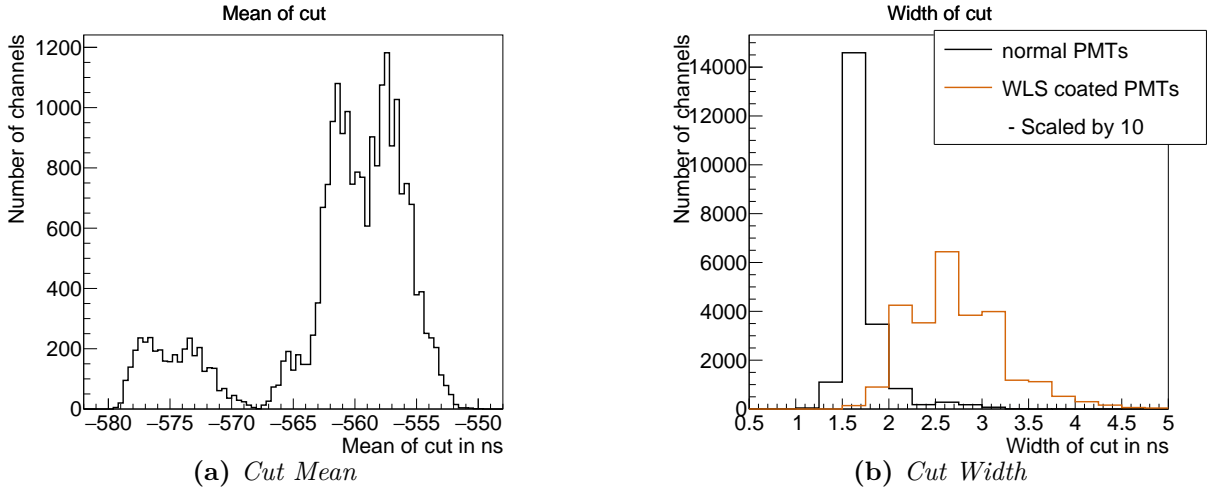
**Figure 6.6** ♦ *Distribution of the mean* **(a)** *and width* **(b)** *of the derived new narrow LE time cut for all channels. The width distribution thereby distinguishes between normal MAPMTs and those that feature a WLS coated front window.*

The resulting LE time distribution using the new derived cuts is presented in figure 6.7. It shows the aligned LE time distribution of all hits, and those correlated to electron rings. Aligned means, that the LE times of all channels are corrected for their individual offset. This offset is the center between the derived "left" and "right" cut values for each individual cut, respectively. Starting with the distribution of all hits, one clearly sees a broad distribution for the leading edge time

---

[5]Hereby the unit is indeed arbitrary, as the parameter in view does not really resemble the signal-to-noise ratio visible in the two dimensional LE-ToT distribution, but rather the sum of the signal-to-noise ratios for different bins.

[6]Those 3900 channels, out of which $\sim 500$ are from actual broken channels in the corresponding DiRICH-FEBs do neither improve, nor deteriorate the spectra discussed in the following (as was found in additional studies). These channels are either at the very inner or very outer rim of the detector, where either way rings are only found very seldom.

**(a)** *LE time of all hits*

**(b)** *LE time of hits in the proximity of electron candidates*
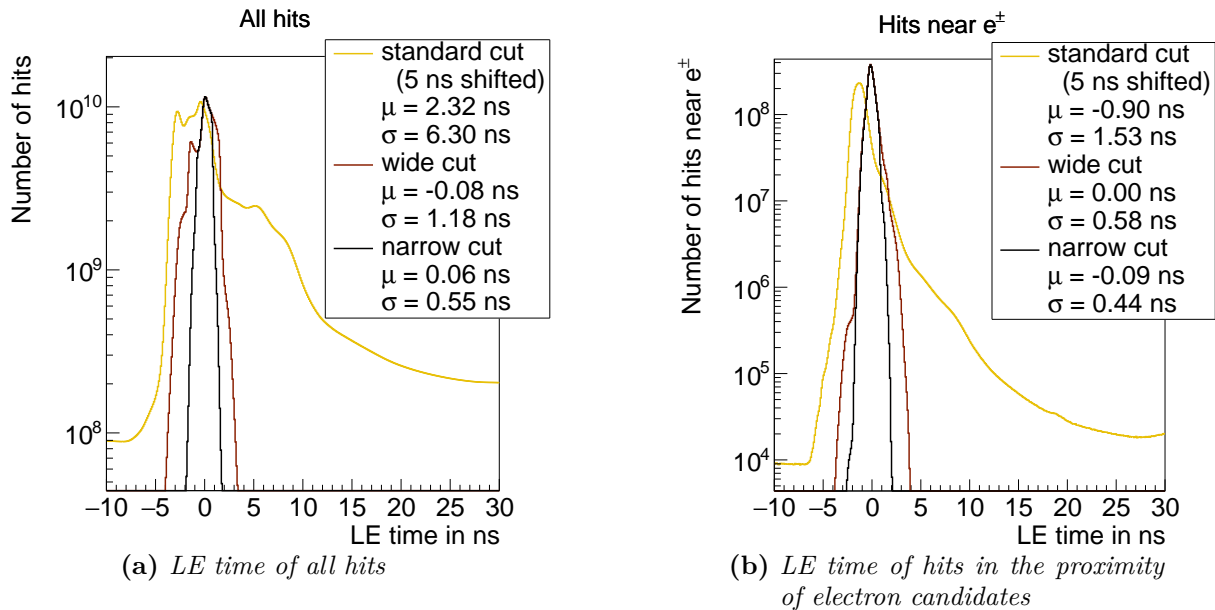
**Figure 6.7 ♦** *Aligned LE time for different LE time cuts, depicted for all hits* **(a)** *and hits in the proximity of electron candidates* **(b)***. The aligned LE time of a hit is retrieved by subtracting the center point between the channel individual left and right cut values from the measured LE time. The aligned time of the standard cut is shifted by an additional* 5 ns*, as the cut window of this cut is asymmetric. Hits are assumed in the proximity of an electron candidate if they are at most separated by* 30 mm *plus an additional* 2° *absolute angular equivalent. The mean μ and standard deviation σ of the distributions are denoted in the legend.*

using the old cut. Less contaminations are visible when applying the newly derived cuts. Still in the wide cut distribution one finds a narrow peak in time before the prompt peak. This peak, being earlier in time but vanishing when requesting the hits to be correlated to electron rings, must again be related to the "blob-like" structures discussed before. Comparing the old to the new cuts, the main peak is much more narrow, leading to a higher peak in the distributions center. This demonstrates that the average LE times for each channel, that correspond to electrons, are now much better approximated. The width of the two distributions using the narrow cut is still found slightly narrowed moving to the electron ring correlated hits. The difference is however small, indicating that nearly all measured background hits are eliminated using this cut. A width of $\sigma_t = 440$ ps however is still nearly double the amount measured in reference measurements [TS18, 61f] using the same readout chain and sensor ($\sigma_t = 256$ ps). This is partially related to the still not properly corrected walk and cross talk contributions which are further discussed in chapter 7.

To test the newly derived cut on the LE time[7], again the $\beta$-momentum spectrum is derived showing the velocity and momentum of all particles having the closest match to RICH rings with a radius between 17 mm and 30 mm. The maximum angular difference between particle track and ring center was set to 2°. The spectrum is derived for the cut described in the beginning

---

[7]Unfortunately, this cut also still includes the ToT cut used in the described standard cut. This is a result of only being able to use large statistics in a reasonable way, using the so called DST-files, which consist of pre-analyzed beamtime data only including already calibrated hits and particle candidates.
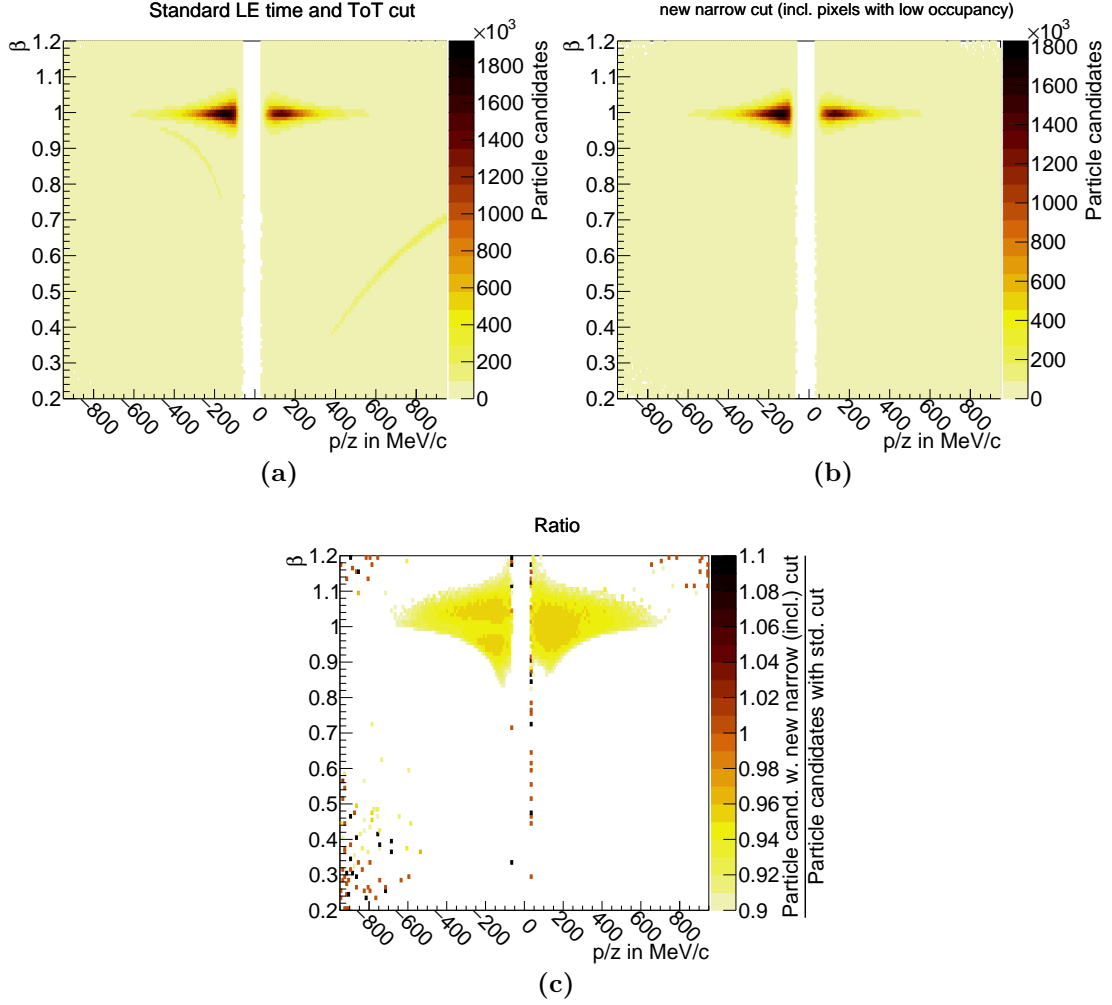
**Figure 6.8** ♦ *β-momentum spectrum of particles matched to rings reconstructed using the old standard cut on LE time (and ToT)* **(a)** *and using the new LE time cut* **(b)***. The ratio of those two distributions is depicted in* **(c)***. The here used cut is the narrow cut described in this section, including also channels, where – due to very low occupancy with electron induced hits – no cut values were retrievable, without additional cut on the LE time. Matched rings require a radius between* 17 mm *and* 30 mm *and a maximum absolute angular distance of* 2°*, where only the closest match is filled into these spectra. The ratio cut is limited to a range of* 1 ± 0.1 *such that the heavily suppressed proton and* π⁻ *contributions are not visible anymore.*

of this section (depicted in Fig. 6.8a) and the newly derived cut (fig. 6.8b). Comparing the $\beta$-momentum distribution of the standard cut to the one derived with the new cuts one finds that proton and $\pi^-$ bands are now more suppressed. With the new cut, these mass bands are not visible anymore, which is the result of an overall reduction of "bad" rings. Those "bad" rings, being induced by several coinciding noise hits, are partially matched to random track candidates found in their proximity. Since electrons occur much less often than pions and protons, the chance of not matching electrons to such "bad" rings is high. Thus, reducing the amount of "bad" rings serves the overall suppression of incorrectly matched particles in the RICH. This is even more obvious, examining the ratio of the two spectra depicted in 6.8c, where except for the electron contribution no other particle is visible anymore. It might however also seem apparent that the cut reduces the number of electrons at $\beta \approx 1$ as here at low momenta a maximum

of only 0.95 is reached, while large momenta show an even lower efficiency ratio of below 90%. To explain why this conclusion is incorrect, one needs to see that the pion mass bands reach into the electron region at $\beta \approx 1$ moving towards large momenta. Assuming that the new LE time cut improves the rejection of $\pi^{\pm}$ it is therefore natural, that the apparent efficiency presented in this figure must drop towards large momenta. To extract a more meaningful distribution one therefore must approximate the amount of falsely reconstructed $\pi^{\pm}$ in the shown distribution, which here will now referred to as background. There are several approaches to estimate this exact contribution. One of them uses the fact, that the spatially uncorrelated $\pi^{\pm}$ (and other particles) must have the same probability to be falsely matched to a ring when rotating them by a certain azimuthal angle $\phi$. Assuming there is no large spatial correlation between different electrons along $\phi$, this rotation procedure should only indicate the amount of background inducing particles matched to rings by chance. This especially holds true, as only very few electrons are registered in the RICH during one event. This method rotates only in terms of $\phi$, as the number of the given particles should mostly be a function of the polar angle $\theta$. This rotation should be chosen rather large, as e.g. electron-pairs from conversion mostly feature small opening angles. Furthermore, an azimuthal angle of $\pm n \cdot 60°$ (with $n \in \mathbb{N}$) should be chosen, as otherwise the shadowing induced by the spokes in the RICH and insensitive regions between the MDC plates repeating every 60° might be shifted onto normally sensitive regions, thereby inducing biases in the background estimation. This method comes with the additional benefit of doing the background approximation always within similar event structures, which is normally not easily achieved doing e.g. mixing of different events, where normally an event categorization (e.g. centrality) needs to be taken into account. For this analysis a $\phi$ angle of 180° is chosen, as it preserves the detector geometry. Other approaches like a 60° rotation and a basic event mixing approach were still tested and result in very similar pictures (see Fig. A.34 in the appendix pg. 199). With this the signal spectrum can be extracted using the derived background through

$$\text{signal} = \text{S}(\beta, p/z) = N_{\text{all}}(\beta, p/z) - N_{\text{background}}(\beta, p/z) \, ,$$

where $N$ can be a function of any observable, and only in this $\beta$-momentum spectrum depends on $\beta$ and $p/z$. Accordingly the signal (S) to noise (B) ratio spectrum is derived as:

$$\text{signal-to-noise ratio} = \frac{\text{S}}{\text{S+B}}(\beta, p/z) = \frac{N_{\text{all}}(\beta, p/z) - N_{\text{background}}(\beta, p/z)}{N_{\text{all}}(\beta, p/z)} \, . \tag{6.1}$$

As the $\beta$-momentum distribution of the signal is quite similar to the already shown bare number of particles[8] only the ratio plot, dividing the signal reconstructed with the new cut by that of the old cut is shown in figure 6.9. In this figure one can now correctly see that the signal efficiency does not get reduced below 90% at large momenta, but stays rather constant at $\sim 94\%$ with large patches at small momenta reaching a maximum of $\sim 96\%$. To understand where this still visible reduction comes from, it is helpful to study the spatially resolved distribution of those lost hits. Figure 6.10a shows the spatially resolved ratio of found "definite electrons", defined by $0.95 < \beta < 1.05$, $|p/z| < 250 \,\text{MeV}/c$ and $m < 50 \,\text{MeV}/c^2$, using the new cut divided

---

[8]Mainly the $\pi^{\pm}$ and proton bands vanish
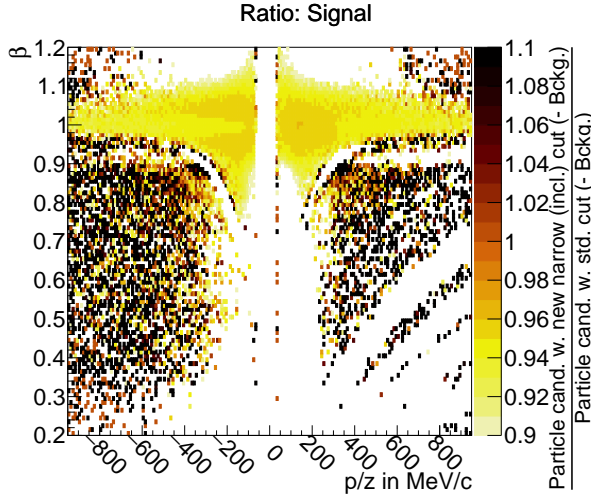
**Figure 6.9 ♦** *β-momentum resolved signal ratio, dividing the signal retrieved using the new narrow cut by the signal gained using the old standard cut on LE time (and ToT). The signal contribution for each cut is derived by counting all particle candidates (in terms of β-momentum) and subtracting the background (*-**Bckg.***). The background is estimated counting the number of particles that are still matched to a ring when their φ-coordinate is rotated by 180°. The narrow cut also includes channels, where no cut values were retrievable (***incl.***). Those channels are not further cut compared to the standard cut. Particle candidates are those that are closest matched to rings with radius between* 17 mm *and* 30 mm *at a maximum absolute angular distance of* 2°*.*

by the ones found with the old cut. Striking is the pattern of many equidistantly spaced spots where the new time cut seems to hinder the proper reconstruction of electron candidates. These spots, always found in the center of the MAPMT are not indicative of reoccurring channels with improperly defined cut parameters, as those would result in an efficiency drop in form of a circular pattern around the improperly cut channel (see example in Fig. A.36 in the appendix pg. 200). Furthermore, figure 6.10c, showing all rings found by the ring finder, in conjunction with figure 6.10d, showing only those rings matched to an electron, indicates that the ring finder has a tendency to find "bad" rings at the exact spots seeing the largest reduction in occupancy here. Thus, the reoccurring pattern are more so an indication of the time cut being applied correctly, reducing the number of electron candidates being incorrectly matched to "bad" ring candidates. Such electron candidates might still be actual electrons, which were produced through conversion after the RICH detector, therefore leaving no detectable trace in the RICH. With this one can conclude, that definitely no badly defined cut parameters in certain channels are the reason for the decreased efficiency in the electron bands.

Apart from that, a partial reduction in the amount of reconstructed rings in the WLS region is apparent. This reduction however also does not go in hand with an overly large reduction in number of hits per channel that are spatially correlated to electrons, shown in figure 6.10b. Instead, this number stays nearly constant over the full detector. This is even more obvious in the slightly widened time window, where nearly the same reduction in the ring reconstruction ratio is observed, but featuring an even lower reduction in the number of hits per channel spatially correlated to electrons (see Fig. A.37 in the appendix pg. 201). From that one can conclude, that the narrow LE time cut reduces slightly the prolonged tail visible in the LE time distribution for WLS coated MAPMTs but does not largely reduce the reconstruction efficiency for rings of the same. Additionally, no large variance of the observed inefficiency is found when dividing the data in ten different bins of beamtime as is shown in figures A.38 and A.39 in the

**(a)** *Spatially resolved ratio of reconstructed rings after background subtraction* ^new cut^/_standard cut_



**(b)** *Spatially resolved ratio of hits correlated to electron rings* ^new cut^/_standard cut_



**(c)** *Number of **all rings** reconstructed using the standard cut*



**(d)** *Number of **all electron rings** reconstructed using the standard cut*
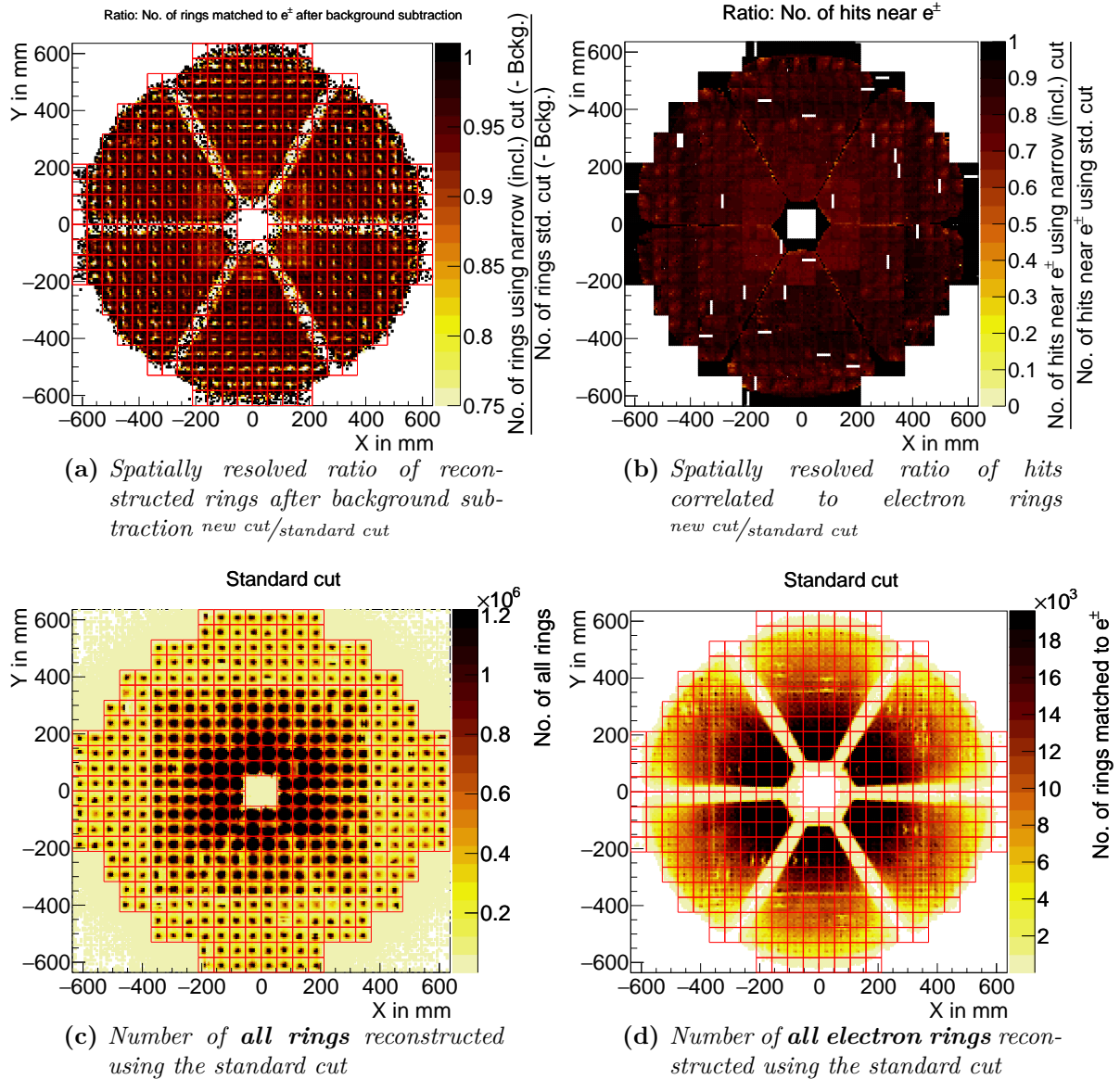
**Figure 6.10** ♦ *Spatially resolved ring **(a)** and hit ratios **(b)** for hits and rings matched to definite e$^\pm$ dividing rings reconstructed with the new LE cut by the ones reconstructed using the old standard cut. Together with the spatially resolved number of all rings **(c)** and the number of rings matched to definite e$^\pm$. Added to the figures are red lines indicating the outlines of the MAPMTs as visual guides. Definite e$^\pm$ are defined by $0.95 < \beta < 1.05$, $|p/z| < 250\,\mathrm{MeV}/c$ and $m < 50\,\mathrm{MeV}/c^2$ and are called matched to a ring, if they are the closest track candidate not farther away than 2°. A hit in a given channel is counted as electron correlated if the channel is situated in the circular area spanned by a radius of 30 mm and absolute angular difference of 2° around a definite e$^\pm$. The used LE time cut includes all channels where no new cut was found, with their original cut values. White spots visible in **(b)** in the detector stem from broken DiRICH-FEB channels, resulting in lower ring reconstruction efficiency to the left and right of these channels, as is visible in **(d)**.*

appendix pg. 202f.. A drastic variation of the leading edge time – as it would be induced when not correcting on basis of the timing information of the HADES-START detector – can thus also be excluded.
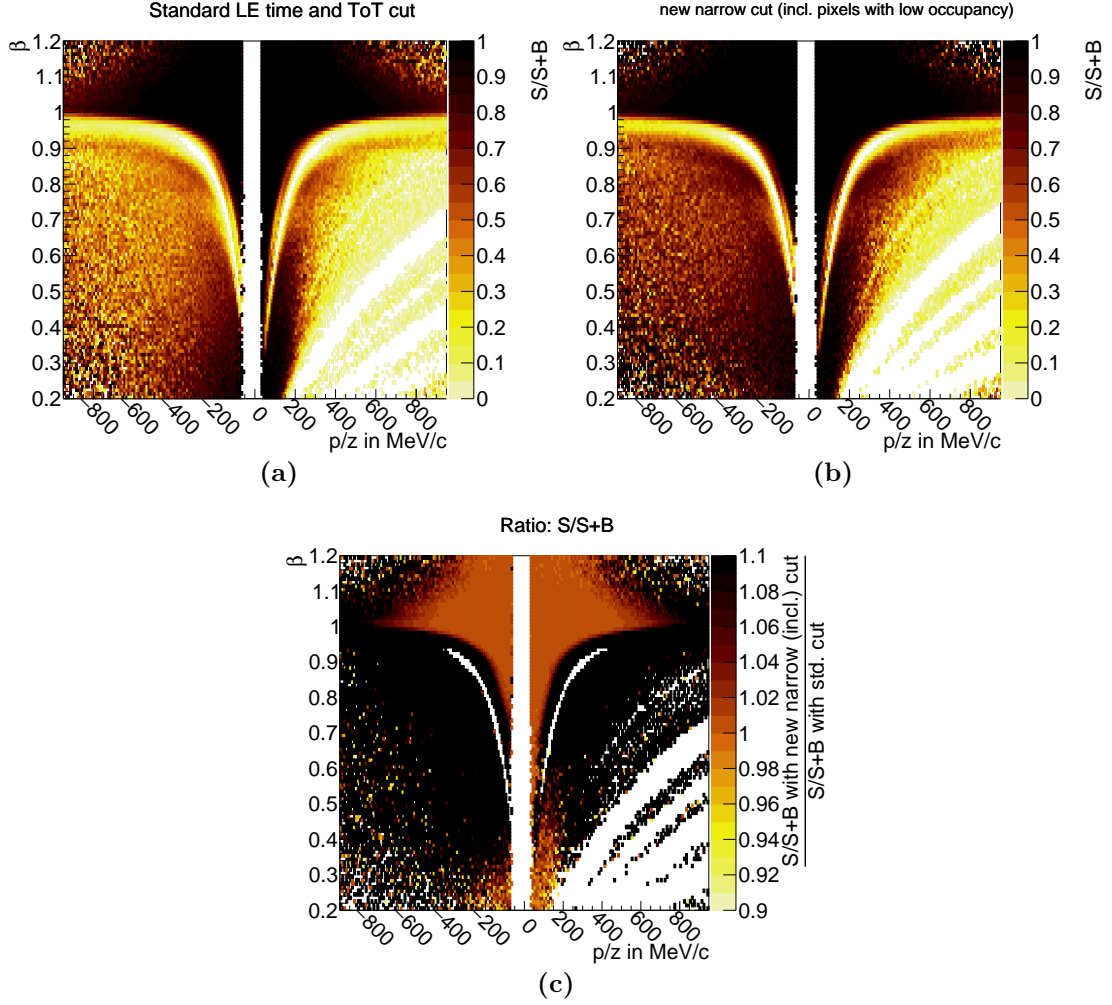
**Figure 6.11 ♦** *β-momentum resolved signal-to-noise ratio for particles matched to rings reconstructed using the old standard cut on LE time (and ToT)* **(a)** *and using the new LE time cut* **(b)**. *The ratio of those two distributions is depicted in* **(c)**. *The used new narrow cut includes all channels where no new cut was found, with their original cut values. The signal-to-noise is calculated using equation* (6.1). *The number of all matched particles is comprised of all particles being the closest match to a RICH ring with radius between* 17 mm *and* 30 mm *having a maximum absolute angular distance of* 2°. *The necessary background is approximated applying the same matching requirement but rotating all particles' φ-coordinate by* 180° *thereby reconstructing the uncorrelated background.*

The resulting $^S/_{S+B}$ for the old cut is found depicted in figure 6.11a with the new cuts $^S/_{S+B}$ ratio plot shown in figure 6.11b. The ratios of the two $^S/_{S+B}$ and simple β-momentum distributions, dividing the new narrow cut's distribution by the one using the old cut is depicted in figures 6.8c and 6.11c.

Studying the $^S/_{S+B}$ plots, the region of largest interest is the electron region at $β \approx 1$. There, the most striking difference between the two spectra is towards large momenta and again best retrievable from the ratio plot. Therein visible is, that moving towards very large momenta, the signal-to-noise ratio improves, reaching levels of above 1.1. The improvement is less visible at lower absolute momenta, where the improvement on the signal-to-noise ratio is lower than

a per-mill. The same is found for the wider time cut depicted in figure A.42b in the appendix pg. 206 [9].

Additional improvements not further elaborated here include sharper rings featuring a reduced $dR$ value and an improved event separation, where events with no reconstructed electron candidate feature significantly less measured photon hits than events with a reconstructed electron candidate[10].

## 6.4 Summary

In this chapter, different timing cuts were established and features of the LE time and ToT distribution discussed on basis of a single channels LE-ToT distribution. The basic LE time and ToT cut introduced in the beginning did clean up the $\beta$-momentum distribution substantially, such that this cut was chosen as standard in the HYDRA-DST production. During the assessment of the single channel LE-ToT distribution it was found the largest background stems from "blob-like" structures and the therethrough induced capacitive cross talk at low ToT and slightly delayed LE times. Other prominent regions in the LE-ToT distribution include scintillation light and capacitive cross talk induced by the main signal. Additionally it was found, that the low ToT hits measured at the same LE time as the main signal are spatially correlated to Cherenkov rings from electrons and can in parts not be explained by charge sharing or cross talk. On basis of this understanding of the LE-ToT distribution a narrow LE time cut was established. This cut improved the signal-to-noise ratio of the $\beta$-momentum distribution. This improvement is small at low momenta but much larger at high momenta, where the pion band reaches significantly into the electron region. The standard $\beta$-momentum distribution showing particle counts was found slightly reduced at the electron region. Even though this normally indicates a reduced efficiency, it was found that the reduction stems from a reduction of "bad" rings artificially matched to particle candidates in the electron region. Thus, the efficiency can be assumed unaffected by the narrow LE time cut. Albeit the improvements gained through the narrow LE time cut, the old cut, still being the current standard in the HYDRA-DST production, is used for the rest of this thesis.

---

[9]The same $S/S+B$ plots are shown for the narrow and wider cut when excluding low occupancy channels in figure A.42 pg. 206 in the appendix. For the sake of completeness also the bare signal ratios are added to the appendix on pg. 205 Fig. A.41.

[10]The interested reader can find according figures in the appendix on pages 207f.

# 7

# Timing precision of the DiRICH readout chain in HADES

In this chapter the best possible timing precision in the HADES detector is derived. This mainly serves the purpose to examine the full capabilities of the DiRICH readout chain as it will be used also in future experiments, partially even with the same photon sensor. There are however some problems deriving the best possible timing precision using HADES data. Firstly, all reconstructed hits in the HADES RICH depend on the HADES-START detector signal, which is used as reference to "calibrate" all RICH hits. The effect of the START detector can however be assumed small, as its timing precision should be in the order of $\sigma = 50\,\mathrm{ps}$ – as was already discussed in subsection 1.3.1 – which is small compared to the timing precision of the MAPMT of

$$\mathrm{FWHM} = (350 \pm 10)\,\mathrm{ps} \,\hat{\approx}\, \sigma = (149 \pm 4)\,\mathrm{ps}$$

provided as transit time spread in [HAM19]. Furthermore, the LE timing is deteriorated due to the present walk for different ToTs already shown in chapter 6, where also the problems correcting this walk are discussed. This chapter will therefore discuss the timing precision on basis of hits within ToT-bands of varying width. Finally, the DiRICH input capacitance[1] and WLS coating on some MAPMTs influence the timing precision. Therefore, these different channel-"types" are analyzed separately from each other, with an additional section focusing solely on the effect of the WLS coating closing this chapter.

## 7.1 Leading Edge timing precision for narrow bins in ToT

To counteract the widening effect of the walk effect present in all channels, one normally tries to approximate the walk and correct for it based on the measured ToT information. As was discussed in chapter 6, this is not easily doable, as different contributions in each channels LE-ToT spectra contribute very different depending on the analyzed channel's average occupancy.

Instead, to extract the theoretically possible timing precision another method of suppressing the effect of the walk is to focus on the timing precision in a small range of ToTs only. Here a varying range of allowed ToTs is chosen, taking into account the varying occupancy of different channels. Starting off the procedure, a ToT bin width is chosen to group the measured LE-ToT pairs of hits into a two dimensional histogram for each channel. Choosing a bin width of 100 ps

---

[1]In HADES two types of input capacitances are used, 1 pF and 10 pF.
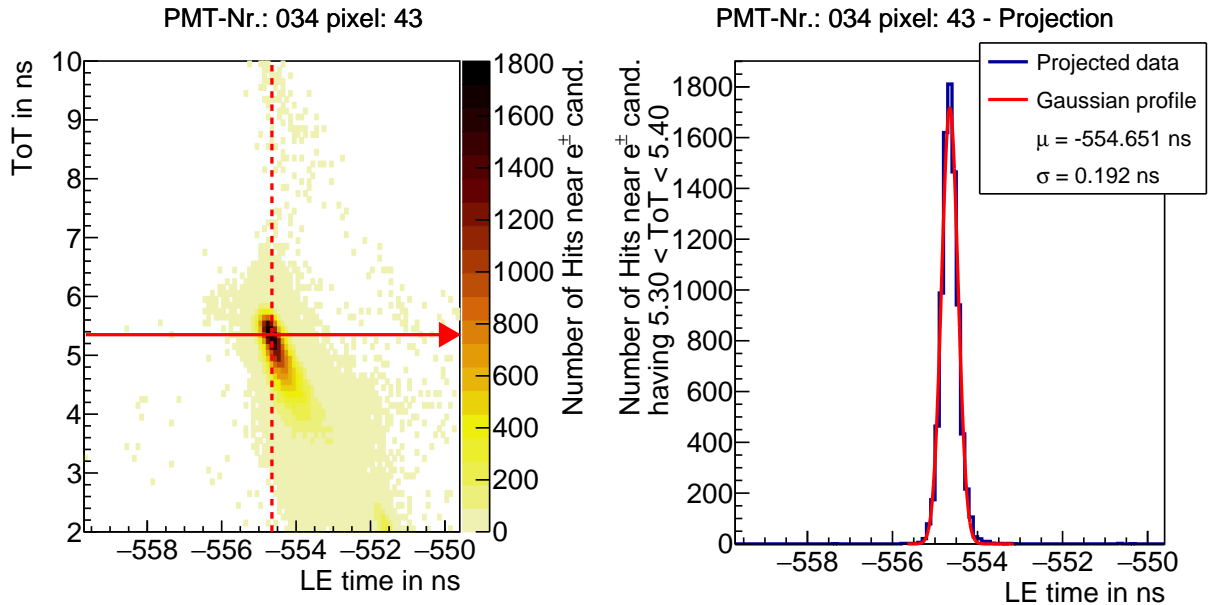
**Figure 7.1 ♦** *Visualization of the projection over a single* 100 ps *ToT bin and fit of a Gaussian profile to that projection to assess the timing precision of a single channel (PMT 34 pixel 43). Using hits measured in this channel while an electron candidate was identified in its proximity a two dimensional LE-ToT histogram is built using a binning of* 100 ps × 100 ps*. Therein the bin with the largest amount of hits is found which is indicated by the intersection of the dashed line and the red arrow. Along the red arrow a projection is made, being depicted on the right. This projection over a single* 100 ps *ToT bin, is fitted with a Gaussian profile, extracting the profiles standard deviation σ as timing precision of that channel.*

in LE and ToT, is a good trade off between a small enough ToT range still featuring enough statistic to extract meaningful information. Using this histogram, the maximum bin is found. If this bin features less than 100 entries, this channel is not used for the further derivation of the timing precision. Using this requirement the timing precision of 23444 out of 27392 channels is extracted. This equals roughly the same amount of channels already discussed in chapter 6. Using all channels meeting the requirement on the number of hits, a projection is made along the LE axis through the found maximum ToT bin ($\text{ToT}_{max}$). This means that for the following channel individual analysis only those hits are taken into account featuring

$$\text{ToT}_{max} - 50\text{ps} < \text{ToT} < \text{ToT}_{max} - 50\text{ps} \ .$$

Using only those hits, a Gaussian profile is fitted to the visible peak in the now one dimensional LE time spectrum. This procedure is visualized exemplary for a single channel in figure 7.1. Indicated in that figure with a red arrow is the chosen projection line, with the resulting projection depicted to the right. The LE time of the maximum LE-ToT bin is additionally marked with the dashed line and used as a starting value for the following fit of the Gaussian profile to the extracted one dimensional projection. The fit with a Gaussian distribution thereby is necessary as some channels still include large amounts of background, mainly due to later LE time-values induced by scintillation. From there the width of this Gaussian distribution is extracted (as depicted in the figure) for each channel and filled into the final timing precision spectrum depicted in figure 7.2. Therein shown are all channels where the timing precision is
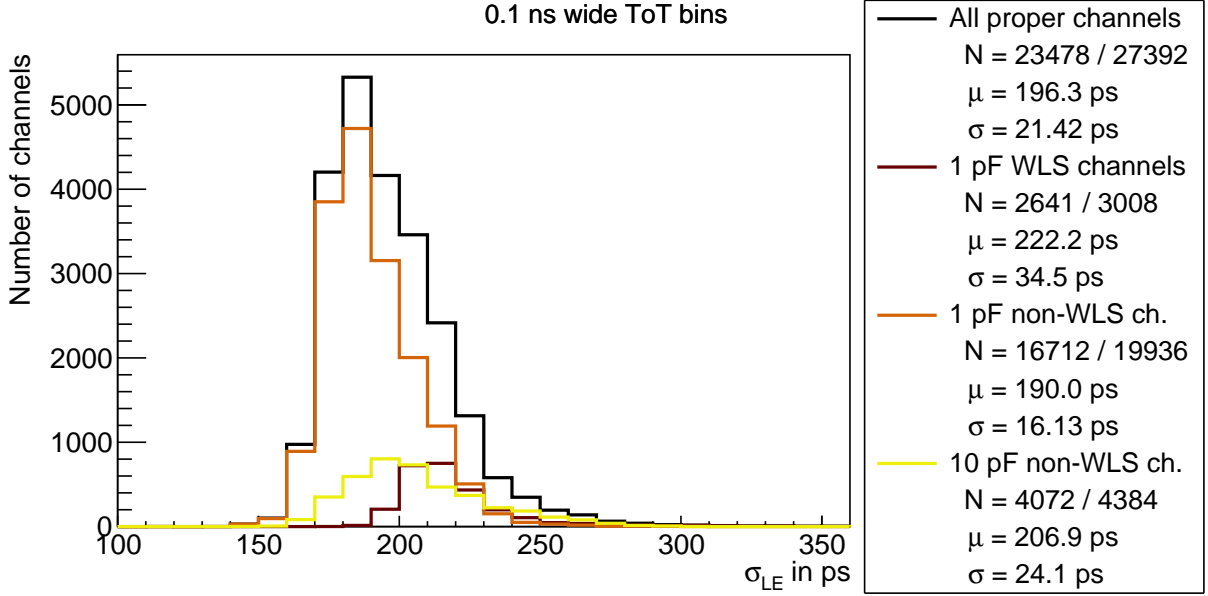
**Figure 7.2** ♦ *Channel individual timing precision being the $\sigma_{LE}$ value of a Gaussian profile fitted to the 100 ps binned LE time distribution of a single channel over a single 100 ps ToT bin. The channel dependent chosen ToT range is that of the 100 ps × 100 ps LE-ToT bin with the largest number of entries. The retrieved timing precisions are separated into three different groups labeled in the legend. Hereby the capacitance refers to the input capacitance of the DiRICH-FEB whereas the WLS is applied to the MAPMT read out. For each group the number of properly fitted channels N is denoted in the legend together with the number of all channels in the detector belonging into that group. Additionally, the sample average timing precision μ and sample spread σ for each group are denoted up to statistically significant precision.*

reconstructible through the described procedure, differentiating between different types of channels. Compared are channels that belong to MAPMTs with WLS coated front window, as well as DiRICH channels with 1 pF input capacitance and 10 pF input capacitance. First examining the overall timing precision one finds, that the average timing precision in the HADES detector given the 100 ps wide ToT bin only amounts to

$$\bar{\sigma}_{\text{LE, HADES}} = (196.8 \pm 0.1)\,\text{ps}\,.$$

This number

$$\bar{\sigma}_{\text{LE, best}} = \sqrt{\bar{\sigma}^2_{\text{LE, HADES}} - \sigma^2_{\text{HADES-START, worst}}} = \sqrt{196.8^2 - 50^2} = (190.3 \pm 0.1)\,\text{ps}\,,$$

is slightly larger than the average timing precision of $\sigma_{\text{MAPMT}} = (149 \pm 4)\,\text{ps}$ of the photon sensor even including the maximum possible timing precision of the HADES-START detector. Comparing only the best possible selection of channels that do not feature the WLS coating as well as the larger input capacitance which are known to deteriorate the timing precision, one only achieves at best a possible timing precision of

$$\bar{\sigma}_{\text{LE, best, 1 pF non-WLS}} = \sqrt{190.4^2 - 50^2} = (183.7 \pm 0.1)\,\text{ps}\,,$$

for the single selected ToT bin of 0.1 ns width. Thereby the found maximum ToT bins do not vary by a lot[2] (which is also later confirmed in chapter 8). For such a small ToT bin also large photon counts on the MAPMT, as they are found in the used data sample, do not majorly spoil the timing precision. This can be seen seen choosing a data sample that allows eight simultaneous hits on the MAPMT at maximum and repeating the analysis procedure, now reaching a similar timing precision of

$$\bar{\sigma}_{\text{LE, HADES,}} = (193.2 \pm 0.2)\,\text{ps}$$

for all MAPMTs and

$$\bar{\sigma}_{\text{LE, HADES, 1\,pF non-WLS}} = (186.6 \pm 0.1)\,\text{ps}$$

for non-WLS coated MAPMTs (see Fig. A.50 in the appendix pg. 211). Also, the LE time bin width can be excluded as a primary source of this wider timing precision, as a binning of 50 ps leads to the very similar result of

$$\bar{\sigma}_{\text{LE, HADES}} = (193.9 \pm 0.1)\,\text{ps}$$

average detector timing precision (see figure A.53 in the appendix pg. 212).

To fully understand the influence of the artificially limited ToT range onto the derived timing precision, figure 7.3 shows the detector average standard deviation (i.e. timing precision) as a function of ToT bin width. Thereby again different channel types are visualized through differently colored lines. Assessing the overall course through the black line one finds a steady increase in the derived detector average timing precision leveling off and reaching its maximum at

$$(346.7 \pm 0.2)\,\text{ps}\ [3].$$

This result now nearly includes the full ToT range, but needs to be handled with care as at those large ToT bin widths the amount of background leads to very asymmetric distributions and thus larger variations in the fit results (cf.e.g. Fig. A.47b appendix pg. 209). This does indicate that the statistic in such a narrow 5 ps ToT bin is not sufficient anymore to robustly extract the standard deviation of the distribution. This is also suggested by slightly inhomogeneous two dimensional ToT-LE distributions found for this fine binning (cf.e.g. figure A.47a appendix pg. 209). However, this means that the chosen 0.1 ns ToT bin gives already the best possible estimate on the timing precision reachable with this data and without extensive walk and occupancy corrections.[4]

Comparing the timing precision of channels with 1 pF input capacitance to those with 10 pF visible in Fig. 7.2, one finds unsurprisingly a slight deterioration of the timing precision in the order of $(18.4 \pm 0.4)\,\text{ps}$. This increase partially goes in hand with an overall increased spread in the observed timing precisions for the different channels. The deterioration of the timing precision is consistent over the full range of checked ToT bin widths as is seen again in

---

[2]The interested reader can find the according figure A.48 in the appendix on page 210

[3]The interested reader finds the according spectra in figure A.51 in the appendix pg. 211

[4]This is consistent also for the low occupancy data that allows only for maximally eight simultaneous hits on the MAPMT (cf. Fig. A.54a appendix pg. 213.)
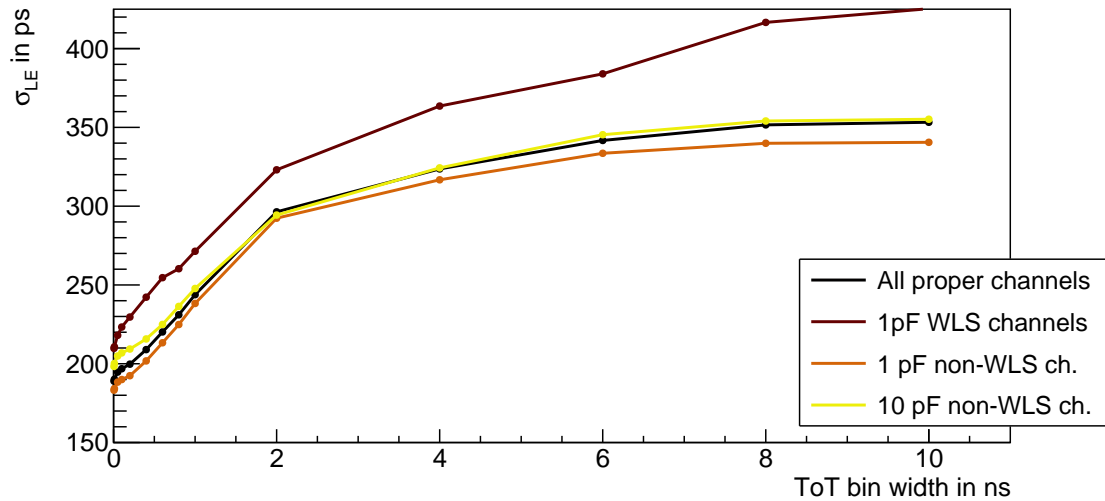
**(a)** *Detector average timing precision*
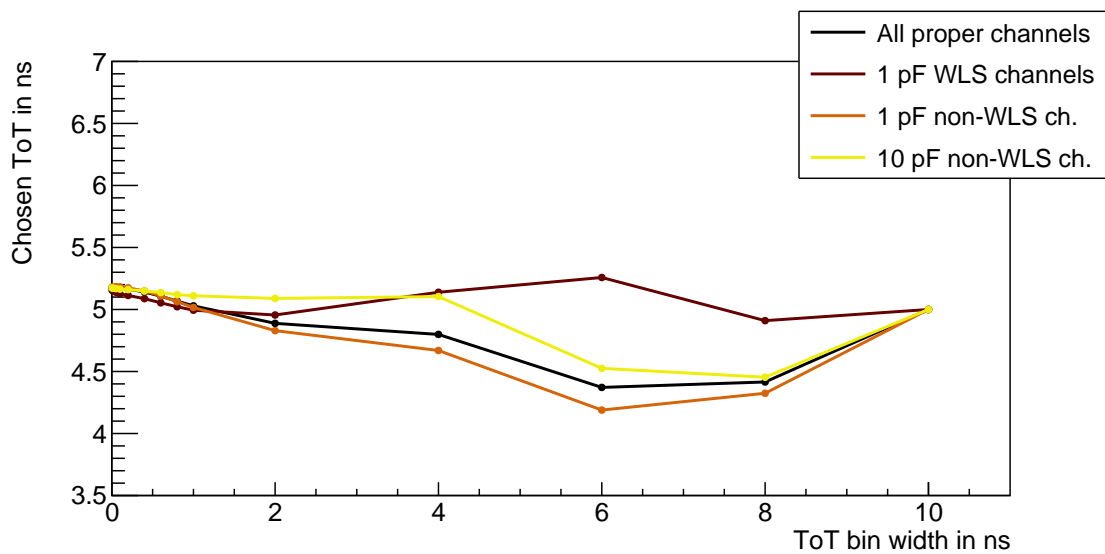


**(b)** *Average ToT bin center*

**Figure 7.3** ♦ *Dependency of the extracted detector average timing precision and the average chosen ToT bin for which the precision was derived onto the chosen ToT bin width. Therefore the averages are taken over three different groups denoted in the legend. The error bars in y-direction indicating the statistical error on the measured points are hereby to small to exceed the marker size. A full distribution for the* 100 ps *ToT bin width is found in* Fig. 7.2 *where also the procedure is laid out.*

figure 7.3. The extend of this deterioration however varies, as does the difference in the average used ToT bin center shown in figure 7.3b. Here the chosen ToT bin for the 10 pF channels stays rather constant only decreasing after 4 ns ToT bin width. In contrast to that, the used ToT bin for channels with 1 pF input capacitance (excluding WLS coated MAPMTs) tends towards lower average ToT values for all ToT bin widths. Hereby the difference in the chosen ToT bin seems not to be correlated with the variation in the extracted timing precision. With this one can conclude, that the deteriorated timing precision indeed results from the larger input capacitance. Comparing the WLS coated MAPMTs to the uncoated MAPMTs the difference in the extracted timing precision is quite consistent over all ToT bin widths, only showing an even

worse performance of the coated MAPMTs towards very large ToT bin widths, where the ToT bin includes low ToTs and thus capacitive cross talk.

## 7.2 Influence of WLS coating on LE timing precision

As was seen before the timing precision of the WLS coated MAPMTs is slightly worse comparing it to uncoated MAPMTs. Hereby the WLS coating is known to induce a prolonged tail in the timing distribution following roughly an exponential decay. This exponential decay results in an asymmetry in the LE time distribution. Thus the deterioration in the derived timing precision for WLS coated MAPMTs on basis of a Gaussian fit must be assumed underestimated. To derive a better comparison between the timing precision with and without WLS coating, this tail is taken into account by fitting a Gaussian profile $G$ convoluted with an exponential decay $Exp$ [5]

$$\mathrm{GExp}(t_{\mathrm{LE}}) = (G * Exp)(t_{\mathrm{LE}}) = \exp\left(-\frac{1}{2}\left(\frac{t_{\mathrm{LE}} - \mu_{\mathrm{LE}}}{\sigma_{\mathrm{LE}}}\right)^2\right) * \exp\left(-t_{\mathrm{LE}}/\tau_{\mathrm{LE}}\right) . \tag{7.1}$$

As the width of this distribution is not extracted easily the decay constant of the fitted exponential decay is used for comparison between WLS coated and uncoated MAPMTs. This
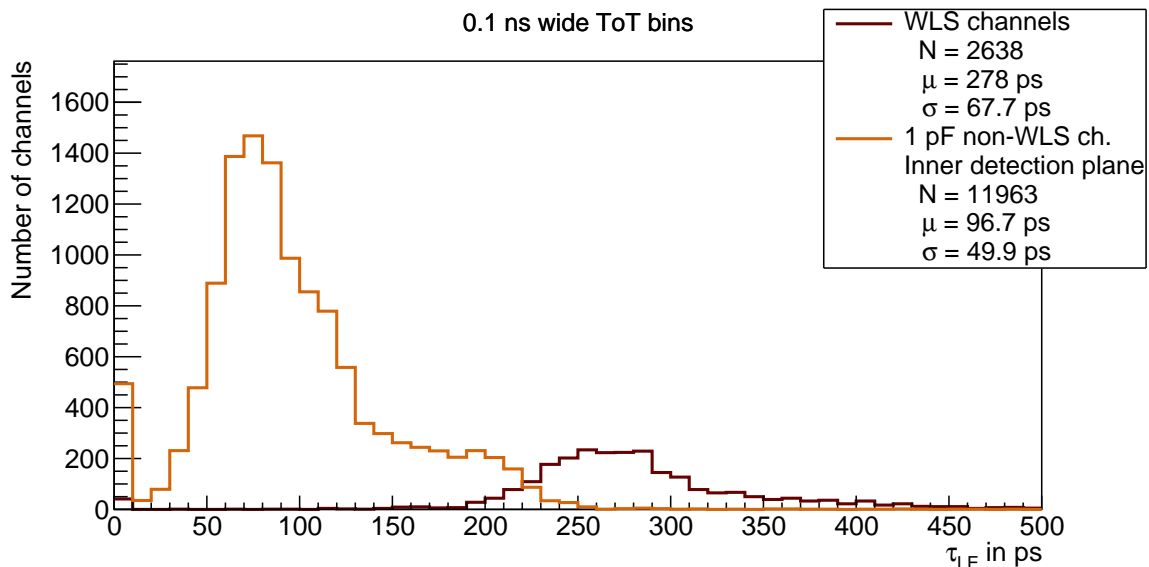


**Figure 7.4 ♦** *Distribution of $\tau$ being the decay constant of a Gaussian-Exponential convolution to approximate the tail of a timing distribution. The convolution is described in equation* (7.1). *Fitted are all* 1 pF *channels situated on the inner photon detection plane. These channels are split into two groups. Channels from WLS coated and uncoated MAPMTs. The mean $\mu$ and standard deviation $\sigma$ of each distribution are denoted in the legend. The fit was carried out over a single* 100 ps *ToT bin using the ToT range of the* 100 ps × 100 ps *LE-ToT bin with the largest number of entries. The bin at zero indicates fits where no exponential decay could be fitted properly and the fit defaulted to a simple Gaussian profile.*

constant is overlayed by the remains of the, falsely to rings associated, contribution from scin-

---

[5] For this, the implementation given by the ROOT class ROOFIT::RooGExpModel was used.

tillation light[6]. Therefore only those MAPMTs should be compared that are spatially not too far separated, as especially with respect to the polar angle $\theta$ the amount of scintillation light varies drastically, being larger towards the inner part of the detector. Therefore, figure 7.4 shows the decay constant $\tau_{LE}$ extracted from the fit for WLS coated MAPMTs and non-WLS coated MAPMTs placed on the inner photon detection plane. In this figure one now sees much clearer the impact of the WLS coating forming a large tail in the timing distribution. The fitted decay constant is roughly tripled by the use of the WLS coating. In that regard even more interesting is the question for which LE time cut widths a significant gain applying the WLS coating can be achieved. Therefore cuts on the LE time of fixed width are applied to the reconstruction. Herefore the left cut values for each channel that were derived in section 6.3 are used as left edges of the cut window with fixed width. Applying these cut windows with different widths of $\{0.75, 1, 1.25, 1.5, 2, 3, 4, 5, 10, 20\}$ ns to the reconstruction one can gain insight into the efficiency enhancement the WLS offers as function of the cut window width. To assess the efficiency, a ratio is derived per channel, dividing the number of hits per channel when an electron is found in the proximity, by the number of electrons which are found in the proximity. The electron candidate is hereby defined again through a cut on $0.95 < \beta < 1.05$, the momentum $|p/z| < 250\,\mathrm{MeV}/c$ and mass $m < 50\,\mathrm{MeV}/c^2$. Furthermore, a found ring with radius $17\,\mathrm{mm} < r_{Ring} < 30\,\mathrm{mm}$ is required that is at most $2°$ separated. The proximate area which is found around this candidate is



**(a)** *1 ns time window*          **(b)** *20 ns time window*
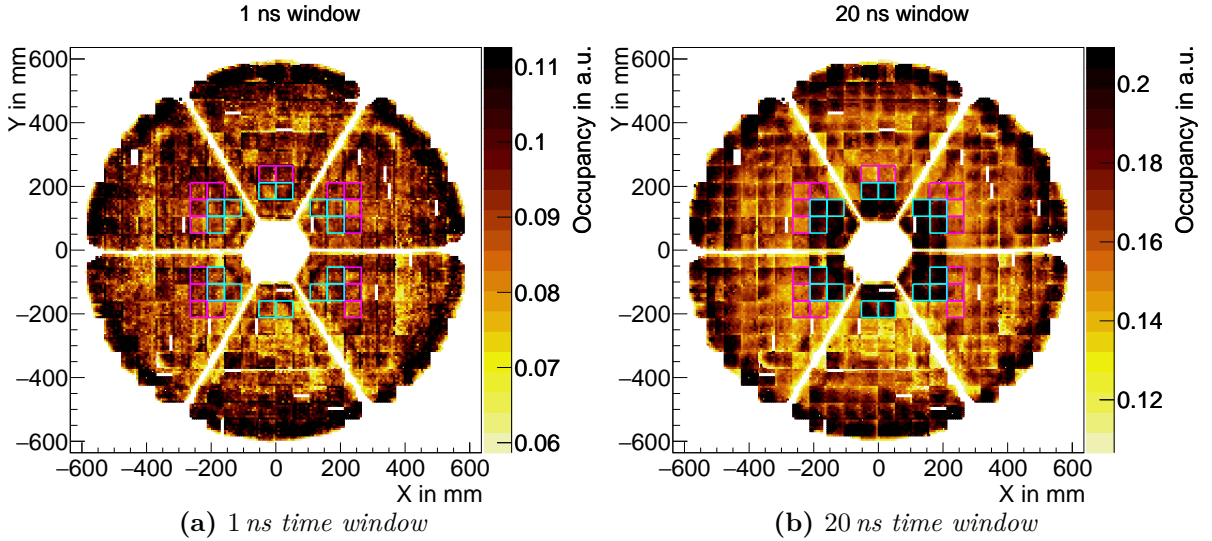
**Figure 7.5** ♦ *Spatially resolved occupancy distribution for a 1 ns* **(a)** *and 20 ns* **(b)** *wide LE time cut. The occupancy is derived per channel and defined by the ratio of number of hits in that channel with an electron candidate in its proximity by the number of electron candidates in its proximity (cf. equation (7.2)). Marked with magenta rectangles are MAPMTs not coated with WLS (and also read out by DiRICHes with 1 pF input capacitance) which are used in the following quantitative analysis and cyan rectangles indicating the accordingly used WLS coated MAPMTs. The same figures additionally requiring a ToT larger than 3 ns is shown in the appendix figure A.55 pg. 214.*

delimited by a circle with radius $30\,\mathrm{mm}$ and an additional angular equivalent of $2°$. Comparing

---

[6]At this point it is worth pointing out, that counterintuitively the WLS also enhances the amount of scintillation light as its region of emittance reaches down into the UV region (as per [SFK15]).

the resulting occupancy per channel

$$\text{Occ.(ch)} = \frac{\text{Number of hits near e}^{\pm} \text{ per channel}}{\text{Number of e}^{\pm} \text{ near channel}} \ , \tag{7.2}$$

spatially resolved for a LE time cut of width 1 ns to one of 20 ns width in figure 7.5, one immediately sees that nearly all efficiency enhancement due to the WLS vanishes when moving to the 1 ns LE time cut. To quantify this dependency of the increase in measured number of photons by using WLS coating with respect to the used LE time cut width, a dedicated analysis is carried out. Using the LE time cut windows with fixed width established before, the average occupancy is measured over all outer WLS coated MAPMTs and their non-WLS coated neighbors. Hereby only those MAPMTs are taken into account that are read out by DiRICH-FEBs with 1 pF input capacitance that do not suffer from shadowing of the spokes in the RICH. The used MAPMTs are also indicated by magenta (non-WLS) and cyan (WLS) rectangles in figure 7.5. This analysis applies an additional ToT cut allowing only ToTs larger than 3 ns to limit the influence of capacitive crosstalk which is enhanced by the enlarged amount of pulses measured on the WLS coated MAPMTs[7]. This analysis is depicted in figure 7.6, where the LE time cut dependent occupancy for the non-WLS coated and WLS coated MAPMTs is plotted as ratio. Thereby the ratio is built comparing each derived occupancy to the occupancy derived for the non-WLS coated MAPMTs at 20 ns. One can immediately retrieve the overall increase in number of measured pulses which reaches 26% after 20 ns. This increase is significantly larger than any other reported increase in the hit multiplicity through WLS, where an increase of $\leq 21\%$ was found [TS18, 61f][Ada+15; Pat19]. This leads to the assumption that still a large contribution of hits from background sources is incorrectly included in this analysis. Large parts
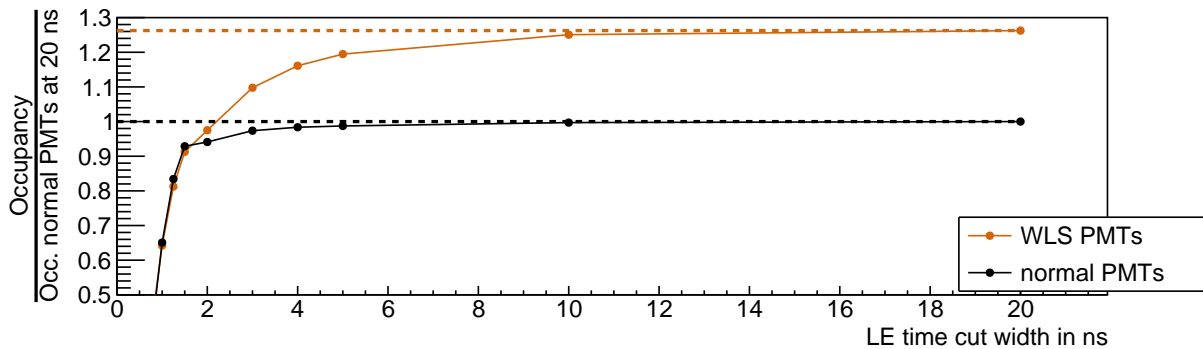


**Figure 7.6 ♦** *Relative average occupancy comparing selected channels from WLS and non-WLS coated MAPMTs for different LE time cut widths. The occupancy in dependence of the LE time cut width is thereby averaged over all respective channels before dividing it by the average occupancy measured in the uncoated MAPMTs at a LE time width of* 20 ns*. Hereby only channels with* 1 pF *input capacitance are used as shown in* Fig. 7.5*, with the occupancy defined through equation* (7.2)*. To suppress low ToT cross talk an additional cut* ToT > 3 ns *is applied. Indicated with dashed lines are the maximum values reached after* 20 ns*, therethrough exhibiting the gain of the WLS coating.*

of this contribution are most likely caused by scintillation light which is also emitted into the UV

---

[7]Unfortunately a measurement without any ToT cut is not possible even without a particular cut on ToT here, as the already existing standard cut discussed in chapter 6 rejects low ToTs.

region (cf. [SFK15]) to which the WLS is more sensitive. The break even point, where the WLS coated and uncoated MAPMTs produce the same amount of hits is found slightly later than 1.5 ns. For smaller LE time cut windows the amount of measured hits by WLS coated MAPMTs is smaller than those of the uncoated MAPMTs. Hereby this can only be a lower limit due to the scintillation light and uncorrected dependence on walk and number of simultaneous MAPMT hits. According to a toy analysis that assumes that the real increase in number of hits due to the WLS coating lies in the order of 20% and scales all measurement points for the WLS coated MAPMTs accordingly, the break even point is found after 2 ns (see Fig. A.57 appendix pg. 215). As the WLS is known to also have an impact on ring sharpness – be it through dispersion or the isotropic photon emission of the WLS coating – a study is made to see if a narrow time cut also reduces the increased $dR$ value. This would again support that any effect of the WLS coating is fully eliminated for narrow LE time cuts. For this purpose, figure 7.7 depicts the $dR$
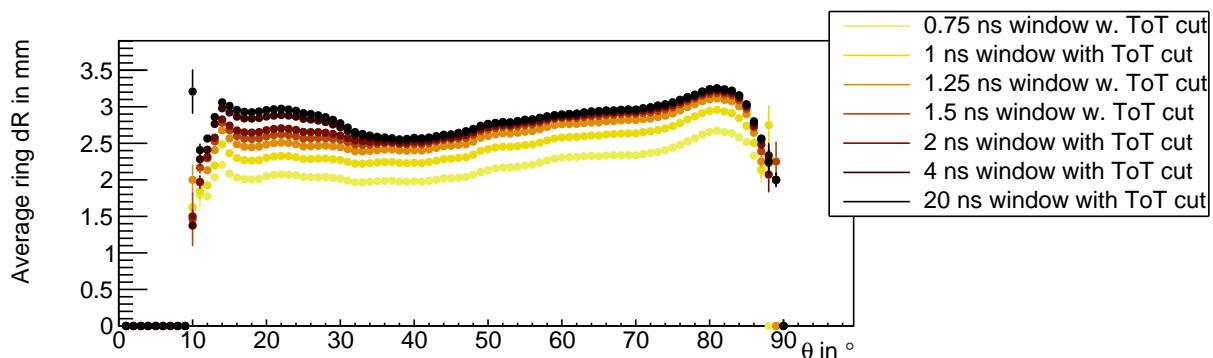


**Figure 7.7 ♦** *Average ring dR distribution over θ for different LE time cut widths with an additional ToT cut of* ToT > 3 ns. *The dR is calculated according to equation* (4.1) *for rings found at most* 2° *separated from an electron candidate with radius r between* 17 mm *and* 30 mm.

distribution with respect to the polar angle $\theta$ for different LE time windows. Hereby also the cut on the ToT > 3 ns is applied. The increased $dR$ towards lower polar angles $\theta$ stems from the WLS coated MAPMTs [8]. This increase in $dR$ gets reduced drastically applying a 1.5 ns wide LE time cut, while the $dR$ in the rest of the detector is mostly unaffected. Narrowing the LE time cut even further by moving to a 1.25 ns wide cut, one now finds the $dR$ reduced over the full detector. Still one sees a slight enhancement of the $dR$ towards lower polar angles. This increase however is in parts not correlated to the WLS coating, as simulations that do not account for the ring broadening effect of the WLS also show a slight increase in $dR$ for smaller polar angles[9]. It is therefore unclear if a complete recuperation of the worse $dR$ using WLS coated MAPMTs is already achieved at 1.25 ns. One does find however that the decrease in the average $dR$ gets indeed very small applying time cuts in the order of 2 ns. The steep drop in $dR$ visible for very narrow time cuts is in parts related to a suppression of overlapping double rings. This gets very obvious when comparing the number of hits near electron candidates added to the appendix (fig. A.59 pg. 216) where the double ring contribution is suppressed for sharper time cuts (further discussed in chapter 8.

---

[8]This is additionally supported by the $x/y$-spatially resolved $dR$ distributions found in figure A.58 appendix pg. A.58.

[9]The interested reader finds an according figure A.85a in the appendix pg. 235

## 7.3 Summary

Throughout this section the effective timing precision of the DiRICH read out chain with H12700 MAPMTs was derived in the context of the HADES RICH. Hereby two main culprits deteriorate the timing precision, the walk, being the dependency of the measured LE time on the measured signal amplitude and thus ToT, and the dependency of the LE time on the occupancy on the MAPMT. In order to retrieve the best possible timing precision using the MAPMTs and the DiRICH readout chain one therefore would need to correct for both of those effects. To still get a good approximation without these corrections in this chapter the LE time precision of only one single ToT bin was studied. It was found that the detector average timing precision in a single 0.1 ns ToT bin reaches below 200 ps. A distinction was made between WLS coated MAPMTs and normal MAPMTs reviling the timing precision being deteriorated by $\sim 30$ ps assuming a Gaussian shaped timing response. Also the influence of the 10 pF input capacitance was found to be in the order of 15 ps. Integrating over the full ToT range an average detector timing precision of $\sim 350$ ps was found. This value would reflect the timing precision when not accounting for any ToT dependent walk and other effects. Further analyses regarding the WLS coated MAPMTs indicated that through the fit of a Gaussian profile convoluted with an exponential tail, the tailedness of the LE time distribution of the WLS coated MAPMTs exceeds that of the normal MAPMTs significantly, leading to the conclusion that the timing precision using solely a Gaussian profile fit artificially improves the timing precision of the WLS MAPMTs retrieved before. This was supported through a dedicated analysis using LE time window cuts of fixed width and extracting the detector response for WLS MAPTMs and normal MAPMTs separately. The gain through use of the WLS coating was found to reach 26% after roughly 10 ns. This value is significantly larger than the gain of the WLS found in other studies which hints towards an improper inclusion of the also enhanced scintillation light efficiency of the WLS in the analysis. The WLS coating however also induced an earlier drop off in the efficiency with respect to the LE time cut width leading to the time cut width at which WLS coated and uncoated MAPMTs see the same amount of hits being slightly after 1.5 ns. This was in parts supported by findings analyzing the ring sharpness, which showed the same trend. Conclusively a coating with a wavelength shifting layer is not beneficial for applications that require a timing precision down to the sub-nanosecond level.

<div align="right">

# 8

</div>

# Using ToT information for background suppression

This section focuses on using the time over threshold (ToT) information to discriminate between single and double photon hits. This information is especially useful to later distinguish single Cherenkov rings from two rings superimposed to one another. Hereby the MAPMT responds to different amounts of light, i.e. different number of simultaneous photon hits in a single pixel, with different signal charges on the anode. This is equal to an increase of the integrated signal pulse, which results in increasing width and signal height. An increase in signal width is measurable in the DiRICH-FEB via time over threshold (ToT) determination. The increase in ToT however does not need to correlate linearly with the amount of light, contrary to the signal integral. Therefore a calibration of each channel's ToT spectra might be necessary, as the position of single and multi-photoelectron peaks in the ToT distribution might vary on a per channel basis.

## 8.1 Uncalibrated ToT sum as proxy for photon multiplicity in single hits

First however a test analysis is made to check if already an uncalibrated use of the ToT information, i.e. simple ToT sum, allows to distinguish between single Cherenkov rings and two rings lying on top of each other. This is done using electron candidates[1] registered in the HADES detector for which at least five hits are registered in the RICH detector in a close-by area[2] around the candidate. All hits in this area are then counted and their ToT summed up. As an additional requirement, the electron candidate is only allowed to have one ring nearby as otherwise the superimposed double rings would already have been recognized by the ring fitter. As the number of measured photons produced by the electrons varies over $\theta$ due to the WLS coating at low $\theta$ and an increased radiator length for larger $\theta$ [3], the analysis here focuses only on a small range in $\theta$. The discussed results are however valid even when integrating over the full range in $\theta$ and especially for all $\theta$ individually (cf. Fig. A.62 pg. 218 appendix). Using the $\theta$-range of $36.5° < \theta < 37.5°$ [4] for the electron candidates, figure 8.1a shows the number of hits and their ToT sum, where one can clearly make out a single and double ring contribution. The

---

[1] The electron candidate is again defined through a cut on $0.95 < \beta < 1.05$, the momentum $|p/z| < 250\,\mathrm{MeV}/c$ and mass $m < 50\,\mathrm{MeV}/c^2$.

[2] Circular area with radius $30\,\mathrm{mm}$ and an added angular difference equivalent of $2°$ around the respective electron candidate.

[3] The interested reader finds the corresponding figure A.61 in the appendix pg. 217.

[4] The $1°$ range around $\theta = 37°$ is chosen as this polar angle is still fully on the inner photon detection plane but still at large enough $\theta$ to feature only minimal signal contributions of WLS coated MAPMTs.

single and double ring contribution are identifiable by two separated Gaussian like peaks visible in both distributions. Both distributions are therefore fitted with two Gaussian profiles and an exponential decay, approximating the underlying background to better examine the separation between the two contributions. These fits are depicted as dashed lines in the same figure with the fitted mean $\mu$ and standard deviation $\sigma$ of both Gaussian profiles denoted in the legend. The fitting range for the binary number of hits distribution as well as the ToT sum distribution starts at the respective onset of each spectrum. The fitting range of both distributions is also cut early, cutting away a long tail which can not be attributed to either of the Gaussian distributions. One is then able to scale the $x$-axis in terms of the first peak's position ($\mu_1$)



**(a)**  **(b)** *x-axis scaled to single ring mean*
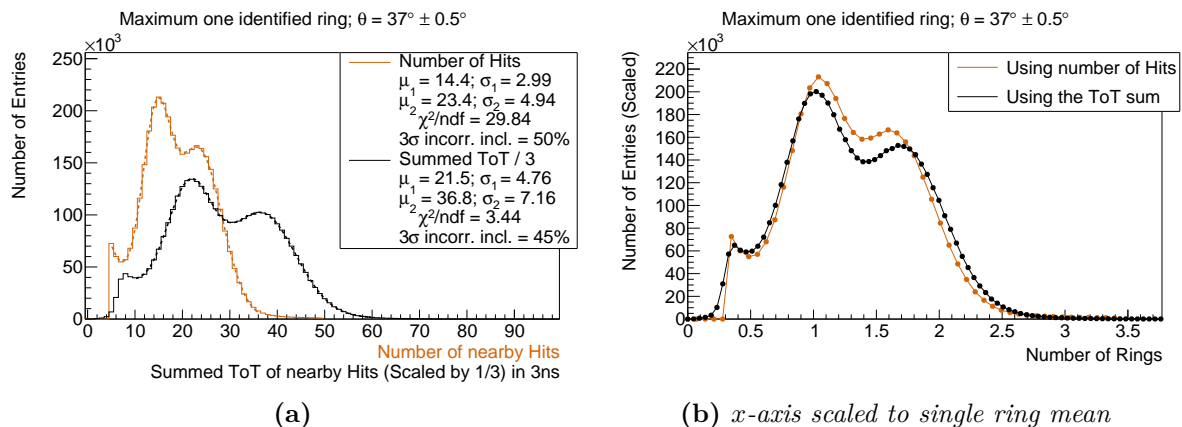
**Figure 8.1** ♦ *Comparison of the distributions counting the number of hits in the proximity of an electron candidate and summing up their hit dependent ToT. Sub-figure* **(a)** *shows the distribution of number of hits and their ToT sum. Hereby all hits are counted in circular areas with radius* 30 mm *and added angular difference equivalent of* 2° *around electron candidates. The reconstructed electron candidate is only allowed to have one reconstructed ring in its proximity and must be reconstructed in the limited polar angle region of* 36.5° < θ < 37.5°. *To retrieve the ToT sum spectrum, the ToT of all those hits is summed up and divided by three for visibility reasons. Each distribution is fitted via two Gaussian distributions for single and double ring contributions and an underlying exponential decrease to approximate the background. The uncertainty on the fit parameters is estimated through fit-range variation and given as the last digit of each parameter. The "3σ incorrect inclusion" percentage is defined via equation* (8.1). *It refers to the amount of incorrectly as single ring identified double rings when cutting on* 3σ *of the single ring distribution. Sub-figure* **(b)** *scales the x-axis for each distribution individually, according to the extracted* $\mu_1$ *from the corresponding fit. The resulting x-axis then corresponds to "number of rings" as the the first peaks center will always be situated at* x = 1. *Hereby the distribution using the ToT sum also has its y-axis scaled accordingly to keep the area below both distributions comparable.*

of each individual distribution for better comparability between the two spectra as is depicted in sub-figure 8.1b. There one finds that the average ToT sum in a double ring shifts further towards twice the amount of that of a single ring, which is less so the case using only binary hit information from the RICH detector. Furthermore, the overall fit quality improved, as seen by the lower $\chi^2/\mathrm{ndf}$ in fig 8.1a. This indicates that approximating the whole spectrum with only two Gaussian profiles and the additional exponential distribution fits the data much better now. Nonetheless since only a subrange of the full distribution is fitted, the overall fit results can only

be reliable on the percent level, which is fine for this qualitative comparison between the original binary hit information and the additional usage of the ToT information. Albeit those benefits, the overall separability between single and double rings seems to have improved only slightly. In order to quantify the separation between single and double ring a good value to compare is the "3$\sigma$ incorrect inclusion"-percentage, which is also noted in the figure's legend. This parameter is described by

$$\text{"3}\sigma \text{ incorr. incl."} = {}^{100}\!/\!_2 \left( erf \left( \frac{1}{\sqrt{2}} \frac{\mu_1 + 3\sigma_1 - \mu_2}{\sigma_2} \right) + 1 \right) \% \tag{8.1}$$

and thus provides the percentual amount of incorrectly identified double rings when cutting on 3$\sigma$ of the single ring distribution. Comparing this number between the distribution using the binary hit information and the distribution using the ToT sum, one finds a slight improvement by using the ToT in the order of 5 pp [5], i.e. $\sim 11\%$. The next step is now to calibrate/align the ToT of the different channels to see if this separation value can still be improved upon. Calibrating hereby refers to the idea, that estimating each channels' single and double photoelectron ToT equivalent would allow to give each measured hit an approximate channel dependent photoelectron equivalent. This calibration would take effects such as slightly different pixel gain or slightly different measurement thresholds into account.

## 8.2 Discussion of ToT spectra on basis of single channels

Before deriving a ToT calibration one must understand the different features of the ToT distribution. Therefore figure 8.2 shows the ToT distribution for two neighboring channels using three different data sets. The first dataset uses the beam data which is correlated to the START detector signal, additionally requiring that an identified electron[6] is in close proximity to the individual channel of which the ToT is added to the ToT distribution. This dataset – from now on called "In-beam" – features photons from single and double rings. Its single channel ToT spectrum thus features contributions from single and double photon hits. The second dataset uses signals from laser data which mostly feature single photon hits except for the outer rim of the detector, where the occupancy is much larger. Only at these positions the ToT spectrum is also comprised of single and double photon hits. The last dataset uses the signals detected at LE times before the beam correlated signals are detected in the RICH[7]. This dataset thus features no beam correlated data and contains only the dark noise of the MAPMTs and the electronic noise always persistent in the detector. Dark noise of MAPMTs is mostly comprised of thermal electron emission from the photo cathode. Such noise must produce the same signal as a normal single photon undergoing the photo effect in the MAPMT's cathode, as the amplification chain is the same for both. In consequence the ToT spectrum from the "off beam" dataset is used best as baseline determining the signal shape for single photoelectron induced ToTs. Examin-

---

[5]pp stands for the percentage point.

[6]$\beta > 0.95$, $|p/z| < 250 \, \text{MeV}/c$, $m < 50 \, \text{MeV}/c^2$, more than 10 hits in a circular area with radius 30 mm and added absolute angular difference equivalent of $4°$.

[7]The dark rate data is taken from $-1000$ ns to $-600$ ns with respect to the trigger signal, whereas the signal correlated to the beam is found at earliest $-580$ ns.
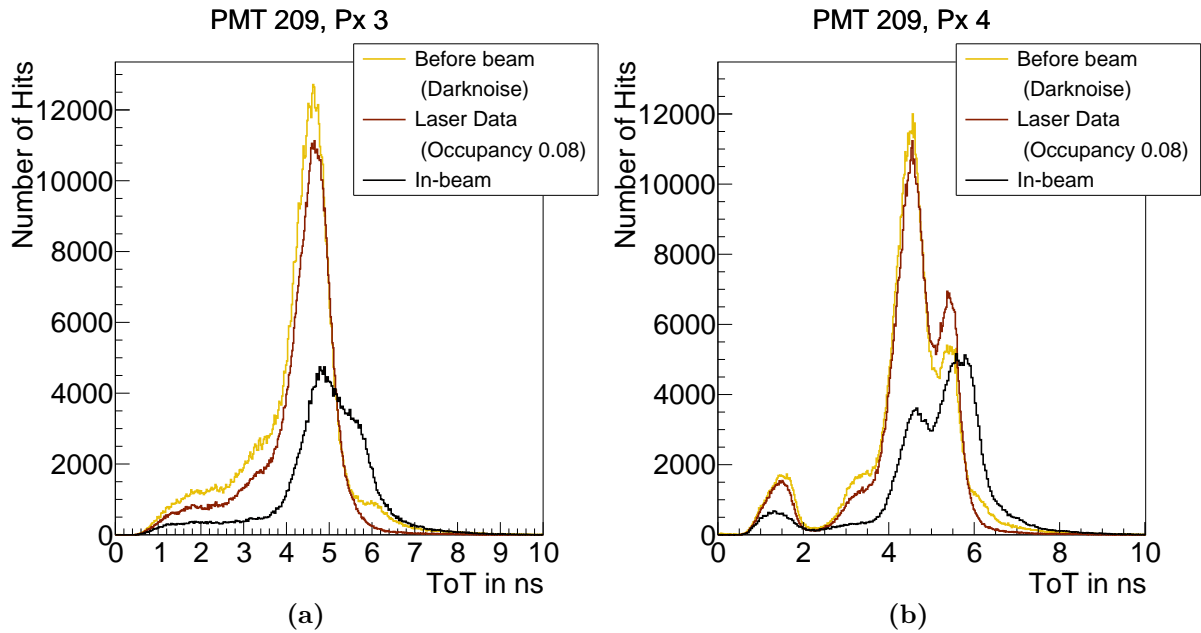
**Figure 8.2** ♦ *ToT spectra from two neighboring channels on the same MAPMT for three different datasets. Before beam refers to the ToT of hits which are registered before any beam induced event, which are dominated by the MAPMT's dark noise. The laser data is taken in between beam events with the laser system attached to the RICH. This data is for most pixels comprised mostly of single photons. The occupancy value hereby refers to the average number of hits per event in this channel. "In-beam" data uses the ToT of signals which are correlated to the detector trigger measured in pixels which are in close proximity to an electron candidate.*

ing figure 8.2a the difference between single and double photoelectron induced signal ToTs is visible in the increasing number of signals with larger ToTs. This increase is only visible in the "In-beam" data, with the laser data's occupancy for this particular channel being 0.08 [8] and thus only single photons reaching the MAPMT's pixel. This increase seems to induce a second peak/bump in the spectrum at approximately 6 ns for this channel. Unfortunately this bump is only an artifact of the signal itself as can be seen in the spectrum of figure 8.2b, where this second peak is also visible for data that is only comprised of single photoelectron induced signals. A second interesting observation can be made studying the difference between the "off-beam" and "In-beam" spectra, where one recognizes that the single photoelectron peak, which would still be the dominant contribution to this spectrum for occupancies of up to 0.72, seems to be lower than the contributions of larger photon counts (for best visibility see e.g. Fig. A.64b in the appendix). This means, that either the single photon contribution is indeed lower than the multi-photoelectron contributions or that the single photon contribution shifts slightly for the "In-beam" data. The reasons for such a shift would not be fully understood, however could be correlated to an overall baseline shift as a result of many pixels being illuminated at the same time, thus introducing a large amount of capacitive cross talk on the MAPMT. To demonstrate that both artifacts are present in many channels, figure A.63 in the appendix pg. 219 shows a random selection of ToT spectra from other channels. Assessing the double peak, or rather

---

[8] An occupancy of 0.08 means that the channel only detected eight signals every 100 trigger pulses induced by the laser.

abnormal dip structure further, the question arises if different input capacitances in the DiRICH low pass input filter show the artifact differently pronounced. This is not easy to check, as different channels show vastly different ToT spectra and markedness of the discussed artifact. An examination by eye did not reveal any major difference between DiRICH-FEBs with 10 pF and 1 pF input capacitance as can be seen in figure A.64 in the appendix pg. 220, where randomly chosen ToT spectra of 10 pF and 1 pF DiRICH-FEBs are compared. There however one sees, that the described artifact seems only to persist for ToT values larger than 3.5 ns. The artifact can be approximately described by a steep drop that is interrupted by a sudden plateau or even increase. Therefore an approximating test is made by checking the derivative of the ToT distribution. This derivative, starting from 3.5 ns ToT, needs to show a local minimum below zero followed by a local maximum above zero and again a local minimum below zero thereafter. To exclude minor fluctuations at least two of the three local maxima caused by this artifact need to exceed the standard deviation of the distributions derivative. The described procedure is shown for a channel with and without the described dip in figure A.65 in the appendix pg. 221. Now, to distinguish between channels showing this abnormal dip structure from channels that do not, the arbitrarily named markedness value is defined. This value is set to one if the channel fulfills the aforementioned criterion that at least two of the three local maxima in the derivative of the ToT distribution exceed the standard deviation of the same distribution. Setting the markedness of all other channels to zero one can now plot the average markedness for each DiRICH-FEB input channel and for each MAPMT pixel in figure 8.3. Albeit the described
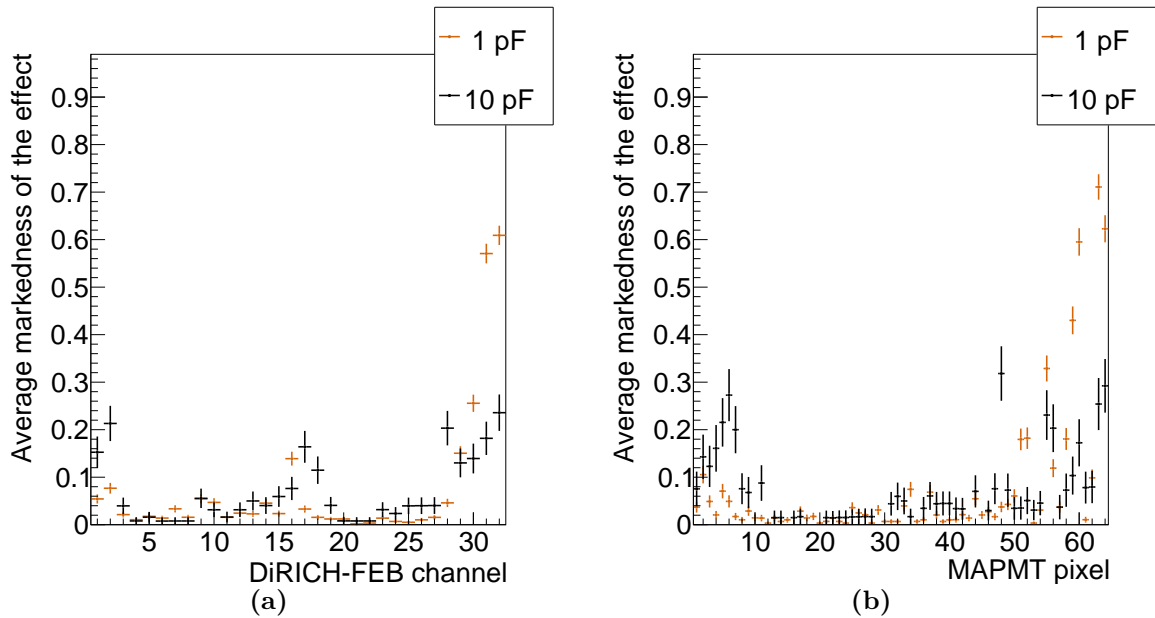


**Figure 8.3 ♦** *Average markedness of different DiRICH channels **(a)** and MAPMT pixels **(b)** separated by the corresponding DiRICH-FEB's input capacitance. The markedness hereby is a proxy to identify channels featuring an atypical dip in their ToT distribution. Those channels receive a markedness value of one, while all others are assigned a markedness of zero. The derivation procedure is shown and described in figure* A.65 *appendix pg.* 221. *The indicated error bars depict the statistical error on each average. The results of these plots can only be seen qualitatively, as the proxy is not fully reliable.*

markedness proxy not being very robust, one still can make out channels, where the average markedness exceeds the globally averaged markedness. On the DiRICH, these channels are channels $1, 2, 16, 17$, and 28–32. Hereby the influence of the input capacitance of the DiRICH seems only minor and overall not consistent over the different channels, meaning that for some channels the markedness of the $10\,\mathrm{pF}$ driven DiRICHes exceeds the markedness of the $1\,\mathrm{pF}$ ones and vice versa. Also when checking the MAPMT pixels one finds the last pixels to exceed the global average. Closer examination however shows, that explicitly channels $64, 63, 60, 59$, and $55$ overshoot the average the most. Hereby pixels $64, 63, 60$, and $59$ correspond to DiRICH channels $31$ and $32$ of two DiRICHes reading out one MAPMT, whereas pixels $62, 61, 58, 57$ correspond to DiRICH channels $15$ and $16$ (cf. Fig. A.66 appendix pg. 222). If one would assume the dip to be an MAPMT artifact there should be no particular reason why channel pairs of two would exhibit the largest markedness of the dip artifact. If however the dip is induced by the DiRICH-FEB one would see exactly pairs of two channels exhibiting the largest markedness, as those are always read out by directly neighboring channels. Therefore, this hints towards the dip indeed being an artifact of the DiRICH channels lying on the very corners of the module. These would be exactly those channels, which did also show an overall increased noise band width as was discussed in section 3.2.3. This behavior would indeed correspond to the effects discussed in [GKR15], where the presence of fixed frequency noise was found to induce dips in the measured ToT spectrum. They describe the effect such that periodic "[. . . ] noise induces a random shift on both the measured leading and trailing edges, correlating them with each other [. . . ] [, which] decreases the probability of obtaining certain periodic values of the ToT"[GKR15, p. 20]. Consequently one would be able to derive this special noise's frequency finding several dips in the spectra. Prime candidate for a fixed frequency noise contribution would be the clock signal with $200\,\mathrm{MHz}$ which is distributed from the DiRICH combiner board via the backplane to all DiRICH-FEBs. This clock, albeit separated via a ground layer in the DiRICH-FEB PCB is routed with respect to the PCB layer structure closest to channels 17–32 (layer one to layer four). It actually lies directly beneath channels 32–29 separated by a ground layer and a $1.1\,\mathrm{V}$ distributive layer. Such a signal would induce $5\,\mathrm{ns}$ separated dips in the ToT spectra. In an attempt to support exactly this theory a Fourier transform of the ToT spectrum was made but failed, as the standard variations in the ToT spectrum exceed those of the dips. Overall, this discussion only being on a qualitative level would need a dedicated measurement in the lab to fully determine the exact culprit leading to such an inhomogeneous ToT distribution.

## 8.3 Deriving a ToT calibration per channel

To still derive a robust calibration procedure albeit the artifacts in the ToT spectra, two different methods are applied "smoothing" the spectrum to ease a later determination of single and double photon contributions. Both those methods are depicted in figure 8.4 applied to two different channels. The first method uses just a coarser binning of the spectrum in $0.25\,\mathrm{ns}$ bins, as already there the effect of having two separate peaks nearly vanishes. The second method uses a symmetric moving average over $\pm0.5\,\mathrm{ns}$ to even further smooth the spectrum. This comes
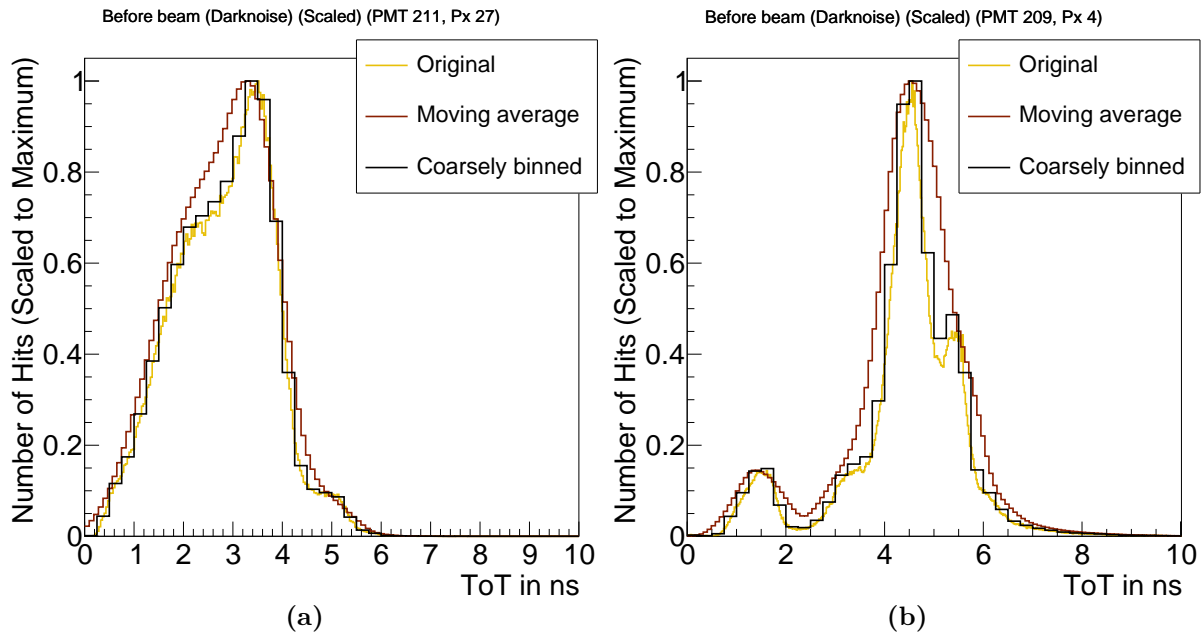
**Figure 8.4** ♦ *ToT spectra comparing different "smoothing"-methods for two different channels. The ToT spectra are extracted from the "off beam" dataset which is mainly comprised of dark noise of the MAPMT. The different histograms are scaled to their maximum to have all presented methods overlay. The "moving average" is taken over a sliding window of 1 ns width, whilst the coarsely binned data fills the data into 0.25 ns bins.*

with the downside of decreasing the separability between single photoelectron peak and noise for channels with low gain (visible in Fig. 8.4a). The smoothened spectra of the "off-beam" data are now fitted with a single Gaussian distribution to retrieve the single photoelectron response for each channel. Special attention is payed to the channels with low gain. There, instead of fitting a Gaussian distribution, the signal is approximated by finding the last local maximum. This local maximum is found moving from largest ToT values to lowest, searching for the three bins after which the spectrum falls again. Those three points are then used in a quadratic extrapolation[9], determining the local maximum. From there the HWHM – and with that, the standard deviation – is found through search for the last ToT value with a number of hits larger than $a/2$, where $a$ is the number of hits at the maximum. With this procedure the single photoelectron response of each channel is extracted. The extracted means and widths are depicted in figure 8.5. One immediately recognizes the inhomogeneity in the fit of the coarsely binned ToT spectra. The visible structure having a period of ca. 0.25 ns can be ascribed to the coarse binning itself, having a bin-width of same size. This effect is not visible in the fits to the spectra smoothed by moving average. Further comparing the two different smoothing procedures a slight shift in the standard deviation becomes visible. Whilst the overall shape, showing an increase of the width towards lower means is consistent for both distributions, the absolute unfolded standard deviations of the moving average data

---

[9]Quadratic extrapolation is carried out through the Lagrange Polynomials

$$y = y_0 \frac{(x - x_1)(x - x_2)}{(x_0 - x_1)(x_0 - x_2)} + y_1 \frac{(x - x_0)(x - x_2)}{(x_1 - x_0)(x_1 - x_2)} + y_2 \frac{(x - x_0)(x - x_1)}{(x_2 - x_0)(x_2 - x_1)} \ .$$

(a) *Fit results from moving average smoothed spectra*

(b) *Fit results from coarsely binned spectra*
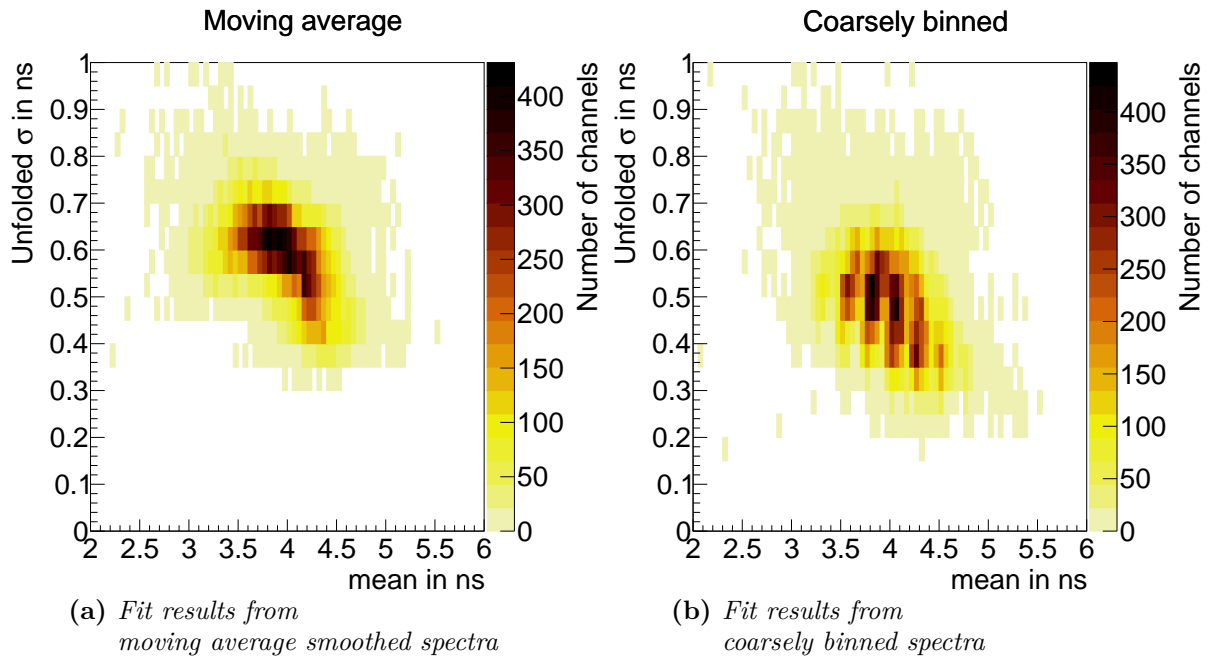
**Figure 8.5** ♦ *Fit results fitting the ToT spectra extracted from the "off-beam" data with two different smoothing methods for each channel. The "off-beam" data is comprised mainly of dark noise from the MAPMT. The moving average method* **(a)** *takes the moving average over 1 ns, whilst the coarsely binned method* **(b)**, *smooths the data by filling it into 0.25 ns bins. The extracted mean is depicted on the x-axis with the unfolded standard deviation on the y-axis. The unfolded standard deviation hereby refers to* $\sigma_{\mathrm{unfolded}} = \sqrt{\sigma^2 - w^2/12}$ *with w being either 0.25 ns or 1.0 ns (for the moving average).*

show a clear shift towards larger values. As the standard deviation is already cleared of the artificial broadening induced by the smoothening procedure, finding an explanation for that is not easy. One explanation would be that the Gaussian distributions fitted to the coarsely binned data still might not include certain features of the full ToT distribution as the smoothening might still not have been wide enough. This assumption would be contradicted by the fact that only very few channels reach standard deviations larger than 0.6. Another explanation would be that the broad moving average of 1 ns fails for small average ToTs as there the noise contribution might already influence the main signal shape and thus the fit results. This would also partially explain the visible kink in the spectrum. The extracted mean positions which are most important moving forward are consistent for both procedures. This is also seen when overlaying all channels' ToT spectra after aligning all their single photoelectron responses to 4 ns, being depicted in figure 8.6. Visibly, the spread in the global ToT distribution gets reduced by aligning all measured ToTs to the channel's single photoelectron peak corresponding ToT, thus testifying that the single photoelectron response of each channel seems approximated well. Albeit the improvement being visible, the overall narrowing of the global ToT spectrum moving from the original spectrum to the aligned one, is not large. This is seen comparing the standard deviations $\sigma$ of all distributions where an improvement of only 0.4 ns is found. This indicates that the supply voltage alignment procedure for the MAPMT HV described in section 2.5 did indeed produce very similar single photoelectron responses in nearly all channels, canceling the strong

MAPMT channel gain dependence of the ToT distributions. Comparing the distributions of both procedures used to smoothen the channel individual ToT distribution to extract the single photoelectron response accordingly, look very similar. This also results in a similar standard deviation of both distributions, where the coarse binning procedure produces only slightly better results. In that regard the channel dependent single photoelectron responses extracted using the coarse binning are used moving forward.
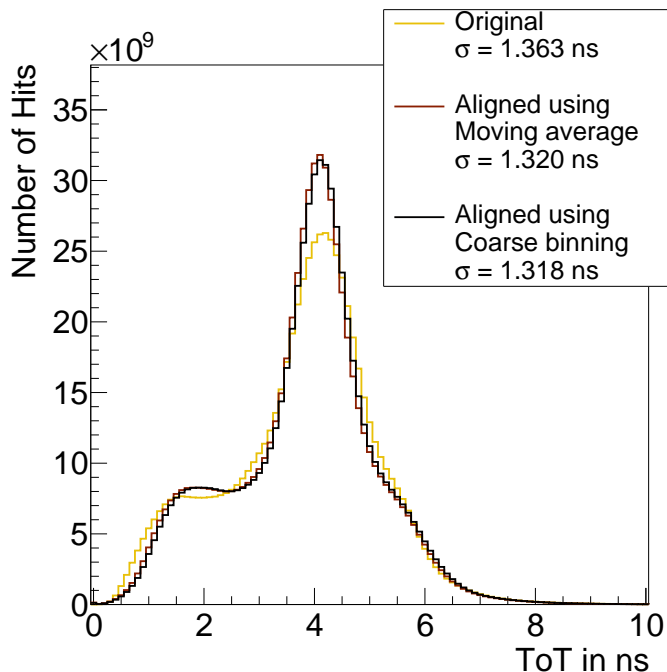


**Figure 8.6 ♦** *Integrated ToT spectra, taking all measured ToTs of all channels using the originally measured ToTs versus ToT distributions obtained using the two different smoothing methods. The alignment is obtained by shifting the single photoelectron ToT to 4 ns using respective offsets per channel. The channel dependent single photoelectron ToT equivalent is thereby derived through fitting each channels ToT spectrum of hits from "off-beam" data. The extracted single photoelectron ToT equivalents are also depicted in figure 8.5.*

With the single photoelectron signal response extracted, only the double photoelectron response is still to be determined. This is best done using the "In-beam" data, where it is known that single and double photons must be registered by most of the pixels. The first intuitive approach would be to simply fit the distribution with several Gaussian distributions, with their integral weights determined by a Poisson distribution according to the occupancy of each pixel. Assuming an occupancy of $occ \approx 0.59$ (which will be elaborated on later) one needs to fit at least three Gaussian distributions[10] for single, double, and triple photon response to the spectrum. Each distribution would feature two free parameters (mean $\mu$ and width $\sigma$) and one common parameter being their occupancy derived integral. For a normal charge spectrum one assumes also the mean and standard deviation to be correlated via $\mu_n = \mu_0 + n \cdot \Delta\mu$ and $\sigma_n = \sqrt{n}\sigma$ respectively (see [Bel+94]). This unfortunately does not necessarily have to be that way for the here used ToT measured spectra, as those do not necessarily scale linearly with respect to the signal charge (compare the toy simulations depicted in figures A.67 and A.68 in the appendix pg. 223f). Nonetheless, different tests are made, leaving all $\mu_n$ and $\sigma_n$ as free parameters, or assuming a logarithmically decreasing gap between the different Gaussian distributions. All these fits lead to very volatile results, depending heavily on the starting parameters. With the fitting procedure not leading to robust results, a simple fit with Gaussian distributions must be discarded.

---

[10]The Gaussian corresponding to the triple photon hit on the MAPMT still contributes with 8.5% to the overall visible spectrum.

The alternative approach used here takes the mean ToT of the "In-beam" data as approximation for the response of channel to larger number of photons. This mean must be derived discarding ToTs of signals from cross talk, which usually have a smaller ToT[11]. Taking the mean ToT is much more robust but comes with the downside, that one must know the occupancy of the analyzed channel such that one can use a Poisson distribution to derive an average number of photons correlated to the average ToT extracted. A good estimate on the average number of photons, if a hit is registered in the corresponding pixel, is 1.51 following the detailed explanations given in the appendix section B.4. Using the derived occupancy one can use a linear function extrapolating between the one photon case derived via the dark noise and the "In-beam" mean derived to find the corresponding number of photons for a measured ToT. This linear extrapolation can be done either using the average difference between single and multi-photoelectron mean of all channels or on a per channel basis. For this analysis the detector global average difference between single and multi-photoelectron peak was found to be 0.74 ns. Both approaches should work fine and deliver similar results if the assumptions that all channels have similar occupancies holds true. The linear approximation must be cut off for ToTs that would lead to "negative number of photon values" as otherwise rings featuring more cross talk which is smaller in amplitude might get their number of correlated photons artificially reduced. Resulting "negative number of photon values" are therefore set to zero.

## 8.4 Calibrated ToT sum as proxy for photon multiplicity in single hits

The results of the two described calibration procedures (globally averaged or channel individual difference between single- and multi-photoelectron peak) are checked again using the same cuts as in the beginning of this chapter[12]. The resulting distributions are depicted in figure 8.7. Now titled "number of photons" are the sums over the photon equivalents extracted from the calibrated ToT using the described procedure. Again all distributions (hits and "photons") are fitted with two Gaussian profiles with an underlying exponential decay (compare sub-figures a/c). Comparing the fit goodness first, both procedures produce nearly the same $\chi^2/\mathrm{ndf}$ values now including the full range of the distribution. Starting from nine to 100 "Number of photons" the $\chi^2/\mathrm{ndf}$ is still much lower than that of the binary hit distribution, which is again only fitted without its tail to large number of hits. Overall both procedures result nearly in the exact same distributions, which is unsurprising, as already discussed before. Scaling the number of hits/"photons" to the extracted mean $\mu_1$ of both distributions one can again produce figures 8.7b/d showing the proxy of number of rings. Herein visible is, that the double ring nearly reaches twice the number of "photons" compared to the single ring distribution. This is of course the wanted result of this calibration procedure. However, with the mean of the second Gaussian distribution representing the double ring's average number of "photons", not reaching exactly

---

[11] This is achieved by taking the mean only over the channel individual range starting from the already extracted single photoelectron position reduced by twice the standard deviation of the same.

[12] Electron candidates detected at $36.5° < \theta < 37.5°$ with only one detected ring nearby. The figures not requesting these two cuts are added to the appendix pgs. 225ff figures A.69 through A.74.

**(a)**



**(b)** *x-axis scaled to single ring mean.*



**(c)**



**(d)** *x-axis scaled to single ring mean.*
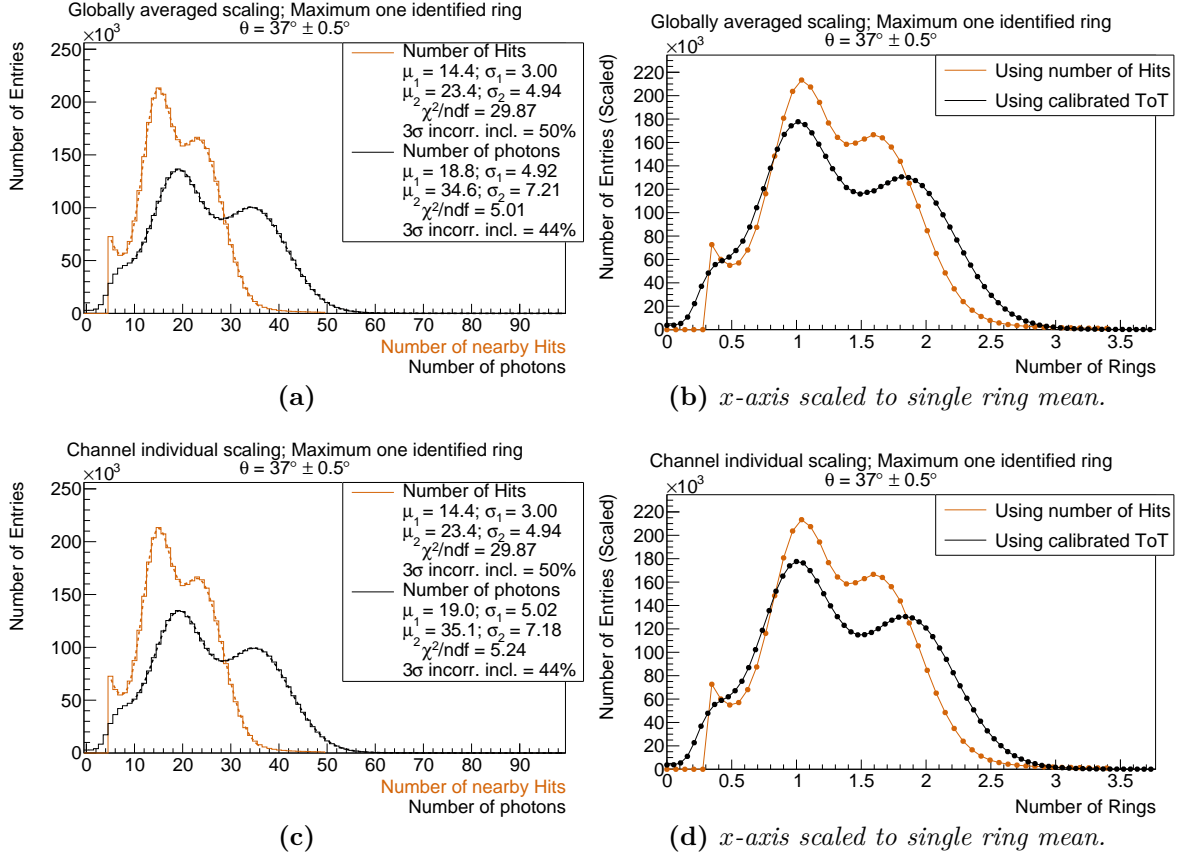
**Figure 8.7** ♦ *Comparison of the distributions counting the number of hits in the proximity of an electron candidate and summing up their channel-based calibrated ToT. Sub-figures* **(a)** *and* **(c)** *show the distribution of number of hits and their calibrated ToT sum, here called "number of photons". Hereby all hits are counted in circular areas with radius* 30 mm *and added angular difference equivalent of* 2° *around electron candidates only allowing for one reconstructed ring in the electron candidates proximity. The channel dependent ToT calibration resulting in the depicted "number of photons" follows a linear extrapolation between the each channels' single photoelectron response (1.0 "photons") and multi-photoelectron response. The latter is extracted using the "In-beam" data to extract a* 1.51 photon *ToT equivalent as mean of this distribution, while the "off-beam" data is used to find the single photoelectron response through fit. Both channel individual ToT distributions are smoothened using* 0.25 ns *wide binning. From there, sub-figure* **(a)** *averages the difference between single and multi-photoelectron response over the full detector. Accordingly, the linear extrapolation uses the single photoelectron response per channel but the detector averaged scaling value, whereas sub-figure* **(c)** *uses both parameters channel dependent. Each distribution is fitted via two Gaussian distributions for single and double ring contributions and an underlying exponential decrease to approximate the background. The uncertainty on the fit parameters is estimated through fit-range variation and given as the last digit of each parameter. The "3σ incorrect inclusion" percentage is defined via equation* (8.1). *It refers to the amount of double rings incorrectly identified as single rings when cutting on* 3σ *of the single ring distribution.*

*Sub-figures* **(b)** *and* **(d)** *scale the x-axis for each distribution, according to the extracted $\mu_1$ from the corresponding fit. Hereby the distribution using the ToT sum also has its y-axis scaled accordingly to keep the area below both distributions comparable. The resulting distribution therethrough indicates the number of rings corresponding to the respective distribution, assuming a double ring would use double the number of hits/"photons".*

twice the amount of the single ring's average number of "photons" one must assume that the used method is not fully sufficient. Therefore, also taking into account the previously observed shift of the single photoelectron peak's position in the "off-beam" data compared to the "In-beam" data, an additional test is made, transforming the ToT into number of "photons" setting the extracted single photoelectron peak position for each channel to 0.9 "photons". This means, that for this transformation the value for the single photoelectron peak position extracted from the "off-beam" data now does not represent 1.0 "photons" but 0.9 "photons". This results in an ever so slight improved ratio of single ring average "photons" to double ring average "photons" (see A.70 in the appendix pg. 226), but no further improvements. Comparing the results of the ToT calibration to simply summing up the hits' ToTs, as was discussed in the beginning of this chapter, one finds only little improvement in the separability of single and double ring contributions. Now showing a 6 pp difference in the "$3\sigma$ incorrect inclusion" percentage which equals an improvement of $\sim 14\%$ and is only one percentage point larger compared to simply summing up the ToTs of all hits and could also well be contributed to variance of the fit. Comparing however the tail of the distributions derived using the calibration, one now sees that this tail is strongly reduced, which was seen less significant using only the bare ToT sum described in the beginning of this chapter. Thus an examination by eye does indicate that the ToT calibration did improve the overall spectrum, as the ratio of "photons" from single to double rings improved and the tail vanished. The bare separability number however did not improve.

The results of the different calibration methods are summarized in table 8.1. Obviously this is first of all again a testament to the gain alignment procedure laid out in section 2.5. Nonetheless this might indicate, that the best possible gain using the ToT to distinguish between single and double rings is already reached. Here comes into play, that many channels contribute to one ring and thus the variances in their uncalibrated ToT might overall cancel out most of the time. Certainly however the conversion from ToT to number of "photons" is not optimal yet, as can be seen comparing the standard deviations of the binary hit- and number of photon distributions. It is found that the expected $\sqrt{N}$ standard deviation for a counting experiment measuring an average of $N$ counts is not reached by neither single nor double ring

$$\sigma_{\text{theo., single ring, Hit}} = \sqrt{14.4} = 3.79 > 3.00 = \sigma_{\text{meas., single ring, Hit}}$$
$$\sigma_{\text{theo., double ring, Hit}} = \sqrt{23.4} = 4.84 \approx 4.94 = \sigma_{\text{meas., double ring, Hit}}$$
$$\sigma_{\text{theo., single ring, ToT}} = \sqrt{19.0} = 4.36 < 5.02 = \sigma_{\text{meas., single ring, ToT}}$$
$$\sigma_{\text{theo., double ring, ToT}} = \sqrt{35.2} = 5.93 < 7.18 = \sigma_{\text{meas., double ring, ToT}} \cdot$$

Such an effect can be caused by inconsistent improvements through ToT usage, which in turn might be traced back to the not fully sufficient globally uniform occupancy estimate. Assuming that one could correct for the broadening in the single and double ring distributions one can calculate the best possible separation retrievable through this theoretically perfect calibration. Thus using $\mu_1 = 19.0$, $\sigma_1 = 4.36$, $\mu_2 = 35.2$, $\sigma_2 = 5.93$ one finds the "$3\sigma$ incorr. incl." value dropping down to 30%. Correcting for the occupancy and the varying ToT artifacts per channel is however very difficult and might, as discussed before, not even be possible.

**Table 8.1** ♦ *Results on the separability between single and double rings based on counting hits, summing their ToT, or counting "photons" using different methods of calibrating the ToT spectrum to retrieve the photon equivalent. The different methods hereby use different single photoelectron peak multiplicities or use the extracted difference between single and multi-photoelectron peak per channel differently. The dark noise multiplier refers to the "photon" count that is given to the single photoelectron peak extracted from the "off-beam" data used in the linear extrapolation. A value of 0.9 means that the extracted mean of each channels' ToT distribution from the "off-beam" data only equals 0.9 "photons" with respect to the "In-beam" data. The difference between single and multi-photoelectron peak which is used for the linear extrapolation can be used per channel or as a global average over all channels, and is accordingly denoted. The hit, ToT sum, or photon count is done in circular areas with radius 30 mm and added angular difference equivalent of 2° around electron candidates. The separation value between single and double rings is based on the "3σ incorrect inclusion" percentage as per equation (8.1). The relevant figures are given as references.*

| | Diff. between single & multi photon peak | Dark noise mult. | $\mu_1$ | $\sigma_1$ | $\mu_2$ | $\sigma_2$ | "3σ incorr. incl." | Fig. |
|---|---|---|---|---|---|---|---|---|
| **Hits** | | | 14.4 | 3.00 | 23.4 | 4.94 | 50% | |
| **ToT sum** | | | 21.5 | 4.76 | 36.8 | 7.16 | 45% | 8.1a |
| **calibrated ToT** | per channel | 1.0 | 19.0 | 5.02 | 35.2 | 7.18 | 44% | 8.7c |
| **calibrated ToT** | global av. | 1.0 | 18.8 | 4.92 | 34.6 | 7.21 | 44% | 8.7a |
| **calibrated ToT** | per channel | 0.9 | 18.6 | 5.28 | 35.4 | 7.47 | 45% | A.74a |
| **calibrated ToT** | global av. | 0.9 | 18.3 | 5.16 | 34.7 | 7.52 | 45% | A.73a |

## 8.5 Summary

Based on the results presented, one concludes that the effect of the ToT usage is visible but small. The separability of single and double rings is improved by roughly 5 pp consistently over many different tests and calibration procedures. Hereby the easiest procedure, just summing up all measured ToTs per ring did produce similar results compared to the more advanced method of calibrating/aligning the individual ToT response per channel first. An additional improvement might be gained by correctly approximating the full shape of the ToT response to different photon multiplicities, as especially there the uncertainty on the differences in channel occupancy would be eliminated.

# 9

# Analytical transformation procedures for the RICH in HADES

A key problem every sub-detector faces is to transform its own local coordinate system into the global detector coordinate system. For the HADES experiment, the common coordinates are the spherical angles $\theta$ and $\phi$[1], which need to be transformed to $x$- and $y$-coordinates in mm corresponding to hit coordinates on the RICH photon detection plane. For the old RICH detector the transformation from a Cartesian to a spherical coordinate system was carried out via mapping each readout pad (which would nowadays correspond to a certain pixel) to a given $\theta/\phi$ coordinate assuming the particles vertex to be at $z = 0$. After that a correction was applied onto the extracted $\theta/\phi$ coordinate taking into account the reconstructed event vertex' $z$-position, i.e. assuming the particle to stem from the event vertex. With the photo sensitive area of the upgraded RICH not resembling the shape of the original photon sensitive plane, a new transformation must be made. This is easiest done simply simulating electrons being emitted into the RICH volume with given $\theta/\phi$ and $z$ coordinates and measuring the ring center positions of the thereby produced ring. For the first analyses after the beamtime an according simulation was made resulting in an $x/y \mapsto \theta/\phi$ map but applying the old additional extrapolation procedure to account for $z$. This however, apart of the now improper usage of the old $z$ transformation, always comes with the downside of depending on the ring-fit, resulting in the gained transformation map always being a function of the applied ring finder/fitter algorithm. As normally the same ring finder/fitter is also used in the final analysis of the data, this obviously does not result in a wrong transformation, but can never be disentangled from the base interrelation between $\theta/\phi$ and $x/y$. This might become problematic for future uses of either different ring finding algorithms or for the use of back-tracking, where the proximity of an electron candidate inside the RICH is checked to determine the probability that the candidate is indeed an electron. Especially for the back-tracking approach, an analytical transformation is handy, as it is normally easy to invert. In this chapter an analytical transformation $x/y \mapsto \theta/\phi$ is derived and validated using both simulated and experimental data. It is then also compared to the aforementioned map based approach. A visualizing flow chart is depicted in figure 9.1 showing the three different approaches – old, map based and analytical – such that the detailed explanations given in the first section are easier to follow. The second section of this chapter moves one step further and tries to develop a transformation that spaces all $x/y$-coordinates such, that all rings have

---

[1]Additionally each particle has a $\rho$ and $z$ parameter, through which their point of closest approach to the beamline is indicated. Hereby $\rho$ refers to the radial distance. These two parameters are not of importance for this chapter, as here every particle is assumed to come from the event vertex.

**Old:**



**Map based:**
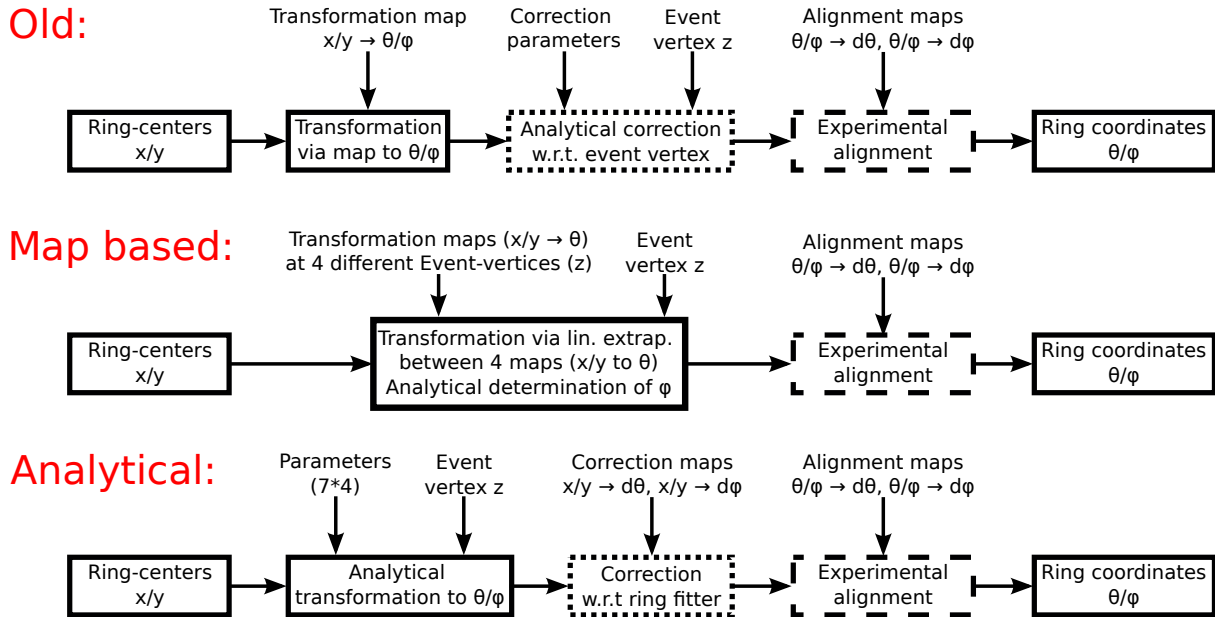


**Analytical:**



**Figure 9.1** ♦ *Flow chart showing the three different methods of transforming the RICH ring $x/y \mapsto \theta/\phi$. All transformations are detailed in the following section with special focus on the analytical transformation. The "Experimental alignment", i.e. the correction for the misalignment of the detector in real life, is visualized as dashed rectangle as it is only necessary for later analysis of real data. The "Correction w.r.t. ring fitter" in the flow chart of the analytical transformation is visualized as dotted rectangle as it is only necessary if one uses the ring fitter. The "Analytical correction w.r.t. event vertex" for the old transformation can (and will) be switched off explicitly later and is thus marked as dotted rectangle.*

the same radius. This transformation follows the same ideas already established during the first section. Such a transformation is especially helpful if the Cherenkov rings are distorted or elliptic but might also help already in the HADES RICH, where only some rings feature artifacts. The derived method is then tested in simulation and its possible benefits for HADES and also other experiments are discussed.

## 9.1 Analytical derivation of a $x/y \mapsto \theta/\phi$ transformation for the RICH

To produce a simple, ring finder/fitter independent transformation one can use geometric calculations. Hereby the easiest part of the transformation is to find the $\phi$ coordinate according to $x/y$. As the detector is spaced equidistantly in $\phi$, the transformation just follows the one of a circle. This means

$$\tan(\phi) = \frac{y}{x}$$

$$\Leftrightarrow \quad \phi = \arctan\left(\frac{y}{x}\right)$$

for $x > 0$, where $\phi = (-\pi/2, \pi/2)$. As the HADES detector has its $\phi = (0, 2\pi)$ negative values of $\phi$ need $2\pi$ to be added. Additionally one needs to extend the transformation accordingly to retrieve the full transformation of

$$
\phi = \begin{cases}
\arctan\left(\frac{y}{x}\right) & \text{for } x > 0, y \geq 0 \text{ Quadrant I} \\
\frac{\pi}{2} & \text{for } x = 0, y > 0 \text{ top} \\
\arctan\left(\frac{y}{x}\right) + \pi & \text{for } x < 0, y > 0 \text{ Quadrant II} \\
\pi & \text{for } x < 0, y = 0 \text{ left} \\
\arctan\left(\frac{y}{x}\right) + \pi & \text{for } x < 0, y < 0 \text{ Quadrant III} \\
\frac{3\pi}{2} & \text{for } x = 0, y < 0 \text{ bottom} \\
\arctan\left(\frac{y}{x}\right) + 2\pi & \text{for } x > 0, y < 0 \text{ Quadrant IV}
\end{cases}
$$

In software this is best implemented via the C-header *math.h*'s internal function *atan2(y,x)* [2]. The according $\theta$ transformation is much harder to follow and needs an explanatory sketch presented in figure 9.2 to understand the following calculations. With the new RICH detector not being fully $\phi$-symmetric anymore, at first view the $\theta$ transformation seems to depend not only on $r = \sqrt{x^2 + y^2}$ but also on the $\phi$ angle, which in turn would lead to yet another $x/y$-dependence. As however only the radial coordinate $r$ at which the staggered photon detection planes intersect changes for a given $\phi$, one can simply calculate two possible transformations for $r(\theta)$. One for the inner photon detection plane, and one for the outer, such that later one only needs to check if either $|x| > w_{\text{inner plane}}$ or $|y| > w_{\text{inner plane}}$ are larger than the width $w$ of the inner plane. Therefore the sketch in figure 9.2 shows only an exemplary slice of the detector at $\phi = 0°$ thus having the intersection of the staggered planes at $371\,\text{mm}$. Starting with the particle vector

$$
\vec{p} = \begin{pmatrix} \sin(\theta) \\ \cos(\theta) \end{pmatrix}
\tag{9.1}
$$

at the target-point $T$

$$
\vec{T} = \begin{pmatrix} 0 \\ z \end{pmatrix}
$$

where $z$ is the vertex position along the beam axis with respect to the origin of the coordinate system which here is the center of the circle, spanning the RICH mirror with radius $r_m$. One then finds the point on the mirror where the particle intersects via solving

$$
(\vec{T} + a \cdot \vec{p})^2 = r_m^2
$$

for $a$ and reinserting it, therewith retrieving point

$$
\vec{P} = \vec{T} + a \cdot \vec{p}.
$$

---

[2]The actual implementation still must foresee that HADES has its $\phi = (0, 2\pi)$, such that *phi = phi > 0 ? phi : 360.+phi* must be added.
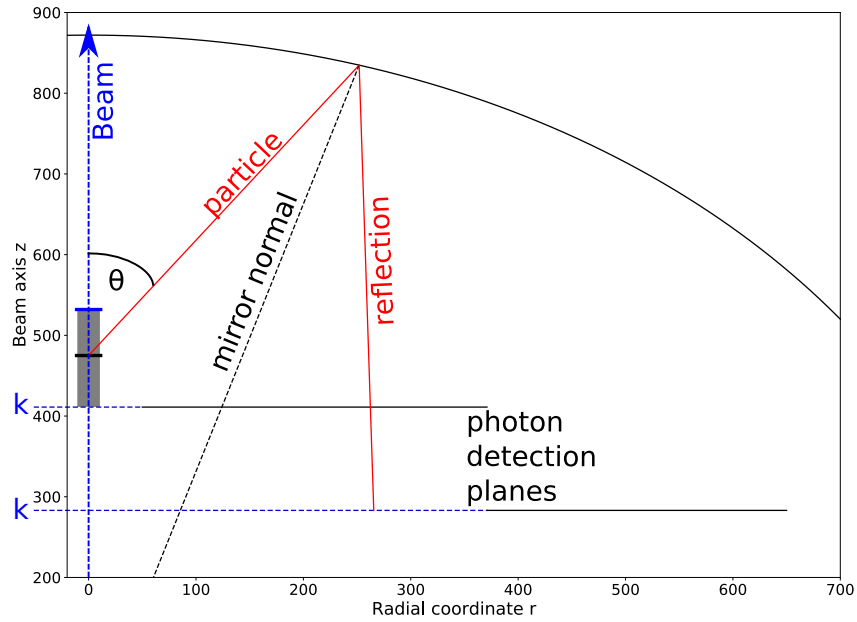
**Figure 9.2** ♦ *Sketch showing a slice of the RICH detector for a single $\phi = 0°$, visualizing where a particle and the Cherenkov-ring center would be reflected onto the photon detection planes. The Beam (blue dashed arrow) in this figure is at $r = 0$ and moves along the y-axis, where $r = \sqrt{x^2 + y^2}$ is the radial coordinate. The vertical axis resembles the beam axis position with respect to the mirror sphere center at $z = 0$, which thereby is also the origin of the mirror normal (black dashed line). $\theta$ is the angle under which the particle is ejected from the target area (gray), where the exact origin of the particle trajectory (red line) is at the position indicated by the black bar. The blue bar at the target area visualizes the zero position of the HYDRA-Framework. The reflection from the mirror sphere (black) then travels towards the two photon detection planes indicated by horizontal black lines. Parameter $k$ describes the vertical positions, i.e. z-positions, of the photon detection planes indicated via two dashed blue lines. The respective width of the detection planes depends on the $\phi$-angle chosen.*

From there one uses the reflection formula for vectors

$$\vec{q} = \vec{d} - 2(\vec{d} \cdot \vec{n})\vec{n},$$

where $q$ is the reflection resulting from the incoming vector $\vec{d}$ which reflects off of the mirror with normal $n$ (which is normalized here). In this case therefore the reflection line is given by

$$\vec{R} = \vec{P} + c(\vec{p} - 2(\vec{p} \cdot \vec{n})\vec{n}) \,,$$

where $c$ is a temporary variable still to be determined, and

$$n = \frac{-\vec{P}}{||-\vec{P}||}$$

the normalized reflection vector, as the center of the mirror sphere is at $(0, 0)$ and therefore

$$\begin{pmatrix} 0 \\ 0 \end{pmatrix} - \vec{P} = -\vec{P} \,.$$

This line of reflection now needs to be intersected with the photon detection plane situated at $k$ with respect to the mirror sphere center through

$$\begin{pmatrix} r \\ k \end{pmatrix} = \vec{R}$$

solving for $c$ and after reinsertion leading to the fully simplified equation[3] where again $r = \sqrt{x^2 + y^2}$ is the radial coordinate for a singular $\phi$.

$$r(\theta; z, k, r_m) = \frac{2kz^2 \sin^3(\theta) + 2kz \cos(\theta) \sin(\theta)\sqrt{-z^2 \sin^2(\theta) + r_m^2} - kr_m^2 \sin(\theta) - r_m^2 z \sin(\theta)}{2z^2 cos^2(\theta) sin^2(\theta) - 2z \sin^2(\theta)\sqrt{-z^2 \sin^2(\theta) + r_m^2} - r_m^2 \cos(\theta)} \, . \tag{9.2}$$

The resulting equation is unfortunately in terms of $r(\theta; z, k, r_m)$ where $z, k, r_m$ are known parameters[4] defined by the event vertex and detector geometry, whilst the actual problem here would require $\theta(r; z, k, r_m)$. Considering the complexity of the formula no easy inversion is possible, and thereby no exact formula in terms of $\theta(r; z, k, r_m)$ can be derived. It is however fully possible to extrapolate the given formula with different polynomials as will be discussed in the following. Plotting the $\theta$-angle for different $r$- and $z$-values results in the figures 9.3a and b. There one can



**(a)** *Inner photon detection plane*

**(b)** *Outer photon detection plane*
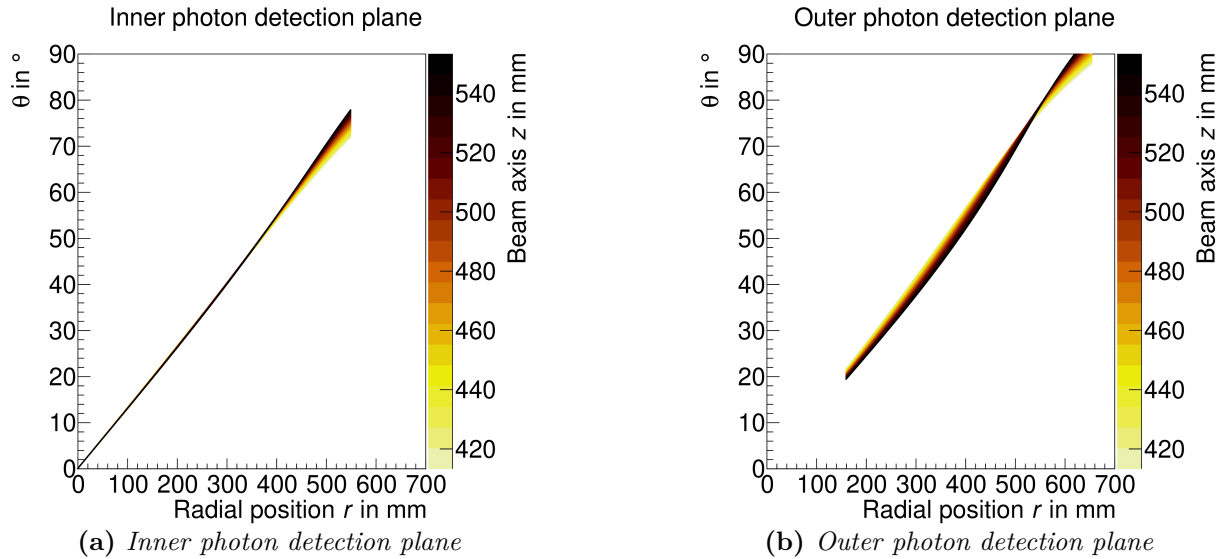
**Figure 9.3 ♦** *Calculated radial position $r(\theta, z)$ of a reconstructed ring in the RICH for a particle with angle $\theta$ emitted at $z$ (beam axis). The $\theta(r; z, k, r_m)$ is derived from equation (9.2) where $k = 410.8$ mm **(a)** or $k = 282.8$ mm **(b)** are the positions of the two detection planes w.r.t. the beam axis and $r_m = 872$ mm is the mirror radius. The z-axis refers to the position along the beam axis where the mirror sphere center is situated at $z = 0$. Therewith the HYDRA-Framework zero position which marks the definite ending of the target area is at $533.3$ mm, whereas the earliest point of interest is $433.3$ mm. The drawn functions are valid for all azimuthal angles $\phi$, the transition point in r from inner- to outer photon detection plane however differs in $\phi$.*

---

[3]Here the SageMath framework is used to ease the calculation.

[4]Obviously $z$ is only a parameter in that sense that it does not change within one reconstructed event. Over different events however it does change. Also $k$ is only a parameter in the sense that it will take only two different fixed values.

easily see that an approximation via simple polynomials should be capable of approximating the different functions for different target vertices $z$ to quite high precision. Especially the inner photon detection plane behaves nearly linearly for angles up to $50°$ which is roughly the angle to which the inner photon detection plane always reaches. After that the different target vertices result in substantially different function shapes describing $\theta(r)$. The outer photon detection plane unsurprisingly always shows separated functional progressions for different target vertices. Those result in a distinct cross over region, visible at $r \approx 580\,\mathrm{mm}$. Thus, for radial positions more inwards, more upstream (meaning more positive $z$) target segments result in smaller angles, whereas for radial positions more outwards, the opposite is the case. Both transformations, the one for inner and for outer photon detection plane are calculated for much larger (respectively lower) than $50°$, albeit the respective geometry ending latest (earliest) at that point. This is done to help the fitting procedure, as a hard cut at exactly the range of interest resulted in erratic behavior at the edges, most times still including some points of interest leading to bad fitting approximations for those points. For the following transformation a polynomial of $7^{\mathrm{th}}$ degree in $r$ is chosen, where each parameter is a polynomial of $4^{\mathrm{th}}$ degree in $z$, thus giving

$$\theta = a_0 r^0 + a_1 r^1 + ... + a_6 r^3 + a_7 r^7$$

$$\text{with } a_i = b_{i,0} z^0 + b_{i,1} z^1 + b_{i,2} z^2 + b_{i,3} z^3 + b_{i,4} z^4 \ .$$

with the parameters shown in the appendix in figures A.75 and A.76. These parameters are



**(a)** *Inner photon detection plane*  **(b)** *Outer photon detection plane*
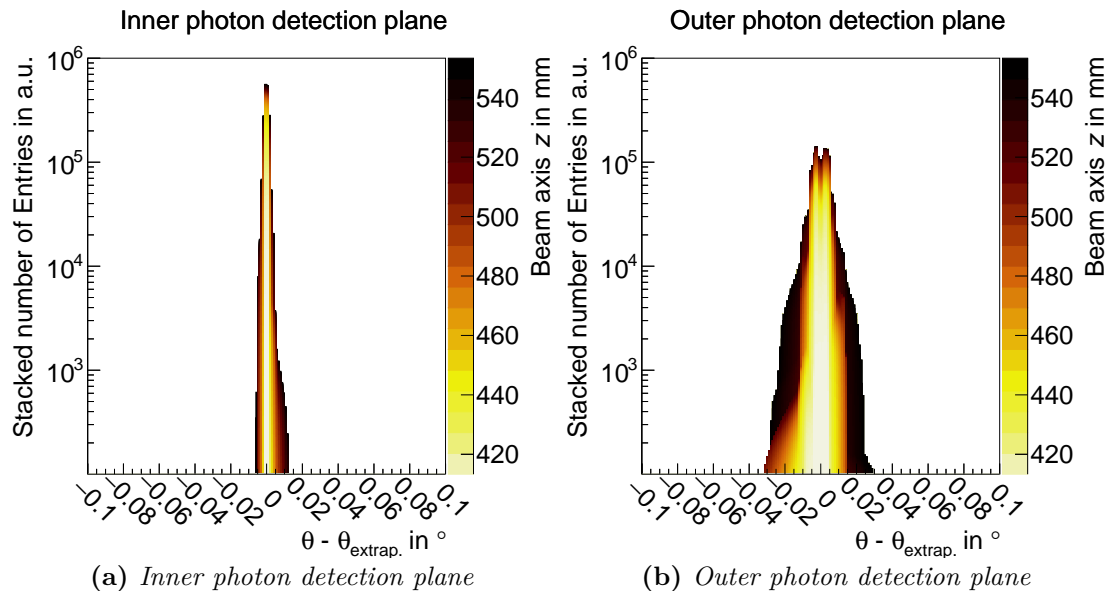
**Figure 9.4** ♦ *Distribution of differences between the analytically calculated $\theta$ in the RICH and the one gained from an extrapolation by a $7^{th}$ degree polynomial in $r$, where each parameter is approximated by a polynomial of $4^{th}$ degree in $z$. This extrapolation is gained through fits at discrete $z$-values, fitting the resulting parameters with respect to $z$ afterwards. The histograms presented are stacked, meaning that all differences $\theta - \theta_{extrap.}$ for different $r$- and $z$-values are filled into the same histograms but with different colors according to the shown $z$-axis. **(a)** shows the inner- and **(b)** the outer photon detection plane. The number of entries is thereby artificial, as infinitely many points of comparison could have been chosen.*

derived by first fitting the functional space for a discrete set of $z$-values and then fitting the resulting points in $z$-$a_i$-space with the described polynomial of $4^{\text{th}}$ degree. With this approximation in place a check is made, comparing the approximated angle $\theta$ with the one derived from the original equation (9.2). This comparison is shown in figures 9.4a and b. Showing no difference much larger than $|0.01°|$ in the region of interest for the inner photon detection plane and no difference much larger than $|0.03°|$ for the outer photon detection plane. Visible is, that moving towards more upstream $z$-values the difference distribution broadens, which is to be expected as for more positive $z$-values the functional progression gets more and more non-linear. A polynomial of $7^{\text{th}}$ degree in $r$ is chosen, as a polynomial of $6^{\text{th}}$ degree did deteriorate the approximation results for the outer photon detection plane severely (cf. Fig. A.77a appendix pg. 230), whereas a polynomial of $8^{\text{th}}$ degree did not lead to large improvements (cf. Fig. A.77c appendix pg. 230 ).

## 9.2 Check of the analytical $x/y \mapsto \theta/\phi$ transformation

To confirm the transformation with data, a simulation is carried out, generating electrons homogeneously distributed in $\phi$ and $\cos\theta$. Generated uniformly at $x = 0\,\text{mm}$, $y = 0\,\text{mm}$, and $z_H = [-80\,\text{mm}, 0\,\text{mm}]$ with respect to the HYDRA-Framework's origin of ordinates[5], the electron vertices are varied along the approximate target area. From there the electrons are emitted uniformly in $\phi = [0°, 360°]$ and according to an $\arccos(x)$ distribution, where x is uniformly distributed, in $\theta = [0°, 90°]$ to account for the larger area which needs to be covered for larger $\theta$ angles. The electrons' momentum is set to $300\,{}^{\text{MeV}}/c$ but of no importance for this study[6]. The generated electrons' $\theta/\phi$ can then be compared to the ones retrieved through the RICH's fitted ring and the derived transformation. With the ring finder now coming into play the analytically derived $x/y \mapsto \theta/\phi$ transformation needs to be corrected with respect to the ring finder/fitter "tendencies" (cf. map-based flow chart in Fig. 9.1 dotted rectangle). For that, a single correction map is added after the initial transformation. This map, spacing along $x/y$, is derived as an average across the full range in $z_H = [-80\,\text{mm}, 0\,\text{mm}]$ using the differences between analytically derived $\theta/\phi$ and simulated $\theta_e/\phi_e$ respectively. In $\phi$ the difference $\Delta\phi = \sin(\theta_e)\phi - \phi_e$, is calculated taking into account the $\theta_e$ angle of the simulated electron, whilst $\Delta\theta = \theta - \theta_e$. This again is done to counteract the smaller Cartesian-space that is covered by $\phi$ at smaller $\theta$. This average difference in $\theta$ and $\phi$ is depicted in figures 9.5a and 9.5b respectively. There one clearly observes the "tendencies" of the ring fitter. Starting on the outer rim, one observes that the ring fitter places the rings more inwards than the actual electron trajectory would suggest. This makes sense and can solely be explained by the ring fitter tending to move the ring-center of only partially visible rings closer towards the actual found hits on the detection plane. The same effect, but reversed is visible on the very inside of the RICH detector, where the ring is placed to slightly larger $\theta$s. Most interesting is the behavior at the transition region from inner to outer photon detection plane. There the ring fitter tends to place the ring which should have its center on the

---

[5]Which is situated at $z = +533.3\,\text{mm}$ with respect to the mirror sphere center.
[6]The interested reader finds depictions of the distribution in the appendix figure A.78 pg. 231

**(a)** *Uncorrected differences in θ*



**(b)** *Uncorrected differences in φ*



**(c)** *Differences in θ including corrective map*



**(d)** *Differences in φ including corrective map*
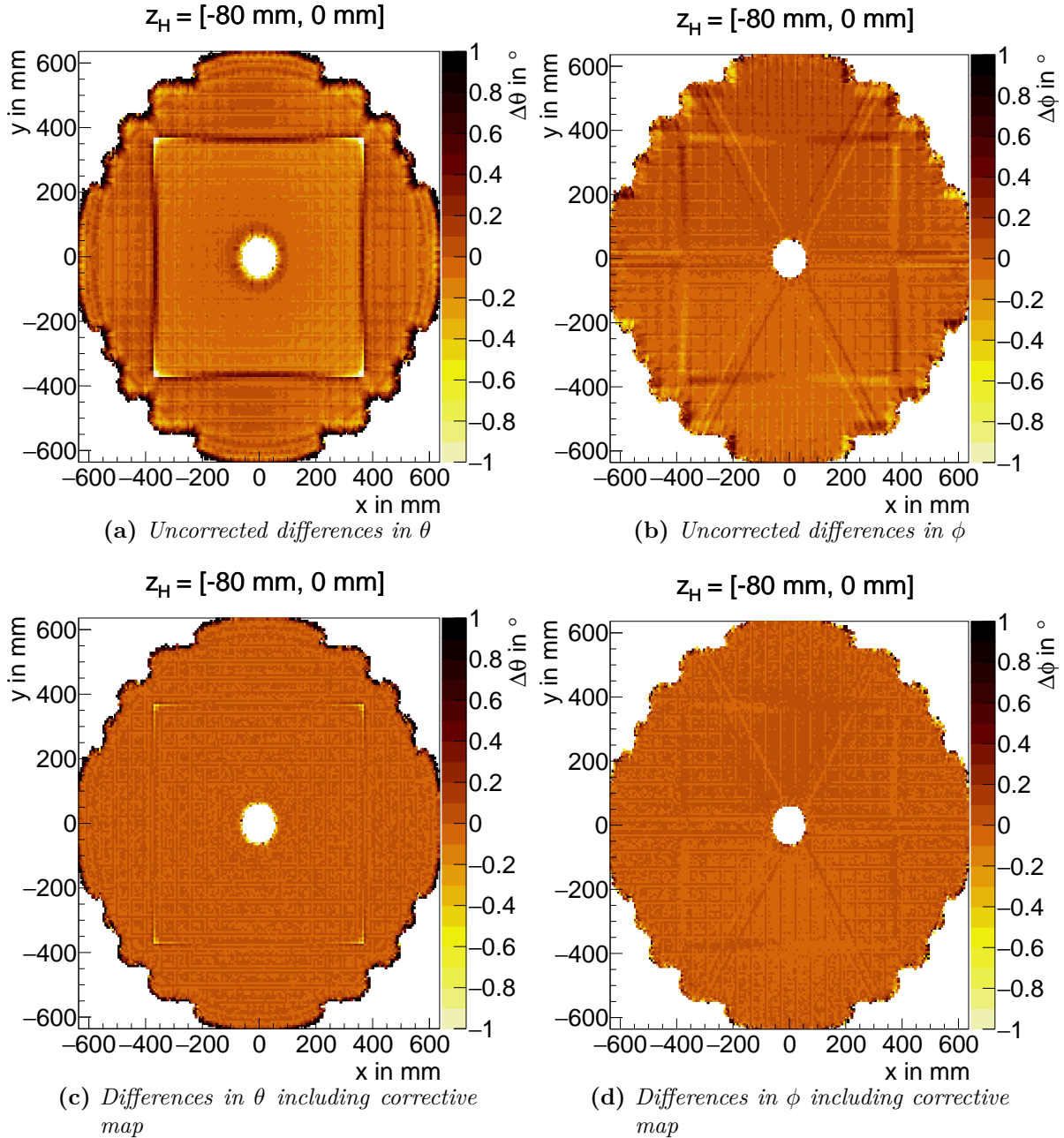
**Figure 9.5** ♦ *Spatially resolved distribution of differences in θ and φ using the new transformation with and without corrective map that accounts for the ring fitter's tendencies. Where $\Delta\theta = \theta - \theta_e$ and $\Delta\phi = \sin(\theta_e)\phi - \phi_e$, with $\theta/\phi$ the reconstructed and $\theta_e/\phi_e$ the simulated electron emission angles. The differences are averaged for each pixel in $x/y$ on the RICH over all electron vertices $z_H = [-80, 0]$ mm. The $1 \times 10^8$ electrons are emitted at $x = 0$ mm, $y = 0$ mm uniformly over $2\pi$. All spatially resolved distributions have a pixel sized $7 \times 7$ mm$^2$ granularity and are artificially cut of at $\pm 1°$.*

outer plane, on the inner plane instead, except at the edges (e.g. $(x, y) = (371$ mm, $371$ mm)) where the opposite happens. This behavior is the result of several different overlaying problems, the ring finder is facing at this transition region. For early target segments (see e.g. figure A.79b in the appendix), meaning more negative $z_H$, the ring fitter places the rings more towards the plane where most photons are registered. This means, that for a ring e.g. lying mostly on the

inner plane, the ring center is found at lower $\theta$s, and vice versa. This results from the fact, that for such low $z_H$ many photons hit the vertical gap between the two photon detection plane and are thus lost. Later target segments ($z_H$ towards 0, see e.g. figure A.79a in the appendix) show the opposite effect, where rings found on the inner plane should actually have their centers on the outer and vice versa. Examining the $\Delta\phi$ distribution one again observes the ring fitter to slightly misplace rings at the transition region from inner to outer photon detection plane. Furthermore, also at the spoke regions, the ring fitter tends to misplace the ring. This again results from part of the ring being shadowed by the spoke and thus the ring fitter placing it closer to the registered photon hits. Same again holds true at the outer rim of the detector.

All of those ring fitter tendencies are taken into account moving towards the data with correction map, as is shown in figures 9.5c and 9.5d[7]. The correction map thereby always uses a bilinear interpolation taking into account the nearest four measured points on the correction map to derive the exact correction for a given $x/y$ to be added onto $\theta$ and $\phi$. This method leads to improper results at the edges of the detector, but is still sufficient. This is visible not only on the outer rim of the detector, but again at the transition region from inner to outer photon detection plane. Still, checking the detector global differences $\Delta\theta$ and $\Delta\phi$, as shown in figure 9.6a a narrow distribution centered at approximately zero is found for both angles. Comparing it to the old transformation (applied on the new RICH) displayed in figure 9.6b a large improvement in $\theta$ and a smaller one in $\phi$ is observed. The improvement in $\theta$ is visible in the more centered mean difference and the much narrower width. In $\phi$ the already afore centered distribution is still exactly centered within errors whilst also here a slight improvement in the width is visible. Having a huge improvement in $\theta$ is unsurprising. There the new detector geometry has, as it depends on $z$, the largest impact. The improvement in $\phi$ can mainly be contributed to an improper handling at the transition from $\phi = 360°$ to $\phi = 0°$ in the old transformation. As there a simple bilinear extrapolation is used to get the exact $x/y$ to $\phi$ transformation from the simulated map, interpolating the jump from $\phi = 360°$ to $\phi = 0°$ incorrectly (compare figure A.81b at $x > 0, y = 0$ in the appendix). Additionally to the already presented improvements one now reaches a spread in $\Delta\theta$ and $\Delta\phi$ which is nearly equal, as would be expected. This again supports that the derived transformation together with the added correction map transforms the different coordinates nearly perfectly. Comparing the resulting spread in $\Delta\theta$ and $\Delta\phi$ to a theoretically estimated best possible spread of $\sigma_{\Delta\theta,\text{ best}} = 0.36$ and $\sigma_{\Delta\phi,\text{ best}} = 0.35$, one sees that only the transformation for $\theta$ could be improved a bit more. This estimate on the best possible spread is derived in the appendix in section B.5 by measuring the spread in the angular matching only in thin slices of $z$.

**Test of the transformation in real data**

The next step is to cross check the transformation using real data. For that, another corrective map needs to be introduced, taking into account the alignment of the RICH with respect to the track reconstructing MDC sub-detector (cf. dashed rectangle in Fig. 9.1). This corrective map

---

[7]For the sake of completeness the same plot for the old transformation is added to the appendix figures A.80 and A.81 pg. 232.

**(a)** *New transformation with corrective map*

**(b)** *Old transformation*
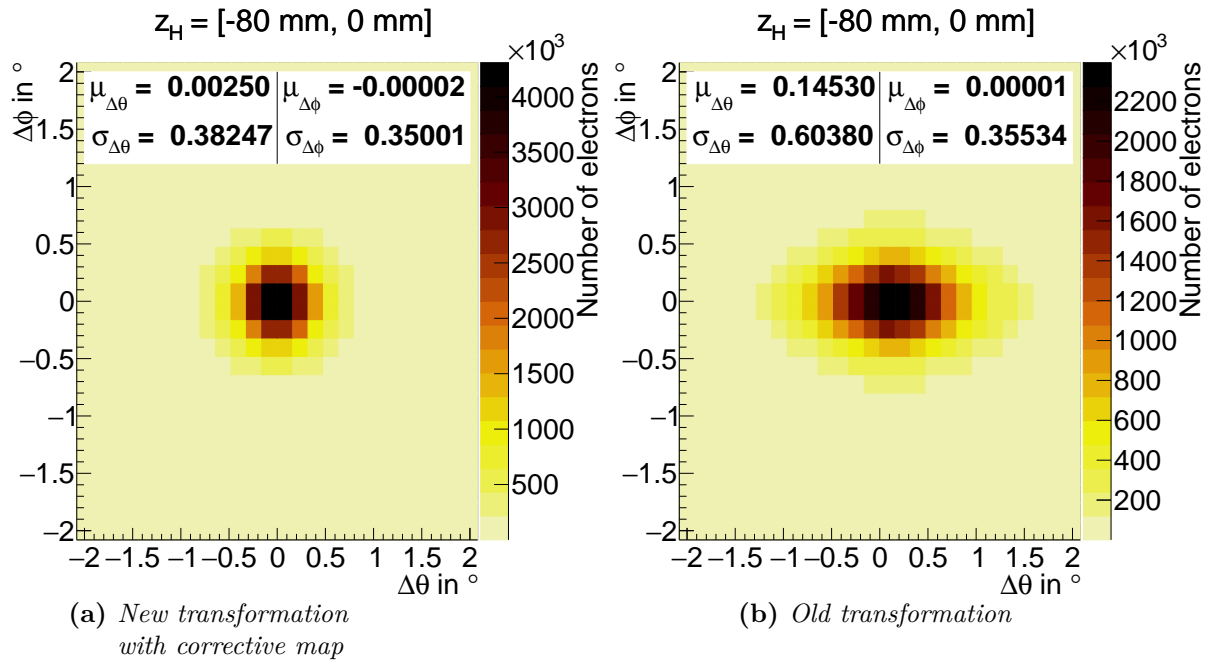
**Figure 9.6 ♦** *Differences in $\theta$ and $\phi$ using the new transformation with corrective map (accounting for ring fitter tendencies) and using the old transformation. All differences are filled into the 2D-histogram spacing over $\Delta\theta = \theta - \theta_e$ and $\Delta\phi = \sin(\theta_e)\phi - \phi_e$, with $\theta/\phi$ the reconstructed and $\theta_e/\phi_e$ the simulated electron emission angles. Using all electron vertices $z_H = [-80, 0]$ mm for $1 \times 10^8$ electrons emitted at $x = 0$ mm, $y = 0$ mm uniformly over $2\pi$. Denoted are the sample mean $\mu$ and sample standard deviation $\sigma$ along $\Delta\theta$ and $\Delta\phi$ separately. The last digit of the mean is the statistical uncertainty therein.*

not only corrects for any misalignment between RICH and MDC but also for the RICH intrinsic misalignment of the mirror-tiles (cf Fig. A.82 appendix pg. 233). As data sample $\pi^0$-Dalitz decays are chosen, as those should mostly come from the target vertex. The simple cut chosen is based on two checks. First finding electrons via $0.95 < \beta < 1.05$, $|p/z| < 250\,\mathrm{MeV}/c$ and $m < 50\,\mathrm{MeV}/c^2$. Then checking if a possible pair for that electron exists with opening angle $OA > 9°$, decay vertex $z_d$ in proximity of event vertex $z_e$ through $z_e - 20\,\mathrm{mm} < z_d < z_e + 20\,\mathrm{mm}$, and mass of the mother particle $m_{\mathrm{mother}} < 150\,\mathrm{MeV}/c^2$. Figure 9.7a shows the deviations in $\theta$ compared between the old transformation (with and without $z$-correction), this analytical transformation and a transformation interpolating linearly between four maps $(x/y \mapsto \theta)$ at four different $z$-positions. The maps for the last transformation are derived from a dedicated simulation by Semen Lebedev [Leb20], and aligned afterwards using the same single "alignment" map used for the analytical transformation. This "map based" approach is added to the flow chart in the beginning of this chapter in figure 9.1 as "Map based:" transformation. This is feasible, as this alignment map is only used to account for the experimental misalignment between RICH and MDC, which should be the same for both transformations being derived or finally corrected based on the same geometry used in simulation. $\Delta\theta$ is now the difference between the transformed $\theta$ and the one reconstructed by the MDC $\theta_{\mathrm{MDC}}$. A Voigt profile, being a convolution of a Gaussian- and a Cauchy-Lorentz profile, is fitted to the four different distributions, approximating the peaked structure with the long tails better than a sole fit with a Gaussian profile. Therewith one finds,

**(a)** *$\Delta\theta$ for different RICH transformations with fitted Voigt profile*

**(b)** *Area below fitted Voigt profile*
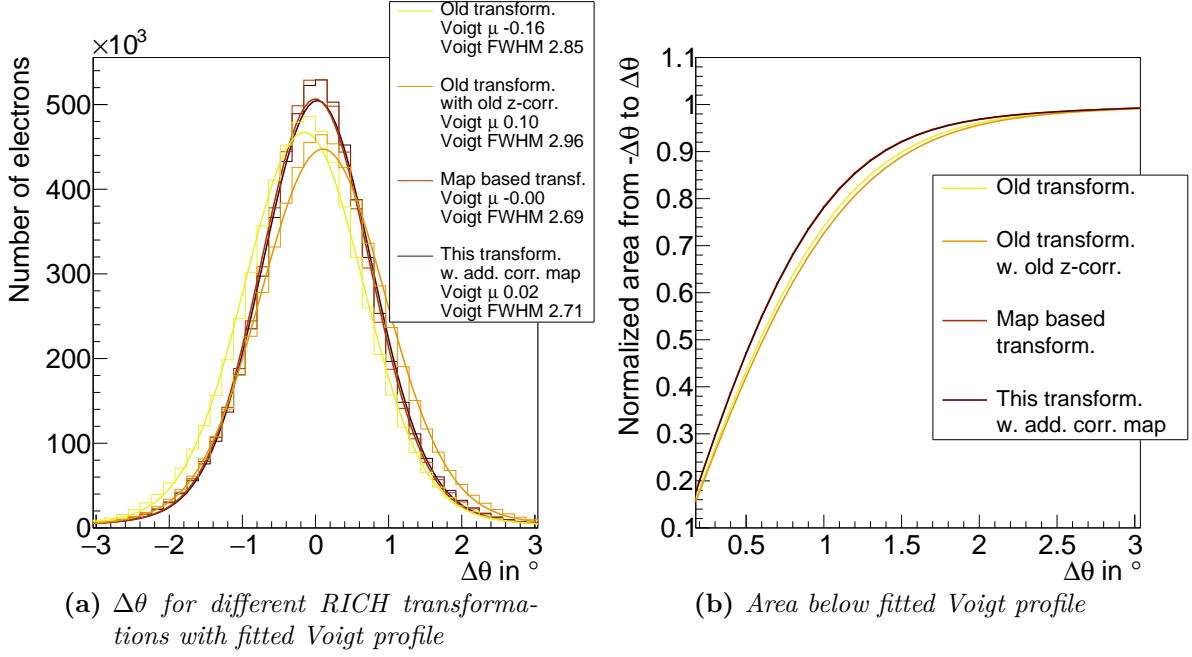
**Figure 9.7** ♦ *Comparison of $\Delta\theta = \theta - \theta_{\mathrm{MDC}}$ for different RICH transformations, transforming the ring centers in $x/y$ to $\theta/\phi$. Thereby $\theta_{\mathrm{MDC}}$ is the polar angle of the particle candidate as reconstructed by the MDC. The chosen particle candidates need to fulfill $0.95 < \beta < 1.05$, $|p/z| < 250\,\mathrm{MeV}/c$ and $m < 50\,\mathrm{MeV}/c^2$ to be assumed electrons. Furthermore, they must build a possible pair with another electron candidate with opening angle $OA > 9°$, decay vertex $z_d$ in proximity of event vertex $z_e$ through $z_e - 20\,\mathrm{mm} < z_d < z_e + 20\,\mathrm{mm}$, and mass of the mother particle $m_{\mathrm{mother}} < 150\,\mathrm{MeV}/c^2$. Those candidates are assumed to be mostly part of a $\pi^0$-Dalitz decay. Each distribution, using the old transformation, using the old transformation with the old correction for different z-vertices, using the here described transformation with additional corrective map to account for ring fitter tendencies, and the solely map based extrapolation, are fitted with a Voigt profile. A Voigt profile is thereby the convolution of a Gaussian- and a Cauchy-Lorentz profile, where the Full-Width-Half-Maximum of the Voigt profile is calculated through $FWHM_V \approx 0.5346 \cdot FWHM_L + \sqrt{0.2166 \cdot FWHM_L^2 + FWHM_G^2}$, with $FWHM_L$ being the FWHM of the Lorentz profile and $FWHM_G$ the one of the Gaussian profile respectively (according to [OL77]). Sub-figure **(b)** uses the fitted profiles to estimate the area below each distribution respectively, taking the range between $-\Delta\theta$ and $+\Delta\theta$.*

that additionally to the nearly perfectly centered mean of both distributions the Full-Width-Half-Maximum (FWHM) is comparable between the transformation derived here and the "map based"-transformation. This is even better visible comparing the integral of the fitted Voigt profiles as is shown in figure 9.7b. Therein both functions are nearly congruent, with the old transformations showing a less steep rise towards larger angular differences. With respect to the older transformations one observes, that the z-correction using the old detector geometry still helps to move the mean slightly towards zero, however at the cost of a heavily deteriorated width. The overall gain moving towards an updated transformation is less extreme compared to the afore presented simulation results. This obviously results from several contributing smearing factors, such as the granularity of the MDC, the uncertainty on the event vertex, as well as deviations induced through multiple scattering. It is however also clear, that the analytical approach presented here works equally well, compared to the brute force multidimensional map

based approach albeit using significantly less parameters, being easier to invert and giving a ring fitter independent handle on the ring track matching.

## 9.3 Test of additional coordinate transformation $x_{\text{old}}/y_{\text{old}} \mapsto x_{\text{new}}/y_{\text{new}}$ unifying ring radii

Similar to the calculations determining the ring center position, one can move even one step further and calculate the different photon hit positions (i.e. positions of the ring circumference). This is done by adding and subtracting the Cherenkov-angle $\theta_c = \arccos(1/n)$ [8] from the $\theta$ in the particle vector $\vec{p}$ as defined in equation (9.1) giving

$$\vec{p_{\pm}} = \begin{pmatrix} \sin(\theta \pm \theta_c) \\ \cos(\theta \pm \theta_c) \end{pmatrix} \ .$$

From there the two lines of reflection building the right side of the ring are found to be

$$\vec{R_{+,1}} = \vec{P_+} + c_{+,1}(\vec{p_+} - 2(\vec{p_+} \cdot \vec{n_+})\vec{n_+}) \ \text{ and}$$
$$\vec{R_{+,0}} = \vec{P} + c_{+,0}(\vec{p_+} - 2(\vec{p_+} \cdot \vec{n})\vec{n}) \ .$$

Where $\vec{R_{+,0}}$ is the corresponding reflection off of the mirror at the ring's center and $\vec{R_{+,1}}$ the off-center reflection (cf. Fig. 9.8). This off-center reflection needs $\vec{P_+}$, which is calculated being the intersection point of $\vec{p_+}$ with the mirror and $\vec{n_+}$ is the corresponding normalized mirror normal. The latter line of reflection again uses the reflection point on the mirror which was already used for the ring center determination before. This means that for this line only the direction changes according to $\vec{p_+}$. The same calculation is done for $\vec{p_-}$ as is depicted in the sketch in figure 9.8, using the same procedure. Also depicted there are the focal planes for the given parameters, being the points at which $\vec{R_{+,1}}$ intersects with $\vec{R_{+,0}}$ or $\vec{R_{-,1}}$ (orange) intersects with $\vec{R_{-,0}}$ respectively (green). Thereby this focal plane heavily depends on the particle vertex. Alternatively one can, like before, also derive the intersecting point of either reflected beam with either of the two photon detection planes. This results in extensively long formulas which can only reasonably derived using mathematical softwares such as SageMath which is used here to solve and simplify. The long formulas of the form $r_{\pm,0/1}(\theta; z, k, r_m, n)$ being the position on the photon detection planes at $z = k$ of the right/left "Cherenkov-photon" ($\pm$) reflected center/off-center (0/1) are found in equation (B.6) appendix pg. 244. Such a calculation is interesting in the sense that one can use the ring radius information for each $\theta$ and $z$ to transform the whole RICH detector in such a way, that the radius stays constant independent of $\theta$ and $z$ as well as the photon detection plane, on which the ring is reconstructed resulting in several benefits. First of all the ring radius distribution would become more flat and narrower, allowing for easier cuts on the ring radius without the necessity for $\theta$-dependence of cut values, distinguishing rings from background. Secondly, and predominantly this might help reconstructing rings at the transition

---

[8]The gas inside the RICH being $C_4H_{10}$ has a refractive index of $n = 1.0014$ at $400\,\text{nm}$ which is the wavelength at which the MAPMT has its highest efficiency.
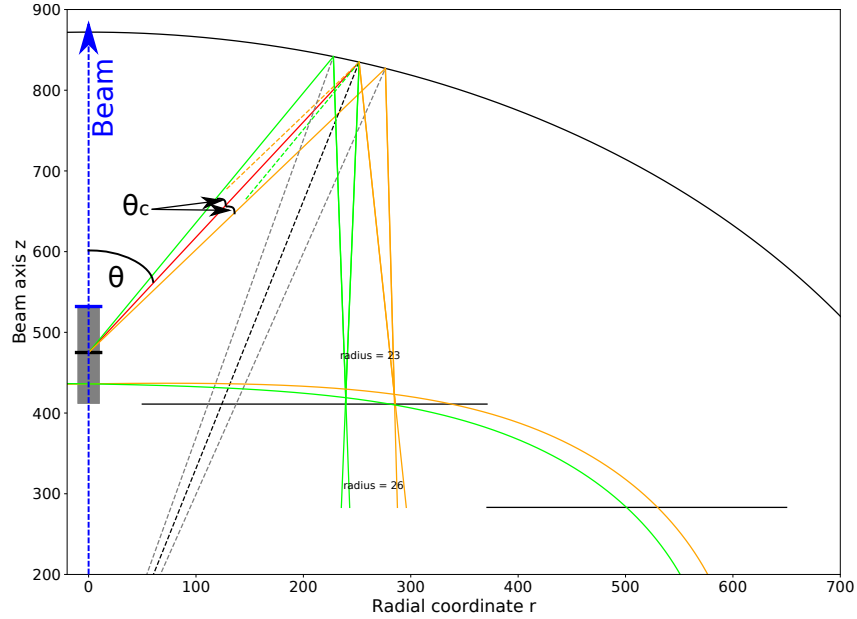
**Figure 9.8 ♦** *Sketch showing a slice of the RICH detector for a single $\phi = 0°$, visualizing the first possible and the last possible Cherenkov photon reflection for the "right" and "left" sides of the Cherenkov ring. The Beam (blue dashed arrow) in this figure is at $r = 0$ and moves along the $y$-axis, where $r = \sqrt{x^2 + y^2}$ is the radial coordinate. The $y$-axis resembles the beam axis position with respect to the mirror sphere center at $z = 0$, which thereby is also the origin of the mirror normals (black/gray dashed lines). $\theta$ is the angle under which the particle is ejected from the target area (gray), where the exact origin of the particle trajectory (red line) is at the position indicated by the black bar. The blue bar at the target area visualizes the zero position of the HYDRA-Framework. The Cherenkov angle $\theta_c$ is added/subtracted from the particle trajectory and calculated via $\arccos(1/n)$ with $n = 1.0014$ for isobutane. The reflections from the mirror sphere (black) then travel towards the two photon detection planes indicated by horizontal black lines. The respective width of the detection planes depends on the $\phi$-angle chosen. The point at which the two left (green) (respectively right (orange)) reflected photon trajectories overlap build uniformly in $\theta$ the focal plane. The radii denoted show the radius of the ring if it reaches the inner or outer photon detection plane.*

region moving from inner to outer photon detection plane which, due to geometrical distortion, can not be reconstructed in the present framework. To explain this, one can imagine that at least some rings where one part is on the inner and one on the outer photon detection plane might fail to be reconstructed[9]. This is the case because the ring fitter can struggle to reconstruct rings where the center part is just cut out, leaving the two ring parts directly next to each other. The final radial transformation $T : r_{old} \mapsto r_{new}$ uses a "arbitrarily chosen" constant ring radius of $r_{Ring} = 23\,\text{mm}$ [10] and is fully detailed in B.6 in the appendix.

The result of the transformation is again tested with single electrons using the same configuration from before ($1 \times 10^8$ electrons, $z_H = [-80, 0]\,\text{mm}$ $x = 0\,\text{mm}$, $y = 0\,\text{mm}$ uniformly over $2\pi$). Using these particles the resulting hit patterns are then transformed from $x/y$ to the new $x_{transf.}/y_{transf.}$ by means of the described transformation. To compare the results of transformed to original reconstruction, the ring finder/fitter is let run using either the transformed coordinates or the

---

[9]A sketch displaying this exact effect is found in Fig. A.83 appendix pg. 233.

[10]The radius is chosen here, as it is close to the actual average ring radius on the detector.

**(a)** *using original x/y coordinates*



**(b)** *using transformed x/y coordinates*
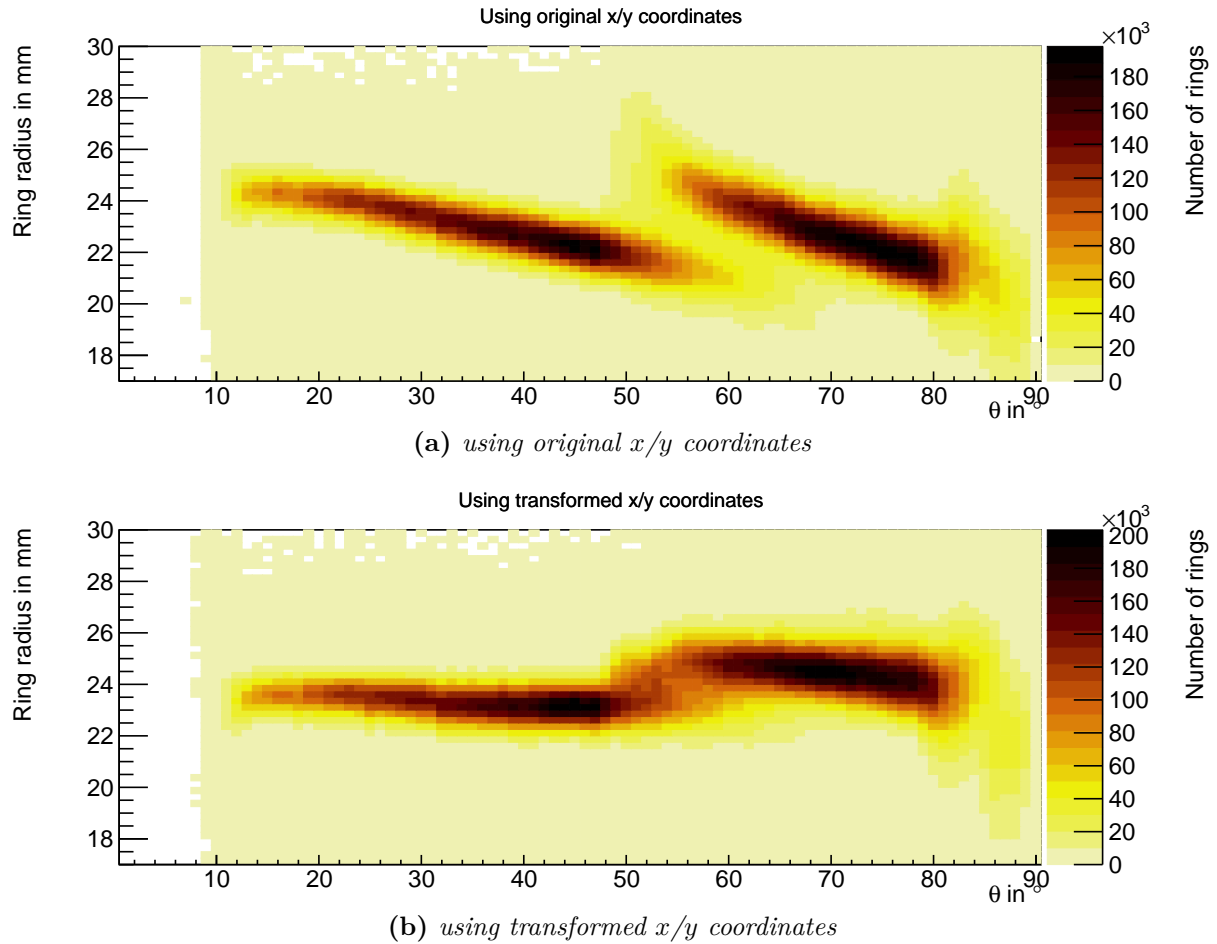
**Figure 9.9 ♦** *Radius distribution over θ using the original* **(a)** *or transformed x/y coordinates* **(b)***. The distribution is derived using $1 \times 10^8$ simulated electrons emitted at $z_H = [-80, 0]$ mm $x = 0$ mm, $y = 0$ mm and distributed uniformly over $2\pi$. Transformation is done using polynomials that approximate a uniform radial distribution of $23$ mm over full θ and φ. Where the radius depends on φ solely due to the position of the transition region between inner and outer photon detection plane.*

original ones. Hereby also the afore discussed new transformation, transforming $x/y$ to $\theta/\phi$ for the old coordinates is taken into account, to keep results independent of a proper angular reconstruction. The radii of all reconstructed rings are then filled into a θ dependent histogram for both, the original and the transformed coordinates. This histogram using the original $x/y$-coordinates is depicted in figure 9.9a. There one finds the ring radius to drop with increasing θ for both photon detection planes individually, resulting in a sudden splitting of the radius distribution at angles of $50°$ to $70°$, where the transition region lies. This is partially counteracted by applying the transformation, as becomes visible in figure 9.9b. Showing a much flatter progression of the ring radius distribution for the inner and outer detection planes. Still, using the transformation, the average radii for inner and outer detection plane are not exactly the same. This is best visible in the figure 9.10a where the average ring radius for each bin in θ is depicted. There one finds the average to be very flat at the set radius of $23$ mm for the inner photon detection plane, while for the outer photon detection plane a slightly curved course at approximately $24$ mm ring radius is visible. Consequently at the transition region a small

**(a)** *Mean progression*



**(b)** *Standard deviation progression*
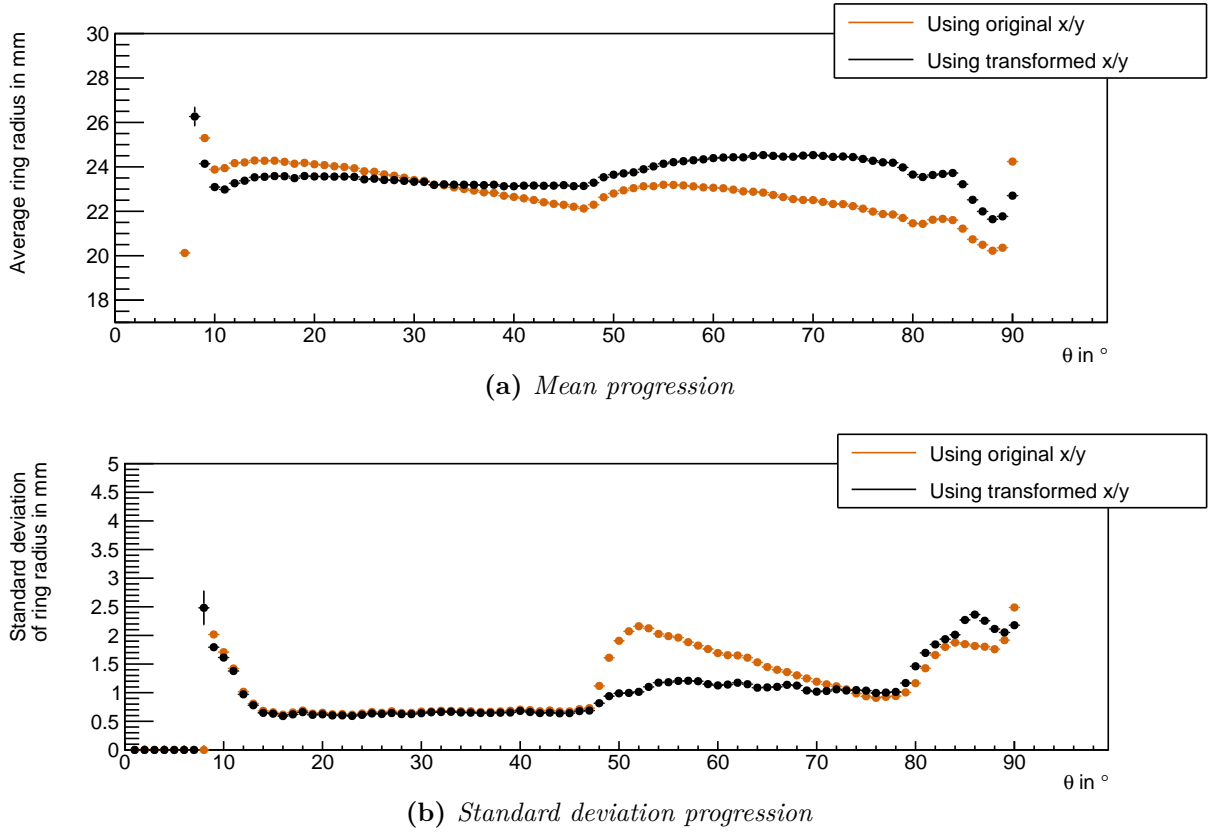
**Figure 9.10** ♦ *Average* **(a)** *and standard deviation* **(b)** *of the simulated ring radius distribution as function of polar angle θ (1°-binning). Comparing the distribution derived based on original (cf.* Fig. 9.9a*) and transformed (cf.* Fig. 9.9b*) x/y coordinates.*

split is visible, separating the rings found on the inner from rings found on the outer photon detection plane. Nonetheless the spread of the radii at the transition region gets narrowed, as is shown in figure 9.10b where the standard deviation of the ring distribution in one $θ$-bin is depicted. From 50° to 70°, where the transition region lies, the standard deviation of the ring radii is much larger for rings reconstructed using the original $x/y$-coordinates. Contrary to that the rings found with the transformed coordinates show a slightly increased spread at largest polar angles. Conclusively this means, that the transformation did nearly reach its goal of achieving a global 23 mm average ring radius. The transformation correctly reduces the spread and flattens the progression of the ring radii for different $θ$, leaving only a slight discrepancy in ring radii reconstructed on the inner and outer photon detection plane. One reason why the transformation is not perfect on the outer photon detection plane might be an incorrect handling of the detector geometry in either simulation or derivation of the transformation polynomials. To exclude this hypothesis the parameters leading to this extrapolation were varied slightly, testing the response of the finally extracted spectra. Here, no major improvement nor deterioration by slight variance of the parameters could be found, leading to the conclusion that the derived formula is still not handled perfectly. Additional investigations checking the ring sharpness through $dR$-distributions (see equation (4.1)) revealed no major improvements using the derived transformation. Therefore the resulting graphics are only comprised in figures A.84 and A.85 in the appendix.

With the radius distribution being expectedly narrowed at the transition region using of the newly transformed $x/y$, the next step is to check if an improvement in reconstructed number of rings at the transition region is visible. To check this, a particle is deemed reconstructed if a ring is found within $4°$ absolute angular difference (equation (4.3)) with a radius between $17\,\mathrm{mm}$ and $30\,\mathrm{mm}$. Again running the analysis using the old coordinates and the transformed ones, the electron reconstruction efficiency[11] is determined per pixel ($7 \times 7\,\mathrm{mm}^2$) by

$$\text{Efficiency} = 1 - \frac{\text{Number of unreconstructed electrons}}{\text{Number of electrons}} \ .$$

Thereby the according pixel for the reconstructed or not reconstructed electron is calculated using the simulated electron and transforming its $\theta/\phi$ to $x/y$. Resulting efficiencies are depicted in figure 9.11a and 9.11b. Therein one finds that the efficiency at the transition region did increase from the $\sim 0.5$ to $\sim 0.9$. It becomes apparent, that indeed some rings are not recoverable, as too few photons hit either of the photon detection planes. The improvement best becomes visible in the fraction of efficiency using the transformed coordinates divided by the efficiency gained using the original coordinates. This fraction is depicted spatially resolved in figure 9.11c and as one dimensional histogram in figure 9.11d. Focusing on the transition region between inner and outer photon detection plane first (e.g. $x = y = 371\,\mathrm{mm}$), one recognizes the significant improvement in the efficiency. This effect becomes largest if the transition region lies at large radii $r$ (e.g. $r = 525\,\mathrm{mm}$ at $\phi = 45°$) reaching an up to nearly twofold increase in efficiency. This is unsurprising as especially at these positions the inclination of the reflected photons becomes such that many photons hit the gap between inner and outer detection plane (cf.e.g. Fig. A.83 appendix pg. 233). Therefore, a proper fit of the remaining photons becomes more important and is harder to get by. The rest of the detector shows a nearly unchanged efficiency as the reconstruction efficiency there is unaffected by the detector geometry. This is also supported by the one dimensional representation, where one finds nearly all bin entries at one, meaning no improvement. The efficiency on the outer rim of the detector shows partial improvement and partial deterioration, thus giving a hard to interpret picture of an overall improvement at these positions. As the main improvement is limited to a small spatial region in the RICH the overall mean improvement only reaches 1.012 over the full detector.

---

[11]Only referring to the efficiency on the RICH level, with no other detector being used in the reconstruction.

**(a)** *Using original x/y coordinates*



**(b)** *Using transformed x/y coordinates*



**(c)** *Fraction of efficiencies*



**(d)** *Fraction of efficiencies*
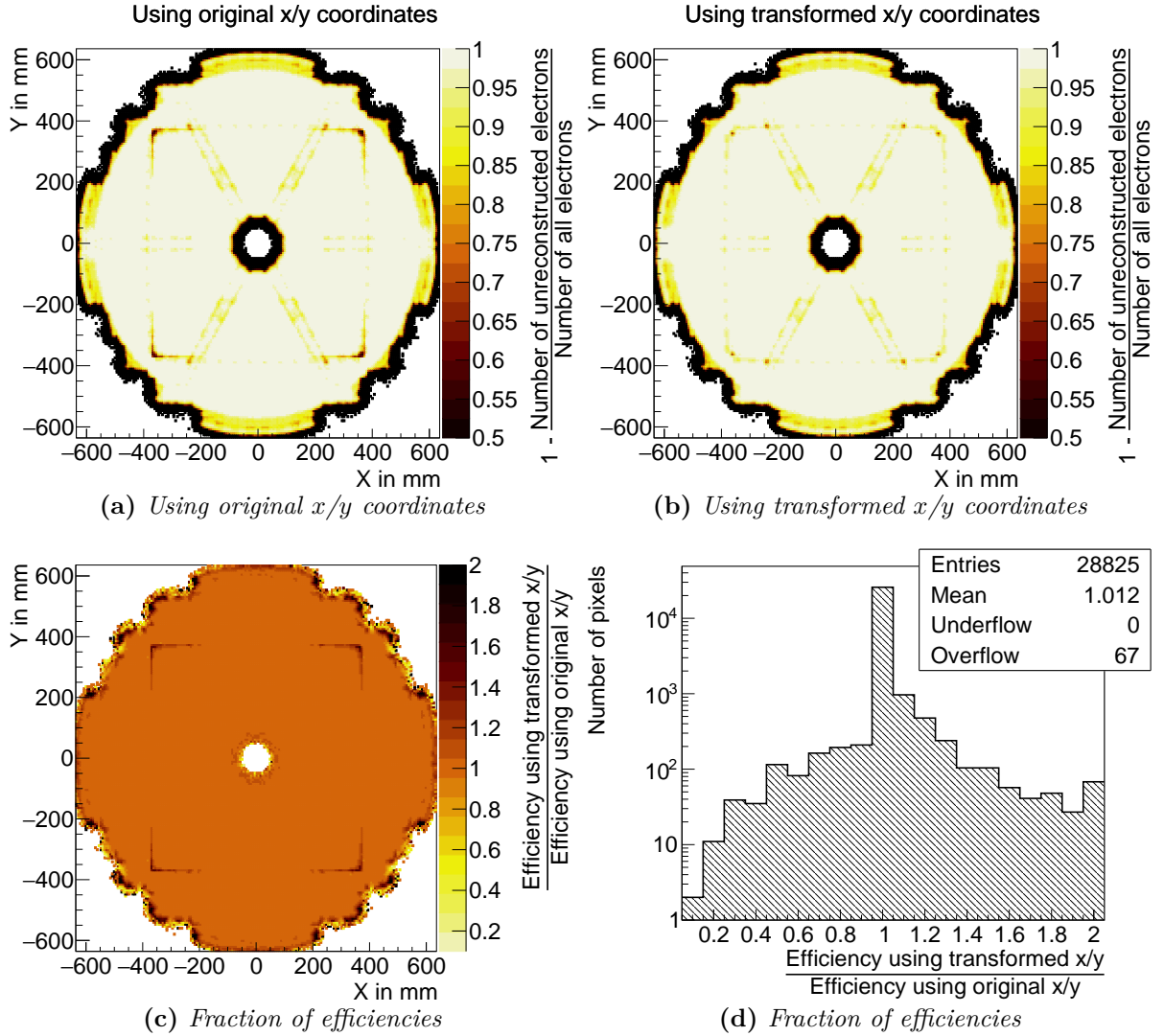
**Figure 9.11** ♦ *Spatially resolved electron reconstruction efficiency using the original* **(a)** *and transformed x/y coordinates* **(b)***. This efficiency distribution is derived using $1 \times 10^8$ simulated electrons emitted at $z_H = [-80, 0]$ mm $x = 0$ mm, $y = 0$ mm and distributed uniformly over $2\pi$. Efficiency is determined via $Efficiency = 1 -$ Number of unreconstructed electrons/Number of electrons in each $7 \times 7$ mm$^2$ pixel. Pixels with no electrons in them, i.e. pixels outside $\theta > 90°$ are discarded.* **(c)** *shows the fraction of* **(b)**/**(a)***, where the largest and lowest values are artificially cut off at values smaller than 0.1 and larger than 2. The color scale is inverted moving from* **(a)**,**(b)** *to* **(c)** *for visibility reasons. Sub-figure* **(d)** *depicts the entries of* **(c)** *as one dimensional histogram. There the mean is noted down to statistical precision in the legend.*

## 9.4 Summary

The first section of this chapter focused on an analytical transformation from the Cartesian RICH coordinate system $x/y$ to the detector global spherical coordinate system $\theta/\phi$ in HADES. The transformation is based on the concept that the detector is at least partially radially symmetric such that a simple transformation of radial coordinate $r$ to $\theta$ is sufficient. Here, this transformation was derived calculating the reflection vector of a particle with given $\theta$ analytically. One could clearly see that this transformation describes the behavior of the detector correctly, in simulation and using real data. One finds that, albeit taking the ring fitter tendencies not into account perfectly, the analytically derived transformation is still comparable to one taking the ring fitter into account perfectly ("map-based" transformation). For the best transformation possible, given the implemented ring fitting routine, it is therefore best to use an approach with different maps for different $z$-positions[12]. Using other reconstruction algorithms or making use of a backtracking-approach however favors the analytical approach presented here. It leaves a clear distinction between the real ring center and the center that is reconstructed using the ring fitter. Additionally, the transformation is more lightweight having only $7 \times 4$ parameters and is extremely easy to invert $(\theta/\phi \mapsto x/y)$.

The second section of this chapter used the already established idea of simply calculating the reflection vector of the particle now taking into account the actual ring projection on the photon detection plane. With the possibility to analytically determine the exact positions of each ring, a transformation was derived which transforms the $x/y$-coordinates such, that all rings have equal radii over the full RICH detector. Hereby the final transformation polynomials were derived through an iterative process. Overall it can be stated that indeed the transformation led to a more flat and, at the transition region from inner to outer photon detection plane, less wide ring radius distribution. A significant improvement of the reconstruction efficiency could be observed at the transition region, increasing the previously low efficiency of $\sim 0.5$ to $\sim 0.9$, leaving only 10% of the rings not reconstructible. For the HADES detector, the improvement is mostly limited to these regions, whereas other detectors that feature more geometric distortions might benefit much more from the approach presented here. Therefore, seeing this test of the "ring radius preserving" transformation more as a proof of concept was a full success.

---

[12]This exact transformation is therefore the current standard in HYDRA.

<div style="text-align: right">

# 10

</div>

<div style="text-align: right">

# Summary and outlook

</div>

In 2019 the HADES detector was used in a measuring campaign studying heavy-ion interactions through Ag+Ag collisions at 1.58A GeV. This beamtime marked the first use of the upgraded RICH detector. The upgrade of this HADES RICH was and is a full success. The way thereto was accompanied by topics discussed throughout this thesis. Starting with the characterization of the photon sensor for the photon detection plane and the readout modules and closing with beamtime data driven analyses on the detector performance and calibrations. In the following, the different topics of this thesis will be summarized and put into context. Hereby focus is also laid on the fact that the future CBM experiment will use the same photon detector and readout system.

## 10.1 Testing the HADES RICH hardware by means of laboratory measurements

Before commissioning of the HADES RICH the photon detector and the readout chain underwent several tests. In this regard, the first part of this thesis dealt with characterizing the photon detector and parts of the readout module.

**Characterization of the HADES RICH photon detector**
The HADES RICH's photon detector is comprised of 428 MAPMTs of type Hamamatsu H12700. These MAPMTs are part of a batch of 1100 MAPMTs, which were bought for CBM and are now in parts used for the HADES RICH upgrade. All 1100 MAPMTs were tested using a dedicated test bench allowing all MAPMTs to be fully characterized in the context of this thesis. The characterization was carried out in terms of dark rate, efficiency, homogeneity, effective area, gain, and afterpulse-probability giving the following averages over all MAPMTs:

| Measurand | Average over 1100 MAPMTs | Requirements |
|---|---|---|
| Efficiency-Index | $0.9711 \pm 0.0021\,(\text{stat.}) \pm 0.0055\,(\text{syst.})$ | $-$ |
| Effective area | $(85.46 \pm 0.04\,(\text{stat.}) \pm 0.42\,(\text{syst.}))\%$ | $\geq 80\%$ |
| Gain | $(2.641 \pm 0.0223\,(\text{stat.}) \pm 0.250\,(\text{syst.})) \times 10^6$ | $> 0.8 \times 10^6$ |
| Dark rate | $(1.014 \pm 0.030\,(\text{stat.}) \pm 0.490\,(\text{syst., max.}))\,\text{kHz}$ | $< 6.4\,\text{kHz}$ |
| Afterpulse-probability | $(0.9271 \pm 0.01701\,(\text{stat.}) \pm 0.047\,(\text{syst.}))\%$ | $< 5\%$ |

Visibly, all measurands are fully in line with the contractually agreed on requirements. In addition to the global averages, also the development with respect to the production time was analyzed. A positive change over the time of production was observed with a decrease in the MAPMTs dark rate, increase in homogeneity, and increase in effective area. On the negative side an increase was found with respect to the afterpulse-probability, whereas all other measurands did only show fluctuations but no in- or decreasing trend. The increased afterpulse-probability is however still fully in line with the given requirements.

Also assessed was the long term stability of the MAPMT characteristics. For this, selected reference MAPMTs were remeasured multiple times over the course of three years. It was found that the dark rate of the MAPMTs decreases over time, reaching their respective minimum latest after half a year. Further, the afterpulse-probability of the MAPMTs increases with time but seems too level off after approximately one and a half years. The steepness of this increase was found varying for different MAPMTs. With the measurement uncertainty on the gain being quite high only one MAPMT exhibited a visible increase. In terms of efficiency of the MAPMTs a slight and hard to interpret decrease over time was found. The counteractive increase in the afterpulse-probability, the variation in gain and the lowering in efficiency are however small. They thus impose, with regards to the overall well working MAPMT, no hazard for HADES nor CBM, both using the same photon sensors.

After surveying all MAPMTs the first step towards the new HADES RICH was made deriving the optimal MAPMT grouping. This is necessary, as always six MAPMTs are supplied with the same high voltage using the DiRICH read out chain, which is employed in the HADES RICH. A gain alignment procedure was developed using different gain classes to group the MAPMTs based on the ten lowest pixel gains, skipping the lowest three, to obtain a measure stable against single pixel outliers. This procedure worked very well and produced a gain-wise very homogeneous detector. This was not only found in low level analyses but was also later supported analyzing the data from the beamtime.

**Measurements of the DiRICH-FEB readout electronics**

After establishing the MAPMT layout for the HADES RICH, tests with regards to the readout electronics were made. First, a routine was developed finding the baseline of the respective DiRICH-FEB channel. This procedure also allowed to analyze the noise band width of the individual DiRICH. Having the tools to measure this noise band width allowed to test the DiRICH in different setup configurations. It was found that, unsurprisingly, higher input capacitances in the input filter, leading to lower low-pass cutoff frequencies, reduced the noise band width in the DiRICH. More interesting was the finding, that the DiRICH modules closest to the DiRICH power module were exposed to a massive noise band width increase, when using the power module's DC/DC converters. This increase could be reduced by means of shielding and through the use of different input capacitances but not fully recuperated. Due to this finding, the idea of using DC/DC converters inside the HADES RICH was omitted instead driving the whole setup using four dedicated low voltage power lines for each DiRICH. There are however ongoing plans to use other DC/DC converters that emit less radiative noise for future experiments like CBM.

On top of the baseline finding procedure, a procedure was developed to derive a threshold for the each channel of the DiRICH MAPMT combination. By differentiating the measured signal rate as a function of threshold, a statistical amplitude spectrum can be derived and further used to derive thresholds for each channel separating electronic noise from actual photon signals. On basis of these spectra a test was made determining the single photoelectron peak positions of all MAPMT DiRICH combinations in the HADES detector. This test was deemed successful but overall not robust enough. Hereby one main problem leading to volatile results was an inhomogeneous illumination of the photon sensors during the measurement. This problem could not be fixed before the beamtime, such that the final decision was made using only fixed thresholds during the Ag+Ag beamtime in 2019.

With the full HADES detector set up, additional tests were made assessing the overall noise situation in the full detector. It was found that the full HADES detector features on average an astonishing 11.5 mV full noise band width after pre.-amplification for the DiRICH-FEBs with 1 pF input capacitance and 8.4 mV on average for those with 10 pF. This very good result indicates that on average measurements would even be possible with a set detection threshold of 20 mV, being more than three times the average half noise band width. This supports the choice of not using DC/DC converters was indeed correct but also indicates that a detector global use of DiRICHes with 10 pF input capacitance might have been an even better choice. Unfortunately this was not possible at the time due to a shortage of 10 pF capacitors.

## 10.2 Tuning the RICH detector's performance on basis of beam data

On basis of this well built detector, the second large part of this thesis dealt with the task of improving the detector response through different calibrating measurements on basis of the beamtime data.

### Prepratory studies

The start was made with prepratory studies slightly before the actual beamtime. Here the impact of the magnetic stray field was studied. A visible but small effect was found observing at maximum a 20% decreased efficiency in less than 2% of all channels when driving the magnet close to its design maximum of 3.2 kA. This impact is negligible as the overall loss in efficiency is very small. Not negligible was the impact of scintillation light from the calcium fluoride window, which was found to introduce an additional photon load of 6.7 kHz per pixel on the MAPMTs. This was measured as integral over all channels using single collisions of Ag on an Ag target, i.e. the same setup used in the final measurement campaign. Based on these findings the window was removed which led, due to the enhanced radiator volume, to a necessary switch in the radiator gas to $C_4H_{10}$.

**Time and ToT cuts**

Using beamtime data, first cuts on leading edge (LE) time and time over threshold (ToT) were discussed. These simple cuts already improved the detector response significantly. Before deriving more narrow time cuts, artifacts visible in every channels' LE and ToT response were iterated. Most interestingly it was found, that most channels exhibit a clear peak at LE times right before the main peak (correlated to reconstructed electron candidates). This peak was not found correlated to electrons reconstructed in the rest of the detector. These artifacts might be correlated to low momenta electrons being scattered at large angles of $\sim 90°$ thus producing Cherenkov light when passing directly over the MAPMTs. This theory was deemed plausible in dedicated simulations not derived in the context of this thesis. Furthermore, the capacitive cross talk contribution could clearly be separated from other low ToT contributions using the LE-ToT spectrum, suggesting to use this representation always when discussing this effect. Indications were found that for some MAPMT pixels a substantial part of signals with low ToT can actually be related to real photon hits, excluding capacitive cross talk and charge sharing as their main source. After understanding most features in the LE-ToT distribution, another attempt was made deriving more narrow time cuts. The effect of these cuts was studied finding a clear improvement of the detector response. The cuts mostly limit the number of "fake" rings that might be randomly matched to other particles than electrons. It is thus suggested to consider these narrow time cuts for future analyses using the HADES RICH.

**Timing precision**

As the LE spectrum does feature many artifacts not easily correctable, in a first attempt an integrated timing precision of 440 ps (RMS) was found. This already very good timing precision was reached without employing any major calibrations and is thus larger than the best possible timing precision reachable with this photon detector and readout chain. For the HADES detector this timing precision is fully sufficient as interaction rates are low and the background in the detector is small. In light of the future CBM experiment, measuring at much higher interaction rates using the same sensor and readout, it is nonetheless interesting to assess the maximum capabilities of the setup. In order to find the timing precision that would be reachable after calibration, the timing precision was analyzed using only LE times in ToT windows of different widths and assuming a Gaussian like time response. By this means, a timing precision with respect to the HADES START detector of

$$\bar{\sigma}_{\text{LE, HADES}} = (196.8 \pm 0.1)\,\text{ps}$$

was found using only a single 100 ps wide ToT windows. It is thus the timing precision one can assume when perfectly correcting for all artifacts in the LE time spectrum. Increasing the ToT window to its maximum width, i.e. including all hits but still assuming a Gaussian like time response, the average timing precision in HADES did decrease to

$$\bar{\sigma}_{\text{LE, HADES}} = (346.7 \pm 0.2)\,\text{ps} \; .$$

This number is therefore the timing precision reachable with little effort invested into calibrating the LE time response of each channel. In future it should therefore be considered to try to correct for ToT dependent walk and additional occupancy dependent shifts (which might be found small enough to neglect). This would not necessarily help the HADES reconstruction but might give detailed information on how to handle the same MAPMT-DiRICH setup in future experiments like CBM. It was found that DiRICH-FEBs with larger input capacitance of $10\,\mathrm{pF}$ reduced these timing precisions by only $\sim 15\,\mathrm{ps}$ on average. Also MAPMTs with WLS coated front window did exhibit worse timing precision. It was observed that the gain of WLS only manifests for timing acceptance windows of larger $> 1.5\,\mathrm{ns}$ (break even point), hence significantly spoiling the timing precision. After $10\,\mathrm{ns}$ the WLS reaches its maximum increase of hits being $+26\%$. This $26\%$ increase must be assumed an overestimation with the analysis technique still partially including background sources.

**Calibrating and using the ToT information**

In a next step it was tried to used the ToT information to improve the separation between single rings and overlapping (maybe even overlaying) double rings. First tested was the impact of a simple uncalibrated ToT sum comparing it to the use of just the hit information. Here, an increase in separability of approximately $11\%$ was found. During derivation of the calibration an artifact in the ToT distribution was found and discussed. This feature of consistent dips in the ToT spectra was established to most probably come from the impact of fixed frequency noise on the ToT measurement. After accounting for this effect a calibration was developed, again testing for improvements in the separability of overlapping rings. Therethrough an improvement in separability of $14\%$ was found, also improving the shape of the reconstructed number of photons per single/double ring spectra. It was estimated that assuming a perfect calibration a theoretical improvement in separation of $30\%$ might be achievable. This however would need a near perfect understanding of the distorted ToT spectra discussed before.

**Detector alignment**

In the last chapter an attempt was made to derive an analytically motivated transformation of RICH coordinates $x/y$ to HADES spherical coordinates $\theta/\phi$. The derivation of this transformation succeeded, however could not exceed the precision of a simple transformation map inferred from simulation. This was mainly deemed to be an impact of the ring finder/fitter tendencies not perfectly correctable using the analytical transformation. The analytical transformation has however much less parameters and is well usable for the so called back tracking approach, where the ring finder might not even be employed.

Based on a very similar calculation like the one used to extract the analytical transformation, a new transformation of the whole RICH detector was obtained. This transformation aimed to produce equally sized rings over the full detector. The transformation was found to work, producing nearly equal ring sizes over the full detector. This is especially interesting at the transition region between inner and outer photon detection plane, where the detector geometry distorts rings the most. There, a loss in the ring reconstruction efficiency due to distorted rings

could be recuperated nearly fully. Therefore one can see this method of analytically transforming the detector towards being more homogeneous as a proof of concept to maybe be incorporated in future experiments that feature more geometric distortions.

## 10.3 Outlook

The DiRICH readout chain together with the Hamamatsu H12700 MAPMT worked very well in the upgraded HADES RICH for the 2019 Ag+Ag beamtime. The low noise, high timing precision and precise spatial resolution already results in a very performant detector with only limited calibration in place. All calibrative measures described throughout this thesis enhanced the detector's performance even further. This will also hold true for the CBM RICH detector soon to be built, which uses the same photon detection setup. Since for CBM the interaction rates and photon density on the photon detection plane will be much higher, even more effort needs to be invested into the calibration. Many methods discussed throughout this thesis, like the gain alignment, baseline and threshold setting are hereby directly transferable. Others like leading edge and time over threshold calibrations need to be tweaked slightly but should then be applied to ensure a best possible working of the CBM RICH. Also an analytical detector transformation should be tested as the rings in the CBM RICH will be more elliptic. Nonetheless one can expect the CBM RICH to work very well with the same detection setup already producing very good results in the HADES RICH.

# List of Figures

# List of Tables

# Appendices

# A
## Additional figures

This appendix holds all additional graphics referenced throughout this thesis but not deemed important enough to be placed into the main text.
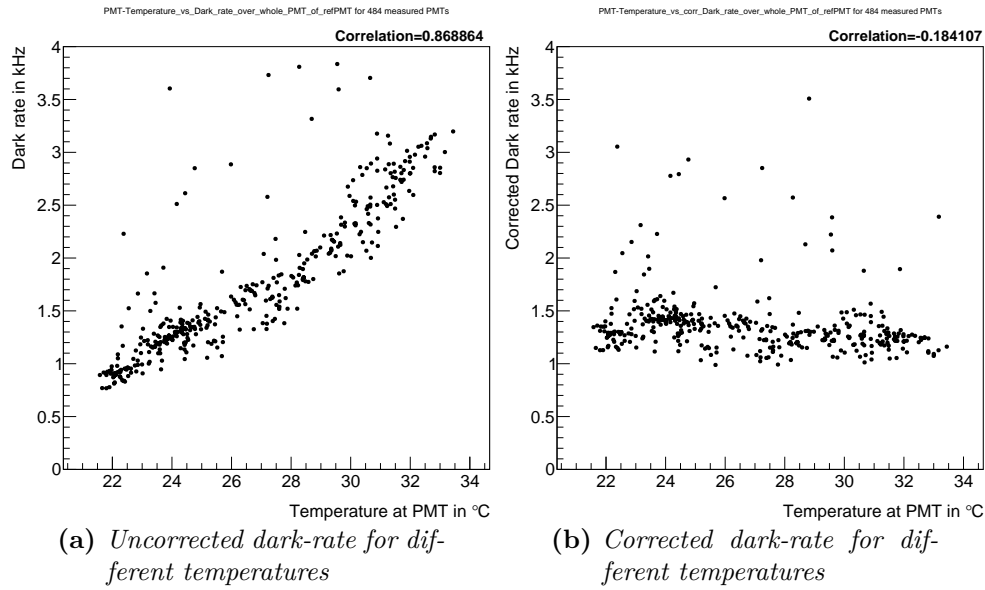
## A.1 Additional figures for Chapter 1
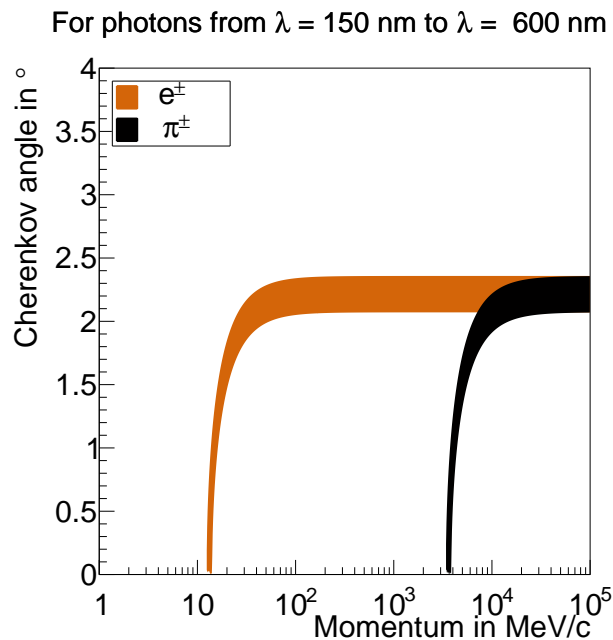


**Figure A.1** ♦ *Cherenkov angle range for electrons ($e^{\pm}$) and pions ($\pi^{\pm}$) at different momenta, assuming the Cherenkov photons to be emitted at wavelengths of $150$–$600$ nm in $C_4F_{10}$. The wavelength dependent refractive index ($n(\lambda)$) is approximated using a Sellmeier Polynomial with parameters $A = 2.375 \times 10^{-07}$ and $\lambda_0 = 73.64$ nm from [Fil+02].*
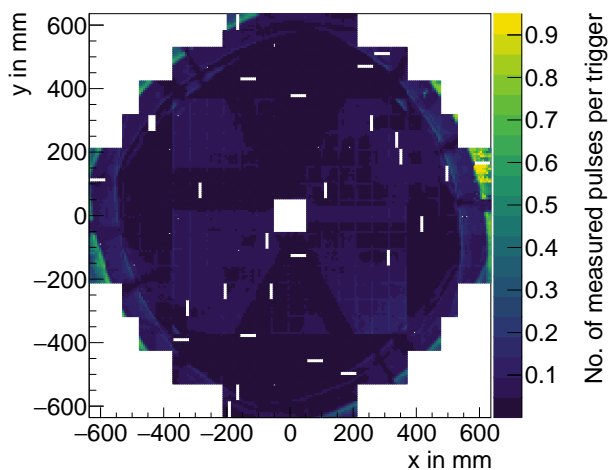


**Figure A.2** ♦ *Measured illumination using the four laser couplings attached to the HADES RICH detector. The intensity is set such, that on average one photon is measured every ten pulses.*

## A.2 Additional figures for Chapter 2



**(a)** *Uncorrected dark-rate for different temperatures*



**(b)** *Corrected dark-rate for different temperatures*

**Figure A.3** ♦ *Scatter plots showing dark-rate for varying temperatures with **(b)** and without **(a)** using an empirical formula correcting for the dark-rates dependence on temperature described in [ST17, pp. 74, 75]. Shown are the dark-rates of the reference MAPMT always inserted into the test bench. The Pearson's correlation coefficient is depicted in the top right of each plot and reads $r_{uncorr.} = 0.87$ and $r_{corr.} = -0.18$.*
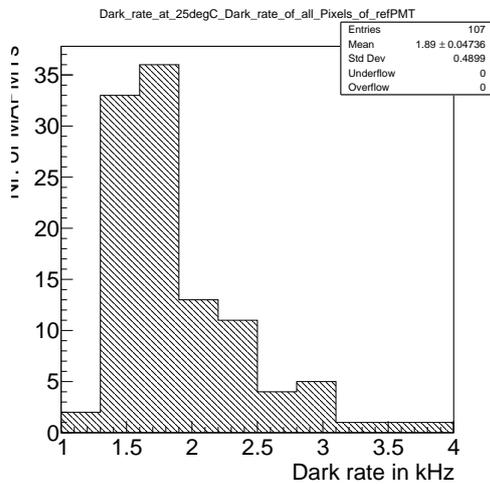


**Figure A.4** ♦ *Distribution of dark-rate for all measurements of the main reference MAPMT before the 10-06-2016. This measurements do not take the dark-rate's dependence on the temperature into account. The standard deviation of this distribution is $\sigma_{dark} = 0.4899\,kHz$ and therefore the systematic uncertainty on this measurand.*
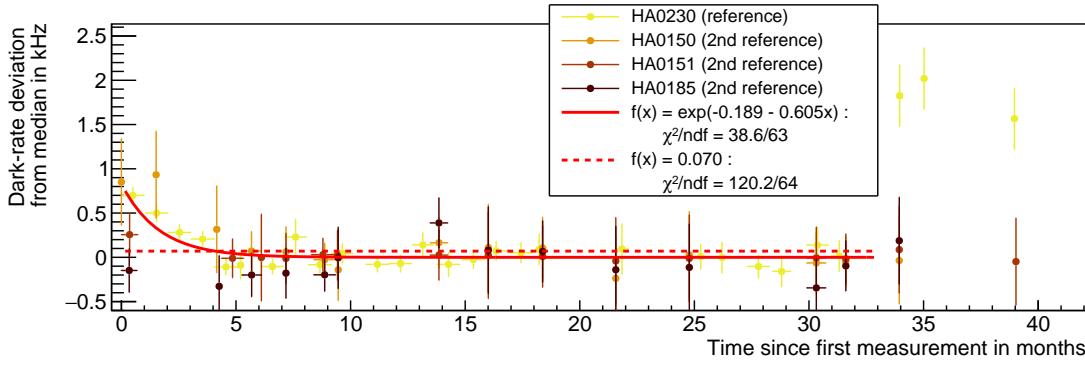
**(a)** *Variation of dark-rate with time. The fits discard measurement data derived after the 33<sup>rd</sup> month due to MAPMT behavior not yet fully understood.*
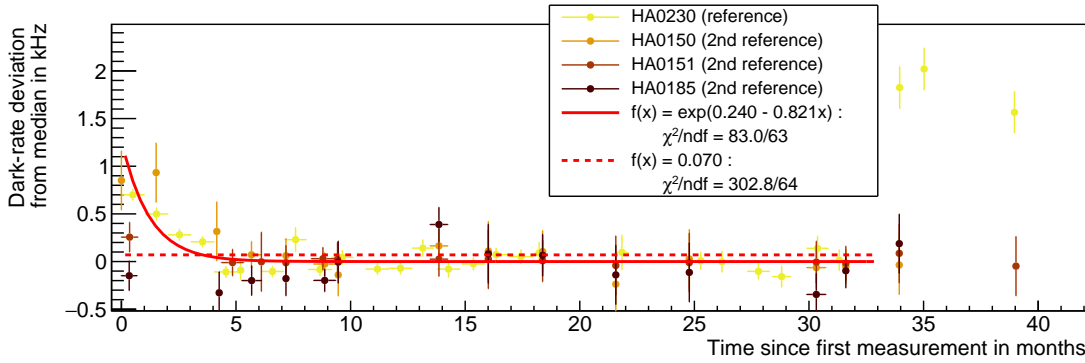


**(b)** *Variation of dark-rate with time assuming uncertainties from [För16, p. 56] on the uncorrected dark-rate i.e. for measurements before the 10-06-2016.*
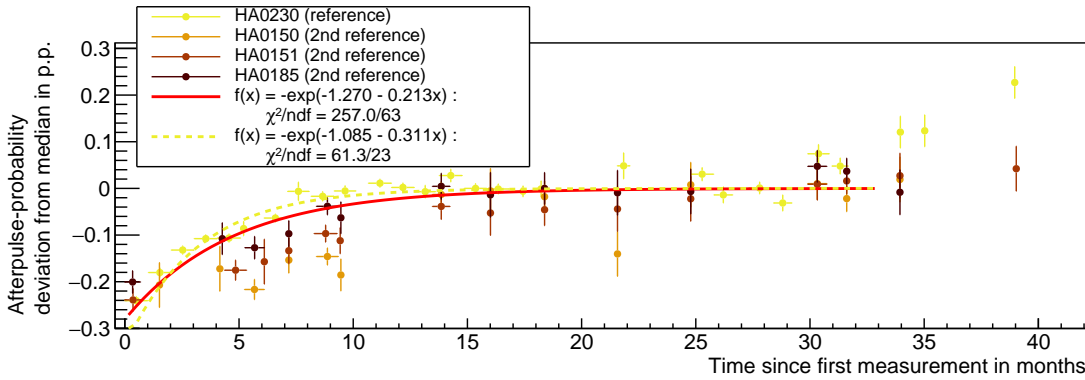


**(c)** *Variation in the aftperpulse-probability over time. Yellow dashed line is only fitted to the main reference MAPMT (HA0230).*
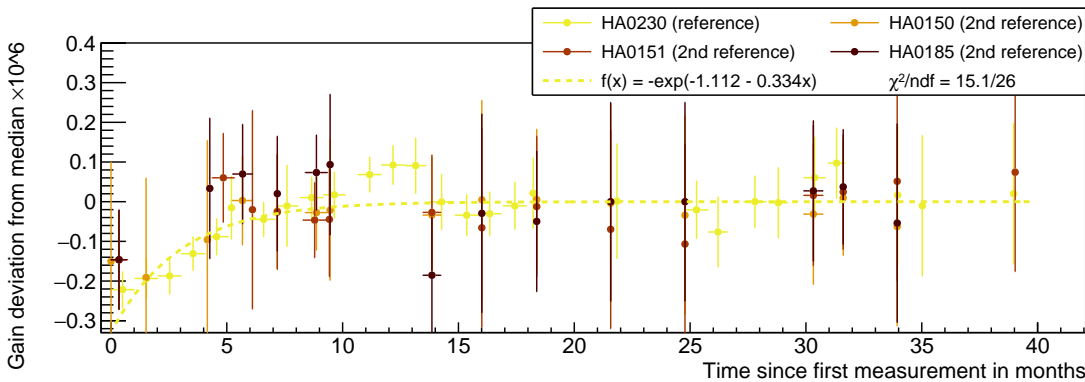


**(d)** *Variation of measured single photoelectron gain of reference MAPMTs. Yellow dashed line is only fitted to the main reference MAPMT (HA0230).*
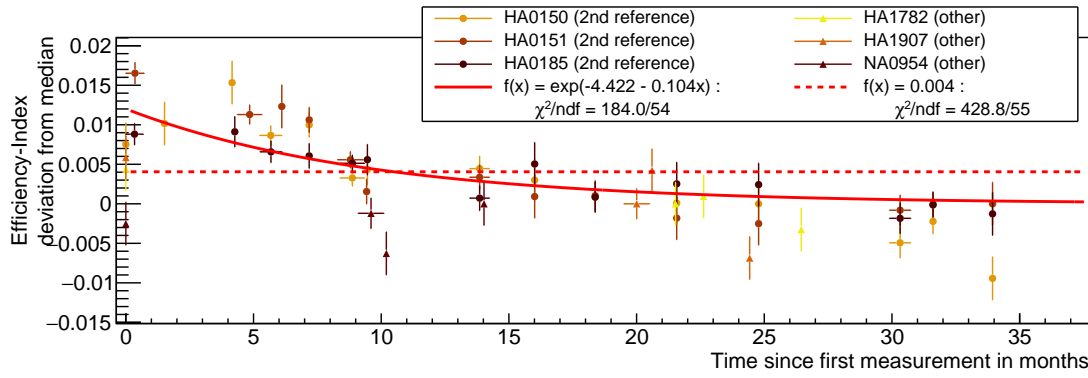
**(e)** *Variation of measured efficiency of secondary reference- plus some additional MAPMTs. Efficiency is always a measure comparing the MAPMTs' efficiency to the efficiency of the main reference MAPMT.*
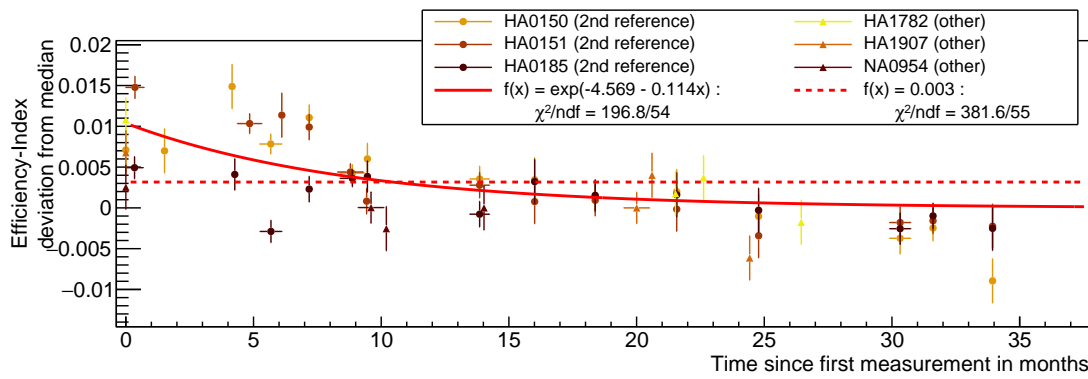


**(f)** *Variation of measured efficiency of secondary reference- plus some additional MAPMTs using a gain dependent threshold. The threshold is hereby set to the 30% single photoelectron peak level for each (also the main reference) MAPMT.*
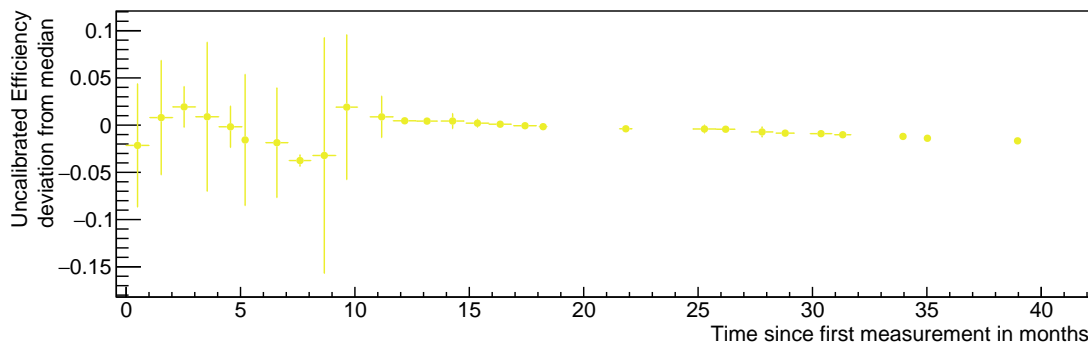


**(g)** *Variation of the "efficiency" measured of the main reference MAPMT. This "efficiency" is heavily dependent on the current light level of the LED used in the test bench. However, these fluctuations are even larger during the early months of measurement.*

**Figure A.5 ♦** *Amalgamation of the dependency of different parameters of the MAPMT w.r.t. the time of measurement. All figures depicted show the difference of the respective measurand comparing it to its MAPMT individual median of all measurement points one year after the first measurement. Depicted are main and secondary reference MAPMTs (for **(e/f)** also additional other MAPMTs) measured differently often in the test bench. Each point depicted averages over all measurements in one month of the given MAPMT, where month zero corresponds to the first month of measurement of that MAPMT. Thus, the uncertainty depicted in x-direction indicates the range of underlying measurements, while the uncertainty in y is the scaled systematic uncertainty ($\sigma/\sqrt{n}$) for n measurements with $\sigma$ as their individual uncertainty. Several exponential and constant fits are applied in order to assess the development of the repsective measurand with all fit results denoted in the legend.*
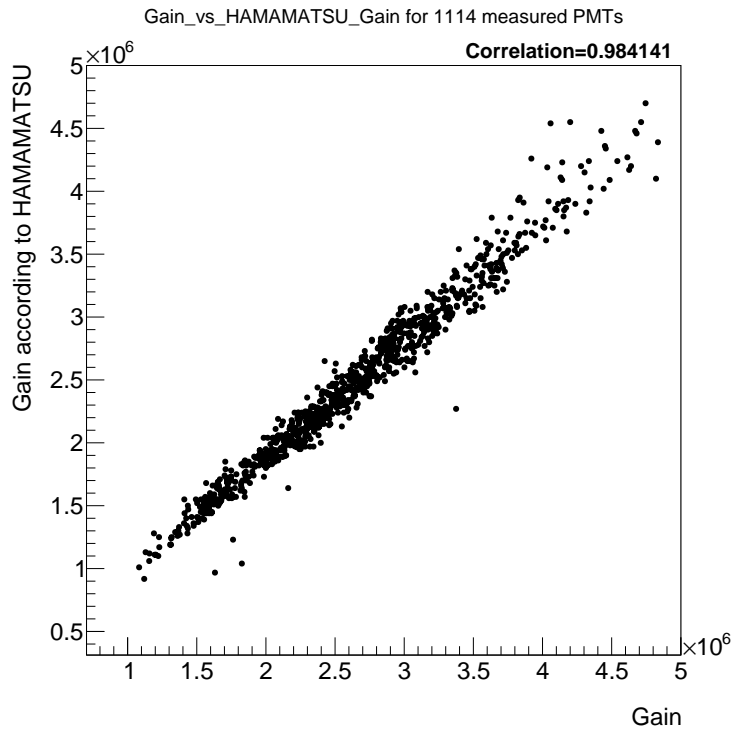
**Figure A.6** ♦ *Scatter plot of gain measured in the test bench and the gain measured by Hamamatsu. The Pearson's correlation coefficient, depicted in the top right, shows a strong correlation between those two measurands.*
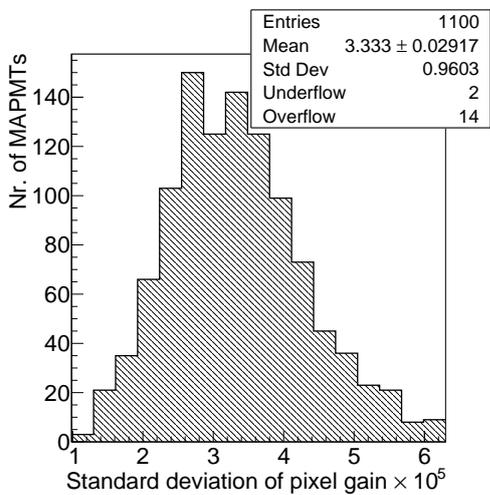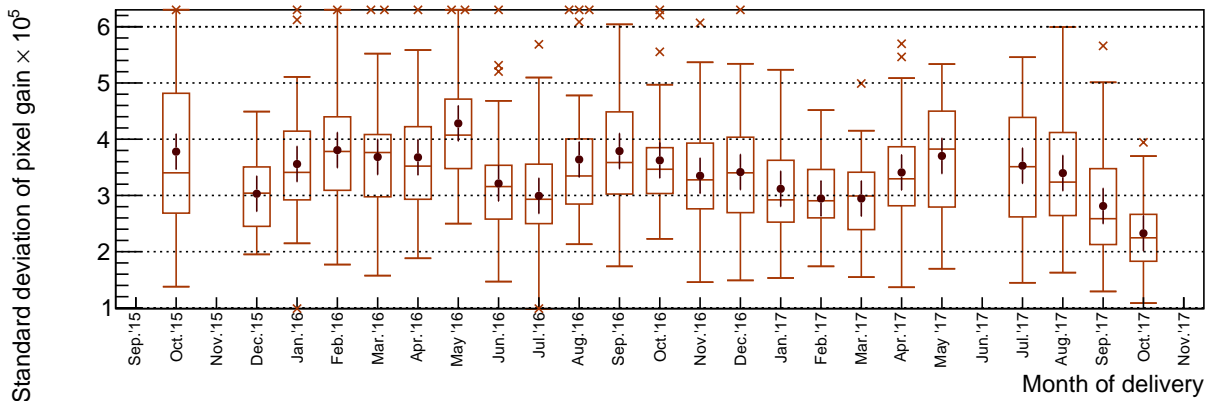


**Figure A.7** ♦ *Standard deviation in the pixel gains of one MAPMT for all 1100 H12700 MAPMTs visualized as box plot separated by delivery month (top) and as histogram (right). In the box plot, the boxes represent the IQR and whiskers a maximum of 1.5 IQR. The horizontal bar inside the box is the median, with the marker (dot) being the arithmetic mean. The Error bars attached to the mean represent the unscaled systematic uncertainty per measurement, as do the bin-widths of the histogram. Outliers are indicated with cross-markers. The systematic uncertainty is approximated using the uncertainty of the average $\sigma_{av.}$ through $\sigma_{std.-dev.} = \sigma_{av.}/\sqrt{2}$*
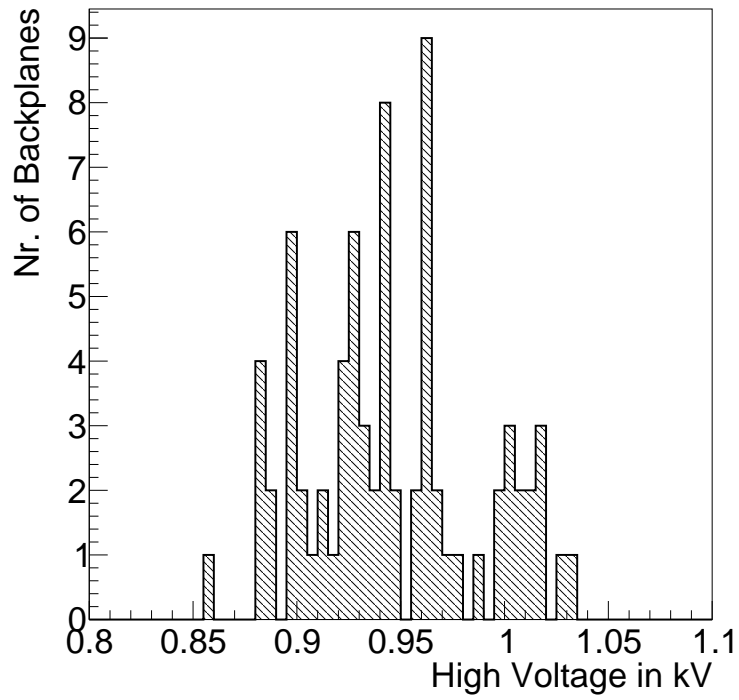
**Figure A.8** ♦ *High Voltage settings for all backplanes in the HADES RICH. These supply voltages are derived by the request that all MAPMTs on all Backplanes should have a gain of $2 \times 10^6$.*

## A.3 Additional figures for Chapter 3
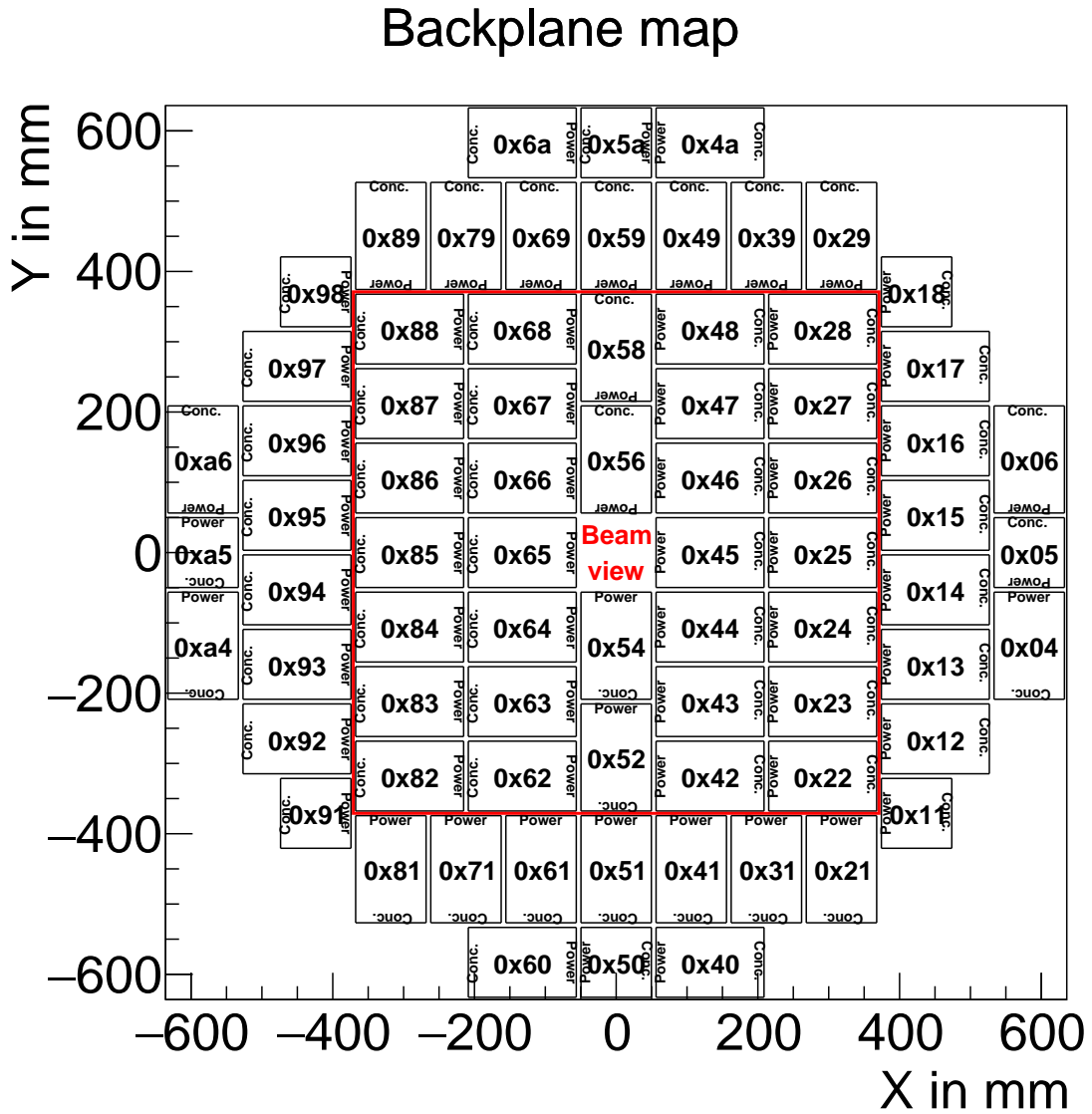
# Backplane map



**Figure A.9** ♦ *Spatial depiction of the arrangement of backplanes in the HADES RICH. Indicated as large red rectangle is the transition region from inner to outer photon detection plane. For each backplane, the side of connector and power board are noted in the figure, thus giving the backplanes orientation. The depiction is in beam view, i.e. from behind the RICH.*
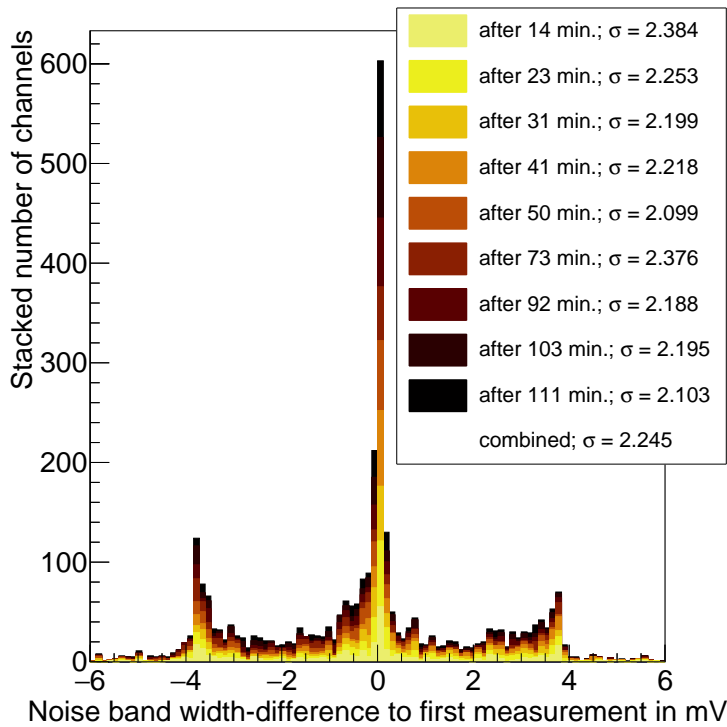
**Figure A.10** ♦ *Difference of the derived noise band width compared to the first measurement in a lab environment. Each color in this stacked plot represents a different measurement in time. The time difference of each measurement to the first measurement as well as the standard deviation σ can be found in the legend.*
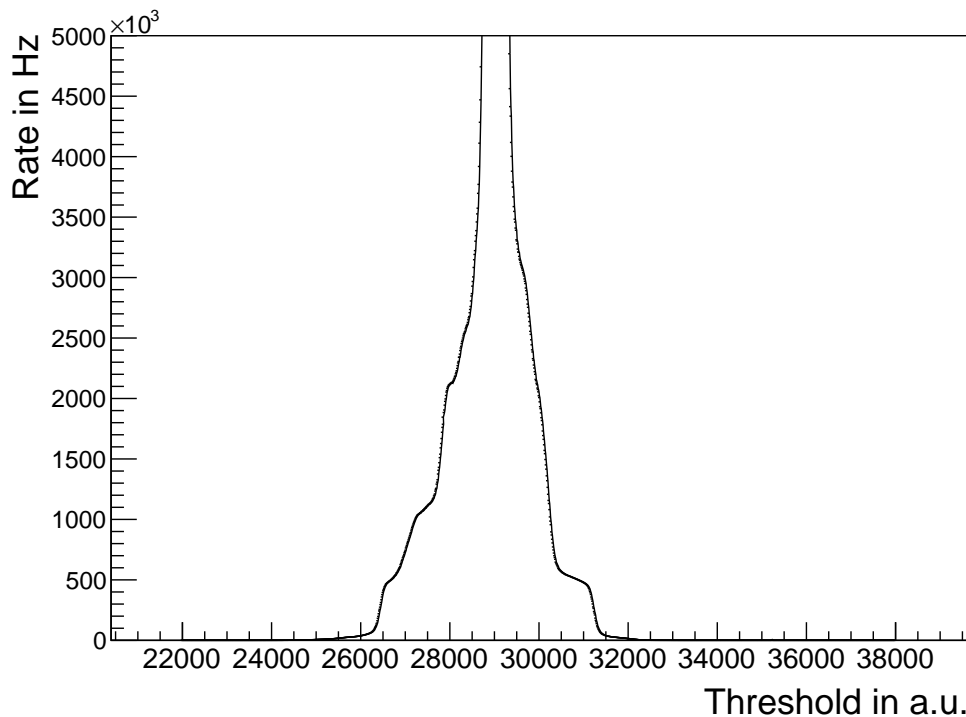


**Figure A.11** ♦ *Noise band of a single DiRICH-FEB channel measured using the unshielded DC/DC power supply of the power board. Measured is the rate above threshold at varying thresholds for a single DiRICH-FEB channel in a lab environment. Showing a stepwise increase of 500 kHz at both sides of the noise band.*

**(a)** *Copper-shielding*                **(b)** *EMV + Copper-shielding*
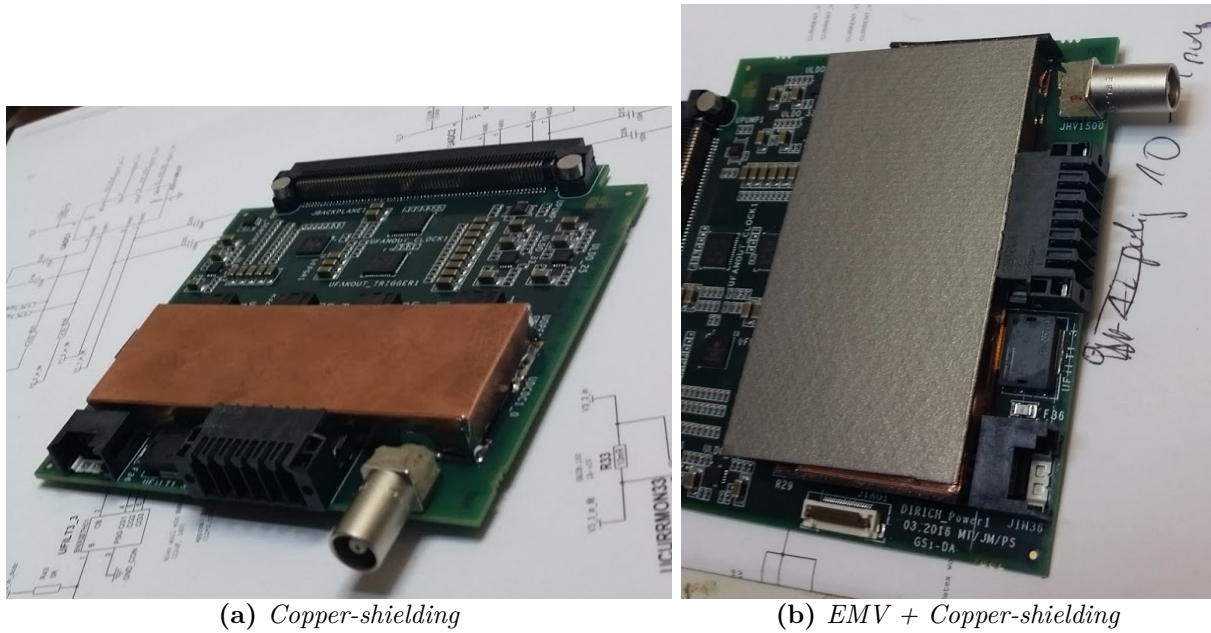
**Figure A.12** ♦ *Pictures of the* 0.5 mm *Copper and* 1 mm *EMV-shielded DC/DC-converter stages on the DiRICH power-board. Informations regarding the EMV shielding (EFR(10) from Kemet Electronics) can be found under* [KEM18]
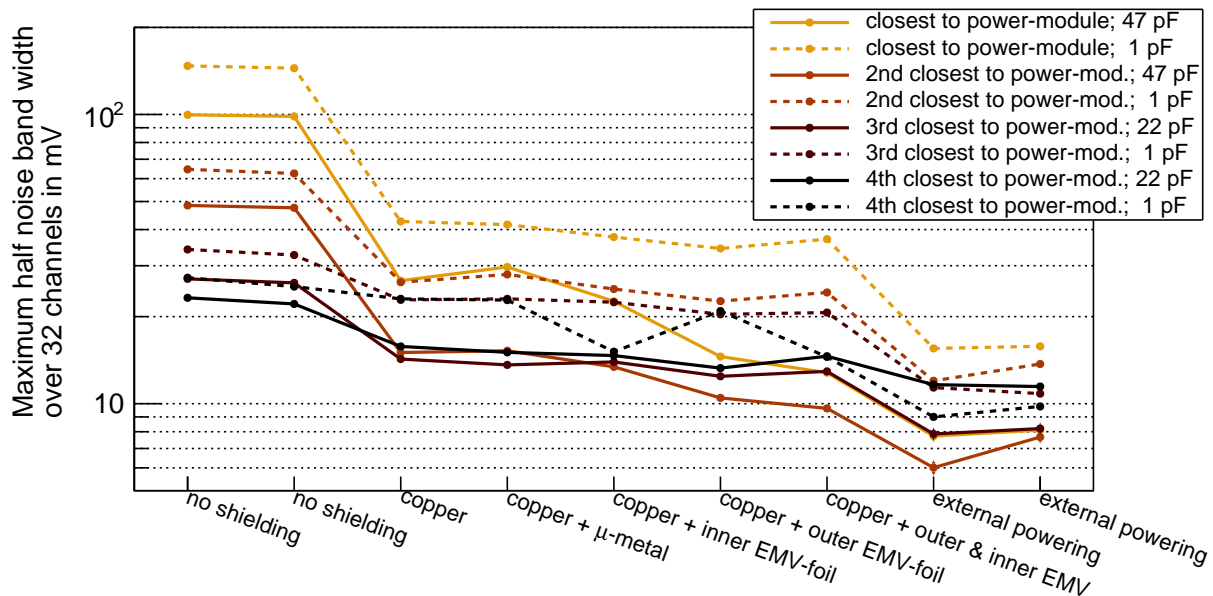


**Figure A.13** ♦ *Maximum half noise band width of 32 channels of one DiRICH-FEB with the use of various shielding materials. All measurements except those marked as "external powering" were made with switched on DC/DC converter stage on the power module. The different DiRICHes have different distances to the power module as indicated in the figures legend. The solid lines refer to DiRICHes with larger input capacities at their input stage. The error bars indicated refer to the systematic uncertainty on the measurement.*
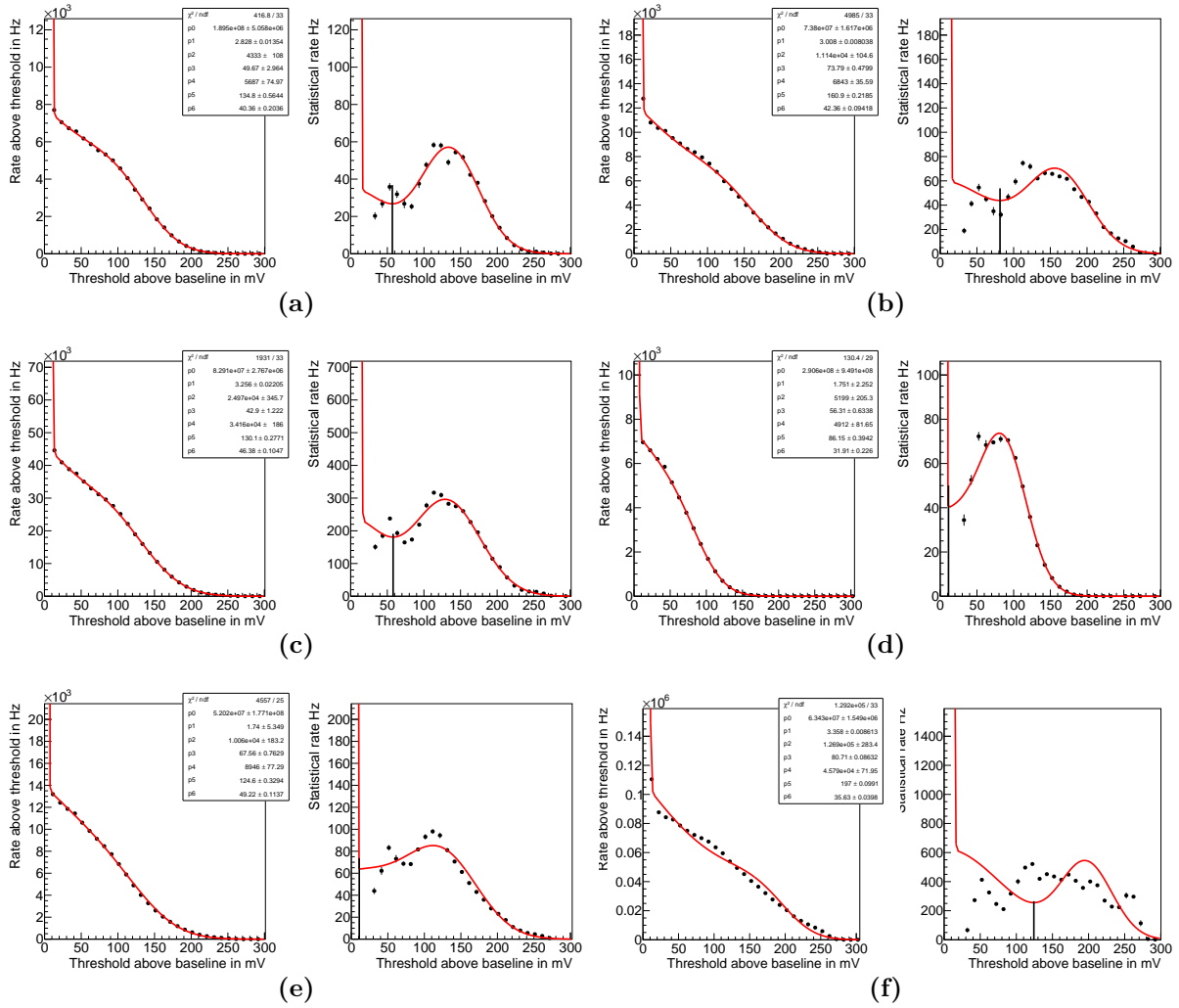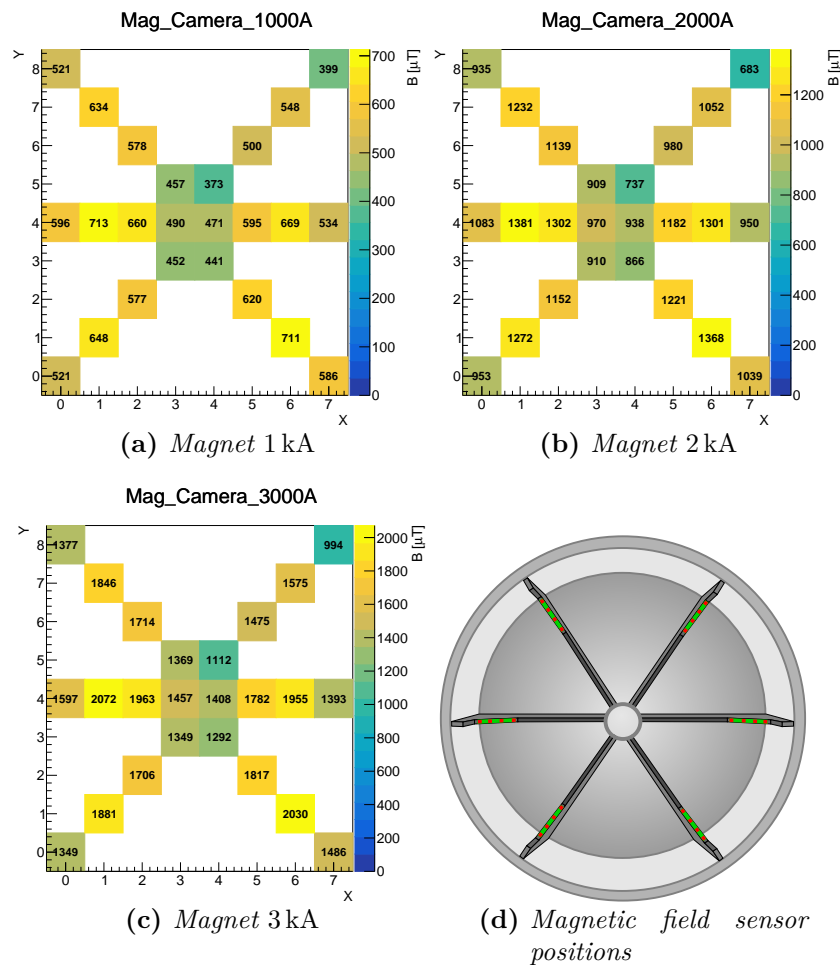
**Figure A.14** ♦ *Amalgamation of different succeeding fits **(a)-(e)** and one fit with $\chi^2/ndf > 1000$ **(f)** fitting the rate above threshold for varying thresholds. Each sub-figure includes two different plots, where the left one shows the measured data and the fit to it, with the right plot showing the derivative of data and fitted functions. The measured data was taken by measuring the rate at each comparative threshold (given in mV after pre-amplification) ten times over 3 s. The displayed error bars are therefore the uncertainty on the median (for the measured data) and propagated for the derivative. The derivative of the data points using the five point stencil hereby struggles if the change in rate between points is extremely large. There fitted function and the derivative of the data differ most. The fit functions are three error functions two of which have their mean fixed at zero to describe the MAPMT's and environmental noise. Parameters* p0, p2, p4 *are the respective areas under the functions. Parameters* p1, p3, p6 *are the σ of each function with* p5 *being the mean of the third error function thus representing the single photon peak position.*
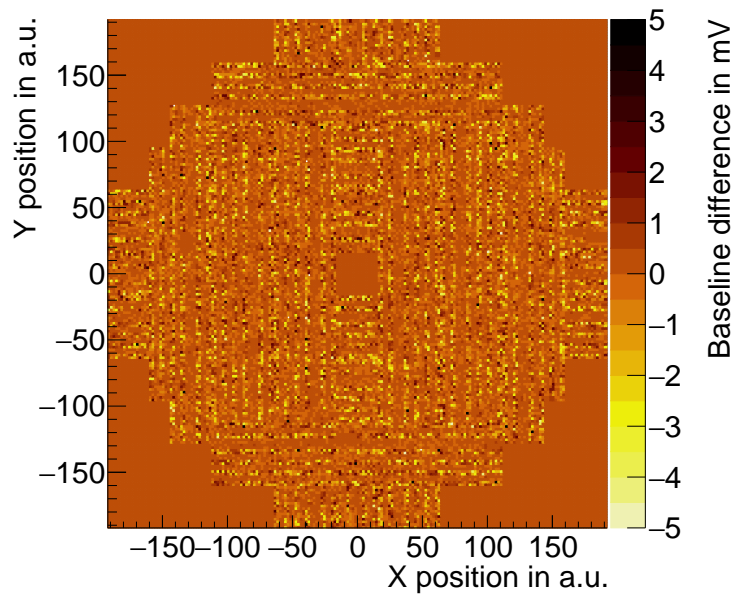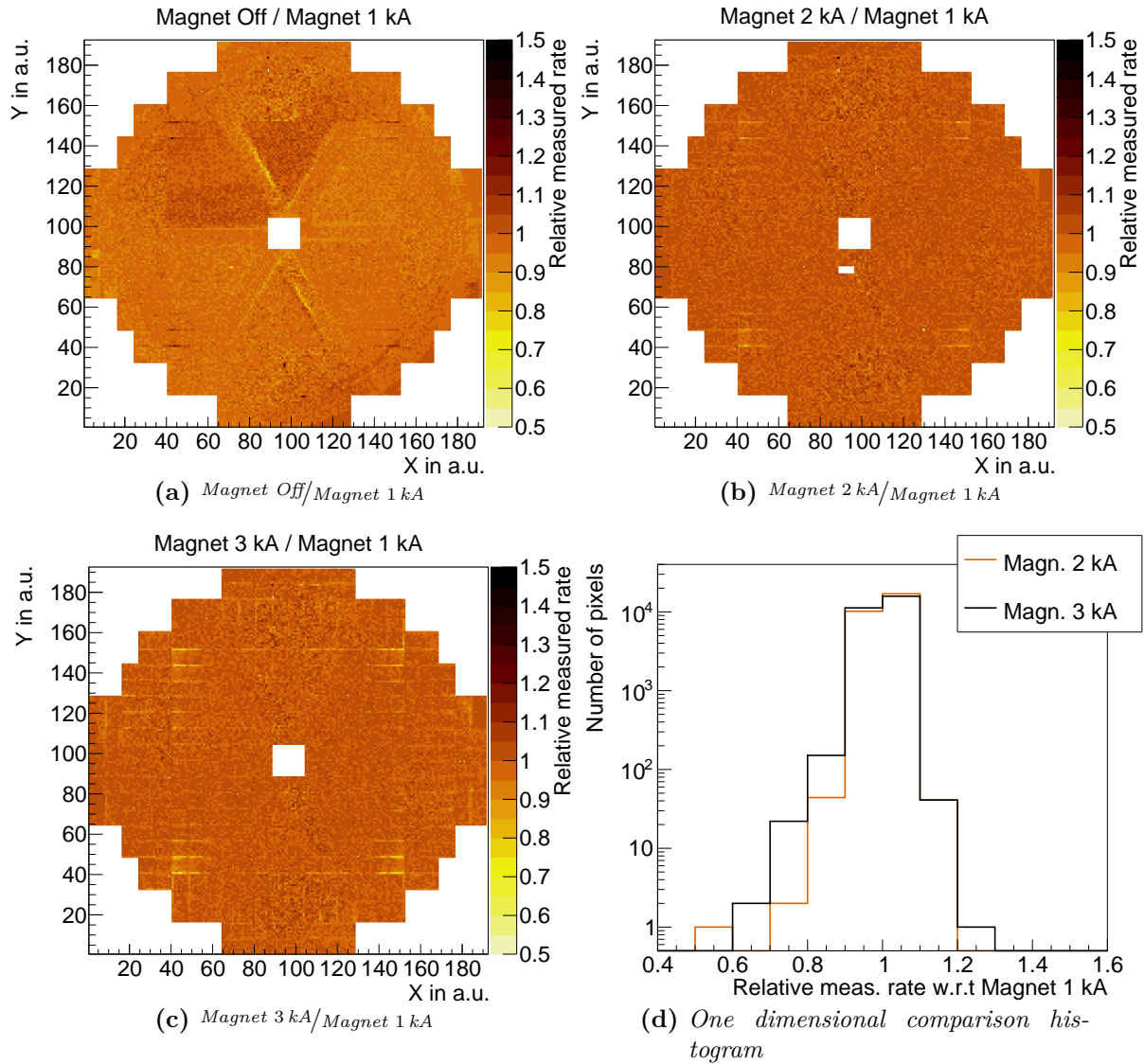
**Figure A.15** ♦ *Spatially resolved baseline differences in mV after pre-amplification for each channel in the fully equipped HADES RICH. The comparison is made between two baseline measurements (201 minutes apart). Unequipped areas or areas without module coverage are depicted with a baseline difference of 0, visualized as large brown areas.*

## A.4  Additional figures for Chapter 5



**(a)** *Magnet* 1 kA



**(b)** *Magnet* 2 kA



**(c)** *Magnet* 3 kA



**(d)** *Magnetic field sensor positions*

**Figure A.16** ♦ *Absolute magnetic field at the HADES RICH for three different magnetic field settings of the HADES magnet. Subfigures* **(a)**–**(c)** *show the absolute magnetic field in* µT *for each four sensors on the six spokes in the RICH, as shown in figure* **(d)***. The shown magnetic field strengths are corrected for the earth's and other magnetic fringe fields. With a soft iron shield around the RICH vessel the outermost sensors always see the smallest field together with the innermost (largest distance to the magnets) sensors. The measurements and graphics are made by Adrian Weber* [Web20a]*.*

**(a)** *Magnet Off/Magnet 1 kA*



**(b)** *Magnet 2 kA/Magnet 1 kA*



**(c)** *Magnet 3 kA/Magnet 1 kA*



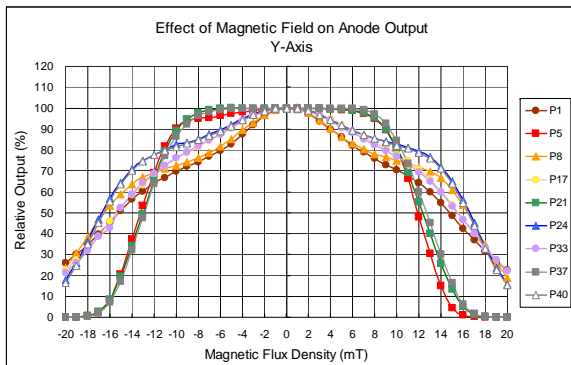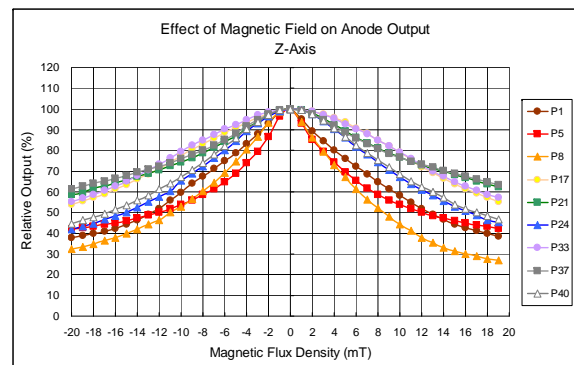**(d)** *One dimensional comparison histogram*

**Figure A.17** ♦ *Spatially resolved relative measured rate in the HADES RICH for different magnetic fields ((a)–(c)) Thereby for all different magnetic currents the average multiplicity per trigger for all pixels in the HADES RICH is normalized to that of the measurement with* 1 kA *magnet current. Subfigure (d) displays these relative measured rates as histogram.*

**Figure A.18** ♦ *Internally shown magnetic field measurements carried out by Hamamatsu on the H12700 MAPMT. This slide was accessed through* [Pau19]*.*
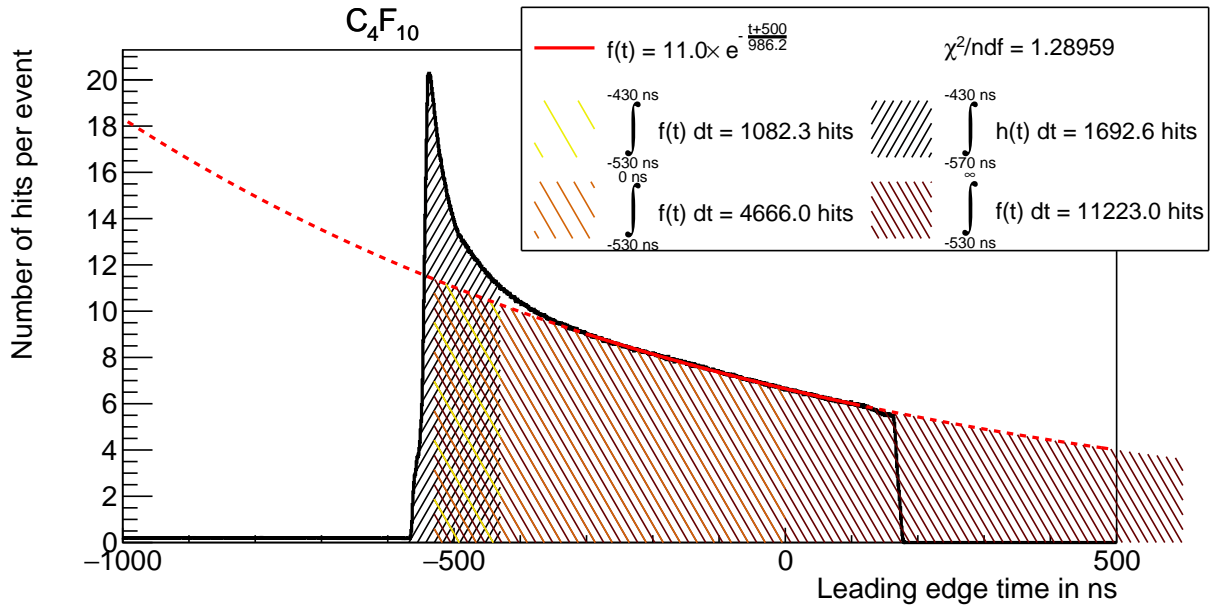
**Figure A.19** ♦ *Distribution of average hits per event over time for an Ag beam on Ag target with $500 \times 10^3$ particles per spill where the RICH radiator is filled with $C_4F_{10}$. An exponential decay is fitted to the tail of the data (solid red line) being mostly comprised of hits from scintillation photons of the $CaF_2$ window, with the dashed line indicating the shape of the function outside of the fitted range. The dashed areas below the distribution and fitted function indicate the integration ranges denoted in the legend, with the brown dashed area exceeding the drawing pad to indicate the integrals upper edge going to infinity.*
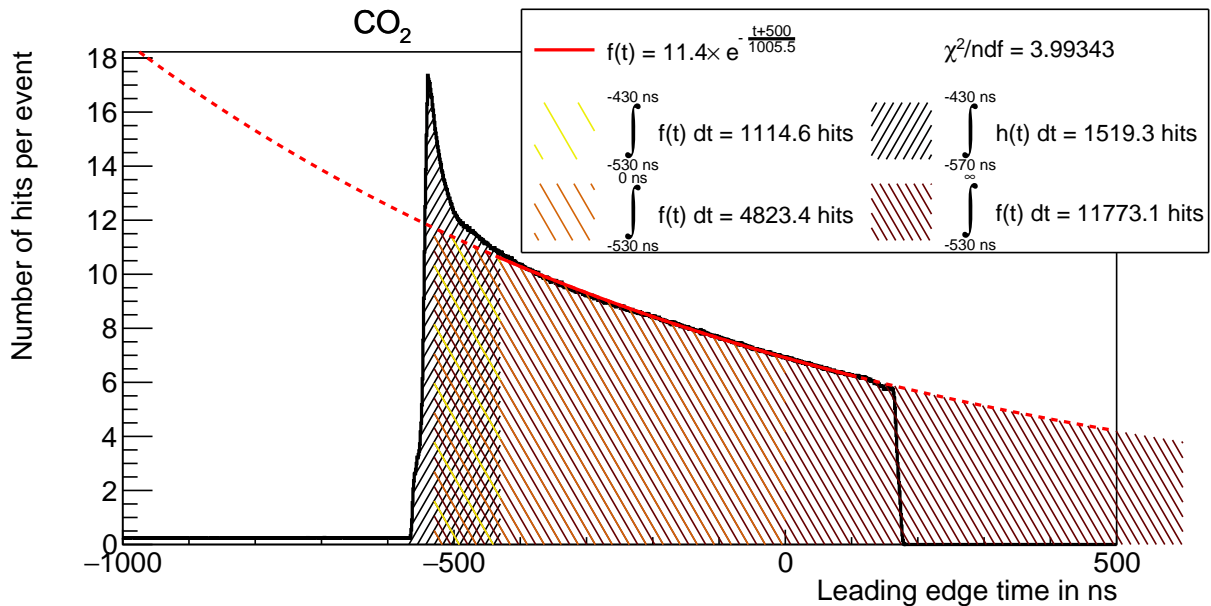


**Figure A.20** ♦ *Distribution of average hits per event over time for an Ag beam on Ag target with $500 \times 10^3$ particles per spill where the RICH radiator is filled with $CO_2$. An exponential decay is fitted to the tail of the data (solid red line) being mostly comprised of hits from scintillation photons of the $CaF_2$ window, with the dashed line indicating the shape of the function outside of the fitted range. The dashed areas below the distribution and fitted function indicate the integration ranges denoted in the legend, with the brown dashed area exceeding the drawing pad to indicate the integrals upper edge going to infinity.*
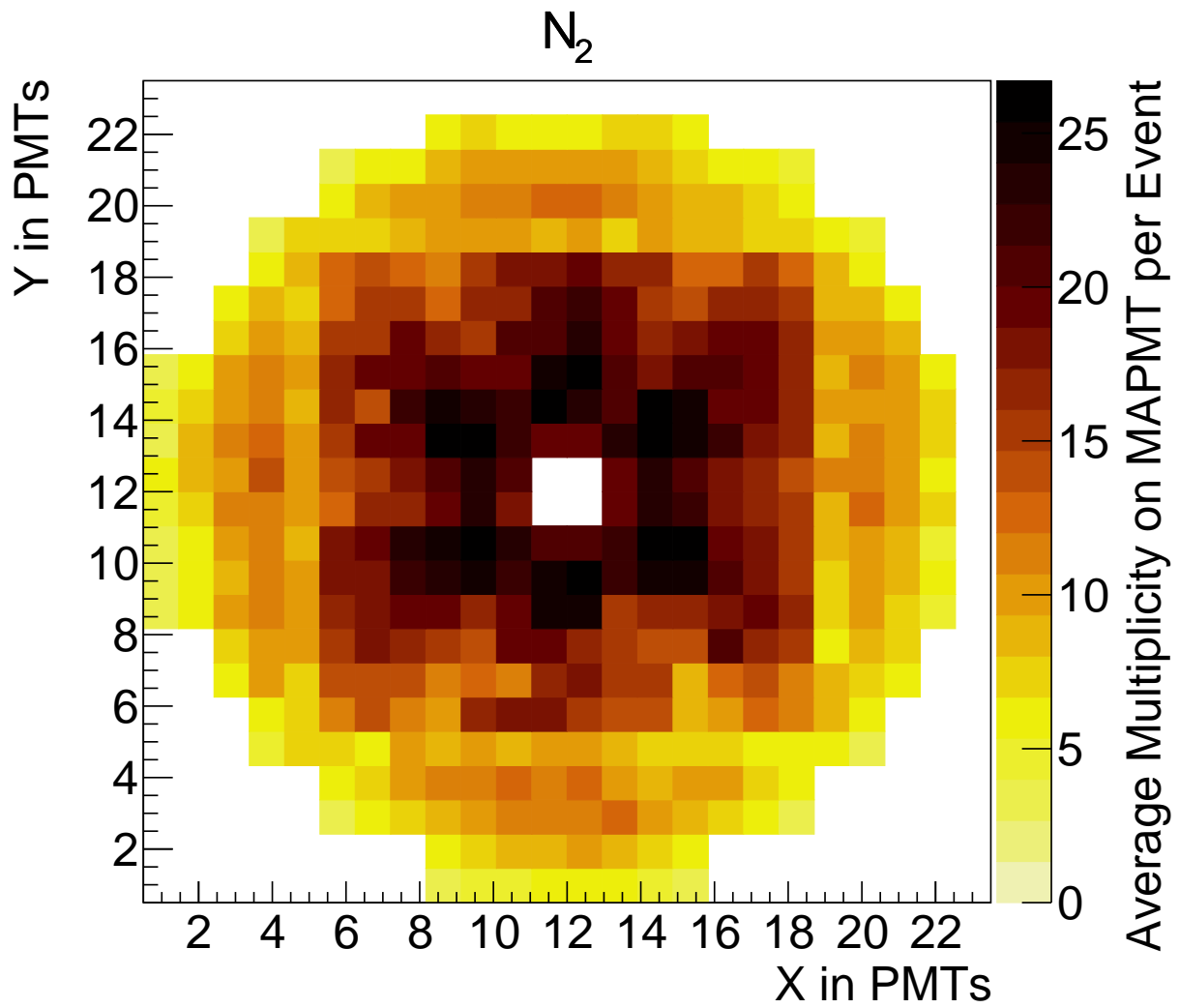
**Figure A.21** ♦ *Spatially resolved distribution of average "late" hits per event for an Ag beam on Ag target with $500 \times 10^3$ particles per spill where the RICH radiator is filled with $N_2$. Late hits indicate hits in the tail of the hit time distribution of the respective event. This time range is mostly being comprised of hits from scintillation photons of the $CaF_2$ window.*

## A.5 Additional figures for Chapter 6
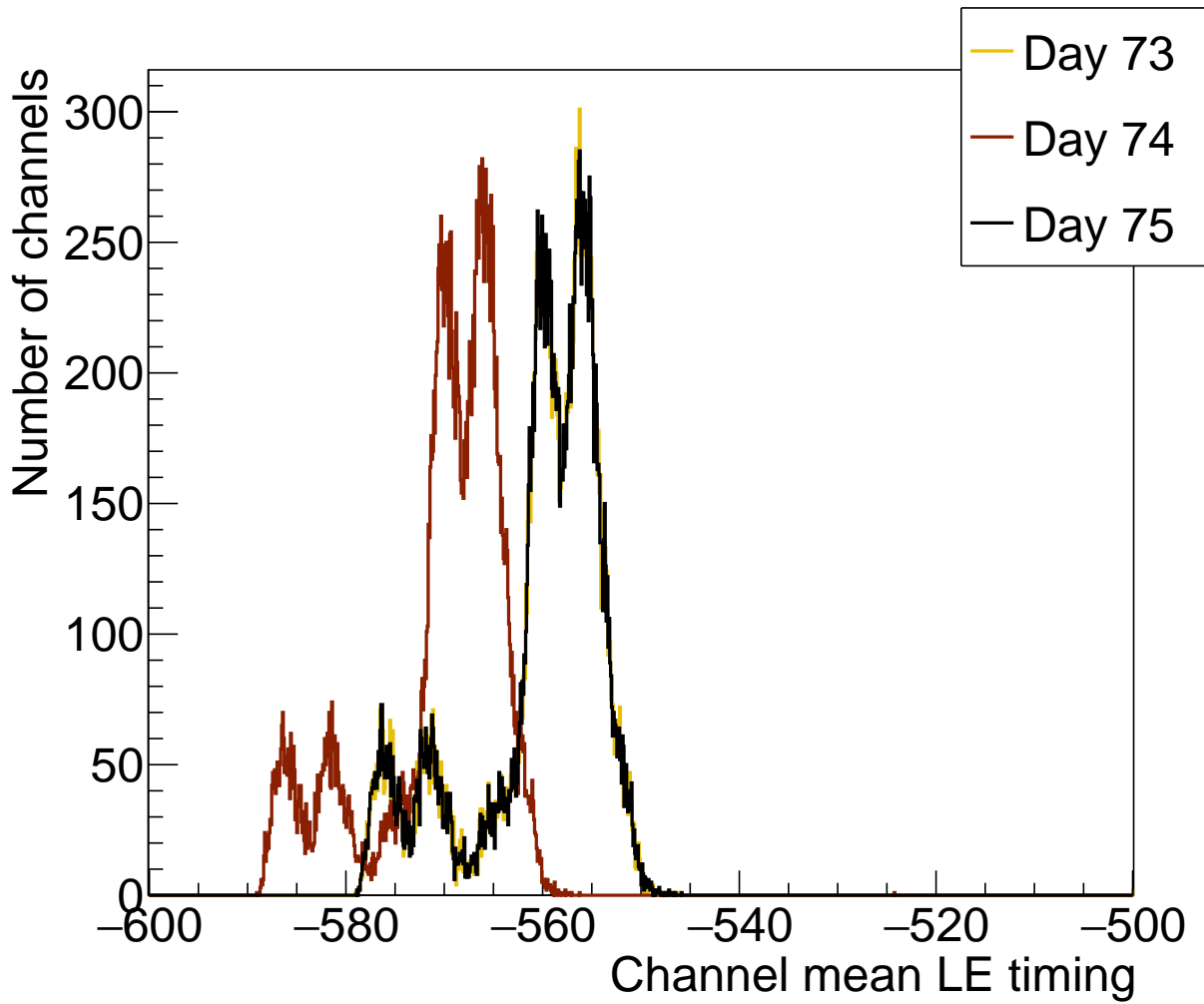


**Figure A.22** ♦ *Measured average LE time for different days of beamtime. Day 74 shows a shifted LE time constant throughout every channel. This shift comes from a shift in the trigger signal, and is correctable using the HADES-Start detectors hit time information. The overall distribution shows distinct peaks, mostly related to the different trigger-cable lengths in the detector.*
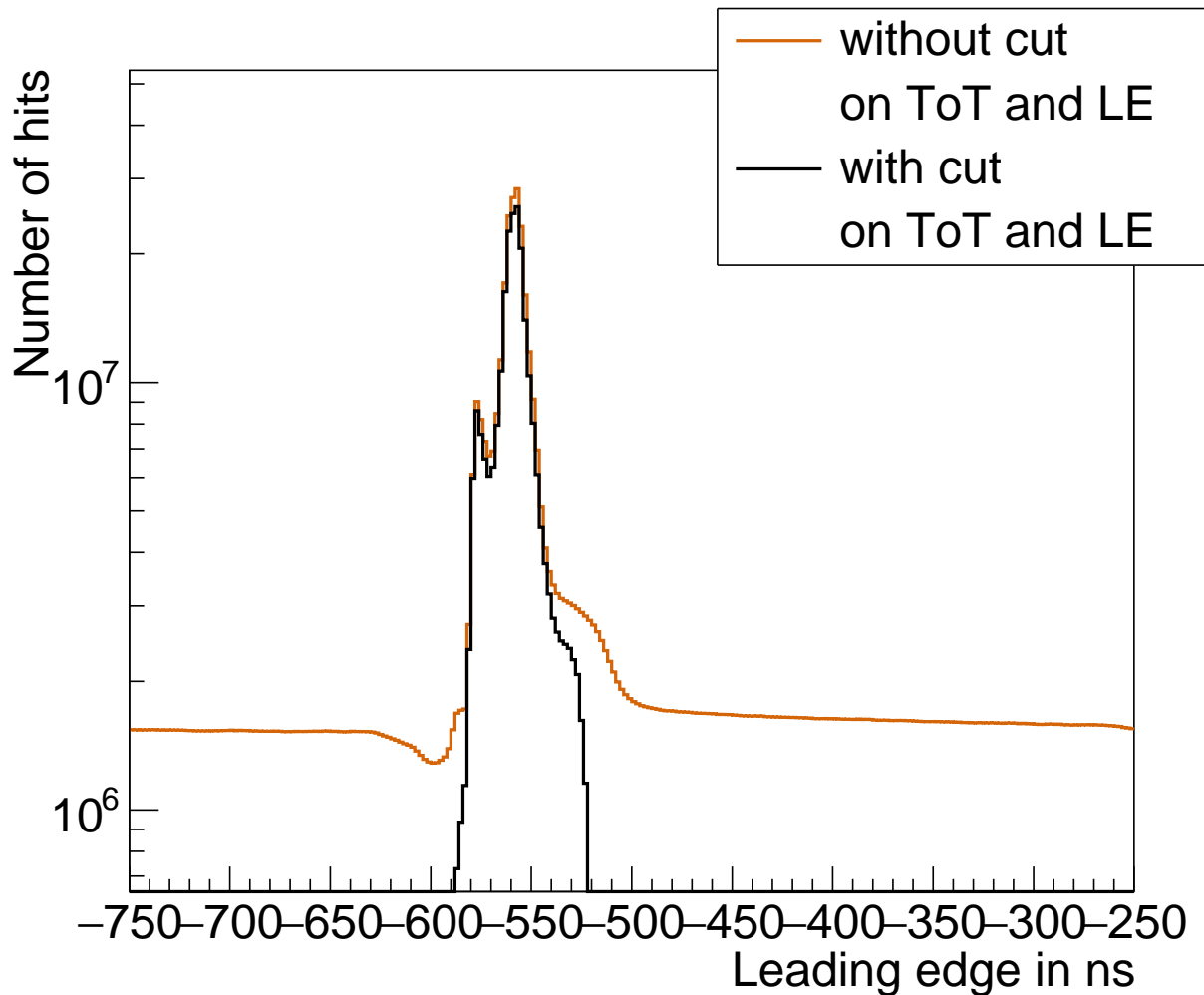
**Figure A.23** ♦ *Leading edge time distribution for every hit (measured by every channel) in the HADES RICH before and after applying the standard LE and ToT cut. This distribution shows all hits integrated over days 65, 74, and 80 of the beamtime. The channel individual hard cut on the LE time is visible in the abrupt increase ($\sim -580$ ns) and decrease ($\sim -520$ ns) in number of hits. The two different peaks correspond to the contribution of different channel groups. Thereby the visible earlier peak results from beam data measured at one arm in the detector, while the rest of the detector feartures nearly the same timing.*

**(a)** *Hits in the proximity of an e$^{\pm}$ cand.*

**(b)** *Hits with less than eight simultaneous hits on the MAPMT*

**(c)** *Ratio*
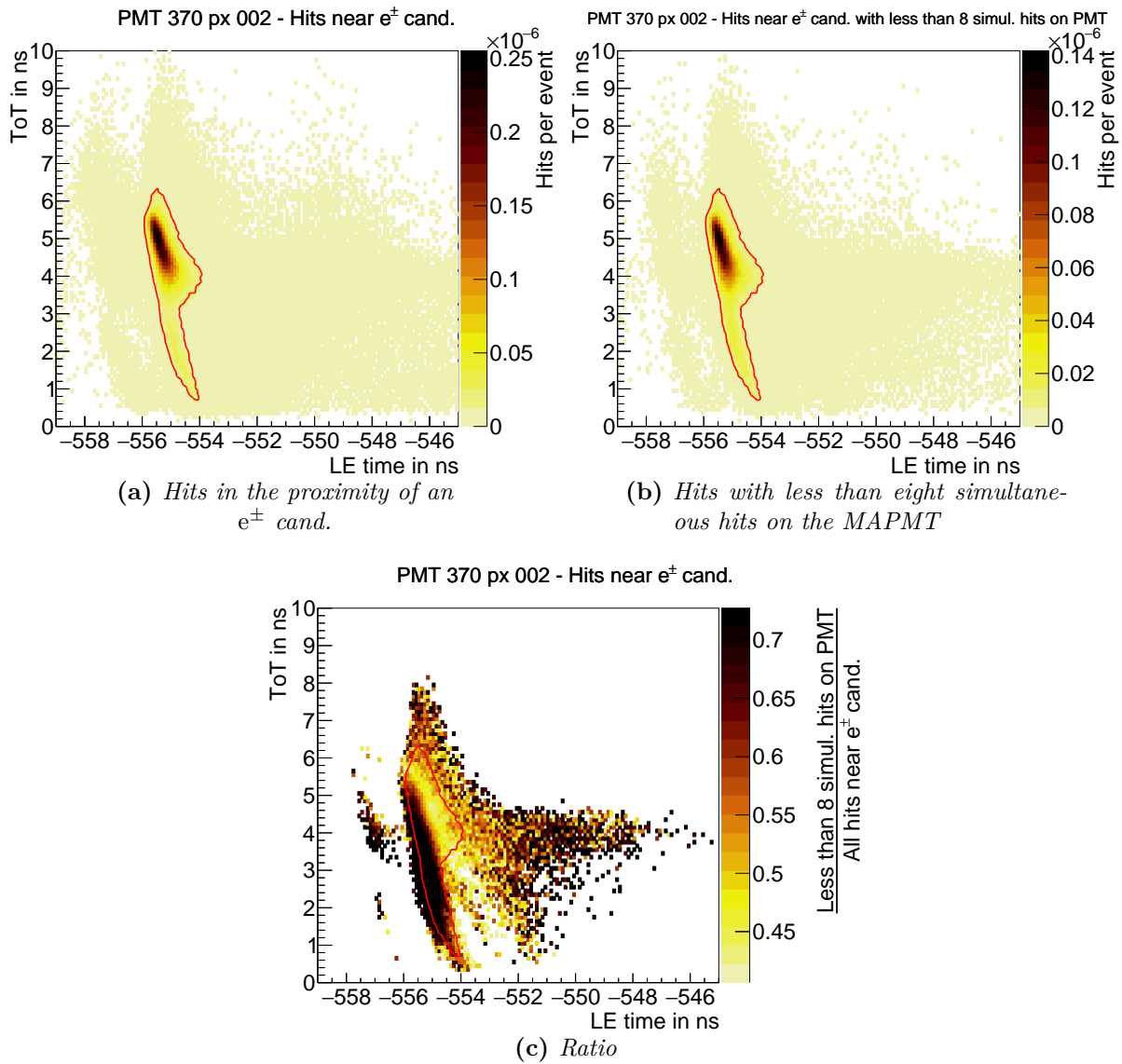
**Figure A.24 ♦** *Single channel (PMT 370 pixel 2) LE-ToT distribution for hits in the proximity of an electron track. Sub-figure **(a)** shows all those hits whereas **(b)** shows only the subsample of hits, where less than eight hits were measured on the MAPMT during the same event. The ratio of the two distributions is shown in **(c)**. The a red line in all sub-figures indicates the "5% of maximum" contour of sub-figure **(b)**, i.e. the outer bound of LE-ToT bins with more than 5% of the maximum entry. The ratio plot features only bins, where in both used distributions more than 5 hits were counted. This ratio plot's z-scale is additionally cut at the upper and lower 10% quantile, to better visualize its inherent features.*

**(a)** *Hits in the proximity of an* $e^\pm$ *cand.*



**(b)** *Hits being the only hit on the MAPMT*



**(c)** *Ratio*
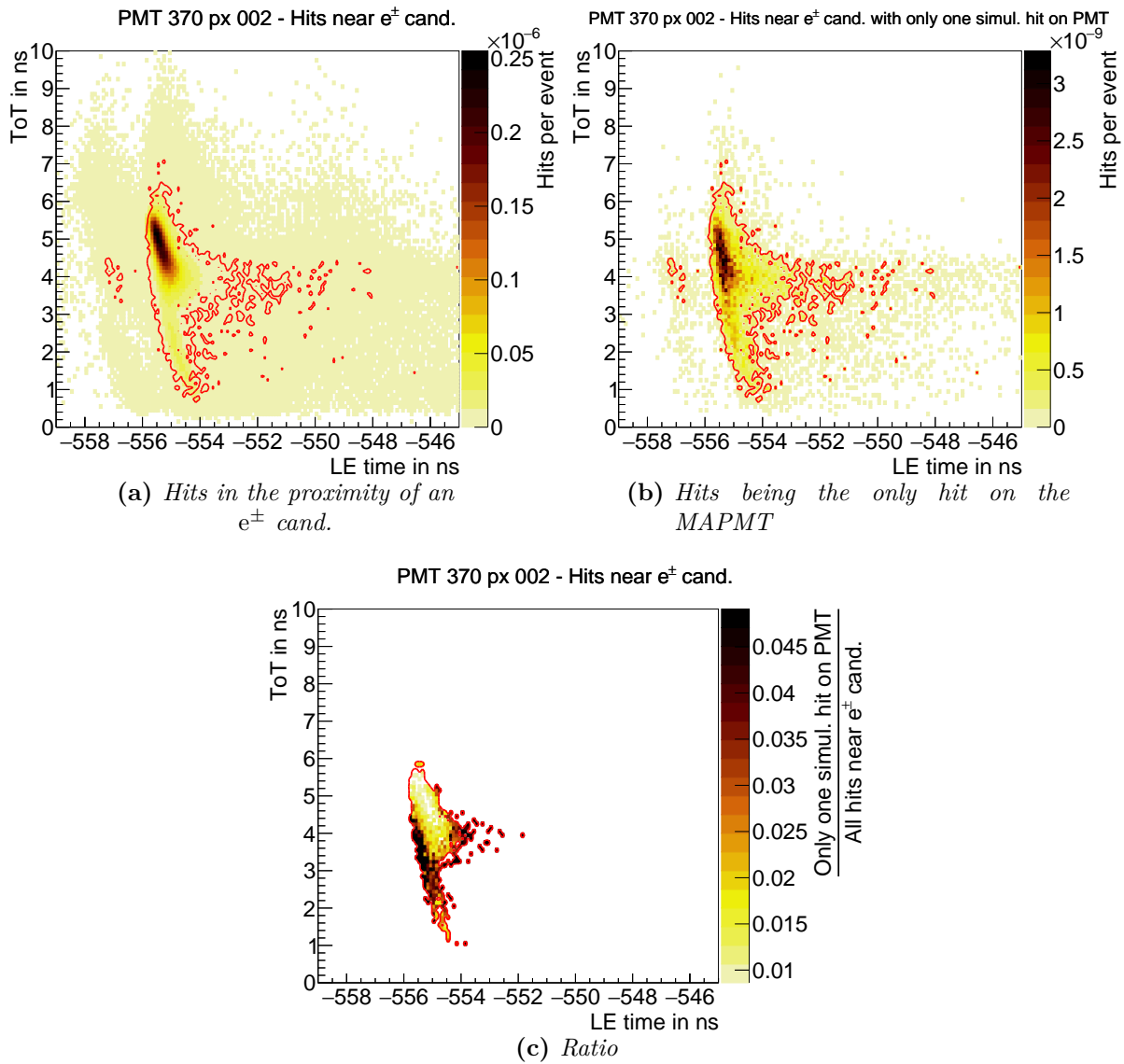
**Figure A.25 ♦** *Single channel (PMT 370 pixel 2) LE-ToT distribution for hits in the proximity of an electron track. Sub-figure **(a)** shows all those hits whereas **(b)** shows only the subsample of hits, where the measured hit is the only hit on the MAPMT during the same event. The ratio of the two distributions is shown in **(c)**. The a red line in all sub-figures indicates the "5% of maximum" contour of sub-figure **(b)**, i.e. the outer bound of LE-ToT bins with more than 5% of the maximum entry. The ratio plot features only bins, where in both used distributions more than 5 hits were counted. This ratio plot's z-scale is additionally cut at the upper and lower 10% quantile, to better visualize its inherent features.*

**(a)** *All hits*

**(b)** *Hits in the proximity of an e$^\pm$ cand.*

**(c)** *Ratio*
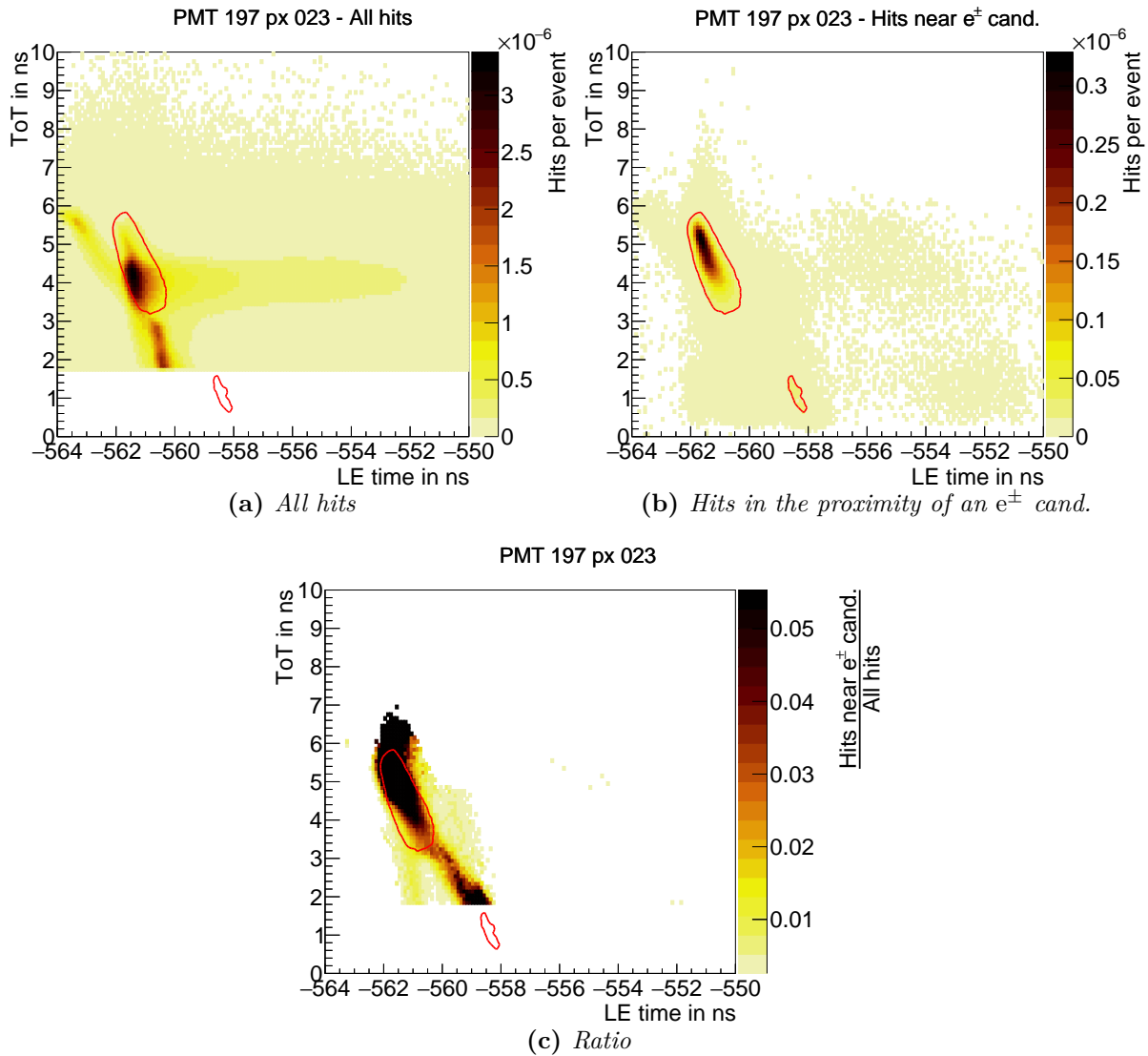
**Figure A.26 ♦** *Single channel (PMT 197 pixel 23) LE-ToT distribution for all hits **(a)**, hits in the proximity of an electron track **(b)** and the fraction of both depicted in **(c)**. Indicated with a red line in all sub-figures is the "5% of maximum" contour from sub-figure **(b)**, i.e. the outer bound of LE-ToT bins with more than 5% of the maximum entry. For technical reasons the spectrum including all hits is cut off at ToTs smaller than the afore derived cut value on the ToT for this channel. Hits are deemed close to a candidate if they are at maximum 30 mm plus an absolute angular equivalent of 2° separated. The ratio plot features only bins, where in both used distributions more than 5 hits were counted. Furthermore this distributions z-scale is artificially cut at the upper and lower 10% quantile, to better visualize its inherent features.*

(a) *All hits*



(b) *Hits in the proximity of an* e$^{\pm}$ *cand.*



(c) *Ratio*

**Figure A.27** ♦ *Single channel (PMT 541 pixel 61) LE-ToT distribution for all hits **(a)**, hits in the proximity of an electron track **(b)** and the fraction of both depicted in **(c)**. Indicated with a red line in all sub-figures is the "5% of maximum" contour from sub-figure **(b)**, i.e. the outer bound of LE-ToT bins with more than 5% of the maximum entry. For technical reasons the spectrum including all hits is cut off at ToTs smaller than the afore derived cut value on the ToT for this channel. Hits are deemed close to a candidate if they are at maximum 30 mm plus an absolute angular equivalent of 2° separated. The ratio plot features only bins, where in both used distributions more than 5 hits were counted. Furthermore this distributions z-scale is artificially cut at the upper and lower 10% quantile, to better visualize its inherent features.*

**(a)** *All hits*

**(b)** *Hits in the proximity of an* e$^\pm$ *cand.*
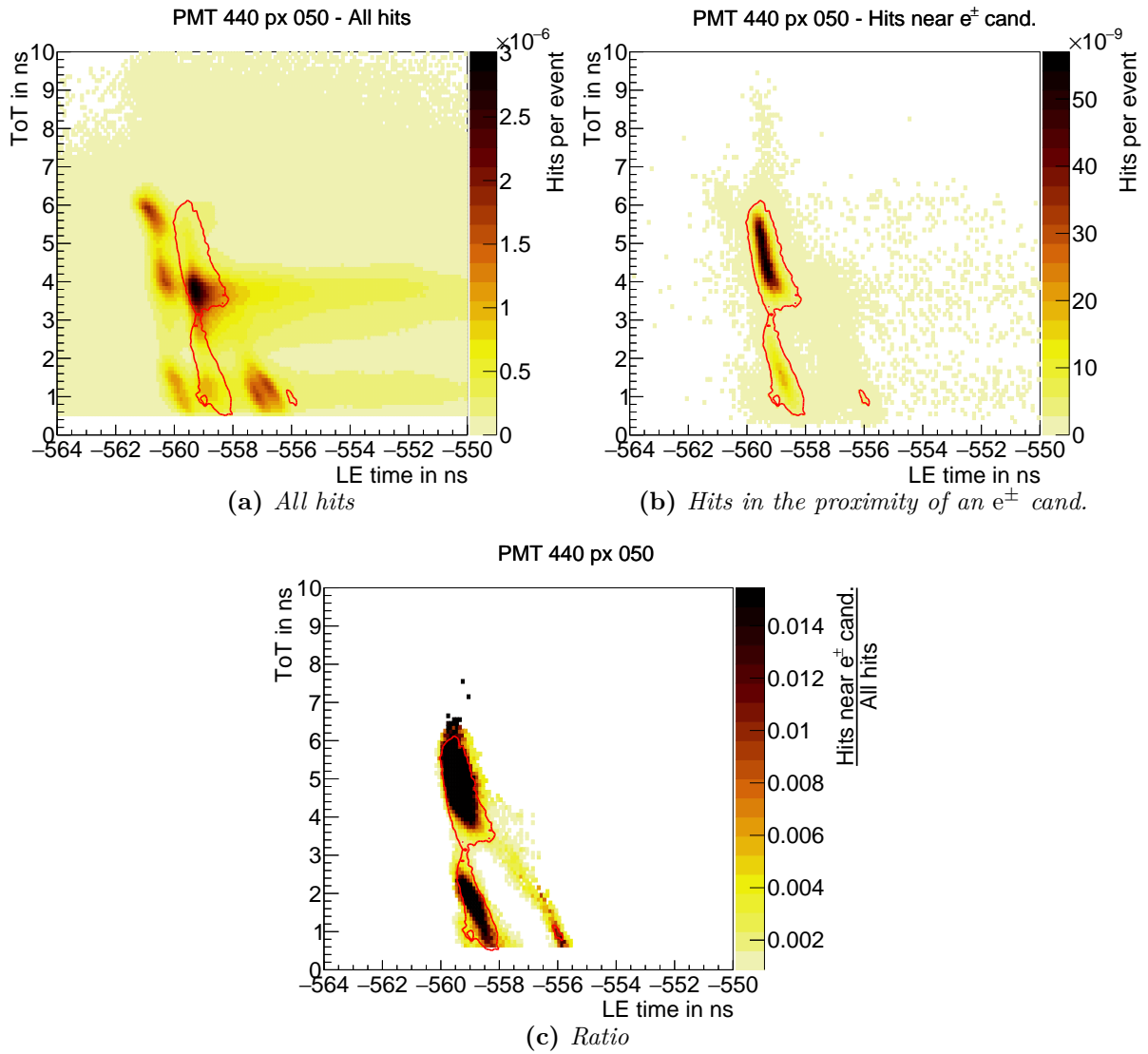
**(c)** *Ratio*

**Figure A.28** ♦ *Single channel (PMT 242 pixel 28) LE-ToT distribution for all hits **(a)**, hits in the proximity of an electron track **(b)** and the fraction of both depicted in **(c)**. This channel is read out by a DiRICH with* 10 pF *input capacitance. Indicated with a red line in all sub-figures is the "5% of maximum" contour from sub-figure **(b)**, i.e. the outer bound of LE-ToT bins with more than 5% of the maximum entry. For technical reasons the spectrum including all hits is cut off at ToTs smaller than the afore derived cut value on the ToT for this channel. Hits are deemed close to a candidate if they are at maximum* 30 mm *plus an absolute angular equivalent of* 2° *separated. The ratio plot features only bins, where in both used distributions more than 5 hits were counted. Furthermore this distributions z-scale is artificially cut at the upper and lower 10% quantile, to better visualize its inherent features.*
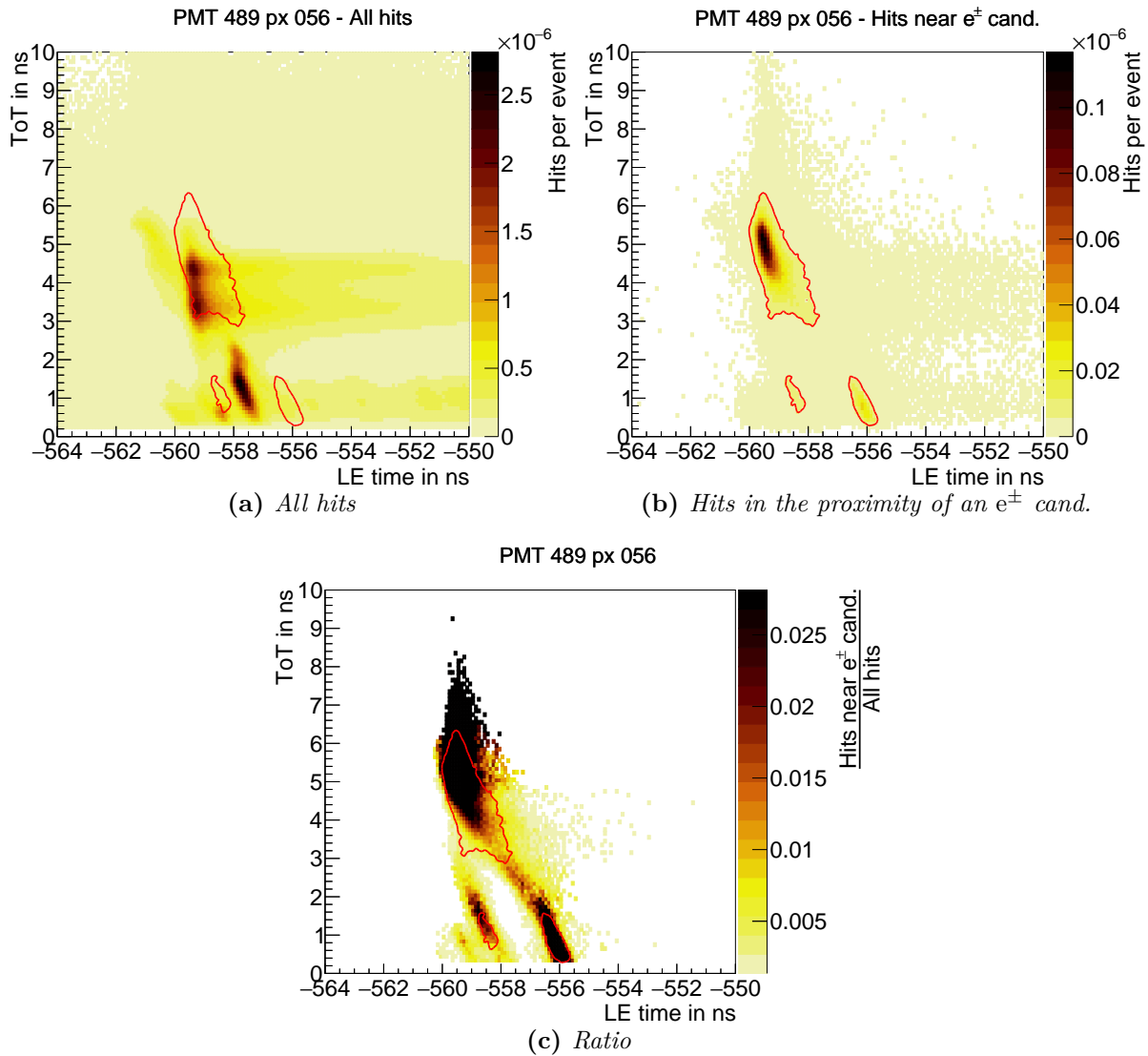
**(a)** *All hits*



**(b)** *Hits in the proximity of an* $e^{\pm}$ *cand.*



**(c)** *Ratio*

**Figure A.29** ♦ *Single channel (PMT 440 pixel 50) LE-ToT distribution for all hits **(a)**, hits in the proximity of an electron track **(b)** and the fraction of both depicted in **(c)**. Indicated with a red line in all sub-figures is the "5% of maximum" contour from sub-figure **(b)**, i.e. the outer bound of LE-ToT bins with more than 5% of the maximum entry. For technical reasons the spectrum including all hits is cut off at ToTs smaller than the afore derived cut value on the ToT for this channel. Hits are deemed close to a candidate if they are at maximum* $30\,\mathrm{mm}$ *plus an absolute angular equivalent of* $2°$ *separated. The ratio plot features only bins, where in both used distributions more than 5 hits were counted. Furthermore this distributions z-scale is artificially cut at the upper and lower 10% quantile, to better visualize its inherent features.*
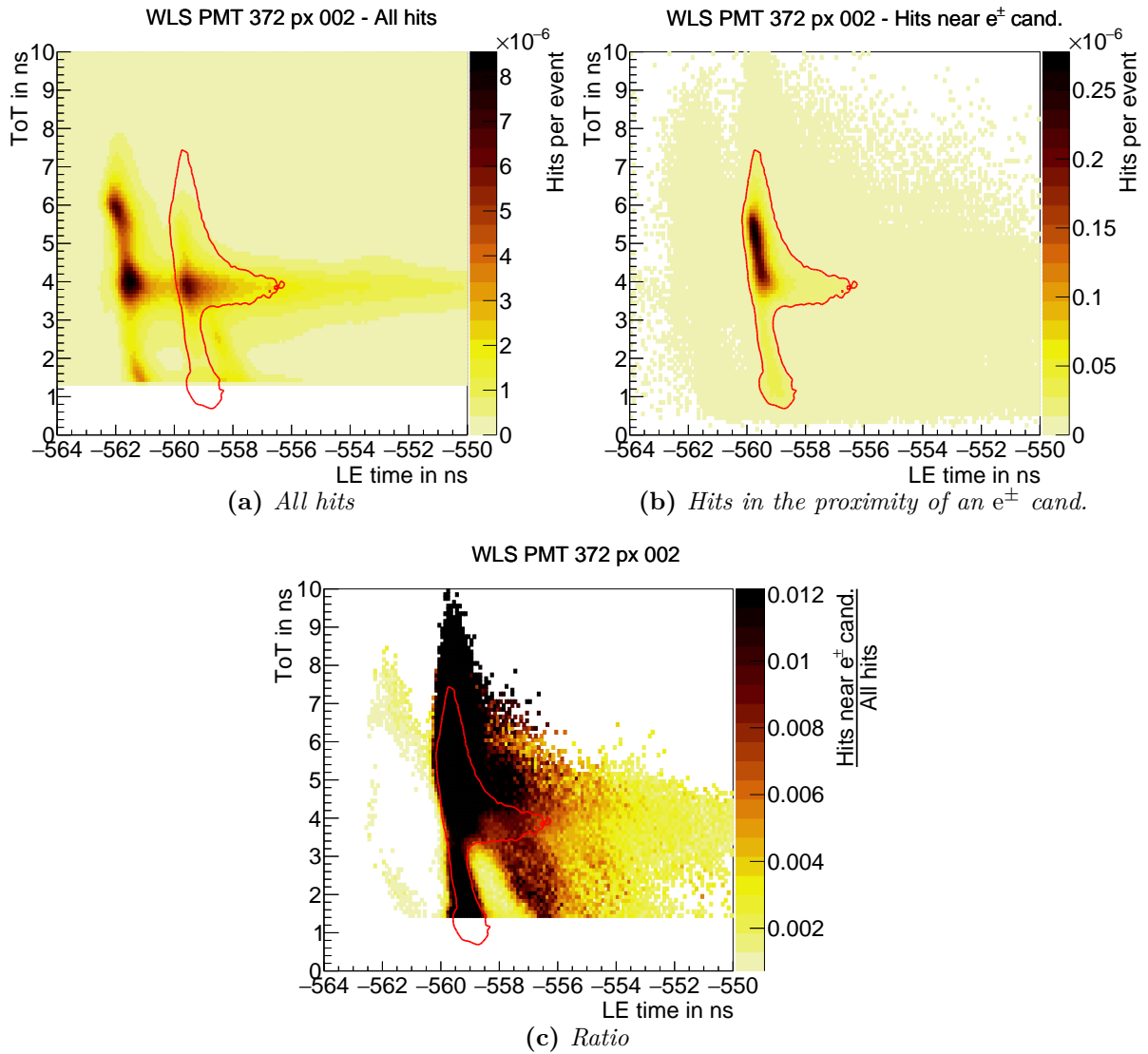
**(a)** *All hits*



**(b)** *Hits in the proximity of an* e$^{\pm}$ *cand.*



**(c)** *Ratio*

**Figure A.30** ♦ *Single channel (PMT 489 pixel 50) LE-ToT distribution for all hits **(a)**, hits in the proximity of an electron track **(b)** and the fraction of both depicted in **(c)**. Indicated with a red line in all sub-figures is the "5% of maximum" contour from sub-figure **(b)**, i.e. the outer bound of LE-ToT bins with more than 5% of the maximum entry. For technical reasons the spectrum including all hits is cut off at ToTs smaller than the afore derived cut value on the ToT for this channel. Hits are deemed close to a candidate if they are at maximum 30 mm plus an absolute angular equivalent of 2° separated. The ratio plot features only bins, where in both used distributions more than 5 hits were counted. Furthermore this distributions z-scale is artificially cut at the upper and lower 10% quantile, to better visualize its inherent features.*
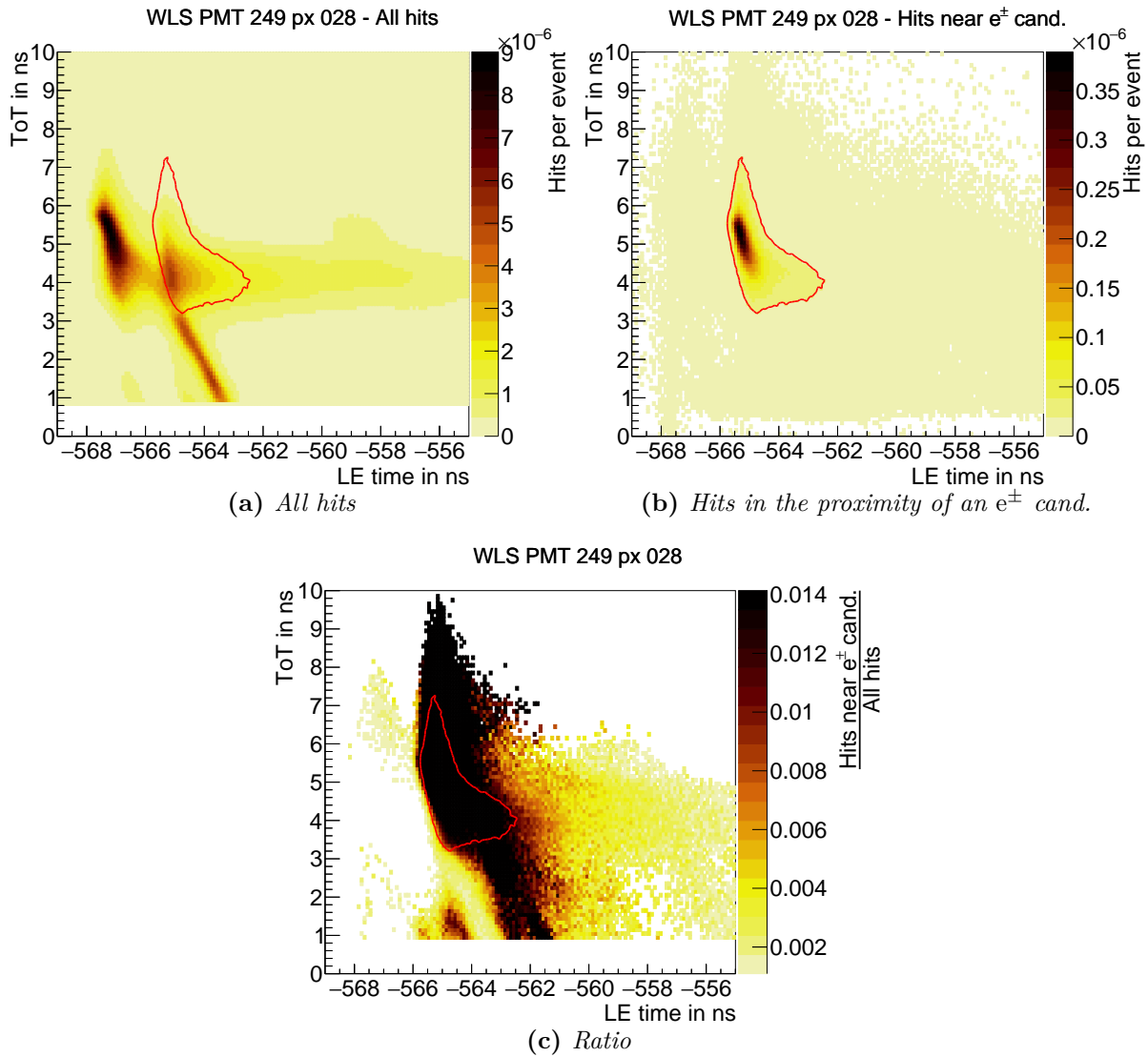
**(a)** *All hits*



**(b)** *Hits in the proximity of an* e$^\pm$ *cand.*



**(c)** *Ratio*

**Figure A.31** ♦ *Single channel (PMT 372 pixel 2 with WLS coated front window) LE-ToT distribution for all hits **(a)**, hits in the proximity of an electron track **(b)** and the fraction of both depicted in **(c)**. Indicated with a red line in all sub-figures is the "5% of maximum" contour from sub-figure **(b)**, i.e. the outer bound of LE-ToT bins with more than 5% of the maximum entry. For technical reasons the spectrum including all hits is cut off at ToTs smaller than the afore derived cut value on the ToT for this channel. Hits are deemed close to a candidate if they are at maximum 30 mm plus an absolute angular equivalent of 2° separated. The ratio plot features only bins, where in both used distributions more than 5 hits were counted. Furthermore this distributions z-scale is artificially cut at the upper and lower 10% quantile, to better visualize its inherent features.*
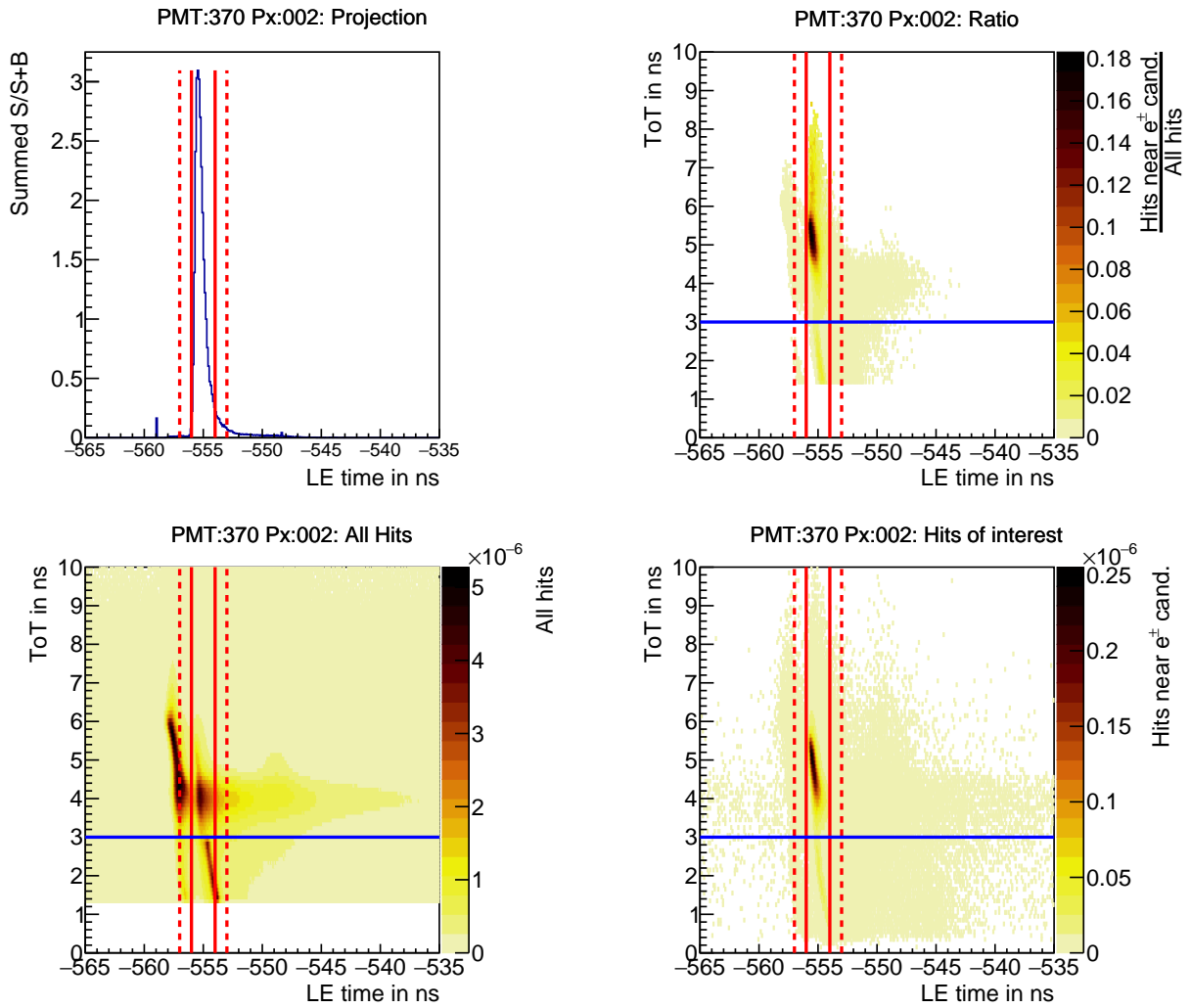
**(a)** *All hits*



**(b)** *Hits in the proximity of an* $e^{\pm}$ *cand.*



**(c)** *Ratio*

**Figure A.32** ♦ *Single channel (PMT 249 pixel 28 with WLS coated front window) LE-ToT distribution for all hits* **(a)**, *hits in the proximity of an electron track* **(b)** *and the fraction of both depicted in* **(c)**. *Indicated with a red line in all sub-figures is the "5% of maximum" contour from sub-figure* **(b)**, *i.e. the outer bound of LE-ToT bins with more than 5% of the maximum entry. For technical reasons the spectrum including all hits is cut off at ToTs smaller than the afore derived cut value on the ToT for this channel. Hits are deemed close to a candidate if they are at maximum* 30 mm *plus an absolute angular equivalent of* 2° *separated. The ratio plot features only bins, where in both used distributions more than 5 hits were counted. Furthermore this distributions z-scale is artificially cut at the upper and lower 10% quantile, to better visualize its inherent features.*
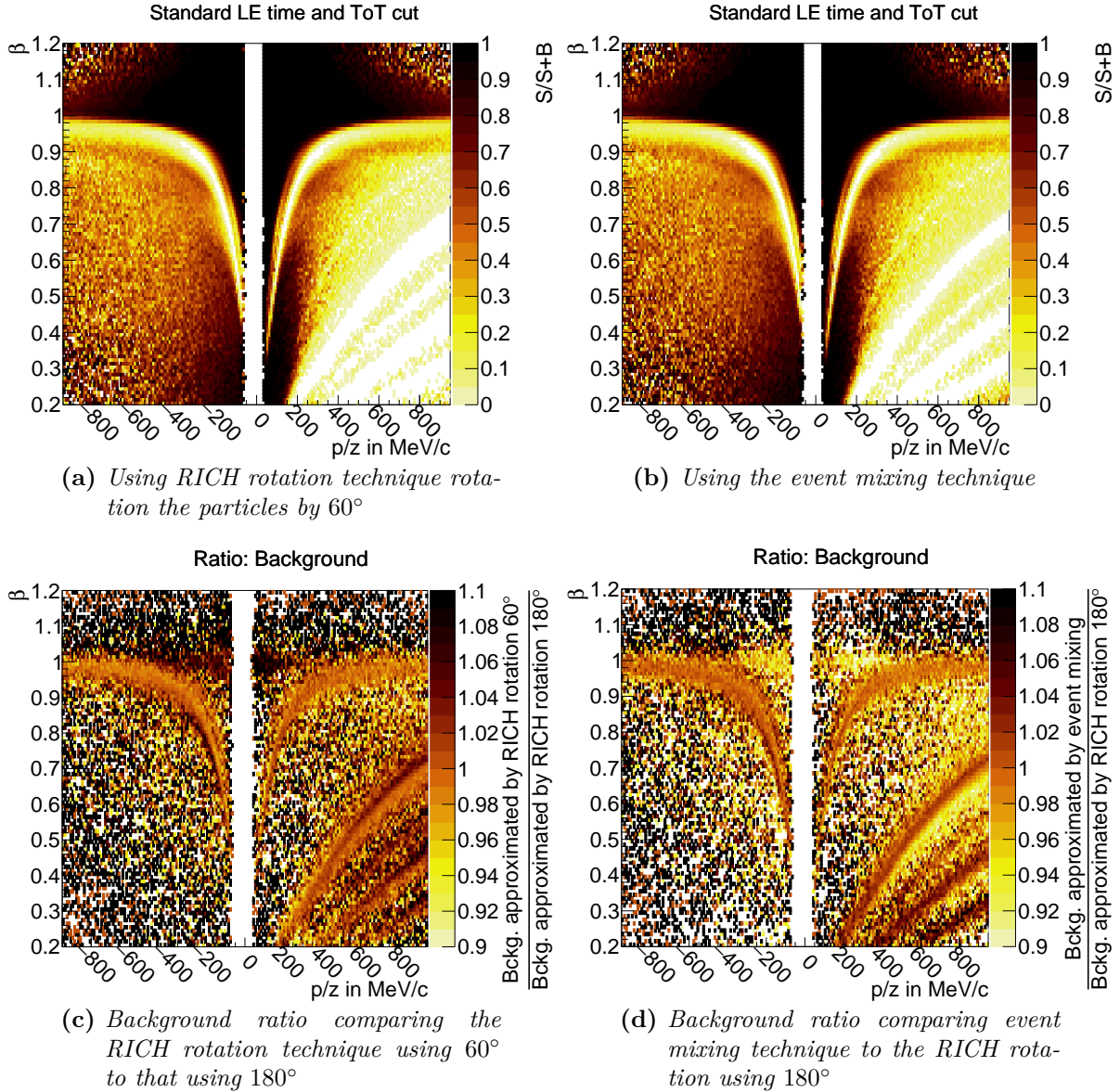
**Figure A.33** ♦ *Amalgamation of differently represented LE-ToT spectra of pmt 370 pixel 2, visualizing the newly derived sharp LE cut. The figure in the top left shows the one dimensional projection of the figure depicted top right, projecting everything above the blue line. The top right figure depicts the ratio of hits in the channel if an electron candidate was nearby divided by all hits measured in this channel i.e. the bottom right figure divided by the bottom left. Hits are deemed close to a candidate if they are at maximum 30 mm plus an absolute angular equivalent of 2° separated. LE-ToT-Bins with less than 5 entries in either of the distributions are discarded. The solid red line visualizes the narrow LE cut whereas the dashed line shows the wide LE cut. The narrow cut is derived finding the first value above 10% of the distributions maximum giving the cuts left edge. The right edge is found being the first LE time value where this threshold is undershot again. The wide cut is derived taking twice the narrow cut's width keeping the center of the cut the same.*

**(a)** *Using RICH rotation technique rotation the particles by 60°*



**(b)** *Using the event mixing technique*



**(c)** *Background ratio comparing the RICH rotation technique using 60° to that using 180°*



**(d)** *Background ratio comparing event mixing technique to the RICH rotation using 180°*

**Figure A.34** ♦ *Comparison of different background approximation techniques. Sub-figure **(a)** shows the signal to noise ratio approximating the background via the RICH rotation technique, wher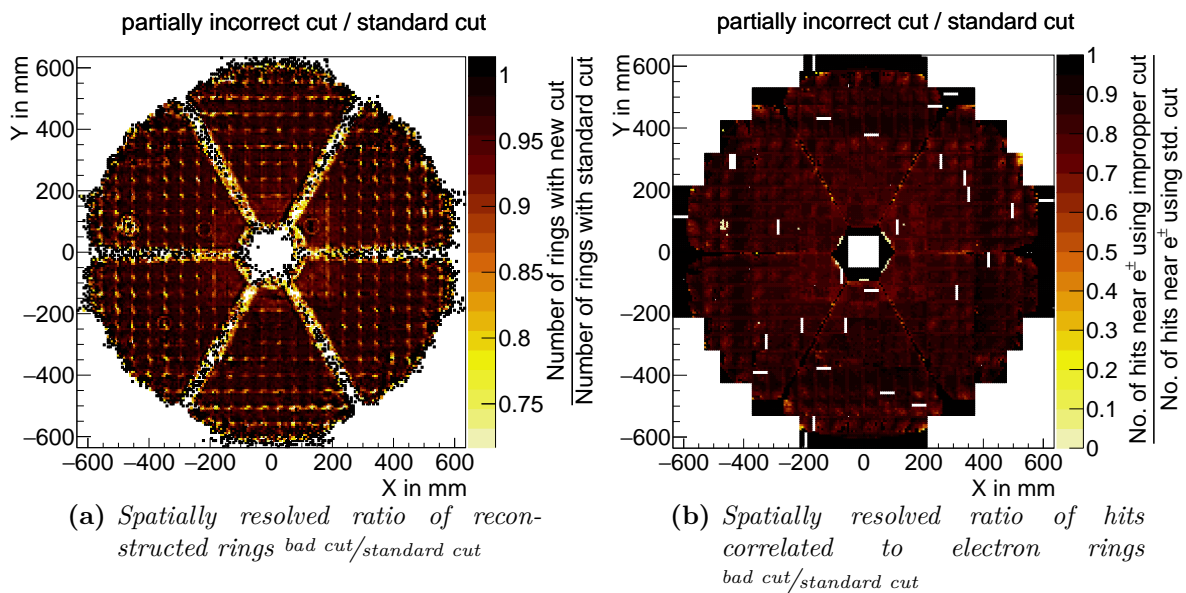e the normal analysis is made rotating all particles' φ-coordinate by a given angle (here 60°, which is normally used as standard). The signal to noise ratio is retrieved taking all reconstructed particle candidates being the closest to rings in the RICH but not farther away than 2° absolute angular difference using formula (6.1). Sub-figure **(a)** shows the signal to noise ratio approximating the background via a reduced event mixing attempt. This procedure sorts events into five different categories according to the particle multiplicity in that event, where each category is separated by 15 particles. The particles of one such category are than combined with the rings from the next recorded event of that category, retrieving therethrough the uncorrelated background. Sub-figures **(c)** and **(d)** depict the ratios of the bare background distributions gained through the different methods of approximation.*
***Both methods are thereby compared to the background estimate retrieved using the RICH rotation technique with rotation of 180°. All methods do result in very similar data, wherever large particle multiplicities are. The electrons are slightly overestimated when using the 60° RICH rotation technique and slightly underestimated when doing the event mixing.***
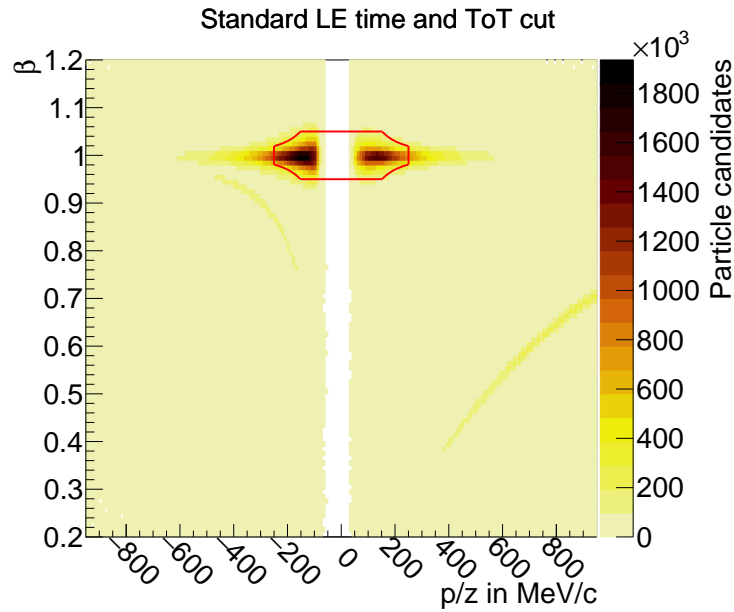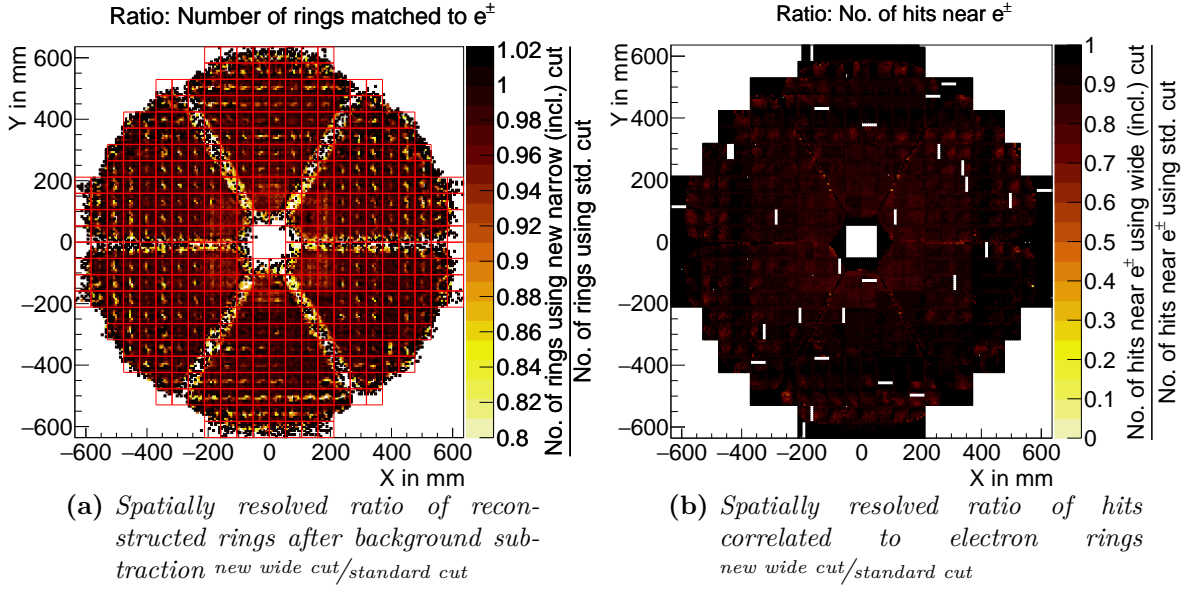
**Standard LE time and ToT cut**

**Figure A.35** ♦ *β-momentum spectrum of particles matched to rings reconstructed using the old standard cut on LE time (and ToT) to visualize the region of "definite electrons" through the red enclosed area. A particle is deemed matched being the closest match to a RICH ring with a radius between $17\,\mathrm{mm}$ and $30\,\mathrm{mm}$ and a maximum absolute angular distance of $2°$. The area is defined through the cuts of $0.95 < \beta < 1.05$, $|p/z| < 250\,\mathit{MeV/c}$ and $m < 50\,\mathit{MeV/c^2}$. This region is dominated by electrons applying only the simplest RICH matching cut, as is visible here.*



(a) *Spatially resolved ratio of reconstructed rings $^{bad\ cut}/_{standard\ cut}$*

(b) *Spatially resolved ratio of hits correlated to electron rings $^{bad\ cut}/_{standard\ cut}$*

**Figure A.36** ♦ *Spatially resolved ratio of reconstructed rings (a) and ratio of reconstructed (to electron rings correlated) hits (b) to visualize the effect of bad LE time cuts. Sub-figure (a) shows the number of rings where an electron candidate was found within $2°$ absolute angular difference using a narrow LE time cut with some badly cut channels divided by the rings found using the standard cut. Here electron candidates are defined by $0.95 < \beta < 1.05$, $|p/z| < 250\,\mathit{MeV/c}$ and $m < 50\,\mathit{MeV/c^2}$ For the new cut, channels where no cut was found, were left with the standard cut values. Sub-figure (b) shows the ratio of number of hits within a circular area spanned around the electron candidate with radius $30\,\mathrm{mm}$ and an additional absolute angular equivalent of $2°$, dividing the hits retrieved by a narrow LE time cut with some badly cut channels divided those retrieved by the standard cut.*
***Visible structures in (a) are, apart of the recurrent equidistantly spaced pattern, ring like shapes at e.g. $(-210, 70)$. In the center of all those ring shapes one finds in (b) a single pixel with deteriorated efficiency.***

(a) *Spatially resolved ratio of reconstructed rings after background subtraction* $^{new\ wide\ cut}/_{standard\ cut}$

(b) *Spatially resolved ratio of hits correlated to electron rings* $^{new\ wide\ cut}/_{standard\ cut}$

**Figure A.37** ♦ *Spatially resolved ring **(a)** and hit ratios **(b)** for hits and rings matched to definite* $e^{\pm}$ *dividing rings reconstructed with the new wide LE time cut by the ones reconstructed using the old standard cut. Added to figure **(a)** are red lines indicating the outlines of the MAPMTs as visual guides. Definite* $e^{\pm}$ *are defined by* $0.95 < \beta < 1.05$, $|p/z| < 250\ MeV/c$ *and* $m < 50\ MeV/c^2$ *and are called matched to a ring, if they are the closest track candidate not farther away than* $2°$. *A hit is assumed electron correlated if it is in the circular area spanned by a radius of* $30\ mm$ *and absolute angular difference of* $2°$ *around a definite* $e^{\pm}$. *Those hits are counted per channel, thereof building the depicted ratio.*

***The used wide LE time has twice the width of the narrow new cut and includes all channels where no new cut was found, with their original cut values. White spots visible in (b) in the detector stem from broken DiRICH-FEB channels.***
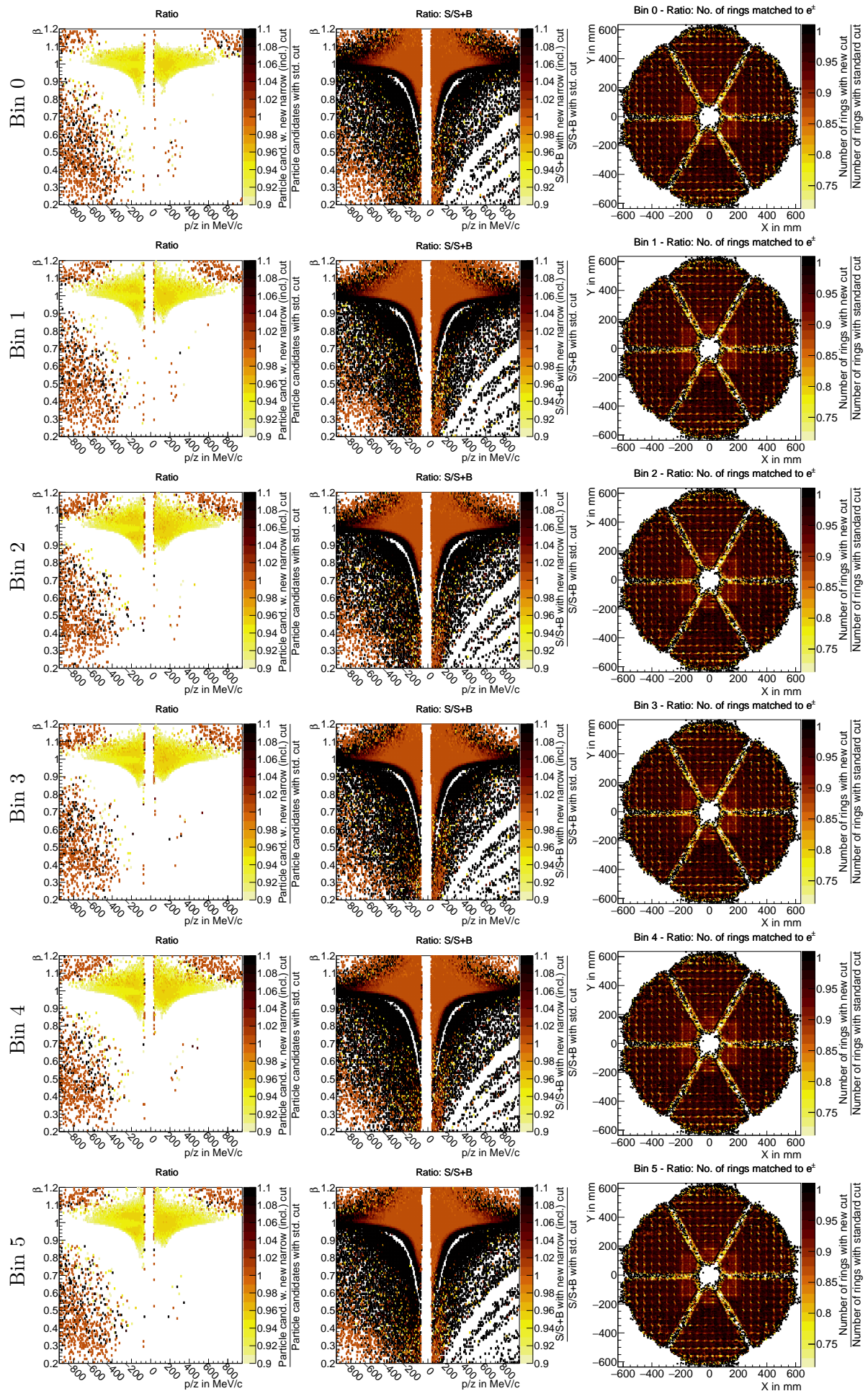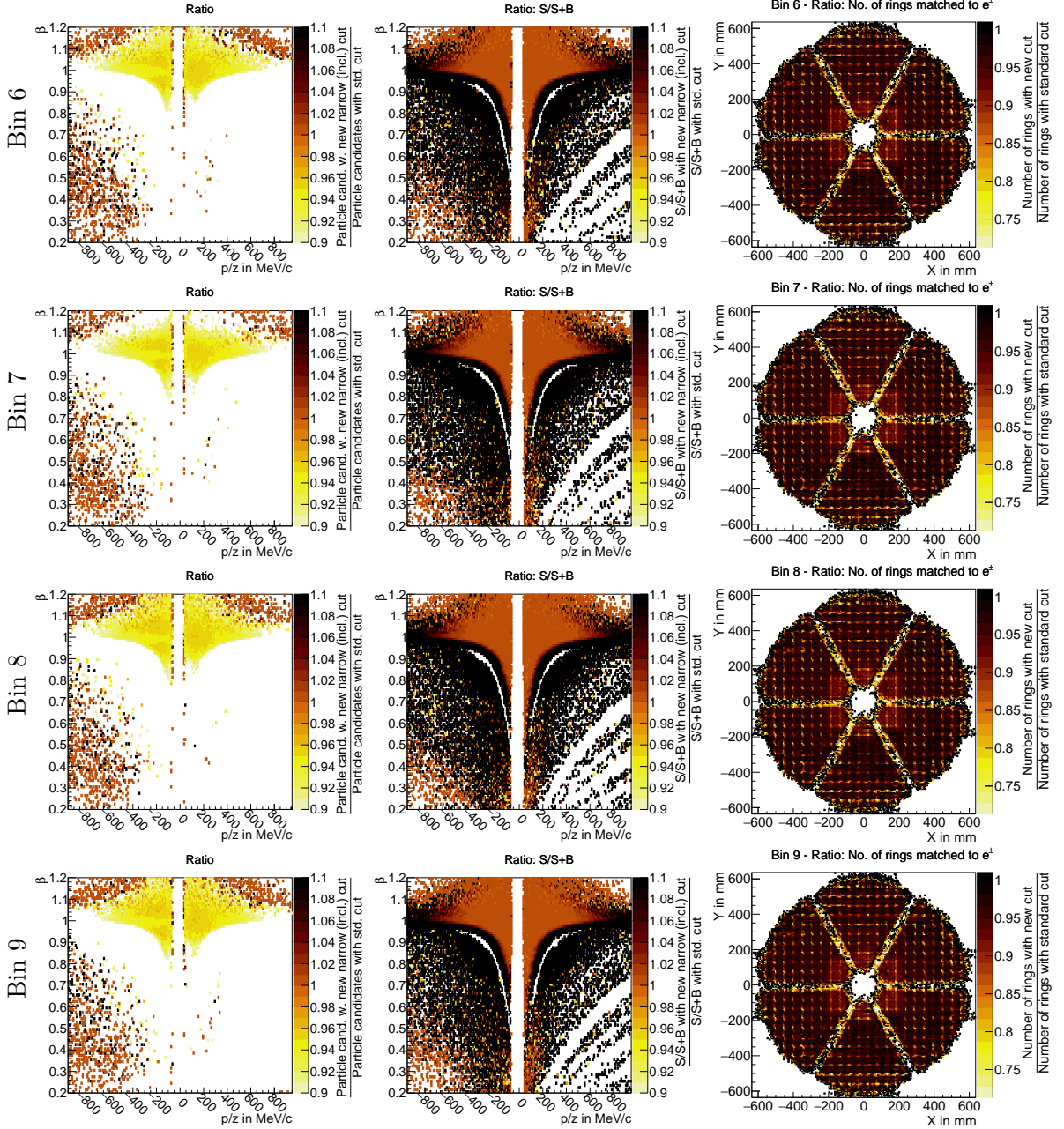
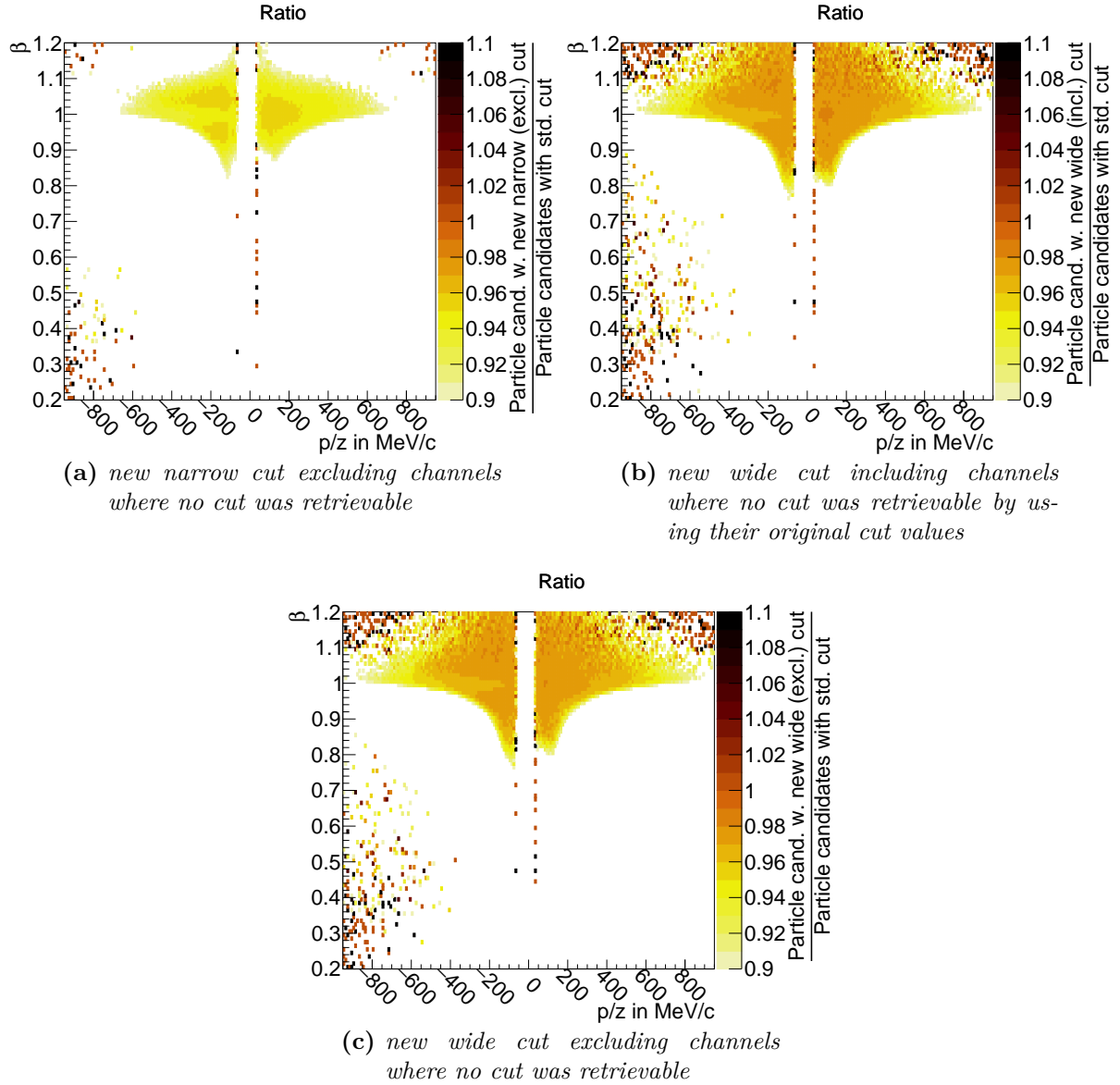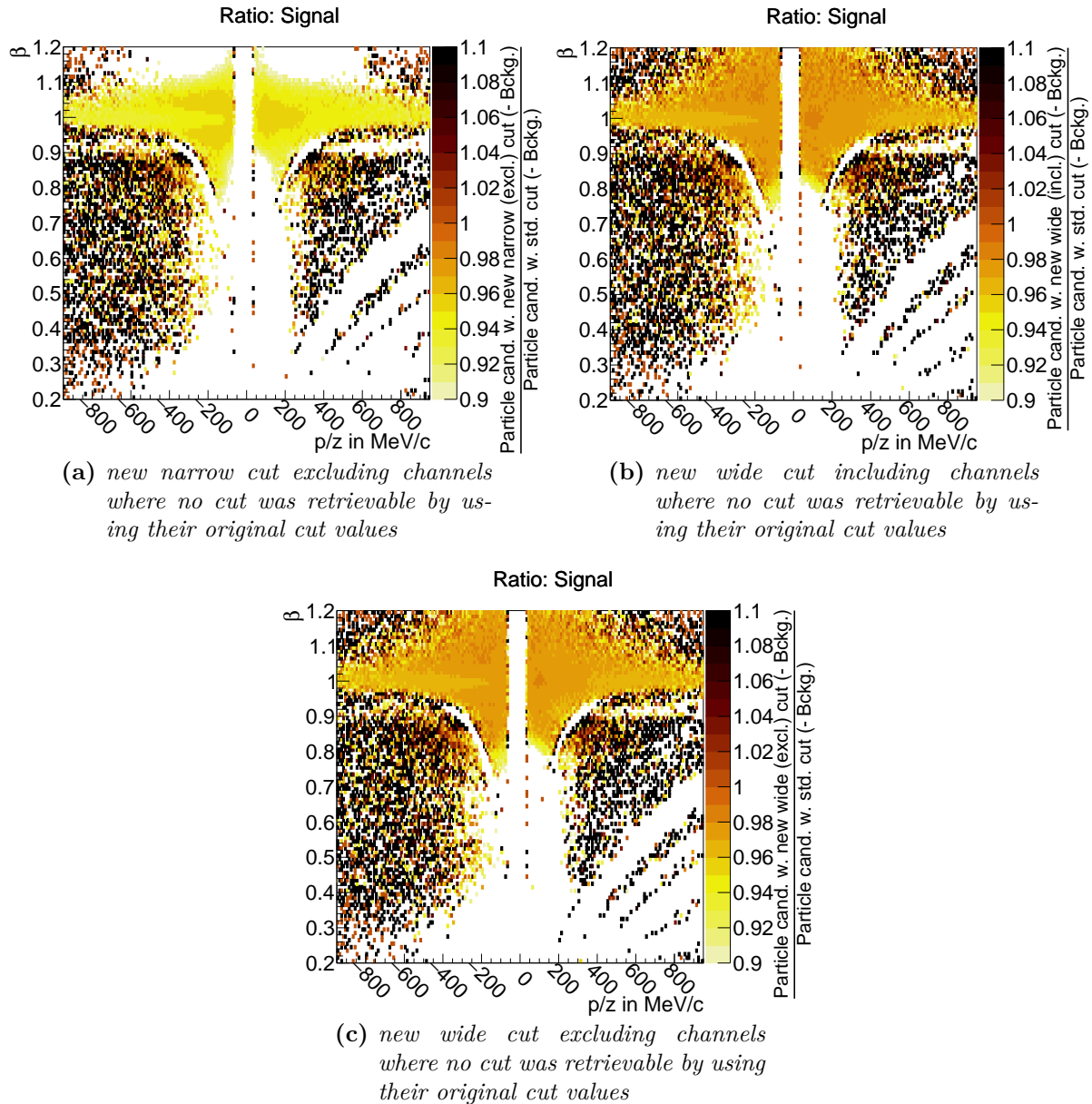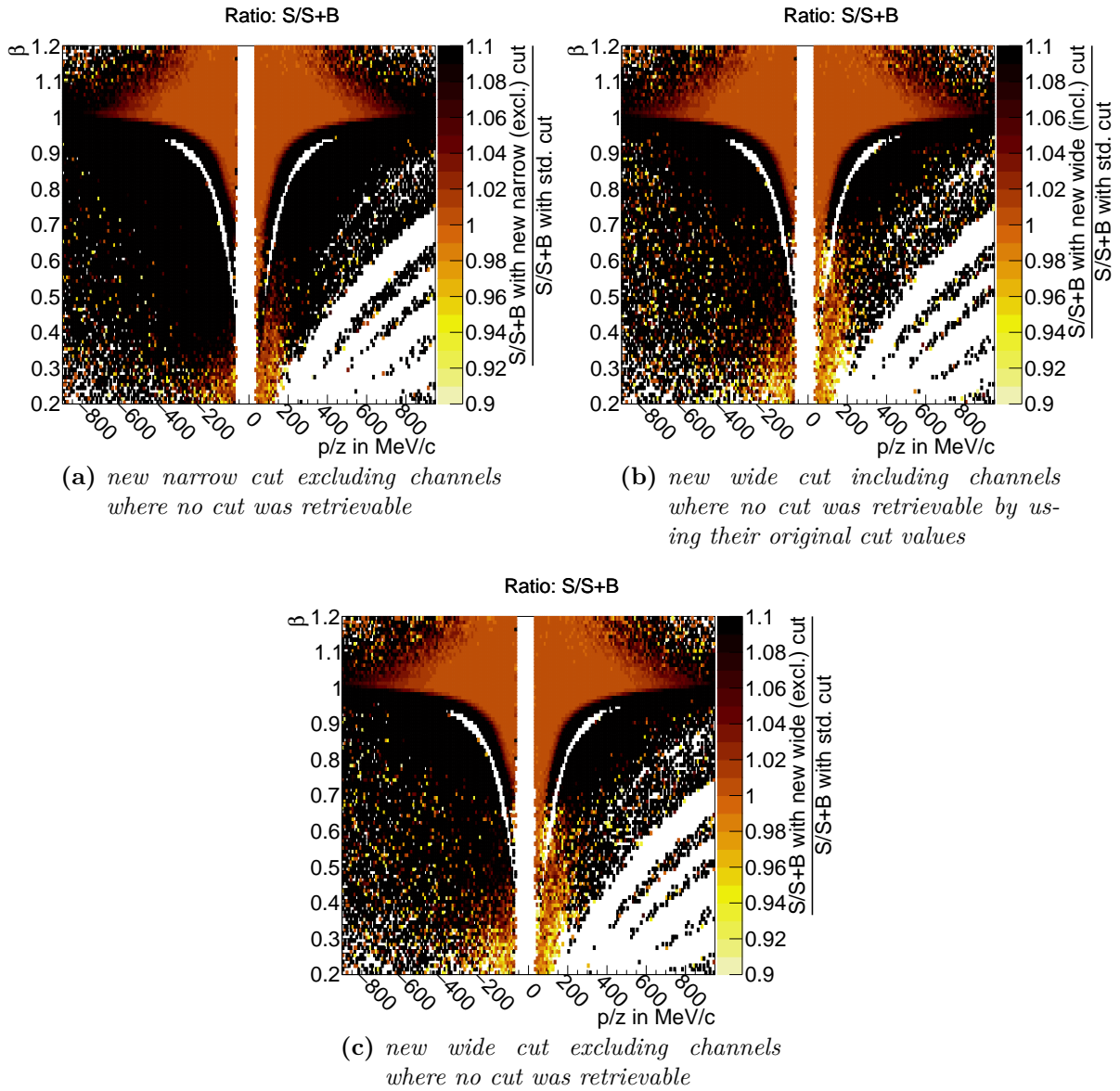**Figure A.38** ♦ *Explanation of this figure is found under the next figure A.39 on the next page.*

**Figure A.39** ♦ *β-momentum ratios, signal to noise ratios and spatially resolved ring ratios for ten different beamtime bins. The beam time bins are in chronologically ascending order and contain each roughly $7 \times 10^8$ events. All these ratio plots always depict each measure comparing the new narrow cut to the standard cut. The cut values include those channels where no new cut value was found using their original cut values. The β-momentum distribution shows all particle candidates with the closest match to a RICH ring with a radius between $17\,\mathrm{mm}$ and $30\,\mathrm{mm}$ and a maximum absolute angular distance of $2°$. The signal to noise ratio plot takes the signal to noise ratio of both cuts and divides it. The signal to noise ratio for each cut is retrieved using equation (6.1) where the background contribution is approximated via applying the same matching requirement but rotating all particles' φ-coordinate by $180°$ thereby reconstructing the uncorrelated background. The spatially resolved ring ratio divides the number of rings matched to definite $e^\pm$ reconstructed with the new LE cut by the ones reconstructed using the old standard cut. Definite $e^\pm$ are defined by $0.95 < β < 1.05$, $|p/z| < 250\,{}^{MeV}\!/c$ and $m < 50\,{}^{MeV}\!/c^2$ and are called matched to a ring, if they are the closest track candidate not farther away than $2°$.*

**(a)** *new narrow cut excluding channels where no cut was retrievable*



**(b)** *new wide cut including channels where no cut was retrievable by using their original cut values*



**(c)** *new wide cut excluding channels where no cut was retrievable*

**Figure A.40 ♦** *Ratio of β-momentum spectra for particles matched to rings reconstructed using different cuts always divided by the standard cut on LE time (and ToT). Compared to the standard cut are the narrow cut excluding channels without new cut values **(a)**, the wide cut also excluding those channels **(c)** and the wide cut including those channels with their old cut values **(b)**. The β-momentum ratio distribution divides all particle candidates with the closest match to a RICH ring with a radius between* 17 mm *and* 30 mm *and a maximum absolute angular distance of* 2° *measured using the new cut by the ones found using the standard cut.*

**(a)** *new narrow cut excluding channels where no cut was retrievable by using their original cut values*



**(b)** *new wide cut including channels where no cut was retrievable by using their original cut values*



**(c)** *new wide cut excluding channels where no cut was retrievable by using their original cut values*

**Figure A.41** ♦ *β-momentum resolved signal ratio, dividing the signal retrieved using different new cuts by the signal measured using the old standard cut on LE time (and ToT). Always compared to the standard cut are the narrow cut excluding channels without new cut values **(a)**, the wide cut also excluding those channels **(c)** and the wide cut including those channels with their old cut values **(b)**. The signal is derived by counting all particle candidates (in terms of β-momentum) and subtracting the number of particles counted when their φ-coordinate is rotated by 180°. Particle candidates are deemed matched if they are the closest candidate to a ring with radius between 17 mm and 30 mm but at maximum separated by an absolute angular distance of 2°.*

**(a)** *new narrow cut excluding channels where no cut was retrievable*

**(b)** *new wide cut including channels where no cut was retrievable by using their original cut values*

**(c)** *new wide cut excluding channels where no cut was retrievable*

**Figure A.42 ♦** *Signal to noise ratio distribution for different cuts not discussed in the main text. Always compared to the standard cut are the narrow cut excluding channels without new cut values **(a)**, the wide cut also excluding those channels **(c)** and the wide cut including those channels with their old cut values **(b)**. The signal to noise ratio plot takes the signal to noise ratio of both cuts and divides it. The signal to noise ratio for each cut is retrieved using equation* (6.1) *where the background contribution is approximated via applying the same matching requirement (closest cand. with max. separation* $2°$ *to ring with* $17\,mm < r < 30\,mm$ *) but rotating all particles'* $\phi$-*coordinate by* $180°$ *thereby reconstructing the uncorrelated background.*

Ratio: Number of rings matched to e$^{\pm}$
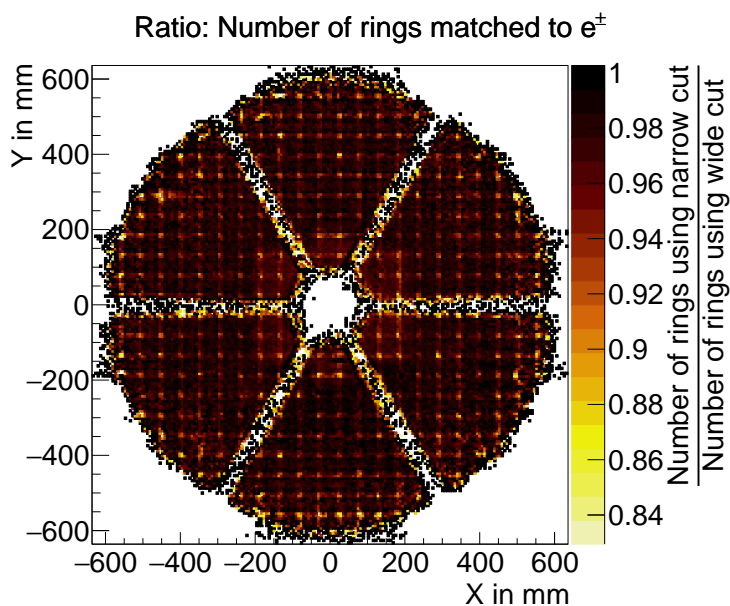


**Figure A.43** ♦ *Spatially resolved ring ratio for rings matched to definite* e$^{\pm}$ *dividing rings reconstructed with the narrow LE cut by the ones reconstructed using the wide LE cut. Definite* e$^{\pm}$ *are defined by* $0.95 < \beta < 1.05$, $|p/z| < 250\,^{MeV}\!/c$ *and* $m < 50\,^{MeV}\!/c^2$ *and are called matched to a ring, if they are the closest track candidate not farther away than* $2°$. *Both used LE time cuts include all channels where no new cut was found, with their original cut values.*
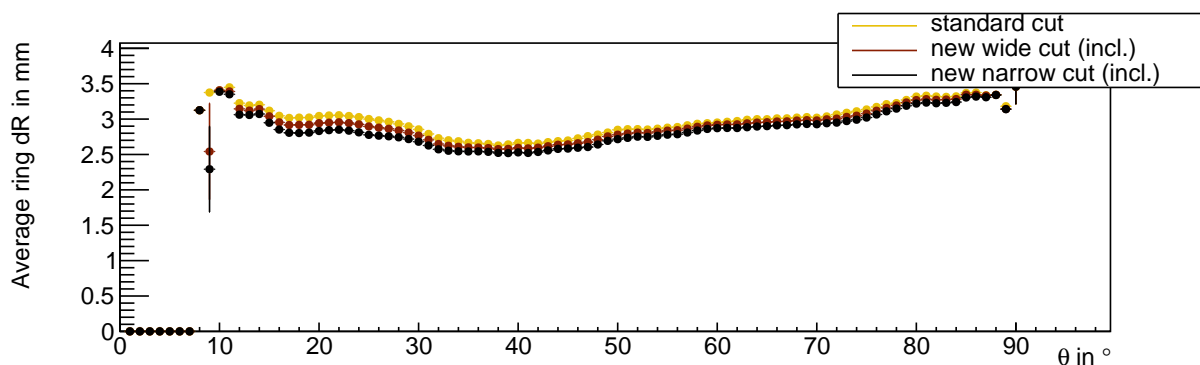


**Figure A.44** ♦ *θ resolved average dR distribution of rings reconstructed with three different cuts on the LE time. The average ring dR of rings matched to definite electron candidates is binned in* $1°$ *wide θ bins. The ring with radius between* $17\,\text{mm}$ *and* $30\,\text{mm}$ *is assumed matched to a definite electron candidate if an electron candidate was found with maximum* $2°$ *difference between ring center and particle candidate. Where the definite electron is defined through* $0.95 < \beta < 1.05$, $|p/z| < 250\,^{MeV}\!/c$ *and* $m < 50\,^{MeV}\!/c^2$. *Angles lower than* $30°$ *contain a significant amount of hits from WLS coated MAPMTs. The new cuts used here include channels where no new cut was found using their original cut values.*
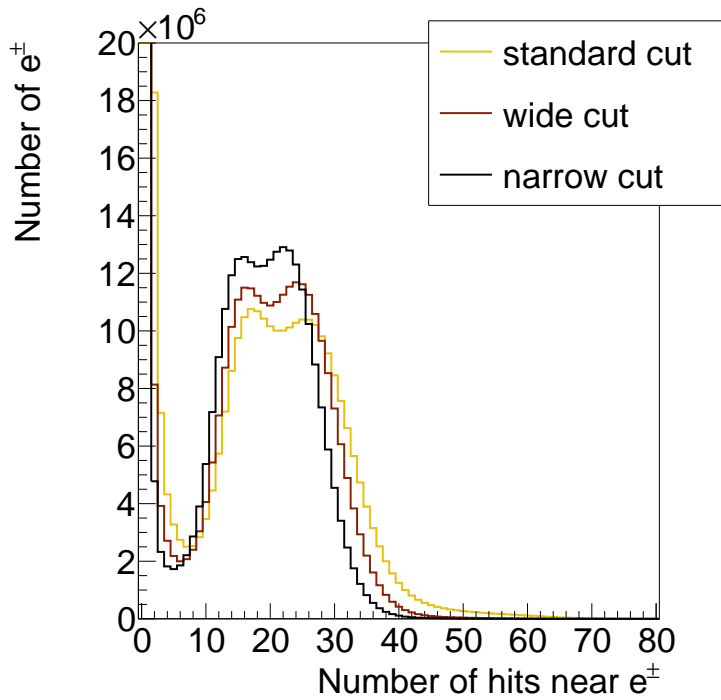
**Figure A.45** ♦ *Number of hits in the vicinity of an electron candidate for different LE time cuts. A hit is deemed in the vicinity of an electron candidate if it is found in the circular area defined by radius 30 mm and an additional absolute angular equivalent of 2°. The large peak towards zero hits (which is cut off in this figure) stems either from particles which were actually no real electrons, or (mostly) from conversion in or behind the RICH detector. The right peak in the double peak structure shows close-by double rings as is further discussed in chapter 8. At very large number of hits (> 40) the afore mentioned "blob-like" structures can be found*



(a) *Using standard cut*



(b) *Using new narrow inclusive cut*
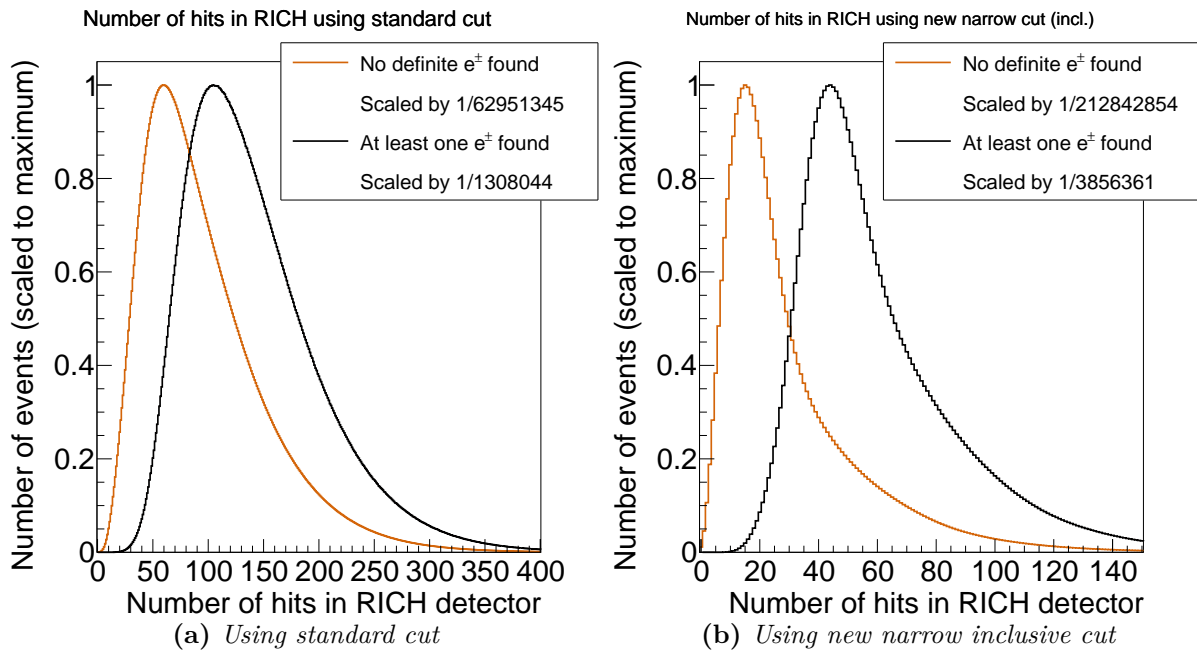
**Figure A.46** ♦ *Number of all hits in the RICH detector for events where no electron candidate was found and events where at least one electron candidate was found. These distributions are separately shown for the old standard cut on LE time (and ToT) (a) and the new narrow cut (b). The narrow cut includes channels where no new cut was found, without any more narrow cut compared to the old cut. The electron candidate is defined by $0.95 < \beta < 1.05$, $|p/z| < 250 \, MeV/c$ and $m < 50 \, MeV/c^2$. All distributions are scaled with regards to their maximum value to keep them visibly comparable. Further, the x-axis of (b) is zoomed in such, that all distributions fill equal amounts of the figure.*

## A.6 Additional figures for Chapter 7



**(a)** 5 ps *ToT binning*



**(b)** 10 ns *ToT binning*
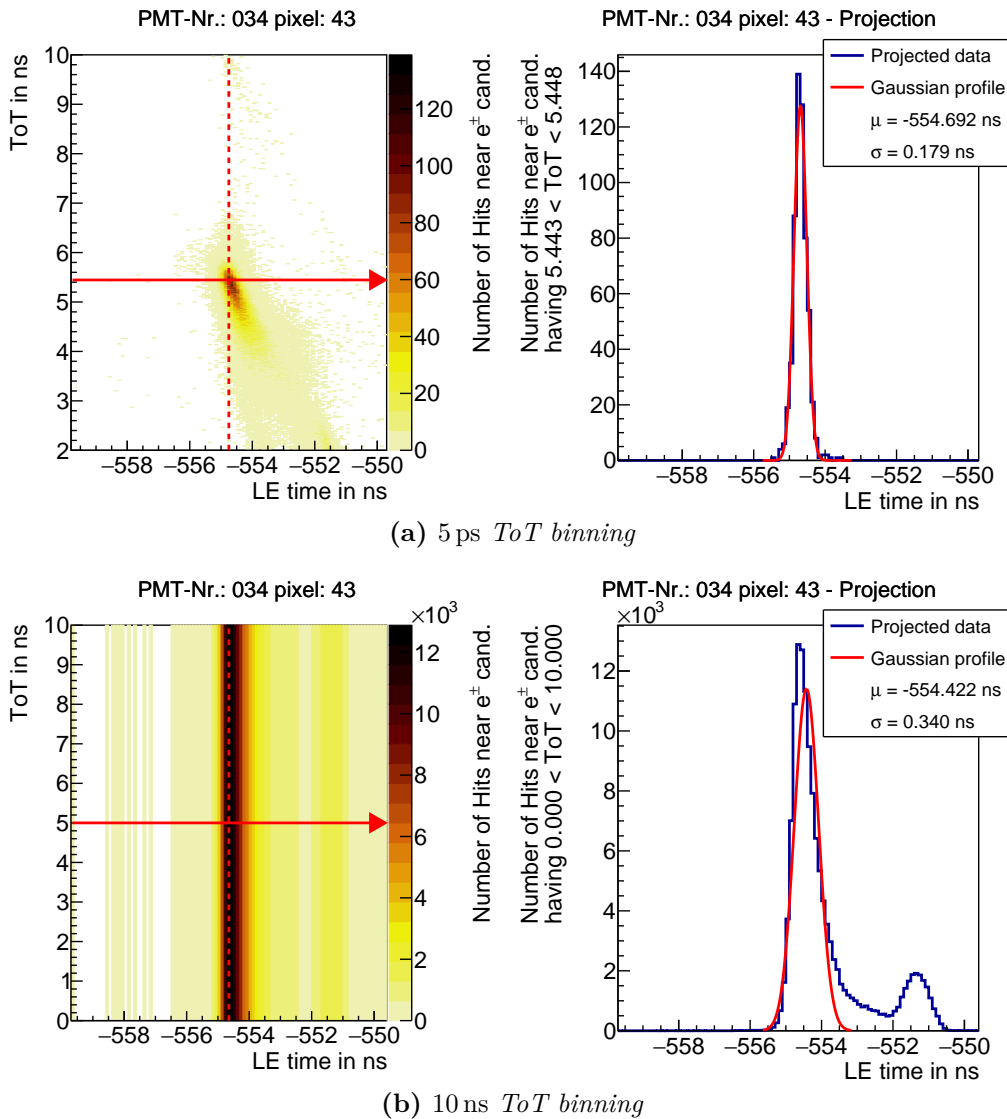
**Figure A.47 ♦** *Visualization of the projection over the full ToT range* **(a)** *and a single* 5 ps *ToT bin* **(b)** *and fit of a Gaussian profile to that projection to assess the timing precision of a single channel (PMT 34 pixel 43). Using hits measured in this channel while an electron candidate was identified in its proximity a two dimensional LE-ToT histogram is built using a binning of* **(a)**:100 ps × 10 ns *and* **(b)**:100 ps × 5 ps*. Therein the bin with the largest amount of hits is found which is indicated by the intersection of the dashed line and the red arrow. Along the red arrow a projection is made, being depicted on the right. This projection, is fitted with a Gaussian profile, extracting the profiles standard deviation σ as timing precision of that channel.*
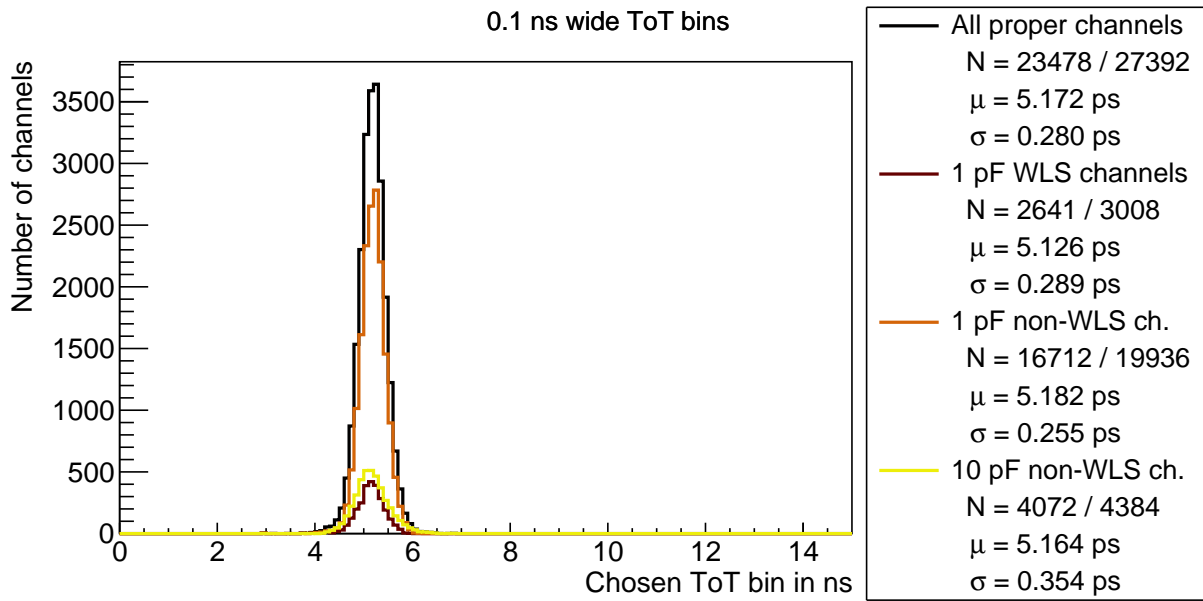
**Figure A.48** ♦ *Distribution of all channel individually chosen ToT bin centers used for the projection over which the timing precision is extracted. Using a* $100\,ps \times 100\,ps$ *binned histogram the depicted ToT is found by being the center ToT of the bin with the largest amount of entries. Average* $\mu$ *and standard deviation* $\sigma$ *are denoted in the legend together with the number of all (later) fitted channels* $N$. *Thereby the channels are also split into three different groups. Hereby the capacitance refers to the input capacitance of the DiRICH-FEB whereas the WLS is applied to the read out MAPMT.*



**(a)** $1\,pF$ *non-WLS channels*



**(b)** $10\,pF$ *non-WLS channels*
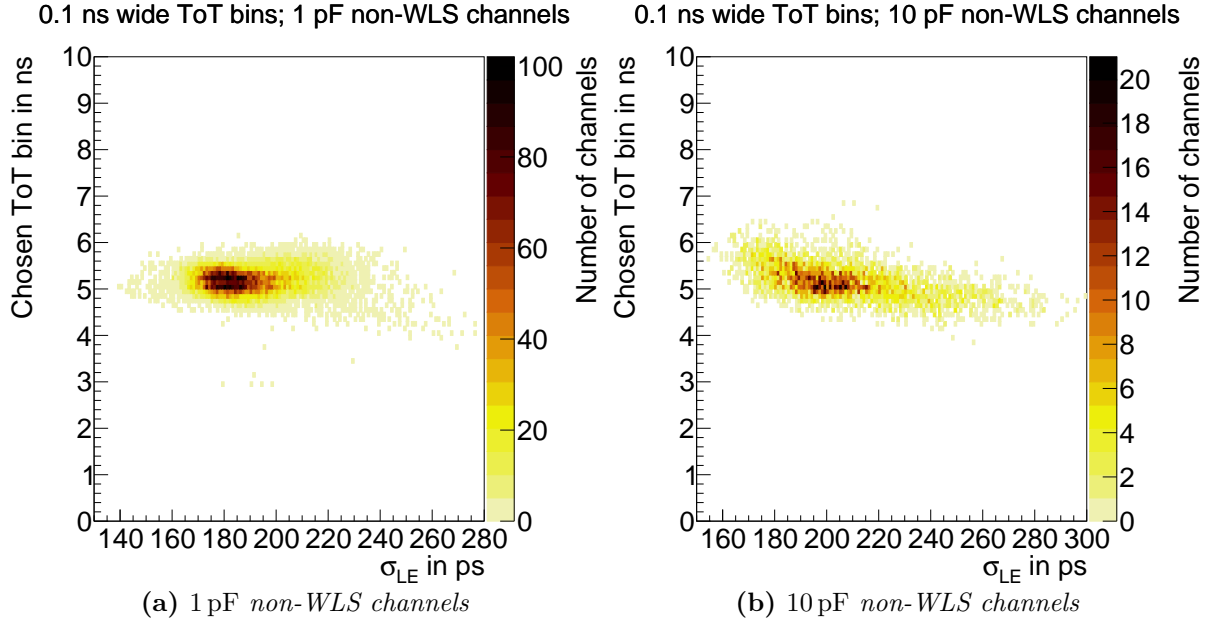
**Figure A.49** ♦ *Two dimensional timing precision* $\sigma_{LE}$ *vs. chosen ToT bin center distribution for* $1\,pF$ *((a)) and* $10\,pF$ *((b)) non-WLS channels. Hereby the capacitance refers to the input capacitance of the DiRICH-FEB whereas the WLS is applied to the read out MAPMT. Using a* $100\,ps \times 100\,ps$ *binned histogram the depicted ToT is found by being the center ToT of the bin with the largest amount of entries. The according timing precision is extracted from a Gaussian profile's standard deviation* $\sigma$ *being fitted to a* $100\,ps$ *wide projection over the corresponding ToT bin.*
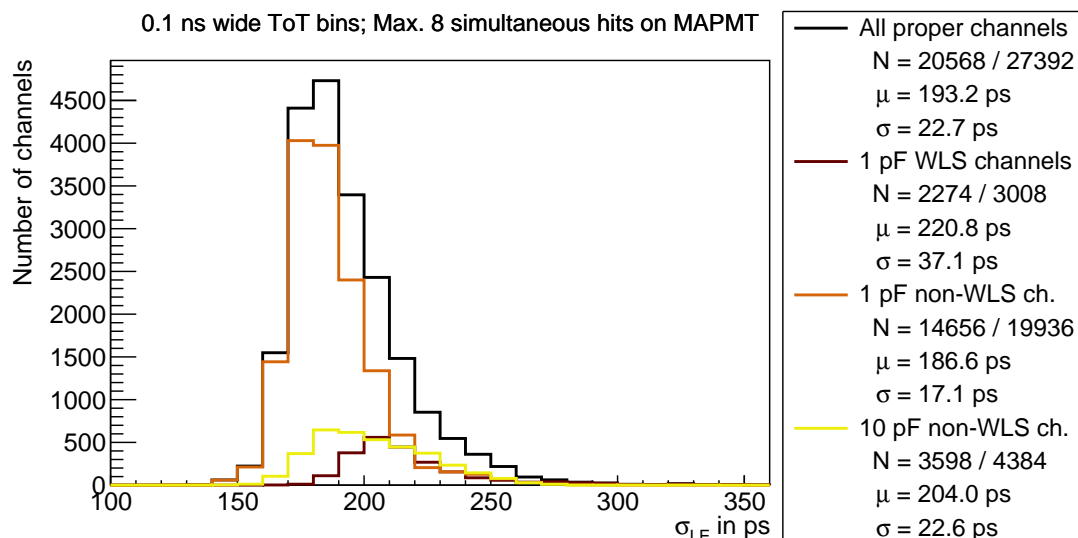
**Figure A.50 ♦** *Timing precision per channel, being the $\sigma_{LE}$ value of a Gaussian profile fitted to the 100 ps binned LE time distribution of the low occupancy data set of a single channel over a single 100 ps ToT bin. The low occupancy data set contains the channel dependent LE-ToT distribution of hits that were measured during an event where no more than eight hits were measured simultaneously on the channel's MAPMT. The channel dependent chosen ToT range is that of the 100 ps × 100 ps LE-ToT bin with the largest number of entries. The retrieved timing precisions are separated into three different groups labeled in the legend. Hereby the capacitance refers to the input capacitance of the DiRICH-FEB whereas the WLS is applied to the read out MAPMT.*
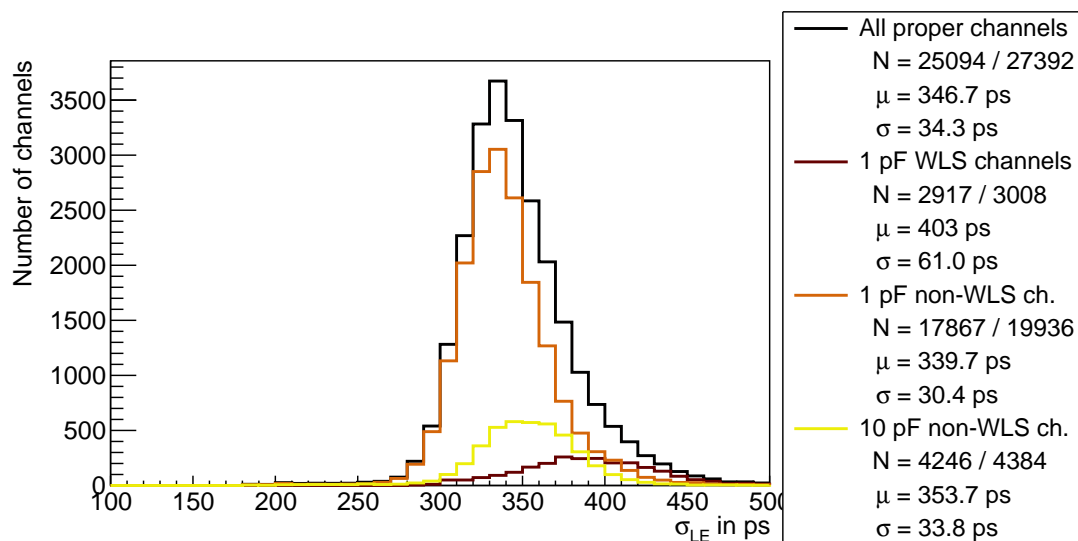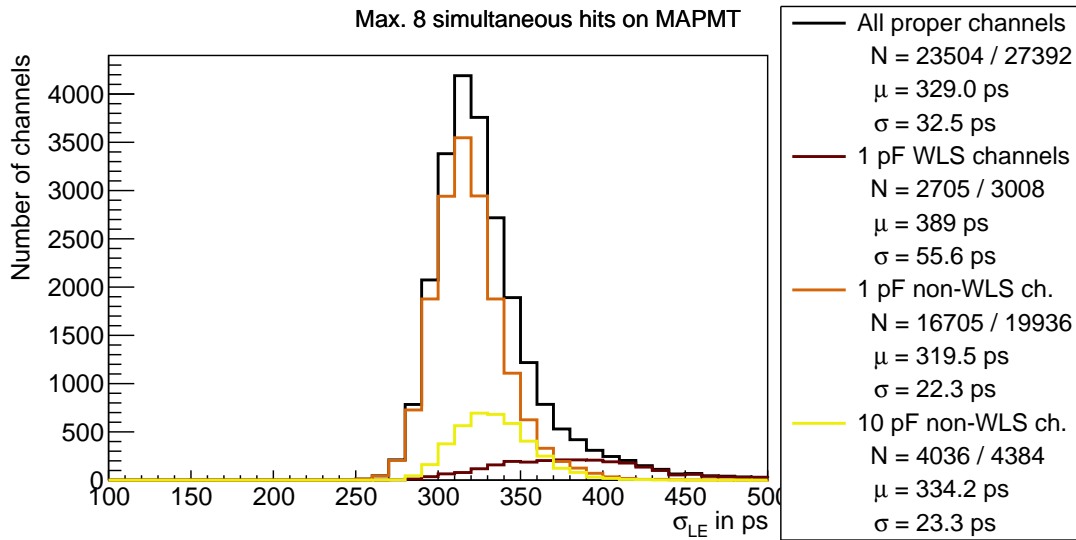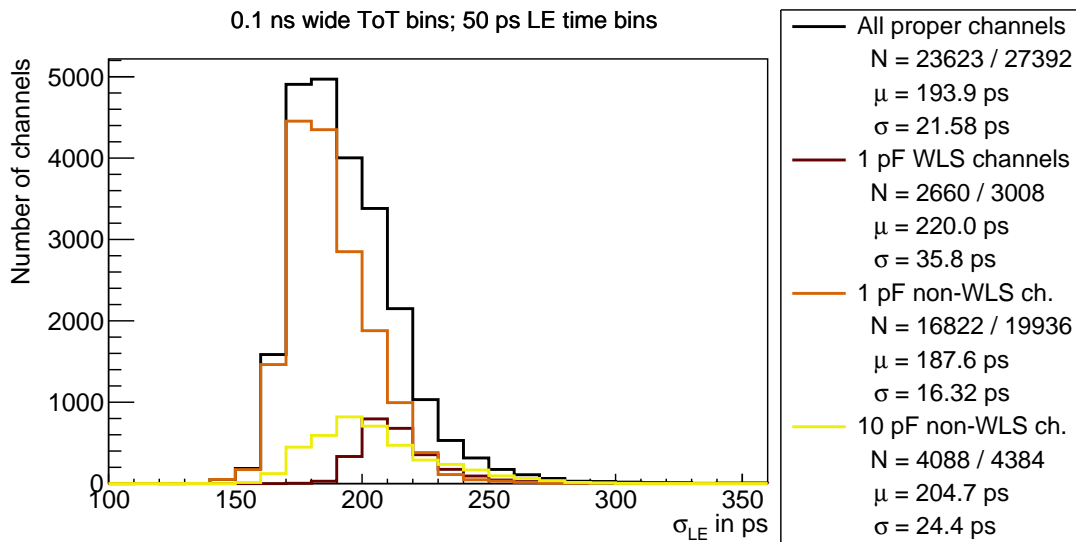


**Figure A.51 ♦** *Timing precision per channel being the $\sigma_{LE}$ value of a Gaussian profile fitted to the 100 ps binned LE time distribution integrated over the full 10 ns ToT range. The retrieved timing precisions are separated into three different groups labeled in the legend. Hereby the capacitance refers to the input capacitance of the DiRICH-FEB whereas the WLS is applied to the read out MAPMT. For each group the number of properly fitted channels N is denoted in the legend together with the number of all channels in the detector belonging into that group. Additionally, the sample average timing precision μ and sample spread σ for each group are denoted up to statistically significant precision for each group.*

211

**Figure A.52** ♦ *Timing precision per channel being the $\sigma_{LE}$ value of a Gaussian profile fitted to the 100 ps binned LE time distribution integrated over the full 10 ns ToT range of the low occupancy data set. The low occupancy data set contains the channel dependent LE-ToT distribution of hits that were measured during an event where no more than eight hits were measured simultaneously on the channel's MAPMT. The retrieved timing precisions are separated into three different groups labeled in the legend. Hereby the capacitance refers to the input capacitance of the DiRICH-FEB whereas the WLS is applied to the read out MAPMT. For each group the number of properly fitted channels N is denoted in the legend together with the number of all channels in the detector belonging into that group. Additionally, the sample average timing precision $\mu$ and sample spread $\sigma$ for each group are denoted up to statistically significant precision for each group.*



**Figure A.53** ♦ *Timing precision per channel being the $\sigma_{LE}$ value of a Gaussian profile fitted to the 50 ps binned LE time distribution of a single channel over a single 100 ps ToT bin. The channel dependent chosen ToT range is that of the 50 ps × 100 ps LE-ToT bin with the largest number of entries. The retrieved timing precisions are separated into three different groups labeled in the legend. For each group the number of properly fitted channels N is denoted in the legend together with the number of all channels in the detector belonging into that group. Additionally, the sample average timing precision $\mu$ and sample spread $\sigma$ for each group are denoted up to statistically significant precision for each group.*
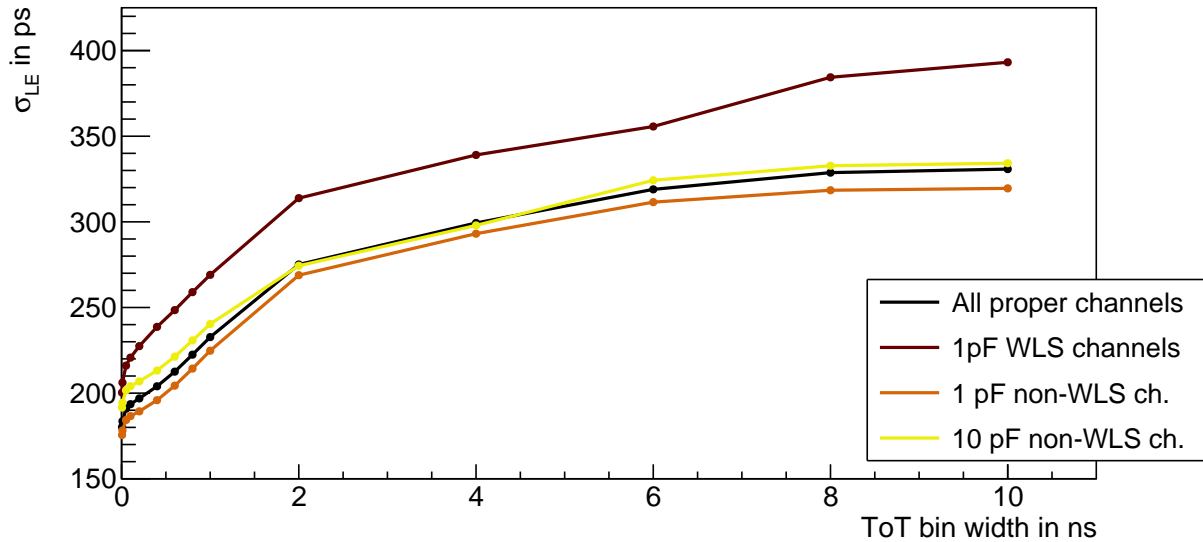
**(a)** *Detector average timing precision*
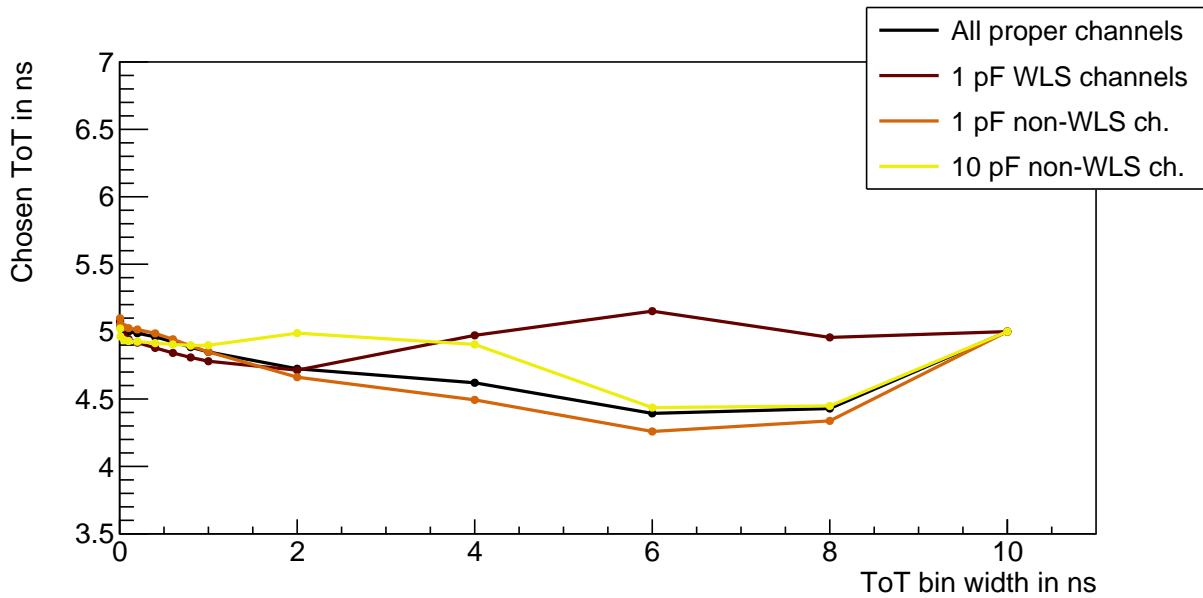


**(b)** *Average ToT bin center*

**Figure A.54 ♦** *Dependency of the extracted detector average timing precision and the average chosen ToT bin for which the precision was derived onto the chosen ToT bin width. This dependency is derived for channel's hit time distributions that require not more than eight simultaneous hits per event on the channel's MAPMT. Herefore the averages are taken over three different groups denoted in the legend. The error bars in y-direction indicating the statistical error on the measured points are hereby to small to exceed the marker size. A full distribution for the* 100 ps *ToT bin width is found in* Fig. A.50 *(appendix pg. 211) where also the procedure is laid out. The same depiction is also found using the full ToT range, i.e.* 10 ns *ToT bin width in Fig. A.52 (appendix pg. 212).*

**(a)** *1 ns wide LE time cut*



**(b)** *20 ns wide LE time cut*
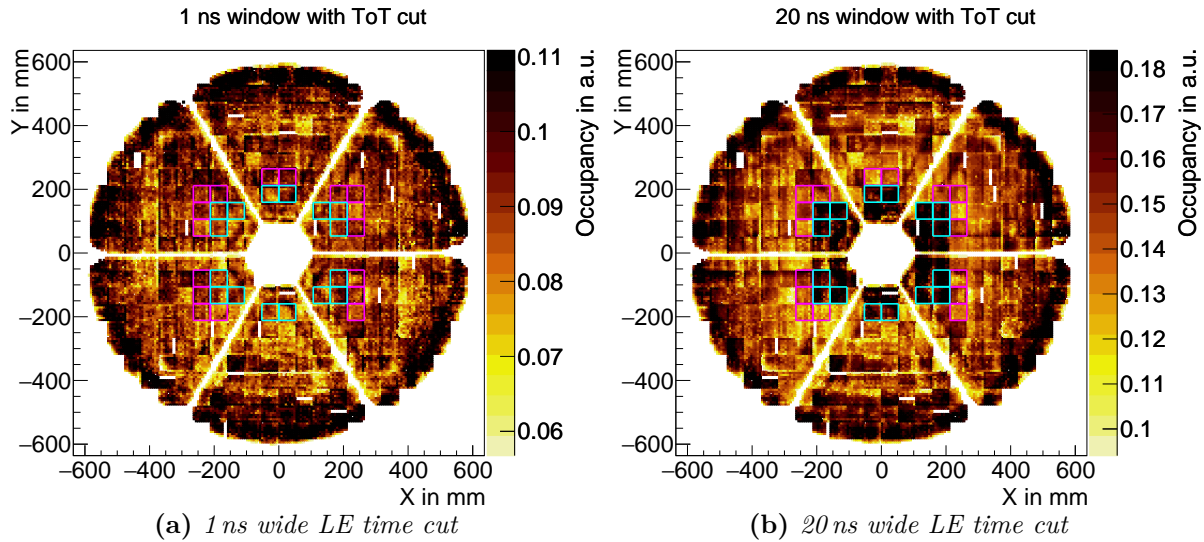
**Figure A.55** ♦ *Spatially resolved occupancy distribution for a 1 ns ((a)) and 20 ns ((b)) wide LE time cut. In this analysis in addition to the applied LE window a ToT cut ToT > 3 ns is applied. The occupancy of each channel is defined by the ratio of number of hits in that channel with an electron candidate in its proximity by the number of electron candidates in its proximity (compare equation (7.2)). The proximate area is defined through a circle with radius 30 mm and an additional angular equivalent of 2° (see equation (B.5)). The electron candidate is defined by 0.95 < β < 1.05, the momentum |p/z| < 250 MeV/c and mass m < 50 MeV/c² requiring additionally a ring in the RICH with 17 mm < $r_{Ring}$ < 30 mm maximally separated by 2°. Marked with magenta rectangles are MAPMTs not coated with WLS (and also read out by DiRICHes with 1 pF input capacitance) which are used in the following quantitative analysis and cyan rectangles indicating the accordingly used WLS coated MAPMTs.*
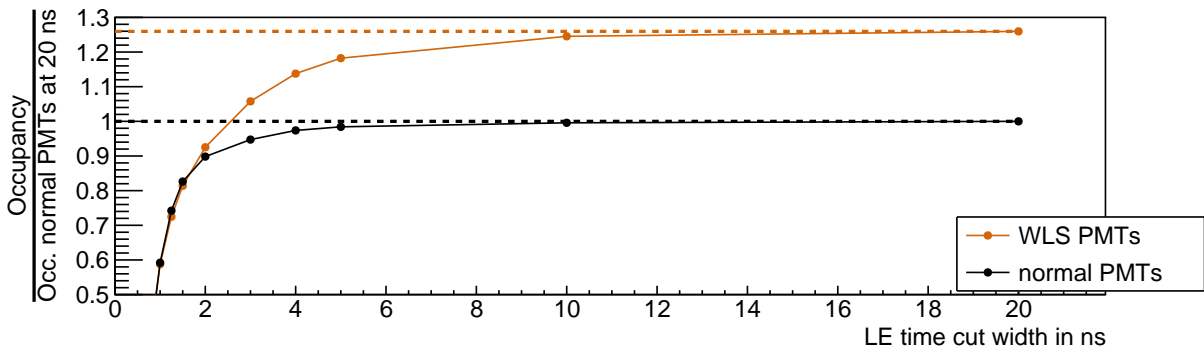


**Figure A.56** ♦ *Relative average occupancy comparing selected channels from WLS and non-WLS coated MAPMTs for different LE time cut widths. The occupancy in dependence of the LE time cut width is thereby averaged over all respective channels before dividing it by the average occupancy measured in the uncoated MAPMTs at a LE time width of 20 ns. Hereby only channels with 1 pF input capacitance are used as shown in Fig. A.55, with the occupancy defined through equation (7.2). For this analysis no additional cut ToT > 3 ns is applied. Indicated with dashed lines are the maximum values reached after 20 ns, therethrough exhibiting the gain of the WLS coating.*
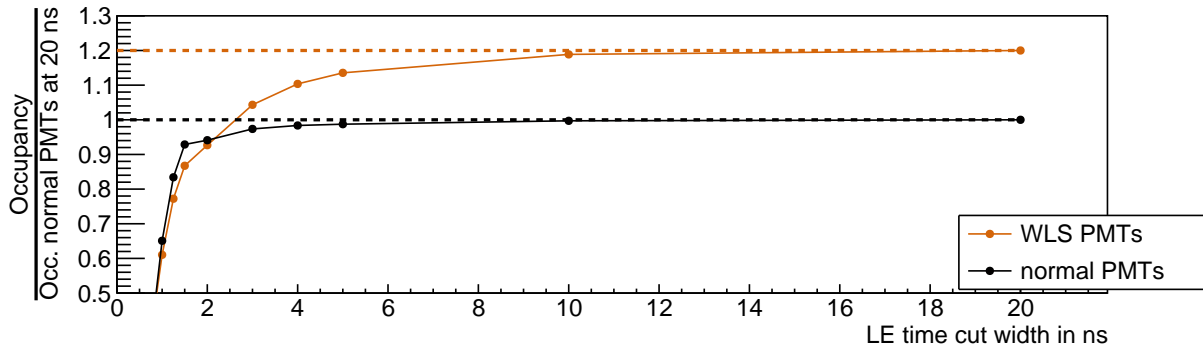
**Figure A.57** ♦ *Toy analysis of the relative average occupancy comparing selected channels from WLS and non-WLS coated MAPMTs for different LE time cut widths. Herefore the WLS gain was explicitly set the WLS gain to 20%, as this value is known to be the approximate gain of the WLS in lab measurements. The occupancy in dependence of the LE time cut width is thereby averaged over all respective channels before dividing it by the average occupancy measured in the uncoated MAPMTs at a LE time width of 20 ns. Hereby only channels with 1 pF input capacitance are used as shown in Fig. A.55, with the occupancy defined through equation (7.2). To suppress low ToT cross talk an additional cut ToT > 3 ns is applied. Indicated with dashed lines are the maximum values reached after 20 ns, therethrough exhibiting the gain of the WLS coating.*
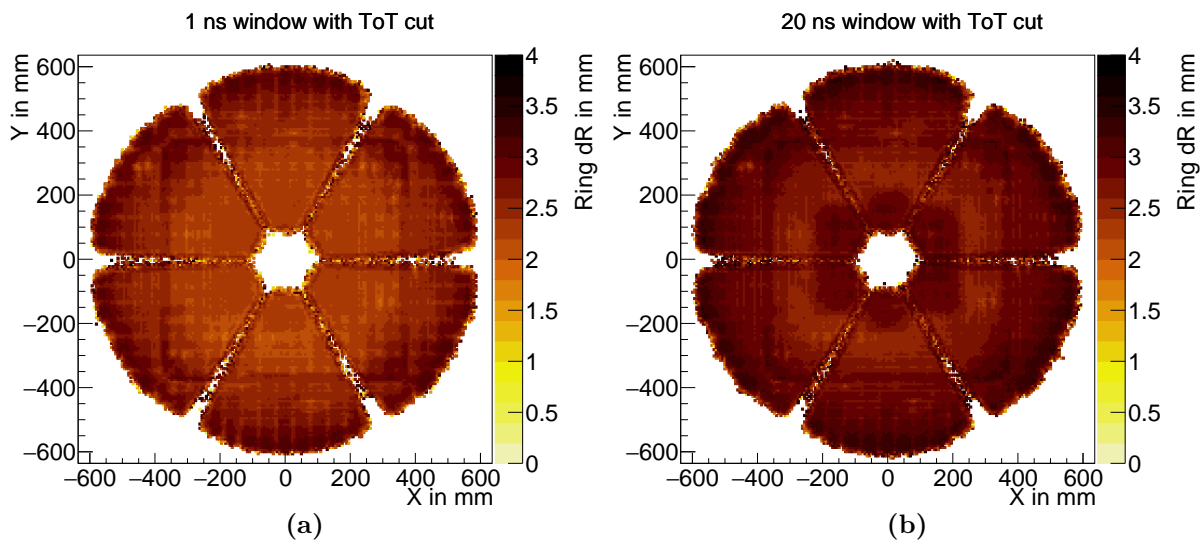


**Figure A.58** ♦ *Spatially resolved distribution of ring dR for 1 ns and 20 ns wide LE time cut windows. For each pixel sized x/y-bin the average ring dR of rings with their ring center in that bin is shown. In addition to the LE time cut an additional ToT cut of ToT > 3 ns is applied. The dR is calculated according to equation (4.1) for rings found at maximum 2° separated from an electron candidate with radius r between 17 mm and 30 mm. Visibly the WLS region in the very inner parts of the detector sees an enhanced dR for a largely opened LE time window.*
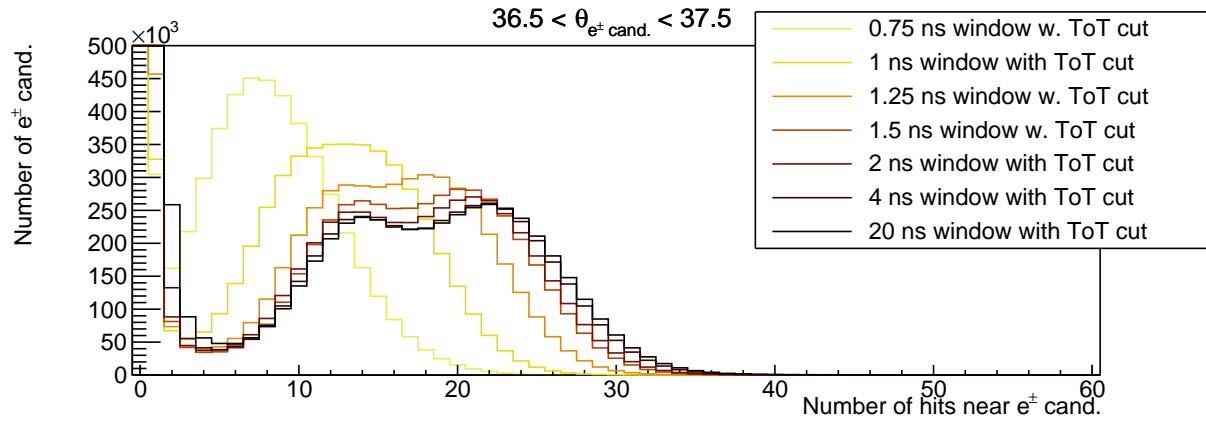
**Figure A.59** ♦ *Number of hits in the proximity of an electron candidate detected at polar angle $36.5° < \theta < 37.5°$ for different LE time cut widths applying an additional ToT cut to suppress cross talk contributions. The proximate area is defined through a circle with radius $30\,\text{mm}$ and an additional angular equivalent of $2°$ (see equation (B.5)). The electron candidate is defined by $0.95 < \beta < 1.05$, the momentum $|p/z| < 250\,^{MeV}/c$ and mass $m < 50\,^{MeV}/c^2$ requiring additionally a ring in the RICH with $17\,mm < r_{Ring} < 30\,mm$ maximally separated by $2°$.*
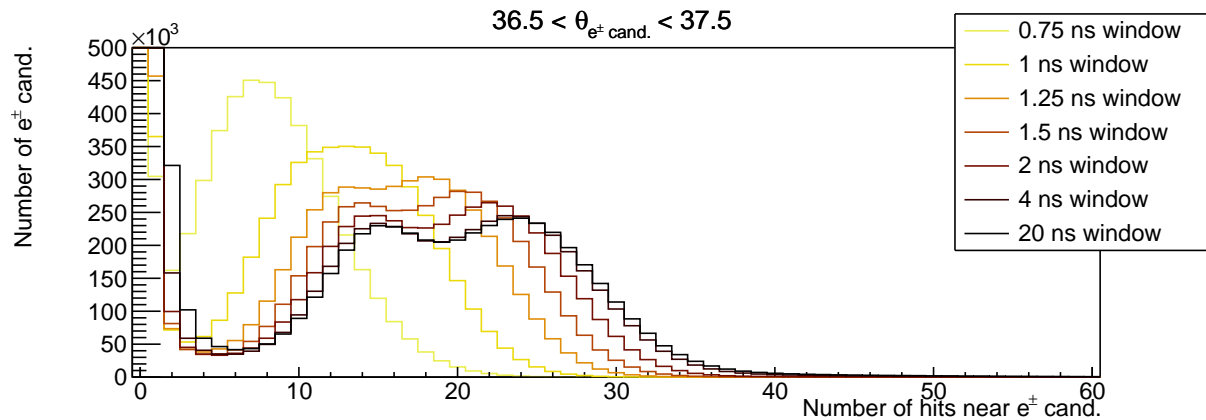


**Figure A.60** ♦ *Number of hits in the proximity of an electron candidate detected at polar angle $36.5° < \theta < 37.5°$ for different LE time cut widths applying no additional ToT cut. The proximate area is defined through a circle with radius $30\,\text{mm}$ and an additional angular equivalent of $2°$ (see equation (B.5)). The electron candidate is defined by $0.95 < \beta < 1.05$, the momentum $|p/z| < 250\,^{MeV}/c$ and mass $m < 50\,^{MeV}/c^2$ requiring additionally a ring in the RICH with $17\,mm < r_{Ring} < 30\,mm$ maximally separated by $2°$.*
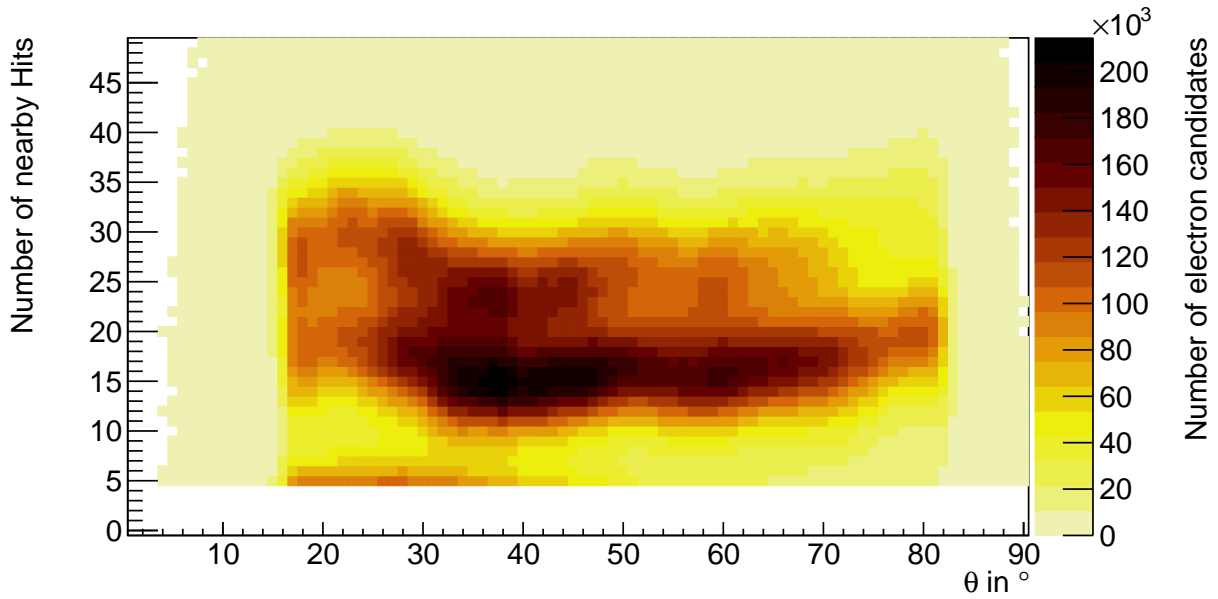
**Figure A.61** ♦ *θ resolved number of hits in the vicinity of electron candidates distribution. A hit is deemed close if it is found in the circular area with radius 30 mm plus an additional 2° angular difference equivalent (see equation (B.5)). The electron candidate is defined through its velocity $0.95 < \beta < 1.05$, the momentum $|p/z| < 250\,MeV\!/c$ and mass $m < 50\,MeV\!/c^2$. Visibly the distribution varies over θ, exhibiting an increase at very small θ where WLS coated MAPMTs are located and towards larger θ where the electron traversed path through the radiator gets the longest. Also visible are the two distinct peaks over nearly the full θ range. These peaks are induced by the single and double ring contributions.*

## A.7 Additional figures for Chapter 8



**(a)**

**(b)** *x-axis scaled to single ring mean*

**(c)** *Max. one ring identified*

**(d)** *Max. one ring identified; v.s.*

**(e)** *Max. one ring at $\theta \approx 37°$*

**(f)** *Max. one ring at $\theta \approx 37°$; v.s.*
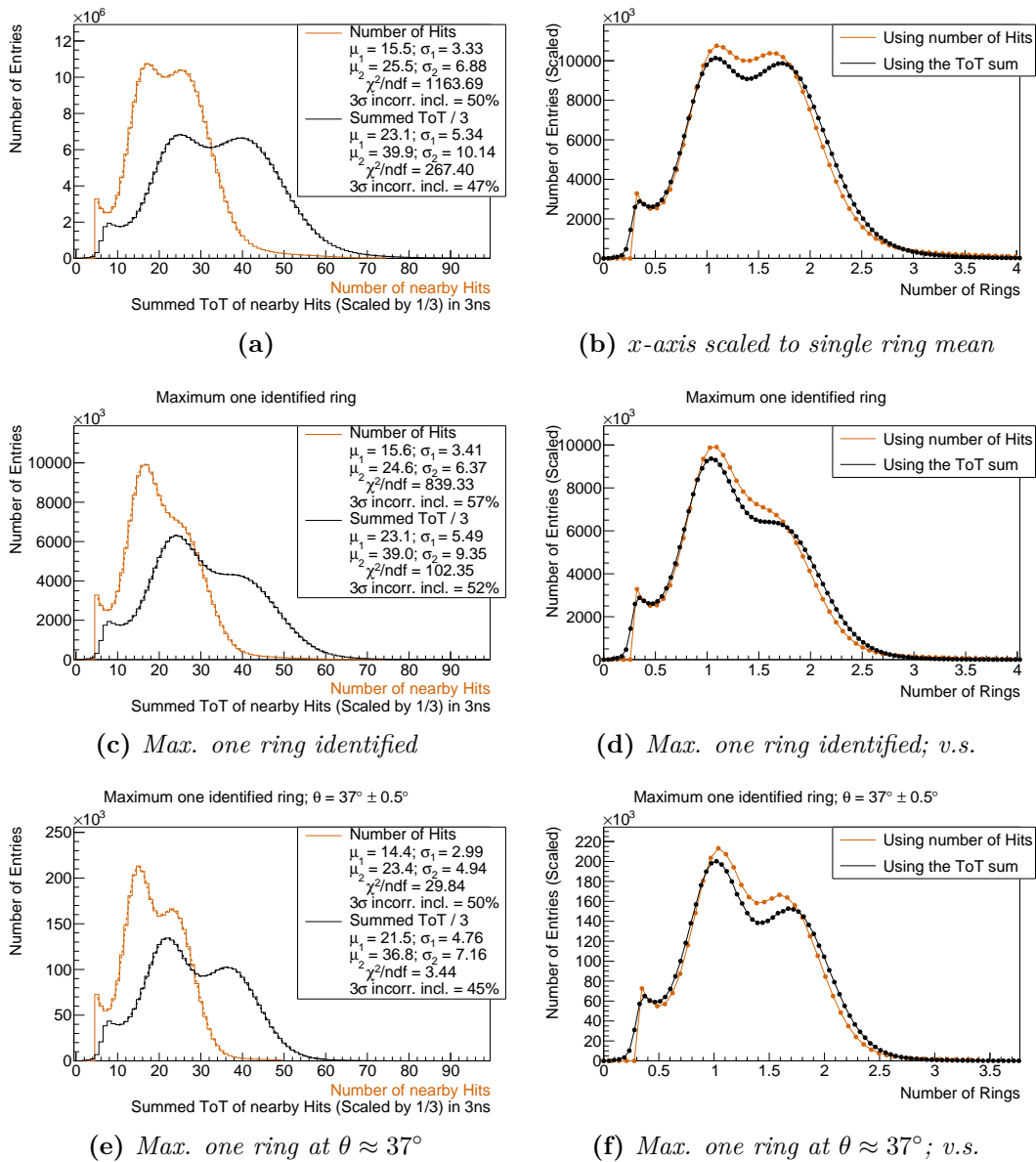
**Figure A.62** ♦ *Comparison of the distributions counting the number of hits in the proximity of an electron candidate and summing up their hit dependent ToT. Sub-figures (a)/(c)/(e) show the distribution of number of hits and their ToT sum. Hereby all hits are counted in circular areas with radius 30 mm and added angular difference equivalent of 2° around electron candidates. To retrieve the ToT sum spectrum, the ToT of all those hits is summed up and divided by three for visibility reasons. For sub-figure (a) any number of rings is allowed in the corresponding area, whereas (c)/(e) only allow for one reconstructed ring in the electron candidates proximity. Sub-figure (e) additionally requires the electron candidate to be reconstructed within polar angle $36.5° < \theta < 37.5°$. Each distribution is fitted via two Gaussian distributions for single and double ring contributions and an underlying exponential decrease to approximate the background. The "3σ incorrect inclusion" percentage is defined via equation (8.1). Sub-figures (b)/(d)/(f) scale the x-axis for each distribution individually, according to the extracted $\mu_1$ from the corresponding fit. The resulting x-axis then corresponds to "number of rings" as the the first peaks center will always be situated at $x = 1$. Hereby the distribution using the ToT sum also has its y-axis scaled accordingly to keep the area below both distributions comparable.*
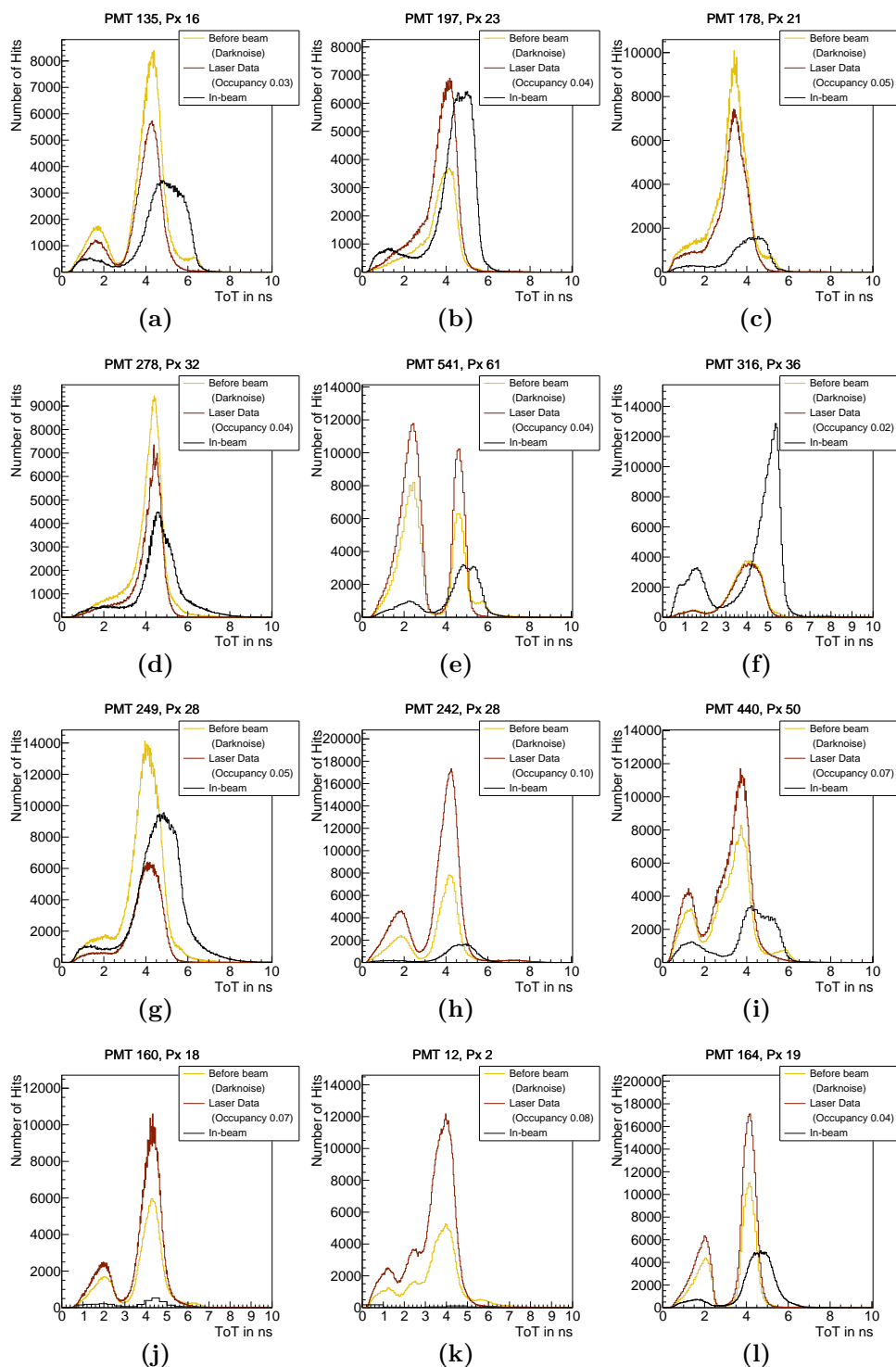
**Figure A.63** ♦ *Single ToT spectra for different randomly chosen channels. Plotted are three different datasets. "Before beam" refers to the ToT of hits which were registered before any beam induced event, which are dominated by the MAPMT's dark noise. The "laser data" is taken in between beam events with the laser system attached to the RICH. This data is for most pixels comprised mostly of single photons. The occupancy value hereby refers to the average number of hits per event in this channel. "In-beam" data uses the ToT of signals which are correlated to the detector trigger measured in pixels which are in close proximity to an electron candidate.*
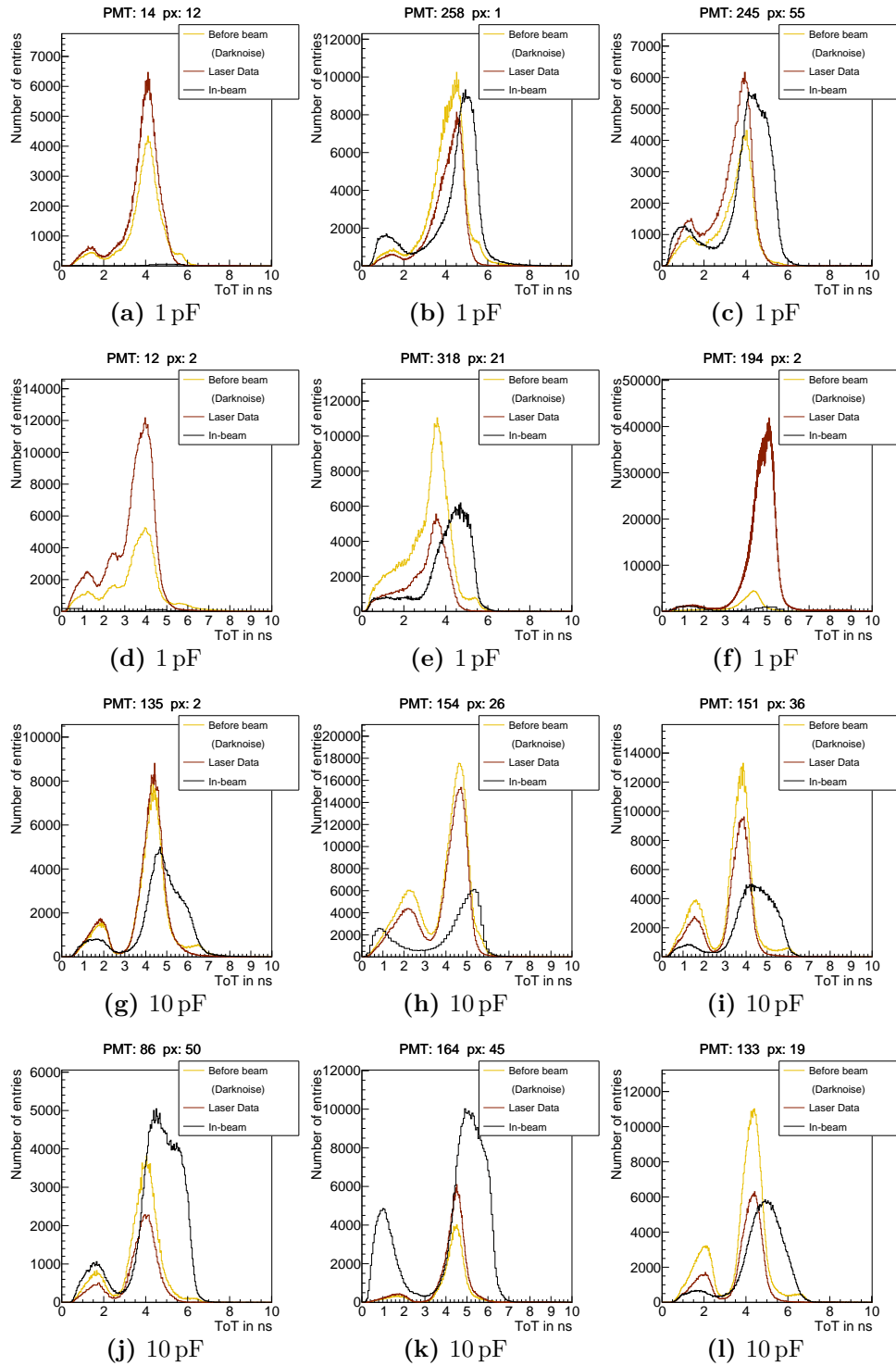
**Figure A.64 ♦** *Single ToT spectra for different input capacities (1 pF and 10 pF). Plotted are three different datasets. Before beam refers to the ToT of hits which were registered before any beam induced event, which are dominated by the MAPMT's dark noise. The laser data is taken in between beam events with the laser system attached to the RICH. This data is for most pixels comprised mostly of single photons. The occupancy value hereby refers to the average number of hits per event in this channel. "In-beam" data uses the ToT of signals which are correlated to the detector trigger measured in pixels which are in close proximity to an electron candidate.*

**(a)** *Markedness of one*



**(b)** *Markedness of zero; No three maxima*



**(c)** *Markedness of zero; Second maximum not larger than zero*
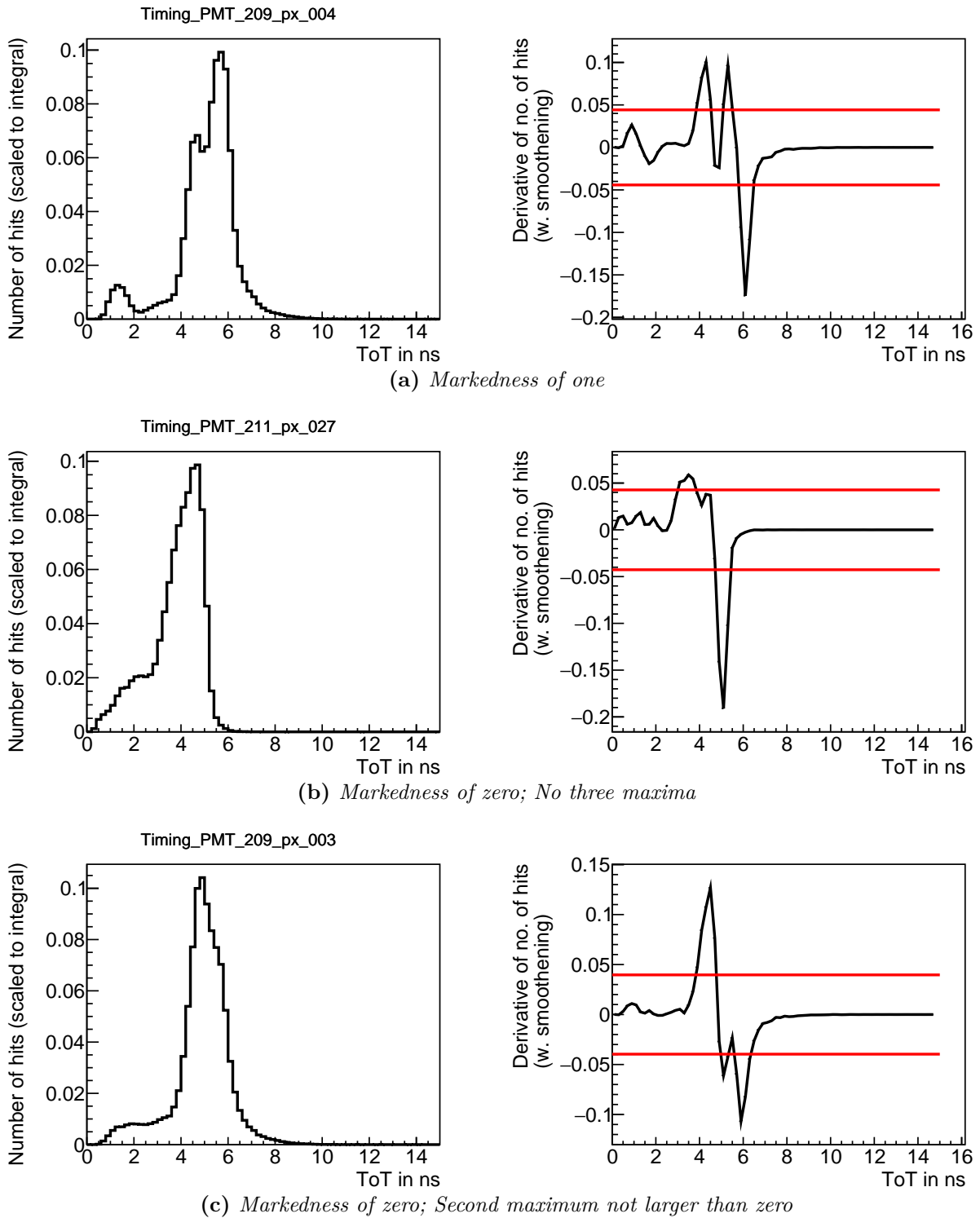
**Figure A.65 ♦** *Visualization of the markedness derivation procedure by means of three different channels. The left sub-figure shows for the channel's ToT distribution scaled to its integral. The derivative of this spectrum shown in the right sub-figures is calculated using a numeric derivative of eights' accuracy order with red lines indicating its standard deviation. Starting from a ToT value of $3.5\,$ns the derivative must show a local minimum smaller than zero followed by a local maximum larger than zero followed again by a local minimum smaller than zero, with at least two out of those three maxima exceeding the standard deviation of the derivative spectrum, for the channel to receives a markedness value of one. This is shown in sub-figure **(a)**. Sub-figures **(b)** and **(c)** show channels with markedness zero.*
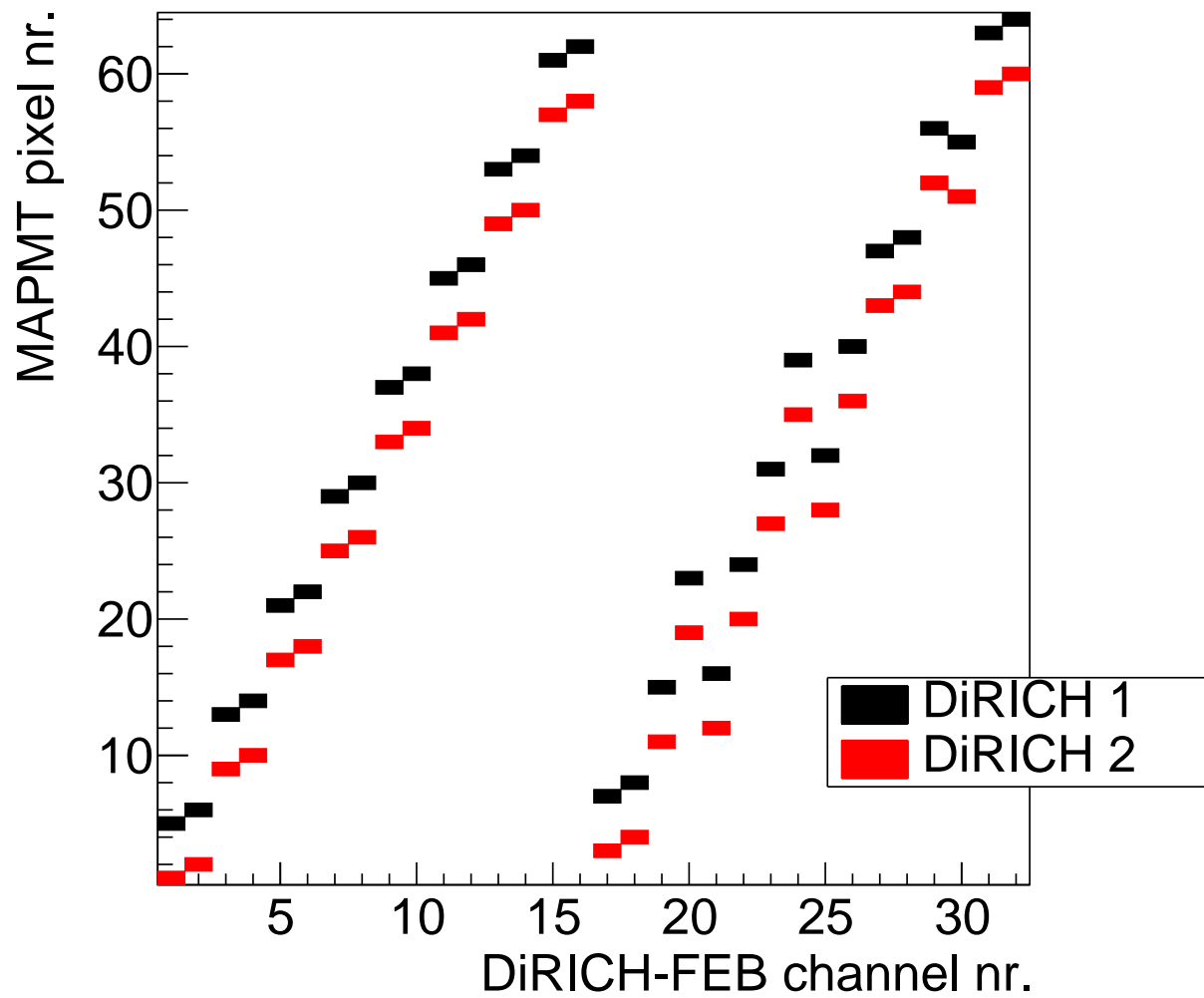
**Figure A.66 ♦** *Assignment matrix between MAPMT pixel and DiRICH-FEB channel. As each MAPMT is read out by two DiRICH-FEBs, each DiRICH channel might be assigned to one of two MAPMT pixels.*

**(a)** *Charge distribution*

**(b)** *Charge distribution*

**(c)** *ToT distribution*

**(d)** *ToT distribution*

**(e)** *Single photon ToT distribution*

**(f)** *Double photon ToT distribution*
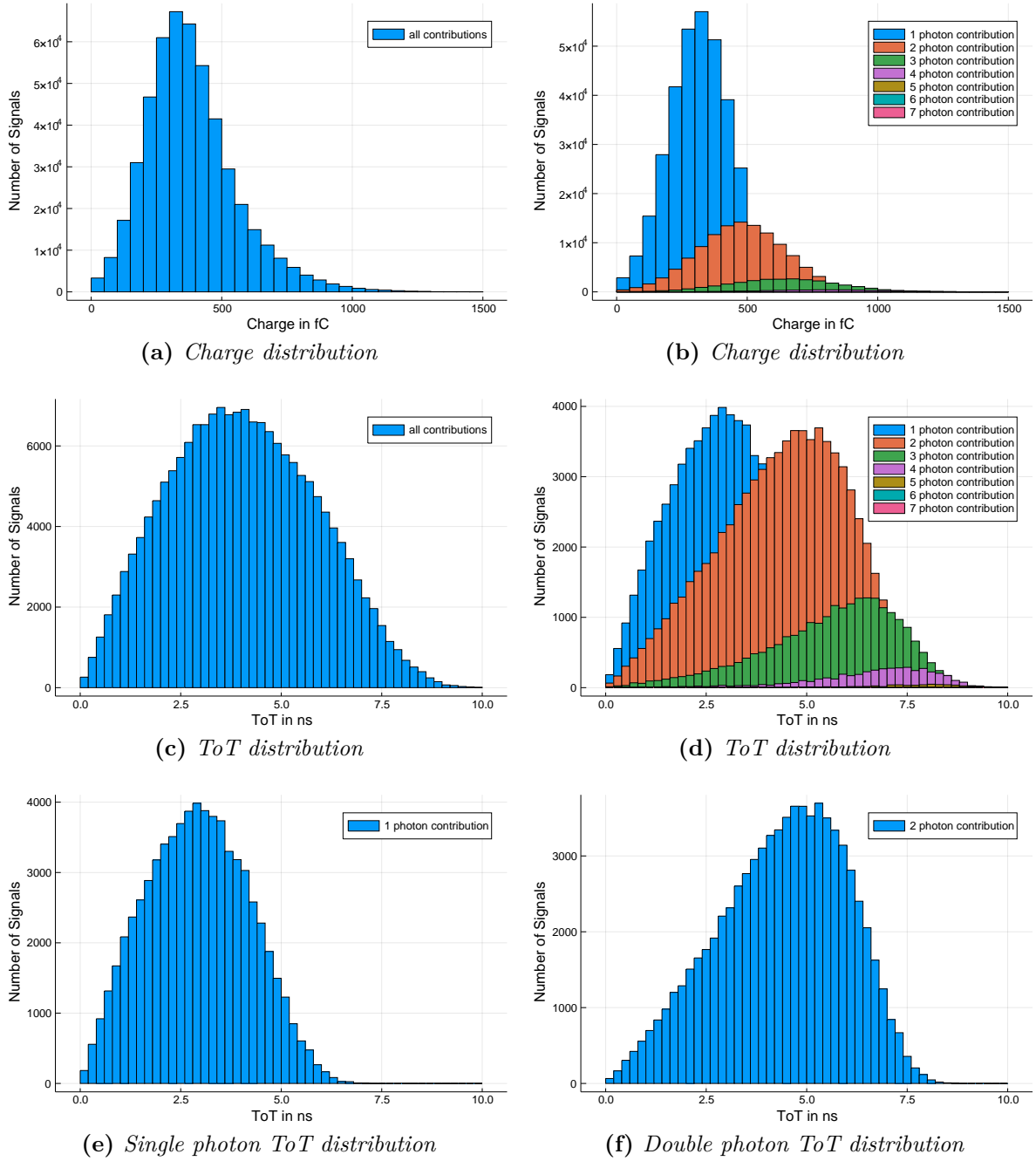
**Figure A.67 ♦** *Toy simulation to get a feeling for the ToT response for different number of photons. The charge distribution (sub-figures **(a)**,**(b)**) is generated according to [Bel+94] using a random number generator following a Poisson distribution, i.e. Poisson($-\ln(1 - occ)$), with the occupancy set to $occ = 0.5$ giving the number of photons and an according Gaussian distributed random number Normal($\mu_1 + (n-1)\Delta\mu$, $\sigma\sqrt{n}$) where n is the number of photons and $\mu_1 = 320\,fC$, $\Delta\mu = 160\,fC$, and $\sigma = 120\,fC$ are given constants, giving the charge. The ToT (sub-figures **(c)**–**(f)**) for each charge is calculated using $2\sqrt{2}\sigma \cdot \sqrt{-\ln\left(\sqrt{2\pi}\sigma \cdot {}^{thr}/_{A\cdot 25\cdot 50\,\Omega}\right)}$, with A being the charge of the pulse and $thr = 70\,mV$, and $\sigma = 3.0\,ns$ being given constants. Visibly the single photon contribution **(e)** moves from a Gaussian distribution using the charge information to an Extreme Value Distribution (see [Wol16a]) whereas the double photon contribution **(f)** is more shaped like a Gumbel (see [Wol16b]) distribution. This obviously depends heavily on the parameters chosen, but is always nonlinear.*

**(a)** *Standard deviation of the 1–7 photon contributions for different signal and threshold setups.*

**(b)** *Mean ToT for different occupancies, i.e. photon counts for different signal and threshold setups.*
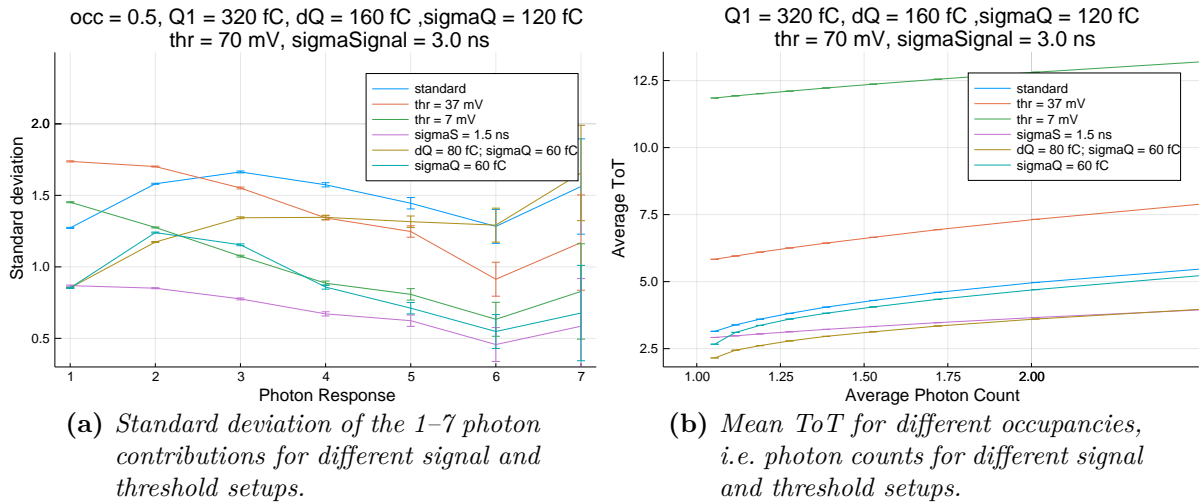
**Figure A.68** ♦ *Behavior of the mean ToT for a given light level (b) and standard deviations of the different single- /multi-photon peaks for different signal shapes and threshold setups extracted from a toy simulation. Following the in figure* A.67 *described procedure with the parameters noted at the top of this figure (where $Q \hat{=} \mu$), always only one parameter was altered as denoted in the figures legend. The uncertainties given only refer to the systematic uncertainties. The average photon count is calculated via $x = {}^{-ln(1-occ)}/_{occ}$. Hereby the standard deviation behaves very differently for each different parameter setup, whereas the average ToT nearly always scales more or less linear with the given average photon count.*

Figures A.69 through A.74 always show the same analysis with slightly different parameter setups. Shown is always a comparative number of hits and number of photons distribution, where both hits and photons are counted in circular areas with radius 30 mm and added angular difference equivalent of 2° around electron candidates. At most one ring correlated to the electron candidate is allowed. Thereby two different analyses are shown. One taking only electrons emitted in the $\theta$ range of $36.5° < \theta < 37.5°$, and the other one integrating over the full $\theta$-range. The ToT spectra through which the linear calibration is derived is smoothened via a simple coarse binning of 0.25 ns. The one photon ToT equivalent, which is assumed to be single photons, is then extracted from "off-beam" data which is mostly comprised of dark noise from the MAPMT. The according photon level (number of photons for the extracted ToT) is then either set to 0.9 "photons" or 1.0 "photons". The second photon level is extracted from the "in-beam" data and is assumed to be 1.51 "photons" globally for all channels. The distance between the two photon-ToT equivalents is then either used on a per channel basis or as a global average in the linear extrapolation together with the extracted single photon equivalent ToT. Sub-figures **(a)** always show the plain distributions together with a fit, depicted as a dashed line. The fit is comprised of two Gaussian distributions for single and double ring contributions and an underlying exponential decrease to approximate the background. The legend shows the important fit parameters, of which the uncertainty is estimated through fit-range variation and given as the last digit of each parameter. Also shown is the "$3\sigma$ incorrect inclusion" percentage defined via equation (8.1). This percentage refers to the amount of incorrectly as single ring identified double rings when cutting on $3\sigma$ of the single ring distribution. Sub-figures **(b)** show the same picture but with the $x$-axis scaled for each distribution according to the extracted $\mu_1$ from their fit. This results in the $\mu_1$ of each distribution ending up at a $x$-value of one. For the number of photons also the $y$-axis is scaled accordingly to keep the area below both distributions comparable. In the caption of each figure keywords are denoted to help an ad-hoc understanding of the corresponding figures.



**(a)**

**(b)** *x-axis scaled w.r.t single ring mean.*
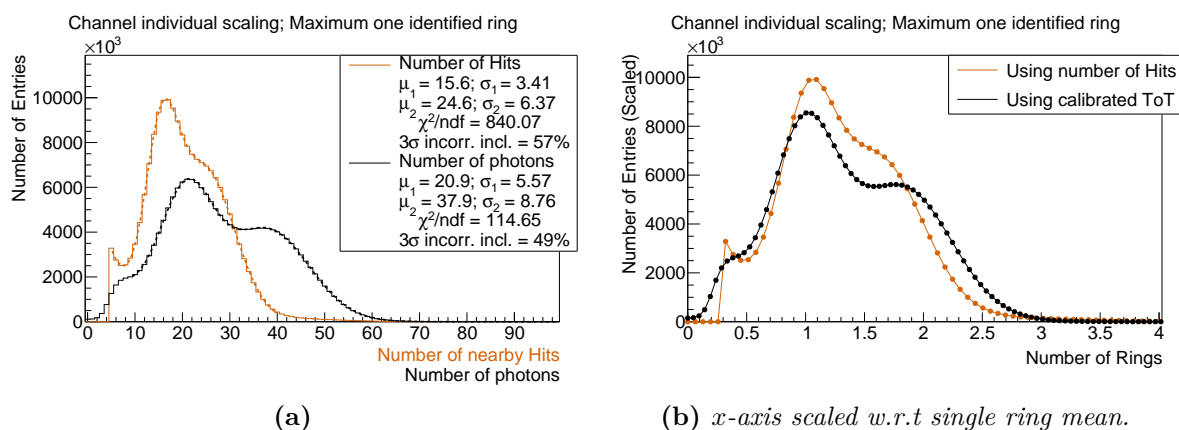
**Figure A.69** ♦ *Maximum one ring near electron candidate. Coarsely binned ToT smoothening. Per channel difference between single (1.0 "photons") and multi-photon ToT equivalent. Full explanation on page 225.*

**(a)**

**(b)** *x-axis scaled w.r.t single ring mean.*
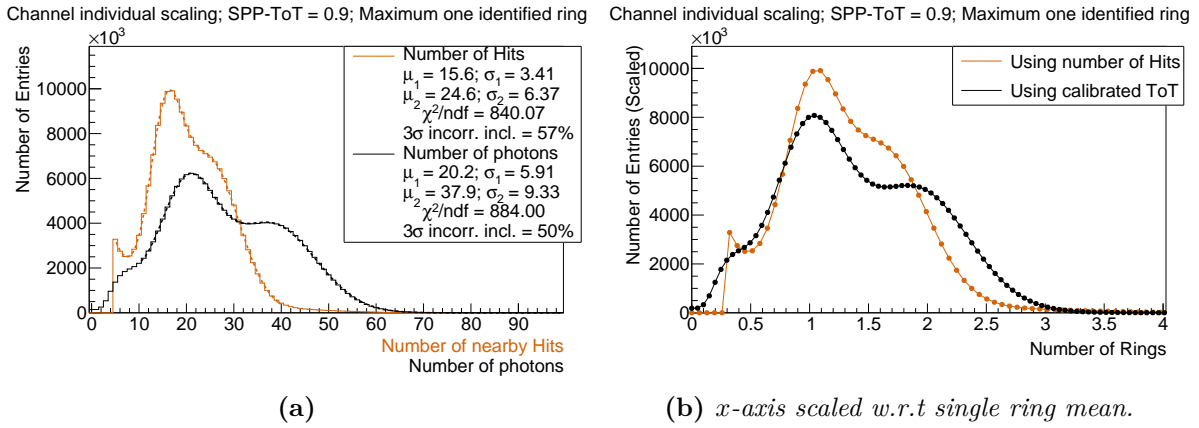
**Figure A.70** ♦ *Maximum one ring near electron candidate. Coarsely binned ToT smoothening. Per channel difference between single (0.9 "photons") and multi-photon ToT equivalent. Full explanation on page 225.*



**(a)**

**(b)** *x-axis scaled w.r.t single ring mean.*
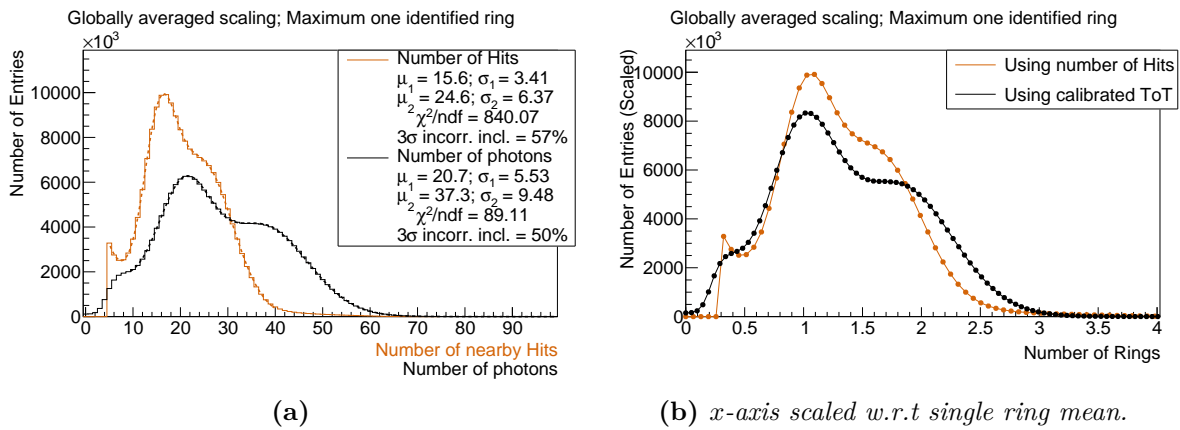
**Figure A.71** ♦ *Maximum one ring near electron candidate. Coarsely binned ToT smoothening. Global average difference between single (1.0 "photons") and multi-photon ToT equivalent. Full explanation on page 225.*



**(a)**

**(b)** *x-axis scaled w.r.t single ring mean.*

**Figure A.72** ♦ *Maximum one ring near electron candidate. Coarsely binned ToT smoothening. Global average difference between single (0.9 "photons") and multi-photon ToT equivalent. Full explanation on page 225.*

**(a)**

**(b)** *x-axis scaled w.r.t single ring mean.*

**Figure A.73** ♦ *Maximum one ring near electron candidate. Coarsely binned ToT smoothening. Global average difference between single (0.9 "photons") and multi-photon ToT equivalent. Electron candidate emitted in $36.5° \leq \theta < 37.5°$. Full explanation on page 225.*
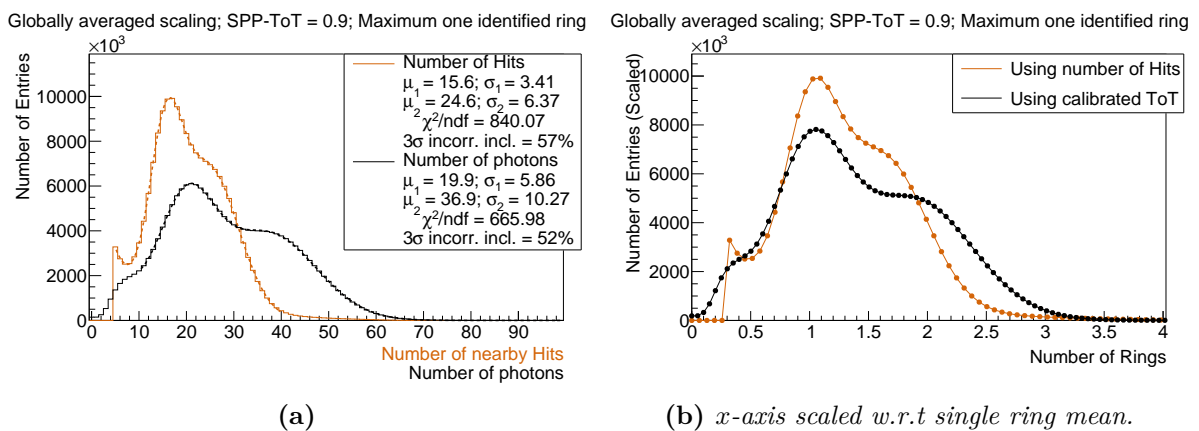


**(a)**

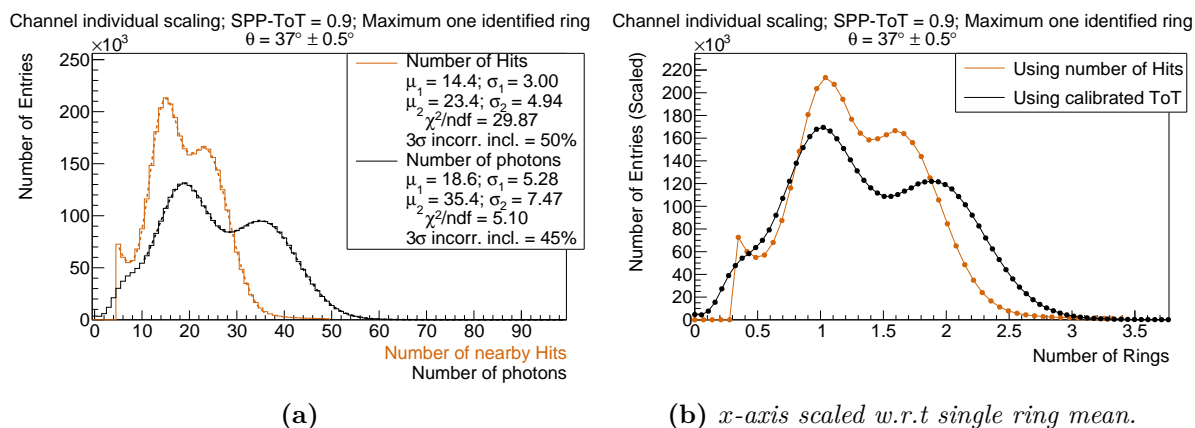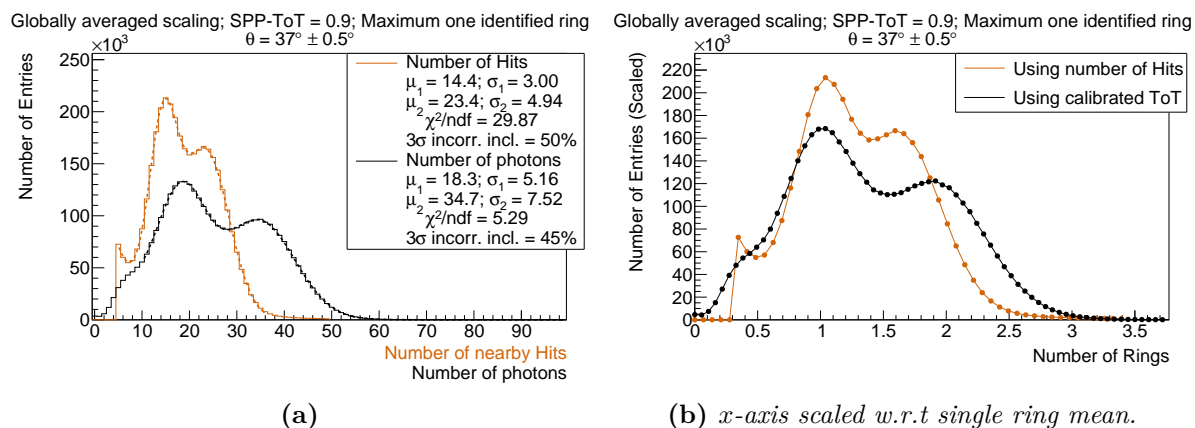**(b)** *x-axis scaled w.r.t single ring mean.*

**Figure A.74** ♦ *Maximum one ring near electron candidate. Coarsely binned ToT smoothening. Per channel difference between single (0.9 "photons") and multi-photon ToT equivalent. Electron candidate emitted in $36.5° \leq \theta < 37.5°$. Full explanation on page 225.*

## A.8  Additional figures for Chapter 9
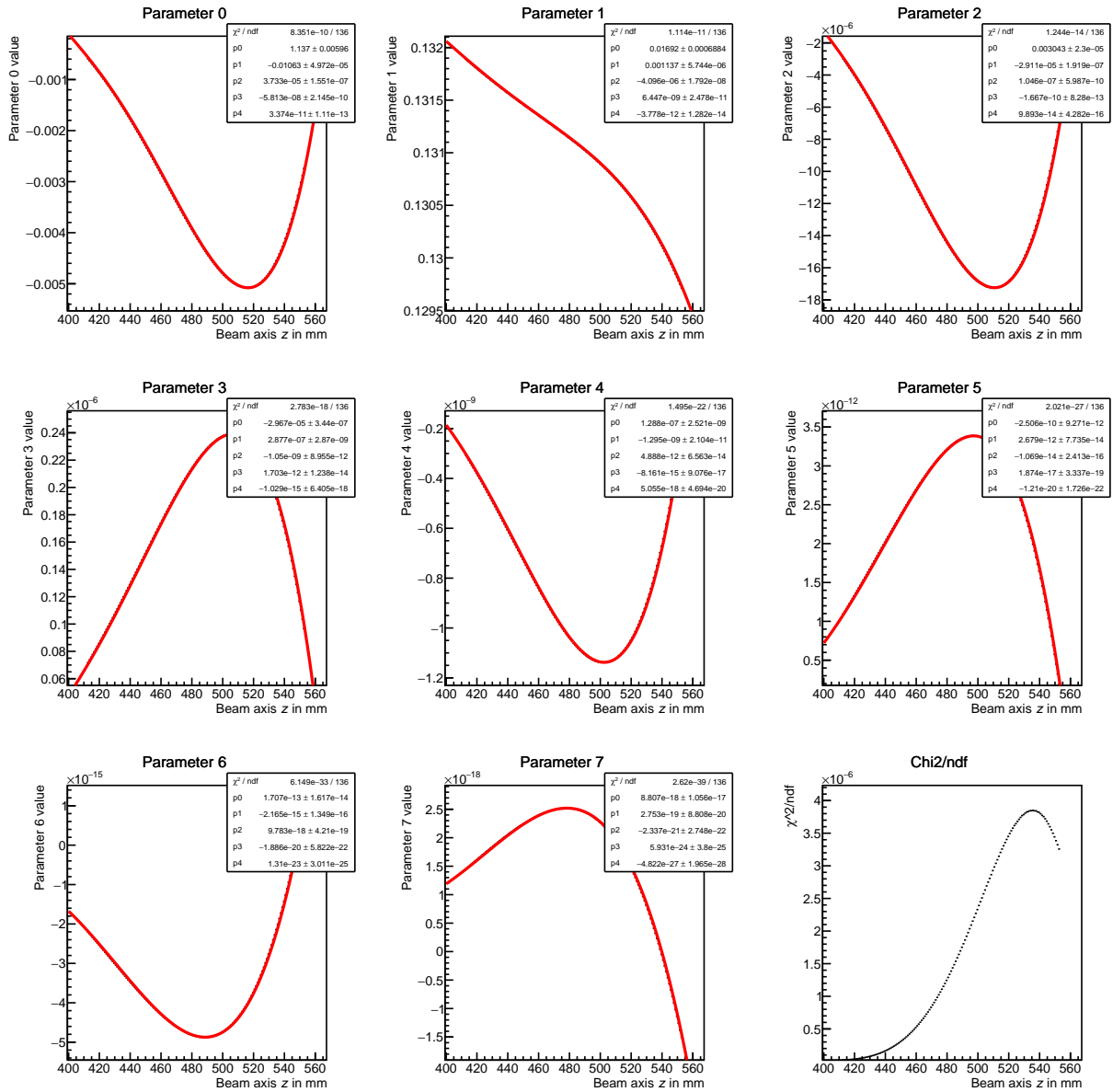


**Figure A.75 ♦** *Parameters for the polynomial of $7^{th}$ degree describing the inner photon detection plane's dependency $r(\theta)$ in terms of the beam axis coordinate $z$. The mirror sphere center is situated at $z = 0$. The last graph gives the $\chi^2/ndf$ for the different fits of the $7^{th}$ degree. The $\chi^2/ndf$ however is slightly arbitrary, as an artificially large number of points can be chosen for the fit. Each parameter itself is fitted with a polynomial of $4^{th}$ degree, thereby fitting the dependency on $z$. All fit parameters are denoted in the legend.*
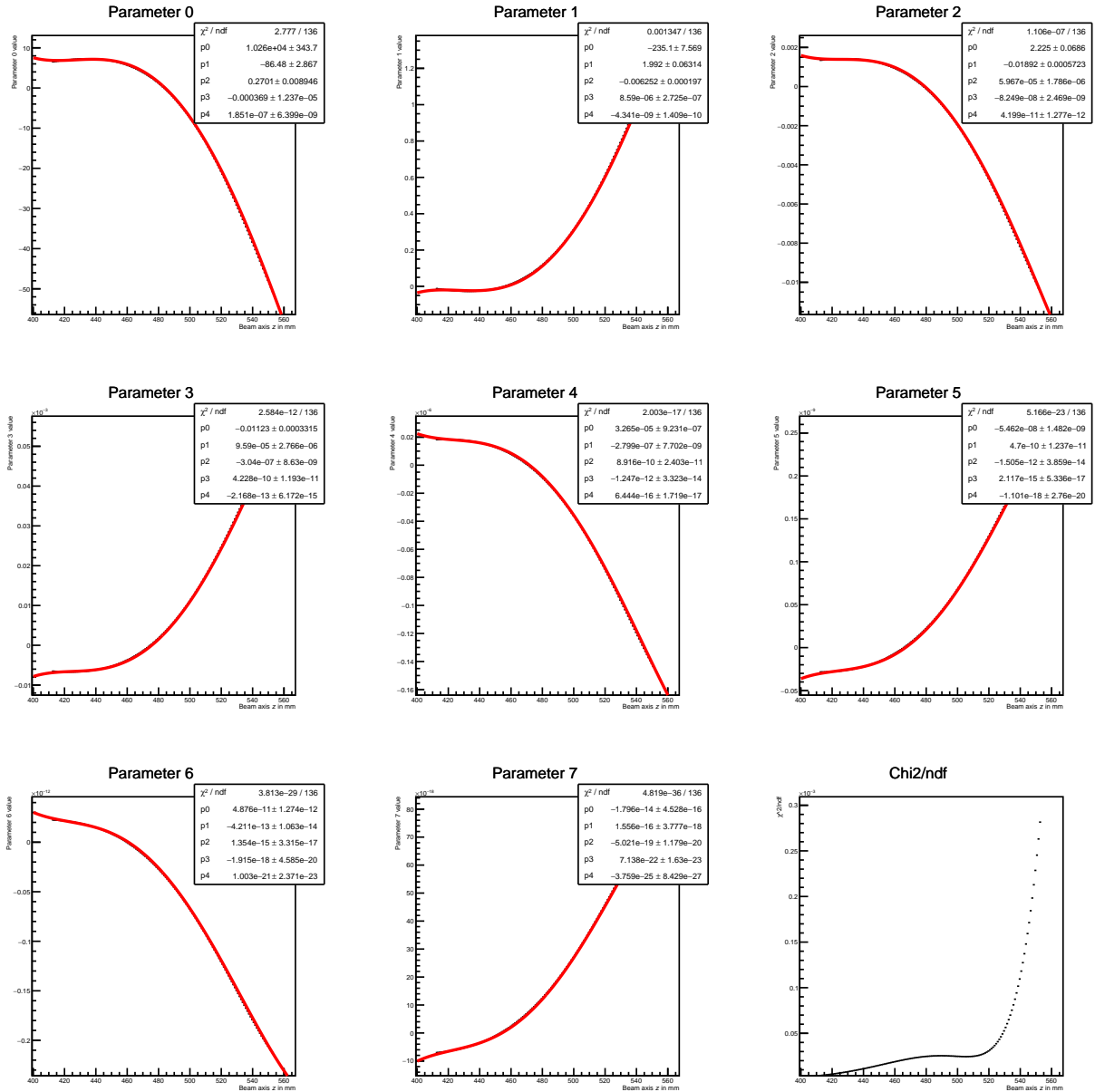
**Figure A.76** ♦ *Parameters for the polynomial of $7^{th}$ degree describing the outer photon detection plane's dependency $r(\theta)$ in terms of the beam axis coordinate $z$. The mirror sphere center is situated at $z = 0$. The last graph gives the $\chi^2/ndf$ for the different fits of the $7^{th}$ degree. The $\chi^2/ndf$ however is slightly arbitrary, as an artificially large number of points can be chosen for the fit. Each parameter itself is fitted with a polynomial of $4^{th}$ degree, thereby fitting the dependency on $z$. All fit parameters are denoted in the legend.*

**(a)** *Using polynomial of $6^{th}$ degree in $r$*
*Inner photon detection plane*

**(b)** *Using polynomial of $6^{th}$ degree in $r$*
*Outer photon detection plane*

**(c)** *Using polynomial of $8^{th}$ degree in $r$*
*Inner photon detection plane*

**(d)** *Using polynomial of $8^{th}$ degree in $r$*
*Outer photon detection plane*
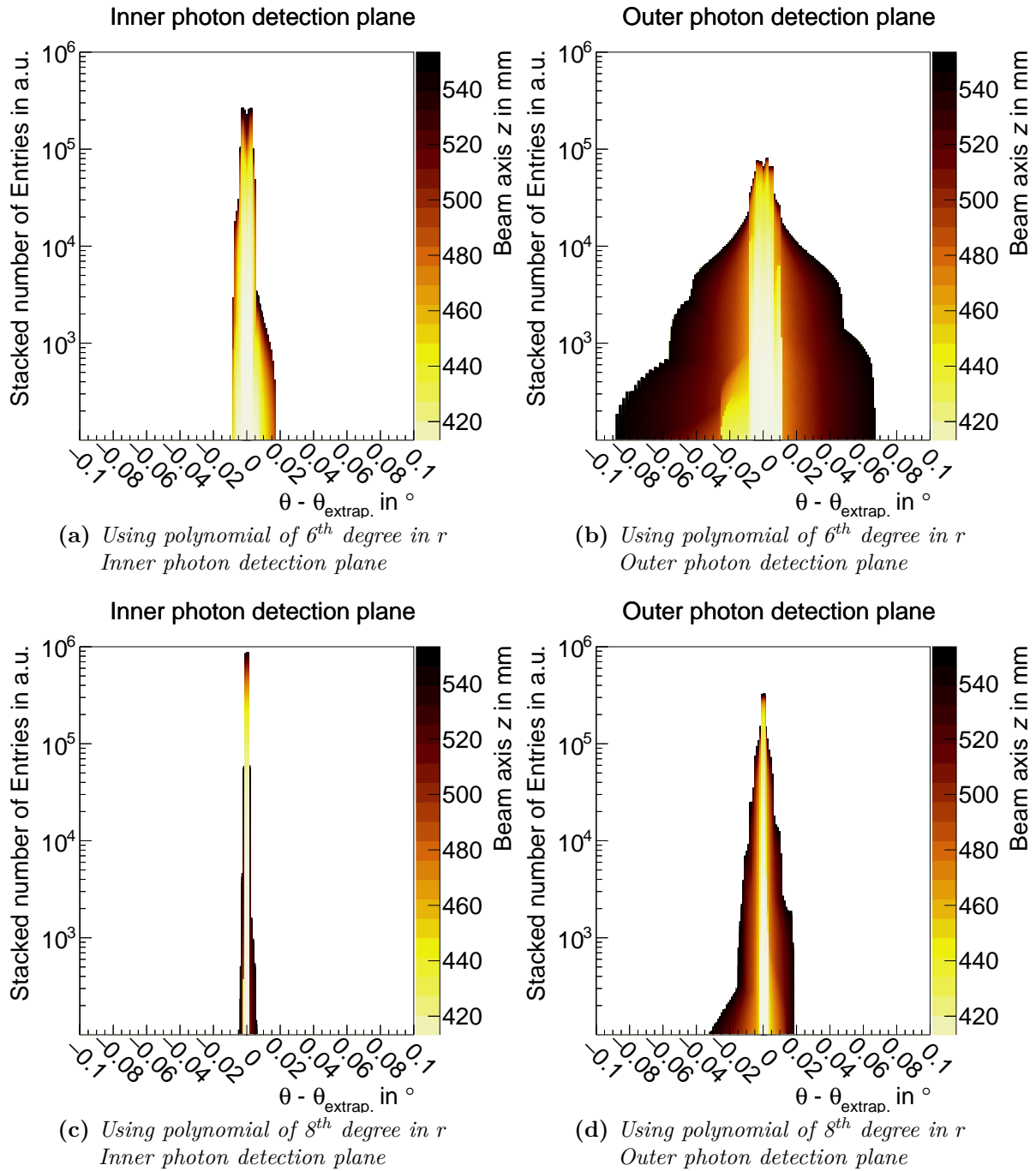
**Figure A.77** ♦ *Difference between the analytically derived $\theta$ and the one gained from the extrapolation using a $6^{th}$ **(a)**/**(b)** and $8^{th}$ **(c)**/**(d)** degree polynomial in $r$, where each parameter is approximated by a polynomial of $4^{th}$ degree in $z$. This extrapolation is gained through fits at discrete $z$-values, fitting the resulting parameters with respect to $z$ afterwards. The histograms presented are stacked, meaning that all differences $\theta - \theta_{extrap.}$ for different $r$- and $z$-values are filled into the same histograms but with different colors according to the shown $z$-axis. **(a)** hereby shows the inner- and **(b)** the outer photon detection plane. The number of entries is thereby artificial, as infinitely many points of comparison could have been chosen.*

**(a)** *electron z vertices*



**(b)** *electron θ/φ emission angles*
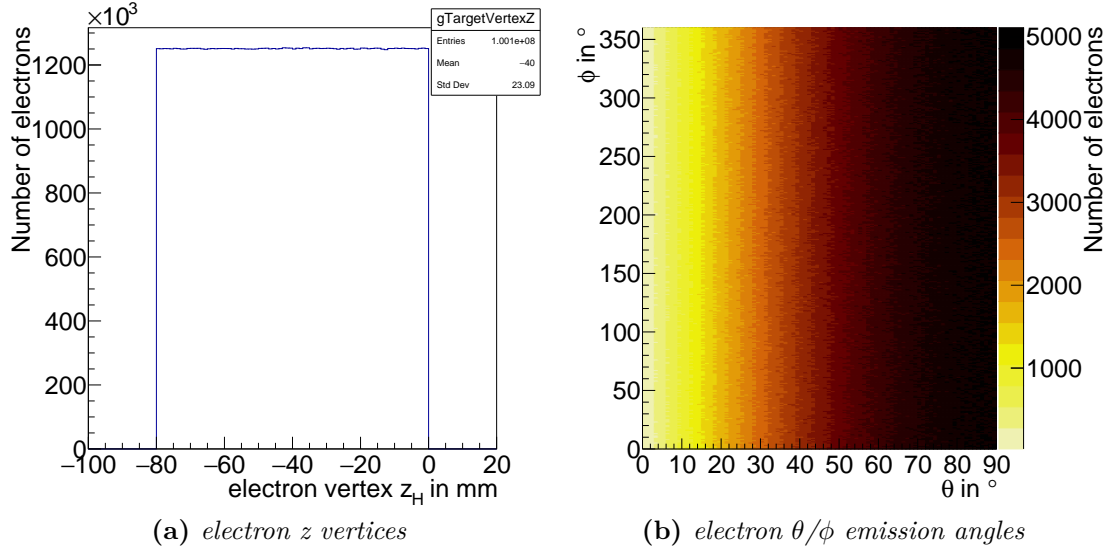
**Figure A.78** ♦ *Vertices **(a)** and emission angles **(b)** of electrons used for the electron simulation to check the new $x/y \to \theta/\phi$ transformation for the RICH detector. The vertex along $z_H$ refers to the beam axis in the HYDRA coordinate system, where the target spans roughly from $-80$ mm to $0$ mm. $z_H = 0$ is situated at $z = 533.3$ mm with respect to the mirror sphere center at $z = 0$. Electrons are emitted uniformly in $\phi = [0°, 360°]$ and according to an $\arccos(x)$ distribution, where $x$ is uniformly distributed, in $\theta = [0°, 90°]$ to account for the larger area which needs to be covered for larger $\theta$ angles.*



**(a)** *Upstream target segment*



**(b)** *Downstream target segment*
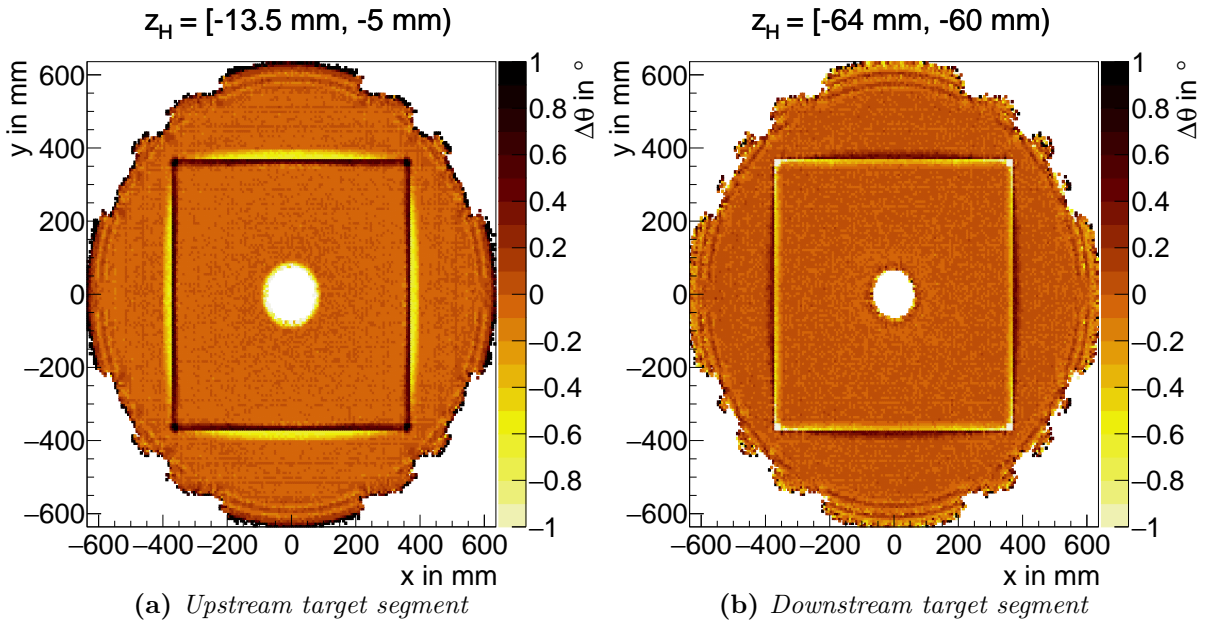
**Figure A.79** ♦ *Spatially resolved distribution of differences in $\theta$ for more negative $z_H$ (upstream target segment (a)) and $z_H$ close to zero (downstream target segment (b)). Using the new transformation with and without corrective map, accounting for ring fitter tendencies. Where $\Delta\theta = \theta - \theta_e$, with $\theta/\phi$ the reconstructed and $\theta_e/\phi_e$ the simulated electron emission angles. The differences are averaged for each $x/y$ pixel on the RICH averaging over all particles having their vertices in the respective range. The simulated $1 \times 10^8$ electrons are emitted at $x = 0$ mm, $y = 0$ mm uniformly over $2\pi$. All spatially resolved distributions have a pixel sized $7 \times 7$ mm$^2$ granularity and are artificially cut of at $\pm 1°$.*

**(a)** *Upstream target segment*

**(b)** *Downstream target segment*
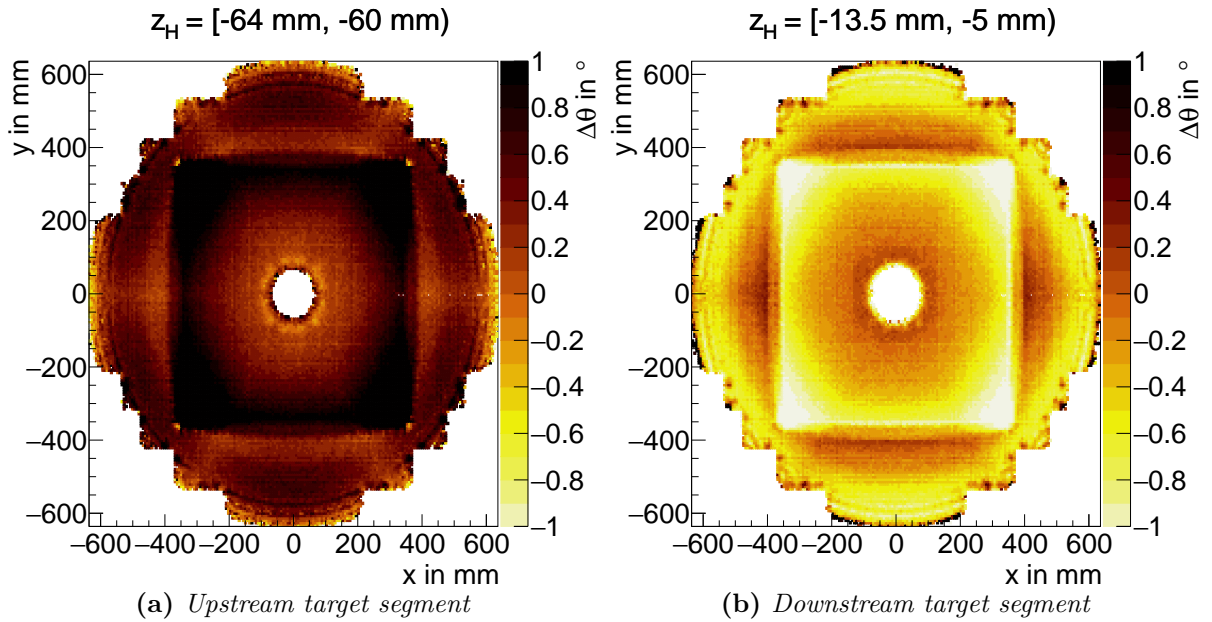
**Figure A.80** ♦ *Spatially resolved distribution of differences in $\theta$ using the old transformation for more negative $z_H$ (upstream target segment (a)) and $z_H$ close to zero (downstream target segment (b)). Where $\Delta\theta = \theta - \theta_e$, with $\theta/\phi$ the reconstructed and $\theta_e/\phi_e$ the simulated electron emission angles. The differences are averaged for each $x/y$ pixel on the RICH averaging over all particles having their vertices in the respective range. The simulated $1 \times 10^8$ electrons are emitted at $x = 0\,\mathrm{mm}$, $y = 0\,\mathrm{mm}$ uniformly over $2\pi$. All spatially resolved distributions have a pixel sized $7 \times 7\,\mathrm{mm}^2$ granularity and are artificially cut of at $\pm1°$.*



**(a)** *Differences in $\theta$*
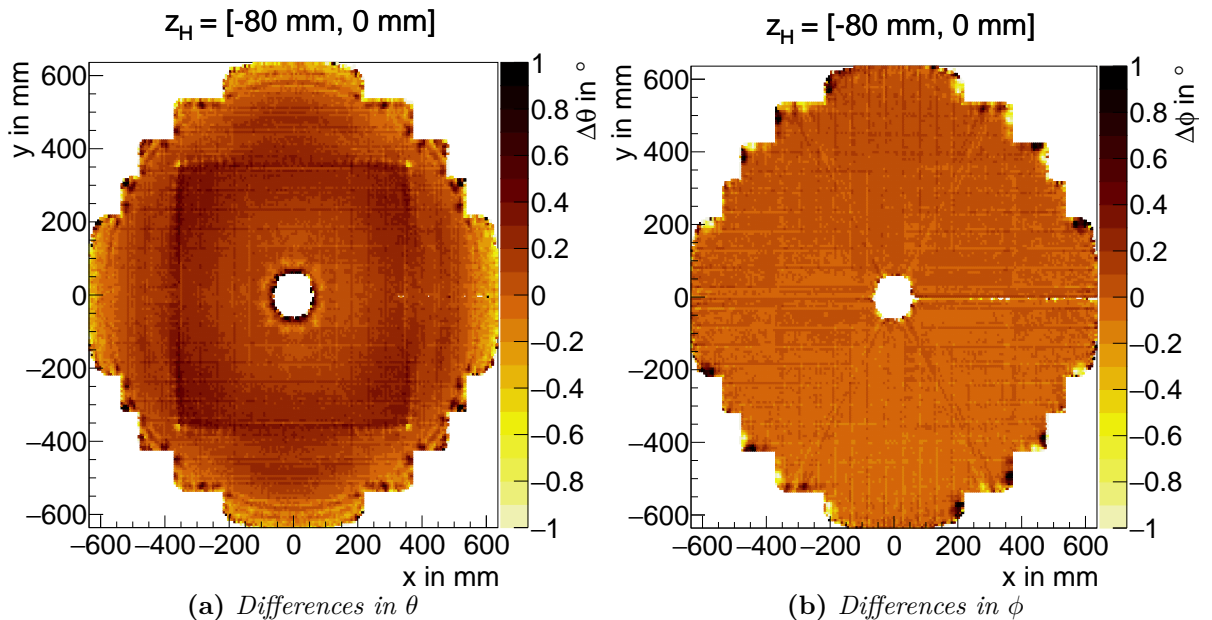
**(b)** *Differences in $\phi$*

**Figure A.81** ♦ *Spatially resolved distribution of differences in $\theta$ and $\phi$ using the old transformation. Where $\Delta\theta = \theta - \theta_e$ and $\Delta\phi = \sin(\theta_e)\phi - \phi_e$, with $\theta/\phi$ the reconstructed and $\theta_e/\phi_e$ the simulated electron emission angles. The differences are averaged for each $x/y$ pixel on the RICH over all electron vertices $z_H = [-80, 0]\,\mathrm{mm}$. The $1 \times 10^8$ electrons are emitted at $x = 0\,\mathrm{mm}$, $y = 0\,\mathrm{mm}$ uniformly over $2\pi$. All spatially resolved distributions have a pixel sized $7 \times 7\,\mathrm{mm}^2$ granularity and are artificially cut of at $\pm1°$.*
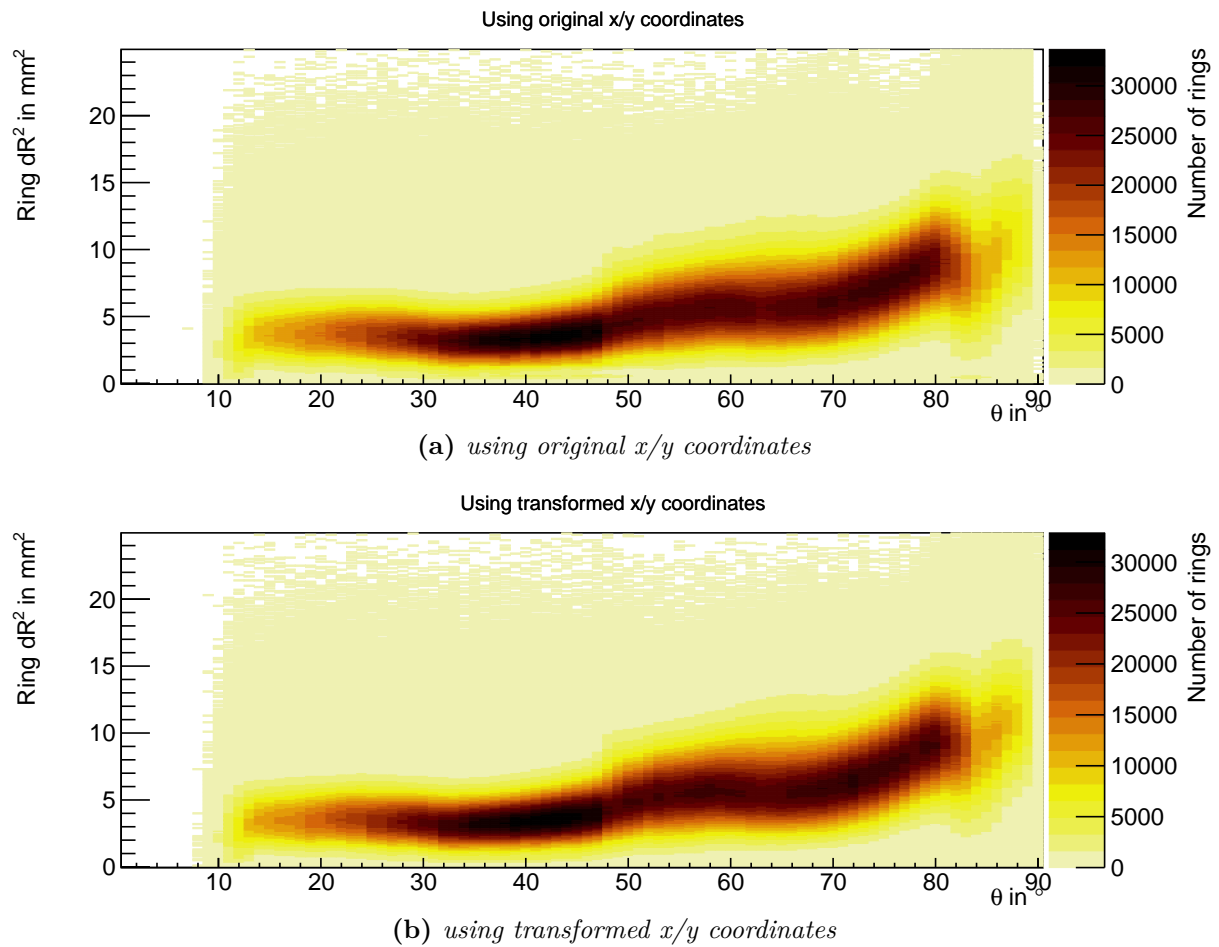
**(a)** *Differences in θ*
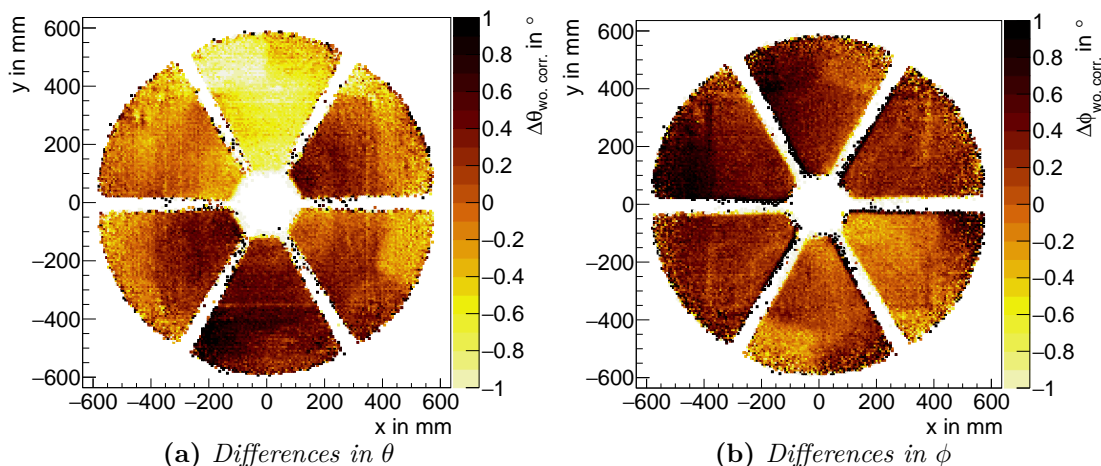


**(b)** *Differences in φ*

**Figure A.82** ♦ *Spatially resolved distribution of differences in θ and φ with respect to real data. The transformation used is the map based transformation but **not applying the experimental alignment**. Thus this figure represents the angular differences between simulation and real data. Where $\Delta\theta = \theta - \theta_{MDC}$ and $\Delta\phi = \sin(\theta_{MDC})\phi - \phi_{MDC}$, with $\theta/\phi$ the reconstructed and $\theta_{MDC}/\phi_{MDC}$ the emission angles reconstructed by the MDC. The electron candidates used are from $\pi^0$-Dalitz decays defined by electrons with opening angle $OA > 9°$, decay vertex $z_d$ in proximity of event vertex $z_e$ through $z_e - 20\,mm < z_d < z_e + 20\,mm$, and $m_{mother} < 150\,^{MeV}\!/c^2$.*
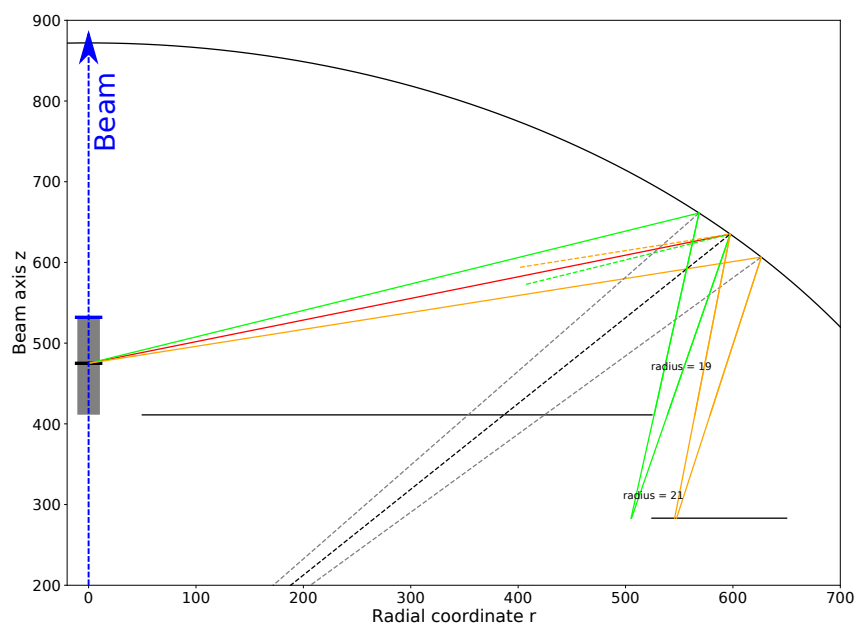


**Figure A.83** ♦ *Sketch showing a slice of the RICH detector for a single $\phi = 45°$, visualizing the first possible and the last possible Cherenkov photon reflection for the "right" (orange) and "left" (green) "sides" of the Cherenkov ring. The Beam in this figure is at $r = 0$ and moves along the y-axis, where $r = \sqrt{x^2 + y^2}$ is the radial coordinate. The y-axis resembles the beam axis position with respect to the mirror sphere center at $z = 0$, which thereby is also the origin of the mirror normals (black/gray dashed lines). $\theta = 75°$ is the angle under which the particle is ejected from the target area (gray), where the exact origin of the particle trajectory (red line) is at the position indicated by the black bar. The blue bar at the target area visualizes the zero position of the HYDRA-Framework. The reflections from the mirror sphere (black) then travel towards the two photon detection planes indicated by horizontal black lines. For this special case, the "left" side of the Cherenkov ring is not detected by any photon sensor, as it hits the vertical gap between the two photon detection planes.*

**(a)** *using original x/y coordinates*



**(b)** *using transformed x/y coordinates*

**Figure A.84** ♦ *Distribution of $dR^2$ over $\theta$ using the original- **(a)** or transformed $x/y$ coordinates **(b)**. $dR^2$ thereby is the sum of the squared differences between each hit and the ring, divided by the number of hits. The distribution is derived using $1 \times 10^8$ simulated electrons emitted at $z_H = [-80, 0]$ mm $x = 0$ mm, $y = 0$ mm and distributed uniformly over $2\pi$. Transformation was done using polynomials that approximate a uniform radial distribution of $23$ mm over full $\theta$ and $\phi$. Where the radius depends on $\phi$ solely due to the position of the transition region between inner and outer photon detection plane.*
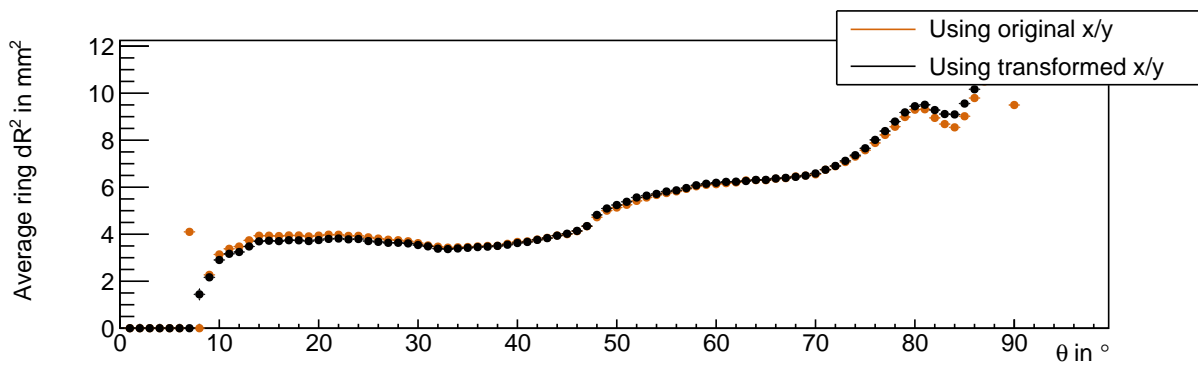
(a) *Mean progression*
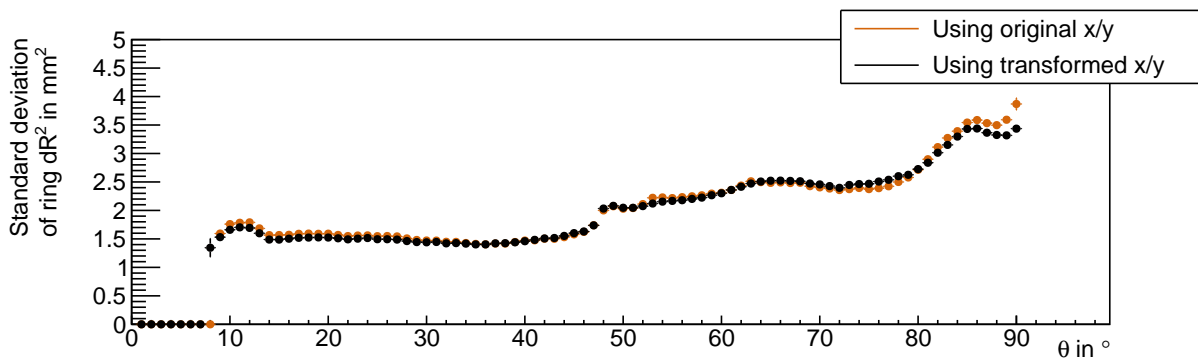


(b) *Standard deviation progression*

**Figure A.85** ♦ *Average **(a)** and standard deviation **(b)** of the $dR^2$ distribution as function of $\theta$ (1°-binning) for original and transformed $x/y$ coordinates. Comparing the distribution derived based on original (cf. Fig. A.84a) and transformed (cf. Fig. A.84b) $x/y$ coordinates.*

# B

## Detailed explanations

This appendix gives more in-depth explanations to some of the procedures and derivations touched on during the main part of this thesis.

## B.1 Differentiation procedure for integrated rate spectra

This section will further elaborate on how to derive a statistical pulse amplitude spectrum from a measured integrated one. This derivation is done by always comparing the rate at one threshold with the rate at another e.g. larger threshold. The resulting difference must then be the rate of pulses with a pulse amplitude in-between those two thresholds. Phrased differently, one derives the derivative of the originally obtained rate spectrum. For obvious reasons this only holds true if the uncertainty on the two measured rates is low compared to the rate measured, thus resulting not in a "real" pulse amplitude spectrum but only in a "statistical" one. The basis for this differentiation is the median of the measured rates $\tilde{r}(x)$, with $x$ being the different thresholds. This median is derived of ten measurements each 3 seconds long. It helps to reject sudden spikes in the measured rates and thus leads to an overall more homogeneous "integrated" pulse amplitude spectrum. The statistical rate $r'(x)$ is derived through differentiation via the five-point stencil

$$r'(x) \approx -\frac{-\tilde{r}(x + 2h) + 8\tilde{r}(x + h) - 8\tilde{r}(x - h) + \tilde{r}(x - 2h)}{12h} \, , \tag{B.1}$$

where $h$ is the difference in mV between one threshold setting and the next. The additional negation of the whole formula is necessary, as otherwise, the ever decreasing rate for increasing thresholds would result in an always negative statistical rate. This way of calculating the derivative has the benefit of combining interpolation with the derivative in one step[1].

---

[1]A way of representing the five-point stencil is the derivative of the quartic Lagrange "interpolating" polynomial.

## B.2  Procedure to build raw hits from single edges in HYDRA

In the RICH unpacker in HYDRA, (leading and trailing) edges measured by each DiRICH channel are combined using the following pseudocode.

---

**Algorithm 1** Code to build raw hits from single edges in HYDRA (HRich700Trb3Unpacker)

---

1: **for** *channel* in all DiRICH channels **do**
2:     Retrieve cut values on leading edge and time over threshold from database
3:     $LE_{\text{low}}$, $LE_{\text{high}}$
4:     $ToT_{\text{low}}$     ▷ Channel individual time over threshold cut retrieved from Database. $0\,\text{ns}$ minimum.
5:     $ToT_{\text{high}}$               ▷ Retrieved from Database. $15\,\text{ns}$ standard
6:     **for** $LE$ in all leading edges of this *channel* **do**
7:         **if** $LE < LE_{\text{low}}$ **or** $LE > LE_{\text{high}}$ **then continue**
8:         **end if**
9:         **for** $TE$ in all unused trailing edges (of this *channel*) with $TE > LE$ **do**
10:             $ToT = TE - LE$
11:             **if** $ToT < ToT_{\text{low}}$ **then continue**     ▷ Discard this trailing edge but see if the current LE can be combined with the next one
12:             **else if** $ToT > ToT_{\text{high}}$ **then break**         ▷ Discard the current LE
13:             **else**
14:                 addRawHit($LE$,$ToT$)    ▷ Build RICHRawHit hit with this LE and TE pair **break**         ▷ Move on to next LE and mark this TE as used
15:             **end if**
16:         **end for**
17:     **end for**
18: **end for**

---

## B.3 Hit track matching for RICH (photon) hits

The check if a bare hit is in the vicinity of a track candidates is split into two parts. First a check is made if the hit distance to the track is not larger than a fixed radius $r_{\text{max}}$. If this is not the case, an additional check needs to be made that takes into account the track position's uncertainty. Starting with the first check a hit is naturally assumed in the vicinity of a track, if its radial distance $\Delta r$ is lower than a given fixed radius $r_{\text{max}}$.

$$\Delta x = x_{\text{hit}} - x_{\text{track}}$$
$$\Delta y = y_{\text{hit}} - y_{\text{track}} \tag{B.2}$$
$$\Rightarrow \Delta r = \sqrt{\Delta x^2 + \Delta y^2} \leq r_{\text{max}} . \tag{B.3}$$

Where $x_{\text{hit}}/y_{\text{hit}}$ are the center coordinates of the fired pixel and $x_{\text{track}}/y_{\text{track}}$ result from the (reverse) transformation of $\phi_{\text{track}}/\theta_{\text{track}}$ to "pixel coordinates" in the RICH. If the hit is found in this region it is assumed to belong to the according track. If $\Delta r$ is slightly larger than $r_{\text{max}}$ one needs to check if the uncertainty on the track's position would still allow for the hit to be assumed close. The track's position $x_{\text{track}}/y_{\text{track}}$ in the RICH is not precise but is allowed to vary within the $dQA$ limit, this variation also needs to be taken into account. This limit on the angular variation ($dQA$) is hard to apply to the current Cartesian coordinates. Therefore an imaginary rim-point ($x_{\text{rim}}$,$y_{\text{rim}}$) is generated, indicating the position of the hit when moving it the distance of $r_{\text{max}}$ closer to the track.
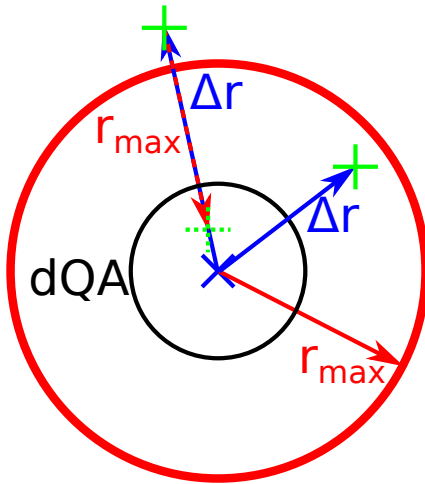


**Figure B.1** ♦ *Illustration of the hit track matching. Green plusses mark photon hits, while the blue cross depicts the track position. For the photon hit outside of the maximum distance $r_{max}$ the imaginary rim point (green dotted plus) is generated through "moving" the photon hit by $r_{max}$ towards the track position. This imaginary point is then checked if it still lies within the dQA area (black) around the track. The dQA circle is depicted artificially large for visibility reasons.*

This is shown in figure B.1 using equations (B.4). Here, one (green) point can directly be assumed correlated to the track as its $\Delta r$ is smaller than $r_{\text{max}}$. The other (green) point lies further away. Thus the imaginary rim-point is calculated first according to

$$x_{\text{rim}} = (1 - {r_{\text{max}}}/{\Delta r}) \cdot \Delta x + x_{\text{track}}$$
$$y_{\text{rim}} = (1 - {r_{\text{max}}}/{\Delta r}) \cdot \Delta y + y_{\text{track}} . \tag{B.4}$$

This resulting rim-point can then be transformed back to spherical coordinates such that a cut

on $dQA$ is applicable

$$dQA = \sqrt{\Delta\theta(x_{\rm rim}, y_{\rm rim})^2 + \Delta\phi(x_{\rm rim}, y_{\rm rim})^2} \,, \tag{B.5}$$

$$\text{with } \Delta\theta_{\rm rim} = \theta_{\rm rim} - \theta_{\rm track}$$

$$\text{and } \Delta\phi_{\rm rim} = \sin(\theta_{\rm track})(\phi_{\rm rim} - \phi_{\rm track}) \,,$$

where again the $dQA$ needs to be smaller than the given maximum $dQA_{\rm max}$, for the hit to be assumed to belong to the according track. In the following chapters this artificial and slightly different $dQA$ is named "absolute angular equivalent".

## B.4 Estimation on average number of photons per pixel

This number can be derived from the average number of pixels per ring divided by the average number of photons. The number of pixels per ring can be estimated via a quick simulation. Using the average ring radius of $\sim 23\,\text{mm}$ and average $dR$ – which is the average quadratic distance between hits and their ring – of $\sim 9\,\text{mm}$ one can simulate the average number of pixels that could see photons[2] to be 42.36. This is shown in figure B.2. The average number of photons per ring is found to be 25 as can be seen in figure B.3. With this one derives the occupancy to be $occ \approx 0.59$ and with that the average number of photons if a hit is registered to be $\overline{P_\lambda(n > 0)} \approx 1.51$ according to a Poisson distribution

$$P_\lambda(n) = \frac{\lambda^n}{n!}e^{-\lambda} \Rightarrow P_\lambda(0) = e^{-\lambda}$$

$$\Rightarrow occ = 1 - e^{-\lambda} \Leftrightarrow \lambda = -ln(1 - occ)$$

$$\Rightarrow P_\lambda(0) = 1 - occ$$

---

[2] Taking into account the $2\sigma = 6\,\text{mm}$ region around the ring and therefore 95% of all photons that would be emitted in the ring according to a Gaussian profile. This is very much in line with the encircled area with radius 30 mm over which hit summation is carried out.
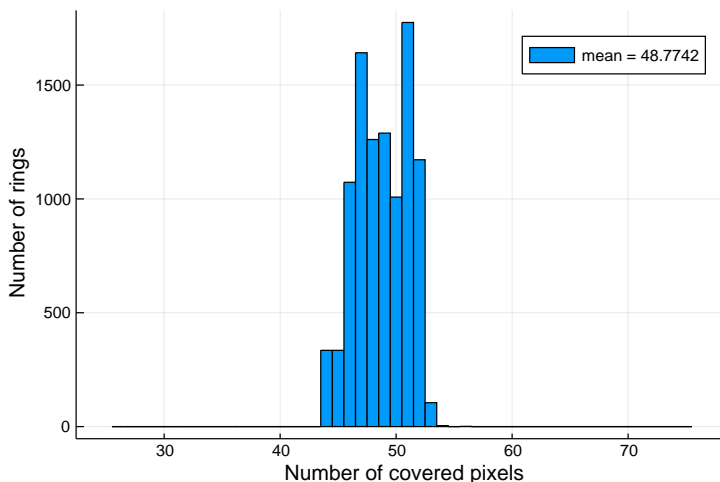


**Figure B.2** ♦ *Simulated number of pixels per ring. The toy simulation is based on randomizing the center of the ring on a grid with $7 \times 7\,\text{mm}^2$ pixels and counting the number of pixels, where $^1/_9$ of the pixel is covered by the ring-ribbon. The ring-ribbon is the ring shaped area with width of $\pm 6\,\text{mm}$ around the ring center with a radius of $23\,\text{mm}$. The mean of $49\,\text{pixels}$ can be taken from the legend.*
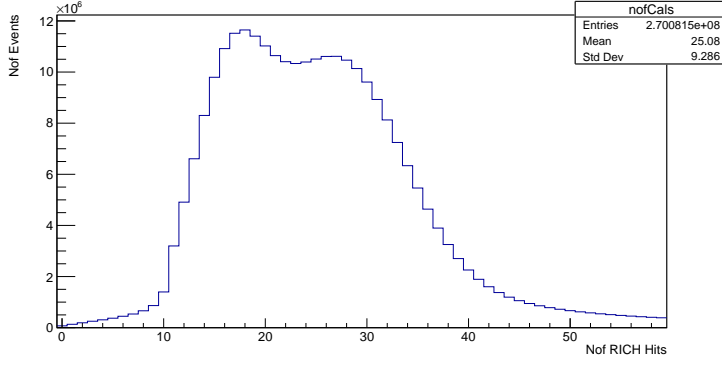
**Figure B.3** ♦ *Number of hits in an area around the electron candidate. They are counted in circular areas with radius* 30 mm *and added angular difference equivalent of* 2° *around electron candidates. With one ring being required in the proximity of the same candidate. The mean of* 25 *hits can be taken from the legend.*

$$\overline{P_\lambda(n)} = \sum_{n=0}^{\infty} n \cdot P_\lambda(n)$$

$$\Rightarrow \overline{P_\lambda(n > 0)} = \sum_{n=1}^{\infty} \frac{n \cdot P_\lambda(n)}{1 - P_\lambda(0)}$$

$$\Rightarrow \overline{P_\lambda(n > 0)} = \frac{\overline{P_\lambda(n)}}{1 - P_\lambda(0)}$$

$$\Rightarrow \overline{P_{occ}(n > 0)} = \frac{\overline{P_{\lambda=-ln(1-occ)}(n)}}{occ}$$

$$\Rightarrow \overline{P_{occ}(n > 0)} = \frac{-ln(1 - occ)}{occ} \; .$$

This approximation however only holds true if the probability for a pixel to see photons from e.g. a close double ring is the same for all pixels, which seems to be the case for all pixels not on the outer rim nor on the most inner part of the detector. Here one only finds a slightly larger occupancy for the WLS coated MAPMTs and a lower occupancy on the outer rim and the spoke regions of the detector as is depicted in figure B.4. These derived occupancies are not robust on the per channel level which means that only global parameters for occupancy and thus average photon count per event should be used.
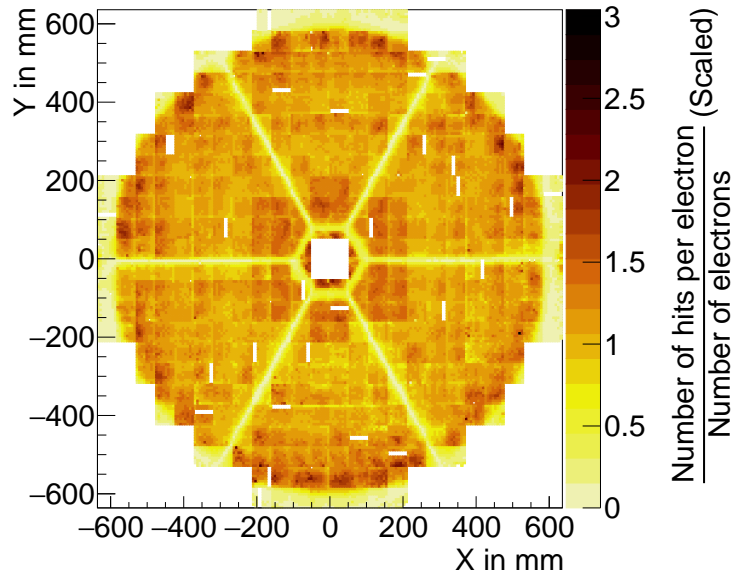
**Figure B.4** ♦ *Scaled occupancy derived via dividing the detected number of hits correlated to an electron candidate for each pixel by the number of electrons which would be able to leave a detectable signal in the same pixel. Measuring the number of hits correlated to an electron candidate is done by checking if a hit was detected in a pixel when a electron candidate was in a circular ares with radius* 30 mm *and added angular difference equivalent of* 2°*. The number of detectable signals from electron candidates is derived via counting the number of times where an electron candidate was in the same circular area. The quotient is then scaled by terms of the detector mean. Visibly the outer rim and spokes show significantly lower occupancy. The slight increase close before the outer rim comes from close double rings, where the second electron candidate was not detected by the rest of the detector. Same holds true for the very inner part of the detector. Overall the detector seems very homogeneously illuminated.*

## B.5  Approximation of the best possible ring matching resolution

The best possible ring matching resolution achievable taking into account the resolution reducing pixel size of the MAPMTs and the ring fitting uncertainties can be approximated focusing on a small area/volume in $x/y$ and $z$. In this small volume the average standard deviation in the difference distribution between $\theta/\phi$ towards the correct $\theta/\phi$ must reflect the best possible resolution. For this test, the $z$-range is divided into 15 segments (the same as for the target in the HADES experiment), taking the standard deviation $\sigma$ in $\theta$ and $\phi$ for each pixel on an $x/y$-map dividing the HADES detector into $192 \times 192$ regions [3]. Each standard deviation of this three dimensional pixel $(x/y/z)$ is filled into the stacked histograms depicted in figures B.5a for $\theta$ and b for $\phi$. The median is taken for each slice in $z$ individually taking the average over all medians in the end as estimator for the maximum resolution possible. Using the median, large outliers are discounted, focusing more on the peak region visible in the figure. Obviously this method is flawed to a certain degree, as the granularity in $x/y$ but especially in $z$ must lead to a slight overestimation of the best possible resolution. In that regard it is interesting to observe that both $\sigma_{\Delta\theta}$ and $\sigma_{\Delta\phi}$ show a similar increasing trend for more negative $z_H$ and $z_H$ approaching

---

[3]192 is actually the maximum number of pixels along $x$ or $y$

**(a)** *Standard deviation in $\theta$*



**(b)** *Standard deviation in $\phi$*
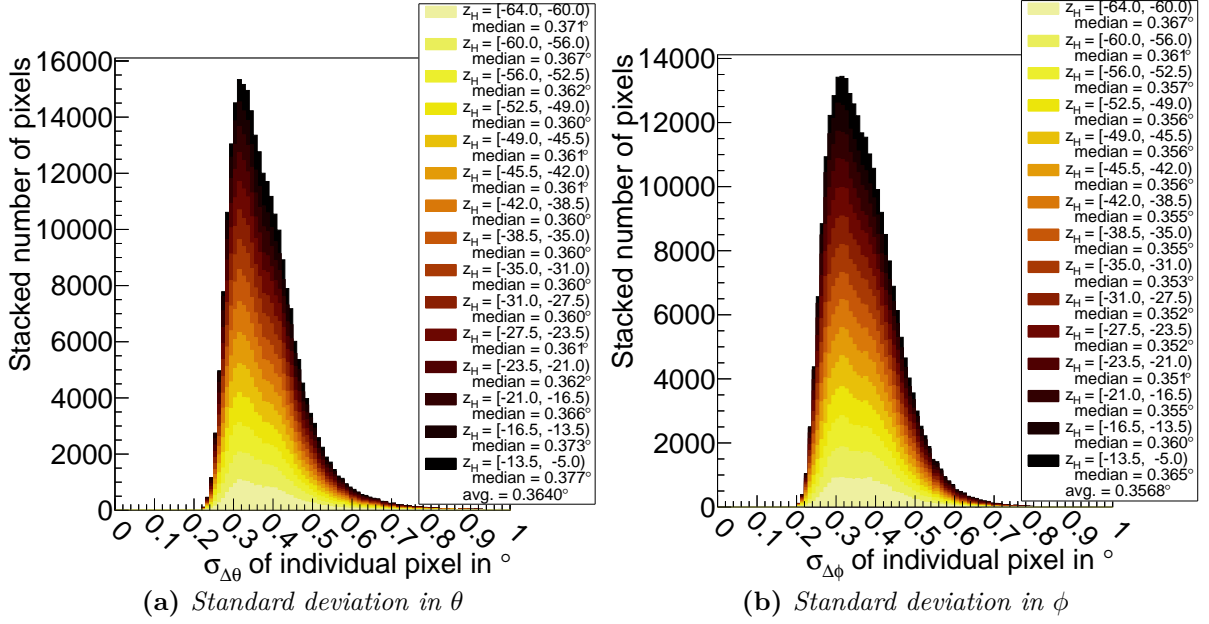
**Figure B.5** ♦ *Standard deviations in the difference distribution between $\theta$ **(a)** and $\phi$ **(b)** of the RICH ring and the $\theta_e/\phi_e$ of a simulated electron for different reconstruction positions in the RICH. $\theta/\phi$ are thereby transformed from the ring-center $x/y$-position using the here described method. The standard deviation is derived inside of $7 \times 7\,\mathrm{mm}^2$ pixels in $x/y$ for the measured ring position and larger bins in $z_H$ for the electron vertex' position along the beam axis. This means that one entry in the histogram is the standard deviation in the respective angular difference for all rings whose center is in one single bin in $x/y$ and whose corresponding simulated electron are emitted inside one bin in $z_H$. Each bin in $z_H$ is given a different color, as referenced in the legend. The median over the standard deviation of all pixels in $x/y$ is taken for each bin in $z_H$ individually. The average over all those medians is also denoted in the legend. The $1 \times 10^8$ electrons are simulated with vertices $z_H = [-80, 0]\,\mathrm{mm}$ emitted at $x = 0\,\mathrm{mm}$, $y = 0\,\mathrm{mm}$ uniformly over $2\pi$.*

zero, thus showing that indeed different $z_H$ regions lead to an overestimation. It is further supporting to find, that at $\sigma_{\Delta\theta}$ and $\sigma_{\Delta\phi}$ both have their averaged median over the different $z_H$ at approximately $0.36°$. The results are furthermore consistent with the old transformation in place (cf. B.6). Still, this way of approximation overestimates the maximum possible resolution slightly, as becomes clear through comparison with the gained results from before. There the new transformation led to a global standard deviation in $\phi$ in the order of $\sigma_{\Delta\phi} = 0.35001$, being lower than the here determined maximum resolution, but still larger than the lowest maximum resolutions found for different $z_H$. It is nonetheless soothing to find, that the resulting standard deviations in $\phi$ of all transformations are close to each other indicating that nearly maximum possible resolution is reached. This behaves differently for $\theta$, where the standard deviation is even still exceeding the overestimated best possible resolution This is explicable by the problem of only using one corrective map in $\theta$, where already large differences in the ring fitters behavior are found comparing the transformation at different $z$-values to another (cf. again Fig. A.79 appendix pg. 231).

**(a)** *Standard deviation in θ*

**(b)** *Standard deviation in φ*
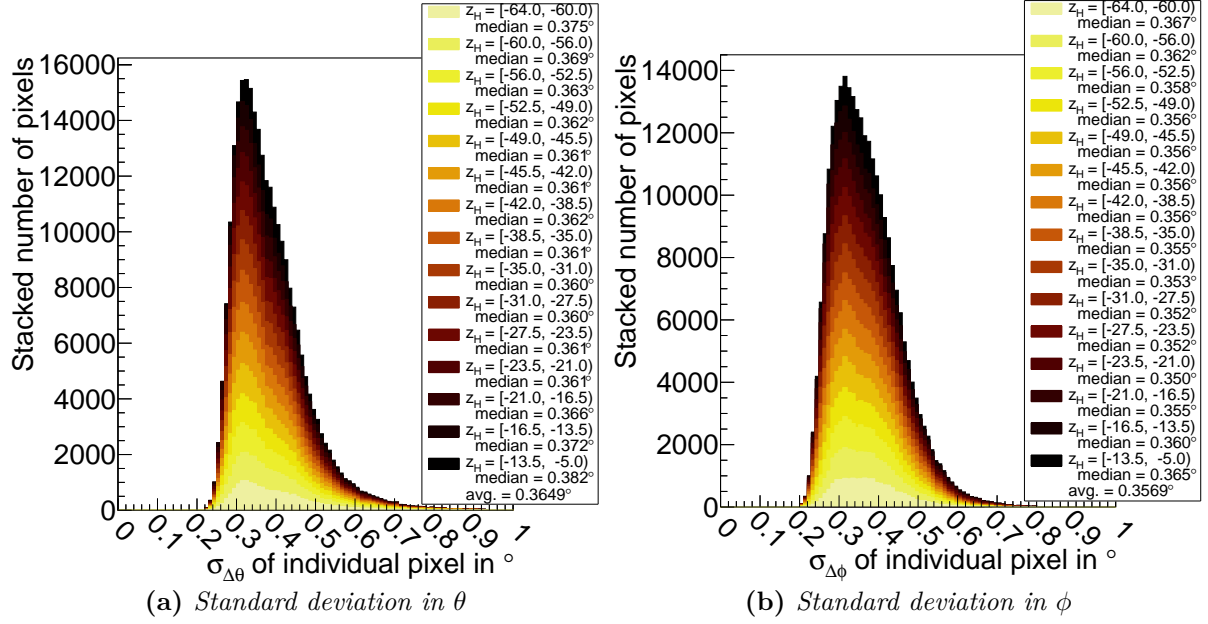
**Figure B.6 ♦** *Standard deviations in the difference distribution between θ **(a)** and φ **(b)** of the RICH ring and the $\theta_e/\phi_e$ of a simulated electron. θ/φ are thereby transformed from the ring-center x/y-position using the old method used in Hydra. The standard deviation is derived inside of $7 \times 7\,\mathrm{mm}^2$ pixels in x/y for the measured ring position and larger bins in $z_H$ for the electron vertex' position along the beam axis. This means that one entry in the histogram is the standard deviation in the respective angular difference for all rings whose center is in one single bin in x/y and whose corresponding simulated electron was emitted inside one bin in $z_H$. Each bin in $z_H$ is given a different color, as referenced in the legend. The median over the standard deviation of all pixels in x/y is taken for each bin in $z_H$ individually. The average over all those medians is also denoted in the legend. The $1 \times 10^8$ electrons are simulated with vertices $z_H = [-80, 0]\,\mathrm{mm}$ emitted at $x = 0\,\mathrm{mm}$, $y = 0\,\mathrm{mm}$ uniformly over $2\pi$.*

## B.6 Detailed derivation of a coordinate transformation $x_{\mathrm{old}}/y_{\mathrm{old}} \mapsto x_{\mathrm{new}}/y_{\mathrm{new}}$ unifying ring radii

The transformation uses

$$r_{\pm,0}(\theta; \dots) = \frac{2kz^2 s_\theta^3 - kr_m^2 s_\theta - r_m^2 z s_\theta + (2kzc_\theta s_\theta \pm (2kzs_\theta^2 - r_m^2)e)f \mp (2kz^2 c_\theta s_\theta^2 - kr_m^2 c_\theta)e}{2z^2 c_\theta s_\theta^2 - r_m^2 c_\theta \pm 2f(ezc_\theta s_\theta \mp zs_\theta^2) \pm (2z^2 s_\theta^3 - r_m^2 s_\theta)e}$$

$$r_{\pm,1}(\theta; \dots) = -\left( kr_m^2 c_c^4 + 2kr_m^2 c_c^2 s_c^2 + kr_m^2 s_c^4 - az^2 c_c s_c^2 - a^3 c_c - (r_m^2 c_c^2 s_c^2 + r_m^2 s_c^4)z \right) \qquad \text{(B.6)}$$

$$\cdot \frac{2bs_c\left(\frac{(z-bc_c)c_c}{d} - \frac{bs_c^2}{d}\right)/d + s_c}{r_m^2 c_c^5 + 2r_m^2 c_c^3 s_c^2 + r_m^2 c_c s_c^4 - 2(c_c^3 s_c^2 + c_c s_c^4)z^2 + 2a(c_c^2 s_c^2 + s_c^4)z} - bs_c \text{ , with}$$

$$c_\theta = \cos(\theta) \qquad s_\theta = \sin(\theta)$$

$$c_c = \cos(\theta \pm \theta_c) \qquad s_c = \sin(\theta \pm \theta_c)$$

$$a = \sqrt{r_m^2 - z^2 s_c^2} \qquad b = zc_c - a$$

$$d = \sqrt{(-z + bc_c)^2 + (bs_c)^2} \qquad e = \sqrt{n^2 - 1} \qquad f = \sqrt{-z^2 s_\theta^2 + r_m^2} \text{ ,}$$

which describes the position on the photon detection planes at $z = k$ of the right/left "Cherenkov-photon" ($\pm$) reflected center/off-center (0/1). To retrieve the radial transformation being $T : r_{old} \mapsto r_{new}$ therefrom, the easiest way is to use an iterative approach with the ring radius as a arbitrary constant of $r_{Ring} = 23\,\text{mm}$ [4]. Focusing first on a single $\theta$ for explanatory purposes one finds the four intersection points with one detection plane $(r_{\pm,0/1}(\theta; z, k, r_m, n))$. Two left points building the left part of the ring $r_{old,left}$ through averaging and two right points building the right side of the ring $r_{old,right}$. Requesting all rings to have the same radius of $r_{Ring} = 23\,\text{mm}$ in the new transformation, those derived points need to translate to new points through

$$T(r_{old,\ left}) \mapsto r_{new,\ left} = r_{old,\ left}$$
$$T(r_{old,\ right}) \mapsto r_{new,\ right} = T(r_{old,\ left}) + 2r_{Ring} = r_{old,\ left} + 2r_{Ring}\,.$$

This is of course only easily derivable here, as only one $\theta$ is looked at and for all following derivations $r_{new,left}$ ($\neq r_{old,left}$) needs to be reconstructed using the transformation $T$. Thus one can only build the transformation recursively. After choosing the first point as shown here for e.g. $\theta = 0°$, all following $r_{new,right}$ are approximated by extrapolating the range between the already derived points linearly. This is easily possible as with a slightly increasing $\theta$ the next $T(r_{old,left})$ should always lie in-between the previously derived $r_{new,left}$ and $r_{new,right}$ This way of extrapolation therefore might only deliver slightly incorrect results for the very first steps. However, the transformation derived in this way is only valid for rings on one photon detection plane. This is especially critical, as the transformation for each plane is derived through summation and might already differ quite substantially at the transition point between the two staggered planes. An easy way of continuing the transformation linearly between the two planes is to add the difference between the two transformations, at the exact transformation point, to the points of the outer transformation.

$$r_{new,\ outer,\ ctd.} = r_{new,\ outer} + (T_{outer}(r_{old,\ planechange}) - T_{inner}(r_{old,\ planechange}))\,.$$

This continuation is therefore dependent on $\phi$ as $r_{old,\ planechange} = {}^{371\,\text{mm}}/\cos(\phi)$ with $371\,\text{mm}$ being the width of the inner photon detection plane at $\phi = 0°$. This approach is however incorrect in the sense that it does not take the constant ring radius into account at the transition. A better way of transforming linearly between the two planes is to transform not at the same $r_{old,\ planechange}$ but rather using the same angle $\theta$ for inner and outer plane. This corresponds to

$$r_{new,\ outer,\ ctd.} = r_{new,\ outer} + (T_{outer}(r_{old,\ \theta,\ outer}) - T_{inner}(r_{old,\ \theta,\ inner}))\,,$$

where $r_{old,\ \theta,\ inner} = r_{old,\ planechange}$ which means that exactly that one $\theta$ is taken, where the ring center on the inner plane lies at the transition point. Respectively $r_{old,\ \theta,\ outer}$ refers to the old position on the outer plane where the particle with the same $\theta$ would have its ring center. Thereby, depending on the particle vertex $z$, $r_{old,\ \theta,\ inner}$ can, but must not necessarily equal $r_{old,\ \theta,\ outer}$. Furthermore, $r_{old,\ \theta,\ outer}$ might very well be a position which does not exist in the real detector, as particles for certain $\theta$ and $z$ combinations, i.e. large $\theta$ and low $z$, do

---

[4]The radius is chosen here, as it is close to the actual average ring radius on the detector.

pass the inner photon detection plane at larger radial coordinates $r$ than they pass the outer photon detection plane (see a similar effect in figure A.83 in the appendix pg. 233). The resulting transformations are again approximated with polynomials in $r$, where each parameter is a polynomial in $z$. Transformations $T_{\text{inner}}(r_{\text{old, inner}})$ and $T_{\text{outer}}(r_{\text{old, outer}})$ are found to be well approximated by polynomials of $7^{\text{th}}$ degree in $r$ and $4^{\text{th}}$ in $z$. The polynomial approximating the correct transition between inner and outer transformation is more linear in $r$ but follows a more complex functional shape in $z$ and it thus of $5^{\text{th}}$ degree[5] in $r$ and $5^{\text{th}}$ degree in $z$. The polynomial approximating the transformation from the new $r_{\text{new}}$ to $\theta$ is chosen of order 6 in $r$ for inner and outer plane and of order 4 in $z$ for the inner plane but of order 5 in $z$ for the outer plane.

---

[5]Choosing a polynomial of larger degree made the fit result less robust over different $z$

# References

[Abl+17]  T. Ablyazimov et al. "Challenges in QCD matter physics –The scientific programme of the Compressed Baryonic Matter experiment at FAIR". In: *The European Physical Journal A* 53.3 (Mar. 2017), p. 60. DOI: `10.1140/epja/i2017-12248-y`. URL: `https://doi.org/10.1140/epja/i2017-12248-y`.

[Ada+05]  John Adams et al. "Experimental and theoretical challenges in the search for the quark gluon plasma: The STAR Collaboration's critical assessment of the evidence from RHIC collisions". In: *Nucl. Phys. A* 757 (2005), pp. 102–183. DOI: `10.1016/j.nuclphysa.2005.03.085`. arXiv: `nucl-ex/0501009`.

[Ada+15]  J. Adamczewski-Musch et al. "Influence of wavelength-shifting films on multianode PMTs with UV-extended windows". In: *Nuclear Instruments and Methods in Physics Research Section A: Accelerators, Spectrometers, Detectors and Associated Equipment* 783 (2015), pp. 43–50. DOI: `https://doi.org/10.1016/j.nima.2015.02.014`. URL: `https://www.sciencedirect.com/science/article/pii/S0168900215001953`.

[Ada+17]  J. Adamczewski-Musch et al. "The RICH detector of the CBM experiment". In: *Nuclear Instruments and Methods in Physics Research Section A: Accelerators, Spectrometers, Detectors and Associated Equipment* 876 (2017). The 9th international workshop on Ring Imaging Cherenkov Detectors (RICH2016), pp. 65–68. DOI: `https://doi.org/10.1016/j.nima.2017.01.052`. URL: `https://www.sciencedirect.com/science/article/pii/S0168900217301109`.

[Ama17]  Weber Adrian Amatus. "Entwicklung von FPGA basierter Ausleseelektronik fur den HADES RICH upgrade und CBM RICH Detektor - online TDC Kalibrierung und DAC Schwellen Erzeugung". Master's Thesis. Heinrich-Buff-Ring 16, 35392, Gießen: II. Physikalisches Institut, Justus-Liebig-Universität, Giessen, Sept. 2017. URL: `https://indico.gsi.de/event/6440/contributions/29547/attachments/21461/27039/Masterthesis_AdrianWeber.pdf`.

[And+14]  O. V. Andreeva et al. "Forward scintillation hodoscope for nuclear fragment detection at the high acceptance dielectron spectrometer (HADES) setup". In: *Instrum. Exp. Tech.* 57 (2014), pp. 103–119. DOI: `10.1134/S0020441214020146`.

[Arn+88]  R. Arnold et al. "A ring imaging Cherenkov detector, the DELPHI barrel RICH prototype: Part B: Experimental studies of the detector performance for particle identification". In: *Nuclear Instruments and Methods in Physics Research Section A: Accelerators, Spectrometers, Detectors and Associated Equipment* 270.2 (1988), pp. 289–318. DOI: `https://doi.org/10.1016/0168-9002(88)90696-1`. URL: `https://www.sciencedirect.com/science/article/pii/0168900288906961`.

[Bel+94]  E.H. Bellamy et al. "Absolute calibration and monitoring of a spectrometric channel using a photomultiplier". In: *Nuclear Instruments and Methods in Physics Research Section A: Accelerators, Spectrometers, Detectors and Associated Equipment*

339.3 (1994), pp. 468–476. DOI: https://doi.org/10.1016/0168-9002(94)90183-X. URL: http://www.sciencedirect.com/science/article/pii/016890029490183X.

[Bla+09]  A. Blanco et al. "In-beam measurements of the HADES-TOF RPC wall". In: *Nuclear Instruments and Methods in Physics Research Section A: Accelerators, Spectrometers, Detectors and Associated Equipment* 602.3 (2009). Proceedings of the 9th International Workshop on Resistive Plate Chambers and Related Detectors, pp. 691–695. DOI: https://doi.org/10.1016/j.nima.2008.12.091. URL: https://www.sciencedirect.com/science/article/pii/S0168900208019645.

[Bor+10]  Szabolcs Borsanyi et al. "Is there still any $T_c$ mystery in lattice QCD? Results with physical masses in the continuum limit III". In: *JHEP* 09 (2010), p. 073. DOI: 10.1007/JHEP09(2010)073. arXiv: 1005.3508 [hep-lat].

[Cal+15]  Marta Calvi et al. "Characterization of the Hamamatsu H12700A-03 and R12699-03 multi-anode photomultiplier tubes". In: *JINST* 10.09 (2015), P09021. DOI: 10.1088/1748-0221/10/09/P09021. arXiv: 1506.04302 [physics.ins-det].

[Fil+02]  T.A Filippas et al. "Precision measurements of gas refractivity by means of a Fabry–Perot interferometer illustrated by the monitoring of radiator refractivity in the DELPHI RICH detectors". In: *Nuclear Instruments and Methods in Physics Research Section B: Beam Interactions with Materials and Atoms* 196.3 (2002), pp. 340–348. DOI: https://doi.org/10.1016/S0168-583X(02)01291-0. URL: https://www.sciencedirect.com/science/article/pii/S0168583X02012910.

[FK04]  Z. Fodor and S. D. Katz. "Critical point of QCD at finite T and mu, lattice results for physical quark masses". In: *JHEP* 04 (2004), p. 050. DOI: 10.1088/1126-6708/2004/04/050. arXiv: hep-lat/0402006.

[Foe13]  Klaus Foehl. *RICH two types.* from KlausFoehl, licenced under CC BY-SA 3.0 (https://creativecommons.org/licenses/by-sa/3.0/). Mar. 2013. URL: https://commons.wikimedia.org/wiki/File:RICH_two_types02_2013-03-15.svg.

[För16]  Jörg Förtsch. "Aufbau und Charakterisierung eines Serienteststandes für HAMAMATSU H12700 MAPMTs und erste Messergebnisse". Master's Thesis. Gaußstraße 20, 42119, Wuppertal: University of Wuppertal, Aug. 2016. URL: https://astro.uni-wuppertal.de/fileadmin/physik/astro/mainpage/publications/theses/Diplom/Foertsch-MSc.pdf.

[Fri18]  Jürgen Friese. *Mail with subject: "RICH goes green".* private communication via mail on 2018-04-18 10:17. Apr. 2018.

[Fri21]  Jürgen Friese. *Mail with subject: "Laser-System".* private communication via mail on 2021-04-07, 14:13. Apr. 2021.

[FT91]    I. Frank and Ig. Tamm. "Coherent Visible Radiation of Fast Electrons Passing Through Matter". In: *Selected Papers*. Ed. by Boris M. Bolotovskii, Victor Ya. Frenkel, and Rudolf Peierls. Berlin, Heidelberg: Springer-Verlag Berlin Heidelberg, 1991, pp. 29–35. DOI: `10.1007/978-3-642-74626-0_2`. URL: `https://doi.org/10.1007/978-3-642-74626-0_2`.

[FU20]    Roger Forty and Olav Ullaland. "Particle Identification: Time-of-Flight, Cherenkov and Transition Radiation Detectors". In: *Particle Physics Reference Library: Volume 2: Detectors for Particles and Radiation*. Ed. by Christian W. Fabjan and Herwig Schopper. Cham: Springer International Publishing, 2020, pp. 281–335. DOI: `10.1007/978-3-030-35318-6_7`. URL: `https://doi.org/10.1007/978-3-030-35318-6_7`.

[GKR15]   F. Gonnella, V. Kozhuharov, and M. Raggi. "Time over threshold in the presence of noise". In: *Nuclear Instruments and Methods in Physics Research Section A: Accelerators, Spectrometers, Detectors and Associated Equipment* 791 (2015), pp. 16–21. DOI: `https://doi.org/10.1016/j.nima.2015.04.028`. URL: `http://www.sciencedirect.com/science/article/pii/S0168900215005161`.

[Haa19]   Robin Haas. "Analyse von blobartigen Strukturen in der MAPMT Photodetektorebene des HADES-RICH Detektors in Ag+Ag-Kollisionen bei 1,58 AGeV Strahlenergie". Bachelor's Thesis. Heinrich-Buff-Ring 16, D-35392, Gießen: Justus Liebig Universität Giessen, Sept. 2019.

[HAD17]   HADES Collaboration. *Proposals for experiments at SIS18 during FAIR Phase-0*. Tech. rep. HADES. Darmstadt, 2017, 102 p. DOI: `10.15120/GSI-2019-00976`. URL: `https://repository.gsi.de/record/220071`.

[HAM19]   HAMAMATSU PHOTONICS K.K. *H12700 Datasheet*. accessed on 2020-07-28 14:53. 2019. URL: `https://www.hamamatsu.com/resources/pdf/etd/H12700_H14220_TPMH1379E.pdf`.

[Har17]   Szymon Harabasz. "Reconstruction of virtual photons from Au+Au collisions at 1.23 GeV/u". PhD thesis. Darmstadt: Technische Universität, 2017. URL: `http://tuprints.ulb.tu-darmstadt.de/6605/`.

[KEM18]   KEMET Electronics Corporation. *Flex Suppressor® Noise Suppression Sheet*. accessed on 2020-08-18 16:17. Sept. 2018. URL: `https://docs.rs-online.com/fd96/0900766b8171640a.pdf`.

[Kop14]   Jan Martin Kopfer. "Development of a prototype camera and Monte Carlo studies for the optimisation of the CBM-RICH detector". Dissertation. Gaußstraße 20, 42119, Wuppertal: University of Wuppertal, Feb. 2014. URL: `https://astro.uni-wuppertal.de/fileadmin/physik/astro/mainpage/publications/theses/PhD/Kopfer-Diss.pdf`.

[Kor+20]  Grzegorz Korcyl et al., eds. *A Users Guide to the TRB3 and FPGA-TDC Based Platforms*. TRB Collaboration, GSI, Aug. 2020. URL: `http://jspc29.x-matter.uni-frankfurt.de/docu/trb3docu.pdf`.

[Kor+21]   G. Kornakov et al. "Performance study and calibration strategy of the HADES scintillator TOF Wall with fast digital readout". 2021. URL: `https://arxiv.org/pdf/2103.07416`.

[Kor13]    Georgy Kornakov Van. "New advances and developments on the RPC tof wall of the HADES experiment at GSI". PhD thesis. U. Santiago de Compostela (main), 2013.

[Leb+10]   S. Lebedev et al. "Ring recognition and electron identification in the RICH detector of the CBM experiment at FAIR". In: *Journal of Physics: Conference Series* 219.3 (Apr. 2010), p. 032015. DOI: `10.1088/1742-6596/219/3/032015`. URL: `https://doi.org/10.1088/1742-6596/219/3/032015`.

[Leb20]    Semen Lebedev. *Mail with subject: "updates in code"*. private communication via mail on 2020-06-22 14:11. June 2020.

[Leh+15]   G. Lehaut et al. "Scintillation properties of N2 and CF4 and performances of a scintillating ionization chamber". In: *Nuclear Instruments and Methods in Physics Research Section A: Accelerators, Spectrometers, Detectors and Associated Equipment* 797 (2015), pp. 57–63. DOI: `https://doi.org/10.1016/j.nima.2015.05.050`. URL: `http://www.sciencedirect.com/science/article/pii/S0168900215007093`.

[Leo94]    William R. Leo. *Techniques for Nuclear and Particle Physics Experiments*. Springer-Verlag Berlin Heidelberg, 1994. DOI: `10.1007/978-3-642-57920-2`. URL: `https://www.springer.com/de/book/9783540572800`.

[Man21]    Mankiewicz. *NEXTEL Velvet Coating 811-21 – 9218 schwarz*. accessed on 2021-04-07, 18:31. Apr. 2021. URL: `https://www.nextel-coating.com/produkt/nextel-velvet-coating-811-21/`.

[Mar06]    Jochen Markert. "Untersuchung zum Ansprechverhalten der Vieldraht-Driftkammern niedriger Massenbelegung des HADES Experimentes". Dissertation. Johann Wolfgang Goethe-Universität, 2006. URL: `https://core.ac.uk/download/pdf/14502808.pdf`.

[Mar17]    Jochen Markert. *Tracking tutorial*. Talk given at the HADES Analysis Workshop 2017. Last accessed on 2021-04-03 15:48. May 2017. URL: `https://indico.gsi.de/event/5849/attachments/19695/24755/JMarkert_tracking_2013.pdf`.

[Mic+11]   J Michel et al. "The upgraded HADES trigger and data acquisition system". In: *Journal of Instrumentation* 6.12 (Dec. 2011), pp. C12056–C12056. DOI: `10.1088/1748-0221/6/12/c12056`. URL: `https://doi.org/10.1088/1748-0221/6/12/c12056`.

[Mik+06]   V.B. Mikhailik et al. "Scintillation properties of pure CaF2". In: *Nuclear Instruments and Methods in Physics Research Section A: Accelerators, Spectrometers, Detectors and Associated Equipment* 566.2 (2006), pp. 522–525. DOI: `https://doi.org/10.1016/j.nima.2006.06.063`. URL: `http://www.sciencedirect.com/science/article/pii/S0168900206012034`.

[MK14]     *2012 Asia-Europe-Pacific School of High-Energy Physics: Fukuoka, Japan 14 - 27 Oct 2012. 1st Asia-Europe-Pacific School of High-Energy Physics.* Comments: 8 lectures, 285 pages, published as CERN Yellow Report https://cds.cern.ch/record/1443909. CERN. Geneva: CERN, 2014. DOI: `10.5170/CERN-2014-001`. URL: `http://cds.cern.ch/record/1443909`.

[OL77]     J.J. Olivero and R.L. Longbothum. "Empirical fits to the Voigt line width: A brief review". In: *Journal of Quantitative Spectroscopy and Radiative Transfer* 17.2 (1977), pp. 233–236. DOI: `https://doi.org/10.1016/0022-4073(77)90161-3`. URL: `http://www.sciencedirect.com/science/article/pii/0022407377901613`.

[Pat19]    Vivek Patel. *Timing studies for COSY data.* Talk given at the CBM RICH meeting Gießen. Viewed on 2021-03-18 20:28. Sept. 2019. URL: `https://indico.gsi.de/event/9430/contributions/40852/attachments/32613/41696/timing_Cosy.pdf`.

[Pau19]    Christian Pauly. *Redirected graphic through mail with subject: "Magnet Test".* private communication via mail on 2019-02-25, 21:34. Feb. 2019.

[Pie+14]   J. Pietraszko et al. "Radiation damage in single crystal CVD diamond material investigated with a high current relativistic 197Au beam". In: *Nuclear Instruments and Methods in Physics Research Section A: Accelerators, Spectrometers, Detectors and Associated Equipment* 763 (2014), pp. 1–5. DOI: `https://doi.org/10.1016/j.nima.2014.06.006`. URL: `https://www.sciencedirect.com/science/article/pii/S0168900214007013`.

[Pie19a]   Jurek Pietraszko. *Picture of Ag target.* Picture uploaded internally. Viewed on 2021-04-01 17:14. Feb. 2019. URL: `http://web-docs.gsi.de/~webhades/media/logbook/mar19/Target_AgAg_window_pictures/20190411_103156.jpg`.

[Pie19b]   Jurek Pietraszko. *T0 setup for Ag beam in 2018/2019.* Talk uploaded internally. Viewed on 2021-04-01 17:14. Feb. 2019. URL: `http://web-docs.gsi.de/~webhades/media/logbook/mar19/T0Setup_2018.pptx`.

[Poc+95]   J. Pochodzalla et al. "Probing the Nuclear Liquid-Gas Phase Transition". In: *Phys. Rev. Lett.* 75 (6 Aug. 1995), pp. 1040–1043. DOI: `10.1103/PhysRevLett.75.1040`. URL: `https://link.aps.org/doi/10.1103/PhysRevLett.75.1040`.

[PT18]     V. Patel and M. Traxler. "The HADES-RICH upgrade using Hamamatsu H12700 MAPMTs with DiRICH FEE + Readout". In: *Journal of Instrumentation* 13.03 (Mar. 2018), pp. C03038–C03038. DOI: `10.1088/1748-0221/13/03/c03038`. URL: `https://doi.org/10.1088/1748-0221/13/03/c03038`.

[Ros20]    Adrian Rost. "Design, installation and commissioning of new read-out electronics for HADES ECAL and diamond detectors for T0-reconstruction and beam diagnostics". PhD thesis. Darmstadt: Technische Universität Darmstadt, 2020. URL: `http://tuprints.ulb.tu-darmstadt.de/12235/`.

## References

[SFK15]    K. Schmidt-Sommerfeld, J. Friese, and T. Kunz. "Feasibility study for a MAPMT readout of the HADES RICH". In: *Scientific Report 2014*. Vol. 2015-1. GSI Report. Darmstadt: GSI Helmholtzzentrum für Schwerionenforschung, 2015, p. 33. DOI: `10.15120/GR-2015-1-MU-NQM-HADES-29`. URL: `https://repository.gsi.de/record/183805`.

[Spi21]    Simon Spies. *Hades Logos Webpage*. accessed on 2020-04-03 12:44. 2021. URL: `https://hades-wiki.gsi.de/foswiki/bin/view/Collaboration/HadesLogos`.

[ST17]    *CBM Progress Report 2016*. Tech. rep. Darmstadt, 2017, pp. 74, 75. URL: `https://repository.gsi.de/record/201318`.

[Svo+14]    O. Svoboda et al. "Electromagnetic calorimeter for the HADES@FAIR experiment". In: *JINST* 9 (2014). Ed. by Pietro Govoni et al., p. C05002. DOI: `10.1088/1748-0221/9/05/C05002`.

[The+09]    The HADES Collaboration et al. "The high-acceptance dielectron spectrometer HADES". In: *Eur. Phys. J. A* 41.2 (2009), pp. 243–277. DOI: `10.1140/epja/i2009-10807-5`. URL: `https://doi.org/10.1140/epja/i2009-10807-5`.

[TK17]    M. Traxler and H. Kayan. *DiRICH3*. accessed on 2020-10-05 14:01. Nov. 2017. URL: `http://jspc29.x-matter.uni-frankfurt.de/trb/schematics/dirich3_all.pdf`.

[Tos+07]    Hakamata Toshikazu et al., eds. *PHOTOMULTIPLIER TUBES - Basics and Applications*. Third Edition (3a). Hamamatsu Photonics K.K., 2007. URL: `https://www.hamamatsu.com/resources/pdf/etd/PMT_handbook_v3aE.pdf`.

[TS18]    *CBM Progress Report 2017*. Tech. rep. CC BY 4.0. Darmstadt, 2018. DOI: `10.15120/GSI-2018-00485`. URL: `https://repository.gsi.de/record/209729`.

[Uğu+13]    C. Uğur et al. "264 Channel TDC Platform applying 65 channel high precision (7.2 psRMS) FPGA based TDCs". In: *2013 IEEE Nordic-Mediterranean Workshop on Time-to-Digital Converters (NoMe TDC)*. 2013, pp. 1–5. DOI: `10.1109/NoMeTDC.2013.6658234`.

[Vic20a]    Vicor Corporation. *ZVS Regulators PI33xx-x0*. accessed on 2020-08-19 10:37. Aug. 2020. URL: `http://www.vicorpower.com/documents/datasheets/ds_pi33xx.pdf`.

[Vic20b]    Vicor Corporation. *ZVS Regulators PI33xx-x1*. accessed on 2020-08-19 10:37. Apr. 2020. URL: `http://www.vicorpower.com/documents/datasheets/ds_pi33xx-01.pdf`.

[Web20a]    Adrian Weber. *Mail with subject: "RE: Daten von Magnet Feld Messung 2019"*. private communication via mail on 2020-10-29 14:08. Oct. 2020.

[Web20b]    Adrian Weber. *Mail with subject: "RE: Daten von Magnet Feld Messung 2019"*. private communication via mail on 2020-10-29, 15:20. Oct. 2020.

[Wol16a]    Wolfram Research (2007). *ExtremeValueDistribution*. accessed on 2020-12-31 12:57. 2016. URL: `https://reference.wolfram.com/language/ref/ExtremeValueDistribution.html`.

[Wol16b]    Wolfram Research (2007). *GumbelDistribution.* accessed on 2020-12-31 12:57. 2016. URL: `https://reference.wolfram.com/language/ref/GumbelDistribution.html`.

[Zei+99]    K. Zeitelhack et al. "The HADES RICH detector". In: *Nuclear Instruments and Methods in Physics Research A* 433 (Aug. 1999), pp. 201–206. DOI: `10.1016/S0168-9002(99)00371-X`.

# Acknowledgments

Throughout the course of such a doctoral thesis and the way to it, one comes across many people that shape oneself and this thesis. It is sheer impossible to mention everybody, however I want to thank you all no matter how large or small your contribution was. Without you this thesis would not exist as it is.

I obviously want to thank Prof. Dr. Karl-Heinz Kampert for letting me write my thesis in this beautiful group of colleagues on this wonderful and interesting experiment. In addition to that, he always provided me with immensely useful feedback and agreed on refereeing this thesis. Especially the last points also hold true for Prof. Dr. Claudia Höhne whose feedback during many meetings was of utmost importance to me. Meeting nearly every week discussions were manifold and always fruitful.

I further would like to thank Dr. Christian Pauly who, since 2013, finds time everyday to support me. Answering any question, sometimes even before I realized having them, guiding me experimentally and personally and last but not least proofreading this thesis. Much attention to detail was also given by the HADES RICH group coordinator Dr. Jürgen Friese starting many important discussions and thus shaping my thesis and work tremendously. But not only him, also to all other HADES RICH commilitones I would like to express my deepest thanks. Jan Otto, Marten Becker, Adrian Weber and Semen Lebedev without them at many points throughout my thesis clever ideas would have remained hidden from me. Additionally I want to add my gratitude towards Dr. Tariq Mahmoud, Jordan Bendarouach and all others of the Gießen HADES/CBM working group. I also want to thank all members of the HADES collaboration, without their efforts certainly the full detector used throughout this thesis would not work as good as it does. In addition to that, I also want to show my gratitude to Michael Traxler, Jan Michel and the TRB collaboration for their unconditional support.

Particularly I also want to thank my colleagues of our Wuppertal HADES/CBM group. I am extremely grateful to Dr. Ievgenii Kres helping me in too many regards in order to actually list them. Dr. Sascha Reinecke who always had an open ear during all the time we worked together from reaching my Bachelors till starting my PhD. Furthermore, I thank Dennis Pfeifer for his unrestricted commitment to any work I needed help with. Vivek Patel for great discussions not only limited to topics in physics. Dr. Jan Kopfer who actually accompanied me during my first baby steps in this working group. Also I want to thank our newest additions Tetiana Povar and Pavish Subramani for inspiring discussions.

Also I want to thank Dr. Julian Rautenberg for always having an open ear, not only in terms of technical questions. I thank Ingrid Schaarwächter and Monika Starke for their coordination of all administrative issues and being permanent contact persons.

# Declaration of Authorship

## English

I hereby declare that the thesis submitted is my own unaided work. All direct or indirect sources used are acknowledged as references.

This thesis was not previously presented to another examination board and has not been published.

## Deutsch

Hiermit versichere ich, die vorliegende Arbeit selbstständig und unter ausschließlicher Verwendung der angegebenen Literatur und Hilfsmittel erstellt zu haben.

Die Arbeit wurde bisher in gleicher oder ähnlicher Form keiner anderen Prüfungsbehörde vorgelegt und auch nicht veröffentlicht.

Wuppertal, den _____          _____

(Jörg Förtsch)